The IceCube Collaboration:

Contributions to the 31st International Cosmic Ray Conference*

Łódź, Poland, 7-15 July 2009

---

*Includes some related papers submitted by individual members of the Collaboration

This page intentionally left blank

IceCube COLLABORATION

R. Abbasi[24], Y. Abdou[18], M. Ackermann[36], J. Adams[13], J. Aguilar[24], M. Ahlers[28], K. Andeen[24], J. Auffenberg[35], X. Bai[27], M. Baker[24], S. W. Barwick[20], R. Bay[7], J. L. Bazo Alba[36], K. Beattie[8], J. J. Beatty[15,16], S. Bechet[10], J. K. Becker[17], K.-H. Becker[35], M. L. Benabderrahmane[36], J. Berdermann[36], P. Berghaus[24], D. Berley[14], E. Bernardini[36], D. Bertrand[10], D. Z. Besson[22], M. Bissok[1], E. Blaufuss[14], D. J. Boersma[24], C. Bohm[30], J. Bolmont[36], S. Böser[36], O. Botner[33], L. Bradley[32], J. Braun[24], D. Breder[35], T. Castermans[26], D. Chirkin[24], B. Christy[14], J. Clem[27], S. Cohen[21], D. F. Cowen[32,31], M. V. D'Agostino[7], M. Danninger[30], C. T. Day[8], C. De Clercq[11], L. Demirörs[21], O. Depaepe[11], F. Descamps[18], P. Desiati[24], G. de Vries-Uiterweerd[18], T. DeYoung[32], J. C. Diaz-Velez[24], J. Dreyer[17], J. P. Dumm[24], M. R. Duvoort[34], W. R. Edwards[8], R. Ehrlich[14], J. Eisch[24], R. W. Ellsworth[14], O. Engdegård[33], S. Euler[1], P. A. Evenson[27], O. Fadiran[4], A. R. Fazely[6], T. Feusels[18], K. Filimonov[7], C. Finley[24], M. M. Foerster[32], B. D. Fox[32], A. Franckowiak[9], R. Franke[36], T. K. Gaisser[27], J. Gallagher[23], R. Ganugapati[24], L. Gerhardt[8,7], L. Gladstone[24], A. Goldschmidt[8], J. A. Goodman[14], R. Gozzini[25], D. Grant[32], T. Griesel[25], A. Groß[13,19], S. Grullon[24], R. M. Gunasingha[6], M. Gurtner[35], C. Ha[32], A. Hallgren[33], F. Halzen[24], K. Han[13], K. Hanson[24], Y. Hasegawa[12], J. Heise[34], K. Helbing[35], P. Herquet[26], S. Hickford[13], G. C. Hill[24], K. D. Hoffman[14], K. Hoshina[24], D. Hubert[11], W. Huelsnitz[14], J.-P. Hülß[1], P. O. Hulth[30], K. Hultqvist[30], S. Hussain[27], R. L. Imlay[6], M. Inaba[12], A. Ishihara[12], J. Jacobsen[24], G. S. Japaridze[4], H. Johansson[30], J. M. Joseph[8], K.-H. Kampert[35], A. Kappes[24,a], T. Karg[35], A. Karle[24], J. L. Kelley[24], P. Kenny[22], J. Kiryluk[8,7], F. Kislat[36], S. R. Klein[8,7], S. Klepser[36], S. Knops[1], G. Kohnen[26], H. Kolanoski[9], L. Köpke[25], M. Kowalski[9], T. Kowarik[25], M. Krasberg[24], K. Kuehn[15], T. Kuwabara[27], M. Labare[10], S. Lafebre[32], K. Laihem[1], H. Landsman[24], R. Lauer[36], H. Leich[36], D. Lennarz[1], A. Lucke[9], J. Lundberg[33], J. Lünemann[25], J. Madsen[29], P. Majumdar[36], R. Maruyama[24], K. Mase[12], H. S. Matis[8], C. P. McParland[8], K. Meagher[14], M. Merck[24], P. Mészáros[31,32], E. Middell[36], N. Milke[17], H. Miyamoto[12], A. Mohr[9], T. Montaruli[24,b], R. Morse[24], S. M. Movit[31], K. Münich[17], R. Nahnhauer[36], J. W. Nam[20], P. Nießen[27], D. R. Nygren[8,30], S. Odrowski[19], A. Olivas[14], M. Olivo[33], M. Ono[12], S. Panknin[9], S. Patton[8], C. Pérez de los Heros[33], J. Petrovic[10], A. Piegsa[25], D. Pieloth[36], A. C. Pohl[33,c], R. Porrata[7], N. Potthoff[35], P. B. Price[7], M. Prikockis[32], G. T. Przybylski[8], K. Rawlins[3], P. Redl[14], E. Resconi[19], W. Rhode[17], M. Ribordy[21], A. Rizzo[11], J. P. Rodrigues[24], P. Roth[14], F. Rothmaier[25], C. Rott[15], C. Roucelle[19], D. Rutledge[32], D. Ryckbosch[18], H.-G. Sander[25], S. Sarkar[28], K. Satalecka[36], S. Schlenstedt[36], T. Schmidt[14], D. Schneider[24], A. Schukraft[1], O. Schulz[19], M. Schunck[1], D. Seckel[27], B. Semburg[35], S. H. Seo[30], Y. Sestayo[19], S. Seunarine[13], A. Silvestri[20], A. Slipak[32], G. M. Spiczak[29], C. Spiering[36], M. Stamatikos[15], T. Stanev[27], G. Stephens[32], T. Stezelberger[8], R. G. Stokstad[8], M. C. Stoufer[8], S. Stoyanov[27], E. A. Strahler[24], T. Straszheim[14], K.-H. Sulanke[36], G. W. Sullivan[14], Q. Swillens[10], I. Taboada[5], O. Tarasova[36], A. Tepe[35], S. Ter-Antonyan[6], C. Terranova[21], S. Tilav[27], M. Tluczykont[36], P. A. Toale[32], D. Tosi[36], D. Turčan[14], N. van Eijndhoven[34], J. Vandenbroucke[7], A. Van Overloop[18], B. Voigt[36], C. Walck[30], T. Waldenmaier[9], M. Walter[36], C. Wendt[24], S. Westerhoff[24], N. Whitehorn[24], C. H. Wiebusch[1], A. Wiedemann[17], G. Wikström[30], D. R. Williams[2], R. Wischnewski[36], H. Wissing[1,14], K. Woschnagg[7], X. W. Xu[6], G. Yodh[20], S. Yoshida[12]

[1]III Physikalisches Institut, RWTH Aachen University, D-52056 Aachen, Germany
[2]Dept. of Physics and Astronomy, University of Alabama, Tuscaloosa, AL 35487, USA
[3]Dept. of Physics and Astronomy, University of Alaska Anchorage, 3211 Providence Dr., Anchorage, AK 99508, USA
[4]CTSPS, Clark-Atlanta University, Atlanta, GA 30314, USA
[5]School of Physics and Center for Relativistic Astrophysics, Georgia Institute of Technology, Atlanta, GA 30332. USA
[6]Dept. of Physics, Southern University, Baton Rouge, LA 70813, USA
[7]Dept. of Physics, University of California, Berkeley, CA 94720, USA
[8]Lawrence Berkeley National Laboratory, Berkeley, CA 94720, USA
[9]Institut für Physik, Humboldt-Universität zu Berlin, D-12489 Berlin, Germany
[10]Université Libre de Bruxelles, Science Faculty CP230, B-1050 Brussels, Belgium
[11]Vrije Universiteit Brussel, Dienst ELEM, B-1050 Brussels, Belgium
[12]Dept. of Physics, Chiba University, Chiba 263-8522, Japan

[13]*Dept. of Physics and Astronomy, University of Canterbury, Private Bag 4800, Christchurch, New Zealand*
[14]*Dept. of Physics, University of Maryland, College Park, MD 20742, USA*
[15]*Dept. of Physics and Center for Cosmology and Astro-Particle Physics, Ohio State University, Columbus, OH 43210, USA*
[16]*Dept. of Astronomy, Ohio State University, Columbus, OH 43210, USA*
[17]*Dept. of Physics, TU Dortmund University, D-44221 Dortmund, Germany*
[18]*Dept. of Subatomic and Radiation Physics, University of Gent, B-9000 Gent, Belgium*
[19]*Max-Planck-Institut für Kernphysik, D-69177 Heidelberg, Germany*
[20]*Dept. of Physics and Astronomy, University of California, Irvine, CA 92697, USA*
[21]*Laboratory for High Energy Physics, École Polytechnique Fédérale, CH-1015 Lausanne, Switzerland*
[22]*Dept. of Physics and Astronomy, University of Kansas, Lawrence, KS 66045, USA*
[23]*Dept. of Astronomy, University of Wisconsin, Madison, WI 53706, USA*
[24]*Dept. of Physics, University of Wisconsin, Madison, WI 53706, USA*
[25]*Institute of Physics, University of Mainz, Staudinger Weg 7, D-55099 Mainz, Germany*
[26]*University of Mons-Hainaut, 7000 Mons, Belgium*
[27]*Bartol Research Institute and Department of Physics and Astronomy, University of Delaware, Newark, DE 19716, USA*
[28]*Dept. of Physics, University of Oxford, 1 Keble Road, Oxford OX1 3NP, UK*
[29]*Dept. of Physics, University of Wisconsin, River Falls, WI 54022, USA*
[30]*Oskar Klein Centre and Dept. of Physics, Stockholm University, SE-10691 Stockholm, Sweden*
[31]*Dept. of Astronomy and Astrophysics, Pennsylvania State University, University Park, PA 16802, USA*
[32]*Dept. of Physics, Pennsylvania State University, University Park, PA 16802, USA*
[33]*Dept. of Physics and Astronomy, Uppsala University, Box 516, S-75120 Uppsala, Sweden*
[34]*Dept. of Physics and Astronomy, Utrecht University/SRON, NL-3584 CC Utrecht, The Netherlands*
[35]*Dept. of Physics, University of Wuppertal, D-42119 Wuppertal, Germany*
[36]*DESY, D-15735 Zeuthen, Germany*
[a]*affiliated with Universität Erlangen-Nürnberg, Physikalisches Institut, D-91058, Erlangen, Germany*
[b]*on leave of absence from Università di Bari and Sezione INFN, Dipartimento di Fisica, I-70126, Bari, Italy*
[c]*affiliated with School of Pure and Applied Natural Sciences, Kalmar University, S-39182 Kalmar, Sweden*

Acknowledgments

We acknowledge the support from the following agencies: U.S. National Science Foundation-Office of Polar Program, U.S. National Science Foundation-Physics Division, University of Wisconsin Alumni Research Foundation, U.S. Department of Energy, and National Energy Research Scientific Computing Center, the Louisiana Optical Network Initiative (LONI) grid computing resources; Swedish Research Council, Swedish Polar Research Secretariat, and Knut and Alice Wallenberg Foundation, Sweden; German Ministry for Education and Research (BMBF), Deutsche Forschungsgemeinschaft (DFG), Germany; Fund for Scientific Research (FNRS-FWO), Flanders Institute to encourage scientific and technological research in industry (IWT), Belgian Federal Science Policy Office (Belspo); the Netherlands Organisation for Scientific Research (NWO); M. Ribordy acknowledges the support of the SNF (Switzerland); A. Kappes and A. Groß acknowledge support by the EU Marie Curie OIF Program; J. P. Rodrigues acknowledge support by the Capes Foundation, Ministry of Education of Brazil.

1339: IceCube
Albrecht Karle, for the IceCube Collaboration (Highlight paper)

0653: All-Sky Point-Source Search with 40 Strings of IceCube
Jon Dumm, Juan A. Aguilar, Mike Baker, Chad Finley, Teresa Montaruli, for the IceCube Collaboration

0812: IceCube Time-Dependent Point Source Analysis Using Multiwavelength Information
M. Baker, J. A. Aguilar, J. Braun, J. Dumm, C. Finley, T. Montaruli, S. Odrowski, E. Resconi for the IceCube Collaboration

0960: Search for neutrino flares from point sources with IceCube (0908.4209)
J. L. Bazo Alba, E. Bernardini, R. Lauer, for the IceCube Collaboration

0987: Neutrino triggered high-energy gamma-ray follow-up with IceCube
Robert Franke, Elisa Bernardini for the IceCube collaboration

1173: Moon Shadow Observation by IceCube
D.J. Boersma, L. Gladstone and A. Karle for the IceCube Collaboration

1289: IceCube/AMANDA combined analyses for the search of neutrino sources at low energies
Cécile Roucelle, Andreas Gross, Sirin Odrowski, Elisa Resconi, Yolanda Sestayo

1127: AMANDA 7-Year Multipole Analysis (0906.3942)
Anne Schukraft, Jan-Patrick Hülß for the IceCube Collaboration

1418: Measurement of the atmospheric neutrino energy spectrum with IceCube
Dmitry Chirkin for the IceCube collaboration

0785: Atmospheric Neutrino Oscillation Measurements with IceCube
Carsten Rott for the IceCube Collaboration

1565: Direct Measurement of the Atmospheric Muon Energy Spectrum with IceCube (0909.0679)
Patrick Berghaus for the IceCube Collaboration

1400: Search for Diffuse High Energy Neutrinos with IceCube
Kotoyo Hoshina for the IceCube collaboration

1311: A Search For Atmospheric Neutrino-Induced Cascades with IceCube
(0910.0215) Michelangelo D'Agostino for the IceCube Collaboration

0882: First search for extraterrestrial neutrino-induced cascades with IceCube
(0909.0989) Joanna Kiryluk for the IceCube Collaboration

0708: Improved Reconstruction of Cascade-like Events in IceCube
Eike Middell, Joseph McCartin and Michelangelo D'Agostino for the IceCube Collaboration

1221: Searches for neutrinos from GRBs with the IceCube 22-string detector and sensitivity estimates for the full detector
A. Kappes, P. Roth, E. Strahler, for the IceCube Collaboration

0515: Search for neutrinos from GRBs with IceCube
K. Meagher, P. Roth, I. Taboada, K. Hoffman, for the IceCube Collaboration

0393: Search for GRB neutrinos via a (stacked) time profile analysis
Martijn Duvoort and Nick van Eijndhoven for the IceCube collaboration

0764: Optical follow-up of high-energy neutrinos detected by IceCube (0909.0631)
Anna Franckowiak, Carl Akerlof, D. F. Cowen, Marek Kowalski, Ringo Lehmann, Torsten Schmidt and Fang Yuan for the IceCube Collaboration and for the ROTSE Collaboration

0505: Results and Prospects of Indirect Searches for Dark Matter with IceCube
Carsten Rott and Gustav Wikström for the IceCube collaboration

1356: Search for the Kaluza-Klein Dark Matter with the AMANDA/IceCube Detectors (0906.3969), Matthias Danninger & Kahae Han for the IceCube Collaboration

0834: Searches for WIMP Dark Matter from the Sun with AMANDA (0906.1615)
James Braun and Daan Hubert for the IceCube Collaboration

0861: The extremely high energy neutrino search with IceCube
Keiichi Mase, Aya Ishihara and Shigeru Yoshida for the IceCube Collaboration

0913: Study of very bright cosmic-ray induced muon bundle signatures measured by the IceCube detector
Aya Ishihara for the IceCube Collaboration

1198: Search for High Energetic Neutrinos from Supernova Explosions with AMANDA (0907.4621)
Dirk Lennarz and Christopher Wiebusch for the IceCube Collaboration

0549: Search for Ultra High Energy Neutrinos with AMANDA
Andrea Silvestri for the IceCube Collaboration

1372: Selection of High Energy Tau Neutrinos in IceCube
Seon-Hee Seo and P. A. Toale for the IceCube Collaboration

0484: Search for quantum gravity with IceCube and high energy atmospheric neutrinos, Warren Huelsnitz & John Kelley for the IceCube Collaboration

0970: A First All-Particle Cosmic Ray Energy Spectrum From IceTop
Fabian Kislat, Stefan Klepser, Hermann Kolanoski and Tilo Waldenmaier for the IceCube Collaboration

0518: Reconstruction of IceCube coincident events and study of composition-sensitive observables using both the surface and deep detector
Tom Feusels, Jonathan Eisch and Chen Xu for the IceCube Collaboration

0737: Small air showers in IceTop
Bakhtiyar Ruzybayev, Shahid Hussain, Chen Xu and Thomas Gaisser for the IceCube Collaboration

1429: Cosmic Ray Composition using SPASE-2 and AMANDA-II
K. Andeen and K. Rawlins For the IceCube Collaboration

0519: Study of High pT Muons in IceCube (0909.0055)
Lisa Gerhardt and Spencer Klein for the IceCube Collaboration

1340: Large Scale Cosmic Rays Anisotropy With IceCube (0907.0498)
Rasha U Abbasi, Paolo Desiati and Juan Carlos Velez for the IceCube Collaboration

1398: Atmospheric Variations as observed by IceCube
Serap Tilav, Paolo Desiati, Takao Kuwabara, Dominick Rocco,
Florian Rothmaier, Matt Simmons, Henrike Wissing for the IceCube Collaboration

1251: Supernova Search with the AMANDA / IceCube Detectors (0908.0441)
Thomas Kowarik, Timo Griesel, Alexander Piégsa for the IceCube Collaboration

1352: Physics Capabilities of the IceCube DeepCore Detector (0907.2263)
Christopher Wiebusch for the IceCube Collaboration

1336: Fundamental Neutrino Measurements with IceCube DeepCore
Darren Grant, D. Jason Koskinen, and Carsten Rott for the IceCube collaboration

1237: Implementation of an active veto against atmospheric muons in IceCube DeepCore
Olaf Schulz, Sebastian Euler and Darren Grant for the IceCube Collaboration

1293: Acoustic detection of high energy neutrinos in ice: Status and results from the South Pole Acoustic Test Setup (0908.3251 – revised)
Freija Descamps for the IceCube Collaboration

0903: Sensor development and calibration for acoustic neutrino detection in ice (0907.3561)
Timo Karg, Martin Bissok, Karim Laihem, Benjamin Semburg, and Delia Tosi
for the IceCube collaboration

PAPERS RELATED TO ICECUBE

0466: A new method for identifying neutrino events in IceCube data
Dmitry Chirkin

0395: Muon Production of Hadronic Particle Showers in Ice and Water
Sebastian Panknin, Julien Bolmont, Marek Kowalski and Stephan Zimmer

0642: Muon bundle energy loss in deep underground detector
Xinhua Bai, Dmitry Chirkin, Thomas Gaisser, Todor Stanev and David Seckel

0542: Constraints on Neutrino Interactions at energies beyond 100 PeV with Neutrino Telescopes
Shigeru Yoshida

0006: Constraints on Extragalactic Point Source Flux from Diffuse Neutrino Limits
Andrea Silvestri and Steven W. Barwick

0418: Study of electromagnetic backgrounds in the 25-300 MHz frequency band at the South Pole
Jan Auffenberg, Dave Bessony, Tom Gaisser, Klaus Helbing, Timo Karg, Albrecht Karle,and Ilya Kravchenko

IceCube

Albrecht Karle*, for the IceCube Collaboration

*University of Wisconsin-Madison, 1150 University Avenue, Madison, WI 53706

Abstract. **IceCube is a 1 km^3 neutrino telescope currently under construction at the South Pole. The detector will consist of 5160 optical sensors deployed at depths between 1450 m and 2450 m in clear Antarctic ice evenly distributed over 86 strings. An air shower array covering a surface area of 1 km^2 above the in-ice detector will measure cosmic ray air showers in the energy range from 300 TeV to above 1 EeV. The detector is designed to detect neutrinos of all flavors: ν_e, ν_μ and ν_τ. With 59 strings currently in operation, construction is 67% complete. Based on data taken to date, the observatory meets its design goals. Selected results will be presented.**

Keywords: **neutrinos, cosmic rays, neutrino astronomy.**

I. INTRODUCTION

IceCube is a large kilometer scale neutrino telescope currently under construction at the South Pole. With the ability to detect neutrinos of all flavors over a wide energy range from about 100 GeV to beyond 10^9 GeV, IceCube is able to address fundamental questions in both high energy astrophysics and neutrino physics. One of its main goals is the search for sources of high energy astrophysical neutrinos which provide important clues for understanding the origin of high energy cosmic rays.

The interactions of ultra high energy cosmic rays with radiation fields or matter either at the source or in intergalactic space result in a neutrino flux due to the decays of the produced secondary particles such as pions, kaons and muons. The observed cosmic ray flux sets the scale for the neutrino flux and leads to the prediction of event rates requiring kilometer scale detectors, see for example[1]. As primary candidates for cosmic ray accelerators, AGNs and GRBs are thus also the most promising astrophysical point source candidates of high energy neutrinos. Galactic source candidates include supernova remnants, microquasars, and pulsars. Guaranteed sources of neutrinos are the cosmogenic high energy neutrino flux from interactions of cosmic rays with the cosmic microwave background and the galactic neutrino flux resulting from galactic cosmic rays interacting with the interstellar medium. Both fluxes are small and their measurement constitutes a great challenge. Other sources of neutrino radiation include dark matter, in the form of supersymmetric or more exotic particles and remnants from various phase transitions in the early universe.

The relation between the cosmic ray flux and the atmospheric neutrino flux is well understood and is based on the standard model of particle physics. The observed diffuse neutrino flux in underground laboratories agrees with Monte Carlo simulations of the primary cosmic ray flux interacting with the Earth's atmosphere and producing a secondary atmospheric neutrino flux[2].

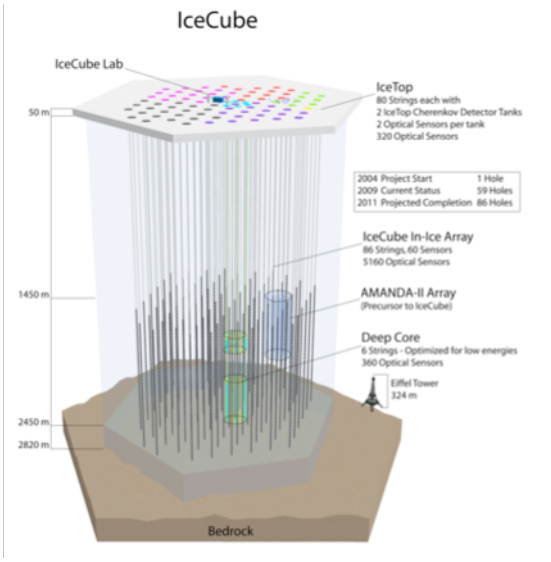

Fig. 1 Schematic view of IceCube. Fifty-nine of 86 strings are in operation since 2009.

Although atmospheric neutrinos are the primary background in searching for astrophysical neutrinos, they are very useful for two reasons. Atmospheric neutrino physics can be studied up to PeV energies. The measurement of more than 50,000 events per year in an energy range from 500 GeV to 500 TeV will make IceCube a unique instrument to make precise comparisons of atmospheric neutrinos with model predictions. At energies beyond 100 TeV a harder neutrino spectrum may emerge which would be a signature of an extraterrestrial flux. Atmospheric neutrinos also give the opportunity to calibrate the detector. The absence of such a calibration beam at higher energies poses a difficult challenge for detectors at energies targeting the cosmogenic neutrino flux.

II. DETECTOR AND CONSTRUCTION STATUS

IceCube is designed to detect muons and cascades over a wide energy range. The string spacing was chosen in order to reliably detect and reconstruct muons in the TeV energy range and to precisely calibrate the detector using flashing LEDs and atmospheric muons. The optical properties of the South Pole Ice have been measured with various calibration devices[3] and are used for modeling the detector response to charged particles. Muon reconstruction algorithms[4] allow measuring the direction and energy of tracks from all directions.

In its final configuration, the detector will consist of 86 strings reaching a depth of 2450 m below the surface. There are 60 optical sensors mounted on each string equally spaced between 1450m and 2450m depth with the exception of the six Deep Core strings on which the sensors are more closely spaced between 1760m and 2450m. In addition there will be 320 sensors deployed in 160 IceTop tanks on the surface of the ice directly above the strings. Each sensor consists of a 25cm photomultiplier tube (PMT), connected to a waveform recording data acquisition circuit capable of resolving pulses with nanosecond precision and having a dynamic range of at least 250 photoelectrons per 10ns. With the most recent construction season ending in February 2008, half of the IceCube array has been deployed.

The detector is constructed by drilling holes in the ice, one at a time, using a hot water drill. Drilling is immediately followed by deployment of a detector string into the water-filled hole. The drilling of a hole to a depth of 2450m takes about 30 hours. The subsequent deployment of the string typically takes less than 10 hours. The holes typically freeze back within 1-3 weeks. The time delay between two subsequent drilling cycles and string deployments was in some cases shorter than 50 hours. By the end of February 2009, 59 strings and IceTop stations had been deployed. We refer to this configuration as IC59. Once the strings are completely frozen in the commissioning can start. Approximately 99% of the deployed DOMs have been successfully commissioned. The 40-string detector configuration (IC40) has been in operation from May 2008 to the end of April 2009.

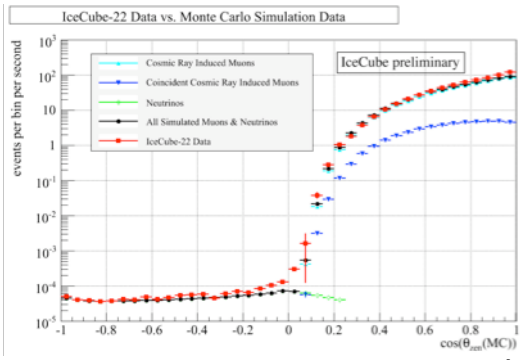

Fig. 2 Muon rate in IceCube as a function of zenith angle[5].The data agree with the detector simulation which includes atmospheric neutrinos, atmospheric muons, and coincident cosmic ray muons (two muons erroneously reconstructed as a single track.)

III. MUONS AND NEUTRINOS

At the depth of IceCube, the event rate from downgoing atmospheric muons is close to 6 orders of magnitude higher than the event rate from atmospheric neutrinos. Fig. 2 shows the observed muon rate (IC22) as a function of the zenith angle[5].

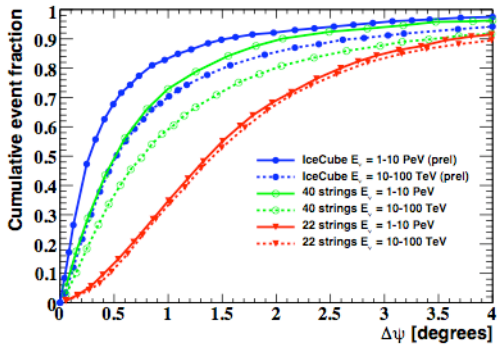

Fig. 3 The angular resolution function of different IceCube configurations is shown for two neutrino energy ranges samples from an E^{-2} energy spectrum.

IceCube is effective in detecting downward going muons. A first measurement of the muon energy spectrum is provided in the references[6].

A good angular resolution of the experiment is the basis for the zenith angle distribution and much more so for the search of point sources of neutrinos from galactice sources, AGNs or GRBs. Figure 3 shows the angular resolution of IceCube for several detector configurations based on high quality neutrino event selections as used in the point source search for IC40[7]. The median angular resolution of IC40 achieved is already 0.7°, the design parameter for the full IceCube.

The muon flux serves in many ways also as a calibration tool. One method to verify the angular resolution and absolute pointing of the detector uses the Moon shadow of cosmic rays. The Moon reaches an elevation of about 28° above the horizon at the South Pole. Despite the small altitude of the Moon, the event rate and angular resolution of IceCube are sufficient to measure the cosmic ray shadow of the Moon by mapping the muon rate in the vicinity of the Moon. The parent air showers have an energy of typically 30 TeV, well above the energy where magnetic fields would pose a signifi-

cant deviation from the direction of the primary particles. Fig. 4 shows a simple declination band with bin size optimized for this analysis. A deficit of ~900 events (~4.2σ) is observed on a background of ~28000 events in 8 months of data taking. The deficit is in agreement with expectations and confirms the assumed angular resolution and absolute pointing.

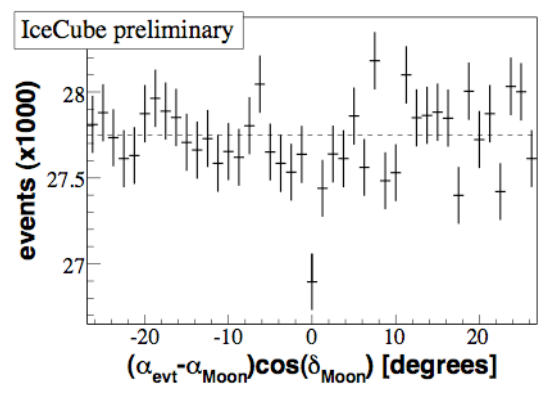

Fig. 4 4.2σ deficit of events from direction of Moon in the IceCube 40-string detector confirms pointing accuracy.

The full IceCube will collect of order 50 000 high quality atmospheric neutrinos per year in the TeV energy range. A detailed understanding of the response function of the detector at analysis level is the foundation for any neutrino flux measurement. We use the concept of the neutrino effective area to describe the response function of the detector with respect to neutrino flavor, energy and zenith angle. The neutrino effective area is the equivalent area for which all neutrinos of a given neutrino flux impinging on the Earth would be observed. Absorption effects of the Earth are considered as part of the detector and folded in the effected area.

Figure 5 provides an overview of effective areas for various analyses that are presented at this conference. First we note that the effective area increases strongly in the range from 100 GeV to about 100 TeV. This is due to the increase in the neutrino-nucleon cross-section and, in case of the muons, the workhorse of high energy neutrino astronomy, due to the additional increase of the muon range. Above about 100 GeV, the increase slows down because of radiative energy losses of muons.

The IC22[8] and IC80 as well as IC86 (IC80+6 Deep core) atmospheric ν_μ area are shown for upgoing neutrinos. The shaded area (IC22) indicates the range from before to after quality cuts. The effective area of IC40 point source analysis[7] is shown for all zenith angles. It combines the upward neutrino sky (predominantly energies < 1PeV) with downgoing neutrinos (predominantly >1 PeV). Also shown is the all sky $\nu_\mu + \nu_\tau$ area of IC80.

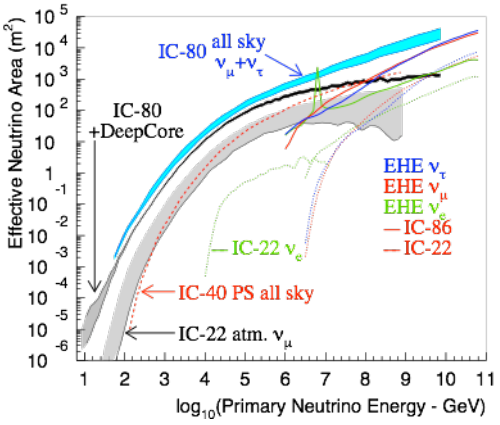

Fig. 5 The neutrino effective area is shown for a several IceCube configurations (IC22, IC 40, IC86), neutrino flavors, energy ranges and analysis levels (trigger, final analysis).

The ν_e effective area is shown for the current IC22 contained cascade analysis[9] as well as the IC22 extremely high energy (EHE) analysis[10]. It is interesting to see how two entirely different analysis techniques match up nicely at the energy transition of about 5 PeV.

The cascade areas are about a factor of 20 smaller than the ν_μ areas, primarily because the muon range allows the detection of neutrino interactions far outside the detector, increasing the effective detector volume by a large factor. However, the excellent energy resolution of contained cascades will benefit the background rejection of any diffuse analysis, and makes cascades a competitive detection channel in the detector where the volume grows faster than the area with the growing number of strings.

The figure illustrates why IceCube, and other

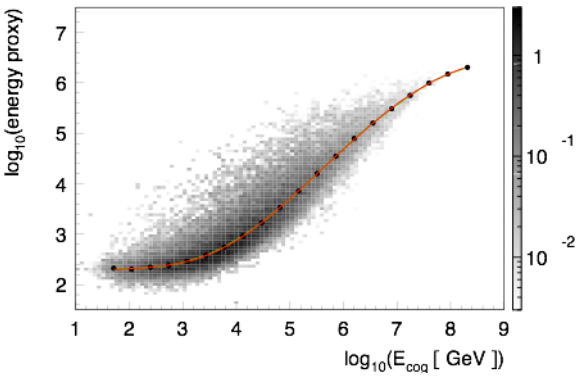

Fig. 6 The energy resolution for muons is approximately 0.3 in log(energy) over a wide energy range

large water/ice neutrino telescopes for that matter, can do physics over such a wide energy range. Unlike typical air shower cosmic ray or gamma ray detectors, the effective area increases by about 8 orders of magnitude ($10^{-4}m^2$ to $10^{+4}m^2$) over an energy range of equal change of scale (10 GeV to 10^9 GeV). The analysis at the vastly different energy scales re-

quires very different approaches, which are presented in numerous talks in the parallel sessions[11, 45].

The measurement of atmospheric neutrino flux requires a good understanding of the energy response. The energy resolution for muon neutrinos in the IC22 configuration is shown in Fig. 6 [8]. Over a wide energy range (1 – 10000 TeV) the energy resolution is ~0.3 in log(energy). This resolution is largely dominated by the fluctuations of the muon energy loss over the path length of 1 km or less.

IV. ATMOSPHERIC NEUTRINOS AND THE SEARCH FOR ASTROPHYSICAL NEUTRINOS

We have discussed the effective areas, as well as the angular and energy resolution of the detector. Armed with these ingredients we can discuss some highlights of neutrino measurements and astrophysical neutrino searches.

Figure 7 shows a preliminary measurement obtained with the IC22 configuration. An unfolding procedure has been applied to extract this neutrino flux. Also shown is the atmospheric neutrino flux as published previously based on 7 years of AMANDA-II data. The gray shaded area indicates the range of results obtained when applying the procedure to events that occurred primarily in the top or bottom of the detector. The collaboration is devoting significant efforts to understand and reduce systematic uncertainties as the statistics increases. The data sample consists of 4492 high quality events with an estimated purity of well above 95%. Several atmospheric neutrino events are observed above 100 TeV, pushing the diffuse astrophysical neutrino search gradually towards the PeV energy region and higher sensitivity. A look at the neutrino effective areas in Fig. 5 shows that the full IceCube with 86 strings will detect about one order of magnitude more events: ~50000 neutrinos/year.

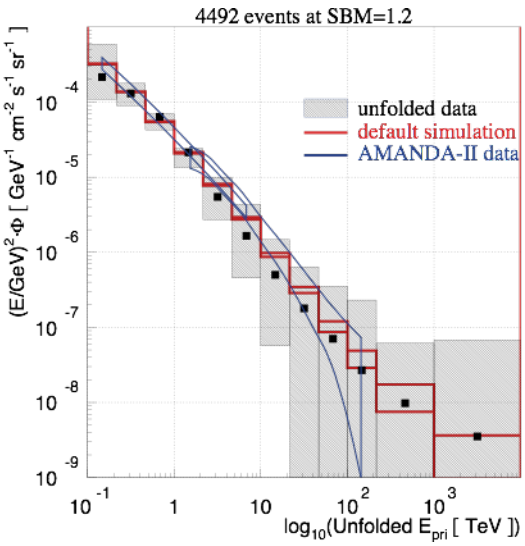

Fig. 7 Unfolded muon neutrino spectrum[8] averaged over zenith angle, is compared to simulation and to the AMANDA result. Data are taken with the 22 string configuration.

The search for astrophysical neutrinos is summarized in Fig. 8. While the figure focuses on diffuse fluxes, it is clear that some of these diffuse fluxes may be detected as point sources. Some examples of astrophysical flux models that are shown include AGN Blazars[46], BL Lacs[47], Pre-cursor GRB models and Waxman Bahcall bound[48] and Cosmogenic neu-

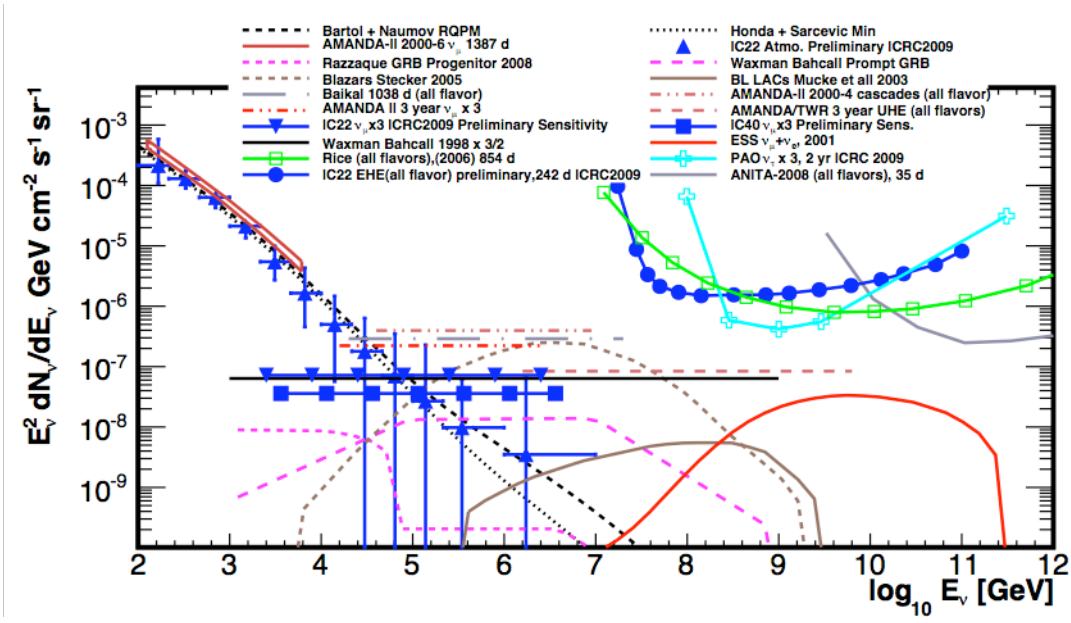

Fig. 8 Measured neutrino atmospheric neutrino fluxes from AMANDA and IceCube are shown together with a number of models for astrophysical neutrinos and several limits by IceCube and other experiments

trinos[49].

The following limits are shown for AMANDA and IceCube:

- AMANDA-II, 2000-2006, atmospheric muon neutrino flux[50]
- IceCube-22 string, atmospheric neutrinos, (preliminary)[8]
- AMANDA-II, 2000-2003, diffuse E^{-2} muon neutrino flux limit[51]
- AMANDA-II, 2000-2002, all flavors, not contained events, PeV to EeV, E^{-2} flux limit[52]
- AMANDA-II, 2000-2004, cascades, contained events, E^{-2} flux limit[53]
- IceCube-40, muon neutrinos, throughgoing events, preliminary sensitivity[29]
- IceCube-22, all flavor, throughgoing, downgoing, extremely high energies (10 PeV to EeV)[10]

Also shown are a few experimental limits from other experiments, including Lake Baikal[54] (diffuse, not contained), and at higher energies some differential limits by RICE, Auger and at yet higher energies energies from ANITA.

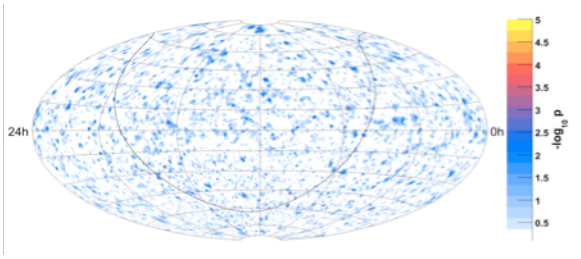

Fig, 9: The map shows the probability for a point source of high-energy neutrinos on the atmospheric neutrino background. The map was obtained by operating IceCube with 40 strings for half a year[7]. The "hottest spot" in the map represents an excess of 7 events. After taking into account trial factors, the probability for this event to happen anywhere in the sky map is not significant. The background consists of 6796 neutrinos in the Northern hemisphere and 10,981 down-going muons rejected to the 10^{-5} level in the Southern hemisphere.

The skymap in Fig. 9 shows the probability for a point source of high-energy neutrinos. The map was obtained from 6 months of data taken with the 40 string configuration of IceCube. This is the first result obtained with half of IceCube instrumented. The "hottest spot" in the map represents an excess of 7 events, which has a post-trial significance of $10^{-4.4}$. After taking into account trial factors, the probability for this event to happen anywhere in the sky map is not significant. The background consists of 6796 neutrinos in the Northern hemisphere and 10,981 down-going muons rejected to the 10^{-5} level in the Southern hemisphere. The energy threshold for the Southern hemisphere increases with increasing elevation to reject the cosmic ray the muon background by up to a factor of ~10^{-5}. The energy of accepted downgoing muons is typically above 100 TeV.

This unbinned analysis takes the angular resolution and energy information on an event-by-event basis into account in the significance calculation. The obtained sensitivity and discovery potential is shown for all zenith angles in the figure.

V. SEARCH FOR DARK MATTER

IceCube performs also searches for neutrinos produced by the annihilation of dark matter particles gravitationally trapped at the center of the Sun and the Earth. In searching for generic weakly interacting massive dark matter particles (WIMPs) with spin-

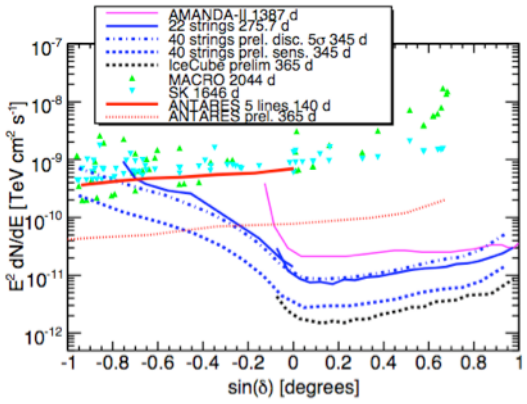

Fig. 10 Upper limits to E^{-2}-type astrophysical muon neutrino spectra are shown for the newest result of ½ year of IC40 and a number of earlier results obtained by IceCube and other experiments.

independent interactions with ordinary matter, IceCube is only competitive with direct detection experiments if the WIMP mass is sufficiently large. On the other hand, for WIMPs with mostly spin-dependent interactions, IceCube has improved on the previous best limits obtained by the SuperK experiment using the same method. It improves on the best limits from direct detection experiments by two orders of magnitude. The IceCube limit as well as a limit obtained with 7 years of AMANDA are shown in the figure. It rules out supersymmetric WIMP models not excluded by other experiments. The installation of the Deep Core of 6 strings as shown in Fig. 1 will greatly enhance the sensitivity of IceCube for dark matter. The projected sensitivity in the range from 50 GeV to TeV energies is shown in Fig. 11. The Deep Core is an integral part of IceCube and relies on the more closely spaced nearby strings for the detection of low energy events as well as on a highly efficient veto capability against cosmic ray muon backgrounds using the surrounding IceCube strings.

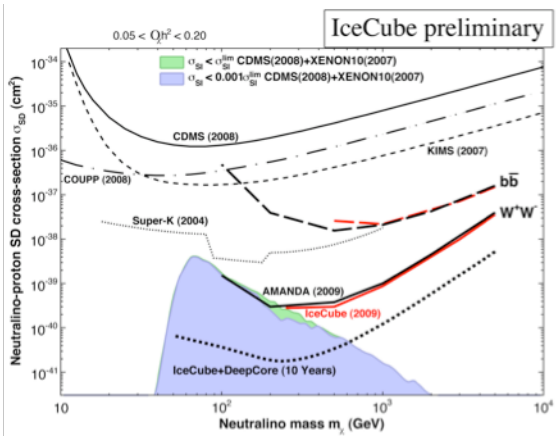

Fig. 11 The red boxes show the upper limits at 90% confidence level on the spin-dependent interaction of dark matter particles with ordinary matter[18, 20]. The two lines represent the extreme cases where the neutrinos originate mostly from heavy quarks (top line) and weak bosons (bottom line) produced in the annihilation of the dark matter particles. Also shown is the reach of the complete IceCube and its DeepCore extension after 5 years of observation of the sun. The shaded area represents supersymmetric models not disfavored by direct searches for dark matter. Also shown are previous limits from direct experiments and from the Superkamiokande experiment.

VI. COSMIC RAY MUONS AND HIGH ENERGY COSMIC RAYS

IceCube is a huge cosmic-ray muon detector and the first sizeable detector covering the Southern hemisphere. We are using samples of several billion downward-going muons to study the enigmatic large and small scale anisotropies recently identified in the cosmic ray spectrum by Northern detectors, namely the Tibet array[55] and the Milagro array[56]. Fig. 12 shows the relative deviations of up to 0.001 from the average of the Southern muon sky observed with the 22-string array[11]. A total of 4.3 billion events with a median energy of 14 TeV were used. IceCube data shows that these anisotropies persist at energies in excess of 100 TeV ruling out the sun as their origin. Having extended the measurement to the Southern hemisphere should help to decipher the origin of these unanticipated phenomena.

IceCube can detect events with energies ranging

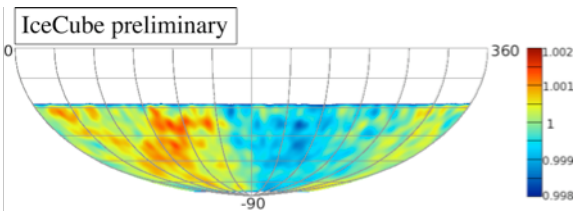

Fig.12 The plot shows the skymap of the relative intensity in the arrival directions of 4.3 billion muons produced by cosmic ray interactions with the atmosphere with a median energy of 14 TeV; these events were reconstructed with an average angular resolution of 3 degrees. The skymap is displayed in equatorial coordinates.

from 0.1 TeV to beyond 1 EeV, neutrinos and cosmic ray muons.

The surface detector IceTop consists of ice Cherenkov tank pairs. Each IceTop station is associated with an IceCube string. With a station spacing of 125 m, it is efficient for air showers above energies of 1 PeV. Figure 13 shows an event display of a very high-energy (~EeV) air shower event. Hits are recorded in all surface detector stations and a large number of DOMs in the deep ice. Based on a preliminary analysis some 2000 high-energy muons would have reached the deep detector in this event if the primary was a proton and more if it was a nucleus. With 1 km^2 surface area, IceTop will acquire a sufficient number of events in coincidence with the in-ice detector to allow for cosmic ray measurements up to 1 EeV. The directional and calorimetric measurement of the high energy muon component with the in-ice detector and the simultaneous measurement of the electromagnetic particles at the surface with IceTop will enable the investigation of the energy spectrum and the mass composition of cosmic rays.

Events with energies above one PeV can deposit

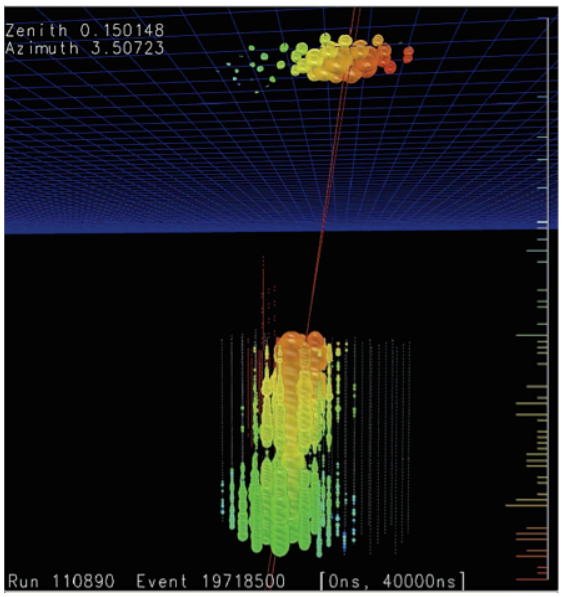

Fig. 13 A very high energy cosmic ray air shower observed both with the surface detector IceTop and the in-ice detector string array.

an enormous amount of light in the detector. Figure 14 shows an event that was generated by flasher pulse produced by an array of 12 UV LEDs that are mounted on every IceCube sensor. The event produces an amount of light that is comparable with that of an electron cascade on the order of 1 PeV. Photons were recorded on strings at distances up to 600 m from the flasher. The events are somewhat brighter than previously expected because the deep ice below a depth of 2100m is exceptionally clear.

The scattering length is substantially larger than in average ice at the depth of AMANDA.

Extremely high energy (EHE) events, above about 1 PeV, are observed near and above the horizon. At these energies, the Earth becomes opaque to neutrinos and one needs to change the search strategy. In an optimized analysis, the neutrino effective area reaches about 4000m^2 for IC80 at 1 EeV. IC80 can therefore test optimistic models of the cosmogenic neutrino flux. IceCube is already accumulating an exposure with the current data that makes detection of a cosmogenic neutrino event possible.

IceCube construction is on schedule to completion in February 2011. The operation of the detector stable and data analysis of recent data allows a rapid increase of the sensitivity and the discovery potential of IceCube.

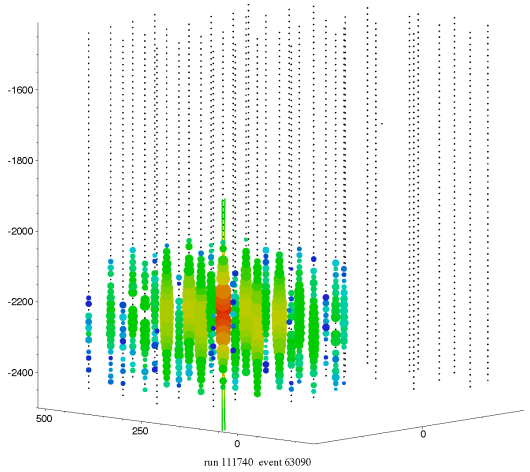

Figure 14: A flasher event in IceCube. Such events, produced by LEDs built in the DOMs, can be used for calibration purposes.

VII. ACKNOWLEDGEMENTS

We acknowledge the support from the following agencies: U.S. National Science Foundation-Office of Polar Program, U.S. National Science Foundation-Physics Division, University of Wisconsin Alumni Research Foundation, U.S. Department of Energy, and National Energy Research Scientific Computing Center, the Louisiana Optical Network Initiative (LONI) grid computing resources; Swedish Research Council, Swedish Polar Research Secretariat, and Knut and Alice Wallenberg Foundation, Sweden; German Ministry for Education and Research (BMBF), Deutsche Forschungsgemeinschaft (DFG), Germany; Fund for Scientific Research (FNRS-FWO), Flanders Institute to encourage scientific and technological research in industry (IWT), Belgian Federal Science Policy Office (Belspo); the Netherlands Organisation for Scientific Research (NWO); M. Ribordy acknowledges the support of the SNF (Switzerland); A. Kappes and A. Groß acknowledge support by the EU Marie Curie OIF Program.

REFERENCES

[1] E. Waxman and J. Bahcall, Phys. Rev. D 59 (1998) 023002

[2] T. Gaisser, *Cosmic Rays and Particle Physics* Cambridge University Press 1991

[3] M.Ackermann et al., J. Geophys. Res. **111**, D13203 (2006)

[4] J.Ahrens et al., Nucl. Inst. Meth. A **524**, 169 (2004)

[5] P. Berghaus for the IceCube Collaboration, proc. Proc. for the XV International Symposium on Very High Energy Cosmic Ray Interactions (ISVHECRI 2008), Paris, France, arXiv:0902.0021

[6] P. Berghaus *et al.*, Direct Atmospheric Muon Energy Spectrum Measurement with IceCube (IceCube collaboration), Proc. of the 31st ICRC HE1.5; astro-ph.HE/arXiv: 0909.0679

[7] J. Dumm *et al.*, Likelihood Point-Source Search with IceCube (IceCube collaboration), Proc. of the 31st ICRC OG2.5D.

[8] D. Chirkin *et al.*, Measurement of the Atmospheric Neutrino Energy Spectrum with IceCube (IceCube collaboration), Proc. of the 31st ICRC HE2.2

[9] J. Kiryluk *et al.*, First Search for Extraterrestrial Neutrino-Induced Cascades with IceCube (IceCube collaboration), Proc. of the 31st ICRC OG2.5; astro-ph.HE/arXiv: 0909.0989

[10] K. Mase *et al.*, The Extremely High-Energy Neutrino Search with IceCube (IceCube collaboration), Proc. of the 31st ICRC HE1.4

[11] R. Abbasi and P. Desiati, JC Díaz Vélez *et al.*, Large-Scale Cosmic-Ray Anisotropy with IceCube (IceCube collaboration), Proc. of the 31st ICRC SH3.2; astro-ph.HE/0907.0498

[12] K. Andeen *et al.*, Composition in the Knee Region with SPASE-AMANDA (IceCube collaboration), Proc. of the 31st ICRC HE1.2

[13] C. Rott et al., Atmospheric Neutrino Oscilaton Measurement with IceCube (IceCube collaboration), Proc. of the 31st ICRC HE2.3

[14] M. Baker *et al.*, IceCube Time-Dependent Point-Source Analysis Using Multiwavelength Information (IceCube collaboration), Proc. of the 31st ICRC OG2.5

[15] J. Bazo Alba *et al.*, Search for Neutrino Flares from Point Sources with IceCube (IceCube collaboration, *to appear in* Proc. of the 31st ICRC OG2.5

[16] M. Bissok *et al.,* Sensor Development and Calibration for Acoustic Neutrino Detection in Ice (IceCube collaboration), Proc. of the 31st International Cosmic Ray Conference, Lodz, Poland (2009) HE2.4; astro-ph.IM/09073561

[17] D. Boersma *et al.*, Moon-Shadow Observation by IceCube (IceCube collaboration), Proc. of the 31st ICRC OG2.5

[18] J. Braun and D. Hubert *et al.*, Searches for WIMP Dark Matter from the Sun with AMANDA (IceCube collaboration), Proc. of the 31st ICRC HE2.3; astro-ph.HE/09061615

[19] M. D'Agostino *et al.*, Search for Atmospheric Neutrino-Induced Cascades (IceCube collaboration), Proc. of the 31st ICRC HE2.2; ; astro-ph.HE/arXiv:0910.0215

[20] M. Danninger and K. Han *et al.*, Search for the Kaluza-Klein Dark Matter with the AMANDA/IceCube Detectors (IceCube collaboration), Proc. of the 31st ICRC HE2.3; astro-ph.HE/0906.3969

[21] F. Descamps *et al.*, Acoustic Detection of High-Energy Neutrinos in Ice (IceCube collaboration), Proc. of the 31st ICRC HE2.4

[22] M. Duvoort *et al.*, Search for GRB Neutrinos via a (Stacked) Time Profile Analysis (IceCube collaboration), Proc. of the 31st ICRC OG2.4

[23] S. Euler *et al.*, Implementation of an Active Veto against Atmospheric Muons in IceCube DeepCore (IceCube collaboration), Proc. of the 31st ICRC OG2.5

[24] T. Feusels *et al.*, Reconstruction of IceCube Coincident Events and Study of Composition-Sensitive Observables Using Both the Surface and Deep Detector (IceCube collaboration), Proc. of the 31st ICRC HE1.3

[25] A. Francowiak *et al.*, Optical Follow-Up of High-Energy Neutrinos Detected by IceCube (IceCube and ROTSE collaborations), Proc. of the 31st ICRC OG2.5

[26] R. Franke *et al.*, Neutrino Triggered High-Energy Gamma-Ray Follow-Up with IceCube (IceCube collaboration), Proc. of the 31st ICRC OG2.5

[27] L. Gerhardt *et al.*, Study of High p_T Muons in IceCube (IceCube collaboration), Proc. of the 31st ICRC HE1.5; astro-ph.HE/arXiv 0909.0055

[28] D. Grant *et al.*, Fundamental Neutrino Measurements with IceCube DeepCore (IceCube collaboration), Proc. of the 31st ICRC HE2.2

[29] K. Hoshina *et al.*, Search for Diffuse High-Energy Neutrinos with IceCube (IceCube collaboration), Proc. of the 31st ICRC OG2.5

[30] W. Huelsnitz *et al.,* Search for Quantum Gravity with IceCube and High-Energy Atmospheric Neutrinos (IceCube collaboration), Proc. of the 31st ICRC HE2.3

[31] A. Ishihara *et al.*, Energy-Scale Calibration Using Cosmic-Ray Induced Muon Bundles Measured by the IceCube Detector with IceTop Coincident Signals (IceCube collaboration), Proc. of the 31st ICRC HE1.5

[32] A. Kappes *et al.*, Searches for Neutrinos from GRBs with the IceCube 22-String Detector and Sensitivity Estimates for the Full Detector (IceCube collaboration), Proc. of the 31st ICRC OG2.4

[33] F. Kislat *et al.*, A First All-Particle Cosmic-Ray Energy Spectrum from IceTop (IceCube collaboration), Proc. of the 31st ICRC HE1.2

[34] M. Kowarik *et al.*, Supernova Search with the AMANDA / IceCube Neutrino Telescopes (IceCube collaboration), Proc. of the 31st ICRC OG2.2

[35] D. Lennarz *et al.*, Search for High-Energetic Neutrinos from Supernova Explosions with AMANDA (IceCube collaboration), Proc. of the 31st ICRC OG2.5; astro-ph.HE/09074621

[36] K. Meagher *et al.*, Search for Neutrinos from GRBs with IceCube (IceCube collaboration), Proc. of the 31st ICRC OG2.4

[37] E. Middell *et al.*, Improved Reconstruction of Cascade-Like Events (IceCube collaboration), Proc. of the 31st ICRC OG2.5

[38] C. Portello-Roucelle *et al.*, IceCube / AMANDA Combined Analyses for the Search of Neutrino Sources at Low Energies (IceCube collaboration), Proc. of the 31st ICRC OG2.5

[39] C. Rott *et al.*, Results and Prospects of Indirect Searches fo Dark Matter with IceCube (IceCube collaboration), Proc. of the 31st ICRC HE2.3

[40] B. Ruzybayev *et al.*, Small Air Showers in IceCube (IceCube collaboration), Proc. of the 31st ICRC HE1.1

[41] A. Schukraft and J. Hülß *et al.*, AMANDA 7-Year Multipole Analysis (IceCube collaboration), Proc. of the 31st ICRC OG2.5; astro-ph.HE/09063942

[42] S. Seo *et al.*, Search for High-Energy Tau Neutrinos in IceCube (IceCube collaboration), Proc. of the 31st ICRC OG2.5

[43] [43] A. Silvestri *et al.*, Search for Ultra–High-Energy Neutrinos with AMANDA (IceCube collaboration), Proc. of the 31st ICRC OG2.5

[44] S. Tilav *et al.*, Atmospheric Variations as Observed by IceCube (IceCube collaboration), Proc. of the 31st ICRC HE1.1

[45] C. Wiebusch *et al.*, Physics Capabilities of the IceCube DeepCore Detector (IceCube collaboration), Proc. of the 31st ICRC OG2.5; astro-ph.IM/09072263

[46] F. W. Stecker. Phys. Rev. D, 72(10):107301, 2005

[47] A. Mücke et al. Astropart. Phys., 18:593, 2003

[48] S. Razzaque, P. Meszaros, and E. Waxman. Phys. Rev. D, 68(8):083001, 2003

[49] R. Engel, D. Seckel, and T. Stanev. Phys. Rev. D, 64(9):093010, 2001

[50] A. Achterberg *et al*. (IceCube collaboration), Phys.Rev.D **79** 102005, 2009

[51] A. Achterberg *et al*. (IceCube collaboration),, Phys. Rev. D **76** 042008 (2007);

[52] Ackerman *et al*. (IceCube collaboration), Astrophys. Jour. **675** 2 1014-1024 (2008); astro-ph/07113022

[53] A. Achterberg, *et al*., Astrophys. Jour. **664** 397-410 (2007); astro-ph/0702265v2

[54] A.V.Avrorin *et al.*, Astronomy Letters, Vol.35, No.10, pp.651-662, 2009; arXiv:0909.5562

[55] M. Amenomori et al. [The Tibet AS-Gamma Collaboration], Astrophys. J. 633, 1005 (2005) arXiv:astroph/0502039

[56] A.A. Abdo et al., Phys. Rev. Lett. 101: 221101 (2008), arXiv:0801.3827

All-Sky Point-Source Search with 40 Strings of IceCube

Jon Dumm*, Juan A. Aguilar*, Mike Baker*, Chad Finley*, Teresa Montaruli*, for the IceCube Collaboration†

*Dept. of Physics, University of Wisconsin, Madison, WI, 53706, USA
†See the special section of these proceedings.

***Abstract*. During 2008-09, the IceCube Neutrino Observatory was operational with 40 strings of optical modules deployed in the ice. We describe the search for neutrino point sources based on a maximum likelihood analysis of the data collected in this configuration. This data sample provides the best sensitivity to high energy neutrino point sources to date. The field of view is extended into the down-going region providing sensitivity over the entire sky. The 22-string result is discussed, along with improvements leading to updated angular resolution, effective area, and sensitivity. The improvement in the performance as the number of strings is increased is also shown.**

***Keywords*: neutrino astronomy**

I. Introduction

The primary goal of the IceCube Neutrino Observatory is the detection of high energy astrophysical neutrinos. Such an observation could reveal the origins of cosmic rays and offer insight into some of the most energetic phenomena in the Universe. In order to detect these neutrinos, IceCube will instrument a cubic kilometer of the clear Antarctic ice sheet underneath the geographic South Pole with an array of 5,160 Digital Optical Modules (DOMs) deployed on 86 strings from 1.5–2.5 km deep. This includes six strings with a smaller DOM spacing and higher quantum efficiency comprising DeepCore, increasing the sensitivity to low energy neutrinos $<\sim 100\,\mathrm{GeV}$. IceCube also includes a surface array (IceTop) for observing extensive air showers of cosmic rays. Construction began in the austral summer 2004–05, and is planned to finish in 2011. Each DOM consists of a 25 cm diameter Hamamatsu photomultiplier tube, electronics for waveform digitization, and a spherical, pressure-resistant glass housing. The DOMs detect Cherenkov photons induced by relativistic charged particles passing through the ice. In particular, the directions of muons (either from cosmic ray showers above the surface, or neutrino interactions within the ice or bedrock) can be well reconstructed from the track-like pattern and timing of hit DOMs.

The 22-string results presented in the discussion are from a traditional up-going search. In such a search, neutrino telescopes use the Earth as a filter for the large background of atmospheric muons, leaving only an irreducible background of atmospheric neutrinos below the horizon. These have a softer spectrum ($\sim E^{-3.6}$ above 100 GeV) than astrophysical neutrinos which originate from the decays of particles accelerated by the first order Fermi mechanism and thus are expected to have an E^{-2} spectrum. This search extends the field of view above the horizon into the large background of atmospheric muons. In order to reduce this background, strict cuts on the energy of events need to be applied. This makes the search above the horizon primarily sensitive to extremely high energy ($>$ PeV) sources.

II. Methodology

An unbinned maximum likelihood analysis, accounting for individual reconstructed event uncertainties and energy estimators, is used in IceCube point source analyses. A full description can be found in Braun *et al.* [1]. This method improves the sensitivity to astrophysical sources over directional clustering alone by leveraging the event energies in order to separate hard spectrum signals from the softer spectrum of the atmospheric neutrino or muon background. For each tested direction in the sky, the best fit is found for the number of signal events n_s over background and the spectral index of a power law γ of the excess events. The likelihood ratio of the best-fit hypothesis to the null hypothesis ($n_s = 0$) forms the test statistic. The significance of the result is evaluated by performing the analysis on scrambled data sets, randomizing the events in right ascension but keeping all other event properties fixed. Uniform exposure in right ascension is ensured as the detector rotates completely each day, and the location at 90° south latitude gives a uniform background for each declination band. Events that are nearly vertical (declination $< -85^\circ$ or $> 85^\circ$) are left out of the analysis, since scrambling in right ascension does not work in the polar regions.

Two point-source searches are performed. The first is an all-sky search where the maximum likelihood ratio is evaluated for each direction in the sky on a grid, much finer than the angular resolution. The significance of any point on the grid is determined by the fraction of scrambled data sets containing at least one grid point with a log likelihood ratio higher than the one observed in the data. This fraction is the post-trial p-value for the all-sky search. Because the all-sky search includes a large number of effective trials, the second search is restricted to the directions of *a priori* selected sources of interest. The post-trial p-value for this search is again

calculated by performing the same analysis on scrambled data sets.

III. Event Selection

Forty strings of IceCube were operational from April 2008 to May 2009 with $\sim 90\%$ duty cycle after a good run selection based on detector stability. The $\sim 3\times10^{10}$ triggered events per year are first reduced to $\sim 1\times10^{9}$ events using low-level likelihood reconstructions and energy estimators as part of an online filtering system on site. These filtered events are sent over satellite to a data center in the North for further processing, including higher-level likelihood reconstructions for better angular resolution. Applying the analysis-level cuts (described below) that optimize the sensitivity to point sources finally yields a sample of $\sim 3\times10^{4}$ events. Due to offline filtering constraints, 144 days of livetime were used to design the analysis strategy and finalize event selection, keeping the time and right ascension of the events blinded. This represents about one-half of the final 40-string data sample. Because the northern sky and southern sky present very different challenges, two techniques are used to reduce the background due to cosmic ray muons.

For the northern sky, the Earth filters out atmospheric muons. Only neutrinos can penetrate all the way through the Earth and interact near the detector to create up-going muons. However, since down-going atmospheric muons trigger the detector at $\sim 1\,\mathrm{kHz}$, even a small fraction of mis-reconstructed events contaminates the northern sky search. Events may be mis-reconstructed due to random noise or light from muons from independent cosmic ray showers coincident in the same readout window of $\pm 10\,\mu\mathrm{s}$. Therefore, strict event selection is still required to reject mis-reconstructed down-going events. This selection is based on track-like quality parameters (the reduced likelihood of the track fit and the directional width of the likelihood space around the best track fit [2]), a likelihood ratio between the best up-going and down-going track solution, and a requirement that the event's set of hits can be split into two parts which both reconstruct as nearly-upgoing. Although the track-like quality parameters have very little declination dependence, these last two parameters only work for selecting up-going neutrino candidates and remove down-going events. This event selection provides an optimal sensitivity to sources of neutrinos in the TeV–PeV energy range.

In the southern sky, energy estimators were used to separate the large number of atmospheric muons from a hypothetical source of neutrinos with a harder spectrum. After track-quality selections, similar but tighter than for the up-going sample, a cut based on an energy estimator is made until a fixed number of events per steradian is achieved. Because only the highest energy events pass the selection, sensitivity is primarily to neutrino sources at PeV energies and above. Unlike for the northern sky, which is a $\sim 90\%$ pure sample of neutrino-induced muons, the event sample in the southern sky is almost entirely well-reconstructed high energy atmospheric muons and muon bundles.

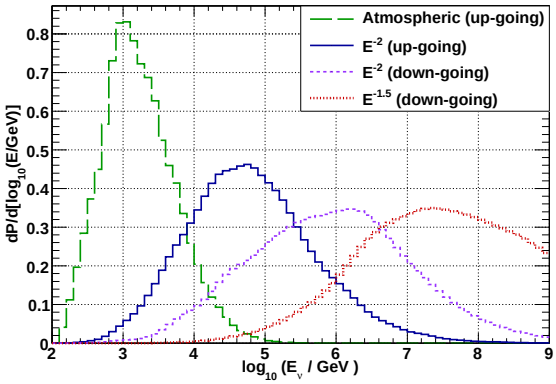

Fig. 1: Probability density (P) of neutrino energies at final cut level for atmospheric and an E^{-2} spectrum of neutrinos averaged over the northern sky and $E^{-1.5}$ in the southern sky.

IV. Performance

The performance of the detector and the analysis is characterized using a simulation of ν_μ and $\bar{\nu}_\mu$. Atmospheric muon background is simulated using CORSIKA [3]. Muon propagation through the Earth and ice are done using MMC [4]. A detailed simulation of the ice [5] propagates the Cherenkov photon signal to each DOM. Finally, a simulation of the DOM, including angular acceptance and electronics, yields an output treated identically to data. For an E^{-2} spectrum of neutrinos the median angular difference between the neutrino and the reconstructed direction of the muon in the northern (southern) sky is 0.8° (0.6°). The different energy distributions in each hemisphere shown in Fig. 1 cause this effect, since the reconstruction performs better at higher energies. The cumulative point spread functions for the 22-, 40-, and 80-string configurations of IceCube are shown in Fig. 2 for two different ranges of energy. Fig. 3 shows the effective area to an equal-ratio flux of $\nu_\mu + \bar{\nu}_\mu$. Fig. 4 shows the 40-string sensitivity to an E^{-2} spectrum of neutrinos for 330 days of livetime and compared to the 22-string configuration of IceCube, as well as ANTARES sensitivity, primarily relevant for the southern sky. The 80-string result uses the same methodology and event selection for the up-going region as this work.

V. Discussion

The previous season of IceCube data recorded with the 22-string configuration has already been the subject of point source searches [7]. The analysis included 5114 atmospheric neutrino events including a contamination of about 5% of atmospheric muons during a livetime of about 276 days. No evidence was found for a signal, and the largest significance is located at

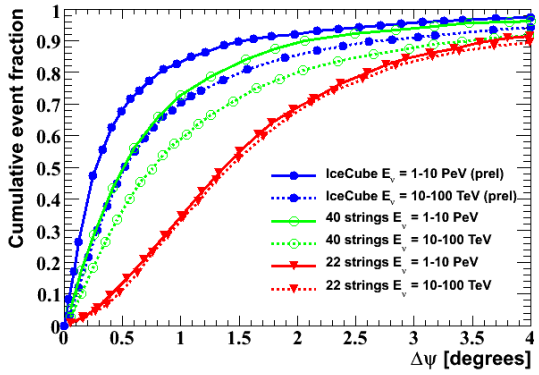

Fig. 2: The point spread function of the 22-, 40-, and 80-string IceCube configurations in two energy bins. This is the cumulative distribution of the angular difference between the neutrino and recostructed muon track using simulated neutrinos. The large improvement between the 22- and 40-string point spread function at high energies is due to an improvement in the reconstruction, which now uses charge information.

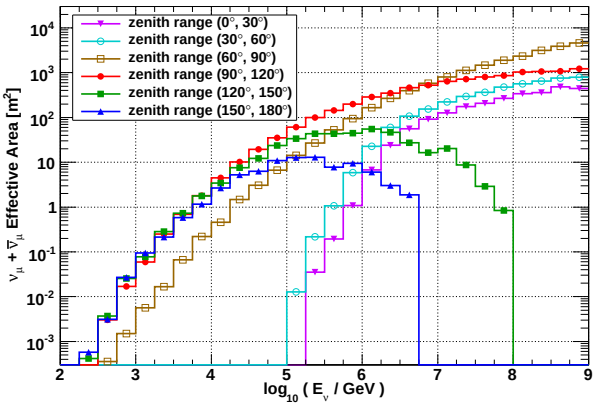

Fig. 3: The IceCube 40-string solid-angle-averaged effective area to an equal-ratio flux of ν_μ and $\bar{\nu}_\mu$, reconstructed within 2° of the true direction. The different shapes of each zenith band are due to a combination of event selection and how much of the Earth the neutrinos must travel through. Since the chance of a neutrino interacting increases with its energy, in the very up-going region high energy neutrinos are absorbed in the Earth. Only near the horizon do muons from $>$PeV neutrinos often reach IceCube. Above the horizon, low energy events are removed by cuts, and in the very down-going region effective area for high energies is lost due to insufficient target material.

153.4° r.a., 11.4° dec. Accounting for all trial factors, this is consistent with the null hypothesis at the 2.2 σ level. The events in the most significant location did not show a clear time dependent pattern, and these coordinates have been included in the catalogue of sources for the 40-string analysis.

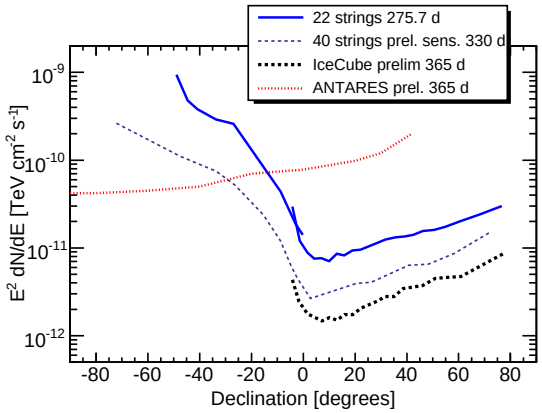

Fig. 4: 40-string IceCube sensitivity for 330 days as a function of declination to a point source with differential flux $\frac{d\Phi}{dE} = \Phi^0(E/\mathrm{TeV})^{-2}$. Specifically, Φ^0 is the minimum source flux normalization (assuming E^{-2} spectrum) such that 90% of simulated trials result in a log likelihood ratio $\log\lambda$ greater than the median log likelihood ratio in background-only trials ($\log\lambda = 0$). Comparison are also shown for the 22-string and the expected performance of the 80-string configuration, as well as the ANTARES [6] sensitivity.

Since the 22-string analysis, a number of improvements have been achieved. An additional analysis of the 22-string data optimized for E^{-2} and harder spectra was performed down to -50° declination with a binned search [8]. These analyses are now unified into one all-sky search which uses the energy of the events and extends to -85° declination. Secondly, a new reconstruction that uses the charge observed in each DOM performs better, especially on high energy events. Third, an improved energy estimator, based on the photon density along the muon track, has a better muon energy resolution.

With construction more than half-complete, IceCube is already beginning to demonstrate its potential as an extraterrestrial neutrino observatory. The latest science run with 40 strings was the first detector configuration with one axis the same length as that of the final array. Horizontal muon tracks reconstructed along this axis provide the first class of events of the same quality as those in the finished 80-string detector.

There are now 59 strings of IceCube deployed and taking data. Further development of reconstruction and analysis techniques, through a better understanding of the detector and the depth-dependent properties of the ice, have continued to lead to improvements in physics results. New techniques in the southern sky may include separating muon bundles of cosmic ray showers from single muons induced by high energy neutrinos. At lower energies, the identification of starting muon tracks from neutrinos interacting inside the detector will be helped with the addition of DeepCore [9].

REFERENCES

[1] J. Braun *et al. Methods for point source analysis in high energy neutrino telescopes*. Astropart. Phys. **29**, 155, 2006.
[2] Neunhoffer, T. Astropart. Phys., 25, 220. 2006.
[3] D. Heck *et al. CORSIKA: A Monte Carlo code to simulate extensive air showers*, FZKA, Tech. Rep., 1998.
[4] D. Chirkin and W. Rhode. Preprint hep-ph/0407075, 2004.
[5] J. Lundberg *et al. Nucl. Inst. Meth.*, vol. A581, p. 619, 2007.
[6] J. A. Aguilar *et al. Expected discovery potential and sensitivity to neutrino point-like sources of the ANTARES neutrino telescope*. in proceedings 30^{th} ICRC, Merida. 2007.
[7] R. Abbasi *et al.* (IceCube Collaboration) *First Neutrino Point-Source Results from IceCube in the 22-String Configuration*. submitted, 2009. astro-ph/09052253
[8] R. Lauer, E. Bernardini. *Extended Search for Point Sources of Neutrinos Below and Above the Horizon*. in proceedings of 2^{nd} Heidelberg Workshop, 2009, astro-ph/09035434.
[9] C. Wiebusch *et al.* (IceCube Collaboration), these proceedings.

IceCube Time-Dependent Point Source Analysis Using Multiwavelength Information

M. Baker*, J. A. Aguilar*, J. Braun*, J. Dumm*, C. Finley*, T. Montaruli*, S. Odrowski†, E. Resconi†
for the IceCube Collaboration‡
*Dept. of Physics, University of Wisconsin, Madison, WI 53706, USA
†Max-Planck-Institut fur Kernphysik, D-69177 Heidelberg, Germany
‡see special section of these proceedings

Abstract. **In order to enhance the IceCube's sensitivity to astrophysical objects, we have developed a dedicated search for neutrinos in coincidence with flares detected in various photon wavebands from blazars and high-energy binary systems. The analysis is based on a maximum likelihood method including the reconstructed position, the estimated energy and arrival time of IceCube events. After a short summary of the phenomenological arguments motivating this approach, we present results from data collected with 22 IceCube strings in 2007-2008. First results for the 40-string IceCube configuration during 2008-2009 will be presented at the conference. We also report on plans to use long light curves and extract from them a time variable probability density function.**

Keywords**: Neutrino astronomy, Multiwavelength astronomy**

I. INTRODUCTION

IceCube is a high-energy neutrino observatory currently under construction at the geographic South Pole. The full detector will be composed of 86 strings of 60 Digital Optical Modules (DOMs) each, deployed between 1500 and 2500m below the glacier surface. A six string Deep Core with higher quantum efficiency photomultipliers and closer DOM spacing in the lower detector will enhance sensitivity to low energy neutrinos. Muons passing through the detector emit Čerenkov light allowing reconstruction with $\lesssim 1^\circ$ angular resolution in the full detector and about 1.5° (median) in the 22 string configuration. In this paper we describe the introduction of a time dependent term to the standard search for steady emission of neutrinos presented in Ref. [3]. We apply it in a search for periodic emission of neutrinos from seven high-energy binary systems and for a neutrino emission coincident with a catalogue of flares occurring when IceCube was taking data in its 22 string configuration. We also describe an extension of the method that uses multi-wavelength (MWL) lightcurves to characterize neutrino emission.

II. TIME DEPENDENT POINT SOURCE SEARCH

An unbinned maximum likelihood ratio method, using a test statistic that compares a signal plus background hypothesis to a background-only one, has been used for the search for point sources of neutrinos in IceCube [1]. We use the angular and energy distribution of events as information to characterize the signal with respect to the background. In the analysis of the 22-string data we use the number of hit DOMs in an event as an energy estimator, while for the 40-string configuration we use a more sophisticated energy estimator based on the photon density along the muon track. The analysis method returns a best-fit number of signal events and spectral index (though with a large error that depends on the number of events near the celestial coordinate being tested).

We use the IceCube 22-string upward-going neutrino event data sample of 5114 events collected in 275 days of livetime between May 31, 2007 and April 5, 2008 (which includes misreconstructed atmospheric muon contamination of about 5%). Selection cuts are based on the quality of the reconstruction, on the angular uncertainty of the track reconstruction ($\sigma < 3^\circ$) and on other variables such as the number of DOMs hit by the direct Čerenkov light produced by muons. Fig 1 shows that the time distribution of these atmospheric neutrino events is consistent with a flat distribution.

Neutrinos from a point source are expected to cluster around the direction of the source and to have a spectrum $\frac{dN}{dE} \propto E^\gamma$ with spectral index $\gamma \sim -2$ as predicted by 1^{st} order Fermi acceleration mechanisms. On the other hand, the background of atmospheric neutrinos is distributed uniformly in right ascension and has an energy spectrum with $\gamma \sim -3.6$ above 100 GeV. We construct a signal probability distribution function (pdf):

$$S_i = \frac{1}{2\pi\sigma_i^2} e^{-\frac{|\vec{x}_i - \vec{x}_s|^2}{2\sigma_i^2}} * E(E_i|\gamma) * T_i, \qquad (1)$$

where σ_i is the reconstructed angular error of the event [2], $\vec{x}_i - \vec{x}_s$ the angular separation between the reconstructed event and the source, E is the energy pdf with spectral index γ, and T_i is the time pdf of the event. The background pdf is given by:

$$B_i = B(\vec{x}_i) * E_{bkg}(E_i) * \frac{1}{L} \qquad (2)$$

where $B(\vec{x}_i)$ is the background event density (a function of the declination of the event), E_{bkg} the energy

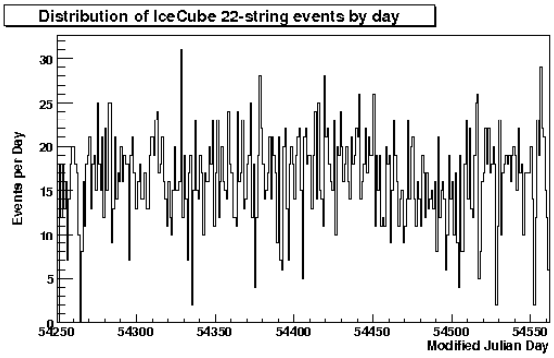

Fig. 1. Time distribution of the 22-string neutrino events.

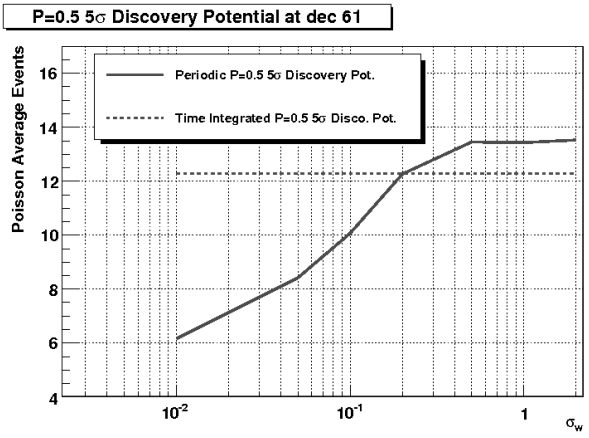

Fig. 2. Comparison of discovery potential at 5σ and 50% probability between the time-integrated and time-dependent methods for LSI +61 303.

distribution of the background, and L the livetime. The background pdf is determined using the data, and the final p-values for these analyses are obtained by comparing scrambled equivalent experiments to data. Scrambled times are drawn from the distribution of measured atmospheric muon event times, taking one event per minute to obtain a constant rate.

The analysis method gives more weight to events which are clustered in space and at energies higher than expected from the atmospheric background. In this work we present the results which include for the first time a time dependent term in the pdf. Results are given in terms of p-values, or the fraction of the scrambled samples with a higher test statistic than found for the data.

III. Binary System Periodicity search

One class of high-energy binary systems, microquasars, includes a compact object with an accretion disk emitting relativistic jets of matter. Jets are assumed to accelerate protons, hence pp and $p\gamma$ interactions are possible. The two microquasars LS 5039 (which is out of the IceCube field of view) and LSI 61 +303 [4] have been observed to emit TeV gamma-rays modulated with the orbital phase of the systems. H.E.S.S. detects the minimum of the photon emission for LS 5039 during the superior conjunction, where the compact object is behind the massive star [5]. The gamma ray modulation can be interpreted as an indication of absorption of gammas emitted from the compact object. Nonetheless, the modulation could be very different in neutrinos, where neutrino production depends on how much matter is crossed by the proton beam on which interactions and decays depend. Since we assume that the modulation is related to the relative position of the accelerator with respect to the observer, we also include in our search objects for which no TeV modulation has yet been observed, using the period obtained from spectroscopic observations of the visible binary partner. We then leave the phase as a free parameter to be fit. Due to low statistics, a Gaussian will be adequate to describe the time modulation. Hence our time-dependent pdf is:

$$T_i = \frac{1}{\sqrt{2\pi}\sigma_w} e^{-\frac{|\phi_i - \phi_0|^2}{2\sigma_w^2}}, \quad (3)$$

where σ_w is the width of the Gaussian in the period, ϕ_i is the phase of the event and ϕ_0 is the phase of peak emission. The phase takes a value between 0 to 1.

We find that this time-dependent method has a better discovery potential than the time-integrated analysis if the sigma of the emission is less than about 20% of the total period (Fig. 2). Since there are more degrees of freedom, the time-dependent analysis will perform worse if neutrinos are emitted over a large fraction of the period.

We examined seven binary systems, listed in Tab. I, covering a range of declinations and periods. There was no evidence of periodicity seen for any of the sources tested. The most significant result for this search has a pre-trial p-value of 6%, we expect to see this level of significance from one of our seven trials in 35% of scrambled samples, hence we find no evidence for periodicity.

Object	RA (deg)	Dec (deg)	Period (d)	p-value
LSI +61 303	40.1	+61.2	26.5	0.51
Cygnus X-1	299.6	+35.2	5.6	0.63
Cygnus X-3	308.1	+40.9	0.2	0.09
XTE J1118+480	169.5	+48.0	0.2	0.11
GRS1915	288.8	+10.9	30.8	0.61
SS 433	287.9	+5.0	13.1	0.06
GRO 0422+32	65.4	+32.9	0.2	0.39

TABLE I
System name, equatorial coordinates, period and pre-trial p-value.

IV. Multiwavelength Flares Analysis

In high-energy environments, $p\gamma$ and pp interactions produce pions and kaons that decay into photons and neutrinos. Thus, we expect a correlation between TeV γ and ν_μ fluxes. Blazars and binary systems exhibit

variability, with flares often observed to correlate in several photon wavebands. Hence, if TeV information is not available, we can use X-ray and optical data as well. We use this expected time correlation between photons and neutrinos to suppress the background of atmospheric neutrinos, which have a random distribution in time, by looking for neutrino emission in time windows selected based on MWL information. By restricting our search we need fewer events to achieve a 5σ signal than with the time-integrated search.

We use MWL observations to create a catalogue of flares from blazars and binary systems which have states of heightened non-thermal emission. We determine the time window of our search based on the MWL data to characterize the time and duration of peak brightness.

A. Selection of Flares

To collect a list of interesting flares we monitored alerts such as Astronomer's Telegram or GCN for sources observed undergoing a change of state which may produce heightened neutrino emission. The selected catalogue is presented in Tab. II and illustrated here:

- **3C 454.3** flares were measured by AGILE GRID during July 24-30, 2007 [8] and again during Nov. 12-22, 2007 [9].
- **1ES 1959+650** was seen by INTEGRAL in a hard flux state (Nov. 25-28 2007 [6]). Later Whipple obtained a few measurements around December 2-7 [7] which we also selected for investigation.
- **Cygnus X-1** had a "giant outburst" seen by Konus-Wind and Suzaku-WAM [10]. These giant outbursts have been modeled in [11].
- **S5 0716+71** was seen flaring in GeV, optical and radio bands during two periods, September 7-13, 2007 and Oct 19-29, 2007 [12].

B. Method and Results

We tested two methods to search for neutrino flares: the first case (hereafter the "box method"), uses a pdf which counts only events which fall inside the selected time window:

$$T_i = \frac{H(t_{max} - t_i)H(t_i - t_{min})}{t_{max} - t_{min}}, \qquad (4)$$

where H is the Heaviside step function, and t_{min} and t_{max} are fixed from MWL data. The second case is to find a best-fit Gaussian to describe the neutrino emission, fitting the mean of the flare and its duration inside the selected time window. The time factor in the source term will be:

$$T_i = \frac{1}{\sqrt{2\pi}\sigma_t} e^{-\frac{|t_i - t_0|^2}{2\sigma_t^2}} \qquad (5)$$

where t_0 is the peak emission and σ_t is the width. The Gaussian search method yields more information about the flare, such as width and time of the peak of the emission, and also can use events outside of the time window. To focus the search on correlation with photon emission instead of an all-year search, we confined the mean to the time window, and the sigma can not be longer than the time window. The Gaussian introduces two additional parameters to fit, while the box method has no additional parameters over the time-integrated search.

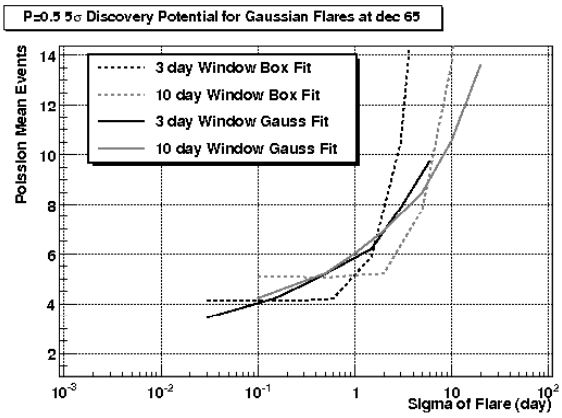

Fig. 3. Comparison of the box and Gaussian method for the flare search. The mean number of events needed for a $5-\sigma$ detection is plotted against the width of neutrino emission.

To compare the two methods, we generated signal events with Gaussian time distributions of different widths to add to scrambled data. Our figure of merit is the minimum flux required for 50% probability of 5σ discovery. We find the box method outperforms the Gaussian unless the FWHM of the signal function is less than 10% or greater than 110% of the width of the time window. We show the discovery potential curves for time windows of 3 and 10 days in Fig. 3. We also tested the possibility that the time window we chose based on MWL information is not centered on a neutrino flare by injecting events with an offset in the window, still finding a region where the box requires fewer events for discovery. Hence the box method, which performs better than the Gaussian method in a broad part of the signal parameter space was selected for providing the final p-values.

We found that 5 of 7 flares we examined were best fit by 0 source events, while S5 0716+71 and 1ES 1959+650 each showed one contributing event during a flare. Considering that we looked at 7 flares, the post trials p-value is 14% for the most significant result, the 10 day flare of S5 0716+71. This value is compatible with background fluctuations.

Source	Alert Ref.	Time Window	p-value
1ES 1959+650	[6]	MJD 54428-54433	1
1ES 1959+650	[7]	MJD 54435.5-54440.5	0.08
3C 454	[8]	MJD 54305-54311	1
3C 454	[9]	MJD 54416-54426	1
Cyg X-1	[10]	MJD 54319.5-54320.5	1
S5 0716+71	[12]	MJD 54350-54356	1
S5 0716+71	[12]	MJD 54392-54402	0.02

TABLE II
FLARE LIST: SOURCE NAME, REFERENCES FOR THE ALERT, INTERVAL IN MODIFIED JULIAN DAY, PRE-TRIAL P-VALUE.

V. Future developments: Analysis Based on Long Light Curves

With the advent of Fermi, long and regularly sampled high energy γ-ray light curves will be available soon. The Fermi public data [13] already provide a first glimpse of the variable behavior of bright sources and the quality of the data. We plan to analyze Fermi light curves using the method described in [14]. Following this approach, the analysis of long light curves will provide:

- A systematic selection of flaring periods: until now the selection of flaring periods is biased because detections are often triggered by alerts. The monitoring of the sky provided by Fermi will eliminate this.
- A systematic criterion to define the threshold for a flare: once enough data will be accumulated, the flare statistics will provide a characteristic level and a standard deviation. With a safe 3σ threshold, flaring periods cannot be confused with intrinsic fluctuations of the detector and can be selected uniformly across the entire period considered.
- The possibility to select more than one flare in the same light curve, to estimate the frequency of the high states.
- A non-parametric time dependent signal pdf.

Our analysis of long Fermi light curves is still in development and for the moment limited by the relatively short duration of the Fermi data taking. We illustrate the method using the light curve collected by RXTE-ASM for Mkn 421 (Fig. 4). About 10 years of RXTE-ASM data are analyzed in order to extract a characteristic level of the source and determine flaring periods, as in [14]. For example here the threshold for flaring has been fixed at the 3σ level that corresponds to 1.7 RXTE/ASM count/sec. Interpreting periods selected above this level with the Maximum Likelihood Block algorithm provides the time dependent pdf (see Fig. 5).

While the rate of events observed in IceCube is approximately stable over timescales of a few days, the variability of the background has to be considered if longer periods are tested. The main source of variations of the observed event rates are changes in the detector uptime. These will be implemented in the description of the background.

VI. Conclusions

We have presented the results of a time dependent analysis of the IceCube 22 string data sample. We searched for a periodic time structure of neutrinos from binary systems, and neutrinos in coincidence with high flux states from sources for which other experiments issued alerts. Results in all cases were consistent with background fluctuations. We also provide insight on how MWL information may in the future be directly used to create a time pdf to analyze correlations of photon and neutrino emission.

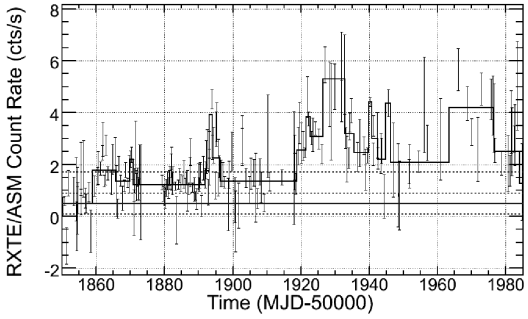

Fig. 4. Subperiod of Mkn 421 light curve collected by ASM/RXTE for illustration of the method.

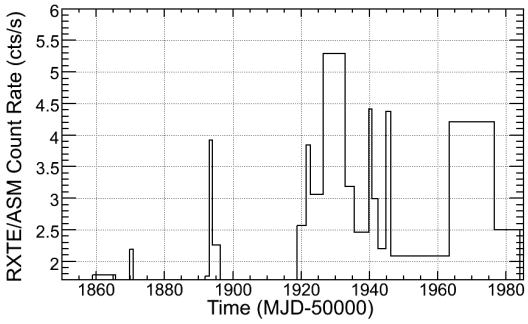

Fig. 5. The time pdf resulting from application of the 3σ threshold described in the text to the Mkn 421 light curve.

References

[1] J. Braun *et al.*, Astropart. Phys. **29**, 299 (2008)
[2] T. Neunhöffer, Astropart. Phys. **25**, 220 (2006)
[3] J. Dumm *et al.*, for the IceCube Collaboration, these proceedings.
[4] J. Albert *et al.*, 2009, ApJ **693**, 303
[5] F. Aharonian *et al.*, 2006 A&A **460**, 743
[6] E. Bottacini *et al.*, http://www.astronomerstelegram.org/?read=1315
[7] VERITAS collab. http://veritas.sao.arizona.edu/documents/summary1es1959.table
[8] S. Vercellone *et al.*, 2008, ApJ **676**, L13
[9] S. Vercellone *et al.*, 2009, ApJ **690**, 1018
[10] S. Golenetskii, *et al.*, GCN 6745, Aug 10 2007
[11] G.E. Romero, M.M. Kaufman Bernado and I.F. Mirabel, 2002, A&A **393**, L61
[12] M. Villata *et al.*, 2008, A&A **481**, L79
[13] http://fermi.gsfc.nasa.gov/ssc/data/access/lat/msl_lc/
[14] E. Resconi *et al.*, arXiv:0904.1371.

Search for neutrino flares from point sources with IceCube

J. L. Bazo Alba*, E. Bernardini*, R. Lauer*, for the IceCube Collaboration†

*DESY, D-15738 Zeuthen, Germany.
†see special section of these proceedings

***Abstract*. A time-dependent search for neutrino flares from pre-defined directions in the whole sky is presented. The analysis uses a time clustering algorithm combined with an unbinned likelihood method. This algorithm provides a search for significant neutrino flares over time-scales that are not fixed a-priori and that are not triggered by multiwavelength observations. The event selection is optimized to maximize the discovery potential, taking into account different time-scales of source activity and background rates. Results for the 22-string IceCube data from a pre-defined list of bright and variable astrophysical sources will be reported at the conference.**

***Keywords*: IceCube, Neutrino Flares, Clustering.**

I. Introduction

Several astrophysical sources are known to have a variable photon flux at different wavelengths, showing flares that last between several minutes to several days. Hadronic models of Active Galactic Nuclei (AGNs) predict [1][2] neutrino emission associated with these multi-wavelength (MWL) emissions. Time integrated analyses are less sensitive in this flaring scenario because they contain a higher background of atmospheric neutrinos and atmospheric muons. Therefore a time dependent analysis is more sensitive because it reduces the background by searching smaller time scales around the flare. A direct approach that looks for this correlation using specific MWL observations is reported in [3].

In order to make the flare search more general, and since MWL observations are scarce and not available for all sources, we take an approach not triggered by MWL observations. We apply a time-clustering algorithm (see [4]) to pre-defined source directions looking for the most significant accumulation in time (flare) of neutrino events over background, considering all possible combinations of event times. One disadvantage of this analysis is the increased number of trials, which reduces the significance. Nevertheless, for flares sufficiently shorter than the total observation period, the time clustering algorithm is more sensitive than a time integrated analysis. The predicted time scales are well below this threshold.

II. Flare search algorithm

The time clustering algorithm chooses the most promising flare time windows based on the times of the most signal-like events from the analyzed data. Each combination of these event times defines a search time window (Δt_i). For each Δt_i a significance parameter λ_i is calculated. The algorithm returns the best λ_{max} corresponding to the most significant cluster. The significance can be obtained using two approaches: a binned method, as in the previous implementation [4], and an improved unbinned maximum likelihood method [5] which enhances the performance.

The unbinned maximum likelihood method defines the significance parameter by:

$$\lambda = -2\log\left[\frac{\mathcal{L}(\vec{x}_s, n_s = 0)}{\mathcal{L}(\vec{x}_s, \hat{n}_s, \hat{\gamma}_s)}\right], \qquad (1)$$

where $\vec{x}_s$ is the source location, $\hat{n}_s$ and $\hat{\gamma}_s$ are the best estimates of the number of signal events and source spectral index, respectively, which are found by maximizing the likelihood, ($\mathcal{L}$):

$$\mathcal{L} = \prod_{i=1}^{n_{tot}} \left(\frac{n_s}{n_{tot}} S_i + \left(1 - \frac{n_s}{n_{tot}}\right) B_i\right) \qquad (2)$$

The background probability density function (pdf), B_i, calculated purely from data distributions, is given by:

$$B_i = P_i^{space}(\theta_i, \phi_i) P_i^{energy}(E_i, \theta_i) P_i^{time}(\theta_i), \qquad (3)$$

where P^{space} describes the distribution of events in a given area (a zenith band of 8° is used for convenience). In a simple case this probability would be flat because of random distribution of background events. However, due to applied cuts, Earth absorption properties and detector geometry, this probability is dependent on zenith, θ_i, and azimuth, ϕ_i. The irregular azimuthal distribution caused by the detector geometry is shown in Fig. 1. For time integrated analyses covering one year the dependence on the azimuth is negligible because the exposure for all right ascension directions is integrated. However, an azimuth correction becomes important for time scales shorter than 1 day, reaching up to 40% difference, thus it should be included in time dependent analyses. P^{space} has value unity when integrated over solid angle inside the test region (i.e. zenith band).

The energy probability P_i^{energy} is determined from the energy estimator distribution and depends on the zenith coordinate. In the southern sky an energy sensitive event selection is the most efficient way to reduce the atmospheric muon background. This energy cut decreases with zenith angle, thus creating a zenith dependence

of the energy. Therefore a zenith dependent energy probability, shown in Fig. 2, is needed. Note that for the northern sky this correction is small.

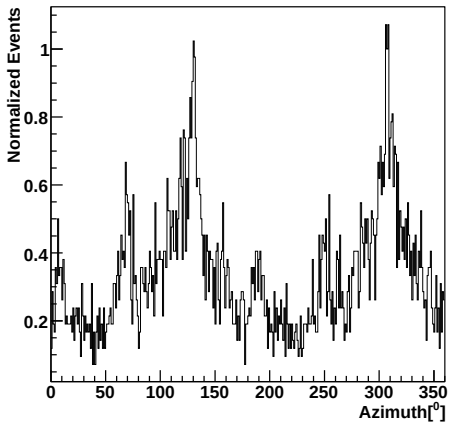

Fig. 1. Normalized azimuth distribution of the data sample reported in [9].

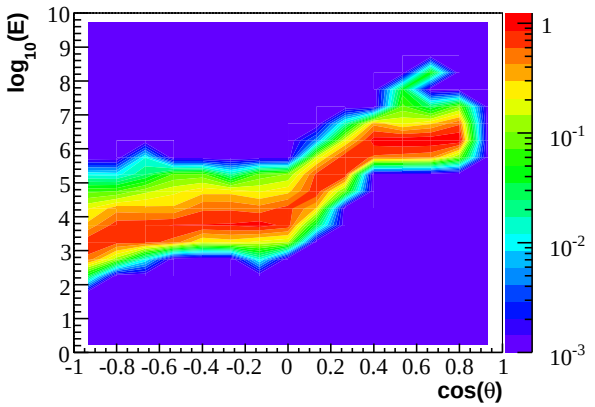

Fig. 2. Background energy pdf from data as a function of the energy estimator and zenith angle. The ultra high energy sample [10] is used. The southern sky corresponds to $\cos(\theta) > 0$.

Given the low statistics at final sample level, estimating the background by counting events inside a time window would introduce significant errors for short time scales. Therefore another approach is used, namely, to fit the event rates in the entire observed period as a function of time. Two regions of the sky (South and North) are distinguished because they have different properties. The northern sky sample consists mostly of atmospheric neutrinos which do not show a significant seasonal variation, therefore a constant fit is used. For the southern sky, a sinusoidal fit is used because it is dominated by a background of high energy atmospheric muons which have seasonal variation. These fits are shown in Fig. 3 and include the necessary correction for the uptime[1] of the detector. It has been verified that the time modulations for different zenith bands within a half hemisphere are the same, thus allowing us to use all events inside the half hemisphere for the fit of the rates.

[1]The uptime takes into account the inefficiency periods and data gaps after data quality selection.

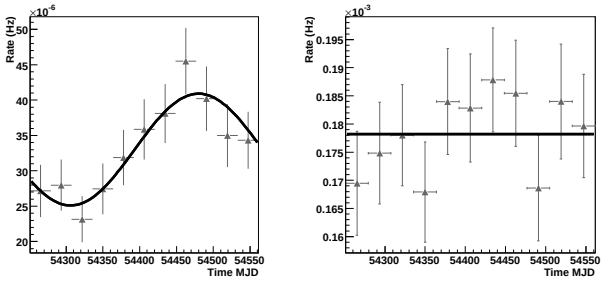

Fig. 3. Uptime corrected rates and their fits for the southern (left) and northern (right) skies.

The signal pdf, S_i, is given by:

$$S_i = P_i^{space}(\mid \vec{x}_i - \vec{x}_s \mid, \sigma_i) P_i^{energy}(E_i, \theta_i, \gamma_s), \quad (4)$$

where, the spatial probability, P_i^{space} is a Gaussian function of $\mid \vec{x}_i - \vec{x}_s \mid$, the space angular difference between the source location, $\vec{x}_s$, and each event's reconstructed direction, $\vec{x}_i$, and σ_i, the angular error estimation of the reconstructed track. The estimator used for σ_i is the size of the error ellipse around the maximum value of the reconstructed event track likelihood. The energy probability, P_i^{energy}, constructed from signal simulation, is a function of the event energy estimation, E_i, the zenith coordinate, θ_i, and the assumed energy spectral index of the source, γ_s ($E^{-\gamma_s}$). A projection of P_i^{energy} for the whole sky is shown in Fig. 4. For a given θ_i and γ_s the energy pdf is normalized to unity over E_i. For the energy a dedicated estimator of the number of photons per track length is used. No flare time structure is assumed (i.e. taken to be flat in time). Therefore there is no need to include a time dependent term in the signal pdf.

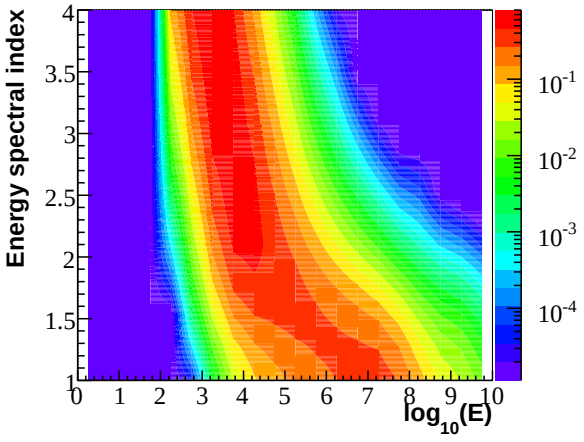

Fig. 4. Projection for the whole sky of the energy component of the signal pdf as a function of the energy estimator and energy spectral index. The ultra high energy sample [10] is used.

TABLE I
LIST OF VARIABLE ASTROPHYSICAL SOURCES AND THEIR DETECTION PROBABILITY (TIME VARIABLE AND TIME INTEGRATED) FOR A SIMULATED FLARE OF 7 DAYS WITH AN E^{-2} ENERGY SPECTRUM AND POISSON MEAN OF 5 INJECTED EVENTS. THE EQUIVALENT STEADY FLUX CORRESPONDS TO 5 EVENTS INJECTED AT ANY TIME IN THE FULL ICECUBE DATA-TAKING PERIOD (276 DAYS).

Source	Type	dec [°]	ra [°]	Detection Probability (3σ) (%)		Eq. flux $\times 10^{-11}$ TeVcm^{-2}s^{-1}
				Time Variable	Time Integrated	
GEV J0540-4359	LBL	-44.1	84.7	46.8	24.5	57.5
GEV J1626-2502	FSRQ	-25.5	246.4	85.6	80.8	30.9
GEV J1832-2128	FSRQ	-21.1	278.4	77.1	72.1	21.2
GEV J2024-0812	FSRQ	-7.6	306.4	37.5	14.4	3.0
3C 279	FSRQ	-5.8	194.1	26.1	9.8	2.4
3C 273	FSRQ	2.0	187.3	50	12.4	1.2
CTA 102	FSRQ	11.7	338.1	36.2	13.6	1.0
GEV J0530+1340	FSRQ	13.5	82.7	31.4	10.1	1.1
3C 454.3	FSRQ	16.1	343.5	70.1	12.2	1.2
GEV J0237+1648	LBL	16.6	39.7	69	11	1.2

We use a binned method implementation of the time clustering algorithm as a crosscheck of our new unbinned analysis. In the case of the binned method, a circular angular search bin (2.5° radius) around the source direction is used. The times of the events that define the search time windows (Δt_i) are given by all the events inside this angular bin. The significance parameter is obtained from Poisson statistics, given the number of expected background events inside the bin and the observed events in each cluster with multiplicity[2] m. The expected number of background events is calculated by integrating, in the given time window, the fit to the rates, as described above. This calculation takes into account the zenith dependence of the background, in zenith bands with the size of the bin, the corresponding uptime factor and the azimuth correction.

The best significance obtained for a cluster is corrected for trial factors by running several Monte Carlo background-only simulations. The simulation is done by creating distributions from data of zenith, azimuth, reconstruction error and energy estimator. The event characteristics are randomly taken from these distributions while considering the correlations between the different parameters. In order to study the performance of the algorithm, we calculate the neutrino flare detection probability as a function of the signal strength and duration of the flare by simulating signal events on top of background events[3]. The properties of signal events are taken from a dedicated signal simulation and depend on the assumed energy spectral index. The Point Spread Function (PSF) is used to smear the events around the source location, thus simulating the effect of the direction reconstruction. For each simulation, a random time is chosen around which signal events are randomly injected inside the time window defined by the flare duration. The flare duration is investigated in the range from 1 day to 15 days, though the algorithm finds the best time window, which could be larger. We constrain the largest flare duration in the algorithm to be less than 30 days, which is sensible from γ-ray observations.

[2]The integral of the Poisson distribution of the background events starts at (m-1) since the beginning and end of the time period are fixed from the data itself.

[3]The number of injected background and signal events is Poisson distributed.

III. SOURCE SELECTION

Since searching for all directions in the sky would decrease the significance, we consider only a few promising sources, thus reducing the number of trials. We select variable bright astrophysical sources in the whole sky. The selected blazars, including Flat Spectrum Radio Quasars (FSRQs) and Low-frequency peaked BL Lacs (LBLs), are taken from the confirmed Active Galactic Nuclei (AGN) in the third EGRET catalogue (3EG) [6]. We also require that they are present in the current latest Fermi catalogue (0FGL) [7]. The criteria for selecting variable and bright source is based on the following parameters thresholds:

- Variability index (3EG) > 1
- Maximum 3EG flux ($E > 100$ MeV) > 40 [10^{-8} ph cm^{-2}s^{-1}]
- Average 3EG flux ($E > 100$ MeV) > 15 [10^{-8} ph cm^{-2}s^{-1}]
- Inside visibility region of IceCube.

The selected source list consists of 10 directions (Table I) that are going to be tested with the time clustering algorithm. Models like [2] favor fluxes of higher energy neutrinos from FSRQ sources. Given the absorption of neutrinos at different energies in the Earth and the event cut strategy, southern sky FSRQs are more favored by these models because of their higher energy range of sensitivity.

IV. DATA SAMPLES

IceCube[8] 22-string data from 2007-08 is used. It spans 310 days with an overall effective detector uptime of 88.9% (i.e. 276 days). The whole sky (declination range from -50° to 85°) is scanned. Different selection criteria are applied for the northern and southern skies. Previously obtained reconstructed datasets are used: the standard point source sample for the northern sky [9] (5114 events, declination from -5° to 85°, 1.4° sky-averaged median angular resolution) and the dedicated ultra high energy sample for the southern sky [10] (1877 events in the whole sky, declination from -50° to 85°,

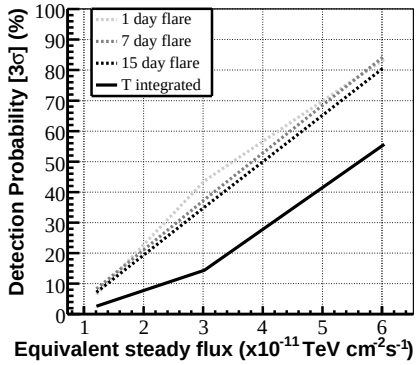

(a) Southern sky at (dec=-7.6, ra=306.4)

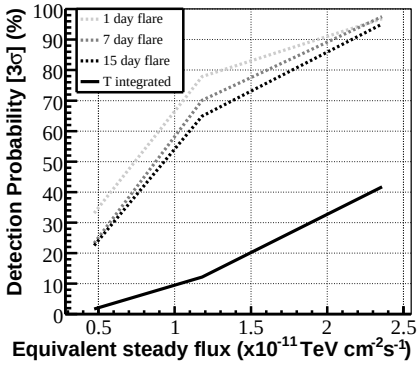

(b) Northern sky at (dec=16.1, ra=343.5)

Fig. 5. Detection probability (3σ) for two source directions. The curves correspond to different time duration of the flares as function of the injected flux with a E^{-2} energy spectrum, using an unbinned time variable method (dashed), compared to a time integrated method (solid). The same mean number of events are injected into the time-windows (1, 7, 15, and 276 days) at each point on the x-axis, which is labeled with the equivalent flux corresponding to the full 276 day period.

1.3° sky-averaged median angular resolution). The first sample is optimized, within an unbinned method, for the optimal sensitivity to both hard and soft spectrum sources. The second sample was optimized for a binned method at ultra high energies. Therefore it should be noted that the binned method results are much better in the southern sky than in the northern sky. Nevertheless, the unbinned method, for an E^{-2} energy spectrum still performs better in the southern sky.

The energy containment in these two regions is different, with ranges from TeV to PeV and from PeV to EeV, in the northern and southern sky respectively. Event tracks are obtained with a multi-photoelectron [4] (MPE) [11] reconstruction which improves the angular resolution for high energies.

V. Results

The probability of a 3σ flare detection using this time variable analysis (time clustering algorithm) for a given number of injected signal events (i.e. Poisson mean of 5 events) with a E^{-2} energy spectrum inside a seven-day window is shown for all sources in Table I. For comparison purposes, time-integrated detection probabilities integrated over the whole 22-string IceCube data period (276 days) are also given. In the northern sky, the same simulated signal was on average four times more likely to be detected at 3σ with the unbinned time variable search than with the time integrated search, and in the southern sky, on average about twice as likely with the time variable search. The gain is not as substantial as in the northern sky because the discovery potential without time properties is already greater since for the same number of injected signal events the background is relatively smaller. A more detailed example for two sources, at the southern and northern skies, for different time scales and signal fluxes is presented in Fig. 5. For shorter flare durations the detection probability increases and is well above a time integrated search. It can be seen that there is a different behaviour for each part of the sky. This is caused by the different type of backgrounds (high energy atmospheric muons in the south and atmospheric neutrinos in the north) and the difference in number of final events in each sample (less events in the southern sky) due to the different selection cuts.

[4]The MPE reconstruction takes the arrival time distribution of the first of N photons using the cumulative distribution of the single photon pdf.

VI. Summary

We have presented the sensitivity of the time clustering algorithm using an unbinned maximum likelihood method. This is an improvement over the previous performances using a binned method and time integrated analyses. The search window for variable sources has been extended to the southern sky. IceCube 22-string data will be analyzed using this method looking for neutrinos flares with no a priori assumption on the time structure of the signal.

References

[1] D. F. Torres and F. Halzen, Astropart. Phys. **27** (2007) 500.
[2] A. Atoyan and C. D. Dermer, New Astron. Rev. **48** (2004) 381.
[3] M. Baker *et al.* for the IceCube Collab.: Contributions to this conference.
[4] K. Satalecka *et al.* for the IceCube Collab.: Contributions to the ICRC, Merida, Mexico, July 3-11, pages 115-118, (2007).
[5] J. Braun *et al.*, Astropart. Phys. **29** (2008) 299.
[6] P. L. Nolan *et al.*, The Astrophysical Journal. Vol. 597, No 1, (2003) pp. 615-627.
[7] A. A. Abdo *et al.*, Fermi LAT Collaboration, (2009). arXiv:0902.1340
[8] A. Karle *et al.*, for the IceCube Collab.: ARENA Proceedings (2008).
[9] J. L. Bazo Alba *et al.* for the IceCube Collab.: NOW 2008 Proceedings. Nucl. Phys. B (Proc. Suppl.) Vol. 188 (2009) pp. 267-269. arXiv:0811.4110
[10] R. Lauer *et al.* for the IceCube Collab.: Proceedings 2nd Heidelberg Workshop "HE γ-rays and ν's from Extra-Galactic Sources", (2009). arXiv:0903.5434
[11] J. Ahrens et al. for the AMANDA Collab., Nucl. Instrum. Meth. A 524 (2004) 169.

Neutrino triggered high-energy gamma-ray follow-up with IceCube

Robert Franke*, Elisa Bernardini* for the IceCube collaboration†
*DESY Zeuthen,D-15738 Zeuthen, Germany
†See the special section of these proceedings.

***Abstract*. We present the status of a program for the generation of online alerts issued by IceCube for gamma-ray follow up observations by Air Cherenkov telescopes (e.g. MAGIC). To overcome the low probability of simultaneous observations of flares of objects with gamma-ray and neutrino telescopes a neutrino-triggered follow-up scheme is developed. This mode of operation aims at increasing the availability of simultaneous multi-messenger data which can increase the discovery potential and constrain the phenomenological interpretation of the high energy emission of selected source classes (e.g. blazars). This requires a fast and stable online analysis of potential neutrino signals. We present the work on a significance-based alert scheme for a list of phenomenologically selected sources. To minimize the rate of false alerts due to detector instabilities a fast online monitoring scheme based on IceCube trigger and filter rates was implemented.**

***Keywords*: IceCube neutrino gamma-ray follow-up**

I. Introduction

A Neutrino Triggered Target of Opportunity program (NToO) was developed already in 2006 using the AMANDA array to initiate quasi-simultaneous gamma-ray follow-up observations by MAGIC. The aim of such an approach is to increase the chance to discover cosmic neutrinos by on-line searches for correlations with established signals (e.g. flares in high-energy gamma-rays) triggered by neutrino observations. For sources which manifest large time variations in the emitted radiation, the signal-to-noise ratio can be increased by limiting the neutrino exposures to most favorable periods. The chance of discovery can then be enhanced (the so called "multi-messenger approach") by ensuring a good coverage of simultaneous data at a monitoring waveband (e.g. gamma-rays). The first realization of such an approach led to two months of follow-up observations of AMANDA triggers by MAGIC, focused on a selected sample of Blazars as target sources [1]. An extension of this program to IceCube and also to optical follow-up observations has been later realized with the ROTSE network of optical telescopes, addressing possible correlations between neutrino multiplets and either GRBs or Supernovae [2].

Multi-messenger studies can be accomplished off-line, searching for correlations between the measured intensity curves in the electromagnetic spectrum and the time of the detected neutrinos. The major limitations encountered so far were due to the scarce availability of information on the electromagnetic emission of the objects of interest, which typically are not observed continuously. Whenever data is available, such an a-posteriori approach is however very powerful, and it is part of the research plans of the IceCube Collaboration. We emphasize that a neutrino telescope at the South Pole is continuously and simultaneously sensitive to all objects located in the northern hemisphere. The investigation of the correlation between the observed properties of the electromagnetic emission and the detected neutrinos is therefore at any time feasible once the relevant electro-magnetic information is available. In other words, on-line and off-line approaches have to be seen as complementary and not mutually exclusive.

In case of variable objects like Blazars, FSRQs as well as Galactic systems like microquasars and magnetars, hadronic models describing the very high energy gamma-rays emission also predict simultaneous high energy neutrinos. Absorption processes might attenuate the gamma-ray luminosity when the objects are brightest in neutrinos, so that an anti-correlation or time-lag might be predicted as well. In all cases, the availability of simultaneous data on high energy gamma-ray emission and (possibly) neutrinos is mandatory to test different scenarios and shed light on the emission mechanisms (e.g. extract information on the optical depth and on other astrophysical source parameters).

II. Selection of target sources

The most interesting objects as a target for gamma-ray follow-up observations of IceCube events are promising sources of TeV neutrinos, which are either known to exhibit a bright GeV flux in gamma-rays and show extrapolated fluxes detectable by Imaging Air Cherenkov Telescopes, or are already detected by IACTs and are variable. Candidates currently being considered are AGNs (HBL, LBL, FSRQs), Microquasars and Magnetars (SGRs). A preliminary source list based on observations with the FERMI [6] and EGRET [3] experiments is based on the following criteria:

- Source is present in both the third EGRET(3EG) and Fermi catalogues;
- Source is classified as variable in the Fermi catalogue;
- Variability Index > 1 in the 3EG catalog (taken from [5]);
- Maximum 3EG flux $> 40 \cdot 10^{-8}\,\mathrm{ph\,cm^{-2}\,s^{-1}}, E > 100\,\mathrm{MeV}$;

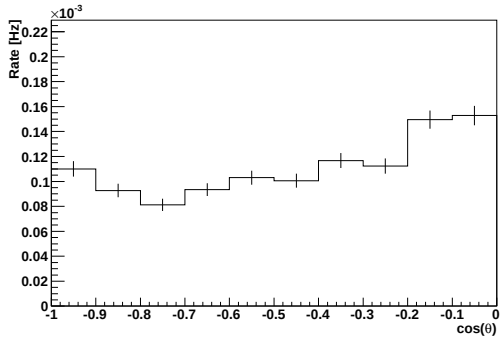

Fig. 1. Predicted rate of atmospheric neutrinos based on Monte-Carlo for IceCube in its 2009/2010 configuration with 59 deployed strings.

- Average 3EG flux $> 15 \cdot 10^{-8}\,\mathrm{ph\,cm^{-2}\,s^{-1}}, E > 100\,\mathrm{MeV}$;
- Difference between the maximum 3EG flux and the minimum 3EG flux $> 30 \cdot 10^{-8}\,\mathrm{ph\,cm^{-2}\,s^{-1}}, E > 100\,\mathrm{MeV}$.

The sources that were selected according to these criteria can be found in Table I.

III. Event selection

The basis for the event selection is an on-line filter that searches for up-going muon tracks. The rate of this filter is about $24\,\mathrm{Hz}$ for IceCube in its 2009/2010 configuration with 59 deployed strings. As the computing resources at the South Pole are limited one can not run more elaborate reconstructions at this rate, so a further event selection has to be done. This so called Level-2 filter searches events that were reconstructed with a zenith angle $\theta > 80^\circ$ ($\theta = 0^\circ$ equals vertically down-going tracks) with a likelihood reconstruction. By requiring a good reconstruction quality the background of misreconstructed atmospheric muons is further reduced. The parameters used to assess the track quality are the likelihood of the track reconstruction and the number of unscattered photons with a small time residual w.r.t. the Cherenkov cone. The reduced event rate of approximately $2.9\,\mathrm{Hz}$ can then be reconstructed with more time intensive reconstructions, like a likelihood fit seeded with ten different tracks (iterative fit). The fit with the best likelihood is used for further cuts. Based on this reconstruction the final event sample is selected by employing a zenith angle cut of $\theta > 90^\circ$ for the iterative reconstruction and further event quality cuts based on this reconstruction. In addition to the already mentioned parameters we also employ a cut on the longest distance between hits with a small time residual compared to their expected arrival time calculated from the track geometry when projected on the reconstructed track. The resulting rate of atmospheric neutrinos as predicted by Monte Carlo as a function of zenith angle can be seen in Figure 1.

IV. The time-clustering algorithm

The timescale of a neutrino flare is not fixed a-priori and thus a simple rolling time window approach is not adequate to detect flares. The time clustering approach that was developed for an unbiased neutrino flare search [7] looks for any time frame with a significant deviation of the number of detected neutrinos from the expected background. The simplest implementation uses a binned approach where neutrino candidates within a fixed bin around a source are regarded as possible signal events. To exploit the information that can be extracted from the estimated reconstruction error and other event properties like the energy an unbinned maximum-likelihood method is under development.

If a neutrino candidate is detected at time t_i around a source candidate the expected background $N_{\mathrm{bck}}^{i,j}$ is calculated for all other neutrino candidates j with $t_j < t_i$ from that source candidate. To calculate $N_{\mathrm{bck}}^{i,j}$ the detector efficiency as a function of the azimuth angle and the uptime has to be taken into account. The probability to observe the multiplet (i, j) by chance is then calculated according to

$$\sum_{k=N_{\mathrm{obs}}^{i,j}-1}^{\infty} \frac{(N_{\mathrm{bck}}^{i,j})^k}{k!} e^{-N_{\mathrm{bck}}^{i,j}} \qquad (1)$$

where N_{obs} is the number of detected on-source neutrinos between t_j and t_i. It has to be reduced by 1 to take into account the bias that one only does this calculation when a signal candidate is detected. As typical flares in high energy gamma-rays have a maximal duration of several days we constrain our search for time clusters of neutrinos to three weeks.

If the cluster with the highest significance exceeds a certain threshold (e.g. corresponding to $5\,\sigma$) the detector stability will be checked and an alert will be send to an Cherenkov telescope to initiate a follow-up observation.

V. Data quality

Data quality is very important for any online alert program to minimize the rate of false alerts due to detector or DAQ instabilities. IceCube has a very extensive monitoring of the DAQ and South Pole on-line processing. However, most of the information is only available with a certain delay after data-taking and thus not useful for follow-up program which requires fast alerts. To ensure that alerts are only sent for neutrino multiplets that where detected during stable running conditions a simple but powerful stability monitoring scheme has been developed. It is based on a continuous measurement of the relevant trigger and filter rates and their respective ratios in time bins of 10 minutes. These values are then compared to a running average of these rates over approximately four days to detect significant deviations. The running average is necessary as slow seasonal changes in the atmosphere and faster weather changes influence the rate of atmospheric muons which dominate the Level-2 rate. An example of this behaviour

TABLE I
PRELIMINARY CANDIDATE SOURCE LIST FOR NEUTRINO TRIGGERED FOLLOW-UP OBSERVATIONS. THE TYPE OF AGN HAS BEEN TAKEN FROM [4]

Source name	Blazar type	Dec. [°]	RA [°]	max. 3EG flux [10^{-8} cm^{-2}s^{-1}]	min. 3EG flux [10^{-8} cm^{-2}s^{-1}]	avg. 3EG flux [10^{-8} cm^{-2}s^{-1}]
3C 273	FSRQ	2.0	187.3	48.3	8.5	15.4
CTA 102	FSRQ	11.7	338.1	51.6	12.1	19.2
GEV J0530+1340	FSRQ	13.5	82.7	351.4	32.4	93.5
3C 454.3	FSRQ	16.1	343.5	116.1	24.6	53.7
GEV J0237+1648	LBL	16.6	39.7	65.1	11.6	25.9

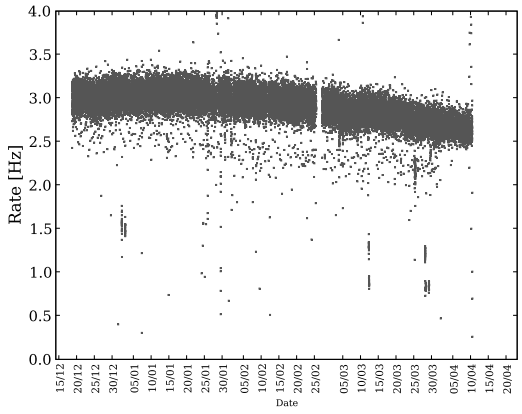

Fig. 2. Rate of the Level-2 online filter for four months (December 2008 till April 2009) in 10-minute bins with IceCube in its 2008/2009 configuration with 40 deployed strings. The Level-2 filter is an online filter that is used for different follow-up observation programs. The slow change in the rate is due to seasonal variations in the atmospheric muon background rate caused by pressure changes in the atmosphere.

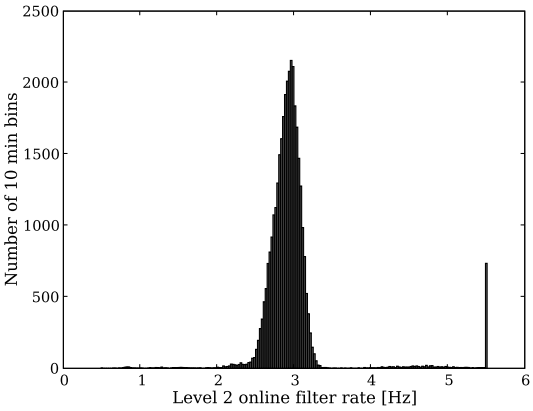

Fig. 3. Histogram of the rates of the online Level-2 filter of IceCube in its 2008/2009 configuration with 40 deployed strings for the four months shown in figure 2. The bin at a value of 5.5 Hz contains all entries bigger than 5.5 Hz.

can be seen in Figures 2 and 3. This system was tested off-line on data from IceCube in its 40-string configuration and proved to correlate very well with the extensive off-line detector monitoring. The fraction of data that has to be discarded due to detector or software problems was about 6 %, which includes all periods in Figures 2 and 3 that significantly deviate from the average. This method will be implemented online for IceCube in its 2009/2010 configuration with 59 deployed strings.

VI. SIGNIFICANCE CALCULATION

Under the hypothesis that all the neutrinos are of atmospheric origin, the probability of observing at least N_{obs} multiplets above the significance threshold and detecting at least N_{coinc} coincident gamma-ray flares is given by:

$$\sum_{m=N_{\text{obs}}}^{+\infty} \frac{(N_{\text{bck}})^m}{m!} e^{-N_{\text{bck}}} \sum_{j=N_{\text{coinc}}}^{m} \frac{m!}{j!(m-j)!} (p_{\text{gam}})^j (1-p_{\text{gam}})^{m-j} \tag{2}$$

where the first term describes the Poisson probability of observing at least N_{obs} neutrino multiplets with N_{bck} background expected, and the second term describes the probability of observing at least N_{coinc} out of m – the running number of observed multiplets, larger or equal to N_{obs} – each with a probability of p_{gam}. We note that this probability can be calculated anytime a-posteriori, once a realistic knowledge of the probability p_{gam} to detect a gamma-ray flare in a time window Δt is available. In order to avoid statistical biases it is mandatory, however, that the statistical test is defined a-priori, i.e. that the conditions to accept an observation and defining a coincidence are previously fixed. Methods on how the to reliably estimate the probability p_{gam} of detecting a gamma-ray flare in a time window Δt, which is influenced by the source elevation and weather conditions, from the frequency of the observed gamma-ray flares are under development. The significance calculated above also does not account for the trial factor correction due to the selection of three or more objects, which can however be calculated as the product of the individual terms corresponding to each source. The probability of having at least one coincidence in any of the proposed sources is, for example:

$$P = 1 - \prod_{i=1}^{N_{\text{Sources}}} P_i^0 \tag{3}$$

where $P^0{}_i$ is the probability of having zero coincidences at the source i.

VII. THE GAMMA-RAY FOLLOW-UP OBSERVATION SCHEME

We propose an observation scheme as follows:

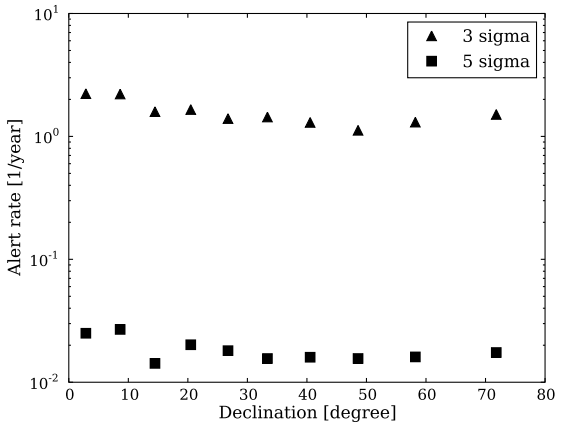

Fig. 4. Preliminiary alert rate from atmospheric neutrino background for IceCube in its 2009/2010 configuration with 59 deployed strings for an alert threshold for the multiplet significance corresponding to 3σ (upper points) and 5σ (lower points) and a bin size of 2°.

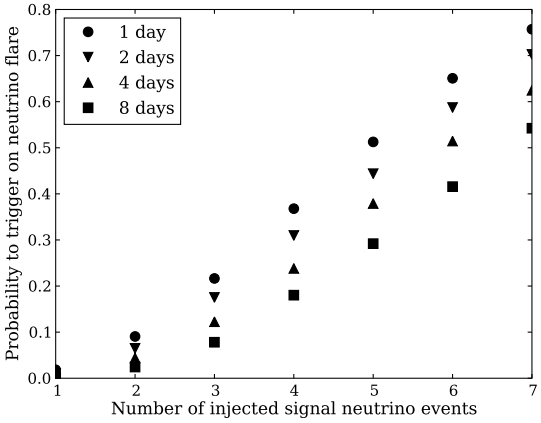

Fig. 5. Preliminary discovery probability for a certain number of injected on-source neutrino events for different flare durations for a source at a declination of 26°. The discovery probability is defined here as the probability to detect a $5\,\sigma$ deviation with the time-clustering method. This does not contain the probability of the gamma-ray observation.

- Up to 1 day after receiving an IceCube alert from one of the pre-defined directions, the source is scheduled to be observed as soon as visible and observation conditions allow.
- If the gamma-ray observation is possible, it will continue for one hour.
- The results of the on-line analysis will be checked and, if there is a positive hint (above 3 σ) the gamma-ray observations may be extended. In case of a positive observation (i.e. a gamma-ray flux trespassing the pre-defined threshold defining a flare), the opportunity to trigger multi-wavelength observations should then be considered. Due to the irreducible background of atmospheric neutrinos (Figure 1) one can estimate the alert rate for different zenith regions (Figure 4) for thresholds corresponding to 3σ and 5σ. The on-source bin has been preliminarily chosen to have a radius of 2°.

Based on a simple Monte Carlo simulation that does not take into account detector features like the azimuth dependent efficiency we calculated the discovery probabilities for different numbers of injected on-source events (see Figure 5) at a declination of 26°. The discovery probability is defined here as the probability to detect a $5\,\sigma$ deviation with the time clustering method.

VIII. Status

The event selection and software to calculate the significance of a neutrino cluster are implemented and ready to be deployed at the South Pole. As IceCube in its 2009/2010 configuration with 59 deployed strings is considerably bigger than the previous detector configuration the stability monitoring needs to be checked with the first weeks of physics data. Pending the approval of the follow-up program by a Cherenkov telescope collaboration we then aim for a timely implementation of this program.

IX. Outlook

Besides enhancing the chance to discover point sources of neutrinos, the gamma-ray follow-up approach here discussed can increase the chance of detecting unusual gamma-ray emission of the selected objects. It also can provide an important contribution to the understanding of the flaring behavior of a few emitters of high energy gamma-rays in a way complementary to X-ray observations. Most relevant, it can provide a series of coincidences and therefore represent an important input to dedicated multi-wavelength follow-up observations, which will assess in more details the phenomenology of the potential sources. In fact – thanks to the existing communication infrastructures of multi-wavelength campaigns – the observation of gamma-ray flares can start a monitoring of the objects at other wavelengths (e.g. X-ray) that would further complement the information that are discussed here.

References

[1] M. Ackermann *et al.* , Proc. 29th ICRC, arXiv:astro-ph/0509330.
[2] Kowalski, M. and Mohr, A., Astropart. Phys., Vol. 27, (2007) pp. 533-538, arXiv:astro-ph/0701618.
[3] Hartman *et al.* , The Astrophysical Journal Supplement Series, Vol. 123, No. 1. (1999), pp. 79-202.
[4] Nandikotkur G., Jahoda K.M., Hartman R.C., 2007, ApJ, 657, 706.
[5] Nolan P.L. *et al.* , The Astrophysical Journal. Vol 597, No 1, (2003) pp. 615-627.
[6] Fermi Collab. Submitted to Astrophysical Journal Supplement (2009).
[7] K. Satelecka *et al.* for the IceCube collaboration, Proc. 30th ICRC, pp. 115-118.

Moon Shadow Observation by IceCube

D.J. Boersma*, L. Gladstone† and A. Karle†
for the IceCube Collaboration‡

*RWTH Aachen University, Germany
†Department of Physics, University of Wisconsin, Madison, WI 53706, USA
‡see special section of these proceedings

***Abstract*. In the absence of an astrophysical standard candle, IceCube can study the deficit of cosmic rays from the direction of the Moon. The observation of this "Moon shadow" in the downgoing muon flux is an experimental verification of the absolute pointing accuracy and the angular resolution of the detector with respect to energetic muons passing through. The Moon shadow has been observed in the 40-string configuration of IceCube. This is the first stage of IceCube in which a Moon shadow analysis has been successful. Method, results, and some systematic error studies will be discussed.**

***Keywords*: IceCube, Moon shadow, pointing capability**

I. Introduction

IceCube is a kilometer-cube scale Cherenkov detector at the geographical South Pole, designed to search for muons from high energy neutrino interactions. The arrival directions and energy information of these muons can be used to search for point sources of astrophysical neutrinos, one of the primary goals of IceCube.

The main component of IceCube is an array of optical sensors deployed in the glacial ice at depths between 1450 m and 2450 m. These Digital Optical Modules (DOMs), each containing a 25 cm diameter photomultiplier tube with accompanying electronics within a pressure housing, are lowered into the ice along "strings." There are currently 59 strings deployed of 86 planned; the data analyzed here were taken in a 40 string configuration, which was in operation between April 2008 and April 2009. There are 13 lunar months of data within that time. In this analysis we present results from 8 lunar months of the 40 string configuration.

For a muon with energy on the order of a TeV, IceCube can reconstruct an arrival direction with order 1° accuracy. For down-going directions, the vast majority of the detected muons do not originate from neutrino interactions, but from high energy cosmic ray interactions in the atmosphere. These cosmic ray muons are the dominant background in the search for astrophysical neutrinos. They can also be used to study the performance of our detector. In particular, we can verify the pointing capability by studying the shadow of the Moon in cosmic ray muons.

As the Earth travels through the interstellar medium, the Moon blocks some cosmic rays from reaching the Earth. Thus, when other cosmic rays shower in the Earth's atmosphere and create muons, there is a relative deficit of muons from the direction of the Moon. IceCube detects these muons, not the primary cosmic rays. Since the position and size of the Moon is so well known, the resulting deficit can be used for detector calibration. The idea of a Moon shadow was first proposed in 1957 [1], and has become an established observation for a number of astroparticle physics experiments; some examples are given in references [2], [3], [4], [5]. Experiments have used the Moon shadow to calibrate detector angular resolution and pointing accuracy [6]. They have also observed the shift of the Moon shadow due to the Earth's magnetic field [7]. The analysis described here is optimized for a first observation, and does not yet include detailed studies such as describing the shape of the observed deficit. These will be addressed in future studies.

II. Method

A. Data and online event selection

Data transfer from the South Pole is limited by the bandwidth of two satellites; thus, not all downgoing muon events can be immediately transmitted. This analysis uses a dedicated online event selection, choosing events with a minimum quality and a reconstructed direction within a window of acceptance around the direction of the Moon. The reconstruction used for the online event selection is a single (i.e., not iterated) log-likelihood fit.

The online event selection is defined as follows, where δ denotes the Moon declination:

- The Moon must be at least 15° above the horizon.
- At least 12 DOMs must register each event.
- At least 3 strings must contain hit DOMs.
- The reconstructed direction must be within 10° of the Moon in declination.
- The reconstructed direction must be within $40^\circ/\cos(\delta)$ of the Moon in right ascension; the $\cos(\delta)$ factor corrects for projection effects.

These events are then sent via satellite to the northern hemisphere for further processing, including running the higher-quality 32-iteration log-likelihood reconstruction used in further analysis.

The Moon reached a maximum altitude of 27° above the horizon ($\delta = -27^\circ$) in 2008, when viewed from

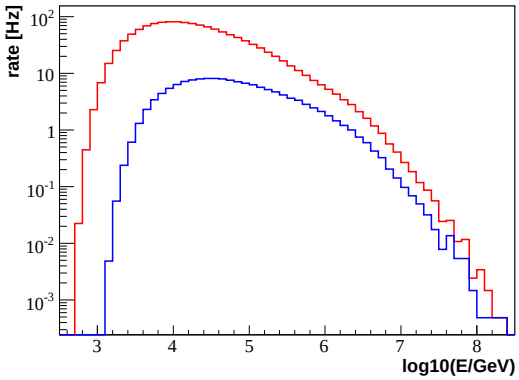

Fig. 1. The energy spectrum of (simulated) CR primaries of muons (or muon bundles) triggering IceCube. Red: all events; blue: primaries with $\delta > -30°$.

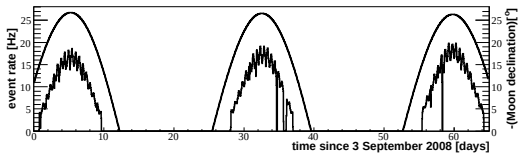

Fig. 2. The rate of events passing the Moon filter (in Hz, lower curve) averaged hourly, together with the position of the Moon above the horizon at the South Pole (in degrees, upper curve), plotted versus time over 3 typical months.

the IceCube detector. The trigger rate from cosmic ray muons is more than 1.2 kHz in the 40 string configuration, but most of those muons travel nearly vertically, and thus they cannot have come from directions near the Moon. Only $\sim 11\%$ of all muons that trigger the detector come from angles less than $30°$ above the horizon. Furthermore, muons which are closer to horizontal (and thus closer to the Moon) must travel farther before reaching the detector. They need a minimum energy to reach this far (see Fig. 1): the cosmic ray primaries which produce them must have energies of at least 2 TeV.

Three typical months of data are shown in Fig. 2, along with the position of the Moon above the horizon. The dominant shape is from the strong increase in muon flux with increasing angle above the horizon: as the Moon rises, so do the event rates near the Moon. This can be seen clearly in the correlation between the two sets of curves. There is a secondary effect from the layout of the 40 strings. One dimension of the detector layout has the full width (approximately 1km) of the completed detector, while the other is only about half as long. When the Moon is aligned with the short axis, fewer events pass the filter requirements. This causes the 12 hour modulation in the rate.

B. Optimization of offline event selection and search bin size

A simulated data sample of 10^5 downgoing muon events was generated using CORSIKA [8].

A set of cuts was developed using the following estimated relation between the significance S, the efficiency

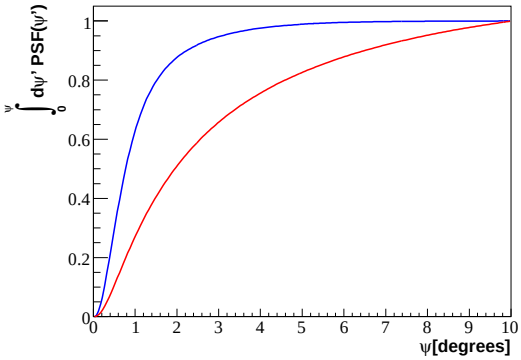

Fig. 3. The x-axis shows the angular difference ψ between the true and reconstructed track. The y-axis shows the fraction of events with this or lower angular error. The blue curve shows the event sample after offline event selection, and the red curve shows the event sample after online event selection.

η of events passing the cut, and the resulting median angular resolution $\Psi_{\rm med}$ of the sample:

$$S(\text{cuts}) \propto \frac{\sqrt{\eta(\text{cuts})}}{\Psi_{\rm med}(\text{cuts})} \qquad (1)$$

Since the deficit is based on high statistics of events in the search bin, this function provides a good estimator for optimizing the significance.

The following cuts were chosen:

- At least 6 DOMs are hit with light that hasn't been scattered in the ice, allowing a -15 nsec to +75 nsec window from some minimal scattering.
- Projected onto the reconstructed track, two of those hits at least 400 meters apart.
- The 1σ estimated error ellipse on the reconstructed direction has a mean radius less than $1.3°$.

The cumulative point spread function of the sample after the above quality cuts is shown as the blue line in Fig. 3.

The size $\Psi_{\rm search}$ of the search bin is optimized for a maximally significant observation using a similar $\sqrt{N}$-error based argument and the resulting relation, which follows. Using the cumulative point spread function of the sample after quality cuts, we have:

$$S(\Psi_{\rm search}) \propto \frac{\int_0^{\Psi_{\rm search}} PSF(\psi')d\psi'}{\Psi_{\rm search}} \qquad (2)$$

Maximizing this significance estimator gives an optimal search bin radius of $0.7°$. This analysis uses square bins with an area equal to that of the optimized round bin, with side length $1.25°$.

C. Calculating significance

To show that the data are stable in right ascension α, we show, in Fig. 4, the number of events in the central declination band. The errors shown are $\sqrt{N}$. The average of all bins excluding the Moon bin is 27747, which is plotted as a line to guide the eye. The Moon bin has 852 events below this simple null estimate. This represents a 5.2σ deficit using $\sqrt{N}$ errors.

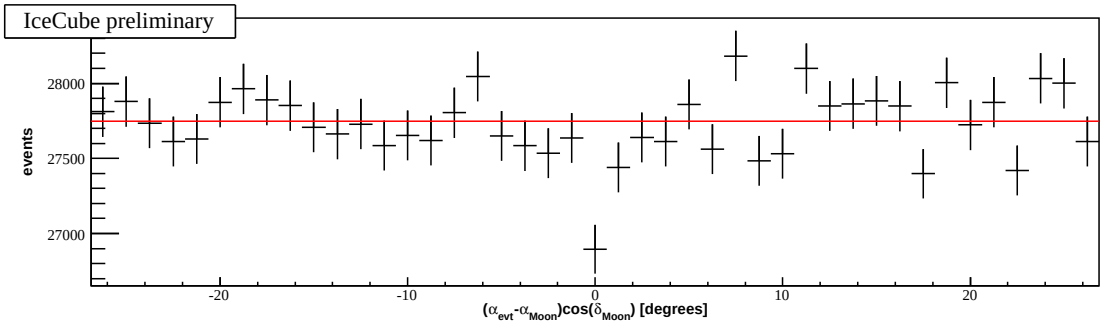

Fig. 4. Number of events per $1.25°$ square bin, relative to the position of the Moon. The declination of the reconstructed track is within $0.625°$ bin from the declination of the Moon. The average of all bins except the Moon bin is shown as a redline to guide the eye.

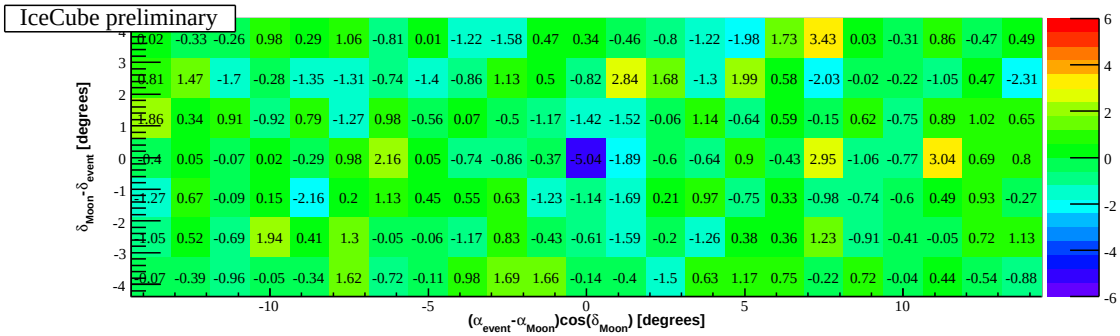

Fig. 5. The significance of deviations in a region centered on the Moon.

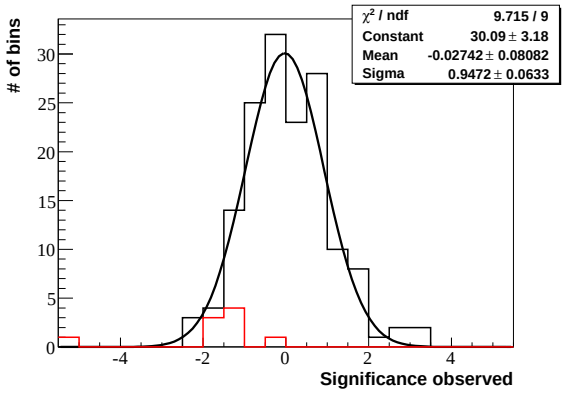

Fig. 6. Each of the deviations shown in Fig. 5 is plotted here. The deviations of the central 9 bins are shown in red. The surrounding bins are shown with a black line histogram, and fit with a Gaussian curve.

Although this shows that the data are stable, this error system is vulnerable to variations in small data samples. Although we don't see such variations here, we considered it prudent to consider an error system which takes into account the size of the background sample.

We used a standard formula from Li and Ma [9] for calculating the significance of a point source:

$$S = \frac{N_{\rm on} - \alpha N_{\rm off}}{\sqrt{\alpha(N_{\rm on} + N_{\rm off})}}. \qquad (3)$$

where $N_{\rm on}$ is the number of events in the signal sample, $N_{\rm off}$ is the number of events in the off-source region, and α is the ratio between observing times on- to off-source. We take α instead as the ratio of on- to off-source areas observed, since the times are equal.

The above significance formula is applied to the Moon data sample in the following way. The data are first plotted in the standard Moon-centered equatorial coordinates, correcting for projection effects with a factor of $\cos(\delta)$. The plot is binned using the $1.25° \times 1.25°$ bin size optimized in the simulation study. Each bin successively is considered as an on-source region. There is a very strong declination dependence in the downgoing muon flux, so variations of the order of the Moon deficit are only detectable in right ascension. Thus, off-source regions are selected within the same zenith band as the on-source region. Twenty off-source bins are used for each calculation: ten to the right and ten to the left of the on-source region, starting at the third bin out from the on-source bin (i.e., skipping two bins in between).

III. Results

For a region of 7 bins or $8.75°$ in declination δ and 23 bins or $28.75°$ in right ascension α around the Moon, the significance of the deviation of the count rate in each bin with respect to its off-source region was calculated, as described in section II-C. The result is plotted in Fig. 5. The Moon can be seen as the 5.0σ deficit in the central bin, at $(0, 0)$.

To test the hypothesis that the fluctuations in the background away from the Moon are distributed randomly around 0, we plot them in Fig. 6. The central 9 bins, including the Moon bin, are not included in the Gaussian

fit, but are plotted as the lower, shaded histogram. The width of the Gaussian fit is consistent with 1; therefore, the background is consistent with random fluctuations.

IV. Conclusions and Future Plans

IceCube has observed the shadow of the Moon as a 5.0σ deviation from event counts in nearby regions, using data from 8 of the total 13 lunar months in the data taking period with the 40-string detector setup. From this, we can conclude that IceCube has no systematic pointing error larger than the search bin, 1.25°.

In the future, this analysis will be extended in many ways. First, we will include all data from the 40 string detector configuration. We hope to repeat this analysis using unbinned likelihood methods, and to describe the size, shape, and any offset of the Moon Shadow. We will then use the results of these studies to comment in more detail on the angular resolution of various reconstruction algorithms within IceCube. This analysis is one of the only end-to-end checks of IceCube systematics based only on experimental data.

LG acknowledges the support of a National Defense Science and Engineering Graduate Fellowship from the American Society for Engineering Education.

References

[1] G.W. Clark, *Arrival Directions of Cosmic-Ray Air Showers from the Northern Sky* October 15, 1957, Physical Review Vol 108, no 2.

[2] A. Karle for the HEGRA collaboration, *The Angular Resolution of the Hegra Scintillation Counter Array at La Palma*, Ann Arbor 1990 Proceedings, High Energy Gamma-Ray Astronomy 127-131.

[3] Giglietto, N. *Performance of the MACRO detector at Gran Sasso: Moon shadow and seasonal variations*, 1997, Nuclear Physics B Proceedings Supplements, Volume 61, Issue 3, p. 180-184.

[4] M.O. Wasco for the Milagro collaboration, *Study of the Shadow of the Moon and the Sun with VHE Cosmic Rays*, 1999 arXiv:astro-ph/9906.388v1

[5] The Soudan 2 collaboration, *Observation of the Moon Shadow in Deep Underground Muon Flux*, 1999 arXiv:hep-ex/9905.044v1

[6] The Tibet AS Gamma Collaboration, M. Amenomori, *et al.* , *Multi-TeV Gamma-Ray Observation from the Crab Nebula Using the Tibet-III Air Shower Array Finely Tuned by the Cosmic-Ray Moon's Shadow*, arXiv:astro-ph/0810.3757v1

[7] L3 Collaboration, P. Achard *et al.* , *Measurement of the Shadowing of High-Energy Cosmic Rays by the Moon: A Search for TeV-Energy Antiprotons* Astropart.Phys.23:411-434,2005, arXiv:astro-ph/0503472v1

[8] D. Heck, J. Knapp, J.N. Capdevielle, G. Schatz, T. Thouw, *CORSIKA: A Monte Carlo Code to Simulate Extensive Air Showers*, FZKA 6019 (1998)

[9] Li, T.-P. and Ma, Y.Q., *Analysis methods for results in gamma-ray astronomy* 1983, ApJ 272,317

IceCube/AMANDA combined analyses for the search of neutrino sources at low energies

Cécile Roucelle*, Andreas Gross*, Sirin Odrowski*, Elisa Resconi*, Yolanda Sestayo*
for the IceCube Collaboration†
**MPIK, Heidelberg, Germany*
†*See the special section of these proceedings*

***Abstract*. During the construction of IceCube, the AMANDA neutrino telescope has continued to acquire data and has been surrounded by IceCube strings. Since the year 2007, AMANDA has been fully integrated for data acquisition and joint IceCube/AMANDA events have been recorded. Because of the finer spacing of AMANDA phototubes, the inclusion of AMANDA significantly extends the detection capability of IceCube alone for low energy neutrinos (100 GeV to 10 TeV). We present the results of two analyses performed on the 2007-2008 Icecube (22 string) and AMANDA data. No evidence of high energy neutrino emission was observed; upper limits are reported.In 2008-09, IceCube acquired data in a 40 string configuration together with the last year of operation of AMANDA. Progress on the analysis of this new combined IceCube/AMANDA sample are presented as well. In addition, a novel method to study an extended region surrounding the most active parts of Cygnus with these datasets is described here.**

***Keywords*: Neutrino astronomy, galactic sources, IceCube, AMANDA, DeepCore**

I. INTRODUCTION

Recent detections by Cherenkov telescopes provide evidence of particle acceleration up to TeV energies in astrophysical sources [1]. The TeV γ-ray emission from these sources could arise from the acceleration of electrons (production of γ-rays via inverse Compton scattering) or the acceleration of hadrons (production of γ-rays through the decay of neutral pions produced in pp/pγ interactions). In the later scenarios, the γ-ray production would be accompanied by the neutrino production since charged pions, like neutral pions, would be generated and decay within the source. The detection of high-energy neutrinos would thus be an unambiguous proof for the acceleration of hadrons in these sources. In particular, galactic TeV γ-ray sources present the bulk of their γ-ray emission at energies lower than a few TeV. The spectrum from these sources is soft with a typical spectral index ($|\Gamma| > 2$) and often exhibits an exponential cut-off at a few TeV. Both observations suggest a break in the neutrino spectrum below 100 TeV. Accordingly, the flux from these sources would differ from the standard spectral index of -2 for neutrino sources. Additionnaly, they represent "low energy" sources (TeV) for IceCube and would be challenging to detect. To enhance the sensitivity to this type of sources, an analysis comprising both the IceCube and the AMANDA detector has been performed. The higher density of optical modules in AMANDA than in IceCube provides a sufficient increase in the number of hits that reconstruction of low energy, neutrino-induced events is possible. This increase in statistics particularly benefits searches for sources with steeply falling spectra (see Sec. III and Sec.IV). A first analysis has been made using the 22 string configuration of IceCube in combination with the AMANDA detector; the results are presented in this proceeding. A new sample of data has been collected with IceCube-40 and AMANDA and is under analysis. We present here the general scheme for this analysis, with particular emphasis on a specific development to enhance the detection sensitivity for extended active regions in the galactic plane.

II. GALACTIC SOURCES : THE γ-ν CONNECTION

Since neutrino and γ-rays are expected to be produced together in hadronic acceleration processes, the neutrino spectrum can be inferred from the observed γ-ray spectrum of the source by a two-step procedure:

1 - The γ-ray spectrum from a source is fitted assuming a pp interaction model obtained using the parametrizations given in [4]. Possible γ-ray absorption is estimated and corrected for before the fit.
2 - With the obtained proton distribution and the target density, the expected neutrino spectrum is estimated.

The Crab Nebula γ-ray energy spectrum has been measured in details by the H.E.S.S. experiment [8]. It is described by a power law with spectral index (Γ) of -2.4 and has a γ-ray energy cutoff at $\sim$14 TeV. Although numerous arguments attribute the γ-ray production from this source to e^+/e^- acceleration, its status as a standard candle argues for its use as a reference for neutrino astronomy. Moreover, the establishment of sufficiently low upper limits by IceCube on the neutrino emission could bring new constraints on the possible hadron acceleration at this source. Assuming that γ-rays from the Crab Nebula originate from hadronic processes (decay of π^0 mesons generated from pp interactions at the source) and that their absoption is negligible, the ν spectrum obtained is:

$$\Phi = 3 \times 10^{-7} e^{-E/7\mathrm{TeV}} (E/\mathrm{GeV})^{-2.4} \mathrm{GeV}^{-1} \mathrm{cm}^{-2} \mathrm{s}^{-1} \quad (1)$$

In the following, we use this computed spectrum as a reference ("Crab Nebula spectrum") to estimate the sensitivity of analyses to low energy sources.

III. ICECUBE-22/AMANDA: RESULTS

During the two deployment seasons 2003-2004 and 2004-2005 at the South Pole, the data acquisition system (DAQ) of AMANDA was significantly upgraded to provide nearly deadtime-less operation and full digitization of the electronic readout [2]. This was achieved by using Transient Waveform Recorders (TWR). The new DAQ system allowed for the reduction of the multiplicity trigger threshold and, consequently, of the energy threshold to $\sim$50 GeV. By being optimally sensitive to neutrinos under 1 TeV, AMANDA thus complements IceCube well and was integrated into the full IceCube analysis starting in January 2006.

A. Data sample and methods

The IceCube 22-string run represents 276 days taken between May 2007 and April 2008. Within this period, the AMANDA detector was taking jointly with IceCube for 143 days. Nevertheless, since the 2006-07 deployment season, every time the AMANDA detector is triggered, a readout request is sent to the IceCube detector. Events are then merged for processing. The trigger rates are strongly dominated by downgoing, atmospheric muons produced in cosmic ray air showers above the detector. They outnumber atmospheric neutrinos by a factor $\sim 10^6$. This background is largely eliminated by limiting the analysis to upgoing muons using a fast reconstruction algorithm which is applied to all of the data. The selected events are then further pared down by applying a cpu-intensive, likelihood-based reconstruction algorithm that accounts for the properties of the ice and then cutting on the fit direction and fit quality parameters. In this analysis, these cuts were optimized to obtain the best discovery potential for a source with a "Crab Nebula" spectrum (Eqn. 1). As low energy events are mainly due to the dominant atmospheric neutrino background, a significantly larger number of events is obtained with this selection than with other IceCube-22 point source searches [12].

In total, 8727 events are selected, of which 3430 are combined IceCube/AMANDA events. Despite the smaller size of AMANDA (1/6 of the volume of IceCube-22) and its shorter livetime (less than 60% wrt. IceCube-22), the contribution of AMANDA to the combined detector sample, particularly at low energies, is clearly visible in the energy distribution simulated atmospheric neutrinos retained at the final event selection in the analysis (Fig. 1). As a consequence, the sensitivity achieved with this approach for a source with a spectrum similar to the one expected for the Crab Nebula (Γ=-2.4; cut-off at 7 TeV) is better than the one achieved with the IceCube only analysis (Fig. 2). Even though, for a harder spectrum (Γ=-2;no cutoff), the standard IceCube only analysis remains better adapted.

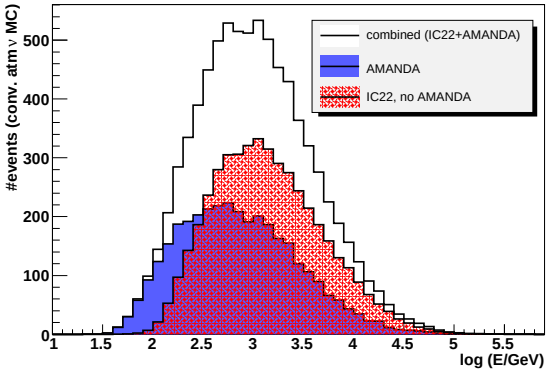

Fig. 1. Event energy distribution for simulated atmospheric neutrinos at the final level of the galactic point source analysis normalized to the livetime of the IceCube 22 strings data taking (276 days) for IceCube only events and to the combined IceCube+AMANDA livetime (143 days) for the AMANDA and combined events.

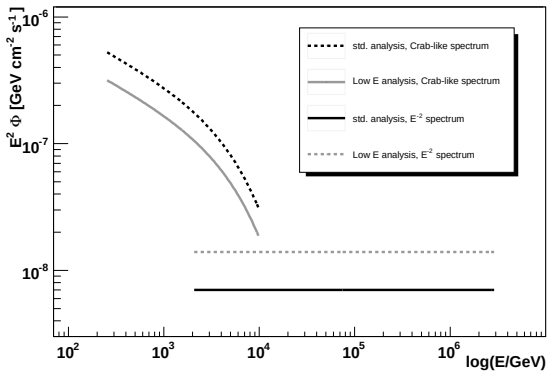

Fig. 2. Sensitivity for a source spectrum with Γ=-2 and a "Crab" spectrum (Γ=-2.4; cut-off at 7 TeV). This analysis (gray) is compared to the standard IceCube only analysis (black).

B. Search on an a priori selected list of point sources

With this dataset, a search for neutrino emission was performed for a list of four, preselected sources: the Crab Nebula, Cas A, SS 433 and LS I +61 303. For three of them, the γ-ray spectrum is known ([8]-[11]), so we optimized the analysis for the expected corresponding neutrino spectrum (for SS 433, which has no measured γ-ray spectrum, the optimisation was made with respect to a test spectrum with a spectral index Γ=-2.4 and a cut-off at 7 TeV). The test-statistic for the analysis is the log likelihood ratio of the signal hypothesis with best fit parameters to the pure background hypothesis. This method is widely used in IceCube [7]. This test-statistic provides an estimate for the significance of a deviation from background (pre-trial p-value) at a position in the sky. The post-trial p-value is then determined by applying the analysis to randomized samples. With this method, the lowest pre-trial p-value (p=0.14) was obtained for the Crab Nebula. This p-value or a lower one can be achieved in 37% of randomized samples. This excess is therefore not significant. The number of

signal events detected and their associated pre-trial p-values are summarized in the table below. Based on the γ-ray observations, the expected neutrino spectral index and possible cut-off energies have been calculated using the method described in Sec. II and are indicated in the same table.

Source	Γ_ν	ν cut-off	Nb. of signal events	p-value (pre-trial)
Crab Nebula	-2.39	7 TeV	3.3	0.14
Cas A	-2.4	-	-1.9	0.65
SS433	-	-	-0.9	0.67
LSI+61 303	-2.8	-	-0.4	0.47

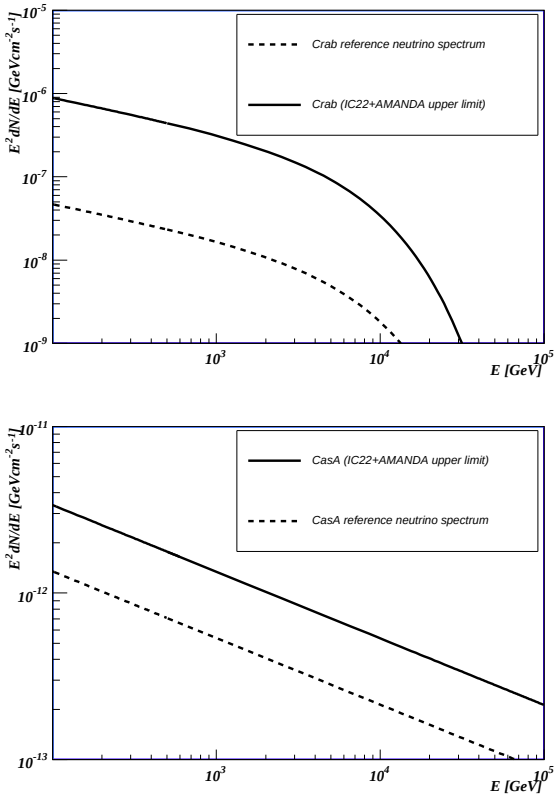

Fig. 3. *Top:* Crab upper limit obtained for this study compared to the reference neutrino spectrum computed for the Crab as in section II using [4] for modeling. *Bottom:* Cas A upper limit obtained for this study compared to its reference neutrino spectrum.

Upper limits on the neutrino flux were derived from the number of events observed in the direction of the different sources with this analysis. The limits obtained for the Crab Nebula and Cas A are presented in Fig. 3 and compared to their expected neutrino spectrum. The limit that can be set by this IceCube-22/AMANDA analysis is for example for the Crab Nebula a factor 18.9 above the expected reference spectrum. This calculation was also made for the case of Cas A (Fig. 3, bottom). This source was detected by HEGRA up to 10 TeV without evidence of high energy cut-off [9]. We extrapolate the power-law γ-ray spectrum given in [10] up to higher energies.

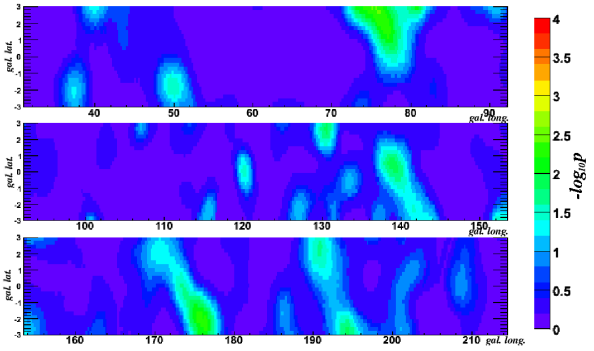

Fig. 4. Galactic plane scan (longitude : $31.5° < l < 214.5°$, latitude : $-3° < b < 3°$) pretrial significance map for IceCube-22/AMANDA. The strongest excess at l=75.875°, b=2.675° (pre-trial p-value = 0.0037). 95% of randomized datasets yielded a more significant excess.

C. Galactic plane scan

In addition to these sources, we performed an unbinned point source search of the galactic plane in the nominal field of view of IceCube (longitude : 31.5°<l<214.5°, latitude -3°<b<3°). The result of this search is shown Fig. 4. The most significant deviation from background observed in this galactic plane unbiased search is seen at l=75.875°, b=2.675° in galactic coordinates. The pre-trial p-value at this location is 0.0037. For 95% of the randomized datasets (reproducing a pure background hypothesis) an equal or lower probability is found and thus the observed excess is not significant.

IV. IceCube-40/AMANDA: expectations

A. Data sample

For the dataset acquired between April 17, 2008 and February 2nd 2009 with the IceCube 40 strings configuration, the total livetime of the IceCube was 268.7 days, and the AMANDA sub-detector performed much better than for the 2007/8 season with a total livetime of 240 days on the same period, corresponding to almost 90% of the IceCube livetime. As a consequence, even with the doubling of the size of IceCube, the relative number of combined IceCube-40/AMANDA events compared to the IceCube-40 only events remain comparable to the ratios obtained with the IceCube-22/AMANDA dataset. The data is still under processing for the selection of neutrino candidates and final exploitation will be made in the near future. Beyond replicating the galactic plane scan and the search for the same list of *a priori* selected sources with these new data, we will search for multiple unresolved sources in the Cygnus region applying a new analysis strategy.

B. Extended sources: Multi-Point Source analysis

A particular interest is given to active regions of the galactic plane, where several accelerators might contribute to a possible neutrino signal. The Cygnus region is a very active star-forming region located at

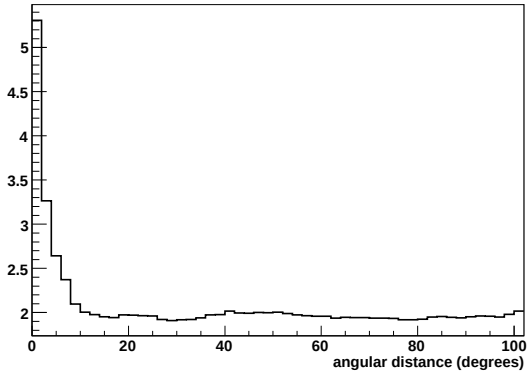

Fig. 5. Number of event pairs (distant of less than 2°) for the signal case divided by the average histogram of random cases with the MPS method for a simulated case presenting 3 sources (yielding each 8 events in the detector) randomly distributed in a region of 11°x7°.

galactic longitude $65^\circ < l < 85^\circ$. Recently, the Milagro collaboration measured both a diffuse TeV γ-ray emission and a bright, extended TeV source [5]. These observations suggest the presence of cosmic rays sources which accelerate hadrons that subsequently interact with the local, dense interstellar medium to produce γ-rays and possibly neutrinos through pion decay. Estimates of the neutrino emission from the zone of diffuse γ-ray emission are reported in [6].

The current point source search method is optimized for resolveable sources. However, to study extended regions like the Cygnus region, this method is not optimal. A better analysis for these cases takes advantage of the possibility of clustering of neutrino events in the totality of the region to improve the detection probability. In this multi-point source (MPS) analysis, we construct a two-point correlation function in which each neutrino candidate that pointed inside the region of study is paired with all other neutrino candidates. A test statistic is then obtained from the number of "close" pairs for which the angular separation is at most 2 degrees, the bin size for achieving the best signal to noise ratio (for IceCube-22/AMANDA data). An excess in the number of these close pairs would indicate an emission from astrophysical sources in the chosen region. This method is sensitive not only to clustered signal that would come from a single source, but also would take advantage of the presence of a diffuse signal.

To illustrate the potential of this method, we give an example of its performance for the IceCube-22/AMANDA configuration. Using the point-spread function obtained from the data (median value: 1.5°), we inserted simulated neutrino events from three possible sources in the IceCube-22/AMANDA dataset. Each simulated source yielded eight events in the detector and was positioned randomly within a region of 11°x7° centered around Cygnus. Fig. 5 shows the histogram of event pairs for the signal case divided by the average histogram of random cases. The first bin thus corresponds to the excess of "close pairs". In order to evaluate the significance associated with this excess, the number of close pairs in 10^7 scrambled sky maps is used. The excess obtained in this example has a p-value of 3×10^{-7}, corresponding to a 5σ detection. For the same configuration, the standard point source analysis [12] is less sensitive as it would require 11 events from each of the sources to reach a detection at the 5σ level (instead of just 8). This analysis will be applied to the unblinded data for IceCube-22/AMANDA and IceCube-40/AMANDA in the near future. For IceCube-22/AMANDA, we will use a region surrounding the most active sources observed by Milagro on Cygnus to define our primaries ($72^\circ < l < 83^\circ$; $-3^\circ < b < 4^\circ$).

V. Conclusion and outlook

Numerous galactic sources observed with γ-rays present a soft spectrum and possibly a cut off at an energy E <100 TeV. Under the hypothesis that acceleration of hadrons explains the γ-ray emission, the associated neutrino spectrum should exhibit a similar cut-off. The merging of the AMANDA and IceCube detector offers an enhancement in sensitivity for the search for these sources. The results of the IceCube-22/AMANDA configuration show no significant excess either for a systematic galactic plane scan on the parts visible for IceCube or for a list of *a priori* selected sources. The data acquired with the IceCube-40/AMANDA configuration are under study and an additional analysis allowing the investigation of the extended Cygnus region will be added. The AMANDA detector, which was shut down on May 15, 2009 as part of the startup of the physics run for the IceCube 59-string configuration detector, paved the road for the development of a nested, higher granularity detector array within IceCube. A new detector array of this type, called "IceCube DeepCore", is under construction [13]. It will consist of at least six strings instrumenting the deep ice (below 2100m) deployed in the center of IceCube and will be completed during the 2009-2010 deployment season.

References

[1] F. A. Aharonian et al., 2006a, ApJ, **636**, 777
[2] W. Wagner, [AMANDA Coll.], ICRC 2003
[3] A. Gross, C. Ha, C. Rott, M. Tluczykont, E. Resconi, T. DeYoung, G. Wikstroḿ, [IceCube Coll.], ICRC 2007, arXiv:0711.0353
[4] S. R. Kelner et al. 2006, PhRvD, **74**, 034018
[5] A. A. Abdo et al, ApJ, **688**, 1078, arXiv:0805.0417
[6] S. Gabici, A. M. Taylor, R. J. White, S. Casanova, F. A. Aharonian, Astropart.Phys. 29 (2008) 180. arXiv:0806.2459
[7] J.Braun et al., Astropart. Phys. 29 (2008) 299.
[8] F. Aharonian et al. [H.E.S.S. coll], A&A **457** (2006)899.
[9] F. Aharonian et al. [H.E.S.S. coll], A&A, **370** (2001)112
[10] J. Albert et al., A&A, **474**, (2007)937
[11] J. Albert et al., 2006, Sci, **312**, 1771
[12] R. Abbasi et al. [IceCube coll], under pub., arXiv:0905.2253
[13] C. Wiebusch [IceCube coll.] these proceedings

AMANDA 7-Year Multipole Analysis

Anne Schukraft*, Jan-Patrick Hülß* for the IceCube Collaboration†

**III. Physikalisches Institut, RWTH Aachen University, Germany*
†*see the special section of these proceedings*

***Abstract*. The multipole analysis investigates the arrival directions of registered neutrino events in AMANDA-II by a spherical harmonics expansion. The expansion of the expected atmospheric neutrino distribution returns a characteristic set of expansion coefficients. This characteristic spectrum of expansion coefficients can be compared with the expansion coefficients of the experimental data. As atmospheric neutrinos are the dominant background of the search for extraterrestrial neutrinos, the agreement of experimental data and the atmospheric prediction can give evidence for physical neutrino sources or systematic uncertainties of the detector. Astrophysical neutrino signals were simulated and it was shown that they influence the expansion coefficients in a characteristic way. Those simulations are used to analyze deviations between experimental data and Monte Carlo simulations with regard to potential physical reasons. The analysis method was applied on the AMANDA-II neutrino sample measured between 2000 and 2006 and results are presented.**

***Keywords*: Neutrino astrophysics, Anisotropy, AMANDA-II**

I. Introduction

The AMANDA-II neutrino detector located at South Pole was constructed to search for astrophysical neutrinos. These neutrinos could originate from many different Galactic and extragalactic candidate source types such as Active Galactic Nuclei (AGN), supernova remnants and microquasars. The detection of neutrinos is based on the observation of Cherenkov light emitted by secondary muons produced in charged current neutrino interactions. This light is observed by photomultipliers deployed in the Antarctic ice. Their signals are used to reconstruct the direction and the energy of the primary neutrino.

AMANDA-II took data between 2000 and 2006. The background of atmospheric muons is reduced by selecting only upward-going tracks in the detector, as only neutrinos are able to enter the detector from below. This restricts the field of view to the northern hemisphere.

The data is filtered and processed to reject misreconstructed downward-going muon tracks [1]. The final data sample contains 6144 neutrino induced events between a declination of 0° and $+90^\circ$ with a purity of $> 95\%$ away from the horizon.

II. Analysis Principle

The idea of this analysis is to search for deviations of the measured AMANDA-II neutrino sky map from the expected event distribution for atmospheric neutrinos, which constitute the main part of the data sample [2]. A method to study such anisotropies is a multipole analysis, which was also used to quantify the Cosmic Microwave Background fluctuations. The analysis is based on the decomposition of an event distribution $f(\theta,\phi) = \sum_{i=1}^{N_{\text{events}}} \delta(\cos\theta_i - \cos\theta)\delta(\phi_i - \phi)$ into spherical harmonics $Y_l^m(\theta,\phi)$, where θ and ϕ are the zenith and azimuth of the spherical analysis coordinate system. The expansion coefficients are

$$a_l^m = \int_0^{2\pi} d\phi \int_{-1}^{1} d\cos\theta \; f(\theta,\phi) Y_l^{m*}(\theta,\phi). \qquad (1)$$

They provide information about the angular structure of the event distribution $f(\theta,\phi)$. The index l corresponds to the scale of the angular structure $\delta \approx \frac{180^\circ}{l}$ while m gives the orientation on the sphere. The expansion coefficients with $m = 0$ depend only on the structure in the zenith direction of the analysis coordinate system. Averaging over the orientation dependent a_l^m yields the multipole moments

$$C_l = \frac{1}{2l+1} \sum_{m=-l}^{+l} |a_l^m|^2. \qquad (2)$$

They form an angular power spectrum characteristic for different input neutrino event distributions.

The initial point of this analysis is the angular power spectrum of only atmospheric neutrino events. Therefore, neutrino sky maps containing 6144 atmospheric neutrino events according to the Bartol atmospheric neutrino flux model [3] are simulated and numerically decomposed with the software package GLESP [4]. Statistical fluctuations are considered by averaging over 1000 random sky maps, resulting in a mean $\langle C_l \rangle$ and a statistical spread σ_{C_l} of each multipole moment.

The same procedure is applied to simulated sky maps containing atmospheric and different amounts of signal neutrinos with a total event number of likewise 6144 events. The influence of the signal neutrinos on the angular power spectrum is studied in terms of the pulls

$$d_l = \frac{\langle C_l \rangle - \langle C_{l,\text{atms}} \rangle}{\sigma_{C_{l,\text{atms}}}}. \qquad (3)$$

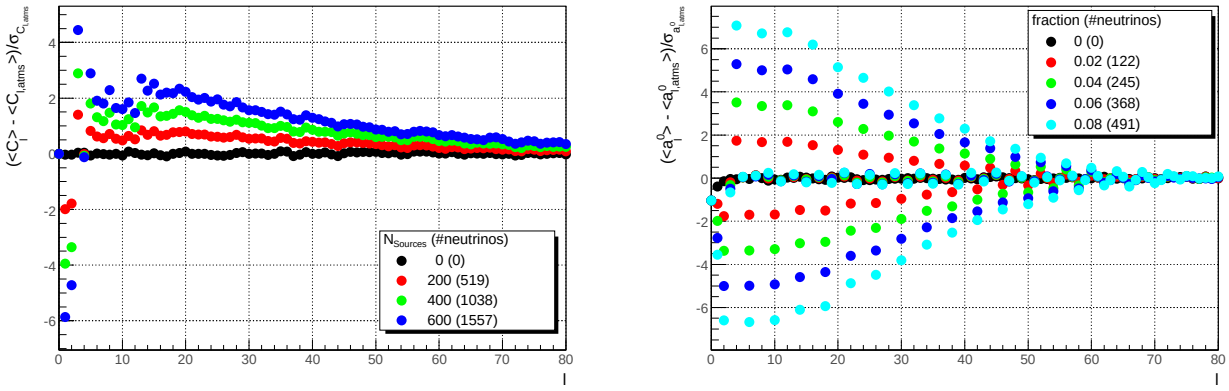

(a) (b)

Fig. 1. (a): Pull plot for the multipole moments C_l of the isotropic point source model. Sources are simulated with a mean source strength $\mu = 5$ and an E_ν^{-2} energy spectrum. The number of sources N_{sources} on the full sphere is varied. The corresponding number of signal neutrinos on the northern hemisphere is given in brackets. The errors bars are hidden by the marker symbols. (b): Pull plot for the expansion coefficients a_l^0 of the cosmic ray interaction model with the Galactic plane in Galactic coordinates. The fraction of neutrinos in the sky map originating from the Galactic plane is varied. The corresponding number of signal neutrinos is given in brackets. The errors bars are hidden by the marker symbols.

III. Signal Simulation

The different models for candidate neutrino sources investigated in this analysis are:

1) Isotropically distributed point sources
2) A diffuse flux from FR-II galaxies and blazars [5]
3) AGN registered in the Véron-Cetty and Véron (VCV) catalog [6]
4) Galactic point sources such as supernova remnants or microquasars
5) Cosmic rays interacting in the Galactic plane.

All simulated pointlike neutrino sources are characterized by a Poissonian distributed source strength with mean μ and an energy spectrum $E_\nu^{-\gamma}$. The relative angular detector acceptance depends on the neutrino energy and therefore on the spectral index of the simulated neutrino source. Signal neutrinos are simulated according to this acceptance considering systematic fluctuations. The total number of signal neutrinos in a sky map of the northern hemisphere with N_{sources} simulated sources on the full-sky is therefore given by $\sim 0.5 \cdot \mu \cdot N_{\mathrm{sources}}$. Additionally the angular resolution is taken into account. It dominates over the uncertainty between the neutrino and muon direction.

The spectral index of pointlike sources is varied between $1.5 \leq \gamma \leq 2.3$. As the spectral index of atmospheric neutrinos is close to 3.7, signal and background neutrinos underlie different angular detector acceptances. Thus, additionally to the clustering of events around the source directions also the shape of the total angular event distribution is used to identify a signature of signal neutrinos in the angular power spectrum [7].

Neutrinos from our Galaxy disturb the atmospheric event distribution by their bunching within the Galactic plane modeled by a Gaussian band along the Galactic equator. Neutrinos produced in cosmic ray interactions with the interstellar medium of our Galaxy are assumed to follow the $E^{-2.7}$ primary energy spectrum.

A further topic (model 6) that can be studied with a multipole analysis are neutrino oscillations. The survival probability of atmospheric muon neutrinos depends on the neutrino energy and the traveling length of the neutrino as well as the mixing angle θ_{23} and the squared mass difference Δm^2_{23}. The traveling length can be expressed by the Earth's radius and the zenith angle of the neutrino direction [7]. Thus, the neutrino oscillations disturb the angular event distribution of atmospheric neutrinos. With the assumption of $\sin^2(2\theta_{23}) \approx 1$ the squared mass difference remains for investigation. Due to the relatively high energy threshold of 50 GeV the effect is small.

IV. Evaluation of the Power Spectra

The deviations from a pure atmospheric angular power spectrum caused by signal neutrinos are studied by the pulls. These pulls are exemplarily shown in Fig. 1a for the model of isotropic point sources. The behaviour of the pulls is characteristic for each signal model. Different multipole moments carry different sensitivity to the neutrino signal. The absolute value of the pull increases linearly with the amount of signal neutrinos in the sky maps. Each pull has a predefined sign.

The deviation of a particular sky map with multipole moments C_l from the pure atmospheric expectation $\langle C_{l,\mathrm{atms}} \rangle$ is quantified by a significance indicator D^2 defined as

$$D^2 = \frac{1}{l_{\max}} \sum_{l=1}^{l_{\max}} \mathrm{sgn}_l \cdot w_l \cdot \left(\frac{C_l - \langle C_{l,\mathrm{atms}} \rangle}{\sigma_{C_{l,\mathrm{atms}}}} \right)^2, \quad (4)$$

where $l_{\max}$ determines the considered multipole moments. The term in brackets is the pull between the

particular sky map and the mean of the atmospheric expectation as defined in Eq. 3. The factors

$$w_l = \frac{\langle C_l \rangle - \langle C_{l,\mathrm{atms}} \rangle}{\sqrt{\sigma^2_{C_l} + \sigma^2_{C_{l,\mathrm{atms}}}}} \quad (5)$$

are defined to weight the pulls according to their expected sensitivity to the signal. For each neutrino signal model one dedicated set of weights w_l is determined. Due to the linear increase of the pulls with the signal strength the strength chosen to calculate w_l is arbitrary.

The weight factors w_l carry the expected sign of the pulls. sgn_l is the sign of the measured pull. Thus, the D^2 calculated for the particular sky map is increased if the observed deviation has the direction expected for the signal model and reduced otherwise.

Due to the weighting of the pulls, the sensitivity becomes stable for high $l_{\max}$. A choice of $l_{\max} = 100$ is sufficient to provide best sensitivity to all investigated signal models.

The D^2 of a sky map is interpreted physically by the use of confidence belts. Therefore, 1000 sky maps for every signal strength within a certain range are simulated and the D^2-value for each sky map is calculated separately to obtain the D^2 distributions. The calculation of the average upper limit at 90% confidence level assuming zero-signal is used to estimate the sensitivity of the analysis to different astrophysical models apriori.

As the multipole analysis is applied to a wide range of astrophysical topics, the trial factor of the analysis becomes important. The trial factor raises with each new set of weights used to evaluate the experimental data. For this reason, models with almost similar weights are combined to a common set of weights and only six sets are remaining.

If the signal signatures show up only in the zenith direction of the analysis coordinate system the expansion coefficients a_l^0 are more sensitive than the multipole moments C_l. The reason is, that the expansion coefficients with $m = 0$ are independent from the azimuth ϕ and contain the pure information about the zenith direction θ. A signal only depending on θ causes only statistical fluctuations but no physical information in the other expansion coefficients. Therefore, the signal has only power in the a_l^0. The analysis method stays exactly the same in these cases, except that all C_l are replaced by the a_l^0. This is related to the models of neutrinos from the Galactic plane and from sources of the VCV catalog, which show north-south-symmetries of the neutrino signals in Galactic and supergalactic coordinates, respectively. Unlike the multipole moments C_l, the a_l^0 do not average over different orientations. Therefore, the analysis of the a_l^0 strongly depends on the used coordinate system. An example for pulls of a_l^0 for the model of a diffuse neutrino flux from the Galactic plane is shown in fig. 1b. The characteristic periodic behavior of the pulls is explained by the symmetry properties of the spherical harmonics.

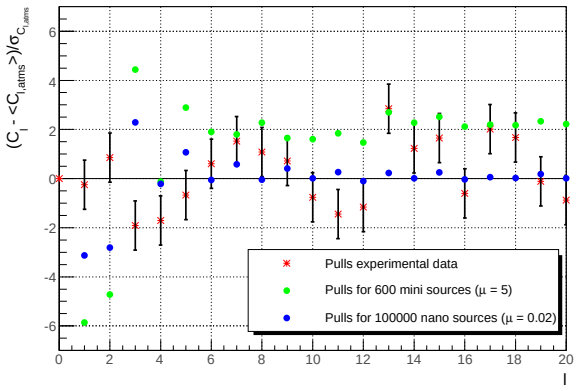

Fig. 2. Pull plot for the experimental multipole moments C_l. Expected pulls for typical model parameters of isotropic point sources are shown for comparison. The error bars symbolize the statistical fluctuation expected for an atmospheric neutrino sky map.

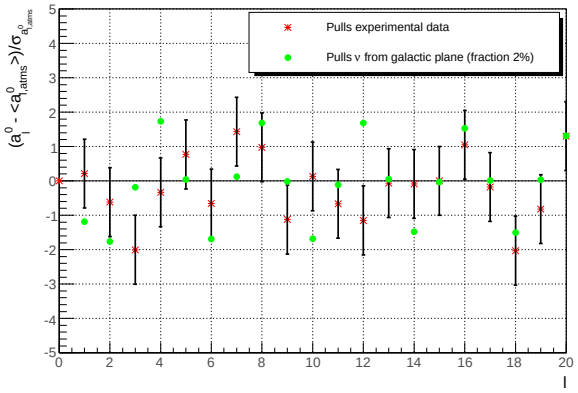

Fig. 3. Pull plot for the experimental expansion coefficients a_l^0 in Galactic coordinates. Expected pulls for typical parameters of cosmic ray interactions with the Galactic plane are shown for comparison. The error bars symbolize the statistical fluctuation expected for an atmospheric neutrino sky map.

V. Experimental Results

The experimental data is analyzed in two steps. First, the experimental data is tested for its compatibility with the pure atmospheric neutrino hypothesis. Secondly, the experimental pulls are compared with the expectations for the different investigated neutrino models.

The pulls of the experimental data are shown for the multipole moments C_l in Fig. 2 and for the expansion coefficients a_l^0 in Galactic coordinates in Fig. 3. To compare the measured data with the expected event distribution, a D^2 is calculated for the multipole moments C_l and the expansion coefficients a_l^0 for transformations into equatorial, Galactic and supergalactic coordinates separately. As no signal model is tested $\mathrm{sgn}_l = w_l = 1$ is assumed. A comparison with the corresponding D^2 distributions results in the p-values giving the probability to obtain a D^2 which is at least as extreme as the measured one assuming that the pure atmospheric neutrino hypothesis is true (Table I).

The statistical consistency of C_l and a_l^0 in equatorial coordinates with the atmospheric expectation is marginal. Rotating to inclined coordinate systems, e.g. Galactic and supergalactic, the consistency improves. The deviation from the pure atmospheric expectation is not compatible with any of the signal models (see Fig. 2, 3 for examples). The discrepancy may be attributed to uncertainties in the theoretical description of the atmospheric neutrino distribution, or to a contribution of unsimulated background of down-going muons misreconstructed as up-going, or to the modeling of properties of the AMANDA detector.

TABLE I
P-VALUES FOR THE COMPATIBILITY OF EXPERIMENTAL DATA AND PURE ATMOSPHERIC NEUTRINO HYPOTHESIS.

Observable	p-value
C_l	0.02
a_l^0, Equatorial	0.02
a_l^0, Galactic	0.15
a_l^0, Supergalactic	0.70

The signal models are tested by calculating the D^2-values of the experimental data using the corresponding sign and weight factors. As the observed deviations do not fit any of the investigated signal models the physical model parameters are constrained. Due to the observed systematic effects affecting mainly the multipole moments C_l and the equatorial expansion coefficients a_l^0 no limits on the models analyzed in the corresponding coordinate systems (models 1, 2 and 6) are derived. The other models are less affected. The limits given below do not include these systematic effects.

A limit on the source strength assuming the VCV source distribution (model 3) is calculated for those sources closer than 100 Mpc to the Earth. In this model all sources are expected to have the same strength and energy spectrum. For a typical spectral index of $\gamma = 2$ the average source flux is limited by the experimental data to a differential source flux of $\mathrm{d}\Phi/\mathrm{d}E \cdot E^2 \leq 1.6 \cdot 10^{-10}\,\mathrm{GeV\,cm^{-2}\,s^{-1}\,sr^{-1}}$ in the energy range between 1.6 TeV and 1.7 PeV.

For the random Galactic sources (model 4), the number of sources is constrained assuming the same source strength and energy spectrum for all sources as well. For a spectral index of $\gamma = 2$, the limit on the number of sources is set by AMANDA to $N_{\mathrm{sources}} \leq 39$ assuming a source strength of $\mathrm{d}\Phi/\mathrm{d}E \cdot E^2 \leq 10^{-8}\,\mathrm{GeV\,cm^{-2}\,s^{-1}\,sr^{-1}}$ or $N_{\mathrm{sources}} \lesssim 4300$ for sources with $\mathrm{d}\Phi/\mathrm{d}E \cdot E^2 \leq 10^{-10}\,\mathrm{GeV\,cm^{-2}\,s^{-1}\,sr^{-1}}$. For source fluxes in between the limit can be approximated by assuming linearity between N_{sources} and $\log\left(\mathrm{d}\Phi/\mathrm{d}E \cdot E^2\right)$.

The differential flux limit obtained from the experimental data on the diffuse neutrino flux from cosmic ray interactions in the Galactic plane (model 5) is $\mathrm{d}\Phi/\mathrm{d}E \cdot E^{2.7} \leq 3.2 \cdot 10^{-4}\,\mathrm{GeV^{1.7}\,cm^{-2}\,s^{-1}\,sr^{-1}}$. This flux limit is shown in Fig. 4 together with the results of two other AMANDA analyses and two theoretical flux predictions. The seven year multipole analysis provides currently the best limit. However, it is still not in reach of the theoretical predictions.

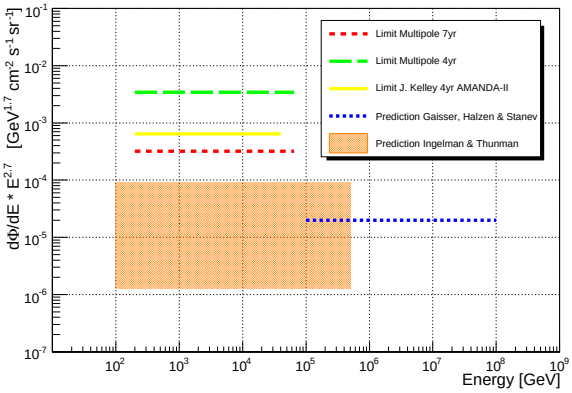

Fig. 4. Limit of the 7yr multipole analysis on the diffuse neutrino flux from cosmic ray interactions in the Galactic plane in dependence of the valid energy range. The limit is compared with two other analyses [2], [8] and two theoretical predictions [9], [10].

VI. Conclusion

It is shown that the multipole analysis is sensitive to a wide range of physical topics. Its area of application is in particular the field of many weak sources in transition to diffuse fluxes. With the statistics of seven years of AMANDA data and improvements of the analysis technique the method is now restricted by systematic uncertainties in the atmospheric neutrino zenith distribution of the order of a few percent. Transforming to coordinate systems less affected by the equatorial zenith angle such as the Galactic and supergalactic system physical conclusions are still possible. A compatibility of the measurement with the background expectation of atmospheric neutrinos is observed. Current efforts to better understand the observed systematics would allow an application of the multipole analysis on future high statistic IceCube data.

References

[1] R. Abbasi et al., Phys. Rev. D 79, 062001 (2009).
[2] J.-P. Hülß, Ch. Wiebusch for the IceCube Collaboration, 30^{th} International Cosmic Ray Conference (ICRC 2007), Merida, arXiv:0711.0353.
[3] G. Barr et al., Phys. Rev. D 70, 023006 (2004).
[4] Doroshkevich et al., International Journal of Modern Physics D, Vol 14, No. 2 (2005), http://www.glesp.nbi.dk/.
[5] J. Becker, P. Biermann, W. Rhode, Astroparticle Physics, Vol 23, No. 4 (2005).
[6] M.-P. Véron-Cetty, P. Véron, A&A, 455, 733 (2006).
[7] A. Schukraft, Multipole analysis of the AMANDA-II neutrino skymap, diploma thesis, RWTH Aachen (2009).
[8] J. Kelley for the IceCube Collaboration, 29^{th} International Cosmic Ray Conference (ICRC 2005), Pune, arXiv:0711.0353.
[9] T. Gaisser, F. Halzen, T. Stanev, Phys. Rept., 258:173-236 (1995).
[10] G. Ingelman, M. Thunman, arxiv:hep-ph/9604286 (1996).

This contribution is supported by the German Academic Exchange Service (DAAD).

Measurement of the atmospheric neutrino energy spectrum with IceCube

Dmitry Chirkin* for the IceCube collaboration†

**University of Wisconsin, Madison, U.S.A.*
†*See the special section of these proceedings.*

***Abstract*. The IceCube detector, as configured during its operation in 2007, consisted of 22 deployed cables, each equipped with 60 optical sensors, has been the biggest neutrino detector operating during the year 2007, superseded only by its later configurations. A high quality sample of more than 8500 atmospheric neutrinos was extracted from this single year of operation and used for the measurement of the atmospheric muon neutrino energy spectrum from 100 GeV to 500 TeV discussed here. Several statistical techniques were used in an attempt to search for deviation of the neutrino flux from that of conventional atmospheric neutrino models.**

***Keywords*: atmospheric neutrinos, charm search, IceCube**

I. Introduction

Most of the events recorded by the IceCube detector constitute the background of atmospheric muons that are produced in air showers. Once this background is removed the majority of events that remain are atmospheric neutrino events, i.e., (mostly) muons created by atmospheric neutrinos. Although much smaller, this also constitutes background for the majority of research topics in IceCube (e.g., extra-terrestrial neutrino flux searches), except one: the atmospheric neutrino study. As part of this study we verify that the atmospheric neutrinos observed by IceCube are consistent with previous measurements at lower energies, and agree with the theoretical extrapolations at higher energies. Since much uncertainty remains in the description of the higher energy atmospheric neutrinos, this study could provide interesting constraints on (not yet observed) charm contribution to the atmospheric neutrino production. Since such charm contribution may affect the flux of atmospheric neutrinos in a way similar to extra-terrestrial diffuse contributions, we attempt to look for both simultaneously in a single likelihood approach.

II. Event selection

For this analysis the new machine learning method (*SBM*) described in [1] was employed. The quality parameters used with the event selection method of this paper include and build upon those discussed previously in [2]. Unfortunately the size limit of this proceeding precludes us from discussing all of the event selection quality parameters and techniques; instead we describe one new technique in detail below.

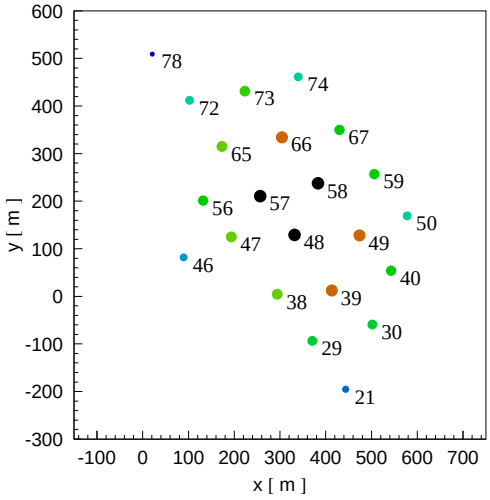

Fig. 1. View of the IceCube 22 string configuration, as used in the run of 2007. The size of the circle and color indicate the relative string weight, used to compute several quality parameters, such as the size of the veto region for contained events, or the total weight, which, much like the number of hit strings, gauges the size of an event and its importance for the analysis.

Events in IceCube are normally formed by the DAQ by combining all hits satisfying the simple majority trigger. The simple majority trigger is defined to combine all hits, which belong to one or more hit sets of at least n different-channel hits within w ns of each other. Typically $n = 8$ or more hits are required to be within $w = 5$ us of each other to satisfy this trigger.

The simple majority trigger combines hits into events only separating them in time. In IceCube a substantial fraction of events so formed turns out to consist of hits originating from two or more separate particles, or bundles of particles, typically unrelated to each other, traveling through well separated (in space) parts of the detector. In order to split up such events and to keep the rate of coincident (now in both time and space) events low, hits in the events were recombined via the use of the *topological trigger*. The definition of this trigger is very similar to that of the simple majority trigger given above: the *topological trigger* combines all *topologically connected* hits, which belong to one or more hit sets of at least n different-channel hits within w ns of each other. Two hits are called *topologically connected* if they satisfy all of the following (the numbers in italics show the values used in the present analysis):

- both hits originate on the detector strings

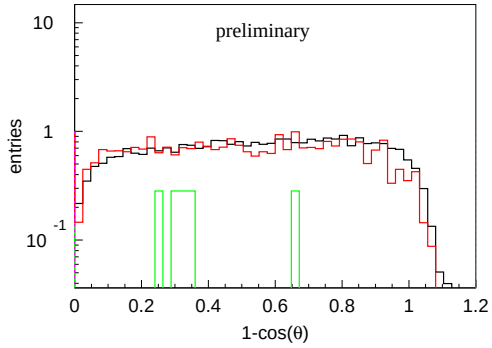

Fig. 2. Zenith angle distribution of remaining data events in 275.5 days of IceCube data (black) comparison with atmospheric neutrino prediction from simulation (red). Several double coincident air shower muon events remain at this level in simulation (shown in green). Vertically up-going tracks are at 0, horizontal tracks are at 1.

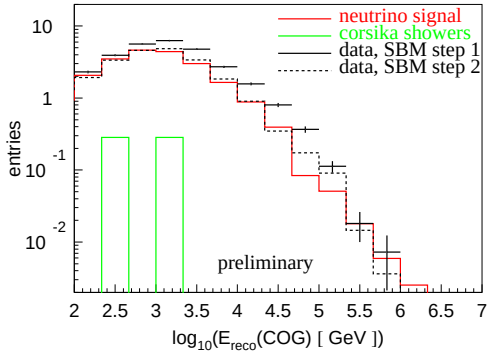

Fig. 3. Reconstructed muon energy at the closest approach point to the center-of-gravity of hits in the event. Data distribution is shown at both steps 1 and 2 of the SBM event selection method [1]. After the $\sim$ 90% purity level is reached in simulation (step 1) it is necessary to remove more events from data that do not look like well-reconstructed muons; this is achieved by comparing data events to simulated muon neutrino events (step 2).

- if both hits are on the same string they should not be separated by more than *30* optical sensors
- the strings of both hits must be within *500* meters of each other
- the $\delta t - \delta r/c$ must be less than *1000* ns.

At least *4* topologically-connected hits within *4* us are required to form a topological triggered set, which is then passed through the simple majority trigger. Just like in the simple majority trigger, the hits not directly connected to each other can belong to the same event if they form topologically-connected sets satisfying the multiplicity condition with at least one and the same hit belonging to both sets.

The required distance between the strings (*500* meters) was left intentionally high to allow easy scaling of the present analysis to higher-string IceCube detector configurations. Still, the rate of unrelated coincident events is much reduced via the use of the topological trigger. More importantly, the fraction of such events after the topological trigger stays at the same low level as the detector grows.

An alternative approach to recognize coincident events by reconstructing them with double-muon hypothesis was tried in a separate effort. In the present work however it is believed that the topological trigger offers several crucial advantages:

- the separation of coincident events is performed at the hit selection level
- the method is faster as it does not require complicated dual-muon fits
- not only 2 but also 3 and more coincident events can be separated
- all of these are kept for the analysis (in the alternative approach coincident events are thrown out)
- noise hits are cleaned very efficiently
- the rate of unresolved coincident events and coincident noise hits is kept at the same low level as the detector grows.

The event selection resulted in 8548 events found in 275.5 days of data of IceCube (see the 22-string configuration in Figure 1), or 31 events per day at $>\sim$ 90% estimated (from simulation) purity level (contaminated by remaining atmospheric muon background). Compare this to expectation from simulation of 29.0 atmospheric neutrino events per day (Figure 2).

III. Atmospheric neutrino spectrum unfolding

Figure 3 compares the measured muon energy distribution for conventional atmospheric neutrino simulation and data at $>\sim$ 90% purity level. The difference between data at steps 1 and 2 of the SBM event selection is due to the presence of events that were unlike those simulated. Such events are removed at step 2 by comparing them to the events in the atmospheric neutrino simulation [1]. At this time the difference between the two data curves should be treated as a measure of (at least some of) the systematic errors introduced by our simulation.

The uncertainty in our measurement of muon energy is $\sim$ 0.3 in $\log_{10}(E_\mu)$ in a wide energy range (from 1 TeV to 100 PeV). A larger smearing, estimated from neutrino simulation (based on [3]), is introduced when matching the muon energy at the location of the detector to the parent neutrino energy.

We tried a variety of unfolding techniques to obtain the distribution of the parent muon neutrinos, including the SVD [4] with regularization term that was the second derivative of the unfolded statistical weight; and iterative Bayesian unfolding [5] with a 5-point spline fit smoothing function (with and without the smearing kernel smoothing). Since we are looking for deviations of the energy spectrum from the power law, the SVD with regularization term that is the second derivative of the log(flux) was selected as our method of choice. Additionally, we chose to include the statistical uncertainties of the unfolding matrix according to [6] (using the equivalent number of events concept as in [7]). The chosen method yielded the most consistent description of spectrum deviations that were studied;

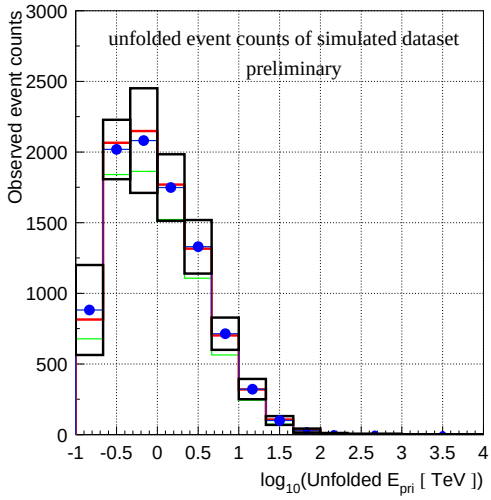

Fig. 4. Unfolded distribution of muon neutrino energies: the original distribution modeled according to [11] (red), median and 90% band of the unfolded result of 10000 simulated sets, drawn from the same simulation (blue dots/lines and black boxes, respectively). A small bias introduced by the regularization term shows up as a slight mismatch between the original and unfolded median bin values. Also shown is the distribution modeled according to [3] (green).

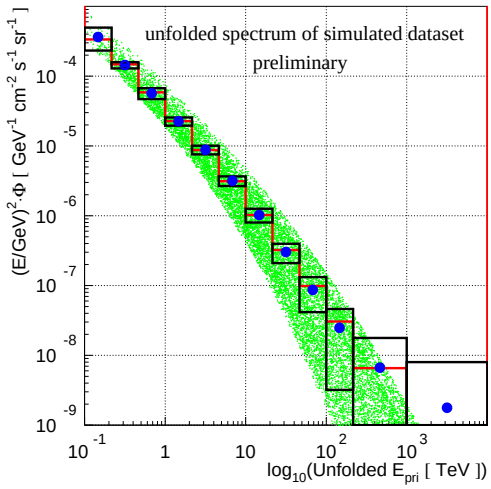

Fig. 5. Unfolded muon neutrino spectrum, averaged over zenith angle, same color designations as in Figure 4. The green points of [3] form a band as they are shown un-averaged, for each zenith angle separately.

also errors estimated from half-width of the likelihood function were reasonable when compared to the spread of unfolded results in a large pool of simulated data sets (see Figures 4 and 5).

It is possible to study the effect of small charm and E^{-2} isotropic diffuse contributions (as the two commonly studied deviations from the conventional neutrino flux models). Injecting known amounts of such contributions into the simulated event sets one computes the 90% confidence belt as in [8], [9], [10] (shown in Figure 6 for statistical weight of events in one of the bins of the unfolded distribution). The following table summarizes the average upper limits for diffuse and RQPM (optimistic) charm models (using conventional neutrino flux description as in [11]):

flux	bin 8	bin 9	bin 10	bin 11
energies, TeV	46.4–	100–	215–	1 – 10 PeV
E^{-2}, $10^{-8}\cdot$	5.48	3.00	3.00	4.06
RQPM (opt) ·	0.74	0.90	1.34	2.44

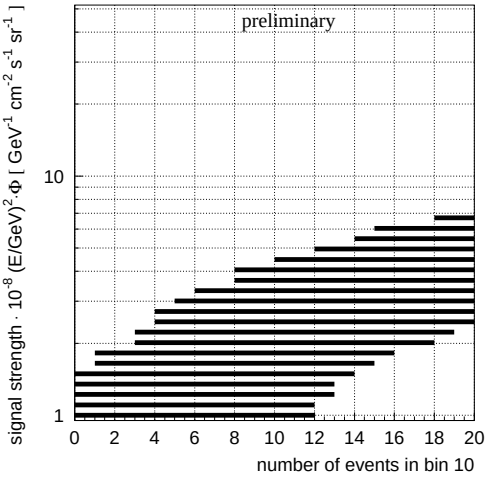

Fig. 6. 90% connfidence belt for E^{-2} isotropic diffuse flux contribution, calculated with 10000 independent simulated sets for bin 10 (neutrino energies 215 TeV-1 PeV)

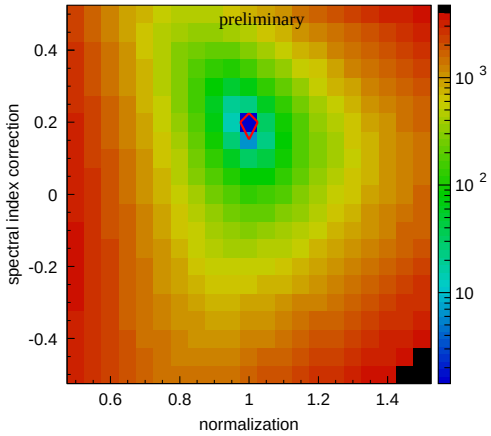

Fig. 7. Likelihood model testing profile for a simulated spectrum with spectral index deviation of $+0.2$ with respect to the reference model. The 90% confidence belt (shown as red contour) is very narrow and widens when systematical errors are taken into account.

IV. Likelihood model testing

The likelihood model testing approach is well-suited to testing the data for specific deviations from the conventional flux model. This approach is based on the likelihood ordering principle of [8] and is easy employ when several deviations are tested for simultaneously [12]. This has recently been used in the analysis of the AMANDA data [13] and is also used in a similar study presented in [14].

As an example, Figure 7 demonstrates the ability to measure the deviation of the conventional flux in overall normalization and spectral index (with 8548 neutrino events in the absence of systematical errors). Figure 8 demonstrates the ability to discern simultaneous charm and diffuse E^{-2} contributions (assuming that the precise

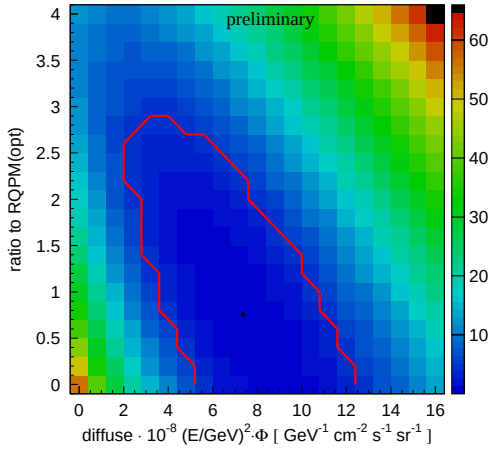

Fig. 8. A 90% confidence belt for a simulated mixed contribution of 2 · RQPM (opt) charm expectation $+6 \cdot 10^{-8} E^{-2}$ isotropic (diffuse) component. This profile includes systematic errors on overall normalization and spectral index of the conventional neutrino flux (allowing them to vary freely).

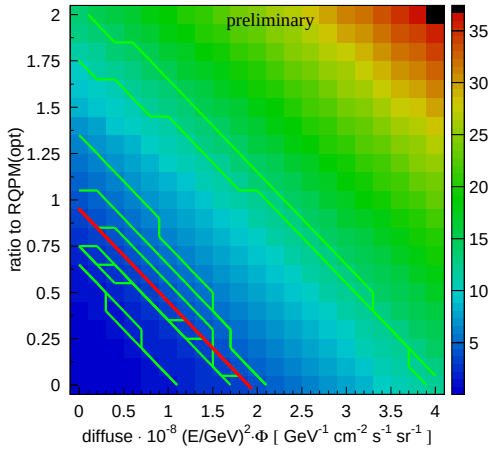

Fig. 9. 90% confidence level upper limit contours shown (in green) for 11 independent simulated data sets (drawn from the same conventional flux parent simulation according to [11]), the "median" upper limit shown in red.

normalization and spectral index of the conventional flux are also unknown). We estimate the median upper limits set by this method on both charm and diffuse E^{-2} components in Figure 9. We used the χ^2 with 2 degrees of freedom approximation to construct the confidence belts; the true 90% levels are even tigher than this (by factor $\sim 1.3 - 1.6$) due to high similarity of effects of both components on the eventual event distribution.

V. Model Rejection Factor

This is a method that optimizes the placement of a cut on the energy observable to maximize sensitivity to an interesting flux contribution, discussed in [15]. The model rejection factor (ratio of $\overline{\mu_{90}}$ to number of expected signal events for a given flux) computed from curves shown in Figure 10 achieves its optimal value with a cut of 224 TeV on the reconstructed muon energy. The corresponding best average upper limit (sensitivity, not including systematics) of $2.14 \cdot 10^{-8}$ is achieved.

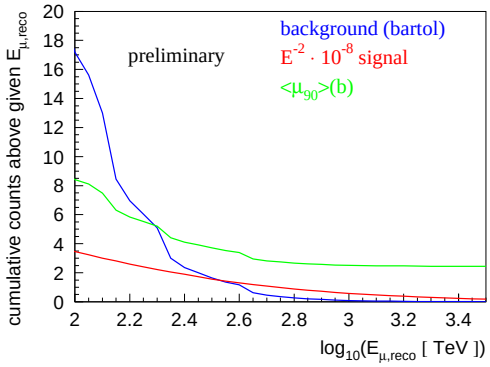

Fig. 10. Cumulative number of E^{-2} diffuse signal events shown in red, number of atmospheric neutrino events shown in blue, the corresponding average upper limit $\overline{\mu_{90}}$ is shown in green.

VI. Conclusions

We present a selection of 8548 muon neutrino events (with $\sim<$ 10% estimated contamintation from the mis-reconstructed air shower muon events) in 275.5 days of IceCube-22 data. An unfolding technique is selected and used to compute the average upper limit on diffuse and charm contributions. We found that the likelihood model testing and the model rejection factor methods both achieve (not surprisingly) somewhat better sensitivities.

Since the study of systematic errors is (at the time of writing of this report) not yet completed, the average upper limits presented here do not contain systematic error effects, and the actual upper limits (or the unfolded spectrum) computed from the data are not yet shown.

References

[1] D. Chirkin, et al., *A new method for identifying neutrino events in IceCube data*, These proceedings
[2] D. Chirkin, et al., *Effect of the improved data acquisition system of IceCube on its neutrino-detection capabilities*, 30th ICRC, Merida, Mexico (arXiv:0711.0353)
[3] M. Honda, et al., Physical Review D, V70, 043008 (2004)
[4] V. Blobel, *An unfolding method for high energy physics experiments*, Advanced statistical techniques in particle physics conference, Durham, 2002
[5] G.D'Agostini, *A multidimensional unfolding method based on Bayes' theorem*, DESY 94-099 (1994)
[6] R. Barlow and Ch. Beeston, *Fitting using finite Monte Carlo samples*, Computer Physics Communications 77 (1993) 219
[7] G. Zech, *Comparing statistical data to Monte Carlo simulation parameter fitting and unfolding*, DESY 95-113 (1995)
[8] G. Feldman and R. Cousins, Physical Review D, V57, 3873 (1998)
[9] K. Münich, J. Lünemann *Measurement of the atmospheric lepton energy spectra with AMANDA-II*, 30th ICRC, Merida, Mexico (arXiv:0711.0353)
[10] S. Gozzini, *Search for Prompt Neutrinos with AMANDA-II*, Ph. D. thesis, Johannes Gutenberg Universität Mainz, 2008
[11] G. Barr, et al., Physical Review D, V70, 023006 (2004)
[12] G. Hill, et al., *Likelihood deconvolution of diffuse prompt and extra-terrestrial neutrino fluxes in the AMANDA-II detector*, 30th ICRC, Merida, Mexico (arXiv:0711.0353)
[13] R. Abbasi et al. (IceCube collaboration), *Determination of the Atmospheric Neutrino Flux and Searches for New Physics with AMANDA-II*, Accepted by Phys. Rev. D., 2009, (arXiv:0902.0675)
[14] W. Huelsnintz and J. Kelley (IceCube collaboration), *Search for quantum gravity with IceCube and high energy atmospheric neutrinos*, these proceedings
[15] G. Hill and K. Rawlins, Astroparticle physics 19 (2003), 393

Atmospheric Neutrino Oscillation Measurements with IceCube

Carsten Rott* **(for the IceCube Collaboration†)**

*Center for Cosmology and AstroParticle Physics, Ohio State University, Columbus, OH 43210, USA
†See special section of these proceedings

***Abstract*. IceCube's lowest energy threshold for the detection of track like events (muon neutrinos) is realized in vertical events, due to IceCube's geometry. For this specific class of events, IceCube may be able to observe muon neutrinos with energies below 100 GeV at a statistically significant rate. For these vertically up-going atmospheric neutrinos, which travel a baseline length of the diameter of the Earth, oscillation effects are expected to become significant. We discuss the prospects of observing atmospheric neutrino oscillations and sensitivity to oscillation parameters based on a muon neutrino disappearance measurement performed on IceCube data with vertically up-going track-like events. We further discuss future prospects of this measurement and the impact of an IceCube string trigger configuration that has been active since 2008 and was specifically designed for the detection of these events.**

***Keywords*: Neutrino Oscillations IceCube**

I. Introduction

The IceCube Neutrino Telescope is currently under construction at the South Pole and is about three quarters completed [1]. Upon completion in 2011, it will instrument a volume of approximately one cubic kilometer utilizing 86 strings, each of which will contain 60 Digital Optical Modules (DOMs). In total, 80 of these strings will be arranged in a hexagonal pattern with an interstring spacing of about 125 m, and 17 m vertical separation between DOMs at a depth between 1450 m and 2450 m. Complementing this 80 string baseline design will be a deep and dense sub-array named DeepCore [2]. For this sub-array, six additional strings will be deployed in the center, in between the regular strings, resulting in an interstring-spacing of 72 m. DeepCore will be densely instrumented in the deep ice below 2100 m, with a vertical sensor spacing of 7 m. This array is specifically designed for the detection and reconstruction of sub-TeV neutrinos. Further, the deep ice provides better optical properties and the usage of high quantum efficiency photomultiplier tubes will enable us to study neutrinos in the energy range of a few tens of GeV. This makes DeepCore an ideal detector for the study of atmospheric neutrino oscillations [2].

In this paper we present an atmospheric neutrino oscillation analysis in progress on data collected with the IceCube 22-string detector during 2007 and 2008. This is an update on a previous report [4], with a larger, more complete background simulation and hence re-optimized selection criteria. An alternative background estimation using the data itself is also discussed.

The goal of this analysis is to measure muon neutrino (ν_μ) disappearance as a function of energy for a constant baseline length of the diameter of the Earth by studying vertically up-going ν_μ. Disappearance effects are expected to become sizable at neutrino energies below 100 GeV in these vertical events. This energy range is normally hard to access with IceCube. However, due to IceCube's vertical geometry, low noise rate, and low trigger threshold the observation of neutrino oscillations through ν_μ disappearance seems feasible. Atmospheric neutrino oscillations have, as of today, not been observed with AMANDA or IceCube.

Based on preliminary selection criteria, we show that IceCube has the potential to detect low-energy vertical up-going ν_μ events and we estimate the sensitivity to oscillation parameters.

II. Atmospheric Neutrino Oscillations

Collisions of primary cosmic rays with nuclei in the upper atmosphere produce a steady stream of muon neutrinos from decays of secondaries ($\pi^\pm, \mathrm{K}^\pm$). These atmospheric neutrinos follow a steeply falling energy spectrum of index $\gamma \simeq 3.7$.

In IceCube these muon neutrinos can be identified through the observation of Cherenkov light from muons produced in charged-current interactions of the neutrinos with the Antarctic ice or the bedrock below. The main difficulty in identifying these events stems from a large down-going high energy atmospheric muon flux, that could produce detector signatures consistent with those produced by up-going muons. These events are the background to this analysis.

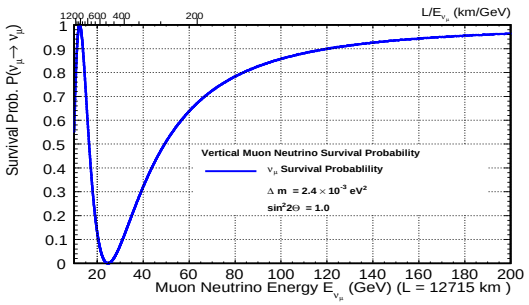

Fig. 1. Muon neutrino survival probability under the assumption of effective 2-flavor neutrino oscillations $\nu_\mu \leftrightarrow \nu_\tau$ as function of energy for vertically traversing neutrinos.

Vertically up-going atmospheric neutrinos travel a distance of Earth diameter, which corresponds to a baseline length L of $12,715$ km. The survival probability for these muon neutrinos can be approximated using the two-flavor neutrino oscillation case and is shown in Figure 1 for maximal mixing and a $\Delta \mathrm{m}^2$ consistent with Super-Kamiokande [6] and MINOS [7] measurements. It illustrates the disappearance effect (large below energies of 100 GeV) we intend to observe.

III. Oscillation Analysis

To probe oscillation effects, our selection criteria need to be optimized towards the selection of low-energy vertical muon events. The selection should also retain some events at higher energies (with no oscillation effects), that could be used to verify the overall normalization. Low energy vertical up-going muons in IceCube predominantly result in registered signals ("hits") on a single string. The muon propagates very closely to one string, such that the Cherenkov light can be sampled well from even low-energy events. The probability of observing hits on a second string is very small due to the large interstring distance of 125 m, and is further suppressed through a local trigger condition known as HLC (Hard Local Coincidence). The HLC condition requires that a DOM only registers a hit if a (nearest or next-to-nearest) neighbor also registers a hit within 1 μs. IceCube was operational in this mode for the 22 and 40-string data.

Given the nature of the signal events, the oscillation analysis can be performed very similarly on the different IceCube string configurations. To verify our understanding of the detector, we perform this analysis in steps. First, we use a subset of the 22-string configuration to develop and optimize the selection criteria, then cross check them on the full 22-string dataset and perform the analysis on the IceCube datasets acquired following the 22-string configuration.

The IceCube 22-string configuration operated between May 31, 2007 and April 5, 2008. In this initial study, we analyze only a small subset of the data acquired over this period with a total livetime of 12.85 days, using randomly distributed data segments of up to 8 hour length collected during the period of 22-string operations. The dataset was triggered with the multiplicity eight DOM trigger and then preselected by a specific analysis filter running at the South Pole, selecting short track-like single string events. The filter requires after removal of potential noise hits, that all hits occur on a single string and that the time difference between the earliest and latest hit be less than 1000 ns. To partially veto down-going muon background it requires no hits in the top 3 DOMs. Further, the hit time difference between at least two adjacent DOMs must be consistent with the speed of light within 25% tolerance, and the first DOM hit in time needs to be near the bottom or top within the series of DOMs hit on the single string. All filter selection criteria are designed to be directionally independent, so that vertical up-going events are collected as well as vertical down-going. The described analysis only uses the up-going sample collected by this filter. The down-going sample could be used in the future for flux normalization purposes, if we succeed in extracting a pure atmospheric neutrino sample against the large down-going atmospheric muon flux [3].

To isolate our signal sample of vertical up-going ν_μ events we apply a series of consecutive selection criteria. We require that the majority of time differences between adjacent DOMs are consistent with unscattered Cherenkov radiation (direct light) off a vertically up-going muon (L4). In addition, a maximum likelihood fit is applied requiring the muon to be reconstructed as up-going (L5). After these selection criteria, the dataset is still dominated by down-going muon background mimicking up-going events. This background is estimated using two CORSIKA [8] samples: one with an energy spectrum according to the Hörandel polygonato model [5] and a second over-sampling at the high energy range. Simulations agree well with data in shape, but the normalization is found to be slightly high. Based on background and signal simulations (atmospheric ν_μ were generated with ANIS [9]) we define a set of tight selection criteria (that do not correlate strongly) and show good signal and background separation. These selection criteria are as follows: Event time length greater than 400 ns (L6), mean charge per optical sensor larger than 1.5 photo-electrons (pe), total charge collected during the first 500 ns larger than 12 pe (L7), and an inner string condition (the trigger string completely surrounded by neighboring strings) (L8). The tight selection criteria were independently optimized at level 5 in order to have high statistics and smoother distributions which would not be available at higher selection levels. Thereafter, we reject all events in the available background CORSIKA sample corresponding to an equivalent detector livetime of at least two days, taking into account the oversampling. Using a conservative approach with two days of livetime equivalent we can set a 90%C.L. upper limit on the possible background contamination in the data sample of 14.8 events, in 12.85 days of livetime. In this sample we further expect 2.13 ± 0.07 (1.68 ± 0.06) signal events (with oscillation effects taken into account) from atmospheric neutrinos. See Table I for event counts as function of the selection criteria. Figure 2 shows the track length distribution after final selection criteria. The track length serves as an energy estimator working well at the energy range of interest since a muon travels roughly 5 m/GeV. As expected, short tracks show larger disappearance effects. Figure 3 shows the fraction of events selected by this analysis that are below a certain muon energy for different track lengths.

The optimization and cross-check on the small subset of available data have been performed in a blind manner. One event was observed after final selection which is consistent with the prediction. This initial result indicates that we understand and model the low-

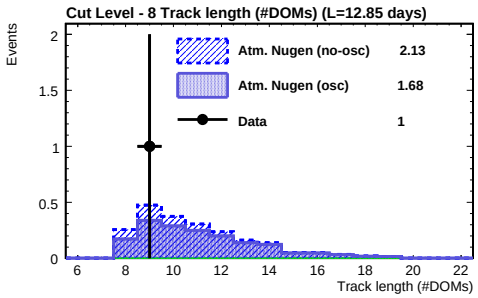

Fig. 2. Expected track length of the signal, with and without oscillations taken into account, and compared to data after final selection criteria. .

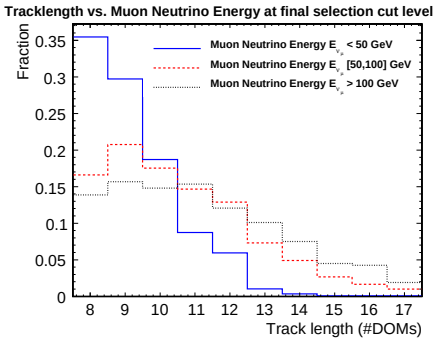

Fig. 3. Fraction of events in a given muon neutrino energy range as function of their track length defined by the number of DOMs hit at final selection.

energy atmospheric neutrino region reasonably well. The analysis on the full dataset is in progress, including a larger background MC sample and a more detailed study of systematic uncertainties. Figure 4 shows the effective area for vertical up-going neutrinos in the 22-string detector at filter level and final selection.

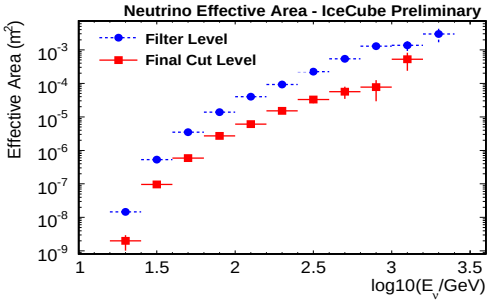

Fig. 4. Average muon neutrino effective area for vertical up-going neutrinos (within 15 degree's of vertical direction) as function of neutrino energy.

IV. Background Estimation

The background has been estimated using CORSIKA simulations. However, due to limited MC statistics there remains a large uncertainty at final selection.

To cross-check the background estimation and to provide a second independent way to obtain a background estimate, we use the data itself to determine the remaining background.

Cut	Corsika	Sig. (with osc)	Effect	Data
L3	$439 \pm 2 \cdot 10^4$	$20.3(17.3) \pm 0.4$	15%	$331 \cdot 10^4$
L4	$54 \pm 2 \cdot 10^3$	$20.0(17.0) \pm 0.3$	15%	$32 \cdot 10^3$
L5	464 ± 175	$11.8(9.7) \pm 0.2$	18%	321
L6	351 ± 171	$10.7(8.8) \pm 0.2$	18%	207
L7	151 ± 41	$9.6(7.9) \pm 0.2$	18%	145
L8	0	$2.1(1.7) \pm 0.08$	21%	1

TABLE I

SUMMARY OF NUMBER OF EVENTS IN DATA AND AS PREDICTED BY SIMULATIONS AS FUNCTION OF THE SELECTION CRITERIA "CUT" LEVEL: L3 - INITIAL PROCESSING (TRIGGER, FILTER), L4/L5 - RECONSTRUCTED TRACK IS VERTICAL UP-GOING, L6/L7 - CHARGE BASED SELECTION CRITERIA, L8 - INNER STRINGS ONLY. SEE TEXT FOR DETAILED DESCRIPTION OF THE SELECTION CRITERIA. EFFECT REFERS TO THE SIZE OF THE DISAPPEARANCE EFFECT.

The nature of the signal events (low energy vertical tracks on a single string) allows us to estimate the background based on the completeness of the veto region defined by the surrounding strings, using geometrical phase-space arguments.

The total number of events observed is the sum of the passing signal events and background faking a signal. The two categories display very different behavior with respect to tightening the selection criteria. Signal events produce predominately real vertical tracks, so that the rate on strings regardless of their position is very similar (see Figure 5).

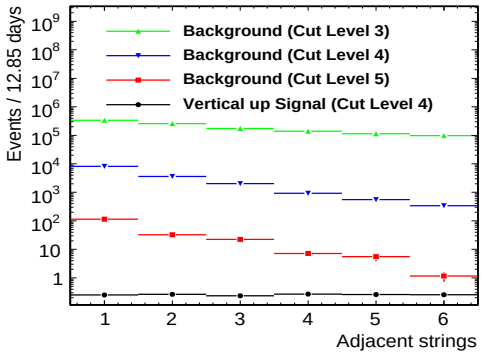

Fig. 5. Number of events for 12.85 days of data at different cut levels as function of number of adjacent strings. The signal prediction is shown for comparison. Note that the number of adjacent strings does not affect the signal as those events are predominately single string events.

Up-going ν_μ of higher energies and non-vertical ν_μ have a small impact on the overall rates. As selection criteria become more stringent, the rates on the strings become more homogeneous as they are dominated by "high quality" low-energy vertical muon neutrino events.

Background behaves very differently under tightening selection criteria, as it becomes more difficult to produce a fake up-going track when the parameter space is taken away and the veto condition tends to have a larger impact.

We determine the ratio between the average number

of events observed on a string with n adjacent strings [1] and those with $n+1$. At a low selection level, the rate on all strings is completely dominated by background. At high selection level, strings having less than four adjacent strings are also background dominated. We use these first three bins to scale the ratio distributions from an earlier selection level to the final selection level. Figure 6 shows the predicted number of events at next-to-final selection level (L7) obtained with this method. The background estimation method from data itself needs to be finalized, including a study of the systematic uncertainites. It provides a cross-check to the predictions from simulation and may ultimately be used as the preferred background estimation method in this analysis.

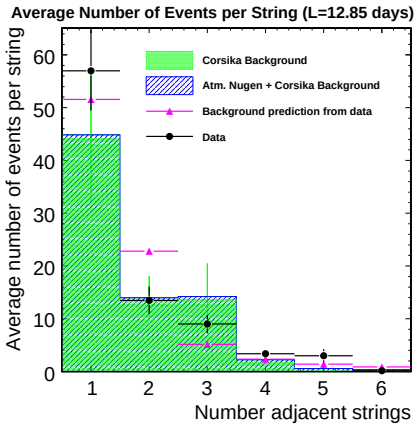

Fig. 6. Average number of events per string at next-to-final selection level (L7) as function number of adjacent strings. Note that the right most bin corresponds to the final selection.

V. Discussion of Sensitivity for 40-string and full IceCube

The IceCube 40-string dataset is in many ways superior to the 22-string dataset. The trigger system has been significantly improved over the 22-string detector through the addition of a string trigger [10], roughly doubling the vertical muon neutrino candidate events per string. In order to reject efficiently against down-going muon background, we require that a string be entirely surrounded by adjacent strings (inner strings criterion) as part of the final selection. The 40-string detector has about a factor of three more inner strings.

Based on the selection criteria for the IceCube 22-string analysis, we have evaluated the sensitivity of the 40-string detector with one year of data using a χ^2-test on the track length distribution. Selection criteria are identical to those presented here, but the number of expected signal events is scaled according to expectation for the 40-string array. We expect about 400 signal events, based on the detector livetime, number of inner strings, and a factor two increase in number of events due to the string trigger. Figure 7 shows the expected sensitivity limits obtained in this way as function of the oscillation parameters. Systematic uncertainties are still being investigated and are not included; They are dominated by the atmospheric neutrino flux uncertainty, optical module sensitivity and ice effects.

[1]We define adjacent strings as those that are within the nominal interstring-distance (roughly 125 m) of the hexagonal detector pattern.

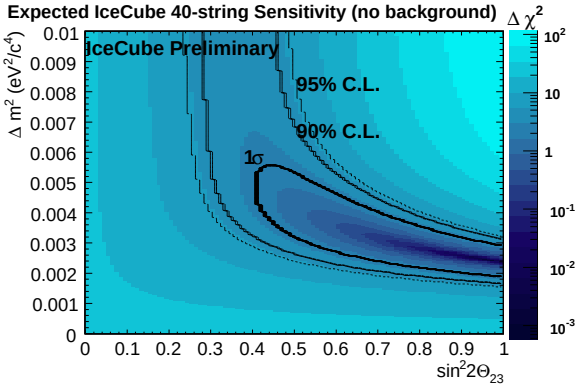

Fig. 7. Expected constraints on oscillation parameters using the IceCube detector in the 40-string configuration under the assumption of zero background .

VI. Conclusions

Preliminary results obtained with a subset of the data collected with the IceCube 22-string configuration active during 2007 and 2008, suggest that IceCube may have sensitivity in the energy range where atmospheric oscillations become important. We estimate the sensitivity to oscillation parameters in the IceCube 40-string dataset and find that IceCube can potentially constrain them, pending the determination of the systematic uncertainties associated with the predicted distributions. Understanding of this energy region is also important for dark matter annihilation signals from the center of the Earth and further provides the groundwork for DeepCore, which will probe neutrinos at a similar and even lower energy range [2].

References

[1] A. Achterberg *et al.* [IceCube Collaboration], Astropart. Phys. **26**, 155 (2006).
[2] D. Grant *et al.* [IceCube Collaboration], Fundamental Neutrino Measurements with IceCube DeepCore, this proceedings.
[3] I. F. M. Albuquerque and G. F. Smoot, Phys. Rev. D **64**, 053008 (2001).
[4] C. Rott [IceCube Collaboration], "Neutrino Oscillation Measurements with IceCube," arXiv:0810.3698.
[5] J. R. Hörandel, Astropart. Phys. 19 (2003) 193.
[6] Y. Ashie *et al.* [Super-Kamiokande Collaboration], Phys. Rev. D **71**, 112005 (2005).
[7] D. G. Michael *et al.* [MINOS Collaboration], Phys. Rev. Lett. **97**, 191801 (2006); P. Adamson *et al.* [MINOS Collaboration], Phys. Rev. Lett. **101**, 131802 (2008).
[8] D. Heck *et al.*, Forschungszentrum Karlsruhe Report FZKA-6019, 1998.
[9] A. Gazizov and M. P. Kowalski, Comput. Phys. Commun. **172**, 203 (2005).
[10] A. Gross *et al.*[IceCube Collaboration], arXiv:0711.0353.

Direct Measurement of the Atmospheric Muon Energy Spectrum with IceCube

Patrick Berghaus* for the IceCube Collaboration†

**University of Wisconsin, Madison, USA*
†*see special section of these proceedings*

***Abstract*. Data from the IceCube detector in its 22-string configuration (IC22) were used to directly measure the atmospheric energy spectrum near the horizon. After passage through more than 10 km of ice, muon bundles from air showers are reduced to single muons, whose energy can be estimated from the total number of photons registered in the detector. The energy distribution obtained in this way is sensitive to the cosmic ray composition around the knee and is complementary to measurements by air shower arrays. The method described extends the physics potential of neutrino telescopes and can easily be applied in similar detectors. Presented is the result from the analysis of one month of IC22 data. The entire event sample will be unblinded once systematic detector effects are fully understood.**

***Keywords*: atmospheric muons, CR composition, neutrino detector**

I. Introduction

While the primary goal of IceCube is the detection of astrophysical neutrinos, it also provides unique opportunities for cosmic-ray physics [1]. One of the most important is the direct measurement of the atmospheric muon energy spectrum.

As shown in figure 1 the energy spectrum of muons produced in cosmic-ray induced air showers has so far been measured only up to an energy of about 70 TeV [2]. The best agreement with theoretical models was found by the LVD detector, with the highest data point located at $E_\mu = 40$ TeV [3]. All these measurements have been performed using underground detectors. Their sensitivity was limited by the relatively small effective volume compared to neutrino telescopes.

With a planned instrumented volume of one cubic kilometer, IceCube will be able to register a substantial amount of events even at very high energies, where the flux becomes very low. The limitation in measuring the muon spectrum is given by its high granularity, and consequent inability to resolve individual muons. Most air showers containing high energy muons will consist of bundles with hundreds or even thousands of tracks. Since the energy loss per unit length can be described by the equation $dE/dx = a + bE$, low-energy muons will contribute disproportionately to the total calorimetric detector response, which depends strongly on the energy of the primary, disfavoring the measurement of individual muon energies.

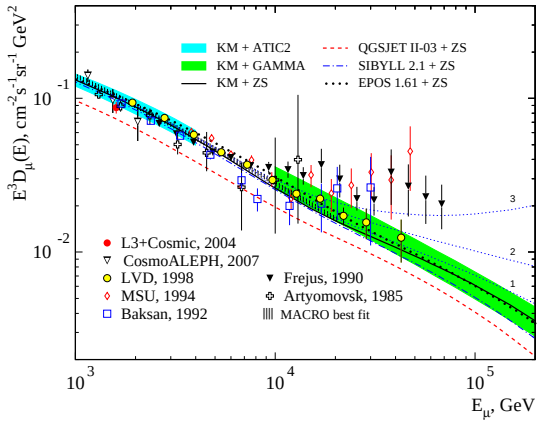

Fig. 1: Muon surface energy spectrum measurements compared to theoretical models [2].

This problem can be resolved by taking advantage of the fact that low energy muons are attenuated by energy losses during passage through the ice. In this analysis, the emphasis was therefore set on horizontal events, where only the most energetic muons are still able to penetrate the surrounding material. The primary cosmic ray interaction in this region takes place at a higher altitude, and therefore in thinner air. The reinteraction probability for light mesons (pions and kaons) is smaller and the flux of muons originating in their decays is maximized.

The main possibilities for physics investigations using the muon energy spectrum are:

- Forward production of light mesons at high energies. While muon neutrinos at TeV energies mostly come from the process $K \rightarrow \nu_\mu + X$, for kinematical reasons muons originate predominantly in pion decays $\pi \rightarrow \nu_\mu + \mu$ [4]. An estimate of the pion production cross section from accelerator experiments gives an uncertainty of

  $$\delta(\sigma_{N\pi}) \simeq 15\% + 12.2\% \cdot log_{10}(E_\pi/500\,\mathrm{GeV})$$

  at $x_{lab} > 0.1$ above 500 GeV [5]. This value should also apply in good approximation to the conventional (non-prompt) muon flux.
- Prompt flux from charm meson decay in air showers [6]. Because of their short decay length, the

reinteraction probability for heavy quark hadrons is negligible. The resulting muon energy spectrum follows the primary energy spectrum with a power law index of $\gamma \approx -2.7$ and is almost constant over all zenith angles. Since the non-prompt muon flux from lighter mesons is higher near the horizon, this means that the relative contribution from charm is lowest, and very challenging to detect.

- Variations of the muon energy spectrum due to changes of the CR composition around the knee. Since the ratio of median parent cosmic ray and muon energy is ≤ 10 at energies [7] above 1 TeV, a steepening of the energy-per-nucleon spectrum of cosmic rays at a few PeV will have a measurable effect on the atmospheric muon spectrum at energies of hundreds of TeV. Comparison of the measured muon spectrum to various phenomenological composition models was the main focus of this analysis.

An additional benefit in the case of neutrino detectors is that a direct measurement of the muon flux will have important implications for neutrino analyses. By reducing the systematic uncertainties on atmospheric lepton production beyond 100 TeV, the detection potential for diffuse astrophysical fluxes will be enhanced. Also, atmospheric muons serve as a "test beam" that allows calibration of the detector response to high-energy tracks.

II. Cosmic Ray Composition Models

Starting from the hypothesis that most cosmic rays originate from Fermi acceleration in supernova shock fronts within our galaxy, the change in the energy spectrum can be explained by leaking of high energy particles. Since the gyromagnetic radius

$$R = \frac{p}{eZB} \simeq (10pc)\frac{E_{prim}[PeV]}{ZB[\mu G]}$$

depends on the charge Z of the particle, for a given energy nuclei of heavier elements are less likely to escape the galactic magnetic field than lighter ones.

The general expression for the flux of primary nuclei of charge Z and energy E_0 is

$$\frac{d\Phi_Z}{dE_0} = \Phi_Z^0 \left[1 + \left(\frac{E_0}{E_{trans}}\right)^{\epsilon_c}\right]^{\frac{-\Delta\gamma}{\epsilon_c}}$$

where the transition energy E_{trans} corresponds to $\hat{E}_p \cdot Z$, $\hat{E}_p \cdot A$ or simply $\hat{E}_p$ for rigidity-dependent, mass-dependent and constant composition models. The parameter ϵ_c determines the smoothness of the transition, and $\Delta\gamma$ the change in the power law index.

Three alternative composition models have been proposed, which all can be fit reasonabkly well to the total cosmic ray flux in the region of the knee [8]. These are:

- Rigidity-Dependent $\Delta\gamma$: This is the default composition used in the IceCube downgoing muon simulation. It is also the one favored by current models of cosmic ray production and propagation in the galactic amgnetic field.
- Mass-Dependent $\Delta\gamma$: An alternative model that also leads to a composition change around the knee. The change in the power law index does not depend on the charge, but on the mass of the nucleus. The best fit proposed in the original paper leads to a smaller value for the transition energy and a steeper spectrum after the cutoff.
- Constant Composition: Here, the composition of the primary cosmic ray flux does not change. The knee is explained by a common steepening in the energy spectrum for all primaries occurring at the same energy.

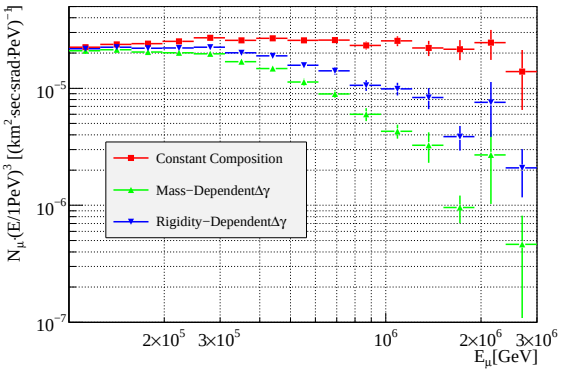

Fig. 2: Atmospheric muon energy spectrum at surface level averaged over the whole sky as simulated with CORSIKA/SIBYLL.

The best measurement of the composition so far was done by KASCADE [9]. Its result was consistent with a steepening of the spectrum of light elements, but depended strongly on the hadronic interaction model used to simulate the air showers (SIBYLL or QGSJET).

The influence of the three composition models on the muon energy spectrum is shown in figure 2. While the spectrum for the constant composition model gradually changes from $E^{-3.7}$ to E^{-4}, the other two show a marked steepening corresponding to the cutoff in the energy per primary nucleon. By accurately measuring the muon energy spectrum, it is therefore possible to significantly constrain the range of allowed cosmic ray composition models in the knee region.

III. Analysis

The data set used in this analysis is based on the IceCube online muon filter, designed to contain all track-like events originating from the region below 70°. It covers the period from June 2006 to March 2007 with an integrated livetime of 275.6 days, during which IceCube was taking data with 22 strings (IC22). A number of quality cuts were applied in order to eliminate background from misreconstructed tracks and to reduce the median error in the zenith angle measurement to

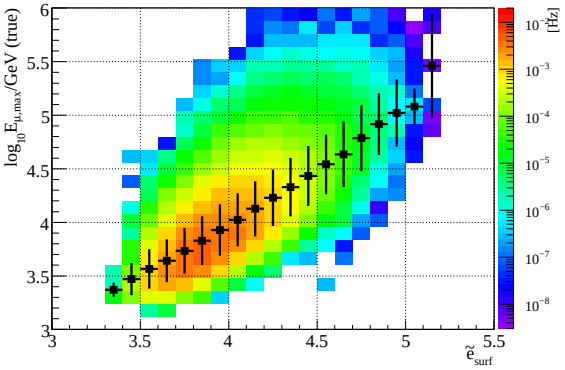

Fig. 3: Relation between energy proxy $\tilde{e}_{surf}$ and true surface energy of most energetic muon in shower. Here and in figure 4 the rigidity-dependent composition model was used.

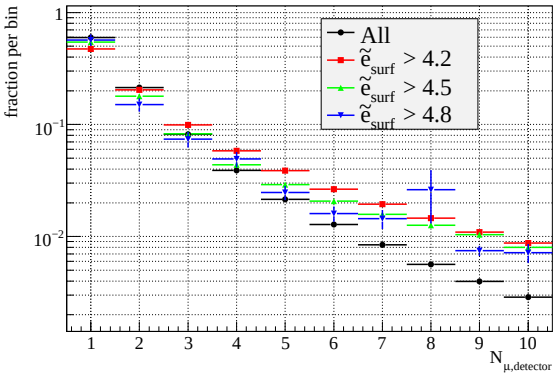

Fig. 4: Simulated muon multiplicity for atmospheric showers at closest approach to the center of the InIce detector for different values of $\tilde{\epsilon}$.

$\approx 0.7°$. The final sample corresponded to an event rate of 0.146 Hz.

$\theta_{zen}[deg]$	d_{vert} [km]	d_{slant} [km]	$E_{\mu}^{thr}[TeV]$
0	1.5	1.5	0.28
70	1.5	4.39	1.12
70	2.5	7.31	2.59
85	1.5	17.21	22.1
85	2.5	28.68	207

TABLE I: Threshold energy for muons passing through ice. The energy values correspond to an attenuation of 99.9%.

To measure the single muon energy spectrum, it is necessary to reduce the background of high-multiplicity bundles, whose total energy depends primarily on the primary cosmic ray [10]. Since there is no possibility to accurately estimate the multiplicity of a downgoing muon bundle, the only way to obtain single muons is by selecting a region close to the horizon to which muons of lower energies cannot penetrate.

The minimum energy required for muons passing through a distance d of ice can be approximated by the equation

$$E_{cut}(d) = (e^{bd} - 1)a/b$$

where $a = 0.163\mathrm{GeVm}^{-1}$ and $b = 0.192 \cdot 10^{-3}\mathrm{m}^{-1}$ [11]. The resulting threshold energies corresponding to vertical tracks and for tracks at the top and bottom of the detector for angles near the horizon are shown in Table I.

Two factors determine the upper energy bound of this analysis. One is the contribution from atmospheric neutrinos, which will eventually dominate the event sample at large depths. The other, and more important, is the finite zenith angle resolution. Using simulated data, it was determined that it effectively limits the measurement of the slant depth to a values below 15 km.

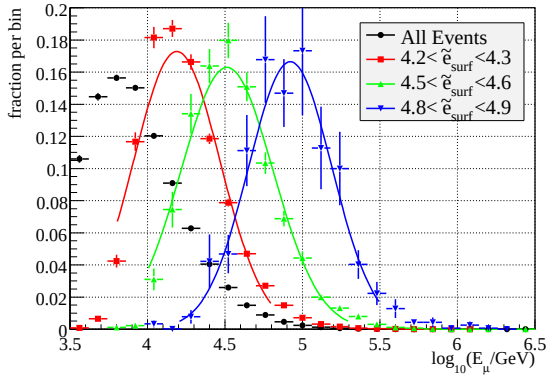

Fig. 5: True surface energy of most energetic muon in shower using rigidity-depending composition model for different values of $\tilde{e}_{surf}$, with fits to Gaussian function. All individual distributions are normalized to unity.

Using the slant depth alone, the range of this analysis is therefore insufficient to probe the region beyond 100 TeV. However, the reach can be extended by incorporating information about the energy of the muon as it passes through the instrumented volume.

For muon tracks in the detector, the energy resolution approaches $\Delta \log_{10}(E) \approx 0.3$ above 10 TeV [12]. This information can be combined with the slant depth to obtain a better estimate for the muon energy at the surface.

A natural way to do this is by defining a surface energy proxy $\tilde{e}$ that behaves as

$\exp(\tilde{e}_{surf}) \propto \log n_{\gamma} \cdot d_{slant}$

where n_{γ} represents the total number of photons measured by the detector. Figure 3 shows the resulting parameter, which has been linerly rescaled in such a way that its value corresponds to the mean $\log(E_{\mu,surf}/GeV)$ for any given bin, provided that the muon energy spectrum is reasonably close to the standard $E^{-3.7}$.

An important criterion for the applicability of the

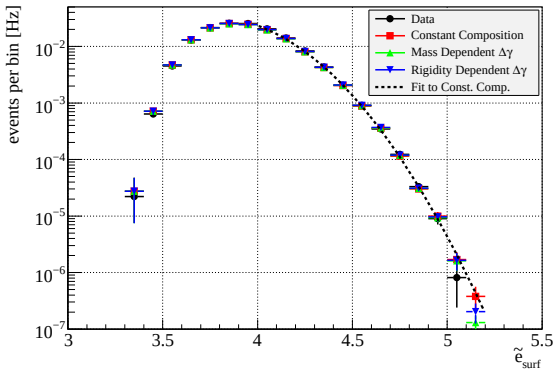

Fig. 6: Data from one month of IC22 at final cut level compared to simulated event rates and fit of empirical function $exp(a + b\tilde{e} + c\tilde{e}^2)$ to constant composition distribution.

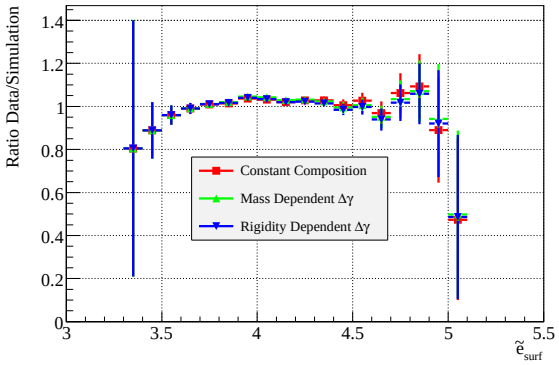

Fig. 7: Ratio of experimental to simulated $\tilde{e}_{surf}$ distributions for one month of IC22 data. Uncertainties are statistical only and exclude systematic detector effects.

energy proxy parameter is that over the entire range of measurement the muon multiplicity remains low, and the influence of high-multiplicity bundles small. Figure 4 confirms that this is indeed the case. It should be noted here that the most energetic muon typically accounts for the dominant contribution to the total energy in the detector, such that other tracks in the bundle can be neglected.

The spread in muon surface energies for a given value of $\tilde{e}_{surf}$ is shown in Figure 5. Around the peak the distributions can be approximated by a Gaussian whose width lies in the range of $\Delta \log_{10} E \approx 0.3 - 0.4$.

IV. Result

Figure 6 shows simulated event rates in dependence of $\tilde{e}_{surf}$ compared to data at final cut level. Almost over the entire range all three models can be approximated by the same empirical fit function. Only in the highest bin can a distinction be made.

The experimental data agrees remarkably well with the simulation, as can be seen more clearly in Figure 7. Despite the steeply falling distribution, the ratio of data to simulation remains very close to one over almost the entire range. For $\tilde{e} > 5$, corresponding to $E_\mu > 100$ TeV, the measurent is based on only three data events.

Using the entire year of IC22 data, the predicted event yield for $5.1 < \tilde{e}_{surf} < 5.2$ based on the constant composition model corresponds to about 10 events. It is therefore unlikely, even neglecting systematic uncertainties, that any of the three models under consideration could definitely be excluded yet. This situation is expected to change as soon as 40-string data can be included in the analysis.

V. Conclusion

This result demonstrates the potential for an accurate measurement of the muon energy spectrum with large neutrino detectors. So far only one month of data has been considered in the analysis, corresponding to about 10% of the entire event sample. Nevertheless, the measurement already covers an energy range almost a factor of three above that of the previous upper limit, with very good agreement between data and simulation.

While it will be difficult to make a definitive statement about the cosmic ray composition around the knee based on IC22 data, it will be possible to confirm the validity of cosmic ray air shower models up to previously inaccessible energy ranges.

At the time of writing, the instrumented volume of the detector has increased by a almost factor of three. Further enlargements are scheduled for the next few years. Future measurements of the muon energy spectrum will benefit from a larger effective area, and a substantial improvement in the angular resolution related to the longer lever arm for horizontal muon tracks within the detector.

Once residual systematic detector uncertainties are resolved, a comprehensive analysis that accounts for both the energy spectrum of individual muons and the total shower energy in the detector will be feasible. The potential for such a combined measurement is unique to large volume detectors.

References

[1] P. Berghaus [IceCube Collaboration], *Proc. of ISVHECRI 2008*, arXiv:0902.0021 [astro-ph.HE].
[2] A. A. Kochanov, T. S. Sinegovskaya and S. I. Sinegovsky, Astropart. Phys. **30** (2008) 219
[3] M. Aglietta *et al.* [LVD Collaboration], Phys. Rev. D **60** (1999) 112001
[4] T. K. Gaisser, Nucl. Phys. Proc. Suppl. **118** (2003) 109.
[5] G. D. Barr, T. K. Gaisser, S. Robbins and T. Stanev, Phys. Rev. D **74** (2006) 094009.
[6] G. Gelmini, P. Gondolo and G. Varieschi, Phys. Rev. D **67** (2003) 017301.
[7] T.K. Gaisser, "Cosmic Ray and Particle Physics," Cambridge University Press, 1990.
[8] J. R. Hörandel, Astropart. Phys. **19**, 193 (2003).
[9] T. Antoni *et al.* [The KASCADE Collaboration], Astropart. Phys. **24**, 1 (2005).
[10] D. Chirkin [AMANDA Collaboration], *Proc. of ICRC 2003*.
[11] D. Chirkin and W. Rhode, arXiv:hep-ph/0407075.
[12] J. Zornoza, D. Chirkin [IceCube Coll.], ICRC 2007, arXiv:0711.0353 (pp. 63-66).

Search for Diffuse High Energy Neutrinos with IceCube

Kotoyo Hoshina* **for the IceCube collaboration†**

*Department of Physics, University of Wisconsin, Madison, WI 53706, USA
†See the special section of these proceedings

***Abstract*. We performed a search for diffuse high energy neutrinos using data obtained with the IceCube 22 string detector during a period 2007-2008. In this analysis we used an E^{-2} spectrum as a typical flux resulting from cosmic ray shock acceleration. Using a likelihood track reconstruction, approximately 5700 track-like neutrinos are extracted from 275.7 days data at an estimated 95% purity level. The expected sensitivities obtained are in a range of $2.2\times10^{-8} \sim 2.6\times10^{-8}$ E^{-2} GeV cm^{-2} s^{-1} sr^{-1} with four different energy estimators. The analysis method and results are presented along with discussions of systematics.**

***Keywords*: IceCube neutrino diffuse**

I. Introduction and detection principle

The IceCube neutrino observatory is the world's largest neutrino telescope under construction at the geographic South Pole. During 2007, it collected data with 1320 digital optical modules(DOM) attached to 22 strings (with 60 optical modules per string). They are deployed in clear glacial ice at depths between 1450 to 2450 meters beneath the surface, where the photon scattering and absorption are known by preceding *in situ* measurements [1]. When a neutrino interacts inside or close to the IceCube detector, DOMs capture Cherenkov photons from secondary charged particles with 10 inch photomultiplier tubes and generate digital waveforms. In most cases, we require at least 8 DOMs to be triggered within a 10 micro second time window. Once the trigger condition is satisfied, all digital waveforms are collected and then processed by online filtering programs to filter out background events. In this analysis we used 275.7 days livetime of data and obtained 5718 candidate neutrino induced events after the final event selection. The event selection process is described in Section II.

The event sample after the selection process mainly consists of atmospheric neutrinos. To separate extraterrestrial high-energy neutrinos from atmospheric neutrinos, one can apply two types of analysis techniques. The first is a point source analysis that uses the direction of the neutrinos to survey high-density event spots (hotspots). The second, called a diffuse analysis, examines the energy spectrum itself and compares it to various physics models. Since the diffuse analysis does not require multiple events from an astrophysical source, it is possible to take into account faint sources that are not significant by themselves in a point source analysis. However, in general, a diffuse analysis requires a better detector simulation. While a point source analysis uses data to search for a hotspot, the diffuse analysis has to rely on simulated parameter distributions under an assumption of a physics model to test observed distributions in the data.

In this analysis we assumed a $\Phi \propto E^{-2}$ energy spectrum for neutrinos from astrophysical sources resulting from shock acceleration processes [2]. Since the atmospheric neutrino flux has a much softer energy spectrum [3][4][5], the signal neutrinos may form a high-energy tail in an energy-related observable over atmospheric neutrinos. The search for an extraterrestrial neutrino component uses the number of events above an energy estimator cut after subtracting a calculated contribution from atmospheric neutrinos. The cut was optimized to produce the best limit setting sensitivity [6]. Results and possible sources of systematics errors are discussed in Section IV.

II. Event Selection

Cosmic ray interactions in the atmosphere create pions, kaons and charmed hadrons which can later decay into muons and neutrinos. The primary background before the event selection is atmospheric muons traveling downward through the ice. Their intensity strongly depends on the zenith angle of the muon: it decreases as the zenith angle increases because a higher zenith angle results in a longer path length from the surface of the Earth to the IceCube detector. The largest zenith angle of atmospheric muons is around 85 degrees and their path length inside the Earth is over 20 km. The first filter is thus designed to select only upward going events. For estimation of the zenith angle, we used a log likelihood reconstruction. In this analysis, the minimum zenith threshold is 90 degrees.

After the zenith angle filter is applied, the remaining data still contains many orders of magnitude more mis-reconstructed background than neutrino-induced events. They are downward going muons, but reconstructed as upward because of poor event quality (low number of triggered DOM, grazing an edge of detector, etc) or two muons that passed through the detector within a trigger time window (coincidence muons) and mis-reconstructed as a single upward going muon [1]. These mis-reconstructed events are effectively rejected by checking fit quality parameters [7]:

[1] This difficulty is mainly caused by scattering of photons in ice. The effective scattering length of Cherenkov photons in IceCube is around 30 m [1].

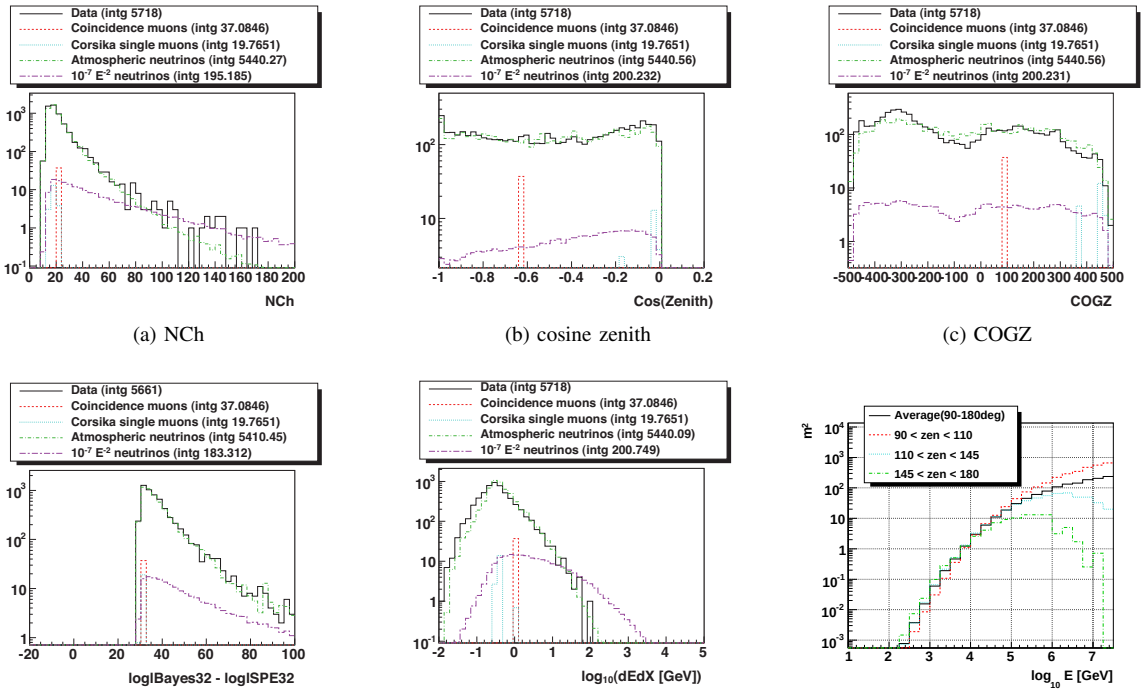

(a) NCh (b) cosine zenith (c) COGZ

(d) log likelihood ratio (e) log10(dEdX) (f) Effective Area

Fig. 1. (a - d) : Comparison of simulations and data for basic parameters after the purification process. COGZ(c) is the z-position of the center of charge-gravity of an event in the IceCube coordinate system. (d) : An alternative energy estimator. See Sec. III. (f) : Effective area of $\nu_\mu + \overline{\nu_\mu}$ after the event selection, in several zenith angle ranges.

- Number of direct hits (NDir) : number of hits which are assumed to result mostly from unscattered Cherenkov photons
- Projected length of direct hits (LDir) : Largest distance of a pair of projections from direct hit positions to a reconstructed track
- Reduced log likelihood : log likelihood result of a reconstructed track divided by number of degrees of freedom
- log likelihood ratio : difference of log likelihood parameters between a fit and a Bayesian fit which is forced to reconstruct as downward going
- smoothness of hits : a parameter for how hits are generated smoothly along a reconstructed track
- log likelihood ratio between single muon fit and Bayesian weighted double muon fit : similar parameter as log likelihood ratio, but uses two Bayesian fits as a hypothesis of coincidence muons

The "direct hits" are defined by the arrival times of photons at each DOM and a reconstruction. Once a reconstruction is determined, at each DOM, we obtain a minimum path and earliest possible arrival times of photons (geometrical hit times) from the Cherenkov light emission point. Some photons may take a longer path because of scattering, which result in a time delay from the geometrical hit time. In this analysis, we chose a time window of [-15ns, 75ns] from the geometrical hit time to accept a hit as a direct hit.

The log likelihood ratio gives a comparison between two fits, a standard likelihood fit and a fit with a zenith-dependent weight which follows a zenith distribution of atmospheric muons. A reliable good quality fit should have a large ratio, while mis-reconstructed atmospheric muons have relatively smaller ratios.

With these quality parameters, we defined a set of cut parameters to purify neutrino-induced events using Monte-Carlo simulation. For atmospheric muons, we generated 10 days of single unweighted CORSIKA muons, 5×10^5 events of energy weighted CORSIKA muons[2], and 7.4 days of unweighted CORSIKA coincidence muons. For atmospheric neutrinos, 2.6×10^7 ν_μ events were generated with an E^{-1} spectrum and re-weighted with a conventional atmospheric neutrino flux [3] plus a prompt neutrino model [4][5]. The optimal cut is chosen to retain as many high energy neutrinos as possible while keeping purity of neutrinos above 95 %.

The optimized cut parameter is then applied to data and compared with Monte-Carlo predictions. In order not to bias the analysis, the highest energy tails of both data and simulation were kept hidden from the analyzer during this final optimization process of cuts. The number of DOMs that has at least one hit (NCh) is used to determine the open window: we compared events which NCh less than 80. Small discrepancies

[2]The power law index of the primary particle is changed to be harder by +1. The effective livetime varies in each primary energy bin, for example, 10 TeV weighted muons correspond to one year of effective livetime. The effective livetime also depends on zenith, e.g. a value of a year for muons around 70 degree.

between data and simulation around the threshold of some quality parameters were observed, mainly because of insufficient statistics of background coincident muon simulation. These events are removed by tightening the cut parameters moderately.

Figs. 1 shows the comparison of data and simulation after the final event selection. The Monte Carlo simulation reproduces data well in most event variables, but discrepancies are still present in some depth dependent variables like COGZ, the z (vertical, or depth) coordinate of the center-of-gravity of the charge in the event (z = 0 in the center of the detector). This systematics is discussed in Sec. IV. The neutrino effective area of ν_μ + $\overline{\nu_\mu}$ after optimal quality cuts for 275.7 days of livetime of IceCube 22 strings is shown in Fig. 1f.

III. Energy estimators and sensitivity

Unlike the previous detector AMANDA, the IceCube detector retains the original waveform by digitizing analog waveforms inside the DOM. This technology allows us to use charge information as an energy estimator. Recently, new techniques for energy reconstruction were developed using the charge information as well as the hit times. In this section, we compare the sensitivity of following energy estimators.

- NCh : number of triggered DOMs. It is simple, but has a relatively strong connection with the track geometry and the ice layers where the muon passed through.
- NPe : Total charge collected by all triggered DOMs of an event. Basically it is similar to NCh, but has a larger and smoother dynamic range than NCh.
- dEdx : A table based energy reconstruction. Using a table generated by a photon propagation program (Photonics [8]), it estimates the energy deposit along a reconstructed track. The reconstruction takes into account the ice properties as a function of depth. [9]
- MuE : a simple energy reconstruction. Similar to dEdx, but uses an homogeneous ice model instead of layered ice photonics tables. [10]

To obtain sensitivities, we assumed no extra-terrestrial signal over a given energy threshold, then calculated the expected upper limit using the Feldman-Cousins method [11]. The Model Rejection Factor [6] is then optimized to have the best sensitivity for E^{-2} test signal flux. Table I shows sensitivities at corresponding energy estimator thresholds. The average number of background neutrinos and $\Phi = 10^{-7}\mathrm{E}^{-2}$ signal neutrinos above the threshold are also predicted.

IV. Results and discussion

Table I also lists the number of data events above the optimized energy thresholds for the four energy estimators. We observed a statistically significant excess of data over the atmospheric neutrino prediction (including prompt atmospheric neutrinos) for all energy estimators except for dEdx. However, disagreements between data and simulation in depth dependences (for example, in COGZ in Fig. 1c) point to unresolved systematics in our simulation. In this section we discuss the effect of the COGZ problem to this analysis.

The depth dependences in the optical properties of the glacial ice, reflecting changes in dust concentration due to climate variations when the ice was formed [1], are taken into account in the detector simulation. However, as Fig. 1c shows, these dependences are not fully reproduced by the simulation. In this analysis, the discrepancy is most severe in the deep part of the detector, for COGZ $<$ -250 m, which is also where most of the highest-energy events lie. The event excess we observed thus could be due to systematics rather than a signal flux.

To test the hypothesis that the excess is due to inaccuracies in our simulation of depth dependences, we repeated the analysis on data from the shallow (COGZ $>$ 0 m) part of the detector and from the deep (COGZ $<$ 0 m) part separately. Fig. 1 shows the COGZ distribution as a function of cosine zenith for the data, atmospheric neutrino simulation, and a subtraction of the simulation from data. To eliminate any bias from hard components like prompt neutrinos or extra-terrestrial neutrinos, we set an additional energy cut NCh $<$ 50 to plot Fig. 1. Fig. 2c indicates that the systematic problems are not specific to the highest energy events. Using events with COGZ $>$ 0 m and cosine zenith less than -0.2, the data and simulation agrees relatively well. We performed the same procedures on the full dataset and no data excess is observed in any of the energy estimators. This result could be compared with the AMANDA diffuse analysis [12] because the majority of hits are recorded by DOMs at depths where AMANDA is deployed. Considering the sensitivities listed in Table II, this result is consistent with the current upper limit for diffuse muon neutrinos 7.4×10^{-8} GeV cm^{-2} s^{-1} sr^{-1}. On the other hand, at COGZ $<$ 0 m with the same zenith cut, we observed an event excess with three energy estimators. Since the sensitivities of the lower COGZ sample are worse than the upper COGZ events, the event excess we observed with the full data set is highly likely due to systematics. Table II summarizes all numbers obtained from the two subsets.

Some of the systematics issues will be resolved with ongoing calibration studies. Our description of the optical ice properties has larger uncertainties in the deep ice, where we so far have relied on extrapolations of the AMANDA measurements in the shallower ice [1], using measurements of dust concentration in Antarctic ice cores for the extrapolation. The ice core data indicate a strong improvement in ice clarity below AMANDA depths, with an estimated increase in average scattering and absorption lengths of up to 40% at depths greater than 2100 m. With such different ice properties in the two parts of the detector, we are investigating our possibly increased sensitivity to systematic error sources that are present at AMANDA depths but become more significant in the deeper, clearer ice. We are also

TABLE I
SENSITIVITIES OF ICECUBE 22 STRINGS 275.7 DAYS WITH VARIOUS ENERGY ESTIMATORS. NO SYSTEMATICS ERROR INCLUDED.

Estimator	MRF (sensitivity)	Energy Threshold	Mean Background	Mean Signal	Data observed
NCh	0.22 ($2.2 \times 10^{-8} E^{-2}$)	NCh $\geq$ 99	9.3	29.4	22
NPe	0.26 ($2.6 \times 10^{-8} E^{-2}$)	log10(NPe) $\geq$ 3.15	6.6	22.5	10
dEdx	0.25 ($2.5 \times 10^{-8} E^{-2}$)	log10(dEdx) $\geq$ 1.4	4.1	19.8	4
MuE	0.24 ($2.4 \times 10^{-8} E^{-2}$)	log10(MuE) $\geq$ 5.05	6.4	28.4	13

TABLE II
SENSITIVITIES OF ICECUBE 22 STRINGS 275.7 DAYS WITH ADDITIONAL COGZ CUT AND COSINE ZENITH CUT (COSθ < -0.2). NO SYSTEMATICS ERROR INCLUDED.

Estimator	COGZ cut	MRF (sensitivity)	Energy Threshold	Mean Background	Mean Signal	Data observed
NCh	COGZ>0	0.41 ($4.1 \times 10^{-8} E^{-2}$)	NCh $\geq$ 68	7.9	15.0	3
NPe	COGZ>0	0.54 ($5.4 \times 10^{-8} E^{-2}$)	log10(NPe) $\geq$ 2.85	8.0	11.3	5
dEdx	COGZ>0	0.50 ($5.0 \times 10^{-8} E^{-2}$)	log10(dEdx) $\geq$ 0.97	7.9	12.2	5
MuE	COGZ>0	0.50 ($5.0 \times 10^{-8} E^{-2}$)	log10(MuE) $\geq$ 4.65	9.9	13.2	7
NCh	COGZ<0	0.47 ($4.7 \times 10^{-8} E^{-2}$)	NCh $\geq$ 80	12.8	15.7	25
NPe	COGZ<0	0.64 ($6.4 \times 10^{-8} E^{-2}$)	log10(NPe) $\geq$ 3.15	2.4	6.4	4
dEdx	COGZ<0	0.58 ($5.8 \times 10^{-8} E^{-2}$)	log10(dEdx) $\geq$ 0.91	15.5	14.0	14
MuE	COGZ<0	0.62 ($6.2 \times 10^{-8} E^{-2}$)	log10(MuE) $\geq$ 5.00	2.9	7.1	6

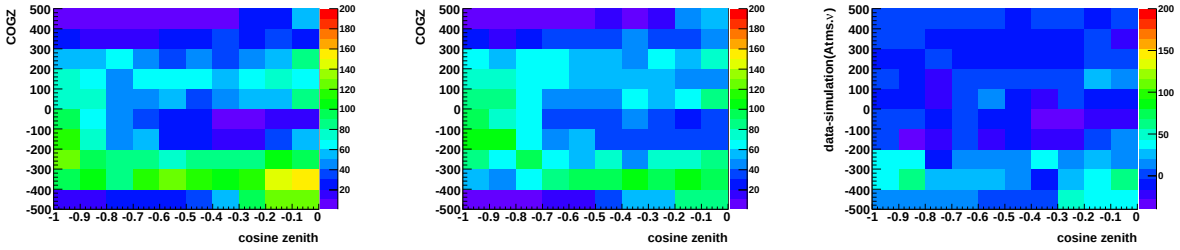

(a) Data (b) Atmospheric ν (c) Data - Atmospheric ν

Fig. 2. (a,b) : Number of Low NCh events at final cut level in COGZ vs cosine zenith. Events contributing to the plot are limited to NCh < 50. (c): Subtraction of plots (a) and (b). The boxes checked with x represent negative values.

improving our photon propagation simulation to better reproduce the data in the clearest ice. This improved simulation will be tested with data from in-situ light sources (LED flashers, nitrogen lasers) and well-reconstructed downward going muons.

Among the four energy estimators, dEdx shows the most stable results. However, all the systematic problems must be understood before we proceed to claim a physics result. The IceCube 22 string configuration is the first detector which allows a detailed study of Monte-Carlo simulation and the detector in the deep ice with reasonable statistics. These results will be essential not only for this analysis, but also for upcoming analysis with the IceCube 40 string configuration.

V. CONCLUSION

Using 275.7 days of upward going muon events collected by the IceCube 22 string configuration, we performed a search for a diffuse flux of high energy extraterrestrial muon neutrinos. The expected sensitivities are around 2.5×10^{-8} GeV cm^{-2} s^{-1} sr^{-1} for an E^{-2} flux using four different energy estimators. We observed an excess of data over that expected from background above the best energy cut with some energy estimators. In order to test the geometric stability of this analysis, we performed the same analysis using two subsets of data divided by a threshold COGZ = 0 m. Having inconsistent results between these two subsets, the data excess we observed is highly likely dominated by systematics. With events at COGZ > 0 m, we observed no data excess with any of the energy estimators, which is consistent with the current upper limit on a diffuse flux of muon neutrinos obtained by the AMANDA diffuse analysis [12]. Many ongoing calibration studies will reveal the unknown systematics in the near future.

REFERENCES

[1] M Ackermann, *et al. Journal of Geophysical Research*, **Vol. 111**, D13203 (2006).
[2] E. Waxman and J. Bahcall, *Phys. Rev.* D **59**, 023002 (1998).
[3] G.D. Barr, T.K. Gaisser, S. Robbins, and T. Stanev, *Phys. Rev. D* **74**, 094009 (2006).
[4] G. Firoentini, A. Naumov, and F.L Villante, *Phys. Lett.* B **510**, 173 (2001).
[5] E.V. Bugaev *et al.* , Il Nuovo Cimento **12C**, No. 1, 41 (1989).
[6] G.C. Hill and K. Rawlins, *Astropart. Phys.* **19**, 393 (2003).
[7] J. Ahrens *et al.* , *Nucl. Inst. Meth.* **A** 524, 169 (2004)
[8] Lundberg, J.; Miocinovic, P. Woschnagg, K. *et al. Nucl. Inst. Meth.* **A** 581, 619 (2007).
[9] S. Grullon *et al.* "Reconstruction of high energy muon events in icecube using waveforms," in Proc. of 30th ICRC (2007).
[10] J.D. Zornoza, D. Chirkin, "Muon energy reconstruction and atmospheric neutrino spectrum unfolding with the IceCube detector", in Proc. of 30th ICRC (2007).
[11] G. Feldman and R. Cousins *Phys. Rev.* D **57** 3873 (1998), G. C. Hill *Phys. Rev.* D 118101 (2003).
[12] A. Achterberg et al., *Phys. Rev.* D, **76**, 042008 (2007).

A Search For Atmospheric Neutrino-Induced Cascades with IceCube

Michelangelo D'Agostino[*] **for the IceCube Collaboration**[†]

[*]*Department of Physics, University of California, Berkeley, CA 94720, USA*
[†]*See the special section of these proceedings.*

Abstract. **The IceCube detector is an all-flavor neutrino telescope. For several years IceCube has been detecting muon tracks from charged-current muon neutrino interactions in ice. However, IceCube has yet to observe the electromagnetic or hadronic particle showers or "cascades" initiated by charged- or neutral-current neutrino interactions. The first detection of such an event signature will likely come from the known flux of atmospheric electron and muon neutrinos. A search for atmospheric neutrino-induced cascades was performed using a full year of IceCube data. Reconstruction and background rejection techniques were developed to reach, for the first time, an expected signal-to-background ratio $\sim$1 or better.**

Keywords**: atmospheric, neutrino, IceCube**

IceCube is a cubic kilometer neutrino telescope currently under construction at the geographical South Pole. With 59 of 86 strings of photomultiplier tubes currently embedded into Antarctica's deep glacial ice, IceCube is already the world's largest neutrino detector [1].

IceCube detects high energy neturinos by observing Cherenkov light from the secondary particles produced in neutrino interactions in ice. In charged-current ν_μ interactions, the outgoing energetic muon emits light along its track through the detector. A hadronic particle shower or cascade is also produced at the neutrino interaction vertex, but this is usually well outside of the instrumented detector volume. In charged-current ν_e interactions, the outgoing electron initiates an electromagnetic (EM) cascade which accompanies the hadronic cascade. Neutral-current interactions of any neutrino flavor produce hadronic cascades.

At the energies relevant for atmospheric neutrinos, both hadronic and EM cascades develop over lengths of only a few meters. In a sparsely instrumented detector like IceCube, they look like point sources of Cherenkov light whose spherical wavefronts expand out into the detector. While muon tracks have been detected by neutrino telescopes, cascade detection has remained an elusive goal for high energy neutrino astrophysics.

The well-studied atmospheric neutrino flux can serve as a calibration source for the cascade detection channel and should provide a valuable proof-of-principle for all-flavor detection. Once neutrino-induced cascades have been detected from the atmosphere, they should also open up a powerful channel for astrophysics analysis.

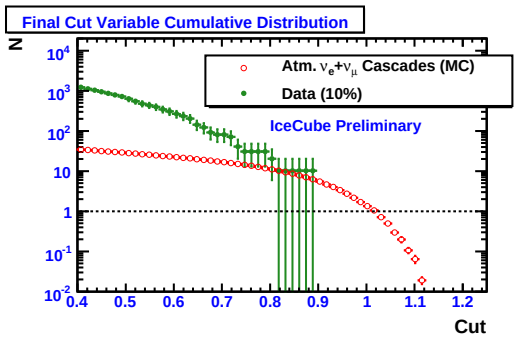

Fig. 1. Number of surviving events as a function of final cut strength for signal Monte Carlo and a 10% sample of the full one year dataset.

Since cascades are topologically distinct from muons, they can be separated from the cosmic ray background over the entire 4π of the sky [2].

The challenge of separating a cascade signal from the overwhelming background of downgoing air-shower muons is significant. In its 22 string configuration, $\sim$10 billion events triggered the IceCube detector in one year of operation. Of these, only $\sim$10,000 are expected to be atmospheric neutrino-induced cascades. Because the atmospheric ν_μ and ν_e fluxes differ [3], these $\sim$10,000 events are unequally distributed among the different cascade signal classes. For each ν_e, we expect $\sim$1.3 ν_μ neutral-current events and $\sim$2.9 ν_μ charged-current events where the hadronic cascade from the interaction vertex is inside the detector (so-called "starting events").

To begin the analysis, a fast filter was developed to run online at the South Pole to select promising candidate events for satellite transmission to the northern hemisphere. The filter selected events with a spherical topology that were not good fits to relativistically moving tracks. After this online filter, each event was reconstructed according to track and cascade hypotheses using hit timing information, and well-reconstructed down-going tracks were thrown out.

A new, analytic energy reconstruction method for cascades was developed that takes into account the significant depth variation of the optical properties of the glacial ice at the South Pole [4]. Several more topological variables with good separation power were also calculated for each event.

The main background for neutrino-induced cascade searches comes from the stochastic energy losses suffered by cosmic ray muons as they pass through the ice surrounding the optical sensors. Two basic variables are

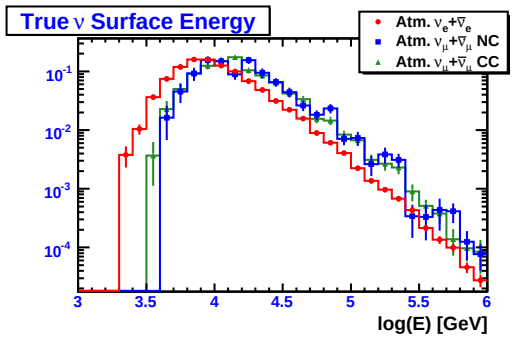

Fig. 2. Monte Carlo distributions of true neutrino energy at the earth's surface for events surviving a final variable cut value of 0.73.

employed to reduce this background. First, we measure how far inside the geometric volume of the detector the reconstructed cascade vertex lies. Muons with a large stochastic energy loss far inside the detector are more likely to leave early hits in outer sensors and can thus be rejected. Second, background separation becomes easier as the cascade energy increases. This is because the more energetic stochastic losses that mimic neutrino-induced cascades would have to come from more energetic muons, which are more likely to leave additional light that will allow for their identification. We therefore expect that more energetic cascades deep inside the detector will be the easiest signal to separate from background.

Along these lines, several neural networks were trained on 12 topological and reconstruction-based variables, including reconstructed energy and a measure of containment within the detector. The product of these variables is taken as the final discriminating cut variable. Figure 1 shows the number of remaining events as a function of the cut on this final variable for events that reconstruct above 5 TeV for signal Monte Carlo and a 10% sub-sample of the available data.

While nothing can yet be concluded from the 10% data sample alone, the full dataset, which will be presented in this talk, may show signs of converging to the signal expectation. Figure 2 shows the true neutrino energy at the earth's surface for the three classes of simulated signal.

REFERENCES

[1] A. Karle for the IceCube Collaboration, "IceCube: Construction Status and First Results," *arXiv:0812.3981*, Dec. 2008.

[2] A. Achterberg et al., "Search for neutrino-induced cascades from gamma-ray bursts with amanda," *The Astrophysical Journal*, vol. 664, no. 1, pp. 397–410, 2007.

[3] G. D. Barr, T. K. Gaisser, P. Lipari, S. Robbins, and T. Stanev, "Three-dimensional calculation of atmospheric neutrinos," *Physical Review D*, vol. 70, no. 2, p. 023006, Jul. 2004.

[4] E. Middell and M. D'Agostino, "Improved reconstruction of cascade-like events in icecube," *These Proceedings*, 2009.

First search for extraterrestrial neutrino-induced cascades with IceCube

Joanna Kiryluk* for the IceCube Collaboration†

* *Lawrence Berkeley National Laboratory and University of California Berkeley, Berkeley, CA 94720, USA*
† *see special section of these proceedings*

***Abstract*. We report on the first search for extraterrestrial neutrino-induced cascades in IceCube. The analyzed data were collected in the year 2007 when 22 detector strings were installed and operated. We will discuss the analysis methods used to reconstruct cascades and to suppress backgrounds. Simulated neutrino signal events with a E^{-2} energy spectrum, which pass the background rejection criteria, are reconstructed with a resolution $\Delta(\log E) \sim 0.27$ in the energy range from ~ 20 TeV to a few PeV. We present the range of the diffuse flux of extra-terrestrial neutrinos in the cascade channel in IceCube within which we expect to be able to put a limit.**

***Keywords*: extraterrestrial, neutrino, IceCube**

I. Introduction

IceCube is a $1\,\mathrm{km}^3$ Cherenkov detector under construction at the South Pole. Its primary goals are to detect high energy extra-terrestrial neutrinos of all flavors in a wide energy range, from $\sim$100 GeV to $\sim$100 EeV, search for their sources, for example active galactic nuclei and gamma ray bursts, and to measure their diffuse flux. When complete, the IceCube detector will be composed of 4800 Digital Optical Modules (DOMs) on 80 strings spaced 125 m apart. In addition there will be 6, more densely populated, Deep Core strings inside the IceCube detector volume. The array covers an area of one km^2 at depths from 1.45 to 2.45 km below the surface [1].

High energy neutrinos are detected by observing the Cherenkov radiation from secondary particles produced in neutrino interactions inside or near the detector. Muon neutrinos in charged current (CC) interactions are identified by the final state muon track [2]. Electron and tau neutrinos in CC interactions, as well as all flavor neutrinos initiating neutral current (NC) interactions are identified by observing electromagnetic or hadronic showers (cascades). A 10 TeV cascade triggers IceCube optical modules out to a radius of about 130 m. Cascades can be reconstructed with good energy resolution, but limited pointing resolution. The good energy resolution and low background from atmospheric neutrinos make cascades attractive for diffuse extraterrestrial neutrino searches [3].

We present expected sensitivities for the diffuse flux of extra-terrestrial neutrinos in the cascade channel in IceCube. This work uses data collected in 2007 with the 22 strings that were deployed in IceCube at that time. The total livetime amounts to 270 days. Ten per cent of the data were used as a "burn" sample to develop background rejection criteria. The results, after unblinding, will be based on the remaining 90% of the data, about 240 days.

II. Data and Analysis

Backgrounds from atmospheric muons, produced in interactions of cosmic rays with nuclei in the Earth's atmosphere form a considerable complication in all neutrino searches in IceCube. A filtering chain developed using Monte Carlo simulations of muon background and neutrino signal was used to reject these backgrounds online and offline.

The atmospheric muon background was simulated with CORSIKA [4]. In addition to the single muon events, which form the dominant background, an appropriate number of overlaying events was passed through the IceCube trigger and detector simulator to obtain a sample of coincident muons. The coincident muon events make a few per cent contribution to the total trigger rate. The signal, electron neutrino events, was simulated using an adapted version of the Monte Carlo generator ANIS [5] for energies from 40 GeV to 1 EeV and with a E^{-2} energy spectrum.

All estimates for the number of signal events later in the text assume an E^{-2} spectrum and flux strength of:

$$\Phi_{model} = 1.0 \times 10^{-6} (\mathrm{E/GeV})^{-2} / (\mathrm{GeV\,s\,sr\,cm^2}). \quad (1)$$

A. Online filtering

The main physics trigger is a "simple multiplicity trigger" (SMT), requiring photon signals in at least 8 DOMs, with the additional requirement of accompanying hits in any of the ± 2 neighboring DOMs, each above a threshold of 1/6 single photoelectron signal and within a 5 μs coincidence window. Averaging over seasonal changes of the trigger rate for IC22 was 550 Hz. The mean SMT rate is generally well reproduced by Monte Carlo simulation, which gives 565 Hz. Assuming the flux given in Eq. 1, approximately 2.7×10^3 electron neutrino events and $\sim 1 \times 10^{10}$ background event are expected to trigger the detector in 240 days.

The backgrounds are suppressed online with first-guess reconstruction algorithms [6]. A first guess track fit assumes that all hits can be projected onto a line, and that a particle producing those hits travels with velocity v_{line}. In addition a simple cut on sphericity

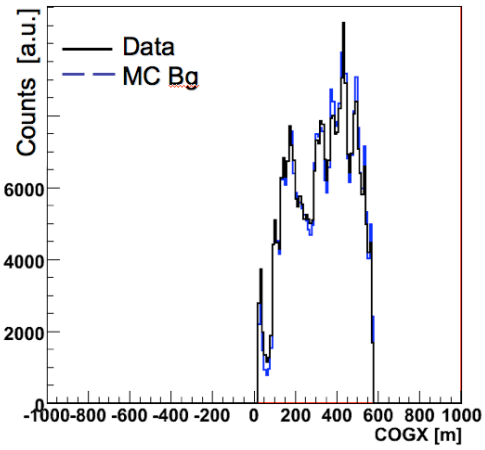

Fig. 1. The reconstructed center-of-gravity (COG) x after online filtering. Data is shown as continuous lines, background Monte Carlo is shown as dashed lines. Monte Carlo data is normalized to the experimental number of events.

of the events ($\text{EvalRatio}_{\text{ToI}}$) is used to select events with hit topology consistent with cascades. Cut values used in online filter are given in Table I. In the case of cascades, the online filter reduced the SMT trigger rate to $\sim$ 20 Hz, or 3.5 % of the total trigger rate. Monte Carlo studies show that the filter retains about 70% of the simulated signal and rejects 97.5% of the simulated background that trigger the detector. The Monte Carlo simulation thus underestimates the overall rate observed in the data. Otherwise main characteristics are well reproduced, Fig. 1 which shows the reconstructed center-of-gravity (COG) x position. The COG is calculated for each event as the signal amplitude weighted mean of all hit DOM positions.

B. Offline filtering

The data, after online filtering and transfer from the South Pole, were passed through more sophisticated algorithms to reconstruct both muon tracks and cascades. This reconstruction uses the maximum-likelihood reconstruction algorithms described in [2], [6].

Several cuts were applied sequentially, and the intermediate data sets are identified as different levels. Level-1 is the trigger level and events passing the online filtering correspond to Level-2. The rates at different levels are summarized in Table I.

At Level-3 events were selected with (i) a reconstructed track zenith angle greater than 73° and (ii) a difference Llh(track)-Llh(cascade) > -16.2 in the likelihood parameters of the track and cascade reonstructions to select cascade-like events. This selection was optimized for the combined efficiency ($\sim$ 80%) in both atmospheric[7] and extra-terrestrial neutrino searches and keeps the data at this level common to both analyses. At Level-4 we require that all cascades originate inside the detector. In IceCube many muon tracks that radiate energetic bremsstrahlung or produce hits in DOMs close to the detector edges can mimic uncontained cascades. To remove this background of partial bright muon events we require that the four earliest hits in the event are inside the fiducial volume of the detector. The boundaries of the fiducial volume in x-y are shown in Fig.2 as continuous lines. In the z direction only an upper boundary was used. It was set at the position of the 8th DOM from the top. Approximately 1% of the background events (data and Monte Carlo) and $\sim$ 13% of the Monte Carlo signal events after online filtering pass Level-3 selections and satisfy the fiducial volume requirement.

At Level-5 we require that the number of hit DOMs (NCh) is greater than 20, that the reconstructed track zenith angle exceeds 69°, and that the event duration, defined as a time difference between the last and first hit DOM, is less than 5 μs. The later cut removes long events, which are mostly coincident double or triple muon events typically with a high multiplicity of hit

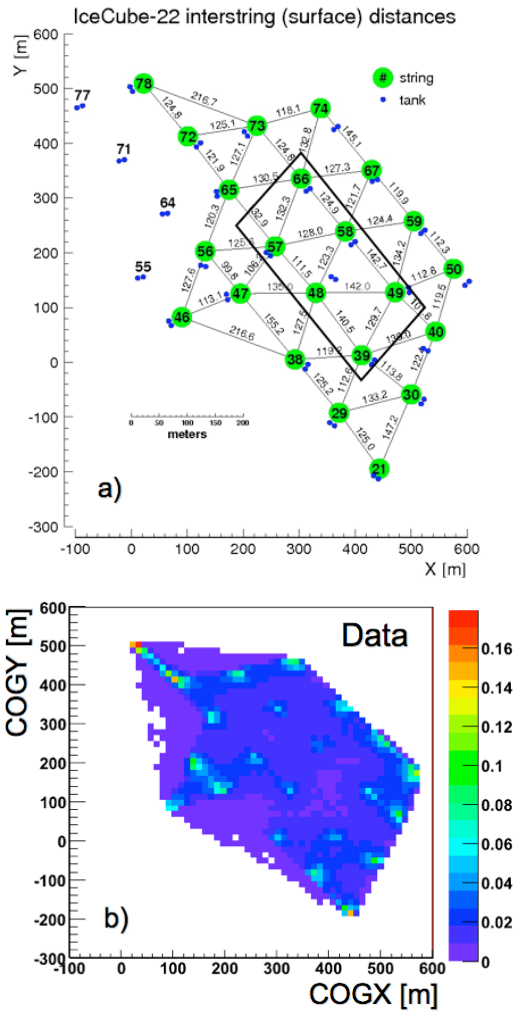

Fig. 2. a) The y versus x positions of the strings in the IC22 detector configuration. b) The reconstructed center-of-gravity (COG) y versus x position from IC22 data after online filtering. The continuous lines show the boundaries of the fiducial volume, which is used in the analyses to restrict the position of the first hits in the event.

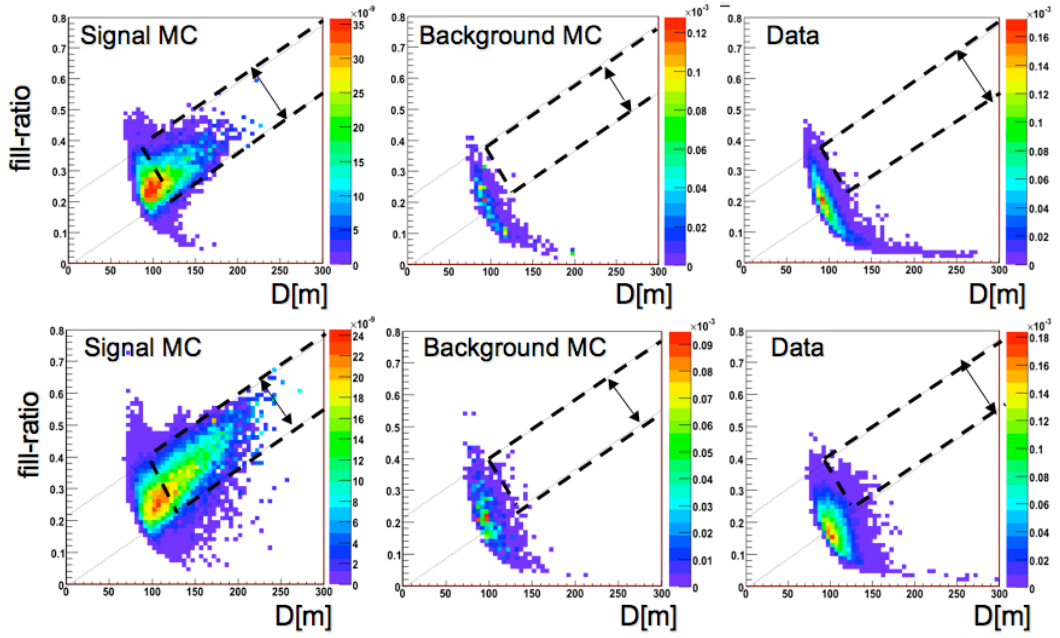

Fig. 3. The fill-ratio versus the distance D (defined in the text) for signal Monte Carlo (left) muon background Monte Carlo (middle) and the data (right) for events with COG-$z > -100$ m (top) and COG-$z < -100$ m (bottom) The dashed lines show the background cut at level 7 used in the analysis.

DOMs.

At Level-6 we require that the reconstructed cascade vertex positions $x(y)$ and COG-$x(y)$ agree to within 60 meters, and that the reduced track and cascade reconstruction likelihood ratio is less than 0.95. For each event we apply the two track reconstruction algorithm and require that the reconstructed tracks coincide to within 1μs. This selection mostly removes background events with coincident muon tracks which are well separated in time.

At Level-7 stringent selections are made on the DOM multiplicity and the fill-ratio. The fill-ratio quantifies the fraction of hit DOMs within a sphere around the reconstructed cascade vertex position with a radius $2 \times D$, where D is the average displacement of the reconstructed cascade vertex with respect to the positions of the hit DOMs in the event. The fill-ratio versus the distance D for signal Monte Carlo, muon background Monte Carlo, and the data for events with COG-$z > -100$m and COG-$z < -100$ m is shown in Fig.3. The presently used version of background Monte Carlo is in good agreement with the data for the top part of the detector, but not for the bottom part of the detector. In the bottom part of the detector, the clear ice (less absorption than at the top of the detector) makes some muons look like cascade (spherical shape and high DOM multiplicity). After applying the cuts on the fill-ratio and the distance D, as shown by the dashed lines in Fig.3 , 135 events from the data burn sample and 11 background Monte Carlo events remained. Almost all of them originate in the bottom part of the detector, as shown in Fig. 3. Remaining 11 Monte Carlo background events correspond to an expected ~ 90 events for the 240 days of the IC22 run.

We placed a final Level-8 cut on the reconstructed energy, $\log E_{\rm reco} > 4.2$, which rejects all remaining background events in the data burn sample and in the background Monte Carlo.

III. Results

The expected number of signal events (NSignal) from a diffuse flux with a strength of $10^{-6}(\mathrm{E/GeV})^{-2}/(\mathrm{GeV \cdot s \cdot sr \cdot cm^2})$ is 52 ν_e events for 240 days of livetime. Signal simulations show that events that pass all background rejection criteria are in the energy range from $\sim$ 20 TeV to a few PeV (with a mean energy of $\sim$ 160 TeV). The energy resolution is $\Delta(\log E) \sim 0.27$, the x and y position resolution is $\sim$ 10 meters. The z position resolution is worse, 25 m, because of a small fraction of events that originated below the detector where no fiducial volume cut was applied.

A burn sample of $\sim 10\%$ of the total IC22 data set and the background Monte Carlo sample were used in developing background rejection criteria. The selections are such that all events in the burn sample and all background Monte Carlo events are rejected, whereas a significant fraction of the signal Monte Carlo events are retained.

The model rejection factor (MRF) defined as: MRF = $\langle \mu_{90} \rangle$ / NSignal, will be used to determine the flux limit:

$$\Phi_{\rm limit} = \mathrm{MRF} \times f(E), \qquad (2)$$

where $f(E)$ is given by Eq.1.

TABLE I
EVENT RATES AT DIFFERENT SELECTION LEVELS FOR EXPERIMENTAL DATA (BURN SAMPLE), ATMOSPHERIC MUONS BACKGROUND MONTE CARLO AND ν_e SIGNAL MONTE CARLO ASSUMING THE FLUX $\Phi_{model} = 1.0 \times 10^{-6}(\mathrm{E/GeV})^{-2}/(\mathrm{GeV \cdot s \cdot sr \cdot cm^2})$

Level	Selection Criteria	Exp Data	Tot Bg MC	Signal MC ν_e
1	Trigger	580 Hz	565 Hz	$2.7 \times 10^3\times$ (240 days)$^{-1}$
2	$v_{\mathrm{line}} < 0.25$ and EvalRatio$_{\mathrm{ToI}} > 0.109$	20 Hz	14 Hz	$1.8 \times 10^3\times$ (240 days)$^{-1}$
3	Zenith $> 73^\circ$ and Llh(track) - Llh(cascade)> -16.2	4 Hz	2.8 Hz	$1.3 \times 10^3\times$ (240 days)$^{-1}$
4	Fiducial Volume (Fig.2)	0.3 Hz	0.15 Hz	$240\times$ (240 days)$^{-1}$
5	$NCh > 20$ and Zenith$_{32iter} > 69^\circ$ and EvtLength $< 5\mu$s	0.02 Hz	0.01 Hz	$165\times$ (240 days)$^{-1}$
6	$\lvert RecoX - COGX\rvert < 60$m and $\lvert RecoY - COGY\rvert < 60$m and ReducedLlh(track) / ReducedLlh(cascade) > 0.95 and RecoTrack1(Time)-RecoTrack2(Time) $< -1\mu$s	0.011 Hz	0.004 Hz	$161\times$ (240 days)$^{-1}$
7	Fill-Ratio (Fig.3)	6.8×10^{-5} Hz	4.3×10^{-6} Hz	$68\times$ (240 days)$^{-1}$
8	NCh> 60 and $\log E_{\mathrm{reco}} > 4.2$	0	0	$52\times$ (240 days)$^{-1}$

The analysis is limited by the currently available background Monte Carlo sample. It is not possible to subtract the simulated residual background contribution with sufficient precision. Thus the sensitivities for the diffuse flux of extraterrestrial neutrino signal, defined as the average upper limit at 90% CL and absence of signal [9], cannot be determined. To give an order of magnitude for the limit, a conservative estimate making no assumptions on background would be $4 \times 10^{-8}(5 \times 10^{-7})(\mathrm{E/GeV})^{-2}/(\mathrm{GeV \cdot s \cdot sr \cdot cm^2})$ for a hypothetical number of observed events after unblinding of 0 (20).

Enclosing, we expect the flux limit from this analysis to be of the same order as the limit on the diffuse flux $\Phi_{\mathrm{limit}} = 1.3 \times 10^{-7}(\mathrm{E/GeV})^{-2}/(\mathrm{GeV \cdot s \cdot sr \cdot cm^2})$ [10] in the cascade channel as obtained from 5 years of AMANDA data. Additional background Monte Carlo events are being generated and systematic uncertainties are currently being studied.

REFERENCES

[1] IceCube, A. Achterberg *et al.*, Astropart. Phys. **26**, 155 (2006); R. Abbasi et al. Nucl. Instrum. Meth. **A601** (2009) 294.
[2] AMANDA , J. Ahrens *et al.*, Nucl. Instrum. Meth. **A524** (2004) 169.
[3] M. Kowalski, JCAP 05 (2005) 010.
[4] D. Heck *et al.*, Tech. Rep. FZKA, 6019 (1998).
[5] A. Gazizov and M. Kowalski, Computer Physics Communications Vol. 172 **3** (2005) 203.
[6] AMANDA, J. Ahrens *et al.*, Phys. Rev. **D67** (2003) 012003.
[7] M. D'Agostino (for the IceCube Collaboration), *A search for atmospheric neutrino-induced cascades with IceCube*, these proceedings.
[8] IceCube, J. Ahrens *et al.*, IceCube Preliminary Design Document (2001).
[9] G. Feldman and R. Cousins, Phys. Rev. **D57** (1998) 3873.
[10] O. Tarasova, M. Kowalski and M. Walter (for the IceCube Collaboration), proceedings of the 30th International Cosmic Ray Conference (ICRC 2007), Merida, Yucatan, Mexico, 3-11 Jul 2007; arXiv:0711.0353 [astro-ph] pages 83-86.

Improved Reconstruction of Cascade-like Events in IceCube

Eike Middell[*†], Joseph McCartin[‡] and Michelangelo D'Agostino[§] for the IceCube Collaboration[¶]

[*]*DESY, D-15735 Zeuthen, Germany*
[†]*Institut für Physik, Humboldt-Universität zu Berlin, D-12489 Berlin, Germany*
[‡]*Dept. of Physics and Astronomy, University of Canterbury, Private Bag 4800, Christchurch, New Zealand*
[§]*Dept. of Physics, University of California, Berkeley, CA 94720, USA*
[¶]*See the special section of these proceedings.*

Abstract. **Cascade-like events are one of the main signatures in the IceCube neutrino detector. This signature includes electromagnetic and hadronic particle showers from charged or neutral current interactions and hence it provides sensitivity to all neutrino flavours. At energies below 10 PeV these cascades have characteristic lengths of only several meters. Compared to the dimensions of the detector they appear as point-like but anisotropic light sources. We present a new approach to the reconstruction of such events. A maximum likelihood algorithm that incorporates the results of detailed simulations of the light propagation in ice, allows for a significantly better analysis of the recorded photon intensities and arrival times. The performance of the algorithm is evaluated in a Monte Carlo study. It suggests that for cascades an angular resolution of 30° is possible.**

Keywords**: IceCube, cascades, reconstruction**

I. Introduction

The IceCube detector [1] is being built at the geographical South Pole. It aims for the detection of neutrinos of cosmic origin, which could answer open questions in astroparticle physics such as the origin of cosmic rays and the nature of dark matter. In its originally planned setup the IceCube detector consists of 4800 digital optical modules (DOMs) on 80 strings. These are horizontally spaced by 125 m and located in depths ranging from 1.45 to 2.45 km, thereby spanning a volume of a cubic kilometer of glacial ice. In order to lower IceCube's energy threshold down to 10 GeV, the DeepCore extension will arrange 6 additional strings in the center of the array. On these strings the DOMs are closer to each other and are located in depths with optimal optical properties.

Each DOM contains a photomultiplier tube (PMT) and the necessary readout electronics. Two digitization devices allow for the measurement of time distributions and intensities of photon fluxes inside the detector: the Analog Transient Waveform Digitizer (ATWD) taking 128 samples over the first 420 ns and the Flash Analog-to-Digital Converter (FADC) taking 256 samples in an interval of 6.4 μs [2]. Presently three quarters of the detector are successfully deployed and are taking data.

Neutrinos can interact in the instrumented volume through neutrino-nucleon or neutrino-electron scattering. The former process dominates. One exception is the resonant scattering of anti-electron neutrinos on atomic electrons at energies of 6.3 PeV, known as the Glashow resonance. The neutrino interaction is not detected directly but it can produce charged particles which emit Cherenkov light in the transparent detector medium. The possible final states of a neutrino interaction depend on the flavour and interaction type. For neutrino astronomy the most prominent neutrino signature is formed by final states with an emerging muon. They allow to deduce the neutrino direction and provide large effective areas because of the large range of the muon.

The signatures of interest here are neutrino induced electromagnetic and hadronic particle showers. Such cascades can originate from all neutrino flavours and occur in many of the interaction scenarios. Assuming that the neutrinos were generated in pion decays one expects a flavour ratio at the source of $\nu_e : \nu_\mu : \nu_\tau = 1 : 2 : 0$. Due to neutrino oscillations this ratio is transformed to $1 : 1 : 1$ before detection, which makes the sensitivity to all flavours important.

Furthermore, electromagnetic cascades allow for a good energy reconstruction, since the number of emitted photons scales linearly with the deposited energy. Hadronic cascades appear similar to electromagnetic ones, with the small correction that for the same deposited energy there are about 20% fewer photons produced [3].

Below 10 PeV cascades have characteristic lengths of several meters. Compared to the distances between the DOMs they appear as point-like light sources. Nevertheless, the angular emission profile of a cascade is anisotropic: the photons originate from one point but they are preferably emitted in the direction of the Cherenkov angle $\Theta_c = 41^\circ$ [4]. Therefore, close to the interaction vertex the neutrino direction can in principle be derived from the angular distribution of the Cherenkov photons. For the large spacing of the DOMs this ability is impaired due to the strong light scattering in the ice [5]. Because of this inherent difficulty of reconstructing the direction of particle showers in ice, studies of these events have been restricted to the search for a diffuse flux of neutrinos. In this situation even a rough estimate

on the neutrino detection would enhance the possibilities of this detection channel.

II. New Approach To Cascade Reconstruction

The existing maximum likelihood reconstruction for cascades [3] does not account for the inhomogeneity of the ice and does not try to reconstruct the neutrino direction. It also does not exploit all the capabilities of the IceCube DAQ.

The aim of the current work is to use all relevant information in the waveforms captured by the DOMs to reconstruct the incident neutrino in a cascade-like event. The point-like but directed cascade can be fully described by 7 parameters: the time and vertex (t,x,y,z) of the neutrino interaction, the deposited energy E and the direction of the neutrino. The latter is described by the two angles zenith Θ and azimuth ϕ. The reconstruction searches for the set of these parameters $\underline{c} = (t,x,y,z,E,\Theta,\Phi)$ that fits the observation best.

A good understanding of the optical properties of the glacial ice is crucial to the IceCube experiment. The instrumented volume is pervaded with dust layers that track historic climatological changes. Since the propagation of light in such an inhomogeneous medium cannot be treated analytically, the Photonics Monte Carlo package [6], [7] has been used. Its simulation results are available in tabulated form. For a given setup of a light source and a DOM these tables allow to make predictions for the mean expected amplitude $\langle\mu(\underline{c})\rangle$ and the photon arrival time distribution $p(t_d,\underline{c})$, where t_d denotes the delay time. For a photon with speed c_{ice} that is emitted at $(t_e,\vec{x}_e)$ and recorded at $(t_r,\vec{x}_r)$ the time $t_d = t_r - t_e - |\vec{x}_r - \vec{x}_e|/c_{ice}$ denotes the additional time the photon takes to reach the receiver over a scattered path rather than a straight line. Scattering in ice can cause delay times up to a few microseconds. Depending on orientation and distance of the cascade with respect to the DOM the arrival time distributions differ in shape (compare Figure 1).

With the tabulated quantities the expected amplitude in a time interval $[t_1,t_2]$ calculates to:

$$\mu(\underline{c}) = f\,\langle\mu(\underline{c})\rangle \int_{t_1}^{t_2} p(t_d,\underline{c})dt_d + R_{\text{noise}}(t_2-t_1) \qquad (1)$$

Two small corrections are applied to the prediction of Photonics. A constant rate R_{noise} accounts for noise hits and a factor f corrects for deviations from the mean amplitude due to the PMT response and charge reconstruction, which is not modelled by Photonics.

With this prediction a likelihood description of the measurement is possible. Assuming a Poisson process for every distinct[1]sample i taken by the ATWD and the FADC in DOM o, one can compare the measured amplitude n_{oi} to the mean expectation μ_{oi} and construct the likelihood:

$$L = \prod_{o,i} \frac{\mu_{oi}(\underline{c})^{n_{oi}}}{n_{oi}!} \exp\{-\mu_{oi}(\underline{c})\}. \qquad (2)$$

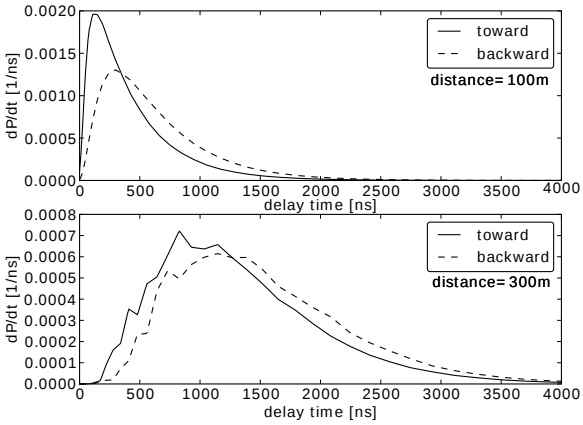

Fig. 1. Tabulated delay time distributions for a DOM at 100 m and 300 m distance to the cascade. The distributions are shown for two orientations of the cascade, pointing either toward or away from the DOM. Photons are increasingly delayed if they either travel larger distances or have to be backscattered to reach the DOM.

By taking the negative logarithm and rearranging the terms one obtains:

$$-\log(L) = \sum_o \langle\mu_o\rangle - n_o \log\langle\mu_o\rangle - \sum_i n_{oi} \log\left(\frac{\mu_{oi}}{\langle\mu_o\rangle}\right) \qquad (3)$$

where $\langle\mu_o\rangle = \sum_i \mu_{oi}$ and $n_o = \sum_i n_{oi}$. The combinatorial term from the Poisson probability has been omitted since it does not depend on the reconstruction hypothesis.

A considerable speedup in the computation results from the fact that in the sum over the samples i only time intervals with $n_{oi} > 0$ contribute. Hence, periods in the DOM readout with no measured charge can be ignored. Practically this is implemented in two steps: first the waveform is scanned for pulses, then these pulses are used to calculate the likelihood.

The cascade reconstruction is performed by searching numerically for the minimum of $-\log(L)$, which is a function of the seven cascade parameters. This minimization is seeded with the time, vertex and direction estimates that one obtains from calculating the center of gravity and tensor of inertia of the hit pattern. These calculations are implemented in IceCube's first-guess reconstruction algorithms. The number of triggered DOMs provides a rough estimate of the deposited energy. The minimization is done by MINUIT with a simplex algorithm that is executed iteratively to improve the result stepwise.

The problem can be significantly simplified if the vertex and the time of the interaction are already known (e.g. when they are determined by another method) and the orientation of the cascade is neglected. Then the likelihood, which now only depends on the cascade energy, provides an energy reconstruction that benefits

[1]In the first 420 ns the readout windows of the ATWD and FADC overlap. One has to choose between both measurements. Because of its precision, the samples from the ATWD are preferred.

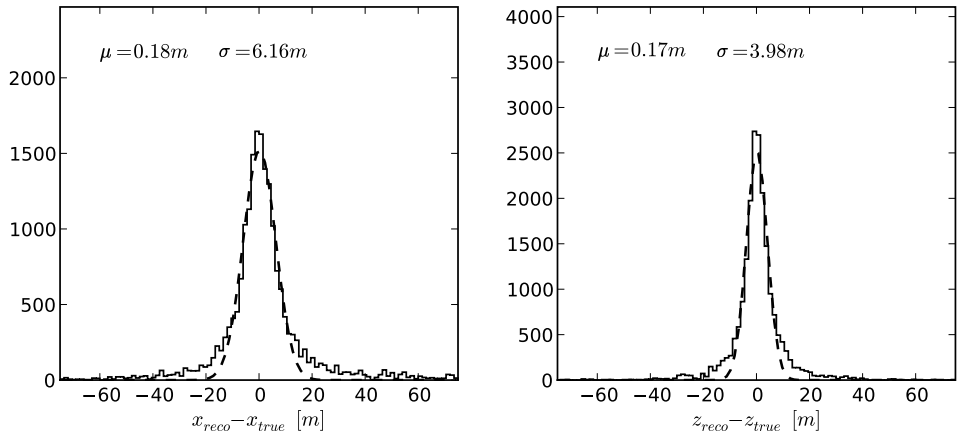

Fig. 2. Offsets between the reconstructed and the true x and z coordinates obtained from an iterative minimization of the 7 dimensional likelihood. Only cascades are selected, whose reconstructed vertex is contained in IC40. The width σ of a fitted Gaussian defines the resolution, which is better for z because of the denser DOM spacing along the string.

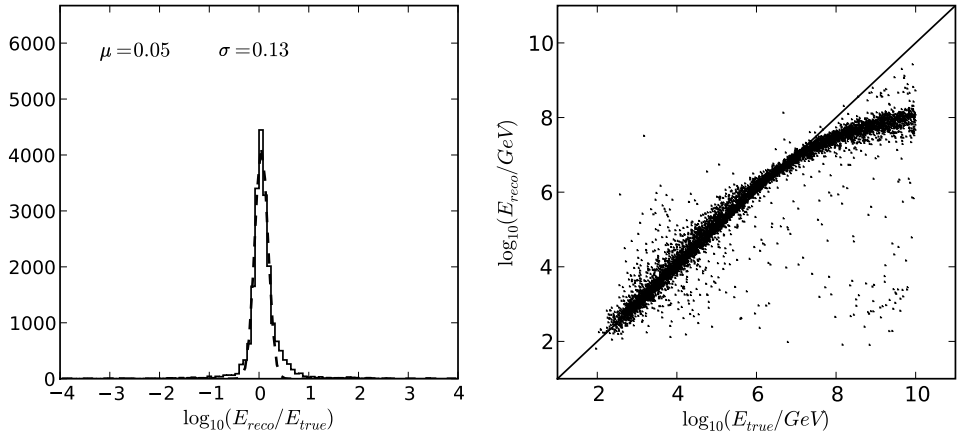

Fig. 3. Left: Offset between the reconstructed and the deposited logarithmic energy for the same event sample. Right: Comparison between the reconstructed and the deposited logarithmic energy. The deviation from the identity line above 10 PeV illustrates the increasing impact of saturation effects on the energy reconstruction.

from the improved light-propagation model. In this case, the search for the minimum is reduced to a numerical root finding problem:

$$\frac{\partial(-\log(L))}{\partial E} = \sum_o \left(\mu_o - \frac{n_o}{1 + \frac{R_{noise}\Delta t}{\mu_o}} \right) = 0 \qquad (4)$$

where Δt denotes the readout window length.

III. Results

The reconstruction algorithm has been tested with a simulated electron neutrino dataset for IceCube in its year 2008 configuration with 40 strings. The primary neutrinos have energies in the range from $10^{1.7}$ GeV to 10^{10} GeV and are weighted to an E^{-2} spectrum. For the simulation of showers the parametrization derived in [4] and implemented in Photonics is used. Lower energetic showers ($<$ PeV) are represented as point-like light source with an anisotropic emission profile. At PeV energies the cascade is split up into several cascades to simulate the elongation due to the LPM effect.

To be part of the further on used event selection, an event has to trigger the detector, the reconstruction must converge (fulfilled by 79%) and the reconstructed vertex has to be located inside the geometric boundaries of the detector (fulfilled by 38%).

To evaluate the resolution of the reconstruction the distribution of offsets between the reconstructed and the true vertex coordinates and energies are shown in Figures 2 and 3. The obtained vertex resolutions are about 7 m in x and y and 4 m in z. This is an improvement with respect to the existing likelihood reconstruction [8]. For the same dataset and selection criteria it yields resolutions of 15 m in x and y and 8 m in z. The better resolution in z results from the smaller distances of only

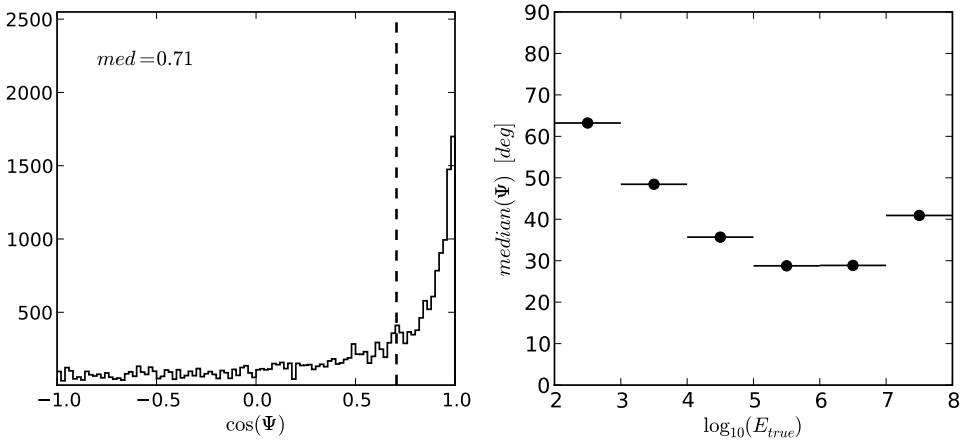

Fig. 4. Left: Distribution of the cosine of the angle between the reconstructed and the true direction. The angular resolution is given by the median. Right: Angular resolution as a function of the energy.

17 m between the DOMs on one string.

The result of the energy reconstruction is shown in Figure 3. A resolution of $\sigma(\log_{10}(E_{reco}/E_{true})) = 0.13$ has been obtained. For large photon fluxes, which can originate from highly energetic or nearby cascades, the saturation of the PMT limits the recorded charge. This affects the energy reconstruction as can be seen in the right plot of Figure 3. Above 10 PeV the reconstructed energy is systematically too low due to the saturation.

A useful measure for the angular resolution is the median of the $\cos(\Psi)$ distribution, where Ψ is the angle between the true and the reconstructed direction. For all events that fulfill the selection criterion this distribution is plotted in the left plot of Figure 4. A study of the energy dependence suggests that for the interesting energy range of 10 TeV to 10 PeV an angular resolution of $30^\circ - 35^\circ$ is possible (right plot in Figure 4). At energies above 10 PeV, the LPM effect leads to an elongation of the cascade and the reconstruction hypothesis of a point-like light source becomes no longer applicable.

IV. Summary and Outlook

A maximum likelihood reconstruction for cascade-like events has been developed. It takes into account the full recorded waveform information as well as the ice properties. A simulation study for the 40 string detector geometry of the year 2008 demonstrates the feasibility of an angular resolution of down to 30°. Compared to muons this is still a very limited precision, but it can provide new opportunities for neutrino searches with cascade-like events. With the angular resolution achieved, the discrimination between upward and downward going neutrinos becomes possible as well as the identification of neutrinos originating from the galactic plane. With the DeepCore extension a further improvement is expected.

The achieved results have to withstand further verification. The next step is to test the performance of the algorithm on measurements with LED and laser light sources in the detector and muon events with bright bremsstrahlung cascades. Several possibilities to enhance the algorithm exist. A different description of saturated DOMs in the likelihood could improve the performance at higher energies. It will be investigated if the shape of the likelihood could be used to estimate the error of the reconstruction. Finally, the presented approach can be extended to reconstruct combined events with more than one light source in the detector.

References

[1] A. Achterberg et al., Astropart.Phys.26:155-173 (2006)
[2] R. Abbasi et al., Nucl.Instrum.Meth.A601:294-316 (2009)
[3] M. Kowalski, PhD-Thesis, Humboldt University to Berlin (2004)
[4] C. Wiebusch, PhD-Thesis, RWTH Aachen, PTHA 95/37 (1995)
[5] M. Ackermann et al., J. Geophys. Res., 111, D13203 (2006)
[6] http://photonics.sourceforge.net
[7] J. Lundberg et al., Nucl.Instrum.Meth.A581:619-631 (2007)
[8] J. Kiryluk et al., in Proc. of 30th ICRC (2007)

Searches for neutrinos from GRBs with the IceCube 22-string detector and sensitivity estimates for the full detector

A. Kappes[*†], **P. Roth**[‡], **E. Strahler**[*], **for the IceCube Collaboration**[§]

[*]*Physics Dept. University of Wisconsin, Madison WI 53703, USA*
[†]*affiliated with Universität Erlangen-Nürnberg, D-91058 Erlangen, Germany*
[‡]*Physics Dept. University of Maryland, College Park MD 20742, USA*
[§]*see special section of these proceedings*

Abstract. **This contribution presents results of searches with IceCube in its 22-string configuration for neutrinos from 41 stacked gamma-ray bursts (GRBs) detected in the northern sky by satellites like Swift. In addition, the capabilities of the full 80-string detector based on a detailed simulation are discussed. GRBs are among the few potential source classes for the highest energy cosmic rays and one of the most puzzling phenomena in the universe. In their ultra-relativistic jets, GRBs are thought to produce neutrinos with energies well in excess of 100 TeV. However, up to now, no such neutrino has been observed. IceCube, currently under construction at the South Pole, is the first km^3 scale neutrino telescope. As such it will have a significantly improved sensitivity compared to the precursor class of 0.01 km^3 neutrino telescopes.**

Keywords**: Gamma-Ray Bursts, Neutrinos, IceCube**

I. INTRODUCTION

Gamma-ray Bursts (GRBs) have been proposed as a plausible source of the highest energy cosmic rays [1] and high energy neutrinos [2]. The prevalent belief is that the progenitors of so called *long-soft* GRBs are very massive stars that undergo core collapse leading to the formation of a black hole. *Short-hard* GRBs are believed to be the product of the merger of binary compact objects such as neutrons stars and black holes leading to the creation of a single black hole. Material is ejected from the progenitor in ultra-relativistic jets. In these jets, electrons and baryons are accelerated to high energies, where the synchrotron radiation from the electrons is observed as the prompt γ-ray signal. Neutrinos are predicted to be produced in the interaction of accelerated baryons with matter or photons in various phases of the GRB: *TeV precursor*—while the jet burrows through the envelope of the progenitor of a long-soft burst [3]; *PeV prompt*—in coincidence with the observed γ-ray signal [2]; *EeV early afterglow*—as the jet collides with interstellar material or the progenitor wind in the early afterglow phase [4].

IceCube is a high energy ($E \gtrsim 1\,\mathrm{TeV}$) neutrino telescope currently under construction at the South Pole [5]. When completed, the deep ice component of IceCube will consist of 5160 digital optical modules (DOMs) arranged in 86 strings frozen into the ice, at depths ranging from 1450 m to 2450 m. Each DOM contains a photo-multiplier tube and supporting hardware inside a glass pressure sphere. The total instrumented volume of IceCube will be $\sim 1\,\mathrm{km}^3$. The DOMs indirectly detect neutrinos by measuring the Cherenkov light from secondary charged particles produced in neutrino-nucleon interactions. Presently, 59 strings are installed and collect data continuously. Construction is scheduled for completion by 2011. AMANDA-II, IceCube's predecessor array, operated between January 2000 and May 2009. It consisted of 677 optical modules arranged on 19 strings with an instrumented volume approximately 60 times smaller than that of IceCube. Searches with AMANDA-II for neutrinos in coincidence with GRBs have been reported with negative results [6], [7].

The two main channels for detecting neutrinos with IceCube are the muon and the cascade channels. Charged current interactions of ν_μ produce muons that, at TeV energies, travel for several kilometers in ice and leave a track-like light pattern in the detector. The detectors are mainly sensitive to up-going muon neutrinos as the Earth can be used to shield against the much larger flux of (up-going) atmospheric muons. Searches for neutrinos from GRBs in the muon channel benefit from good angular resolution ($\sim 1^\circ$ for $E_\nu > 1\,\mathrm{TeV}$) and from the long range of high energy muons. Therefore, we use this channel in our analyses.

II. ICECUBE 22-STRING RESULTS

In our analyses, we search the IceCube 22-string configuration data, collected between May 2007 and April 2008, for muon neutrinos from GRBs in the northern hemisphere. In [8] further analyses using IceCube 22-string data are presented which extend the muon neutrino search to GRBs in the southern sky and use the cascade channel to search for neutrinos of all flavors from GRBs in both hemispheres, respectively.

We perform our searches both in the prompt (defined by the observed γ-ray emission) and the precursor (100 s before the prompt time window) time windows. In order to account for alternative emission scenarios, an additional search is conducted in an extended window from $-1\,\mathrm{h}$ to $+3\,\mathrm{h}$ around the burst. The data outside

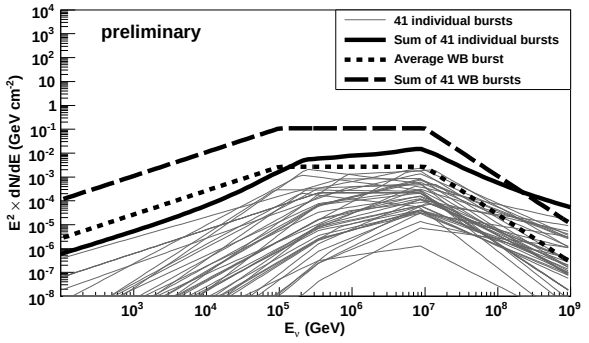

Fig. 1. Neutrino spectra for all 41 GRBs investigated in the analyses. The fluences were calculated for each burst individually using measured bursts parameters following [11]. For comparison, average Waxman-Bahcall GRB fluences (WB, [2]) are shown.

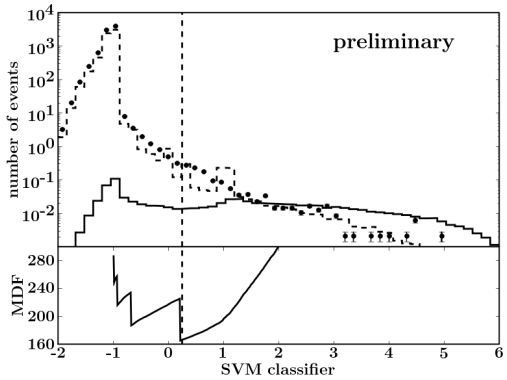

Fig. 2. The SVM classifier distribution of off-time data, simulated backgrounds (dashed), and simulated GRB muon neutrinos (solid). The lower frame displays the MDF resulting from a cut on the SVM classifier. The vertical dashed line shows the final tightened cut at 0.25.

these windows (off-time data) is used to estimate the background in the search windows.

To prevent bias in our analyses, the data within the $-1\,\mathrm{h}$ to $+3\,\mathrm{h}$ window (on-time data) are kept blind during optimization. Only low level quantities of the on-time data are examined in order to determine stability. The remaining, usable off-time data amounts to 269 days of livetime. Of the 48 northern hemisphere bursts detected by satellites (mainly Swift [9]), 7 do not have quality IceCube data associated with them during the prompt/precursor emission windows. For all remaining 41 GRBs, tests show no indications of abnormal behavior of the detector.

As customary, we use the Waxman-Bahcall model as a benchmark for neutrino production in GRBs. The original calculation with this model [2] used average GRB parameters as measured by BATSE [10]. It was refined by including specific details for individual GRBs [11]. Our neutrino calculations follow the latter prescription. For many GRBs the available information is incomplete. In that case we use average parameters in the modeling of the neutrino flux. The individual burst neutrino spectra are displayed in Fig. 1.

Tracks are reconstructed using a log-likelihood reconstruction method [12]. A fit of a paraboloid to the region around the maximum in the log-likelihood function yields an estimate of the uncertainty on the reconstructed direction. Initially, candidate neutrino events are outnumbered (by several orders of magnitude) by downgoing atmospheric muons that are mis-reconstructed as up-going events. Application of data selection criteria allows us to extract a high-purity sample of up-going (atmospheric, and potentially astrophysical) neutrinos.

In order to determine our detector response to the expected GRB neutrinos, we simulate these signal events using ANIS [13]. Background from atmospheric muons is simulated with CORSIKA [14]. Propagation of neutrinos and muons through the Earth and ice are performed with ANIS and MMC [15]. The photon signal at the DOMs is determined from a detailed simulation [16] of the propagation of Cherenkov light from muons and showers through the ice. The simulation of the DOM response takes into account the DOM's angular acceptance and includes a simulation of the DOM electronics. The DOM output is then processed with a simulation of the trigger. Afterwards, the simulated events are treated in the same way as the real data.

A. Binned analysis

We perform a binned analysis searching for emission during the prompt phase. After a loose preselection of events, various quality parameters are combined using a machine learning algorithm. The algorithm used was a Support Vector Machine (SVM) [17] with a radial basis function kernel. The SVM was trained using the off-time filtered data as background and all-sky neutrino simulation weighted to the sum of the individual burst spectra as signal. The optimum SVM parameters (kernel parameter, cost factor, margin) were determined using a coarse, and then fine, grid search with a 5-fold cross validation technique at each node [18].

The resulting SVM classification of events is shown in Fig. 2. The final cut on this parameter is optimized to detect a signal fluence with at least 5σ (significance) in 50% of cases (power) by minimizing the Model Discovery Factor (MDF). The MDF is the ratio between the signal fluence required for a detection with the specified significance and power and the predicted fluence [19]. The angular cut around each GRB is then calculated to keep 3/4 of the remaining signal after the cut on the SVM classifier. In this way, there is one cut on the SVM classifier for all GRBs, but different angular cuts around each GRB according to the angular resolution of the detector in that direction. The SVM cut that returns the best sensitivity is at 0.22. This cut lies directly on a discontinuity in the MDF curve, and so it is tightened away from that discontinuity so that a 1σ underestimation of the background level will not lead to a discovery claim more significant than is appropriate.

B. Unbinned likelihood analysis

We compare the performance of the binned analysis for the prompt emission to that of an unbinned likelihood

analysis. Furthermore, we use the unbinned method to look for neutrino emission in the precursor and extended time window. The unbinned method used here is similar to that described in [20]. The signal, $S(\vec{x}_i)$, and background, $B(\vec{x}_i)$, PDFs are formed from a product of a directional, time and an energy PDF.

Signal PDF: The directional signal PDF is a two-dimensional Gaussian distribution with the two widths being the major and minor axes of the 1σ error ellipse of the paraboloid fit. The time PDF is flat over the respective time window and falls off on both sides with a Gaussian distribution of variable width depending on the duration of the emission. The energy PDF is determined from the distribution of an energy estimator [21] for each GRB individually. The signal PDFs of the GRBs are combined using a weighted sum [22]

$$S_{\rm tot}(\vec{x}_i) = \frac{\sum_{j=1}^{N_{\rm GRBs}} w_j \, S_j(\vec{x}_i)}{\sum_{j=1}^{N_{\rm GRBs}} w_j} \ , \qquad (1)$$

where $S_j(\vec{x}_i)$ is the signal PDF of the jth GRB and w_j is a weight that for of the prompt and precursor window is proportional to the expected number of events in the detector according to the calculated fluences. In the case of the extended window we use $w_j = 1$ for all GRBs.

Background PDF: For the directional background PDF obtained from the off-time data, the detector asymmetries in zenith and azimuth are taken into account by evaluating the data in the detector coordinate system. The time distribution of the background during a GRB can be assumed to be constant, yielding a flat time PDF. The energy PDF is determined in the same way as for the signal PDF with the spectrum corresponding to the Bartol atmospheric neutrino flux [23].

All PDFs are combined in a log-likelihood ratio

$$\ln(\mathcal{R}) = -\langle n_s \rangle + \sum_{i=1}^{N} \ln\left(\frac{\langle n_s \rangle \, S_{\rm tot}(\vec{x}_i)}{\langle n_b \rangle \, B(\vec{x}_i)} + 1\right) \qquad (2)$$

where the sum runs over all reconstructed tracks in the final sample. The variable $\langle n_b \rangle$ is the expected mean number of background events, which is determined from the off-time data set. The mean number of signal events, $\langle n_s \rangle$, is a free parameter which is varied to maximize equation 2 in order to obtain the best estimate for the mean number of signal events, $\langle \hat{n}_s \rangle$.

To determine whether a given data set is compatible with the background-only hypothesis, 10^8 background data sets for the on-time windows are generated from off-time data by randomizing the track times while taking into account the downtime of the detector. For each of these data sets the $\ln(\mathcal{R})$ value is calculated. The probability for a data set to be compatible with background is given by the fraction of background data sets with an equal or larger $\ln(\mathcal{R})$ value.

The analysis is performed on a high-purity up-going neutrino sample after tight selection criteria have been applied. The unbinned likelihood method requires an ~ 1.8 times lower fluence for a 5σ detection than the binned method. The former is therefore used for the results presented in this paper.

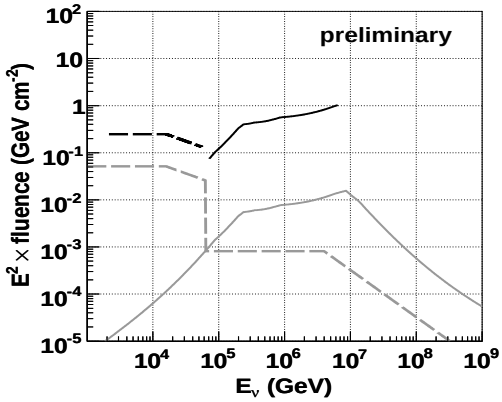

Fig. 3. Light lines—Predicted fluences from the 41 northern hemisphere GRBs for different emission models: prompt (solid, sum of individual spectra as plotted in Fig. 1) and precursor (dashed, [3]). Dark lines—90% C.L. upper limits on the neutrino fluences obtained with the unbinned likelihood analysis.

The unblinding procedure involves applying the likelihood method to the on-time data set after neutrino candidate event selection. For all three emission scenarios the best estimate for the number of signal events ($\langle \hat{n}_s \rangle$) is zero and hence consistent with the null hypothesis. Figure 3 displays preliminary 90% C.L. upper limits for the 41 GRBs on the fluence in the prompt phase (sum of individual spectra as plotted in Fig. 1) of $3.7 \times 10^{-3}\,\mathrm{erg\,cm^{-2}}$ (72 TeV – 6.5 PeV) and on the fluence from the precursor phase [3] of $1.16 \times 10^{-3}\,\mathrm{erg\,cm^{-2}}$ (2.2 TeV – 55 TeV), where the quoted energy ranges contain 90% of the expected signal events in the detector. The limits obtained are not strong enough to constrain the models. The preliminary 90% C.L. upper limit for the wide time window is $2.7 \times 10^{-3}\,\mathrm{erg\,cm^{-2}}$ (3 TeV – 2.8 PeV) assuming an E^{-2} flux.

III. IceCube Sensitivity study for the full detector

Previous studies have estimated the sensitivity of the completed IceCube to neutrino fluxes from GRBs [24], [25]. We present new results using updated information about the detector, improved simulation, and more accurate calculation of the backgrounds.

We utilize the same methods as in the 22-string search to study the sensitivity of the full 86 string detector. We generate a set of fake GRBs by sampling from the populations observed by the Swift [9] and Fermi [26] satellites and taking their observation rates into account. We distribute these bursts isotropically over the sky and randomly in time to produce a set of 142 fake GRBs in the northern sky for a detector livetime of one year, with 6840 s of total emission during the prompt phase. Currently, we use the average Waxman-Bahcall GRB neutrino flux for all bursts [2]. In the future, it will be replaced by individual spectra. To test the precursor phase, we assume each burst has such emission [3]

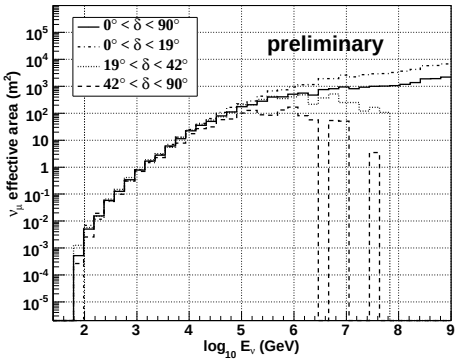

Fig. 4. Muon neutrino effective area for the full IceCube detector as a function of energy. Solid line is averaged over the half sky, while dot-dashed, dotted, and dashed lines represent the most horizontal, middle, and most vertical thirds of the northern sky in $\cos\delta$, respectively.

lasting for 100 s immediately preceeding the observed photons.

As no off-time data is available to determine the background, it is simulated. Atmospheric muons and neutrinos are generated over the full sky and propagated to the detector in the same manner as outlined in section II. The geometry of the full detector is simulated in determining the response to Cherenkov photons. Signal and background are filtered with cuts on quality parameters to create a sample of well-reconstructed, seemingly upgoing events. Further event selection with a machine learning algorithm [27] is then performed to remove the remaining misreconstructed downgoing muons. Afterwards, no atmospheric muons remain in the sample due to the limited amount of Monte Carlo. As no real data is available for comparison, the exact purity of the remaining background sample is unknown, but is estimated to consist of $> 95\%$ atmospheric neutrinos below the horizon, while retaining a large fraction of GRB signal neutrinos. The effective area for different declination bands is shown in Fig. 4. Given the detector angular resolution of $\sim 1^\circ$, we select a search bin radius of 2° around each fake GRB location, retaining 70–90% of signal neutrinos (depending on declination) while dramatically reducing the isotropic background rate. The background is then rescaled to match the emission time window for each burst.

First results of this study indicate that we will be able to detect neutrinos from GRBs in either phase at the 5σ level in greater than 90% of potential experiments within the first few years of operating the full detector. In the event of non-detection, we will be able to set strict upper limits well below the fluences predicted by these models.

IV. Conclusions

We have presented results of searches for muon neutrinos from GRBs with the 22-string configuration of the IceCube detector. These searches covered several time windows corresponding to the various phases of the predicted emission. In all cases, the data were consistent with the background only hypothesis. Hence, we place upper limits on the muon neutrino fluences from the different phases, which, however, are not tight enough to constrain any model yet.

We are also performing a detailed sensitivity study for the full 80-string IceCube detector. The preliminary results of this study show that IceCube will be able to detect the neutrino flux predicted by the leading models with a high level of significance within the first few years of operation or, in the event of no observation, place strong constraints on emission of neutrinos from GRBs.

V. Acknowledgments

A. Kappes acknowledges the support by the EU Marie Curie OIF Program.

References

[1] E. Waxman, *Phys. Rev. Lett.*, vol. 75, p. 386, 1995.
[2] E. Waxman and J. N. Bahcall, *Phys. Rev. Lett.*, vol. 78, p. 2292, 1997.
[3] S. Razzaque, P. Meszaros, and E. Waxman, *Phys. Rev.*, vol. D68, p. 083001, 2003.
[4] E. Waxman and J. N. Bahcall, *ApJ*, vol. 541, p. 707, 2000.
[5] A. Karle, (IceCube Coll.) *et al.*, Preprint arXiv:0812.3981, 2008.
[6] A. Achterberg, (IceCube Coll.) *et al.*, *ApJ*, vol. 664, p. 397, 2007.
[7] ——, *ApJ*, vol. 674, p. 357, 2008.
[8] K. Hoffman, K. Meagher, P. Roth, I. Taboada, (IceCube Coll.) *et al.*, in *this proceedings, ID515*, 2009.
[9] D. N. Burrows *et al.*, *Space Sci. Rev.*, vol. 120, p. 165, 2005.
[10] G. J. Fishman *et al.*, in *Proc. GRO Science Workshop*, GSFC, 1989, p. 2.
[11] D. Guetta *et al.*, *Astropart. Phys.*, vol. 20, p. 429, 2004.
[12] J. Ahrens, (AMANDA Coll.) *et al.*, *Nucl. Inst. Meth.*, vol. A524, p. 169, 2004.
[13] A. Gazizov and M. O. Kowalski, *Comp. Phys. Comm.*, vol. 172, p. 203, 2005.
[14] D. Heck *et al.*, "Corsika: A Monte Carlo code to simulate extensive air showers," FZKA, Tech. Rep., 1998.
[15] D. Chirkin and W. Rhode, Preprint hep-ph/0407075, 2004.
[16] J. Lundberg *et al.*, *Nucl. Inst. Meth.*, vol. A581, p. 619, 2007.
[17] C. Cortes and V. Vapnik, *Machine Learning*, vol. 20, no. 3, p. 273, 1995.
[18] C. Hsu, C. Chang, and C. Lin, "A practical guide to support vector classification," Department of Computer Science, National Taiwan University, Tech. Rep., 2003.
[19] G. C. Hill, J. Hodges, B. Hughey, A. Karle, and M. Stamatikos, in *Proc. PHYSTAT O5: Statistical Problems in Particle Physics*, Oxford, United Kingdom, Sep 2005.
[20] J. Braun, J. Dumm, F. de Palma, C. Finley, A. Karle, and T. Montaruli, *Astropart. Phys.*, vol. 29, p. 299, 2008.
[21] J. Zornoza, D. Chirkin, (IceCube Coll.) *et al.*, in *Proc. International Cosmic Ray Conference (ICRC'07)*, Mérida, Mexico, Aug. 2007.
[22] R. Abbasi, (HiRes Coll.) *et al.*, *ApJ*, vol. 636, p. 680, 2006.
[23] G. D. Barr *et al.*, *Phys. Rev.*, vol. D70, p. 023006, 2004.
[24] J. Ahrens, (IceCube Coll.) *et al.*, *Astropart. Phys.*, vol. 20, p. 507, 2004.
[25] A. Kappes, M. Kowalski, E. Strahler, I. Taboada, (IceCube Coll.) *et al.*, in *Proc. International Cosmic Ray Conference (ICRC'07)*, Mérida, Mexico, Aug. 2007.
[26] A. A. Moiseev *et al.*, *Nucl. Inst. Meth.*, vol. A588, p. 41, 2008.
[27] D. Chirkin, (IceCube Coll.) *et al.*, in *this proceedings, ID0466*, 2009.

Search for neutrinos from GRBs with IceCube

K. Meagher*, P. Roth*, I. Taboada†, K. Hoffman*, for the IceCube Collaboration‡

*Physics Dept. University of Maryland, College Park MD 20742, USA
†School of Physics and Center for Relativistic Astrophysics, Georgia Institute of Technology, Atlanta, GA 30332, USA
‡see special section of these proceedings

***Abstract*. Gamma-ray bursts (GRBs) are one of the few potential sources for the highest energy cosmic rays and one of the most puzzling phenomena in the universe. In their ultra relativistic jets, GRBs are thought to produce neutrinos with energies well in excess of 100 TeV. IceCube, a neutrino telescope currently under construction at the South Pole, will have improved sensitivity to these yet unobserved neutrinos. This contribution describes the methods used for all IceCube neutrino searches from GRBs triggered by satellites. We also present the status of three searches for neutrinos in coincidence with GRBs. The first search seeks to extend existing IceCube 22-string ν_μ searches to the high background southern hemisphere bursts. A second search looks for neutrino-induced cascades with the 22-string configuration of IceCube. Another ν_μ search is planned for the 40-string configuration of IceCube, and its status is presented here. This paper is a companion of another ICRC IceCube contribution that summarizes the IceCube 22-string northern hemisphere ν_μ GRB search results and the expected capabilities of the completed 86-string detector.**

***Keywords*: Gamma-Ray Bursts, Neutrinos, IceCube**

I. INTRODUCTION

Gamma-ray Bursts (GRBs) have been proposed as one of the most plausible sources of the highest energy cosmic rays [1] and high energy neutrinos [2]. The prevalent belief is that the progenitors of so called *long-soft* GRBs are very massive stars that undergo core collapse leading to the formation of a black hole. *Short-hard* GRBs are believed to be the product of the merger of binary compact objects such as neutrons stars and black holes leading to the creation of a single black hole. Material is ejected from the progenitor in ultra-relativistic jets which then produce the observed burst of γ-rays and accelerate particles, including baryons, to high energy. Neutrinos are predicted to be produced in multiple scenarios: while the jet burrows through the envelope of the progenitor of a long-soft burst [3] (TeV precursor), in coincidence with the observed γ-ray signal [2] (prompt) and as the jet collides with interstellar material or the progenitor wind in the early afterglow phase [4] (EeV early afterglow.)

We use the Waxman-Bahcall model as a benchmark for neutrino production in GRBs. The original calculation with this model used average GRB parameters as measured by BATSE [2]. It was refined by including specific details for individual GRBs [5]. Our neutrino calculations follow this latter prescription. For many GRBs the available information is incomplete. In that case we use average parameters in the modeling of the neutrino flux.

IceCube is a high energy ($E \gtrsim 1\,\mathrm{TeV}$) neutrino telescope currently under construction at the South Pole [6]. The total instrumented volume of IceCube will be $\sim 1\,\mathrm{km}^3$. IceCube indirectly detects neutrinos by measuring the Cherenkov light from secondary charged particles produced in neutrino-nucleon interactions. A total of 5160 Digital Optical Modules (DOMs) arranged in 86 strings frozen in the ice are planned. The results presented here correspond to the 22- and 40-string configurations. AMANDA-II [7], IceCube's predecessor array, had an instrumented volume ≈ 60 times smaller than that of the full IceCube. Searches of neutrinos in coincidence with GRBs by AMANDA have been reported with negative results [8], [9].

The two main channels for detecting neutrinos with IceCube are the muon and the cascade channels. Charged current interactions of ν_μ produce muons that, at TeV energies, travel for several kilometers in ice. For the muon channel the detectors are mainly sensitive to up-going muons as the Earth can be used to shield against the much larger flux of down-going atmospheric muons. Because the neutrino-induced muon spectrum from GRBs is expected to be much harder than cosmic-ray induced muons GRB neutrino searches can be extended to the southern hemisphere are shown in section III. Searches for neutrinos from GRBs in the muon channel benefit from good angular resolution ($\sim 1^\circ$ for $E_\nu > 1\,\mathrm{TeV}$) and from the long range of high energy muons. In the cascade channel the detectors are sensitive to all neutrino flavors through various interaction channels. In this case almost all of the neutrino energy is deposited in a narrow cylinder of O(10 m) in length; point-like compared to IceCube dimensions. The cascade channel analyses benefit from good energy resolution (~ 0.1 in $\log_{10} E$) and from 4π sr sensitivity. Complex event topologies can also arise from ν_τ-induced events for energies above $\gtrsim 1$ PeV [10].

II. Satellite Triggered Searches for Neutrinos in Coincidence with GRBs

There are several methods for searching for neutrinos from GRBs. The present contribution and its companion [11] are *satellite triggered searches*. A list of GRB times and sky localizations is obtained from satellites, such as Swift, Fermi and others. From the perspective of IceCube, the ideal GRB that is a source of neutrinos has a high photon fluence, a well measured spectrum, redshift and other electromagnetic properties and is localized with higher accuracy than the pointing resolution of IceCube ($\sim 1^\circ$ for the completed detector). Therefore wide field of view searches are preferable even at the expense of reduced sensitivity. In that respect, Fermi is the main source of GRBs expected to produce neutrinos. Fermi started operations in summer 2008, before this time, the main source of GRBs for study was Swift.

To avoid potential biases, all satellite triggered searches are conducted using *blind* analysis methods. The *on-time* window around each GRB is left unexamined, except for low level quantities that allow to establish the stability of the detector. The length of the on-time window depends on the analysis. The remainder of the data collected by IceCube, or *off-time* window, are used to measure the background experimentally. The on-time window is studied (*unblinded*) only once the analysis procedure has been fully established.

Searches for GRB neutrinos are performed if the detector is determined to have been in a period of stable operation according to general data requirements developed and shared by the IceCube collaboration. In addition the time difference between consecutive events is calculated. At trigger level and for initial event selection criteria the event rate in IceCube is dominated by atmospheric muons produced in cosmic ray showers. Given uncorrelated cosmic rays the time difference between consecutive events is expected to fall exponentially with time and the time constant should correspond to the inverse of the detector event rate. Finally a histogram of the frequency of number of events in 10 s bins is fitted with a Gaussian distribution. Deviations from a normal distribution, measured by a reduced χ^2, indicate periods of high or low detector event rate. Only GRBs corresponding to stable detector periods are considered.

Neutrinos are simulated using an implementation of the ANIS code [12] and atmospheric muons using the CORSIKA air shower simulation package [13]. Propagation of neutrinos and muons through the Earth and ice are performed with ANIS and MMC [14]. The photon signal in the DOMs is determined from a detailed simulation [15] of the propagation of Cherenkov light from muons and showers through the ice. This is followed by a simulation of the DOM electronics and the trigger. The DOM signals are then processed in the same way as the data. The theoretical models tested have been corrected to take into account neutrino oscillations.

III. IceCube 22-string Southern Hemisphere Muon Search

In this analysis we search for muon neutrinos emitted in the prompt phase from GRBs in the southern hemisphere (negative declination). We use filtered data collected with the IceCube detector in its 22-string configuration between May 2007 and April 2008 for bursts with declination $> -40^\circ$. Very low level data taken within two hours of a burst trigger is used for those with declination $< -40^\circ$. In both cases, the data taken ± 20 minutes from the burst trigger is considered to be the on-time window. Following the stability procedure described in section II we find that two of the 42 southern hemisphere bursts do not pass the data quality criteria or have missing data during the prompt emission windows. For the remaining 40 GRBs, these tests show no indications of abnormal behavior of the detector.

Tracks are reconstructed using a log-likelihood reconstruction method [16]. A fit of a paraboloid to the region around the minimum in the log-likelihood function yields an estimate of the uncertainty on the reconstructed direction. Various quality parameters and energy related parameters are derived from the results of some other reconstructions discussed in [16] and [17].

The track quality and energy related variables are combined using a machine learning algorithm. The algorithm used was a Support Vector Machine (SVM) [18] with a radial basis function kernel. One SVM was trained for the filtered dataset after a loose preselection of events and another was trained on the low level dataset. In both cases, off-time background data is taken as the background and all-sky neutrino simulation is used as the signal. The result is an SVM classification between -1 (background-like) and 1 (signal-like) for all events.

An unbinned likelihood method like the one described in [19] was used to search each on-time window. This method avoids using restrictive selection criterion to throw away events but instead uses probability density functions (PDFs) to evaluate whether events are more likely to be signal or background. The signal, $S(\vec{x}_i)$, and background, $B(\vec{x}_i)$, PDFs are each the product of a time, a space, and an SVM PDF.

The space signal PDF is a two-dimensional Gaussian determined from the paraboloid fit. The time PDF is flat over the respective time window and falls off on both sides with a Gaussian distribution with width equal to the time window length. The SVM PDF is determined from the SVM classifier distribution for simulated signal events.

For the space background PDF the detector asymmetries in zenith and azimuth are taken into account by evaluating the off-time data in the detector coordinate system. The time distribution of the background during a GRB is flat over the entire on-time window. The SVM PDF is again determined from the SVM classifier distribution of off-time background data.

All PDFs are combined in an extended log-likelihood function [20] where the sum runs over all reconstructed

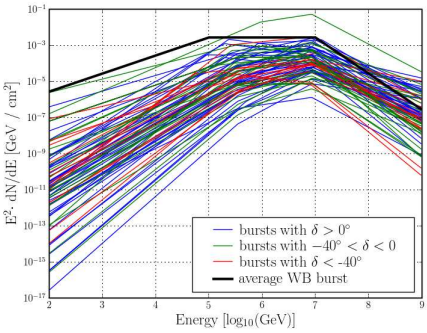

Fig. 1. The calculated neutrino fluxes for all burst triggers taken during IceCube's 22-string operations in different declination bands.

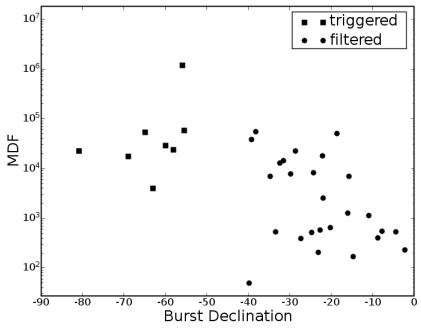

Fig. 2. The 5σ 50% MDF for each burst in the southern hemisphere muon neutrino search.

tracks in the final sample. The variable $\langle n_b \rangle$ is the expected mean number of background events, which is determined from the off-time data set. The mean number of signal events, $\langle n_s \rangle$, is a free parameter which is varied to maximize the expression

$$\ln\left(\mathcal{R}(\langle n_s \rangle)\right) = -\langle n_s \rangle + \sum_{i=1}^{N} \ln\left(\frac{\langle n_s \rangle\, S_{\rm tot}(\vec{x}_i)}{\langle n_b \rangle\, B_{\rm tot}(\vec{x}_i)} + 1\right) \quad (1)$$

in order to obtain the best estimate for the mean number of signal events, $\langle \hat{n}_s \rangle$.

To determine whether a given data set is compatible with the background-only hypothesis, 10^8 background data sets for the on-time windows are generated from off-time data by randomizing the track times while taking into account the downtime of the detector. For each of these data sets the $\ln(\mathcal{R})$ value is calculated. The probability for a data set to be compatible with background is given by the fraction of background data sets with an equal or larger $\ln(\mathcal{R})$ value. The sensitivity of each search is determined by injecting simulated signal events into these randomizations and observing the resultant $\ln(\mathcal{R})$ distribution. This allows for the calculation of the Model Detection Factor (MDF) for each analysis (figure 2). The MDF is the ratio of the lowest signal fluence required for a detection with the required significance and power to the predicted fluence [21].

IV. IceCube 22-string Cascade Search

We are currently conducting a search for neutrino-induced cascades in the prompt phase for 81 GRBs at all declinations in coincidence with data from stable detector periods (see section II for details) collected with IceCube in its 22-string configuration. The on-time period for this analysis is $\pm$ 1 hour. The off-time is the remainder of the data collected by IceCube with 22 strings between May 2007 and April 2008 with a livetime of $\sim$269 days.

The analysis proceeds in three steps. First, a preliminary selection of cascade-like events is performed online at the South Pole. Second, the South Pole filtered data are reconstructed by minimizing log-likelihood functions that take into account the propagation of photons through ice from the source to the digital optical modules [16]. The reconstructions are performed for both a muon hypothesis and a cascade hypothesis. The muon hypothesis reconstruction provides a position, a direction, time and several quality parameters that describe how appropriately the muon hypothesis fits the data. The cascade hypothesis reconstruction provides a candidate neutrino interaction vertex, time, cascade energy and quality parameters. After the reconstruction further selection criteria are applied:

- $L_\mu - L_{cascade} > -16.2$. The difference in the log-likelihood quality parameters for the muon and cascade reconstruction identifies events that are better described by the cascade hypothesis.
- $\theta_\mu > 73°$. Events that match a down-going muon are rejected. Here the $\theta_\mu = 0°$ represents a vertical down-going muon.
- $L_{cascade}/(Nhit - 5) < 8.0$. Cascade events that are low energy or too far from the detector are reconstructed poorly. We use the cascade hypothesis reduced log-likelihood quality parameter to select well reconstructed cascade events.
- $N_{1hit}/N_{hit} < 0.1$. This quantity is a simple cascade energy proxy because it is equivalent to the surface to volume ratio of a spherical pattern of light. N_{1hit} measures the number of DOMs in an event that have only one hit (typically one photo-electron), N_{hit} measures the total number of hits.

For the optimization of the selection criteria we are currently using the Waxman-Bahcall spectrum [2] for the expected $\nu_e + \bar{\nu}_e$ signal. After applying the selection criteria described above, we expect 0.36 ($\nu_e + \bar{\nu}_e$) from 81 GRBs. Because Swift is the main source of GRBs for this analysis, we expect the typical GRB to be about one order of magnitude dimmer than what was assumed for the Waxman-Bahcall spectrum[1]. If a detailed per-burst simulation is performed we expect a significantly lower signal rate. After applying the selection criteria described above $\approx 1.5 \times 10^5$ events remain in the off-time data.

[1]The Waxman-Bahcall model assumed BATSE average GRB parameters, especially $z_{\rm GRB} = 1$, while Swift's mean observed redshift is significantly higher.

For the third and final part of the analysis we discriminate signal from background with a neural network that uses the parameters described above plus the reconstructed energy of the cascade hypothesis and a topological parameter that discriminates long (muon) from spherical (cascade) events. A cut on the neural network parameter provides the final discrimination between signal and background.

V. IceCube 40-string Muon Search

IceCube began operating with 40 strings on April 5 2008 and continues to collect data in this configuration at the time of writing. During this time IceCube remained extremely stable and maintained a livetime of approximately 95%. These additional strings give IceCube a fiducial volume of approximately 0.5 km^3 making it the largest neutrino detector to date. This section will cover the analysis of the northern hemisphere bursts. An analysis of the southern hemisphere bursts will follow.

To date there have been 116 northern hemisphere GRBs reported via GCN circulars during 40-string operations. The launch of the Fermi Gamma-Ray Space Telescope with the Gamma-Ray Burst Monitor (GBM) has greatly increased the number of bursts available for analysis. However, the GBM bursts are usually poorly localized and have 1 sigma uncertainties spanning from 1 to 15 degrees. In addition there are several bursts detected by other satellites of the InterPlanetary Network (IPN), including the brightest burst in the sample, GRB080408B, which result in a total of 48 bursts with localization uncertainties of larger than one degree. In order to search regions of the sky larger than IceCube's angular resolution of approximately 1.5 degrees, new methods must be utilized. Expanding on the unbinned likelihood analysis presented in section III, an extended source hypothesis must be created that takes into account both the GRB's localization error and IceCube's angular uncertainty:

$$S_{\text{space}}(\vec{x}_i) = \frac{1}{N}\int_{4\pi} \mathrm{d}\Omega \cdot e^{\frac{(\vec{r}-\vec{r}_\gamma)^2}{2\sigma_\gamma}+\frac{(\vec{r}-\vec{r}_\nu)^2}{2\sigma_\nu}} \qquad (2)$$

where $\vec{r}_\gamma$ and σ_γ are the location and uncertainty of the GRB as reported in the GCN circular, $\vec{r}_\nu$ and σ_ν are the uncertainty of the IceCube neutrino candidate, and N is a normalization.

Sensitivity studies are currently being performed and will be available soon.

VI. Conclusions

Satellite triggered searches for neutrinos in coincidence with GRBs use many common techniques. The southern hemisphere ν_μ search is a first attempt to extend IceCube's sensitivity to GRBs into the higher background region above the horizon. The cascade search provides sensitivity to all neutrino flavors over 4π sr. The 40-string search provides greater sensitivity due to IceCube's growing effective area and greater number of burst triggers from Fermi.

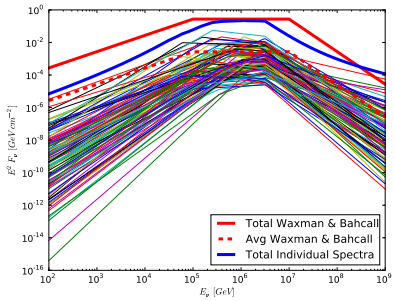

Fig. 3. The Calculated Neutrino Spectrum for 102 of the 116 northern hemisphere bursts for which spectral information was available. The Sum of the Neutrino spectrum is plotted along with the Average Waxman and Bahcall spectrum for a single burst and for 102 bursts.

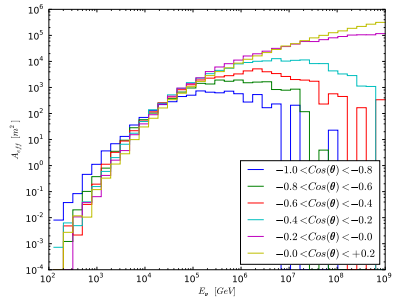

Fig. 4. Effective Area of 40 string IceCube.

References

[1] E. Waxman, *Phys. Rev. Lett.*, vol. 75, p. 386, 1995.
[2] E. Waxman and J. N. Bahcall, *Phys. Rev. Lett.*, vol. 78, p. 2292, 1997.
[3] S. Razzaque, P. Meszaros, and E. Waxman, *Phys. Rev.*, vol. D68, p. 083001, 2003.
[4] E. Waxman and J. N. Bahcall, *ApJ*, vol. 541, p. 707, 2000.
[5] D. Guetta *et al.*, *Astropart. Phys.*, vol. 20, p. 429, 2004.
[6] A. Karle, (IceCube Coll.) *et al.*, in *Proc. International Cosmic Ray Conference (ICRC'09)*, Lodź, Poland, 2009.
[7] E. Andrés, (AMANDA Coll.) *et al.*, *Nature*, vol. 410, p. 441, 2001.
[8] A. Achterberg, (IceCube Coll.) *et al.*, *ApJ*, vol. 664, p. 397, 2007.
[9] ——, *ApJ*, vol. 674, p. 357, 2008.
[10] T. Deyoung, S. Razzaque, and D. F. Cowen, *Astroparticle Physics*, vol. 27, pp. 238–243, Apr. 2007.
[11] A. Kappes, P. Roth, E. Strahler, (IceCube Coll.) *et al.*, in *Proc. International Cosmic Ray Conference (ICRC'09)*, Lodź, Poland, 2009.
[12] A. Gazizov and M. O. Kowalski, *Comp. Phys. Comm.*, vol. 172, p. 203, 2005.
[13] D. Heck *et al.*, *Technical Report FZKA*, vol. 6019, 1998.
[14] D. Chirkin and W. Rhode, "hep-ph/0407075."
[15] J. Lundberg *et al.*, *Nucl. Inst. Meth.*, vol. A581, p. 619, 2007.
[16] J. Ahrens, (AMANDA Coll.) *et al.*, *Nucl. Inst. Meth.*, vol. A524, p. 169, 2004.
[17] J. Zornoza, D. Chirkin, (IceCube Coll.) *et al.*, in *Proc. International Cosmic Ray Conference (ICRC'07)*, Merida, Mexico, Aug. 2007.
[18] C. Cortes and V. Vapnik, *Machine Learning*, vol. 20, no. 3, p. 273, 1995.
[19] J. Braun, J. Dumm, F. de Palma, C. Finley, A. Karle, and T. Montaruli, *Astropart. Phys.*, vol. 29, p. 299, 2008.
[20] R. J. Barlow, *Statistics*. Wiley, 1989.
[21] G. C. Hill, J. Hodges, B. Hughey, A. Karle, and M. Stamatikos, in *Proc. PHYSTAT O5: Statistical Problems in Particle Physics*, Oxford, United Kingdom, Sep 2005.

Search for GRB neutrinos via a (stacked) time profile analysis

Martijn Duvoort* **and Nick van Eijndhoven*** **for the IceCube collaboration†**
*University of Utrecht, The Netherlands
†see special section of these proceedings

***Abstract*. An innovative method to detect high-energy neutrinos from Gamma Ray Bursts (GRBs) is presented. The procedure provides a good sensitivity for both prompt, precursor and afterglow neutrinos within a 2 hour time window around the GRB trigger time. The basic idea of the method consists of stacking of the observed neutrino arrival times with respect to the corresponding GRB triggers. A possible GRB neutrino signal would manifest itself as a clustering of signal candidate events in the observed time profile. The stacking procedure allows to identify a signal even in the case of very low rates.**

We outline the expected performance of analysing four years of AMANDA data (2005–2008) for a sample of 130 GRBs. Because of the extreme optical brightness of GRB080319B, it might be that this particular burst yielded multiple detectable neutrinos in our detector. As such, the method has also been applied to the data of this single burst time profile. The results of this analysis are presented in a separate section.

***Keywords*: GRB Neutrinos AMANDA/IceCube**

I. Introduction

Gamma Ray Bursts are among the most promising sources for high-energy neutrino detection: the accurate localization and timing information presently available, enable very effective background reduction for high-energy neutrino detectors. Yet, no previous search for GRB neutrinos has led to a discovery [1], [2]. As most models of a GRB jet predict neutrino formation simultaneous with the prompt γ emission, previous analyses aim to discover neutrinos that arrive simultaneously with the prompt photons. However, it might be that the main GRB neutrino signal is not simultaneous with the prompt gammas, either in production or arrival at the Earth.

A variety of the models predict the formation of high-energy neutrinos at different stages in the evolution of a GRB. Afterglow models predict a significant neutrino flux a few seconds after the prompt emission [3], [4]. The existence of multiple colliding shells in a GRB jet [5] may also lead to a time difference between high-energy gamma emission and neutrinos. Even if the neutrinos and photons are produced at the same stage of the evolution of the GRB jet, a time difference at the observer may be present: as the jet evolves, it will become transparent for photons at a later stage than for neutrinos. Therefore, neutrinos might be able to escape the source region well before the high-energy photons. This will depend heavily on the actual stage in the evolution of the jet.

For our analysis we use the data of the AMANDA-II detector at the South Pole [6] to look for a neutrino signal. Our analysis method is aimed to be less model dependent than previous GRB analyses. It is insensitive to a possible time difference between the arrival of the prompt photons and the high-energy neutrino signal. We limit the dependence on the expected neutrino spectrum by not using any energy dependent selection criteria. We only use directional selection parameters based on the reconstructed muon track, resulting from an incident muon neutrino [6]. As the detectable number of signal neutrinos in our detector per GRB is very low [7] ($\ll 1$), our method is designed to allow for gaining sensitivity to a GRB neutrino signal by stacking neutrino data of multiple GRBs around their trigger time. Those stacked time profiles can be analysed using the same techniques as the time profile of a single GRB. We first outline the analysis method itself, then we give the results of applying this method to GRB080319B, the most luminous GRB observed to date.

II. The analysis method

We look for signal events correlated with the GRB direction and time. As the background of our detector, which consists of cosmic ray events, is not correlated, we start by filtering the data for a GRB coincidence, both spatially and temporally. The exact selection parameters we use are optimized as outlined in section III.

The GRB data that passes the cuts has a certain time-distribution with respect to the GRB trigger time. The background events that pass the cuts will be uniformly distributed in time with respect to the GRB trigger. A possible GRB signal will be clustered in time. Note that this argument also holds for the case of stacking multiple GRB time windows, which is the main purpose of this analysis method. Here we assume that the intrinsic time difference between photons and neutrinos is a characteristic feature for all GRBs in our sample. Obviously we aim to have all GRB signal neutrinos ending up in the same time-bin. Therefore, the usage of a too small time bin will reduce the sensitivity as signal entries will end up in different bins. Using a too large time bin also reduces the sensitivity as background entries will start to dominate the bins. We estimate the timespread of the neutrino signal to be of the same order of the observed photonic GRB duration: the T_{90} time, defined as the time in which $5\% - 95\%$ of the GRB fluence was detected. This is a safe estimate as the intrinsic

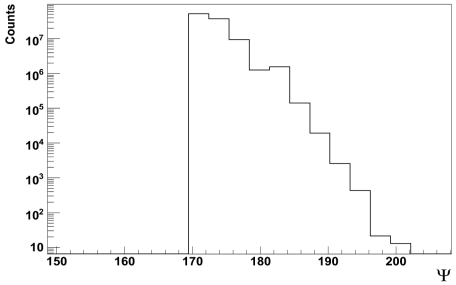

Fig. 1. The Ψ distribution for randomizing 13 entries in 120 bins. (10^8 randomizations)

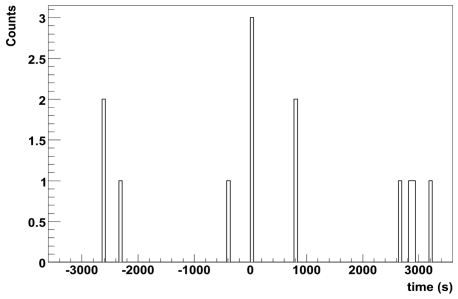

Fig. 2. The time distribution of 3 signal events (at $t = 0$) and 10 randomly distributed events in a 2 hour window using 60 s bin size.

timespread of the neutrino signal will not be larger than that of the photons: as the source region will always be more opaque for photons than for neutrinos, the photon signal will spread more in time than the neutrino signal. We have chosen a conservative bin size of 60 s, resulting in 120 time bins in our 2 hour window.

The probability of observing a certain time distribution given a uniform background distribution, of in total n entries divided over m time bins, is given by the multinomial distribution [8]:

$$p(n_1, n_2, ...n_m|nm) = \frac{n!}{n_1! \cdots n_m!} p_1^{n_1} \cdots p_m^{n_m} \equiv p. \quad (1)$$

Here p_i is the probability of an entry ending up in bin i. In case of a uniform background this is simply m^{-1}. The n_i represents the number of entries in bin i. We derive the bayesian $\Psi \equiv -10 \log p$ [9]:

$$\Psi = -10 \left[\log n! + \sum_{k=1}^{m} (n_k \log p_k - \log n_k!) \right]. \quad (2)$$

If the observation is due to the expected background, a low Ψ value will be obtained. Deviations from the expected background will result in increased Ψ values.

We intend to compare the Ψ value of the observed data, including a possible signal, with the distribution of uniform background Ψ values. We obtain such background sets by (uniformly) randomizing the entries in the two hour time window, keeping the total number of entries constant to what we find in the data. In case of a large signal contribution, this may result in underestimating the significance of the signal. However, for such a high signal contribution we will be able to claim discovery anyway. To claim a discovery we require at least a 5σ level, which means that only a fraction of 5.73×10^{-7} (the corresponding P-value) of all the Ψs of the various background sets is allowed to exceed some threshold Ψ_0. In case the Ψ value of our observed data is larger than Ψ_0, we have a discovery.

In order to reach the necessary accuracy, we perform 10^8 randomizations of all the data events that pass the criteria and calculate the Ψ value of each randomization to obtain a background Ψ distribution. In figure 1 we give one example of our parameter space. Here $n = 13$ entries exist in our simulated observation time window of 120 bins.

As an example, one might observe a time distribution, consisting of 3 signal events in a single bin and 10 randomly distributed background entries, which is shown in figure 2. The Ψ value associated with this distribution equals 186.15. When comparing with the background Ψ distribution of figure 1 it becomes clear that this corresponds to a P-value of 1.13×10^{-3} above the observed $\Psi_0 = 186.15$. For a 5σ discovery we need this fraction to be less than 5.73×10^{-7}. Therefore, observing a time profile like figure 2 will not result in a significant discovery.

III. Optimization of the selection parameters

The significance of our observation is determined by the method outlined in section II. Before we do this we need to optimize the directional parameter values which we use for selecting the final event sample by means of a blind analysis. In order to stay comparable to previous analyses, we will use the standard Model Discovery Factor (MDF) [10], [11] to determine the optimum of our parameter space. At those optimal settings the standard Model Rejection Factor (MRF) [12] is calculated.

The average expected number of background counts per time bin μ_b is calculated by simply dividing the total number of observed entries in the time window by the number of time bins. This is justified by the assumption that the expected signal is much smaller than the background $\mu_\mathrm{b} \gg \mu_\mathrm{s}$. We optimize the selection parameters for a 5σ discovery. The significance we use in the calculation of the MDF is corrected for a trial factor due to the number of bins.

By systematically going through the grid of our parameter space, we reach the parameter values corresponding to a minimum MDF, i.e. we optimize our analysis for discovery. In case of no discovery, the MRF at these settings will provide a flux upper limit. Since we optimize our parameters on the randomized data itself, our background set consists of randomized background plus signal entries. For parameter settings where less than four entries pass, the Ψ statistics cannot result in a discovery: all possible P-value exceed 5.73×10^{-7}. Therefore, we require that at our optimal thresholds, at least four events pass our filter. This is achieved by slightly relaxing the selection criteria.

IV. THE GRB080319B AMANDA ANALYSIS

Even though the expected number of signal neutrinos for an average GRB is extremely low, the atypical GRB080319B might yield an unusually strong neutrino signal justifying an individual neutrino analysis. The analysis of IceCube data [13] was confined to 10 minutes around the GRB trigger time. No neutrino signal was found. We analyse a larger data block from one hour before till one hour after the trigger time, and use the same spectrum as in [13] for our optimization and limit:

$$\frac{dN_\nu}{dE_\nu} = \begin{cases} 6.620 \times 10^{-16} \times E_\nu^{0.59} & \text{if } E_\nu \leq E_1; \\ 0.768 \times E_\nu^{-2.145} & \text{if } E_1 \leq E_\nu \leq E_2; \\ 6.690 \times E_\nu^{-4.145} & \text{if } E_\nu \geq E_2, \end{cases} \quad (3)$$

with the fluence, dN_ν/dE_ν, in (GeV cm^2)$^{-1}$ and the break energies: $E_1 = 322.064$ TeV; $E_2 = 2952.35$ TeV.

For our time profile we use a bin size of 60 s, roughly the T_{90} of this burst. While we expect this to be wide enough for the GRB neutrino signal to fit in one bin, a possible neutrino signal can be spread over two adjacent bins. This obviously lowers the significance of the observation. Therefore, in case we do not find a 5σ result with our initial analysis, we compensate for this binning effect by performing our analysis a second time, where we shift our bins by half a binwidth.

Using a simulated neutrino fluence following the spectrum (3), we obtain the optimum of our parameter space following the method of section III. We find at the optimal parameter settings a 5σ MDF of 123.65 and have six events passing the filter. Based on the GRB spectrum we expect 0.064 signal entries to pass the filter. We find (at 90% confidence level) an MRF of 38.8 for the GRB spectrum. Likewise, using a generic E^{-2} spectrum, we obtain at these settings a limit of $E^2 dN_\nu/dE_\nu = 1.11 \times 10^{-2}$ (GeV cm^2 s)$^{-1}$ at 90% confidence level. Note that these limits are conservative as the Ψ statistics we use to claim discovery is more sensitive than the Poisson statistics on which the MRF is based.

The previous analysis of IceCube data [13] quotes a sensitivity at a fluence of 22.7 times the expected spectrum at 90% C.L. for prompt emission. We find a 90% C.L. limit at 38.8 times the expected spectrum for a neutrino signal arriving in the central bin. This difference

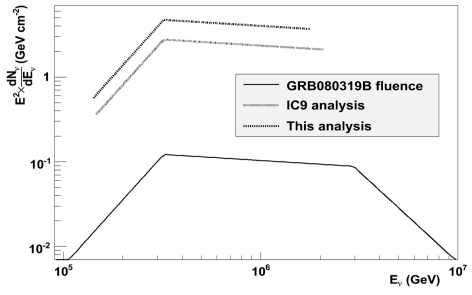

Fig. 3. The 90% C.L. upper limits on the fluence of GRB080319B with respect to the calculated neutrino fluence (3) for both this analysis and the IceCube analysis in its 9 string configuration.

can be seen in figure 3, where the limits of both analyses are given.

The neutrino effective areas for the AMANDA detector for this analysis are given in figure 4. It is given at

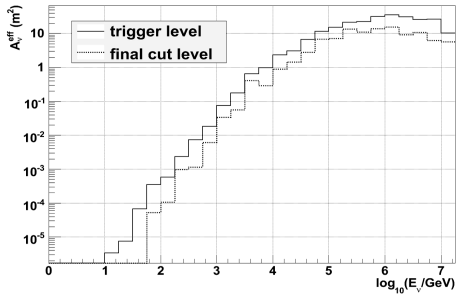

Fig. 4. The neutrino effective area for the position of GRB080319B, both at trigger level and at final cut level.

both trigger level and at the level where all our selections have been applied. The ratio between the 2 histograms is the signal passing rate, which, for the GRB spectrum (3), equals 49.4%.

The time profile we find after unblinding is consistent with the background-only hypothesis. Repeating the analysis with shifted time bins does not change this.

V. THE STACKING ANALYSIS

In this section we present the expected results of analysing the stacked AMANDA data of 130 GRBs between 2005 and 2008. These well-localized bursts are all in the Northern hemisphere to reduce the background due to atmospheric events. The time profile of each GRB is sampled to form a stacked time profile.

Due to the different redshifts of the GRBs in the sample, the effect of cosmological time dilation on the intrinsic time difference between photons and neutrinos will result in a timespread on the arrival of the neutrino signal. This spread will increase for larger time differences. We compensate for this by enlarging the bin sizes for bins further away from the trigger. Each bin will be enlarged by a factor of $\langle z \rangle + 1$, where $\langle z \rangle$ is the average redshift of the GRBs in our sample. We choose to have our central bin range from $-\langle T_{90} \rangle \approx -30$ s to $\langle T_{90} \rangle \approx 30$ s, allowing for a scatter in the neutrino arrival time of the average length of the photon signal. The second bin is a factor of $\langle z \rangle + 1 \approx 3$ larger than the maximum scatter we allow in the center bin and ranges $[30, 120]$ s (and $[-120, -30]$ s). The next bin is again a factor of 3 larger.

The fact that the bins in our time window have unequal sizes does not influence our method. It is simply taken into account by using, for each bin, the correct p_i, the probability for an entry to fall in that bin, see equation (2). Let us consider the same time profile as above (figure 2) with these new bin settings. This leads to the time profile as given in figure 5. Because our time window now has variable binning, the configuration itself changed significantly with respect to the regular

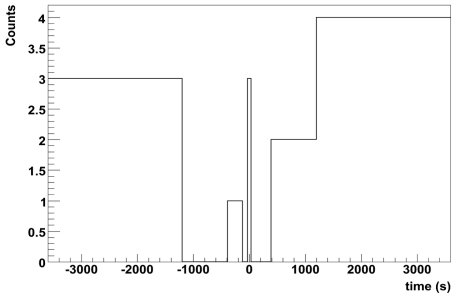

Fig. 5. The time distribution of 3 signal events and 10 randomly distributed events in a 2 hour window. Here we use nine variable time bins as explained in the text.

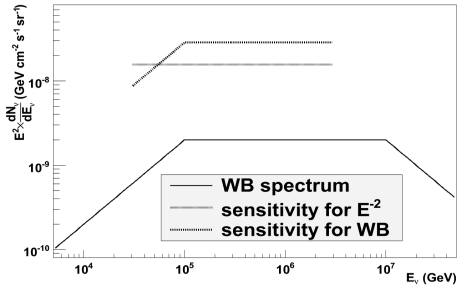

Fig. 6. The sensitivity of this analysis for both a generic E^{-2} and a Waxman-Bahcall (WB) source spectrum (90% C.L.).

case of figure 2. Hence the new Ψ value of our observation (63.44) differs from the previously found value. The background Ψ distribution of figure 1 will change accordingly. Following our example, one can study the

$n_{\rm signal}$	P-value regular 60 s bins	P-value variable bins
1	6.32×10^{-2}	2.36×10^{-1}
2	9.67×10^{-3}	3.77×10^{-2}
3	1.13×10^{-3}	3.14×10^{-3}
4	2.71×10^{-5}	1.80×10^{-4}
5	1.1×10^{-6}	7.8×10^{-6}
6	1×10^{-8}	2.2×10^{-7}

TABLE I
COMPARISON BETWEEN THE SIGNIFICANCE FOR THE CASE OF THE TIME PROFILE OF FIGURE 2 AND THE SAME SITUATION USING THE VARIABLE BINS AS IN FIGURE 5. HERE WE VARY THE AMOUNT OF SIGNAL ENTRIES IN THE CENTER BIN $n_{\rm signal}$; THE 10 BACKGROUND ENTRIES ARE LEFT UNTOUCHED.

effect of the variable binning on the significance of our time profile for different signal strengths. From table I one can see that introducing variable bin sizes slightly lowers the significance of our observations (their P-value) for a signal falling in the center bin.

For the optimization of the selection parameters we use both a Waxman-Bahcall and a generic E^{-2} spectrum. Again, we optimize for discovery using the standard MDF. As a result from the various binsizes, the limit of this analysis depends on the bin size, and therefore depends on the time difference with the GRB trigger. The sensitivity of this analysis for each bin in our

Time range w.r.t. GRB trigger	WB spectrum at 1 PeV (GeV cm^2 s sr)$^{-1}$	$E^2 dN_\nu/dE_\nu$ (GeV cm^2 s sr)$^{-1}$
$[-30, 30]$ s	2.9×10^{-8}	1.55×10^{-8}
$\pm$ $[30, 120]$ s	3.0×10^{-8}	1.58×10^{-8}
$\pm$ $[120, 390]$ s	3.3×10^{-8}	1.76×10^{-8}
$\pm$ $[390, 1200]$ s	4.2×10^{-8}	2.24×10^{-8}
$\pm$ $[1200, 3600]$ s	5.8×10^{-8}	3.09×10^{-8}

TABLE II
THE 90% C.L. SENSITIVITY OF THE STACKING ANALYSIS FOR EACH TIME BIN, FOR BOTH THE WAXMAN-BAHCALL (WB) AND A GENERIC E^{-2} SPECTRUM.

time window are given in table II. For the central bin we have shown the limits in figure 6. Note that these limits only apply to a neutrino signal arriving simultaneously with the prompt photon emission.

VI. DISCUSSION

Currently, the most restrictive muon neutrino upper limit has been determined by AMANDA at $E^2 dN_\nu/dE_\nu \leq 1.7 \times 10^{-8}$ GeV cm^{-2} s^{-1} sr^{-1} based on a sample of over 400 GRBs and for the Waxman-Bahcall spectrum at 1 PeV [2]. For our analysis no energy dependent selection parameters are used and the optimum of the selection parameters is independent of the source spectrum we use. As such, our analysis is less model dependent and it allows for a possible time difference between photons and neutrinos. Furthermore, the stacking procedure provides sensitivity even in the case of very low individual GRB rates. As such, the present analysis has the potential of detecting precursor and afterglow neutrinos in addition to prompt ones.

The method may also be used to analyse the data of individual GRBs. By construction our method is slightly less sensitive compared to a model dependent analysis of a single time bin. The effective area of the complete IceCube detector will be at least $\sim$150 times larger than AMANDA's [14]. Applying our analysis on one year data of the full IceCube, would result in a sensitivity well below the predicted Waxman-Bahcall spectrum.

REFERENCES

[1] Achterberg, A., et al. 2008, Astrophys. J. 674, 357
[2] Achterberg, A., et al. 2007, Astrophys. J. 664, 397
[3] Waxman, E., & Bahcall, J. N. 2000, Astrophys. J., 541, 707
[4] Dai, Z. G., & Lu, T. 2001, Astrophys. J. 551, 249
[5] Dar, A., & De Rujula, A. 2001, arXiv:astro-ph/0105094
[6] Ahrens, J., et al. 2004, Nucl. Instr. Meth. A 524, 169
[7] Halzen, F., & Hooper, D. W. 1999, Astrophys. J. 527, L93
[8] Gregory, P. C. 2005, Bayesian Logical Data Analysis for the Physical Sciences, Cambridge University Press, UK, 2005
[9] van Eijndhoven, N. 2008, Astropart. Phys. 28, 540
[10] Punzi, G. 2003, Statistical Problems in Particle Physics, Astrophysics and Cosmology, 79
[11] Hill, G. C., Hodges, J., Hughey, B., Karle, A., & Stamatikos, M. 2006, Statistical Problems in Particle Physics, Astrophysics and Cosmology, 108
[12] Hill, G. C., & Rawlins, K. 2003, Astropart. Phys. 19, 393
[13] IceCube Collaboration: R. Abbasi 2009, arXiv:0902.0131
[14] Ahrens, J., et al. 2004, Astropart. Phys. 20, 507

Optical follow-up of high-energy neutrinos detected by IceCube

Anna Franckowiak*, Carl Akerlof§, D. F. Cowen*†, Marek Kowalski*, Ringo Lehmann*, Torsten Schmidt‡ and Fang Yuan§
for the IceCube Collaboration¶ and for the ROTSE Collaboration
**Humboldt Universität zu Berlin*
†*Pennsylvania State University*
‡*University of Maryland*
§*University of Michigan*
¶*see the special section in this proceedings*

Abstract. **Three-quarters of the 1 km^3 neutrino telescope IceCube is currently taking data. Current models predict high-energy neutrino emission from transient objects like supernovae (SNe) and gamma-ray bursts (GRBs). To increase the sensitivity to such transient objects we have set up an optical follow-up program that triggers optical observations on multiplets of high-energy muon-neutrinos. We define multiplets as a minimum of two muon-neutrinos from the same direction (within 4°) that arrive within a 100 s time window. When this happens, an alert is issued to the four ROTSE-III telescopes, which immediately observe the corresponding region in the sky. Image subtraction is applied to the optical data to find transient objects. In addition, neutrino multiplets are investigated online for temporal and directional coincidence with gamma-ray satellite observations issued over the Gamma-Ray Burst Coordinate Network. An overview of the full program is given, from the online selection of neutrino events to the automated follow-up, and the resulting sensitivity to transient neutrino sources is presented for the first time.**

Keywords**: Neutrinos, Supernovae, Gamma-Ray Bursts**

I. INTRODUCTION

When completed, the in-ice component of IceCube will consist of 4800 digital optical modules (DOMs) arranged on 80 strings frozen into the ice, at depths ranging from 1450m to 2450m [1]. Furthermore there will be six additional strings densely spaced at the bottom half of the detector. The total instrumented volume of IceCube will be 1 km^3. Each DOM contains a photomultiplier tube and supporting hardware inside a glass pressure sphere. The DOMs indirectly detect neutrinos by measuring the Cherenkov light from secondary charged particles produced in neutrino-nucleon interactions. IceCube is most sensitive to neutrinos within an energy range of TeV to PeV and is able to reconstruct the direction of muon-neutrinos with a precision of $\sim 1°$. The search for neutrinos of astrophysical origin is among the primary goals of the IceCube neutrino telescope. Source candidates include galactic objects like supernova remnants as well as extragalactic objects like Active Galactic Nuclei and Gamma-Ray Bursts [9] [10]. Offline searches for neutrinos in coincidence with GRBs have been performed on AMANDA and IceCube data. They did not lead to a detection yet, but set upper limits to the predicted neutrino flux [13]. While the rate of GRBs with ultra-relativistic jets is small, a much larger fraction of SNe not associated with GRBs could contain mildly relativistic jets. Such mildly relativistic jets would become stalled in the outer layers of the progenitor star, leading to essentially full absorption of the electromagnetic radiation emitted by the jet. Hence, with the postulated presence of mildly relativistic jets one is confronted with a plausible but difficult-to-test hypothesis. Neutrinos may reveal the connection between GRBs, SNe and relativistic jets. As was recently shown, mildly relativistic jets plowing through a star would be highly efficient in producing high-energy neutrinos [5]–[7]. The predicted neutrino spectrum follows a broken power law and Fig. 1 shows the expected signal spectrum for neutrinos produced in kaon and pion decay in the source, simulated using the full IceCube simulation chain. The expected number of signal events is small and requires efficient search algorithms to reduce the background of atmospheric neutrinos (see section II).

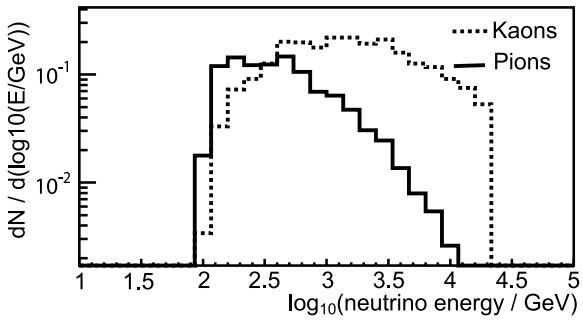

Fig. 1: Neutrino event spectrum in the IceCube detector, from kaon and pion decay in the supernovae-jet model of Ando and Beacom [5].

An optical follow-up program has been started which enhances the sensitivity for detecting high-energy neutrinos from transient sources such as SNe. In this program, the direction of neutrinos are reconstructed online, and if their multiplicity pass a certain threshold, a Target-

of-Opportunity (ToO) notice is sent to the ROTSE-III network of robotic telescopes. These telescopes monitor the corresponding part of the sky in the subsequent hours and days and identify possible transient objects, e.g. through detection of rising supernova light-curves lasting several days. If in this process a supernova is detected optically, one can extrapolate the lightcurve or afterglow to obtain the explosion time [2]. For SNe, a gain in sensitivity of about a factor of 2-3 can be achieved through optical follow-up observations of neutrino multiplets [4]. In addition to the gain in sensitivity, the follow-up program offers a chance to identify its transient source, be it a SN, GRB or any other transient phenomenon.

II. Neutrino Alert System

IceCube's optical follow-up program has been operating since fall of 2008. In order to match the requirements given by limited observing time at the optical telescopes, the neutrino candidate selection has been optimized to obtain less than about 25 background multiplets per year. The trigger rate of the 40 string IceCube detector is about 1000 Hz. The muon filter stream reduces the rate of down-going muons created in cosmic ray showers dramatically by limiting the search region to the Northern hemisphere and a narrow belt around the horizon. The resulting event stream of 25 Hz is still dominated by misreconstructed down-going muons. Selection criteria based on on track quality parameters, such as number of direct hits[1], track length and likelihood of the reconstruction, yield a reduced event rate of 1 event/(10 min). The optimized selection criteria are relaxed to improve the signal efficiency, 50% of the surviving events are still misreconstructed down-going muons, while 50% are atmospheric neutrinos. During the antarctic summer 2008/2009, 19 additional strings were deployed, which have been included in the data taking since end of April 2009. To take into account an enhancement in the rate due to the increased detector volume, the selection criteria have been adjusted and will yield a cleaner event sample containing only 30% misreconstructed muons.
From this improved event sample, neutrino multiplet candidates with a time difference of less than 100 s and with an angular difference (or 'space angle') of less than 4° are selected. The choice of the time window size is motivated by jet penetration times. Gamma-ray emission observed from GRBs has a typical length of 40 s, which roughly corresponds to the duration of a highly relativistic jet to penetrate the stellar envelope. The angular difference is determined by IceCube's angular resolution. Assuming single events from the same true direction, 75% of all doublets are confined to a space angle of 4° after reconstruction. Once a multiplet is found, a combined direction is calculated as a weighted average of the individual reconstructed event directions, with weights derived from the estimated direction resolution of each track. The resolution of the combined direction is up to a factor of $1/\sqrt{2}$ better than that of individual tracks. The multiplet direction is sent via the network of Iridium satellites from the South Pole to the North, where it gets forwarded to the optical telescopes. At this point in time, due to limited parallelization of the data processing at the South Pole a delay of 8 hours is accumulated. In the near future, the online processing pipeline will be upgraded, reducing the latency drastically to the order of minutes.
A total of 14 alerts have passed the selection criteria and were sent to the telescopes within 7 months of operation.

[1]Hits that are measured within [-15ns,75ns] from the predicted arrival time of Cherenkov photons, without scattering, given by the track geometry.

III. Optical Follow-Up Observations

At the moment IceCube alerts get forwarded to the Robotic Optical Transient Search Experiment (ROTSE) [3]. Additions to the list of participating telescopes are planned. ROTSE-III is dedicated to observation and detection of optical transients on time scales of seconds to days. The original emphasis was on GRBs while it more recently has also started a very successful SN program. The four ROTSE-III telescopes are installed around the world (in Australia, Namibia, the USA and Turkey). The ROTSE-III equipment is modest by the standards of modern optical astronomy, but the wide field of view and the fast response permit measurements inaccessible to more conventional instruments. The four 0.45 m robotic reflecting telescopes are managed by a fully-automated system. They have a wide field of view (FOV) of $1.85^\circ \times 1.85^\circ$ imaged onto a 2048 $\times$ 2048 CCD, and operate without filters. The cameras have a fast readout cycle of 6 s. The limiting magnitude for a typical 60 s exposure is around 18.5 mag, which is well-suited for a study of GRB afterglows during the first hour or longer. The typical full width at half maximum (FWHM) of the stellar images is smaller than 2.5 pixels (8.1 arcseconds). Note that ROTSE-IIIs FOV matches the size of the point spread function of IceCube well.
Once an IceCube alert is received by one of the telescopes, the corresponding region of the night sky will be observed within seconds. A predefined observation program is started: The prompt observation includes thirty exposures of 60 seconds length [2]. Follow-up observations are performed for 14 nights. Eight images with 60 seconds exposure time are taken per night. The prompt observation is adjusted to the typical rapidly decaying lightcurve of a GRB afterglow, while the follow-up observation of 14 days permits the identification of an increasing SN lightcurve. Once the images are taken, they are automatically processed at the telescope site. Once the data is copied from the telescopes, a second analysis is performed off-line, combining the images from all sites. Image subtraction is performed according

[2]Once the delay caused by data processing at the South Pole (see section II) is reduced to the order of minutes, the prompt observation will include ten short observations of 5 seconds, ten observations of 20 seconds and twenty long exposures of 60 seconds.

the methods presented in [8]. Here the images of the first night serve as reference, while the images from the following nights are used to search for the brightening of a SN lightcurve.

IV. Sensitivity

The sensitivity of the optical-follow up program is determined by both IceCube's sensitivity to high energy neutrino multiplets and ROTSE-III's sensitivity to SNe. We will distinguish two cases: The first being that no optical counterpart is observed over the course of the program (assuming 25 alerts per year) and the second that a SN is identified in coincidence.

A. No Optical Counterpart Discovered

With no coincident SN observed, one obtains an upper limit on the average number of SNe that could produce a coincidence: $N^{\rm IC}_{\rm ROTSE} < 2.44$ (for 90% confidence level). Constraints on a given model are obtained by demanding that the model does not predict a number in excess of the SN event upper limit. We construct a simple model based on Ando & Beacom type SNe [5]. We introduce two parameters: The first is the rate of SNe producing neutrinos $\rho = (4/3\pi)^{-1}10^{-4}\rho^{\rm SN}_{2e-4}{\rm Mpc}^{-3}{\rm yr}^{-1}$. Note that $\rho^{\rm SN}_{2e-4} = 1$ corresponds to one SN per year in a 10 Mpc sphere, about the rate of all core-collapse SNe in the local Universe [12]. Since we expect only a subset of SNe to produce high energy emission, one can assume $\rho^{\rm SN}_{2e-4} < 1$. The second parameter is the hadronic jet energy $E_{\rm jet} = 3\cdot 10^{51}\epsilon^{\rm jet}_{3e51}{\rm ergs}$ and we choose to scale the flux normalization of the model of Ando & Beacom, F_0, by $\epsilon^{\rm jet}_{3e51}$. Fig. 2 shows the constraints that one can place on the density and jet kinetic energy in the $E_{\rm jet}-\rho$ plane. The basic shape of the constraints that can be obtained in the $E_{\rm jet}-\rho$ plane can be understood from the following considerations. The number of neutrinos depends on the jet energy and the distance: $N_\nu \propto \epsilon^{\rm jet}_{3e51}\cdot r^{-2}$. The program requires at least $N_{\nu,\rm min} = 2$ detected neutrinos in IceCube. A SN with jet energy $\epsilon^{\rm jet}_{3e51}$ produces $N_{\nu,\rm min}$ neutrinos if it is closer than $r_{\rm max}$: $N_{\nu,\rm min} \propto \epsilon^{\rm jet}_{3e51}\cdot r^{-2}_{\rm max}$, which yields $r_{\rm max} \propto (\epsilon^{\rm jet}_{3e51})^{1/2}$. The volume V limited by $r_{\rm max}$ contains $N_{\rm SN} \propto \rho^{\rm SN}_{2e-4}\cdot r^3_{\rm max}$ SN that can produce two neutrinos. Therefore the number of detection $N^{\rm SN}_{\rm IC/ROTSE}$ is given by $N^{\rm SN}_{\rm IC/ROTSE} \propto \rho^{\rm SN}_{2e-4}\cdot(\epsilon^{\rm jet}_{3e51})^{3/2}$. For normalization we use Ando & Beacom-like SNe, which occur at a rate of $\rho^{\rm SN}_{2e-4} = 1$ with GRB-like energies ($\epsilon^{\rm jet}_{3e51} = 1$) and yield $N^{\rm SN,AB}_{\rm IC/ROTSE} = 200$ expected IceCube/ROTSE coincidences per year.

$$N^{\rm SN}_{\rm IC/ROTSE} = N^{\rm SN,AB}_{\rm IC/ROTSE}\rho^{\rm SN}_{2e-4}\cdot(\epsilon^{\rm jet}_{3e51})^{3/2} \qquad (1)$$

According to [11] a non-detection limits the number of IceCube/ROTSE coincidences at a 90% confidence level to $N^{SN}_{\rm IC/ROTSE} < 2.44$. Using Eq. 1 one obtains the two-dimensional constraints on density and hadronic jet energy for this model:

$$\rho^{\rm SN}_{2e-4}(\epsilon^{\rm jet}_{3e51})^{3/2} < 2.44/N^{\rm SN,AB}_{\rm IC/ROTSE} < 0.012, \qquad (2)$$

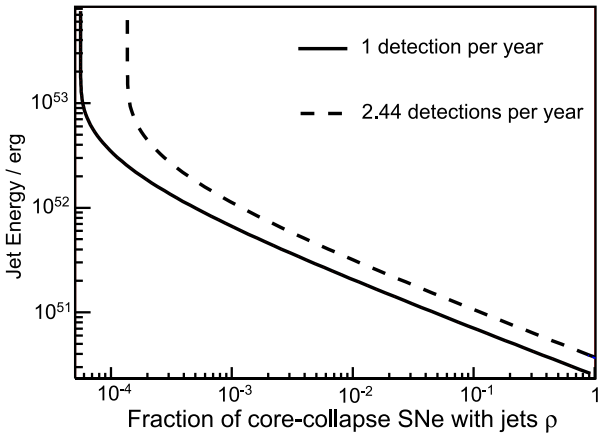

Fig. 2: Sensitivity in the $E_{\rm jet}-\rho$ plane after one year of operation of the 40 string IceCube detector (dashed line—90% CL; solid line—one coincident detection per year).

which is a reasonably good representation of the two dimensional constraints for not too small densities $\rho^{\rm SN}_{2e-4} \gtrsim 10^{-3}$. For GRB-like energies ($\epsilon^{\rm jet}_{3e51} = 1$), it follows that at most one out of 80 SNe produces Ando & Beacom-like jets in its core. Phrased in absolute terms, if no SN will be detected, the rate of SNe with a mildly relativistic jet should not exceed $\rho = 3.1\cdot 10^{-6}{\rm Mpc}^{-3}{\rm yr}^{-1}$ (at 90% confidence level) in our program. The cut-off at small densities visible in Fig. 2 is due to ROTSE-III's limiting magnitude. The sphere (i.e. effective volume) within which ROTSE-III can detect Supernovae has a radius of about 200-300 Mpc. ROTSE-III effectively cannot probe SN subclasses that occur less then once per year within this sphere.

B. Significance in case of a detection

Next we address the case that a SN was detected in the follow-up observations. The task mainly consists of computing the significance of the coincidence. We compute this for one year of data and 25 alerts. Each alert leads to the observation of a $\Delta\Omega = 1.85^\circ\times 1.85^\circ = 3.4$ square degree field, hence over the course of the year ROTSE-III covers a fraction of the sky given by $\Delta\Omega/4\pi \times N_{\rm alerts} = 2.1\cdot 10^{-3}$. Next assume that the time window for a coincident of an optical SN detection and candidate neutrino multipet is given by Δt_d, the accuracy with which we can determine the initial time of the supernova explosion. Studying the lightcurve of supernova SN2008D, which has a known explosion start-time given by an initial x-ray flash, we have developed an accurate way to estimate Δt_d from a SN lightcurve [2]. We fit the light curve data to a model that postulates a phase of blackbody emission followed by a phase dominated by pure expansion of the luminous shell. Explosion times can be determined from the lightcurve with an accuracy of less than 4 hours. A detailed description of this method can be found in [2].

The number of accidental SNe found will be proportional to Δt_d and the total number of SNe per year that ROTSE-III would have sensitivity to detect, if surveying the sky at all times, $N_{\rm ROTSE} \approx 10^4$. Putting all this together the number of random coincidences is:

$$N_{\rm bg} = N_{\rm alerts} N_{\rm ROTSE} \frac{\Delta\Omega}{4\pi} \times \frac{\Delta t_d}{\rm yr} = 0.056 \frac{\Delta t_d}{\rm d}. \quad (3)$$

For $N_{\rm bg} \ll 1$ this corresponds to the chance probability $p = 1 - \exp(-N_{\rm bg}) \approx N_{\rm bg}$ of observing at least one random background event. For $\Delta t_d = 1{\rm d}$ and no other information, the observation of a SN in coincidence with a neutrino signal would have a significance of about 2σ. The significance can be improved by adding neutrino timing information as well as the distance information of the object found. We first discuss the extra timing information. So far we have only required that two neutrinos arrive within 100 s to produce an alert. Thus, in the analysis presented above, the significance for two events 1 s apart would be the same as for 99 s difference. Since the probability p_t to find a time difference less than Δt_ν due to a background fluctuation is given by $p_t = \Delta t_\nu / 100s$ assuming a uniform background, we include the time difference in the chance probability. Next we discuss the use of the SN distance. One can safely assume that there will be a strong preference for nearer SNe, since these are most likely to lead to a neutrino flux large enough to produce a multiplet in IceCube. Using the distance $d_{\rm SN}$ as an additional parameter one can compute the probability to observe a background SN at a distance $d \leq d_{\rm SN}$. The probability is given by the ratio of SNe observed by ROTSE-III within the sphere $d_{\rm SN}$ to all SNe: $p_d = N_{\rm ROTSE}(d)/N_{\rm ROTSE}$. In case of a detection both $d_{\rm SN}$ and Δt_ν will be available. We use a simple Monte Carlo to obtain the significance of this detection. For example the detection of two neutrinos with a temporal difference of Δt_ν =10 s in coincidence with a SN in $d_{\rm SN}$ =20 Mpc distance has a p-value of $5 \cdot 10^{-4}$, which corresponds to 3.5σ, assuming a total of $N_{\rm alerts} = 25$ alerts found in the period of one year.

V. Coincidences with GCN-GRBs

According to current models, about every 15-20th GRB that can be detected by IceCube will produce a neutrino doublet. Hence there is a small possibility that we will find a doublet in coincidence with a GCN alert, a case that we consider separately here. The significance of such a coincidence can be estimated with calculation analogous to Eq. 3. The number of accidental coincidences with a time difference less than Δt is given by:

$$N_{\rm bg} = N_{\rm alerts} N_{\rm GCN} \frac{\Delta\Omega}{4\pi} \times \frac{\Delta t}{\rm yr} = 3.2 \cdot 10^{-8} \frac{\Delta t}{1{\rm s},}. \quad (4)$$

where we have assumed 200 GCN notices and 30 multiplets a year. A coincidence occurs whenever the neutrinos and the GRB overlap within predefined windows in direction and time. For illustrative purposes, if we choose a 1.5-degree directional window and a 4-hour time window (corresponding roughly to IceCube's point spread function and to GRB observations and modeling), Eq. 4 yields an expected background count of $N_{BG} = 4.7 \cdot 10^{-4}$. This corresponds to a 3.5σ effect, or equivalently the expectation of a false positive from background once every 2100 years. We can further reduce the expected background by assuming that the neutrino signal is most likely to be emitted at the same time as the gamma rays. Since the background multiplets will be distributed uniformly across the 4-hour window, we can multiply the chance probability above by the factor

$$p_t = \left| \frac{t_{GRB} - t_\nu}{4 \text{ hours}} \right| \quad (5)$$

where the absolute value is taken since we assume the neutrinos are equally likely to be emitted before the gamma-rays as they are after. Note that our flat probability assumption for the relative emission times of gamma rays and neutrinos from GRBs can, of course, be modified to follow any particular theoretical model. With all these assumptions, if we observe a coincidence that is 300 seconds from the GRB onset time, the chance probability is then given by $N_{BG} \cdot p_t = 4.7 \cdot 10^{-4} \cdot 300/14400 = 9.8 \cdot 10^{-6}$, which corresponds to a 4.4σ result.

VI. Conclusion

We have presented the setup and performance of IceCube's optical follow-up program, which was started in October 2008. The program increases IceCube's sensitivity to transient sources such as SNe and GRBs and furthermore allows the immediate identification of the source. Non-detection of an optical counterpart allows the calculation of a limit on model parameters such as jet energy and density of SN accompanied by jets.
In addition multiplets of neutrinos are tested for coincidences with GCN messages. Even a single coincidence detection would be significant.

VII. Acknowledgments

A. Franckowiak and M. Kowalski acknowledge the support of the DFG. D. F. Cowen thanks the Deutscher Akademischer Austausch Dienst (DAAD) Visiting Researcher Program and the Fulbright Scholar Program.

References

[1] A. Achterberg et al. [IceCube Collaboration], Astropart.Phys. 26:155-173, 2006
[2] D. F. Cowen, A. Franckowiak and M. Kowalski, arXiv:0901.4877
[3] C. W. Akerlof *et al.*, PASP 115:132-140, 2003
[4] M. Kowalski, A. Mohr, Astropart.Phys. 27:533-538,2007
[5] S. Ando, J. Beacom, Phys.Rev.Lett. 95:061103,2005
[6] S. Razzaque, P. Meszaros, E. Waxman, Phys.Rev.Lett. 93:181101, 2004
[7] S. Horiuchi, S. Ando, Phys.Rev. D77:063007,2008.
[8] F. Yuan, C. W. Akerlof, Astropart.Phys. 677:808-812,2008
[9] J. Becker, Phys.Rept. 458:173-246,2008
[10] F. Halzen, D. Hooper, Rept.Prog.Phys. 65:1025-1078, 2002
[11] G. J. Feldman, R. D. Cousins, Phys.Rev. D57:3873-3889,1998
[12] S. Ando, F. Beacom, H. Yuksel, Phys.Rev.Lett. 95:171101, 2005
[13] A. Achterberg et al. [IceCube Collaboration], APJ 674:357-370, 2007

Results and Prospects of Indirect Searches for Dark Matter with IceCube

Carsten Rott* **and Gustav Wikström† for the IceCube collaboration‡.**

*Dept. of Physics and Center for Cosmology and Astro-Particle Physics, Ohio State University, Columbus, OH 43210, USA
†Oskar Klein Centre and Dept. of Physics, Stockholm University, SE-10691 Stockholm, Sweden
‡See special section of these proceedings

***Abstract*. Dark matter could be indirectly detected through the observation of neutrinos produced as part of its self-annihilation process. Possible signatures are an excess neutrino flux from the Sun, the center of the Earth or from the galactic halo, where dark matter could be gravitationally trapped. We present a search for muon neutrinos from neutralino annihilations in the Sun performed on IceCube data collected with the 22-string configuration. No excess over the expected atmospheric background has been observed and upper limits at 90% confidence level have been obtained on the annihilation rate and converted to limits on WIMP-proton cross-sections, for neutralino masses in the range of 250 GeV to 5 TeV. Further prospects for the detection of dark matter from the Sun, the Earth, and the galactic halo will be discussed.**

***Keywords*: Dark Matter, Neutrinos**

I. Introduction

The existence of dark matter can be inferred from a number of observations, among them rotational profiles of galaxies, large scale structures, and WMAP's anisotropy measurement on the cosmic microwave background. Weakly Interacting Massive Particles (WIMPs), 'cold' thermal relics of the Big Bang, are leading dark matter candidates. Besides overwhelming observational evidence for its existence, the properties of dark matter can only be understood through detection of direct or indirect signals from its interactions or through the production at collider experiments. In the Minimal Supersymmetric Standard Model (MSSM) the neutralino is a promising WIMP particle. It is stable and can annihilate pair-wise into Standard Model particles [1]. Galactic WIMPs could be gravitationally captured in the Sun or the Earth and accumulated in their cores [2]. Among the secondary products from the WIMP annihilations we expect neutrinos, which could escape from the center of the Sun or Earth and be detected in neutrino telescopes. Neutrinos are also expected from annihilations in the galactic halo. In IceCube [3] we observe Cherenkov light from relativistic muons in ice. The data analysis is focused on selecting upward-going events in order to separate muons from neutrino interactions from background muons created in cosmic-ray air showers. In this paper we present a search for a neutralino annihilation signal from the Sun with the IceCube 22-string detector. Future sensitivities of IceCube to this signal are discussed, as well as the prospects of observing annihilation signals from the Earth or the galactic halo.

II. The IceCube Neutrino Telescope

The IceCube Neutrino Telescope is a multipurpose detector under construction at the South Pole, which is currently about three quarter completed [3]. Upon completion in 2011, IceCube will instrument a volume of approximately one cubic kilometer of ice utilizing 86 strings, each instrumented with 60 Digital Optical Modules (DOMs). Eighty of these strings will be arranged in a hexagonal pattern with an inter-string spacing of about 125 m and with 17 m vertical separation between DOMs, at a depth between 1450 m and 2450 m. Complementing this 80 string baseline design will be a deep and dense sub-array named DeepCore [4] that will be formed out of seven regular IceCube strings in the center of the array together with six additional strings deployed in between them. In this way, the sub-array will achieve an interstring-spacing of 72 m. The six additional DeepCore strings will have a different distribution of their 60 DOMs, optimizing their design towards a lower energy threshold. The optical sensors will have a vertical spacing of 7 m, will be deployed in deep transparent ice [1] and will consist of high quantum efficiency photomultiplier tubes (HQE PMTs). This will enable us to study neutrinos at energies down to a few 10 GeV. DeepCore will be an extremely interesting detector for the study of WIMPs.

III. Analysis of 22-string data

The 2007 dataset, consisting of 104.3 days livetime with the Sun below the horizon recorded with the IceCube 22-string detector, was searched for a neutrino signal from the Sun [5]. The event sample was reduced in steps from $4.8 \cdot 10^9$ to 6946 events at final level, which constitutes the expected sample of atmospheric

[1]The deep ice is clearer, with a scattering length roughly twice that of the upper part of the IceCube detector. In addition, the deeper location (below 2000 m) provides an improved shielding of cosmic ray backgrounds.

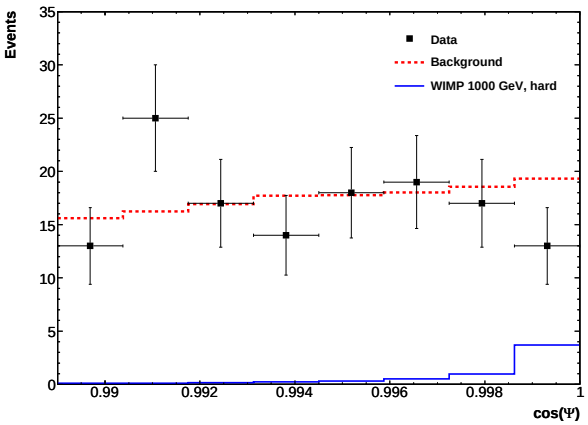

Fig. 1. Cosine of the angle to the Sun, Ψ, for data (squares) with one standard deviation error bars, and the atmospheric background expectation (dashed line). Also shown is a simulated signal ($m_{\tilde{\chi}_1^0}$ = 1000 GeV, hard spectrum) scaled to the found upper limit of $\mu_s = 6.8$ events.

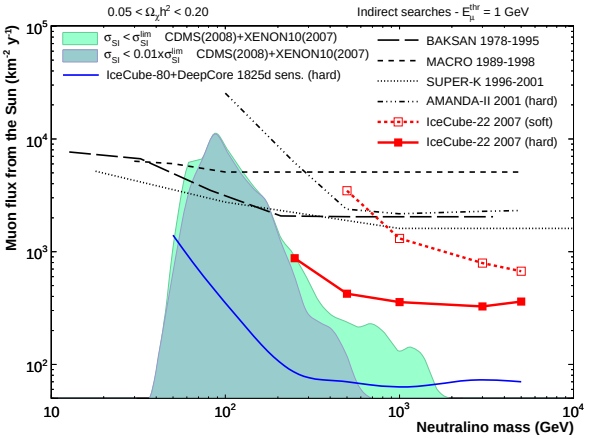

Fig. 2. Upper limits at the 90% confidence level on the muon flux from neutralino annihilations in the Sun for the soft ($b\bar{b}$) and hard (W^+W^-) annihilation channels, adjusted for systematic effects, as a function of neutralino mass [5]. For neutralino masses below m_W $\tau^+\tau^-$ is used as the hard annihilation channel. The lighter [green] and darker [blue] shaded areas represent MSSM models not disfavored by direct searches [20], [21] based on σ^{SI} and $100 \cdot \sigma^{SI}$, respectively. A muon energy threshold of 1 GeV was used when calculating the flux. Also shown are the limits from BAKSAN [15], MACRO [16], Super-K [17], and AMANDA [18], and the expected sensitivity of IceCube with DeepCore.

neutrinos with a contamination of atmospheric muons. Since the analysis is based on comparing the shape of the angular distribution of signal and background (see section III-B), there is no need to achieving a high purity atmospheric neutrino sample at final cut level. Filtering was based on log-likelihood muon track reconstructions, geometry, and time evolution of the hit pattern. Events were required to have a good quality track reconstruction with a zenith angle in the interval 90° to 120°. Multivariate training and selection was done with the help of Support Vector Machines [6]. At the final stages in the analysis, randomized real data were used to model the atmospheric background.

A. *Simulations*

Five WIMP masses: 250, 500, 1000, 3000, and 5000 GeV were simulated using `WimpSim` [7] in two annihilation channels, $b\bar{b}$ (soft channel), and W^+W^- (hard channel), representing the extremes of the neutrino energy distributions. Single and coincident shower atmospheric muon backgrounds were simulated using `CORSIKA` [8]. The atmospheric neutrino background was simulated [9] following the Bartol flux [10]. Charged particle propagation [11] and photon propagation [12], using ice measurements [13], were also simulated.

B. *Results*

The final data sample was used to test the hypothesis that it contains a certain signal level, against the null hypothesis of no signal. The shape of the angular distribution of events with respect to the Sun was used as a test statistic (see Figure 1). The background-only p.d.f. was constructed from data with randomized azimuth angles, while the p.d.f.s for the different signal models tested were obtained from Monte Carlo. A limit was set on the relative strength of the signal p.d.f. using a Feldman-Cousins [14] confidence interval construction. These limits were transformed to a limit on the muon flux above 1 GeV, which is shown in Figure 2 together with previous limits [15], [16], [17], [18], MSSM models [19], and a conservative estimate of the full IceCube sensitivity including DeepCore. The models shown are those not excluded by CDMS [20] and XENON10 [21] based on the spin-independent WIMP-proton cross-section. Models in the darker region require a factor of 100 increase in sensitivity of direct detection experiments in order to be probed by them. Assuming that WIMPs are in equilibrium in the Sun, the limit on the muon flux can be converted to a limit on the spin-dependent WIMP-proton cross-section [22]. These limits are shown in Figure 3 together with previous limits [17], [20], [23], [24], MSSM models, and the IceCube sensitivity.

IV. Earth WIMPs

Dark matter could also be gravitationally trapped at the center of the Earth. Such scenarios are generally not favored due to its less efficient capture of dark matter. However, from an experimental point of view, the searches from dark matter from the center of the Earth are still of interest due to the many unknowns that plague the relic, capture and annihilation processes that enter into the calculation of the expected fluxes. In order to search for an indirect signal from dark matter annihilation from the Earth, IceCube uses muon neutrinos ν_μ that interact in or below the IceCube detector. They produce vertically up-going track-like events, that point back to the center of Earth. We have designed a string trigger [25] for IceCube that is specifically optimized for

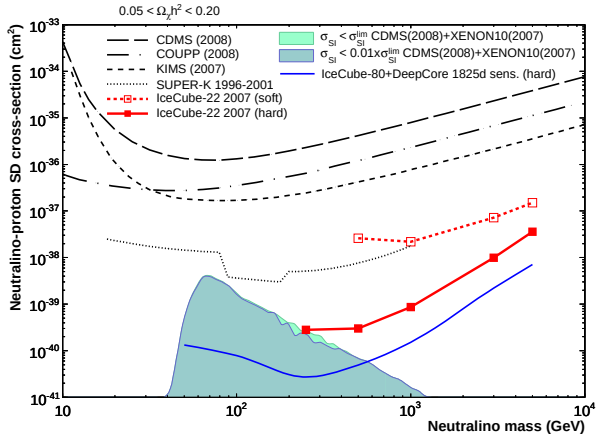

Fig. 3. Upper limits at the 90% confidence level on the spin-dependent neutralino-proton cross-section σ^{SD} for the soft ($b\bar{b}$) and hard (W^+W^-) annihilation channels, adjusted for systematic effects, as a function of neutralino mass [5]. The lighter [green] and darker [blue] shaded areas represents MSSM models not disfavored by direct searches [20], [21] based on σ^{SI} and $100 \cdot \sigma^{SI}$, respectively. Also shown are the limits from CDMS [20], COUPP [24], KIMS [23] and Super-K [17], and the expected sensitivity of IceCube with DeepCore.

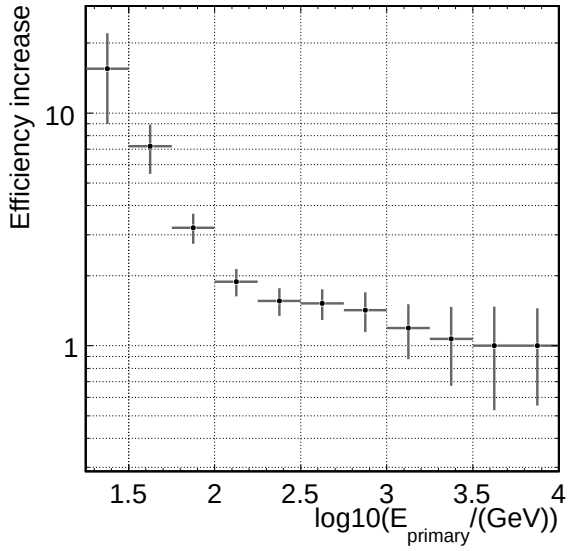

Fig. 4. Impact of the string trigger for the detection of vertically up-going muon neutrinos as function of their energy. The efficiency increase is shown compared to IceCube's multiplicity eight DOM trigger.

this class of events. A similar trigger has also been active in AMANDA. The IceCube string trigger, which selects events with a cluster of hits on a single string, has been active since spring 2008. It requires 5 DOMs to be above threshold in a series of 7 consecutive DOMs, within a time window of 1.5 μs. Due to the low noise environment and this special trigger, IceCube has an energy threshold for these vertical events that can reach below 100 GeV. The increase in efficiency to these events, over the default DOM multiplicity trigger condition, is shown in Figure 4. Based on selection criteria optimized for these vertically up-going events [30], we will derive a sensitivity for the detection of a possible additional muon flux. These results will be shown at the time of the conference.

Interpreting a possible muon flux (induced from muon neutrino interactions in or below the IceCube detector) from WIMP annihilation in the Earth is somewhat more complicated compared to the solar WIMP searches. The escape velocity is relatively small ($v \simeq 15$ km/s at the center) and capture is only possible for low speed WIMPs unless its mass is nearly identical to that of one of the nuclear species in the Earth. WIMPs are typically only expected to be captured after they are bound to the solar system due to previous scattering in the Sun; such capture mechanisms are described in [26], [27], [28]. Contrarily to the Sun, capture and annihilation of WIMPs are generally not in equilibrium in the Earth. Hence, the expected flux of neutrinos from dark matter annihilations strongly depends on how much dark matter was previously accumulated. Models that enhance the collection of dark matter by the Earth therefore also significantly boost expected signals. One such example is an expected boost due to lower velocity WIMPs in the galactic halo from previous dwarf mergers. Such scenarios could boost fluxes at neutrino telescopes by a few orders of magnitude [29].

Such examples show that big uncertainties remain in the overall flux predictions for neutrinos from the center of the Earth. IceCube, with the combination of DeepCore, is an ideal instrument to look for such signals.

V. Halo WIMPs

Besides searches for indirect signals from dark matter annihilation in the center of the Sun and Earth, another promising way is to look directly at the galactic halo. Such a signal could be seen in neutrinos as a large scale flux anisotropy that peaks towards the Galactic Center. IceCube has in the past not performed a dedicated search for such signals. However, theoretical predictions indicate that such a search can provide stringent limits [31], [32] on the dark matter self-annihilation cross-section. They are complementary to Solar WIMP searches, as they probe the dark matter self-annihilation cross-section directly.

The analysis for a neutrino flux anisotropy is still ongoing on the IceCube dataset. We perform this analysis on data collected with the IceCube 40-string configuration. Neutrino-induced muon events are being used to search for a neutrino flux anisotropy towards the direction of the Galactic Center. In its current configuration, IceCube can only access up-going muon neutrinos for the energy range of interest (around and below a TeV) with sufficient background rejection. The region closest towards the Galactic Center, accessible in IceCube with up-going events, is therefore near the horizon. It covers, in part, a distance of about 30° towards the Galactic Center. Using a declination band simplifies the background estimation, as an on and off-source comparison can be performed. Second order effects need to be taken

into account; these include uneven detector exposure-times, as the reconstruction efficiency is a function of the azimuth angle for the tracks in the same declination band. We plan to present the sensitivity using this method at the time of the conference for different signal distributions within the declination bands [33].

For the future, DeepCore is especially promising for the halo WIMP searches, as it lowers the neutrino energy threshold, holds promises for cascade reconstruction and will allow observation of the entire sky. The lower energy threshold will increase expected signal rates, especially to WIMPs with masses of a few hundred GeV and scale with the increase in neutrino effective area. Leading dark matter candidates have masses in the sub-TeV range, so the expected neutrino energy spectrum is at the low energy end of IceCube's sensitivity. The detection of low energy cascades caused by ν_τ, ν_e charged current interactions or neutral current of all neutrino flavors is especially interesting, as the atmospheric neutrino background to this signal is much lower than the muon neutrino background. Even a very limited angular resolution for these cascades, which IceCube might be able to achieve, would benefit the analysis, as it is looking for a large scale anisotropy. The usage of surrounding IceCube strings as veto against down-going muons in DeepCore is expected to give large reductions in this background and enable us to study the entire sky. Simple veto methods have achieved background reductions of four orders of magnitude with excellent signal retention and have potential for greater than 6 orders of magnitude rejection utilizing reconstruction veto methods [34]. Since the Galactic Center, for which the largest flux from dark matter annihilation is expected, is located in the southern hemisphere, this will benefit the analysis in particular.

Expected neutrino fluxes from dark matter self-annihilations in the galactic halo are generally small. Results from PAMELA [35] and Fermi [36] might indicate larger than usual self-annihilation cross-sections of the halo dark matter, this could either be due to unusually large boost factors (clumpiness) well above expectations from dark matter halo simulations, or due to an enhancement in the self-annihilation cross-section (for example Sommerfeld enhancement). Lepton results could also be entirely explainable by astronomical sources (for example pulsars [37]). Regardless of what the source of the recent excess is, it only shows there remains a large uncertainty in any flux predictions for neutrinos from dark matter annihilations or decays in the galactic halo. This, it will be important to check for any such signals with neutrinos.

VI. SUMMARY

IceCube has set the best limits to date on WIMP annihilation in the Sun using 22-string data from 2007. Using data from the completed 86-string detector, which will include the DeepCore low-energy extension, improvements of an order of magnitude are expected. Searches for signals from the Earth and the galactic halo are also expected to give interesting results.

REFERENCES

[1] G. Jungman, M. Kamionkowski and K. Griest, Phys. Rep. **267**, 195 (1996).
[2] W. H. Press and D. N. Spergel, Astrophys. J **296**, 679 (1985).
[3] A. Achterberg *et al.*, Astropart. Phys. **26**, 155 (2006).
[4] D. Cowen for the IceCube coll., Proc. of NEUTEL09, (2009).
[5] R. Abbasi *et al.*, Phys. Rev. Lett. **102**, 201302 (2009).
[6] S. S. Kerthi *et al.*, Neural Comp. **13**, 637 (2001).
[7] M. Blennow, J. Edsjö, T. Ohlsson, JCAP **01**, 021 (2008).
[8] D. Heck *et al.*, FZKA Report **6019** (1998).
[9] A. Gazizov and M. Kowalski, Comput. Phys. Commun. **172**, 203 (2005).
[10] G. D. Barr *et al.*, Phys. Rev. D **70**, 023006 (2004).
[11] D. Chirkin and W. Rhode, hep-ph/0407075v2.
[12] J. Lundberg *et al.*, Nucl. Instr. Meth. A **581**, 619 (2007).
[13] M. Ackermann *et al.*, J. Geophys. Res. **111**, 02201 (2006).
[14] G. J. Feldman and R. D. Cousins, Phys. Rev. D **57**, 3873 (1998).
[15] M. M. Boliev *et al.*, Nucl. Phys. Proc. Suppl. **48**, 83 (1996).
[16] M. Ambrosio *et al.*, Phys. Rev. D **60**, 082002 (1999).
[17] S. Desai *et al.*, Phys. Rev. D **70**, 083523 (2004).
[18] M. Ackermann *et al.*, Astropart. Phys. **24**, 459 (2006).
[19] P. Gondolo *et al.*, JCAP **0407**, 008 (2004).
[20] Z. Ahmed *et al.*, astro-ph/0802.3530.
[21] J. Angle *et al.*, Phys. Rev. Lett. **100**, 021303 (2008).
[22] G. Wikström and J. Edsjö, JCAP **04**, 009 (2009).
[23] H. S. Lee *et al.*, Phys. Rev. Lett. **99**, 091301 (2007).
[24] E. Behnke *et al.*, Science **319**, 933 (2008).
[25] A. Gross *et al.* for the IceCube coll., astro-ph/0711.0353.
[26] J. Lundberg and J. Edsjö, Phys. Rev. D **69**, 123505 (2004).
[27] A. Gould, Astrophys. J. 328, 919 (1988).
[28] A. H. G. Peter, astro-ph/0902.1348.
[29] T. Bruch, A. H. G. Peter, J. Read, L. Baudis and G. Lake, astro-ph/0902.4001.
[30] C. Rott, for the IceCube coll., these proceedings.
[31] H. Yuksel, S. Horiuchi, J. F. Beacom and S. Ando, astro-ph/0707.0196.
[32] J. F. Beacom, N. F. Bell and G. D. Mack, Phys. Rev. Lett. **99**, 231301 (2007).
[33] G. Mack, and C. Rott, forthcoming.
[34] D. Grant *et al.*, for the IceCube coll., these proceedings.
[35] O. Adriani *et al.*, Nature **458**, 607 (2009).
[36] Fermi/LAT Collaboration, arXiv:0905.0025.
[37] H. Yuksel, M. D. Kistler and T. Stanev, astro-ph/0810.2784.

Search for the Kaluza-Klein Dark Matter with the AMANDA/IceCube Detectors

Matthias Danninger* **and Kahae Han† for the IceCube Collaboration‡**

*Department of Physics, Stockholm University, AlbaNova, S-10691 Stockholm, Sweden
†Department of Physics and Astronomy, University of Canterbury, Pr. Bag 4800 Christchurch, New Zealand
‡See special section of these proceedings

Abstract. **A viable WIMP candidate, the lightest Kaluza-Klein particle (LKP), is motivated by theories of universal extra dimensions. LKPs can scatter off nuclei in large celestial bodies, like the Sun, and become trapped within their deep gravitational wells, leading to high WIMP densities in the object's core. Pair-wise LKP annihilation could lead to a detectable high energy neutrino flux from the center of the Sun in the IceCube neutrino telescope.**

We describe an ongoing search for Kaluza-Klein solar WIMPs with the AMANDA-II data for the years 2001-2003, and also present a UED dark matter sensitivity projected to 180 days from a study of data taken with the combined AMANDA II and IceCube detector in the year 2007. A competitive sensitivity, compared to existing direct and indirect search experiments, on the spin-dependent cross section of the LKP on protons is also presented.

Keywords**: Kaluza-Klein, Dark Matter, IceCube**

I. INTRODUCTION

Kaluza-Klein weakly interacting massive particles (WIMP) arising from theories with extra dimensions have come under increased scrutiny [1] alongside WIMP candidates from supersymmetric particle theories, e.g. the neutralino.

Several analyses [2], [3] performed on the data from the AMANDA-II and the IceCube detectors have already put limits on the neutralino induced muon flux from the Sun comparable to that of direct detection experiments. The first excitation of the Kaluza Klein (KK) photon, $B^{(1)}$, in the case of Universal Extra Dimensions (UED) with one extra dimension, annihilates to all standard model particles. This results in the production of a detectable flux of muon neutrinos in the IceCube detector. $B^{(1)}$ is often referred to as the LKP - lightest Kaluza-Klein Particle. KK-momentum conservation leads to the stability of the LKP, which makes it a viable dark matter candidate. Compared to neutralino WIMPs, LKPs come from a relatively simple extension of the Standard Model and, consequently, branching ratios (see Table I) and cross sections are calculated with fewer assumptions and parameter-dependences. This feature allows us to perform a combined channel analysis for an LKP particle. Another consequence of the simple UED model is that with the assumption of a compactified extra dimension scale of around 1TeV, the particle takes a much narrower range of masses [1] from the relic density calculation - ranging from 600 GeV to 800 GeV and 500 GeV to 1500 GeV if coannihilations are accounted for [4]. Moreover, collider search limits rule out LKP masses below 300 GeV [5], [6].

TABLE I
POSSIBLE CHANNELS FOR THE PAIR ANNIHILATION OF $B^{(1)}B^{(1)}$ AND BRANCHING RATIOS OF THE FINAL STATES. FIGURES TAKEN FROM [20].

Annihilation Process			Branching ratio
$B^{(1)}B^{(1)}$	$\rightarrow$	$\nu_e\overline{\nu}_e$, $\nu_\mu\overline{\nu}_\mu$, $\nu_\tau\overline{\nu}_\tau$	0.012
	$\rightarrow$	e^+e^-, $\mu^+\mu^-$, $\tau^+\tau^-$	0.20
	$\rightarrow$	$u\overline{u}$, $c\overline{c}$, $t\overline{t}$	0.11
	$\rightarrow$	$d\overline{d}$, $s\overline{s}$, $b\overline{b}$	0.07

In this paper we describe an ongoing solar WIMP analysis with the (2001) AMANDA data. Furthermore, we derive for the combined geometry of 22 IceCube strings (IC22) and AMANDA (to be referred to as the combined analysis in the rest of the paper) the projected sensitivity on the muon flux and spin-dependent (SD) cross section obtained for LKP WIMPs with data from the year 2007.

The AMANDA-II detector, a smaller predecessor of IceCube with 677 OMs on 19 strings, ordered in a 500m by 200m diameter cylindrical lattice, has been fully operational since 2001 [7]. The IceCube Detector, with its 59^{th} string deployed this season, is much larger with increased spacing between the strings and will have a total instrumented volume of 1km^3 [8]. The set-up in 2007 for the combined analysis consisted of 22 IceCube strings, and the 19 AMANDA strings, with a separate trigger and data acquisition system. The detector geometry for both AMANDA-II and IC22 is shown in Fig. 2a.

II. SIMULATIONS

A solar WIMP analysis can be thought of as using the Earth as its primary physical filter for data, as one only looks at data collected when the Sun is below the horizon at the South Pole, $\Theta_\odot \in [90°, 113°]$. Single[1], μ_{single}, and coincident[2], μ_{coin}, atmospheric muons that come from cosmic ray showers in a zenith angle

[1]atmospheric muons from single CR showers
[2]atmospheric muons from coincident CR showers

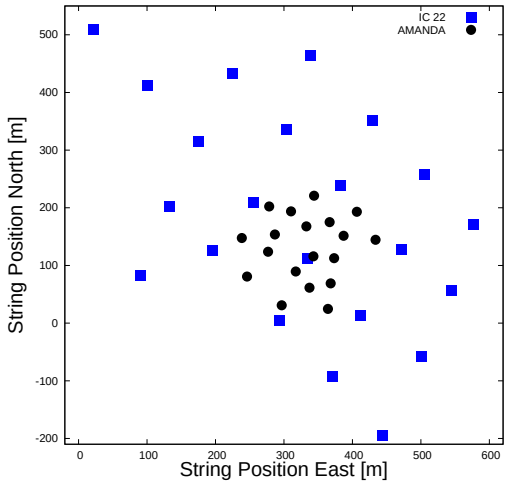

Fig. 1. Top view of the 2007 IceCube+AMANDA detector configuration. The IceCube-22 strings (squares) enclose the AMANDA strings (circles).

range Θ_μ of $[0°, 90°]$, constitute the majority of the background, whereas the near-isotropic distribution of atmospheric neutrinos, ν_{atm}, will form an irreducible background. The atmospheric muon backgrounds are generated using CORSIKA [9] with the Hörandel CR composition model [10]. For the atmospheric neutrino background, produced according to the Bartol model [11], ANIS [12] is used. For the combined analysis, the simulated μ_{single} background has a detector-livetime of 1.2 days, μ_{coin} of 7.1 days and ν_{atm} of 9.8 years. WIMPSIM [13], [14] was used to generate the signal samples for LKP WIMPs, consisting of 2 million events per channel for WIMP masses varying from 250 GeV to 3000 GeV. Individual annihilation channels (three ν's, τ, and t,b,c quarks), contributing to ν_μ's at the detector, were generated for the combined analysis, as well as for the AMANDA only analysis (in the latter case for the energy range from 500 GeV to 1000 GeV). Muon and Čerenkov light propagation in Antarctic ice were simulated using IceCube/AMANDA software such as MMC [15], PTD and photonics [16]. Finally, AMASIM for AMANDA and ICESIM for the combined detector were used to simulate the detector response. The signal detection efficiency of the two detector configurations is given by the effective volume, V_{eff}, which is defined for a constant generation volume, V_{gen}, by

$$V_{eff} = V_{gen} \cdot \frac{N_{obs}}{N_{gen}}, \qquad (1)$$

where N_{obs} is the number of observed LKP events and N_{gen} the number of generated LKP events, undergoing charged-current interaction within V_{gen}. V_{eff} is a good quantity to compare LKP detectability at trigger level for the two analyses, shown in Fig. 2a.

After deadtime correction, 142.5 days of data when the Sun was below the horizon were available in 2001 with a total number of $1.46 \cdot 10^9$ recorded events for the AMANDA analysis. The combined analysis is utilizing a projected total livetime of 180 days of data for the calculated sensitivities in this paper.

The main purpose of the Monte Carlo (MC) simulations of the various background sources is to show that a good agreement with experiment is achieved, demonstrating a sufficient understanding of the detector. Thus, it is viable to assume that the LKP signal samples are simulated correctly within the AMANDA/IceCube simulation-chain and can be used to select the different cut parameters for the higher cut levels $L2,\ L3$ and $L4$, because their difference from background in different parameter distributions can be clearly identified. The actual cut value of each cut level is obtained by maximizing the efficiency function, or a figure-of-merit, for simulated LKP signals and the experimental background sample, which consists of data taken when the Sun was above the horizon and therefore contains no solar WIMP signal. Setting cut values based on experimental background datasets has the advantage that possible simulation flaws are minimized.

III. Filtering

LKP signals are point sources with very distinct directional limitations (zenith angle theta, $\Theta_{zen} = 90° \pm 23°$). Hence, the general strategy of filtering for both analyses is to apply strict directional cuts in early filter levels. $L0$ and $L1$ consist of calibration, reconstruction and making a simple angular cut of $\Theta_{zen} > 70°$ on the first-guess reconstructed track. This leads to a passing efficiency of around 0.7 for all LKP signal samples, and reduction of around 0.002 for both, data and muon background. All events passing the $L0 + L1$ level are reconstructed using log-likelihood methods (llh). $L2$ is a two dimensional cut on the reconstructed llh-fit zenith angle ($\Theta_{zen,llh}$) within $\Theta_\odot$ and the estimated angular uncertainty of the llh track. $L3$ picks reconstructed tracks, which are nearly horizontal and pass the detector, to further minimize vertical tracks associated with background events. The multivariate filter level, $L4$, consists of two different multivariate analysis routines from the TMVA [17] toolkit, namely a support vector machine (SVM) together with a Gaussian fit-function and a neural network (NN). The input variables for the two algorithms are obtained by choosing parameters with low correlation but high discrimination power between background and signal. The individual output parameters are combined in one multivariate cut parameter $Q_{NN} \cdot Q_{SVM}$.

IV. Sensitivity

After the $L4$ cut[3], the muon background reduction is better than a factor $1.16 \cdot 10^{-7}$, which implies that the final sample is dominated by ν_{atm} background. The solar

[3]starting with $L4$, only the combined analysis is discussed

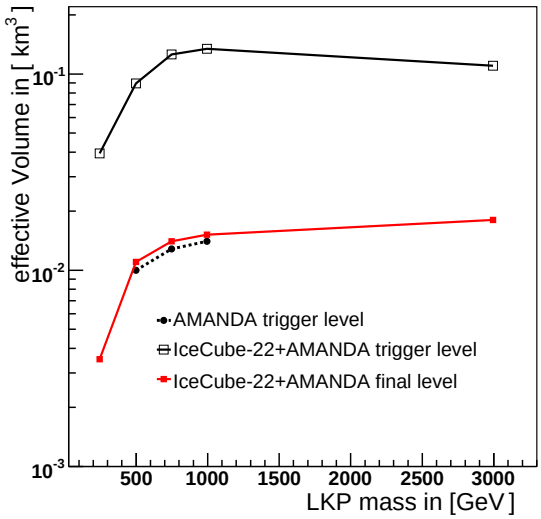

(a) Effective volume

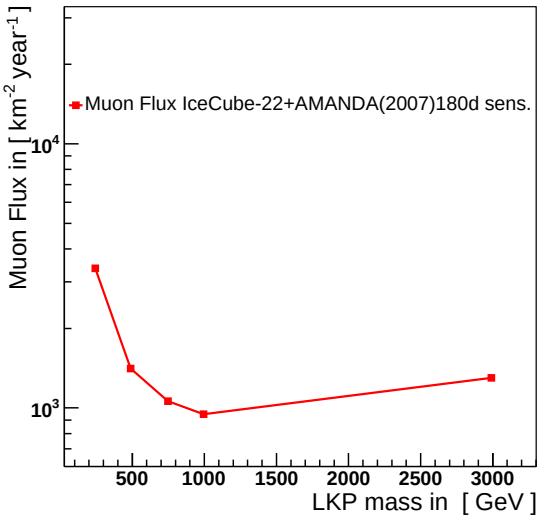

(b) Muon flux sensitivity

Fig. 2. Fig.2a shows the effective volume as a function of LKP mass at trigger level and final cut level for the IceCube-22+AMANDA analysis and at trigger level only for the AMANDA analysis. Fig.2b demonstrates the projected sensitivity to 180 days of livetime on the muon flux from LKP annihilations in the Sun as a function of LKP mass for the IceCube-22+AMANDA detector configuration.

search looks for an excess in neutrino events over the expected background in a specifically determined search cone towards the direction of the Sun with an opening angle Ψ. Events with a reconstructed track direction pointing back towards the Sun within an angle Ψ are kept, where Ψ is optimized to discriminate between the ν_{atm} background and a sum of all seven LKP channels, weighted with the expected branching ratios as listed in Table I.

The expected upper limit, or sensitivity, for an expected number of background events n_{Bg} is

$$\overline{\mu}_s^{90\%}(n_{Bg}) = \sum_{n_{obs}=0}^{\infty} \mu_s^{90\%}(n_{obs}) \frac{(n_{Bg})^{n_{obs}}}{(n_{obs})!} e^{-n_{Bg}} \ , \quad (2)$$

where $\mu_s^{90\%}(n_{obs})$ is the Feldman-Cousins upper limit for the number of observed events, n_{obs} [18]. The model rejection factor [19]

$$MRF = \frac{\overline{\mu}_s^{90\%}}{n_s}, \quad (3)$$

is used to determine the optimum opening angle Ψ of the solar search cone. Here, n_s is the number of surviving LKP events within Ψ.

Under the assumption of no signal detection, it is possible to derive the Feldman-Cousins sensitivity discussed above for the combined detector with a total projected livetime of $T_{live} = 180$ days. The expected number of events after cut level $L4$ are estimated from a processed subset of observational data with a detector livetime of 5.61 days. The results are then extrapolated to the total livetime T_{live}, yielding an expectation of 7140 events. The corresponding expectation from the simulated background samples, $n_{Bg,MC}$, normalized to the data at filter level $L1$ and extrapolated to T_{live}, is $633(\mu_{coin}) + 1038(\mu_{single}) + 5340(\nu_{atm}) = 7011(n_{Bg,MC})$.

The expected sensitivity on the neutrino-to-muon conversion rate $\overline{\Gamma}_{\nu\to\mu}^{90\%}$ is given by

$$\overline{\Gamma}_{\nu\to\mu}^{90\%} = \frac{\overline{\mu}_s^{90\%}}{V_{eff} \cdot T_{live}} \ , \quad (4)$$

where the effective volume V_{eff} is given by eq. 1. For each annihilation channel, one can separately calculate the V_{eff} within the solar search cone, determined by the combined signal p.d.f., $f_S^{all}(x|\Psi)$, and thereby determine a $\overline{\Gamma}_{\nu\to\mu}^{90\%}$ for each channel. Additionally, the combined effective volume, $V_{eff,LKP}$, for the expected ν_{LKP} spectrum is given by the sum of the individual V_{eff} per channel, weighted with the respective branching ratio of each channel. For the neutrino-to-muon conversion rate per single channel, the expected limit on the annihilation rate in the core of the Sun per second is given by,

$$\overline{\Gamma}_A^{90\%} = (c_1(ch, m_{B^{(1)}}))^{-1} \cdot \overline{\Gamma}_{\nu\to\mu}^{90\%} \ , \quad (5)$$

where $c_1(ch, m_{B^{(1)}})$ is an LKP annihilation channel (ch) and energy dependent constant. The sensitivity to the muon flux at a plane at the combined detector is derived via the calculation chain $\overline{\Gamma}_{\nu\to\mu}^{90\%} \to \overline{\Gamma}_A^{90\%} \to \Phi_\mu^{90\%}$ and is performed using the code described in [13], [14]. The results for the final V_{eff} and the predicted sensitivity to a muon flux resulting from LKP induced annihilations in the Sun for the combined IC22 and AMANDA detector 2007 with a total livetime of 180 days are presented in figures 2a and 2b. From the derived ν-to-μ conversion rate, $\overline{\Gamma}_{\nu\to\mu,LKP}^{90\%}$, we can calculate the sensitivity for the annihilation rate in the Sun per second, $\overline{\Gamma}_{A,LKP}^{90\%}$.

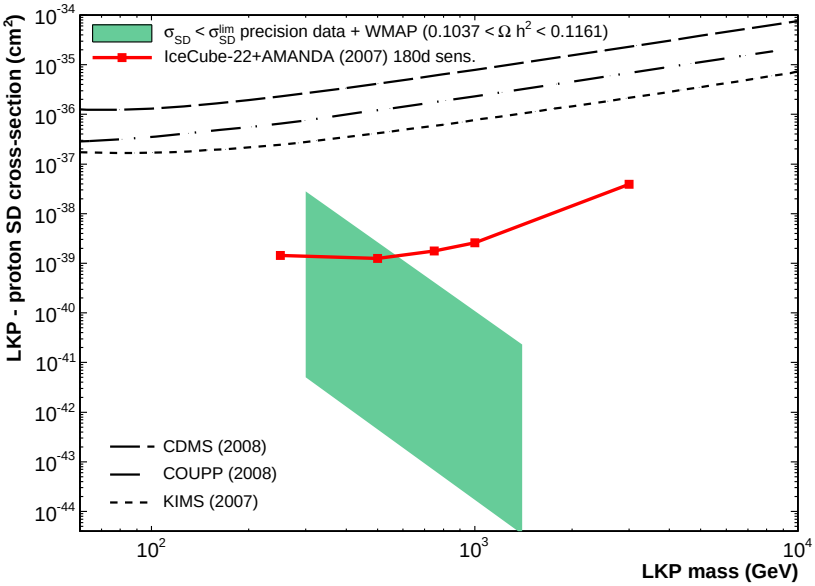

Fig. 3. Theoretically predicted spin-dependent $B^{(1)}$-on-proton elastic scattering cross sections are indicated by the shaded area [22]. The cross-section prediction vary with the assumed mass of the first KK excitation of the quark, constrained by $0.01 \leq r = (m_{q^{(1)}} - m_{B^{(1)}})/m_{B^{(1)}} \leq 0.5$. The current 'best' limits, set by direct search experiments are plotted together with the sensitivity of the combined detector IceCube-22+AMANDA. The region below $m_{B^{(1)}} = 300$ GeV is excluded by collider experiments [5], [6] and $m_{B^{(1)}} > 1500$ GeV is strongly disfavored by WMAP observations [23].

In [20], it is shown that the equilibrium condition between $\Gamma_{A,LKP}$ and the capture rate $C^{\odot}$ is met by LKPs within the probed mass range. Furthermore, the capture rate of LKPs in the Sun is entirely dominated by the spin-dependent component of the $B^{(1)}$-on-proton elastic scattering [21]. Consequently, presuming an equilibrium of $\Gamma_{A,LKP} = C^{\odot}$, the sensitivity for the spin-dependent elastic scattering cross section[4] of $B^{(1)}$ can be calculated as,

$$\sigma_{H,SD} \simeq 0.597 \cdot 10^{-24} \mathrm{pb} \left(\frac{\mathrm{m_{B^{(1)}}}}{1\,TeV}\right)^2 \cdot \left(\frac{\overline{\Gamma}^{90\%}_{A,LKP}}{\mathrm{s}^{-1}}\right). \quad (6)$$

The estimated sensitivity for the spin-dependent cross section for LKPs is displayed in figure 3, along with the most recently published limits from direct search experiments. The theoretical spin-dependent cross section predictions (shaded area) for LKPs are taken from [22] and are plotted for different predictions for the mass of the first KK-excitation of the quark.

V. Conclusion and Outlook

We showed that a competitive result on the spin-dependent cross-section of LKP-on-proton scattering can be obtained with the combined geometry of AMANDA-II and IceCube-22, which explores parts of the unrejected regions in the theoretically predicted LKP-region.

We also described the ongoing solar WIMP analysis of the AMANDA-II data taken during 2001. This will be extended to include 2002 and 2003 data. Furthermore, as the energy signature of ν_μ's induced by LKP annihilations in the Sun is very hard, the fullsized IceCube-80 detector will markedly improve the sensitivity and set strong limits on LKP WIMP theories.

[4]The local density of DM in our galaxy is taken to match the mean density $\overline{\rho}_{DM} = 0.3$ GeV/c^{2}cm^3, and the rms velocity is set to $\overline{v} = 270$ km/s.

References

[1] D.Hooper *et al.* , *The PAMELA and ATIC Signals from Kaluza-Klein Dark Matter* http://arxiv.org/abs/0902.0593.
[2] J.Braun *et al.* , (Searches for WIMP DM from the Sun with AMANDA) ICRC (2009).
[3] R.Abbasi *et al.* , (the IceCube collaboration) arXiv:astro-ph/0902.2460 (14 Feb 2009).
[4] T.Appelquist *et al.* , *Physical Review D* **64** (2001) 035002.
[5] I.Gogoladze *et al.* , *Physical Review D* **74** (2006) 093012.
[6] T.Appelquist *et al.* , *Physical Review D* **67** (2003) 055002.
[7] E.Andres *et al.* , (the AMANDA collaboration) *Astrop. Phys.* **13** (2000) 1.
[8] A.Achterberg *et al.* , (the IceCube collaboration) *Astrop. Phys.* **26** (2006) 155.
[9] D.Heck *et al.* , *FZKA Report* **6019**, Forschungszentrum Karlsruhe (1998).
[10] J.Hörandel, *Astrop. Phys.* **19** (2003) 193.
[11] G.D.Barr *et al.* , *Phys. Review* **D70** (2004) 023006.
[12] A.Gazizov *et al.* , *Comput.Phys.Commun.* **172** (2005) 203.
[13] J.Edsjö, *WimpSim Neutrino Monte Carlo* http://www.physto.se/~edsjo/wimpsim/.
[14] M.Blennow *et al.* , *JCAP* **21** (2008).
[15] D.Chirkin, *Cosmic ray energy spectrum measurement with AMANDA* PhD Thesis, UC Berkley (2003).
[16] J.Lundberg *et al.* , *Nucl.Instr.Meth.* **A581** (2007).
[17] A.Höcker *et al.* , http://tmva.sourceforge.net.
[18] G.J.Feldmann *et al.* , *Phys. Rev.* **D57** (1998) 7.
[19] G.C.Hill *et al.* , *Astrop. Phys.* **19** (2003) 393.
[20] D.Hooper *et al.* , arXiv:hep-ph/0208261v3 (16 Feb 2003).
[21] D.Hooper *et al.* , arXiv:hep-ph/0409272v1 (23 Sep 2004).
[22] S.Arrenberg *et al.* , arXiv:hep-ph/0805.4210v1 (28 May 2008).
[23] M.Tegmark *et al.* , *Physical Review D* **74** (2006) 123507.

Searches for WIMP Dark Matter from the Sun with AMANDA

James Braun[*] **and Daan Hubert**[†] **for the IceCube Collaboration**[‡]

[*]*Dept. of Physics, University of Wisconsin, Madison, WI 53706, USA*
[†]*Vrije Universiteit Brussel, Dienst ELEM, B-1050 Brussels, Belgium*
[‡]*See the special section of these proceedings*

***Abstract*. A well-known potential dark matter signature is emission of GeV - TeV neutrinos from annihilation of neutralinos gravitationally bound to massive objects. We present results from recent searches for high energy neutrino emission from the Sun with AMANDA, in all cases revealing no significant excess. We show limits on both neutralino-induced muon flux from the Sun and neutralino-nucleon cross section, comparing them with recent IceCube results. Particularly, our limits on spin-dependent cross section are much better than those obtained in direct detection experiments, allowing AMANDA and other neutrino telescopes to search a complementary portion of MSSM parameter space.**

***Keywords*: AMANDA WIMP Neutralino**

I. Introduction

Weakly interacting massive particles (WIMPs) with electroweak scale masses are currently a favored explanation of the missing mass in the universe. Such particles must either be stable or have a lifetime comparable to the age of the universe, and they would interact with baryonic matter gravitationally and through weak interactions. The minimal supersymmetric standard model (MSSM) provides a natural candidate, the lightest neutralino [1]. A large range of potential neutralino masses exists, with a lower bound on the mass of the lightest neutralino of 47 GeV imposed by accelerator-based analyses [2], while predictions based on the inferred dark matter density suggest masses up to several TeV [3].

Searches for neutralino dark matter include *direct* searches for nuclear recoils from weak interaction of neutralinos with matter [4], [5] and *indirect* searches for standard model particles produced by neutralino annihilation. Particularly, a fraction of neutralinos interacting with massive objects would become gravitationally bound and accumulate in the center. If neutralinos comprise dark matter, enough should accumulate and annihilate to produce an observable neutrino flux. Searches for a high energy neutrino beam from the center of the Earth [6] and the Sun [7], [8], [9], [10], [11] have yielded negative results. Observations of a cosmic ray electron-positron excess by ATIC [12], PPB-BETS [13], Fermi [14], and HESS [15], along with the anomalous cosmic ray positron fraction reported by PAMELA [16], could be interpreted as an indirect signal of dark matter annihilation in our galaxy [17].

Here we present searches for a flux of GeV–TeV neutrinos from the Sun using AMANDA. We improve on the sensitivity of the previous AMANDA analysis [11] significantly and extend the latest results from IceCube [7] to lower neutralino masses. We observe no neutralino annihilation signal and report limits on the neutrino-induced muon flux from the Sun and the resulting limits on neutralino-proton spin-dependent cross section.

II. Neutrino Detection with AMANDA

The detection of neutrino fluxes above ~ 50 GeV is a major goal of the Antarctic Muon And Neutrino Detector Array (AMANDA). AMANDA consists of 677 optical modules embedded 1500 m to 2000 m deep in the ice sheet at the South Pole, arranged in 19 vertical strings and occupying a volume of ~ 0.02 km^3. Each module contains a 20 cm diameter photomultiplier tube (PMT) optically coupled to an outer glass pressure sphere. PMT pulses ("hits") from incident Cherenkov light are propagated to surface electronics and are recorded as an event when 6–7 hits on any one string or 24 total hits occur within 2.5 μs. The vast majority of the O(10^9) events recorded each year are downgoing muons produced by cosmic ray air showers in the atmosphere above the South Pole. Relativistic charged leptons produced near the detector via charged-current neutrino interactions similarly trigger the detector, with several thousand atmospheric neutrino induced muon events recorded per year. The hit leading edge times, along with the known AMANDA geometry and ice properties [18], allow reconstruction of muon tracks with median accuracy 1.5° – 2.5°, dependent on zenith angle.

AMANDA operated in standalone from 2000–2006 and is currently a subdetector of the much larger ($\sim$ km^3) IceCube Neutrino Observatory [19], scheduled for completion in 2011. The optical module density of AMANDA is much higher than that of IceCube, making AMANDA more efficient for low-energy muons ($\lesssim 300$ GeV) which emit less Cherenkov light.

III. Data Selection and Methods

We describe two separate searches for Solar neutralinos in this proceeding. First, we present a search using a large data sample from 2000–2006 prepared for a high energy extraterrestrial point source search [20], [21]. We also present a search using data from 2001–2003, optimized to retain low energy events [22]. Both analyses are done in two stages; first, neutrino

induced muon events are isolated from the much larger background of downgoing muons, then a search method is used to test for an excess at the location of the Sun.

A. Data Selection

While the Sun is above the horizon, neutrino-induced muons from the Sun are masked by the much larger background of downgoing cosmic ray muons; thus, we select data during the period when the Sun is below the horizon (Mar. 21 – Sept. 21), resulting in 953 days live-time from 2000–2006 and 384 days from 2001–2003. In both analyses, neutrino events are isolated by selecting well reconstructed upgoing muon tracks. Events are first reconstructed with fast pattern matching algorithms, and events with zenith angles $\theta < 80°$ ($\theta < 70°$ for the 2001-2003 analysis) are discarded, eliminating the vast majority of downgoing muons. The remaining events are reconstructed with a more computationally intensive maximum-likelihood reconstruction [23] accurate to 1.5° – 2.5°, and again events with $\theta < 80°$ are discarded.

O(10^6) misreconstructed downgoing muon events remain per year, and these are reduced by cuts on track quality parameters such as track angular uncertainty [24], the smoothness (evenness) of hits along the track [23], and the likelihood difference between the maximum-likelihood track and a forced downgoing likelihood fit using the zenith distribution of downgoing muons as a prior [23]. For the 2000–2006 analysis, 6595 events remain after quality cuts, dominantly atmospheric neutrinos [20], reduced to 4665 events by requiring dates when the Sun is below the horizon. Zenith distributions from 2000–2006 are shown in figure 1.

We consider neutralino masses from 100 GeV to 5 TeV and two extreme annihilation channels: W^+W^- ($\tau^+\tau^-$ for 50 GeV) and $b\bar{b}$, which produce high and low energy neutrino spectra, respectively, relative to the neutralino mass. The fraction of signal events retained depends on the neutrino energy spectrum and varies from 17% for a 5 TeV neutralino mass and W^+W^- channel to 1% for 100 GeV and $b\bar{b}$ channel, relative to trigger level, in the 2000–2006 analysis.

The 2001–2003 analysis is a dedicated neutralino search, unlike the 2000-2006 analysis, and more consideration is given to low energy events. Twelve event observables are considered, and selection criteria based on these observables are optimized separately for three signal classes, dependent on neutralino mass and annihilation channel, to maximize retention of signal events. The signal classes are shown below along with the number of events passing selection criteria.

Class	Channel	m_χ	Final Events
A	W^+W^- $b\bar{b}$	250 GeV – 5 TeV 500 GeV – 5 TeV	670
B	W^+W^- $b\bar{b}$	100 GeV 250 GeV	504
C	$\tau^+\tau^-$ $b\bar{b}$	50 GeV 50, 100 GeV	398

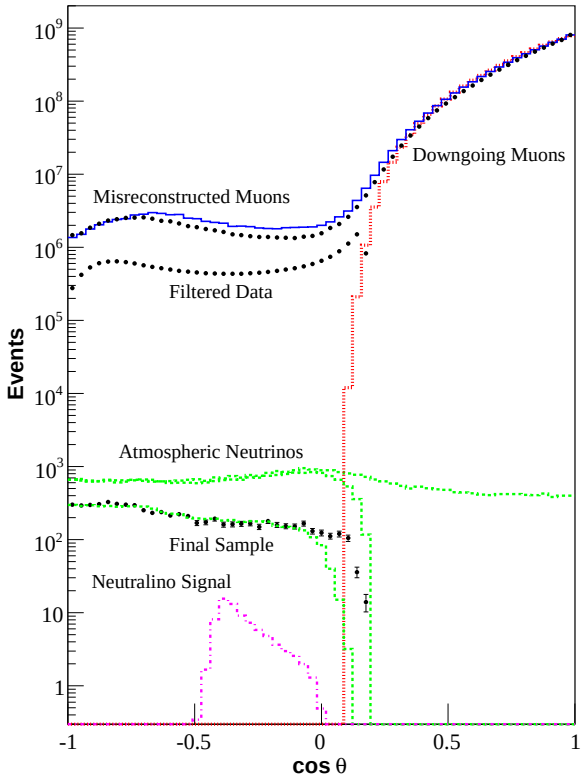

Fig. 1. Reconstructed zenith angles of data (circles) at trigger level, filter level ($\theta < 80°$), and final cut level, true (fine dotted) and reconstructed (solid) zenith angles of CORSIKA [31] downgoing muon simulation at trigger level, reconstructed zenith angles of ANIS [28] atmospheric neutrino simulation at trigger level, filter level, and final cut level (dashed), and reconstructed zenith angles of a neutrino signal from the Sun at final cut level (dash-dotted).

The selection is more efficient than the 2000-2006 analysis, with 21% of signal retained for 5 TeV, W^+W^- channel, to 4% for 100 GeV, $b\bar{b}$ channel. The 2001–2003 analysis additionally considers 50 GeV neutralino masses, with a signal efficiency of 1%–3%.

B. Search Method

Both analyses use maximum-likelihood methods [25] to search for an excess of events near the location of the Sun. The data is modeled as a mixture of n_s signal events from the Sun and background events from both atmospheric neutrinos and misreconstructed downgoing muons. The signal likelihood for the ith event is

$$\mathcal{S}_i = \frac{1}{2\pi\sigma_i^2} e^{-\frac{\psi_i^2}{2\sigma_i^2}}, \qquad (1)$$

where ψ_i is the space angle difference between the event and the Sun, and σ_i is the event angular uncertainty [24]. The background likelihood $\mathcal{B}_i$ is obtained from the zenith distribution of off-source data. The full-data likelihood over all N data events is

$$\mathcal{L} = P(Data|n_s) = \prod_{i=1}^{N} \left(\frac{n_s}{N}\mathcal{S}_i + (1 - \frac{n_s}{N})\mathcal{B}_i \right) \qquad (2)$$

and is numerically maximized to find the best fit event excess $\hat{n}_s$. The likelihood ratio $-2\log\frac{\mathcal{L}(0)}{\mathcal{L}(\hat{n}_s)}$ is approximately χ^2 distributed and provides a measure of significance. Event upper limits are set from this likelihood using the Feldman-Cousins unified construction [26].

C. Signal Simulation and Systematic Uncertainties

Neutrino energy distributions at Earth from neutralino annihilation in the Sun are generated by DarkSUSY [27]. For the 2000–2006 analysis, neutrino events are generated with ANIS [28], with muons propagated using MMC [29], then reweighted to the energy distributions described above. For 2001–2003, the DarkSUSY energy distributions are sampled by WimpSimp [30], and muons are propagated with MMC.

Uncertainties in our signal simulation are dominated by uncertainties in optical module sensitivity and photon propagation in ice. These uncertainties are constrained by comparing the trigger rate of CORSIKA [31] downgoing muon simulation using various hadronic models with the observed AMANDA trigger rate. The effect on signal prediction is measured by shifting the simulated optical module efficiency by these constraints and is 10% for $m_\chi = 5$ TeV, W^+W^- channel, to 21% for $m_\chi = 100$ GeV, $b\bar{b}$ channel. Other sources of uncertainty include event selection (4%–8%) and uncertainty in neutrino mixing angles (5%). For the 2000–2006 analysis, uncertainties total 13%–24% and are included in the limit calculation using the method of Conrad *et al.* [32] as modified by Hill [33]. Uncertainties for 2001–2003 total 23%–38% and are included in the limits assuming the worst case.

IV. Results

The search methods are applied to the final data, and both analyses reveal no significant excess of neutrino-induced muons from the direction of the Sun. A Sun-centered significance skymap from the 2000–2006 analysis (figure 2) shows a 0.8σ deficit from the direction of the Sun. For the 2001–2003 analysis, a deficit of events is observed in classes A and C, and a small excess is seen in class B. Each excess or deficit is within the 1σ range of background fluctuations.

Upper limits on the neutralino annihilation rate in the Sun are calculated from the event upper limit μ_{90} by

$$\Gamma_A = \frac{4\pi R^2 \mu_{90}}{N_A \rho T_L V_{eff}} \Big[\int_0^{m_\chi} \sigma_{\nu N} \frac{dN_\nu}{dE} dE \Big]^{-1}, \quad (3)$$

where R is the Earth-Sun radius, N_A is the Avogadro constant, ρ is the density of the detector medium, T_L is the livetime, and $\sigma_{\nu N}$ is the neutrino-nucleon cross section. The muon neutrino energy spectrum $\frac{dN_\nu}{dE}$ for a given annihilation channel is obtained from DarkSUSY and includes absorption and oscillation effects from transit through the Sun and to Earth. The energy-averaged effective volume V_{eff} is obtained from simulation. Limits on muon flux are given by

$$\Phi_\mu = \frac{\Gamma_A}{4\pi R^2} \int_{1\ GeV}^{m_\chi} \frac{dN_\mu}{dE} dE, \quad (4)$$

and limits on neutralino-proton cross section are calculated according to [34]. These quantities are tabulated in table I for the more restrictive of the two analyses. Muon flux limits, assuming a 1 GeV threshold on muon energy, and spin-dependent cross section limits are shown in figure 3 for both analyses.

V. Discussion

These limits extend the latest IceCube limits to lower neutralino masses and are now beginning to exclude neutralino spin-dependent cross sections allowed by direct detection experiments (figure 3). A 1000-fold improvement over current direct-detection limits [4], [5] does not significantly constrain allowed spin-dependent cross sections; thus, neutrino telescopes will continue to observe a complementary portion of MSSM parameter space over the next several years. IceCube is currently operating with 59 strings and will contain 86 strings when complete in 2011. The DeepCore extension to IceCube [35], six strings with tighter string spacing (72 m), tighter optical module spacing (7 m), and higher PMT quantum efficiency, will be complete in 2010. DeepCore will significantly enhance the sensitivity of IceCube to low energy muons, extending the reach of IceCube to lower neutralino masses.

References

[1] M. Drees and M. M. Nojiri, Phys. Rev. D **47**, 376 (1993).
[2] C. Amsler *et al.*, Phys. Lett. B **667**, 1 (2008).
[3] R. C. Gilmore, Phys. Rev. D **76**, 043520 (2007).
[4] Z. Ahmed *et al.*, Phys. Rev. Lett. **102**, 011301 (2009).
[5] J. Angle *et al.*, Phys. Rev. Lett. **100**, 021303 (2008).
[6] A. Achterberg *et al.*, Astropart. Phys. **26**, 129 (2006).
[7] R. Abbasi *et al.*, arXiv:0902.2460.
[8] M. M. Boliev *et al.*, Nucl. Phys. Proc. Suppl. **48**, 83 (1996).
[9] M. Ambrosio *et al.*, Phys. Rev. D **60**, 082002 (1999).
[10] S. Desai *et al.*, Phys. Rev. D **70**, 083523 (2004).
[11] M. Ackermann *et al.*, Astropart. Phys. **26**, 155 (2006).
[12] J. Chang *et al.*, Nature **456**, 362 (2008).
[13] S. Torii *et al.*, arXiv:0809.0760 (2008).
[14] A. A. Abdo *et al.*, Phys. Rev. Lett. **102**, 181101 (2009).
[15] F. Aharonian *et al.*, arXiv:0905.0105.
[16] O. Adriani *et al.*, Nature **458**, 607 (2009).
[17] L. Bergström, J. Edsjö, and G. Zaharijas, arXiv:0905.0333 (2009).
[18] M. Ackermann *et al.*, J. Geophys. Res. **111**, D13203 (2006).
[19] J. Ahrens *et al.*, Astropart. Phys. **20**, 507 (2004).
[20] R. Abbasi *et al.*, Phys. Rev. D **79**, 062001 (2009).
[21] J. Braun, PhD Thesis, University of Wisconsin (2009).
[22] D. Hubert, PhD Thesis, Vrije Universiteit Brussel (2009).
[23] J. Ahrens *et al.*, Nucl. Inst. Meth. A **524**, 169 (2004).
[24] T. Neunhöffer, Astropart. Phys. **25**, 220 (2006).
[25] J. Braun *et al.*, Astropart. Phys. **29**, 299 (2008).
[26] G.J. Feldman and R.D. Cousins, Phys. Rev. D **57**, 3873 (1998).
[27] P. Gondolo *et al.*, JCAP **0407**, 008 (2004).
[28] A. Gazizov and M. Kowalski, Comput. Phys. Commun. **172**, 203 (2005).
[29] D. Chirkin and W. Rhode, arXiv:hep-ph/0407075 (2004).
[30] L. Bergström, J. Edsjö, and P. Gondolo, Phys. Rev. D **58**, 103519 (1998).
[31] D. Heck *et al.*, FZK, Tech. Rep. FZKA 6019 (1998).
[32] J. Conrad *et al.*, Phys. Rev. D **67**, 012002 (2003).
[33] G.C. Hill, Phys. Rev. D **67**, 118101 (2003).
[34] G. Wikström and J. Edsjö, JCAP **04**, 009 (2009).
[35] D. Cowen *et al.*, in *Proc. of NEUTEL09*, Venice, (2009).
[36] H. S. Lee *et al.*, Phys. Rev. Lett. **99**, 091301 (2007).
[37] E. Behnke *et al.*, Science **319**, 933 (2008).

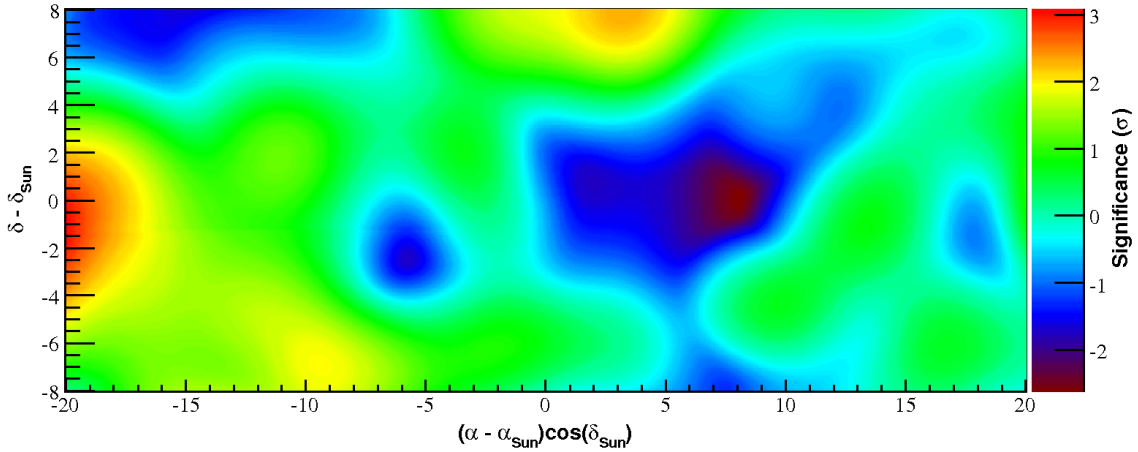

Fig. 2. Sun-centered skymap of event excesses from the 2000–2006 analysis.

$m_\chi(GeV)$	Channel	$V_{eff}(m^3)$	μ_{90}	$\Gamma_A(s^{-1})$	$\Phi_\mu(km^{-2}y^{-1})$	$\sigma^{SI}(cm^2)$	$\sigma^{SD}(cm^2)$
50	$\tau^+\tau^-$	4.31×10^3	6.2	2.11×10^{25}	1.21×10^5	1.84×10^{-40}	4.80×10^{-38}
	$b\bar{b}$	8.62×10^2	8.4	1.32×10^{27}	1.32×10^6	1.15×10^{-38}	3.01×10^{-36}
100	W^+W^-	2.87×10^4	4.5	1.88×10^{23}	6.75×10^3	3.40×10^{-42}	1.52×10^{-39}
	$b\bar{b}$	8.65×10^3	4.5	1.42×10^{25}	4.94×10^4	2.56×10^{-40}	1.14×10^{-37}
200	W^+W^-	3.42×10^5	4.0	9.81×10^{21}	1.09×10^3	4.23×10^{-43}	2.98×10^{-40}
	$b\bar{b}$	9.80×10^3	4.5	1.29×10^{24}	1.13×10^4	5.56×10^{-41}	3.92×10^{-38}
500	W^+W^-	1.31×10^6	3.7	2.07×10^{21}	5.39×10^2	3.51×10^{-43}	3.81×10^{-40}
	$b\bar{b}$	8.87×10^4	4.0	8.52×10^{22}	2.12×10^3	1.45×10^{-41}	1.57×10^{-38}
1000	W^+W^-	2.18×10^6	3.6	1.39×10^{21}	4.18×10^2	7.82×10^{-43}	1.01×10^{-39}
	$b\bar{b}$	2.14×10^5	4.0	2.89×10^{22}	1.26×10^3	1.63×10^{-41}	2.10×10^{-38}
2000	W^+W^-	2.38×10^6	3.6	1.56×10^{21}	3.90×10^2	3.19×10^{-42}	4.52×10^{-39}
	$b\bar{b}$	3.53×10^5	3.9	1.46×10^{22}	9.10×10^2	2.98×10^{-41}	4.23×10^{-38}
5000	W^+W^-	2.07×10^6	3.6	2.20×10^{21}	3.94×10^2	2.66×10^{-41}	3.97×10^{-38}
	$b\bar{b}$	4.59×10^5	3.7	8.91×10^{21}	7.17×10^2	1.08×10^{-40}	1.61×10^{-37}

TABLE I

EFFECTIVE VOLUME, EVENT UPPER LIMIT, AND PRELIMINARY LIMITS ON NEUTRALINO ANNIHILATION RATE IN THE SUN, NEUTRINO-INDUCED MUON FLUX FROM THE SUN, AND SPIN-INDEPENDENT AND SPIN-DEPENDENT NEUTRALINO-PROTON CROSS SECTION FOR A RANGE OF NEUTRALINO MASSES, INCLUDING SYSTEMATICS.

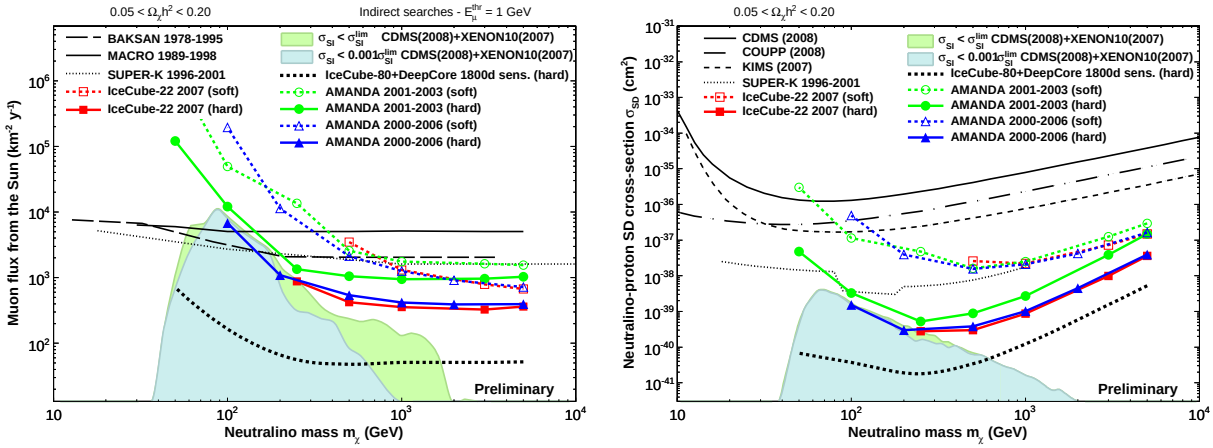

Fig. 3. Preliminary limits on neutrino-induced muon flux from the Sun (left) along with limits from IceCube [7], BAKSAN [8], MACRO [9], and Super-K [10], and limits on spin-dependent neutralino-proton cross section (right) along with limits from CDMS [4], IceCube [7], Super-K [10], KIMS [36], and COUPP [37]. The green shaded area represents models from a scan of MSSM parameter space not excluded by the spin-independent cross section limits of CDMS [4] and XENON [5], and the blue shaded area represents allowed models if spin-independent limits are tightened by a factor of 1000. The projected sensitivity of 10 years operation of IceCube with DeepCore is shown in both figures.

The extremely high energy neutrino search with IceCube

Keiichi Mase*, Aya Ishihara* and Shigeru Yoshida* for the IceCube Collaboration†

**The department of Physics, Chiba University, Yayoi-tyo 1-33, Inage-ku, Chiba city, Chiba 263-8522, Japan*
†*See the special section of these proceedings*

***Abstract*. A search for extremely high energy (EHE) cosmogenic neutrinos has been performed with IceCube. An understanding of high-energy atmospheric muon backgrounds that have a large uncertainty is the key for this search. We constructed an empirical high-energy background model. Extensive comparisons of the empirical model with the observational data in the background dominated region were performed, and the empirical model describes the observed atmospheric muon backgrounds properly. We report the results based on the data collected in 2007 with the 22 string configuration of IceCube. Since no event was found after the search for the EHE neutrinos, a preliminary upper limit on an E^{-2} flux of $E^2\phi_{\nu_e+\nu_\mu+\nu_\tau} \leq 5.6 \times 10^{-7}$ GeV cm^{-2} s^{-1} sr^{-1} (90% C.L.) is placed in the energy range $10^{7.5} < E_\nu < 10^{10.6}$ GeV.**

***Keywords*: neutrinos, IceCube, extremely high energy**

I. Introduction

Extremely high energy cosmic-rays (EHECRs) with energies above 10^{11} GeV are observed by several experiments. Although there is an indication that EHECRs are associated with the matter profile of the universe [1], their origin is still unknown. The detection of cosmogenic EHE neutrino signals with energies greater than 10^7 GeV can shed light on their origin. The cosmogenic neutrinos [2] produced by the GZK mechanism [3] carry information on the EHECR source evolution and the maximum energy of EHECRs at their production site [4]. Thus, EHE neutrinos can provide fundamental information about how and where the EHECRs are produced.

The detection of EHE neutrinos has been an experimental challenge because the very small intensities of expected EHE neutrino fluxes require a huge effective detection volume. The IceCube neutrino observatory, currently under construction at the geographic South Pole, provides a rare opportunity to overcome this difficulty with a large instrumental volume of 1 km^3.

The backgrounds for the EHE neutrino signals are atmospheric muons. The large amount of atmospheric muons come vertically, while the signal comes primarily from zenith angles close to the horizon, reflecting competitive processes of generation of energetic secondary leptons reachable to a detector and absorption of neutrinos due to an increase of the cross-sections. The atmospheric muon backgrounds drop off rapidly with increasing energy. Therefore, a possible EHE neutrino flux will exceed the background in the EHE region ($\gtrsim 10^8$ GeV). The signal is separated from the backgrounds by using angle and energy information.

II. The EHE events and the IceCube detector

At extremely high energies, neutrinos are mainly detected via secondary muons and taus induced during the propagation of EHE neutrinos in the earth [5]. These particles are seen in the detector as a series of energetic cascades from radiative energy loss processes such as pair creation, bremsstrahlung and photonuclear interactions rather than as minimum ionizing particles. These radiative energy losses are approximately proportional to the energies of the muon and tau, making it possible to estimate its energy by observing the energy deposit in the detector.

The Cherenkov light from the particles generated through the radiative processes are observed by an array of Digital Optical Modules (DOMs) which digitize the charges amplified by the enclosed 10" Hamamatsu photomultiplier tubes (PMTs) with a gain of $\sim 10^7$. The total number of photo-electrons (NPE) detected by all DOMs is used to estimate the energy of particles in this analysis. It is found that NPE is a robust parameter for estimating the particle energy.

The data used in this analysis were taken with the 22 string configuration of IceCube (IC22). Each string consists of 60 DOMs and 1320 DOMs in total with 22 strings. The data taking began May, 2007, and continued to April, 2008. This analysis used a specific filtered data to select high energy events, which requires a minimum number of 80 triggered DOMs. The total livetime is 242.1 days after removing data taken with unstable operation. The event rate at this stage is $\sim$1.5 Hz with a 16% yearly variation. Then, 6516 events with NPE greater than 10^4 (corresponding to CR primary energy of about 10^7 GeV and neutrino energy of about 10^6 GeV (with E^{-2} flux)) are selected and used for the further analysis.

III. Background modeling

A. Construction of the empirical model

Bundles of muons produced in CR air showers are the major background for the EHE signal search. Multiple muon tracks with a small geometrical separation resemble a single high energy muon for the IceCube detector. An understanding of the high energy atmospheric muon backgrounds is essential for the EHE signal search.

However, the backgrounds at the relevant energy range ($> 10^7$ GeV) is highly uncertain because of the poorly characterized hadronic interactions and composition of the primary CR where no direct measurement is available.

Therefore, we constructed an empirical model based on the Elbert model [6], optimizing the model to match the observational data reasonably in the background dominant energy region ($10^4 <$ NPE $< 10^5$). The model is then extrapolated to higher energies to estimate the background in the EHE signal region. (See Fig. 1)

The original Elbert model gives a number of muons for a CR primary energy E_0 such as

$$N_\mu = \frac{E_T}{E_0}\frac{A^2}{\cos\theta'}\left(\frac{AE^\mu}{E_0}\right)^{-\alpha}\left(1-\frac{AE^\mu}{E_0}\right)^{\beta}, \quad (1)$$

where A is the mass number of primary CRs with energy of E_0, and θ' is the zenith angle of a muon bundle. α, β and E_T are empirical parameters. The energy weighted integration of the formula relates the total energy carried by a muon bundle ${E_\mu}^{B,surf}$ to the primary CR energy E_0 as,

$$\begin{aligned} {E_\mu}^{B,surf} &\equiv \int_{E_{th}^{surf}}^{E_0/A}\frac{dN_\mu}{dE_\mu}E_\mu dE_\mu \\ &\simeq E_T\frac{A}{\cos\theta'}\frac{\alpha}{\alpha-1}\left(\frac{AE_{th}^{surf}}{E_0}\right)^{-\alpha+1} \quad (2) \end{aligned}$$

where E_{th}^{surf} is a threshold energy of muons contributing to a bundle at surface and depends on the zenith angle. A surface threshold is related to a threshold energy at the IceCube depth E_{th}^{in-ice}, by assuming a proportional energy loss to the bundle energy during propagation. This threshold at the IceCube depth is independent of zenith angle.

With help of a Monte-Carlo (MC) simulation for the detector response as well as the measured CR flux, it is possible to predict the NPE distribution for certain α and E_{th}^{in-ice} parameters. The CR flux used in this analysis is taken from the compilation of several experimental observations in Ref. [7]. The detector response including the Cherenkov photon emission, the propagation in the detector volume and the PMT/DOM response is simulated with the IceCube simulation program. The α and E_{th}^{in-ice} parameters are, then, optimized to express the observed NPE distributions. The best optimized parameters are derived as $\alpha = 1.97$ and $E_{th}^{in-ice} = 1500$ GeV.

With this empirical model, a simple simulation is feasible rather than simulating all muon tracks in a bundle, where the multiplicity can reach ten thousand for CR primary energies of 10^{11} GeV. Therefore, a bundle is replaced by a single track with the same energy as the entire bundle. It is shown in the next section that this substitution works well to express the observational data.

Data generated with CORSIKA [8] (with the SIBYLL high energy hadronic interaction model) are also used. However, the extensive resources required for MC generation precludes production of MC data with energy above 10^{10} GeV. Therefore, the CORSIKA data are mainly used to confirm the empirical model in the background dominant energy region and provide redundant tools to study systematic uncertainty on the background estimation.

The relation between CR primary energy and the NPE (which is the empirical model itself) is independently verified by using information from coincident events with the in-ice and surface detectors. The surface detectors can estimate the CR primary energy and the in-ice detectors give NPE. The relation is found to be consistent with the empirical model we derived.

B. Comparison between observational data and MC

An extensive comparison between the empirical model and the observational data was performed. The empirical model is found to describe the observational data reasonably in most cases. However, a significant difference was found in the z position (depth) of the center of gravity of the event (CoGZ) distribution. Many events are found in the deep part of the detector for the empirical model, while the events concentrate more at the top for the observational data. The difference is only seen for the vertical muons. This is probably due to the simple single muon substitution for the muon bundles in the empirical model. The more energetic single muons penetrate into the deep part, while many low energy muons in the bundles lose energies at the top of the detector for the vertical case. However, for the inclined cases, the bundles are already attenuated before coming to the detector, giving reasonable agreement between the observational data and the empirical model. Therefore, vertical events whose reconstructed zenith angles are less than 37° are not used in this analysis. A simple algorithm is used for the angle reconstruction, based on the time sequence of the first pulses recorded by DOMs.

Several distributions for the observational data and MC data after removing the vertical events are shown in Fig. 1 as well as the expected GZK cosmogenic neutrino signal [4]. As seen in the figure, the empirical model describes the observational data reasonably. The observed CoGZ distribution is also well represented by the empirical model after removing vertical events. The observed data are bracketed by the pure CORSIKA (SIBYLL) proton and iron simulation as expected.

Some up-going events are seen in the observational data, though this is consistent with the empirical background model. It is found that they are horizontally misreconstructed. On the other hand, fewer horizontal events are found for the CORSIKA data sets. This is because the CORSIKA data exhibit a better angular resolution of 1.4° (one sigma) compared to the empirical model of 2.5°. The angular resolution for the observational data is estimated with help of the IceTop geometrical reconstruction. The estimated resolution is 2.5° and consistent with the one of the empirical model. Another difference

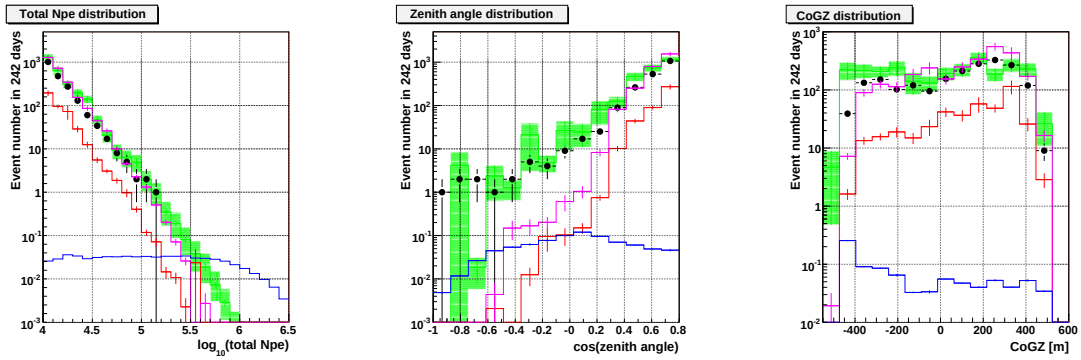

Fig. 1. The total NPE, zenith angle and CoGZ distributions between observational and MC data. The black dots represents observational data, green lines for empirical model (The shade expresses the uncertainty of the model), red for proton (CORSIKA, SIBYLL) and magenta for iron (CORSIKA, SIBYLL). The expected signal from GZK neutrinos[4] is also plotted with blue lines.

between the observational data and the CORSIKA data is found in the CoGZ distribution. The CORSIKA data concentrate more at the top of the detector especially for vertical events. The CORSIKA data also show a narrower distribution in the relation of CR primary energy and the NPE. All these facts seem to indicate that the bundles in CORSIKA consist of more lower energy muon tracks compared to the observational data, leading to bundles with less stochastic energy losses. In order to confirm this hypothesis, more specific investigation is needed.

The GZK signal events populate the EHE region and tend to be horizontal, as described in a previous section. This allows one to discriminate them from the background. The signal is also concentrated in the deep part of the detector because of the more transparent ice there.

IV. Search for EHE neutrino signal

Using the empirical background model, the EHE signal search was performed based on the NPE and zenith angle information. The selection criteria are determined by using only MC data sets that are optimized with the observational data in the background dominated energy region ($10^4 \leq$ NPE $\leq 10^5$), following a blind analysis procedure.

It is found that the large spread of mis-reconstructed events extended to the signal region. We found that the angular resolution is related to the CoGZ position. Events whose CoGZs are at the bottom of the detector (CoGZ < -250 m) and which pass through the edge or outside of the bottom detector are significantly mis-reconstructed horizontal. When an inclined track reaches at the edge of the bottom part of the detector, there is no more detector below, so that the hit timing pattern resembles a horizontal track. The very clean ice at the bottom part of the detector and the biggest dust layer at middle enhance this effect. Therefore, the data sample is divided into two by the CoGZ position as follows.

region A: $-250 <$ CoGZ < -50 m, and CoGZ > 50 m
region B: CoGZ < -250 m, and $-50 <$ CoGZ < 50 m

A clear difference between the backgrounds and the signal is seen in the zenith angle and total NPE relations as shown in Fig. 2. The atmospheric background muon distribution shows a steep fall in NPE and peaks in the vertical direction, while the GZK signal is mainly horizontal and at higher NPE, allowing the discrimination of the backgrounds by rejecting low NPE events and vertically reconstructed events. It is also obvious that the large spread in zenith angle direction for region B due to mis-reconstructed events.

The selection criteria to separate signal from background are determined for region A and B separately. The criteria are determined at first for each zenith angle bins, requiring the background level to be negligible compared to the signal (10^{-4} events per 0.1 cos(zenith angle) bin per 242.1 days). After the optimization for each zenith angle bin, the determined cut-offs in NPE are connected with contiguous lines as shown in Fig. 2.

The expected numbers of signal and background events with the selection criteria are summarized in Table I.

TABLE I
Expected event number

Models	Expected events in 242.1 days
GZK1 [4]	0.16 $\pm$ 0.00 (stat.) $^{+0.03}_{-0.05}$ (sys.)
Atm. muon	(6.3 $\pm$ 1.4 (stat.) $^{+6.4}_{-3.9}$ (sys.)) $\times 10^{-4}$

The effective area for each neutrino flavor averaged over all solid angles with the selection criteria is shown in Fig. 3.

V. Results

The EHE neutrinos are searched for by applying the selection criteria determined in the previous section to the 242.1 days of observed data taken in 2007.

Since no event is found after the search, a 90 % C.L. upper limit for all neutrino flavors (assuming full mixing neutrino oscillations) is placed with the quasi-differential method based on the flux per energy decade ($\Delta \log_{10} E = 1.0$) described in Ref. [9]. A 90 % C.L. preliminary upper limit for an E^{-2} spectrum is also derived as $E^2 \phi_{\nu_e+\nu_\mu+\nu_\tau} \leq 5.6 \times 10^{-7}$ GeV cm^{-2} s^{-1}

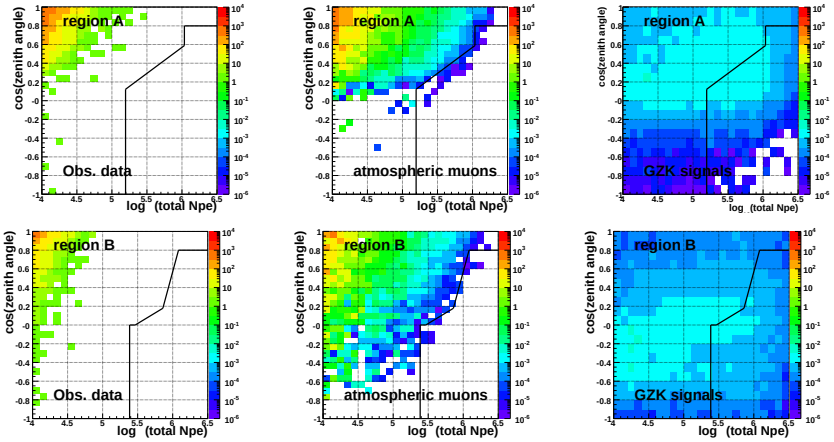

Fig. 2. The zenith angle Vs total NPE. The top plots are for region A and the bottom ones for region B. The plots are for the observational data, the background from the empirical model and the GZK signal[4] from left.

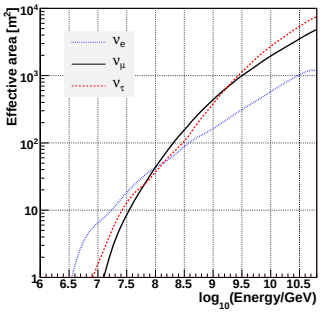

Fig. 3. The effective area for each flavor neutrino after applying the signal selection criteria averaged over all solid angles. Blue dotted line represents ν_e, black solid line for ν_μ and red dashed line for ν_τ.

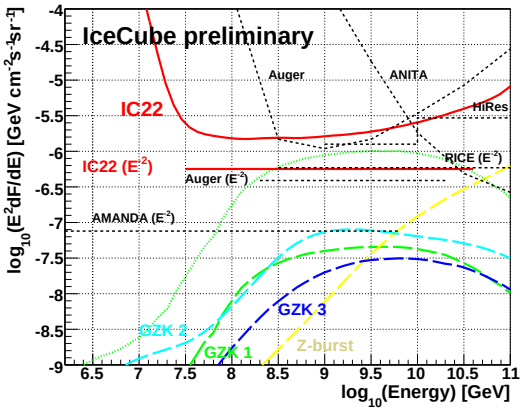

Fig. 4. The preliminary upper limit by the IC-22 EHE analysis (red solid) (all flavor) with the systematics taken into account. The thick long dashed green line represents GZK model 1 [4], light blue is for GZK model 2 [10], blue line is for GZK model 3 [17] and yellow for Z-burst model [11]. The dotted green line is 90 % C.L. upper limit for GZK model 1 by this analysis. The upper limit by other experiments are also shown with dashed lines [12], [13], [14], [15], [16]. Limits from other experiments are converted to all flavors where necessary assuming full mixing neutrino oscillations.

sr^{-1}, where 90 % of the events are in the energy range of $10^{7.5} < E_\nu < 10^{10.6}$ GeV, taking the systematics into account. These preliminary limits as well as results of several model tests are shown in Fig. 4. The derived limit is comparable to the Auger [13] and HiRes [16] limit. The AMANDA limit [12] for an E^{-2} flux is better than the limit by this analysis. This is because AMANDA has a better sensitivity for lower energy and the livetime is about twice as much as this analysis.

The systematics such as detector sensitivity, neutrino cross-section, hadronic interaction model, yearly variation are currently being investigated. The biggest uncertainty comes from the NPE difference observed by the absolutely calibrated light source in situ, and it is estimated to be on the order of 30 %. These systematics are included in the upper limit calculation. The details of the systematics estimation as well as more detail of this analysis will be presented in another paper in preparation.

ACKNOWLEDGEMENTS

We acknowledge the U. S. National Science Foundation, and all the agencies to support the IceCube project. This analysis work is particularly supported by the Japan Society for the Promotion of Science.

REFERENCES

[1] The Pierre Auger Collaboration, Science **318**, 896 (2007).
[2] V. S. Beresinsky and G. T. Zatsepin, Phys. Lett. **28B**, 423 (1969).
[3] K. Greisen, Phys. Rev. Lett. **16**, 748 (1966); G. T. Zatsepin and V. A. Kuzmin, Pisma Zh. Eksp. Teor. Fiz. **4**, 114 (1966) [JETP. Lett. **4**, 78 (1966)].
[4] S. Yoshida and M. Teshima, Prog. Theor. Phys. **89**, 833 (1993).
[5] S. Yoshida *et al.* , Phys. Rev. D **69**, 103004 (2004).
[6] T. K. Gaisser, *Cosmic Rays and Particle Physics* (Cambridge University Press, Cambridge, England, 1990) p206.
[7] M. Nagano and A. A. Watson, Rev. Mod. Phys. **72**, 689 (2000).
[8] D. Heck *et al.* , Report FZKA 6019, (Forschungszentrum Karlsruhe 1998).
[9] X. Bertou *et al.* , Astropart. Phys., **17**, 183 (2002).
[10] O. E. Kalashev, V. A. Kuzmin, D. V. Semkoz, and G. Sigl, Phys. Rev. D **66** 063004 (2002).
[11] S. Yoshida, G. Sigl and S. Lee, Phys. Rev. Lett. **81**, 5505 (1998).
[12] Andrea Silvestri (IceCube), Proc. 31st ICRC (2009).
[13] J. Abraham *et al.* (Auger), Phys. Rev. Lett. **100**, 21101 (2008).
[14] P. W. Gohram *et al.* (ANITA), arXiv:0812.2715v1 (2008).
[15] I. Kravchenko *et al.* (RICE), Phys. Rev. D **73**, 082002 (2006).
[16] R. U. Abbasi *et al.* (HiRes), ApJ **684**, 790 (2008).
[17] R. Engel *et al.* , Phys. Rev. D **64**, 093010 (2001)

Study of very bright cosmic-ray induced muon bundle signatures measured by the IceCube detector

Aya Ishihara* **for the IceCube Collaboration**†
*Department of Physics, Chiba University, Chiba 263-8522, Japan
† See the special section of these proceedings.

***Abstract*. We present the study of cosmic-ray induced atmospheric muon signatures measured by the underground IceCube array, some of which coincide with signals in the IceTop surface detector array. In this study, cosmic-ray primary energies are associated with the total number of photoelectrons (NPEs) measured by the underground IceCube optical sensors with two methods. We found that multiple muons that produce $10^4 \sim 10^5$ NPEs in the IceCube detector in 2008 is corresponding to the cosmic-ray primary energies of $10^7 \sim 10^9$ GeV.**

This association allows us to study cosmic-ray physics using photon distributions observed by the underground detector that are characterized by the properties of muon bundles. It is observed that the detailed NPE space distributions in longitudinal and lateral directions from muon tracks display the ranging-out effect of low energy muons in each muon bundle. The distributions from 2008 high energy muon data samples taken with the IceCube detector are compared with two different Monte Carlo simulations. The first is an extreme case that assumes a single high energy muon in which nearly all of the energy loss is due to stochastic processes in the ice. The other uses the CORSIKA program with SYBILL and QGSJET-II high energy hadron interaction models, in which approximately half of the energy loss is due to ionization of low energy muons.

***Keywords*: IceCube, muon-bundle, high-energy**

I. Introduction

Bundles of muons produced in the forward region of cosmic-ray air showers appear as bright signals in Cherenkov detectors. The multiple-muon tracks with a small geometrical separation (called 'muon-bundles') resemble a muon with a higher energy. Understanding of the background muon bundles using a full air shower MC simulation in the high energy range above 10^7 GeV is limited because the calculation involves poorly characterized hadronic interactions and a knowledge on the primary cosmic ray composition at energies where there is no direct measurement available. The experimental measurement of atmospheric muons provides an independent probe of the hadronic interactions and the primary cosmic-ray compositions.

The IceCube neutrino observatory [1] provides a rare opportunity to access the primary cosmic-ray energies beyond accelerator physics. The IceCube detector located at the geographic South Pole consists of an array of photon detectors which contains a km^3 fiducial volume of clean glacier ice as a Cherenkov radiator. Half of the final IceCube detector (IC40) was deployed by the end of austral summer of 2008. The IC40 detector consists of 40 strings of cable assemblies with an intra-string spacing of 125 m. Each string has 60 optical sensors (DOMs) spacing at intervals of ∼17 m and stretching between depths of ∼1450 m and ∼2450 m in the glacial ice. DOMs are also frozen into tanks located on the surface near the top of each string. The ice-filled tanks constitute an air shower array called IceTop [2]. IceTop can act as an independent air-shower array to measure cosmic-ray spectra as well as trigger simultaneously with the underground detector. This provides a reliable method to study the atmospheric muon bundles.

The data taking with the IC40 detector configuration was performed from April, 2008 through March, 2009. The high energy muon-bundle (HEMu) sample consists of events which measure between 6.3×10^2 and 6.3×10^4 photo-electrons (PEs) in at least 50 underground DOMs. An IceTop coincidence (HECoinc) sample is a subset of the HEMu sample with the additional requirement that IceTop can successfully reconstruct the air shower event. Similarly, samples (called VHEMu and VHECoinc) with higher NPE threshold of 7.0×10^3 are studied. Definitions of samples are summarized in Table I.

Data studied in this paper is taken in the period of July to December 2008 with a livetime of 148.8 days. Event distributions of the samples are presented in Fig. 1.

TABLE I
DEFINITIONS OF SAMPLE CONDITIONS.

	threshold NPE value	IceTop coincidence required
HEMu	6.3×10^2	no
HECoinc	6.3×10^2	yes
VHEMu	7.0×10^3	no
VHECoinc	7.0×10^3	yes

II. Cosmic-ray energy and underground brightness relation

Because the energy losses of muon-bundles are indicators of their energies and multiplicities, measurements of the total energy deposit of muons (E_{loss}) in the detection volume is important for understanding of the nature of muon-bundles. Here, we use the total number of photoelectrons recorded by the all underground DOMs (NPE) as an indicator of E_{loss}. The effective light deposit from

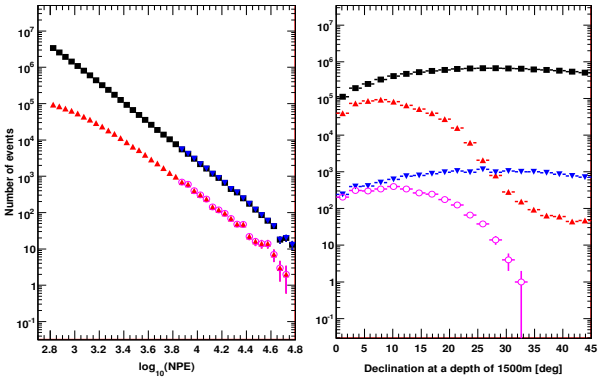

Fig. 1. Atmospheric muon event distributions from 2008 sample as a function of NPE (left) and reconstructed zenith angle θ (right). Filled square denotes HEMu and triangles are HECoinc. Inverse triangles and open circles are that of VHE samples as defined in table I. Coincidence samples show a high detection efficiency for vertical events and the efficiency drops with zenith angles. Event rates decreased by ≈ 2.5 orders of magnitude when NPE is increased by an order of magnitude.

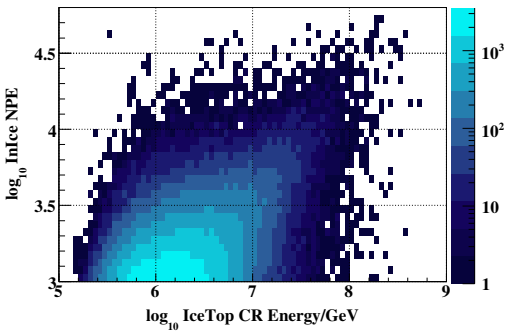

Fig. 2. Event distributions of HECoinc sample as a function of NPE and IceTop reconstructed primary cosmic-ray energies. A clear correlation is observed.

bundles can be parameterized with an effective track length l_0 as [3], [4],

$$\mathrm{NPE} \sim l_0(\eta N_\mu + \xi \Sigma E_\mu) \quad \propto \quad \mathrm{E_{loss}}. \qquad (1)$$

Here, N_μ and ΣE_μ indicate multiplicities and energy sum of underground muons respectively. η and ξ are ionization and radiative energy loss coefficients assumed to be constant with energy. Primary cosmic-ray energies are related to the NPE with two methods. The first method is to directly relate the underground NPEs with IceTop cosmic-ray energy reconstruction results. The other is to construct an empirical model to characterize the event frequencies of underground NPEs from the experimentally measured cosmic-ray surface fluxes [5]. The former method has the advantage that both cosmic-ray energy and underground brightness are consistently measured quantities, while the directional acceptance is limited to near vertical. The latter method requires a model assumption in the underground bundle spectra shape but full angular acceptance is available.

A. IceTop coincidence signals

Figure 2 shows the measured underground NPE distribution as a function of cosmic-ray energies reconstructed by the IceTop air-shower array. The energy determination method by the IceTop array is described in [6]. A clear correlation exhibits that bright underground events are associated with the high energy cosmic-ray induced air showers and each NPE region roughly corresponds to different cosmic-ray energy regimes. For example, it shows that the cosmic-ray primary energy of $\sim 3.0\times10^7$ GeV are associated with 10^4 NPE underground events. As shown in Fig. 1, because of the IceTop coincidence condition, most of events in this sample is near vertical.

B. The empirical model

A high energy muon empirical model is constructed as in [7]. In the model construction, the amount of energy that goes to muon-bundle from cosmic-ray primaries is expressed in terms of energy weighed integral of the Elbert formula [8]. Because a major part of NPEs from muon tracks is expected to be due to the radiative processes in the very bright events, it is assumed in the model that the NPEs from the ionization is negligible compared to the stochastic energy losses, *i.e.* $N_\mu = 1$ in Eq. 1. We then fit experimental data with this model by varying ΣE_μ in Eq. 1 until it reproduces the experimentally observed NPE event rates. The total energy in the bundle ΣE_μ is carried by a single muon and the muon is simulated with [9]. The model is constructed based on the data sample taken in 2007. The present sample from 2008 under study separately confirms the agreement as shown in Fig. 3 above the NPE threshold of 7.0×10^3. Below the threshold value, the model assumption that nearly all energy losses are due to radiative processes is expected to fail. The relation between the true cosmic-ray energy and NPE is shown in Fig. 4. The relation shows reasonable agreement with the experimentally measured relation shown in Fig. 2 in the overlapped acceptance region. An extrapolation of the relation indicates that corresponding primary cosmic-ray energy is increased to 10^9 GeV for the muon bundle signals with 10^5 underground NPE.

III. Energy Losses of Muons in Bundles

A. Muon spectra in bundles

Average muon spectra in a bundle for different total NPE range from CORSIKA MC simulation using SYBILL and QGSJET-II as high energy interaction models with iron primaries and corresponding single muon energy distribution from the empirical model are shown in Fig 5. The plot shows that the number of muons reaching the IceCube depth from CORSIKA simulations increase with their total NPE. While there is a large difference between the muon bundle spectra from the CORSIKA full air-shower simulations and the high energy single muon empirical model, both describe the NPE event rates with a reasonable agreement (Fig 3). There is no significant difference in muon spectra from

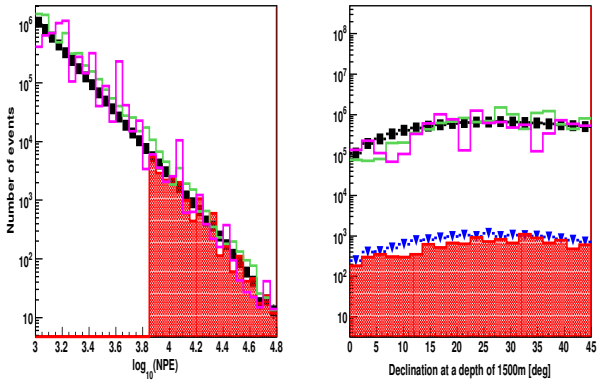

Fig. 3. Event distributions as a function of NPE (left) and reconstructed zenith angle θ (right). Squares and inverse triangles denote 2008 high energy event sample as in Fig. 1. Filled histograms are from the Monte Carlo simulation of the high energy muon empirical model as described in the text. Dark and light colored histograms are from CORSIKA MC simulation using SYBILL and QGSJET-II as high energy interaction models with iron primaries respectively. Event distributions from proton primaries highly underestimate the event rates. It can be seen that all of three MC simulation gives a reasonable agreement with experimental observation.

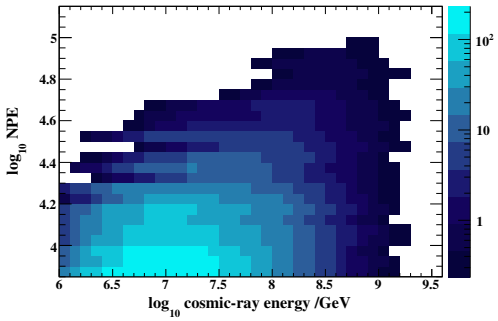

Fig. 4. The correlation between primary cosmic-ray energy to underground NPE from MC simulation with the high energy muon empirical model. A consistent relation obtained with IceTop/underground coincidence measurement is obtained.

SYBILL and QGSJET-II high energy interaction models with iron primary below 4.0×10^4 NPE, but they exhibits some difference for the brighter events which approximately corresponds to the primary cosmic ray energies above $\sim 10^8$ GeV.

The fact that the event rates as a function of the total NPE appear consistent among the three estimations with different muon bundle models indicates that the NPEs of an event insensitive to the energy spectra of muon bundles. It implies that to distinguish whether the observed photon emission is dominated by either the first or the second term in Eq. 1 is difficult with the total NPE. This indicates that the NPE measure is a systematically robust variable when used in analysis as in [7]. On the other hand, to evaluate muon bundle structure in each event, this variable is not sufficient. The nature of muon bundles, such as the muon spectra

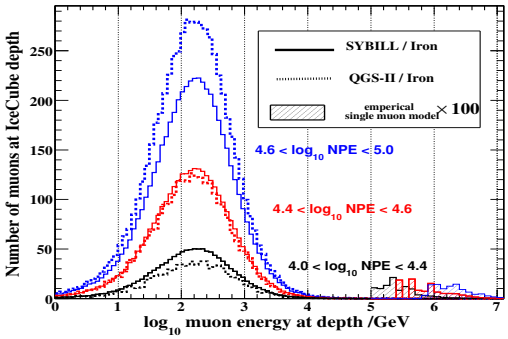

Fig. 5. Average muon MC-truth energy spectra in a bundle in different NPE range are shown for SYBILL, QGSJET-II with iron primaries and the empirical single muon model which is multiplied by 100 for a better visibility. Each of solid and dashed lines represents different NPE regions which approximately correspond to different cosmic-ray primary energies as shown in Fig. 4. In the brightest events, both CORSIKA high-energy models predicts more than 5,000 muons in a bundle reaching the underground detector. The muon in the single muon empirical model has energies between 100 TeV and 10 PeV.

as in Fig. 5, is expected to appear in more detailed NPE distributions along the muon bundle tracks.

B. The lateral and longitudinal NPE distributions

The NPE distributions as functions of distances along and perpendicular to the track are shown in Fig. 6. In the plots, only vertically reconstructed events ($\theta \leq$ 15 degrees) are used. Vertical tracks are suitable for measurement of detailed longitudinal development of the energy losses because the DOM separation in the z direction is only 17 m compared to 125 m in x-y direction. The detected Cherenkov photon profile shows a good correlation with the depth dependence of the measured optical properties of glacier ice. Fig. 6a shows a typical 3-dimensional NPE distributions of an observed high energy muon-bundle track. The lower panels shows averaged NPE distributions in the 2D plane from vertical VHEMu events for 2008 data, SYBILL-iron and the empirical model. There are visible differences in the 2D light deposit distributions between data and models which give similar NPE. The detailed NPE distributions can be further examined as a function of longitudinal distances along tracks at various lateral distances as shown in the Fig. 7. Each solid line denotes different lateral distance with a 50 m interval and the distributions correspond to the slices along the longitudinal distances in the left panel of the Fig. 6b. It can be seen that the NPE observed by each DOM decreases rapidly with lateral distances. The closest longitudinal NPE distribution ($\leq$ 50 m) shows that at the upper IceCube detector $\sim$800 NPEs are observed in each DOM and gradually decreased to $\sim$300 NPEs at the bottom of detector. This is expected to be due to ranging-out of low energy muons in bundles as they travel through the detector. This clearly shows that the longitudinal NPE profiles close to the track is sensitive to the muon energy loss profile. The effect is less visible when photons

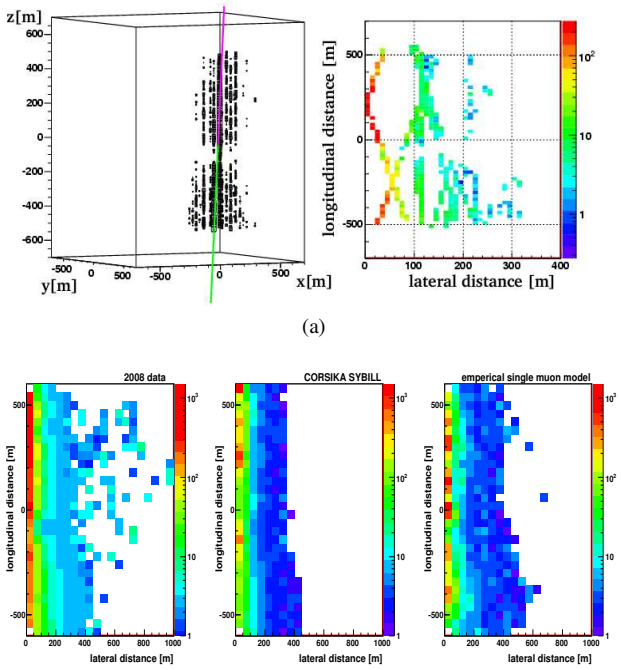

Fig. 6. The lateral and longitudinal NPE distributions from high energy muon-bundle events which produces very bright event signatures. (a) Left: A typical NPE space distributions of a bright event in 2008. The size of squares indicates log_{10} NPE. Solid line indicates the reconstructed direction. There is a loss of photons due to a dusty layer of ice positioning around z = -100 m. Right: The NPEs from each DOM are plotted as functions of distances perpendicular to and along the reconstructed track. Filled bins are the position where the DOMs exist in this lateral and longitudinal two dimensional space and z-axis indicates measured NPEs. When there is more than one DOMs in a bin, NPE averages are calculated. (b) An averaged lateral and longitudinal NPE distribution of vertical bright events. Left: Vertically reconstructed VHEMu sample. Middle: CORSIKA-SYBILL with iron primary. Right: the high energy single muon empirical model.

propagated more than 50 m from the track where the effects of ice properties begin to dominate. The effect of the ice layers with different scattering/absorption properties highly modifies the lateral NPE distributions in this case. The distributions of NPEs close to tracks are suitable to study muon-bundle properties and NPEs at distance reflects the nature of photon propagation through the ice.

IV. Outlook

The various parts of lateral and longitudinal profiles of the NPE distributions in 2-dimensional space are governed by the nature of muon bundles and optical properties of the ice in different way. Specifically, detailed study of the longitudinal NPE profiles at different lateral distances is important for a better understanding of both the muon-bundle and ice property modeling.

The contributions from ionization and radiative energy losses in the obtained lateral and longitudinal NPE distributions are not distinguishable so far. This is because longitudinal NPE profiles shown in Fig. 7 are obtained from multiple events and stochastic nature of energy losses are averaged out. However, a large

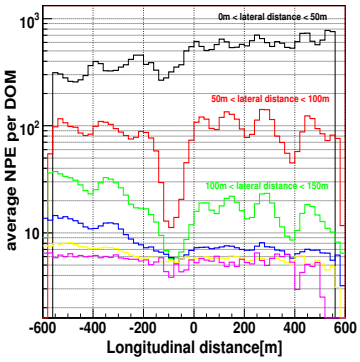

Fig. 7. Averaged longitudinal NPE distributions of the vertical VHEMu event sample. Each solid line denotes longitudinal NPE distributions at various lateral distances with an interval of 50 m. From the top line to the bottom, the intervals corresponding to each line are 0 m∼50 m, 50 m∼100 m, 100 m∼150 m, 150 m∼200 m, 200 m∼250 m and 250 m∼300 m respectively. A clear NPE developments in both longitudinal and lateral directions are visible.

difference between ionization and radiative energy losses is expected to appear in the event-by-event fluctuations of longitudinal/lateral NPE distributions. The sizes of fluctuations from stochastic energy losses are evaluated in [4] using the MMC program [10] and the fluctuations from ionization are expected to be $\propto \sqrt{N_\mu}$.

The deviations of NPE along track from an average NPE per DOM are contributed from variations of ice properties. Because the ice properties does not fluctuate an event-by-event basis, it is possible to distinguish the variation due to ice properties and the fluctuation due to stochastic energy losses. The variations in NPEs near the tracks where less affected from ice properties and also the event-by-event NPE fluctuation at given depth are expected to be sensitive parameters to the stochastic part of the muon bundle energy losses.

V. Acknowledgments

We acknowledge U.S. National Science Foundation, and all the agencies to support the IceCube project. This analysis work is particularly supported by the Japan Society for the Promotion of Science.

References

[1] J. Ahrens *et al.*, Astropart. Phys. **20** 507 (2004); http://icecube.wisc.edu/.
[2] T. Gaisser, in Proceedings of the 30th ICRC, Merida (2007).
[3] Ph.D. thesis, C.H. Wiebusch, Physikalische Institute, RWTH Aachen (1995)
[4] Ph.D. thesis, Predrag Miočinović, UC Berkeley (2001)
[5] M. Nagano and A. A. Watson, Rev. Mod. Phys. **72**, 689 (2000).
[6] F. Kislat, S. Klepser, H. Kolanoski and T. Waldenmaier for the IceCube collaboration, these proceedings
[7] K. Mase, A. Ishihara and S. Yoshida for the IceCube collaboration, these proceedings
[8] T. K. Gaisser, *Cosmic Rays and Particle Physics*, (Cambridge University Press, 1990).
[9] http://www.ppl.phys.chiba-u.jp/JULIeT/
[10] D. Chirkin and W. Rhode, arXiv:hep-ph/0407075

Search for High Energetic Neutrinos from Supernova Explosions with AMANDA

Dirk Lennarz* and Christopher Wiebusch* for the IceCube Collaboration†

**III. Physikalisches Institut, RWTH Aachen University, 52056 Aachen, Germany*
†*See the special section of these proceedings*

***Abstract*. Supernova explosions are among the most energetic phenomena in the known universe. There are suggestions that cosmic rays up to EeV energies might be accelerated in the young supernova shell on time scales of a few weeks to years, which would lead to TeV neutrino radiation. The data taken with the AMANDA neutrino telescope in the years 2000 to 2006 is analysed with a likelihood approach in order to search for directional and temporal coincidences between neutrino events and optically observed extra-galactic supernovae. The supernovae were stacked in order to enhance the sensitivity. A catalogue of relevant core-collapse supernovae has been created. This poster presents the results from the analysis.**

***Keywords*: AMANDA, high energy neutrino astronomy, supernova**

I. Introduction

Almost a hundred years after their discovery, the acceleration mechanisms and sources of the cosmic rays remain an unsolved problem of modern astronomy. Neutrino astronomy can be an important contribution to the solution of this problem. Young supernovae in connection with a pulsar have been proposed as a possible source of cosmic rays with energies up to the ankle. This *pulsar model* can be directly tested by measuring high energetic (TeV) neutrino radiation on time scales of a few weeks to years after the supernova [1][2].

The AMANDA-II neutrino telescope is located in the clear ice at the geographic South Pole and was fully operational since 2000. It reconstructs the direction of high energetic neutrinos by measuring Cherenkov light from secondary muons. The main background are muons and neutrinos produced in air showers in the atmosphere.

This analysis uses 7 years of AMANDA data taken during the years 2000-2006 with a total live-time of 1386 days. The data reconstruction and filtering is described in [3] and the final event sample contains 6595 events. The contamination of mis-reconstructed atmospheric muon events is less than 5% for a declination greater than 5°.

II. Pulsar Model

The liberation of rotational energy from a pulsar can accelerate particles to relativistic energies. Secondary particles, for example pions, are created in the interaction with the expanding supernova envelope and decay into neutrinos and other particles. In this analysis the pulsar model as described in [2] is used. Thermonuclear supernovae have no pulsar inside the envelope and are therefore not considered by this model.

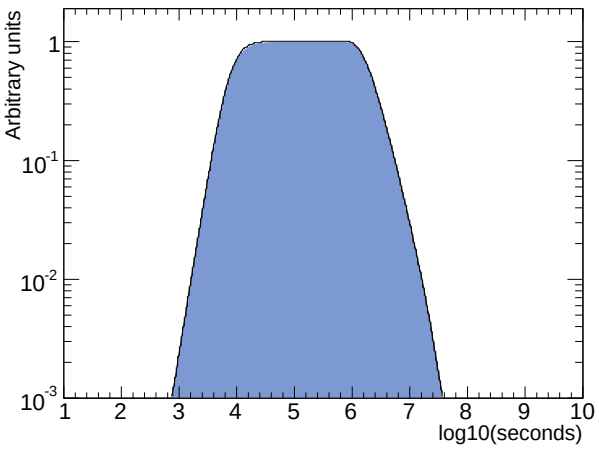

Fig. 1. Typical supernova neutrino model light curve

The phase of powerful, high energetic neutrino emission is limited by two characteristic times: the time at which the pion decay time becomes less than the time between two nuclear collisions (t_π) and the time at which the density of the envelope is sufficiently small for accelerated particles to escape into the interstellar space without interaction (t_c). The supernova neutrino luminosity as a function of time (*model light curve*) is given by:

$$L(t) = \left(1 - \exp\left(-\left(\frac{t_c}{t}\right)^2\right)\right) \cdot \frac{1}{1+(\frac{t_\pi}{t})^3} \cdot \lambda L_0 \left(1+\frac{t}{\tau}\right)^{-2}, \quad (1)$$

where λ is the fraction of the total magnetic dipole luminosity L_0 (in erg/s) that is transferred to accelerated particles and τ the characteristic pulsar braking time.

The shape and length of the model light curve depend on the supernova envelope mass ($\mathrm{M_e}$), uniformity (described by a parameter called ξ) and expansion velocity (V), the pulsar braking time and the maximum pion energy. An E^{-2} neutrino energy spectrum is assumed with an energy cutoff at 10^{14} eV. Fig. 1 shows a typical model light curve for $t_\pi \approx 8 \times 10^3$s and $t_c \approx 2 \times 10^6$s. These values are obtained by choosing $\mathrm{M_e} = 3\mathrm{M_\odot}$, $\xi = 1$, $V = 0.1$c and $\tau = 1$year.

III. Supernova Catalogues

For this analysis a catalogue of supernovae was created. It combines three different electronically available and regularly updated SN catalogues [4][5][6]. A comparison of the three catalogues revealed some inconsistencies in the listed information. A consistent selection was made with special attention to the objects mistaken for a supernova observation, the total number of supernovae and the supernova positions.

Fig. 2 shows the distribution of the 4805 supernovae observed between 1885 and 2008. The clearly visible structure around the celestial equator are supernovae found by the Sloan Digital Sky Survey-II supernova survey. The nearest and best visible supernova for AMANDA was SN2004dj in NGC 2403 at a distance of approximately 3.33 Mpc.

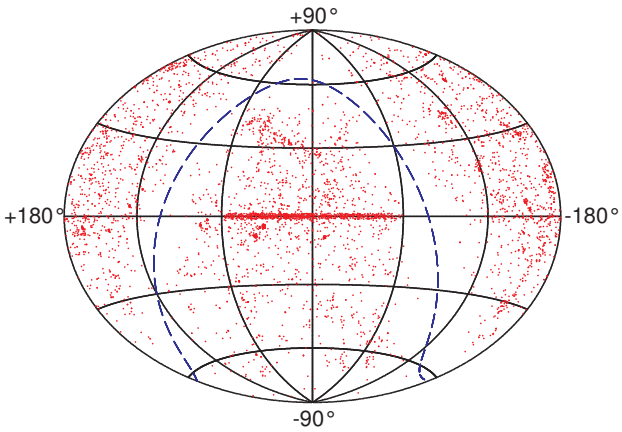

Fig. 2. Distribution of observed supernovae in equatorial coordinates with the galactic plane indicated as dashed line. Due to the background from atmospheric muons only supernovae in the northern hemisphere are relevant.

This analysis searches for directional and temporal coincidences between neutrinos and supernovae. Therefore additional input has to be quantified for each supernova. Firstly, the expected neutrino flux has to be determined from an accurate distance. The supernova distance can be identified with the distance to the host galaxy and can be estimated from the redshift. The redshift estimate is replaced by a measured distance (e.g. Cepheid variables or Tully-Fisher relation) if available. This improves the distance accuracy for nearby supernovae, which are most relevant.

Secondly, the explosion date is needed for the temporal correlation, but only the date of the optical maximum or the discovery date is available. From some well observed SNe (e.g. 1999ex and 2008D) it is known that the optical maximum occurs around 15-20 days after the explosion, which is used as a benchmark. Fig. 3 shows the difference between the date of discovery and the date of maximum for those cases where the light curve was fitted to a template and the date of maximum extrapolated backwards in time or found on old photo plates. The majority of the supernovae are discovered within 20 days after the optical maximum. Hence, the discovery is assumed to be typically 20 days after the optical maximum. The uncertainty of the explosion date is accounted for in the likelihood approach.

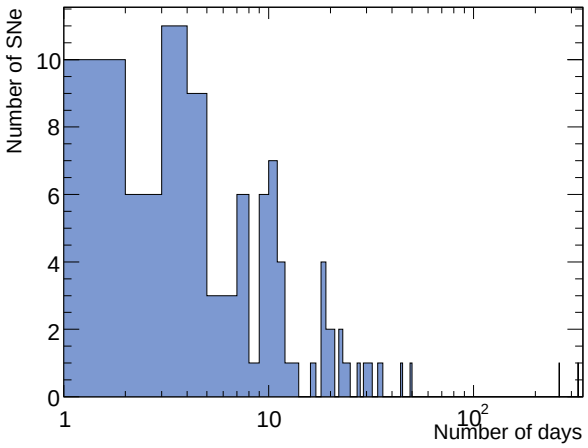

Fig. 3. Number of days between the optical maximum and the discovery if the supernova was discovered after the maximum. A linear one day binning is shown on an logarithmic x-axis.

Thirdly, for the individual supernova the needed input for the pulsar model is not available. Therefore, all supernovae are treated equally. The influence of the model light curve on the analysis is tested by defining two additional sets of parameters which result in light curves with very short and long neutrino emission. Hence, altogether three different model light curves (typical, short, long) are used. The width of the plateau that can be seen in Fig. 1 is 12 days for the typical, 1 day for the short and 76 days for the long light curve. The most realistic assumption for the supernovae in the catalogue is that they have individual realisations of the parameters of the pulsar model and therefore individual light curves between the extreme cases.

IV. Likelihood Approach

A new likelihood approach was developed for this analysis [7]. Its principal idea is to compare all neutrino events from the experimental data sample to every relevant supernova and evaluate the likelihood ratio (LHR) between the hypothesis that this event is signal and the hypothesis of being background. This yields a large value for a good and small value for a bad match. The LHR for all events is summed in order to obtain a cumulative estimator, called Q:

$$Q = \sum_{\mathtt{events}} \frac{\sum_{\mathtt{SN}} p(\vec{a}|\mathtt{SN}) p(\mathtt{SN})}{p(\vec{a}|\mathtt{BG}) p(\mathtt{BG})} \ , \qquad (2)$$

where $\vec{a}$ are characteristic observables of the event.

The advantage of this likelihood definition is that it can be extended to a stacking analysis. Q automatically assigns a small weight to irrelevant combinations of

neutrinos and supernovae, while relevant ones receive a larger weight. Thus, all supernovae from the catalogue can be used in the analysis and no optimisation on the number of sources is needed. Q is a sum of likelihood ratios and therefore its absolute value contains no physical information.

The probabilities in the likelihood sum are constructed from properties of AMANDA, the experimental data sample and the considered model light curve. $p(\mathrm{BG})$ is the probability to have background and is an unknown but constant factor. This probability is eliminated by redefining Q to $Q \cdot p(\mathrm{BG})$.

$p(\vec{a}|\mathrm{BG})$ is the probability that, assuming an event is background, it is observed at its specific time and from its specific direction. It is factorised into a temporal and an angular part. The temporal part corresponds to the AMANDA live-time. However, it cancels out with the corresponding temporal part of $p(\vec{a}|\mathrm{SN})$. AMANDA does not distinguish between signal and background neutrinos and was obviously taking data when the event was measured. The angular probability is constructed with the normalised zenith angle distribution of the experimental data sample (see Fig. 2 in [3]). The azimuth probability is constant, because AMANDA is completely rotated each day and the azimuth is randomised for the relevant time scales of this analysis.

The supernova signal probability consists of $p(\vec{a}|\mathrm{SN})$ and $p(\mathrm{SN})$. The first part depends on the specific event and is the probability that an event from a supernova is observed at a given time from a given direction. $p(\mathrm{SN})$ is the probability to observe a signal from that supernova and is estimated for each supernova.

For $p(\vec{a}|\mathrm{SN})$ two terms are considered. $p(\Psi|\mathrm{SN})$ is the probability that a neutrino from a supernova is reconstructed with an angular difference Ψ relative to the supernova direction. This probability is calculated from the point-spread function, which is obtained from Monte Carlo simulations. The second term $p(t, t_{\mathrm{SN}}|\mathrm{SN})$ yields the probability that a neutrino arrives with a time offset $t - t_{\mathrm{SN}}$ from the explosion date. This probability is taken from a likelihood light curve.

In order to be less model dependent three generic likelihood light curves (typical, short, long) are constructed. They are inspired by the model light curves and constructed conservatively in order to not miss signal by accidentally looking too early or too late. Hence, if the date of the optical maximum is known, the starting time for the likelihood light curves ($t = 0$) is defined to be 30 days earlier. In case only the date of the discovery is known a 50 days earlier starting time is used. This makes sure that the explosion is not missed, because the time shift to the explosion date is overestimated by about 15 days for the optical maximum and up to 35 days for the date of discovery. The likelihood light curves consist of a half Gaussian for $t < 0$, a plateau for $t > 0$ and another half Gaussian after the plateau. The length of the plateau is the full width at 90% of the model light curves and enlarged by the uncertainty of the explosion day. This uncertainty is bigger if only the date of discovery is known. The width of the Gaussian after the plateau is the full width at half maximum (FWHM) after the plateau of the model light curves. Fig. 4 shows the typical likelihood light curve for the date of discovery.

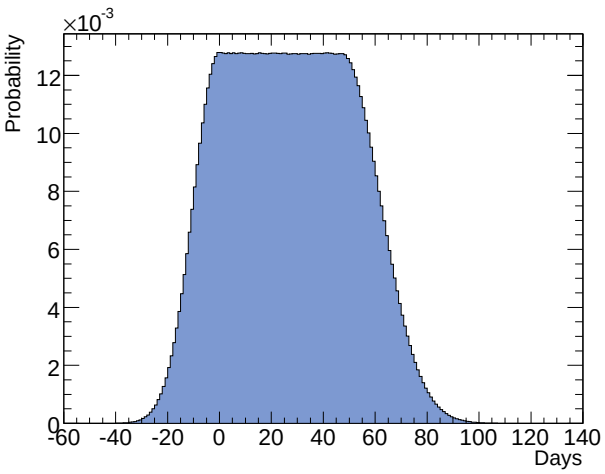

Fig. 4. Typical likelihood light curve

$p(\mathrm{SN})$ depends on the supernova neutrino luminosity, distance and direction. The absolute value of $p(\mathrm{SN})$ is determined by the supernova neutrino luminosity and is a free parameter of this analysis. However, the absolute normalisation is not required, because a constant factor results in a rescaling of Q and hence only relative values are important. All supernovae are assumed to have the same neutrino luminosity at source. $p(\mathrm{SN})$ decreases like the flux with the square supernova distance. AMANDA is not equally sensitive to neutrinos from all directions. Therefore the angular acceptance for different supernova directions is taken into account.

V. Signal and Background Simulation

Q distributions for signal and background simulations are used to construct confidence belts with the Feldman-Cousins approach to the analysis of small signals [8]. Each simulated data sample contains 6595 signal or background events like the experimental data set. Background events are simulated with the zenith angle distribution of the experimental data and the AMANDA live-time. For the signal simulation a model light curve and the AMANDA angular and temporal acceptance is simulated. The angular acceptance includes a random simulation of assumed systematic uncertainties of the measured rate of high energetic muon neutrinos [3]. The simulation of the temporal and angular acceptance reduces signal events from days with low live-time or unfavourable supernova directions.

The confidence belts are used to estimate the sensitivity of the analysis. The sensitivity for the long model light curve is not compatible compared to [3]. Furthermore, if the supernovae have short model light curves, the sensitivity is comparable for the short and

typical likelihood light curves. The typical pulsar model is best detected with the typical likelihood light curve. Therefore the experimental data is analysed with the typical likelihood light curve, because it can cover a larger range of possible parameters.

VI. Experimental Result

Analysing the experimental AMANDA data with the typical likelihood light curve yields:

$$Q_{\text{typical}}^{\text{Exp}} = 0.0059 \ . \tag{3}$$

Fig. 5 shows this value in a Q distribution for background only. The p value of obtaining a Q value equal or bigger than 0.0059 is 73.0%. Hence, the Q value is consistent with background and no deviation from the background only hypothesis is found. Therefore upper limits for the three model light curves are derived.

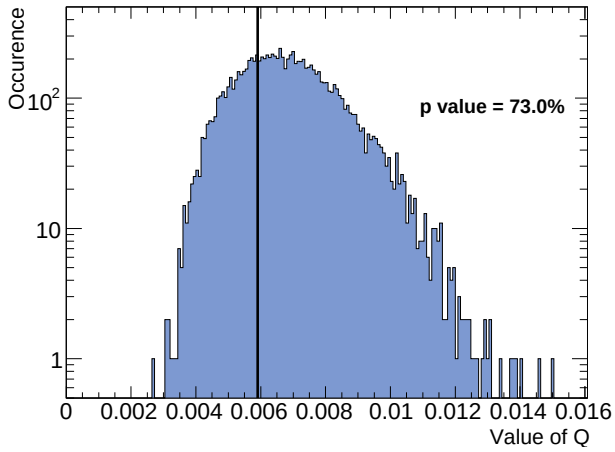

Fig. 5. Q value from analysing the experimental data sample with the typical likelihood light curve (horizontal line) in a distribution for background only.

90% upper limits on the signal strength are derived from the Feldman-Cousins confidence belts. With the help of the signal simulation explained above this value converts to the sum of neutrinos from all supernovae. Assuming the above model ranking of sources and the stacking this limit can also be interpreted as a limit on the number of neutrinos from SN2004dj. Tab. I shows the obtained upper limits for the typical, short and long pulsar model light curve.

Pulsar model	All SNe	SN2004dj
Typical	< 5.4	< 1.0
Short	< 4.1	< 0.9
Long	< 67.3	< 5.9

TABLE I
90% UPPER LIMITS ON THE NUMBER OF NEUTRINOS FROM ALL SUPERNOVA AND FROM SN2004DJ.

The event numbers can be converted to a flux by integrating the AMANDA neutrino effective area with the expected signal energy spectrum (E^{-2} spectrum with cutoff at 10^{14} eV). Assuming the typical pulsar model for all supernovae and taking the average of the effective area over all directions, the 90% upper limit on the flux from all supernovae for the plateau of powerful neutrino radiation (12 days) is:

$$\frac{d\phi}{dE} \cdot E^2 < 5.2 \times 10^{-6} \frac{\text{GeV}}{\text{cm}^2\text{s}} \ . \tag{4}$$

Using the effective area for the direction of SN2004dj, the corresponding 90% upper limit for SN2004dj is:

$$\frac{d\phi}{dE} \cdot E^2 < 8.4 \times 10^{-7} \frac{\text{GeV}}{\text{cm}^2\text{s}} \ . \tag{5}$$

These limits are valid in the energy range from 1.1 TeV to 84.0 TeV.

Assuming that the energy range of the pulsar model as described in [2] can be extended to higher energies, the limits would improve by about 30% and are then valid in the energy range from 1.7 TeV to 2 PeV.

VII. Conclusion

For the first time the neutrino emission from young supernova shells was experimentally investigated. In the context of the pulsar model no deviation from the background only hypothesis was found.

For a galactic supernova the expected flux from the pulsar model should be sufficient to be detectable by IceCube, the AMANDA successor. The sensitivity of this analysis might be enhanced by using an energy estimator in the likelihood and the individual event reconstruction error instead of the energy averaged point-spread function.

References

[1] V. S. Berezinsky and O. F. Prilutsky, *Pulsars and Cosmic Rays in the Dense Supernova Shells*, A&A, **66** (1978), no.3, pp. 325-334
[2] H. Sato, *Pulsars Covered by the Dense Envelopes as High-Energy Neutrino Sources*, Progr. Theor. Phys., **58** (1977), no.2, pp. 549-559
[3] J. Braun et al., *Search for point sources of high energy neutrinos with final data from AMANDA-II*, Phys. Rev. D, **79** (2009), no.6, pp. 062001-1 - 062001-15
[4] List of supernovae from the CBAT, http://cfa-www.harvard.edu/iau/lists/Supernovae.html
[5] Asiago Supernova Catalogue, http://cdsarc.u-strasbg.fr/viz-bin/Cat?B/sn
[6] Sternberg Astronomical Institute (SAI) Supernova Catalogue http://www.sai.msu.su/sn/sncat/
[7] D. Lennarz, *Search for High Energetic Neutrinos from Supernova Explosions with the AMANDA Neutrino Telescope*, Diploma thesis, RWTH Aachen University (2009)
[8] G. J. Feldman and R. D. Cousins, *Unified Approach to the Classical Statistical Analysis of Small Signals*, Phys. Rev. D, **57** (1998), no.7, pp. 3873-3889

Search for Ultra High Energy Neutrinos with AMANDA

Andrea Silvestri* for the IceCube Collaboration†

**Department of Physics and Astronomy, University of California, Irvine, CA 92697, USA.*
†*See the special section of these proceedings.*

***Abstract*. We present results from the search for diffusely distributed Ultra High Energy (UHE) neutrinos performed on data collected in 2003-2005 with the AMANDA experiment. At energies above a few PeV the Earth is opaque to neutrinos, therefore neutrinos must be differentiated from downward going cosmic ray induced (bundles of) muons. A search for a diffuse flux of UHE neutrinos shows no events, leading to a flux limit, summed over all flavors $\mathbf{E^2\Phi_\nu \leq 8.4\times 10^{-8}}$ GeV cm^{-2} s^{-1} sr^{-1} (90% confidence level) for $\mathbf{10^{15.2}}$ eV $< \mathbf{E_\nu} < \mathbf{10^{18.8}}$ eV. This limit is the most stringent placed to date. A number of model predictions different from the $\mathbf{E^{-2}}$ spectrum have been tested and some have been rejected at a 90% C.L. We show that these results can also place a limit on the flux from point sources in the Southern Sky as a function of declination and valid in the same energy range.**

***Keywords*: Diffuse sources, high energy neutrinos, AMANDA**

I. Introduction

Neutrino production from Active Galactic Nuclei (AGN), and other astrophysical sources have been extensively modeled during the past two decades, as described in [1], [2], [3]. Super-massive black holes hosted in the AGNs would accelerate, via a first-order Fermi mechanism, charged particles to ultra high energies. The collision of ultra-relativistic protons with the photon field in the AGN, via pγ and pp-interactions, would then produce high-energy neutrinos. The predicted intensity of neutrinos from these astronomical sources can reach the Earth and be detected by underground neutrino telescopes. Other theoretical calculations as presented in [4], [5], [6] and [2], derive an upper bound to the expected neutrino fluxes from high energy cosmic ray observations. These predictions, based on a model-independent approach, provide also a target for neutrino detector sensitivities. The predicted upper bound (ν_μ and $\bar{\nu_\mu}$ combined) for an E^{-2} spectrum is $\mathrm{E}^2\Phi_\nu^{WB} \leq 2\times 10^{-8}\xi_z$ GeV cm^{-2} s^{-1} sr^{-1}, where ξ_z accounts for cosmological model and source evolution. Using cosmological dependence and source evolution that follows star formation rate over cosmological time gives $\xi_z \sim 3$. Assuming $\nu_\mu/\nu_e = 0.5$ at the source, produced from pγ and pp-collisions, the upper bound on the total flux for all $\nu-$ flavors becomes $\mathrm{E}^2\Phi_\nu^{WB} \sim 9\times 10^{-8}$ GeV cm^{-2} s^{-1} sr^{-1}.

II. Analysis

The analysis results presented in this paper incorporate 3-year of AMANDA data collected in 2003-2005 (detector live-time of 507 days) and are based on work for one year analysis [7] of 2003 data. The Antarctic Muon And Neutrino Detector Array (AMANDA) [8], is the first neutrino telescope constructed in transparent ice, and deployed between 1500 m and 2000 m beneath the surface of the ice at the geographic South Pole in Antarctica. The AMANDA detector uses the Earth to filter out muons generated in the atmosphere on the Northern hemisphere and to search for point and diffuse sources of neutrinos with upward going direction at TeV to 100 TeV energies. However, at energies above PeV the Earth is opaque to neutrinos, therefore ν's must be differentiated from the large background (billions of events per year) of downward going cosmic ray induced (bundles of) muons, which constitutes the primary challenge of this analysis. AMANDA has been taking data with the same detector configuration since 2000, and the data acquisition electronics was upgraded in 2003 by recording full waveforms of the photo-electron (p.e.) pulses from the photomultiplier tubes (PMT) using Transient Waveform Recorders (TWR) [9]. The entire 2003 data set of the AMANDA TWR technology was processed, calibrated and analyzed to perform an atmospheric neutrino analysis and a search for point sources in the Northern hemisphere sensitive at TeV energies [10], [11], which demonstrated the basic capabilities of the novel system to reproduce comparable physics results of the standard system of the AMANDA detector. After demonstrating the physics performance of the TWR technology, the analysis is performed to search for diffusely distributed neutrinos above PeV energies. The full waveforms from the PMT's provide far more information on the light distribution from complex high energy events. However, the new technology produced $\sim$ 85 TB in 3 years, more than an order of magnitude increase w.r.t. the standard AMANDA system. To meet the challenge of large data structure and to simulate comparable data volume new analysis strategies were developed using high performance computing resources. The resources required for this analysis exceeded 2M CPU hours.

The UHE analysis is performed by using the information of multiple p.e.'s from the PMT waveforms. The initial level of the analysis is defined by eliminating over 90% of the background by retaining only events

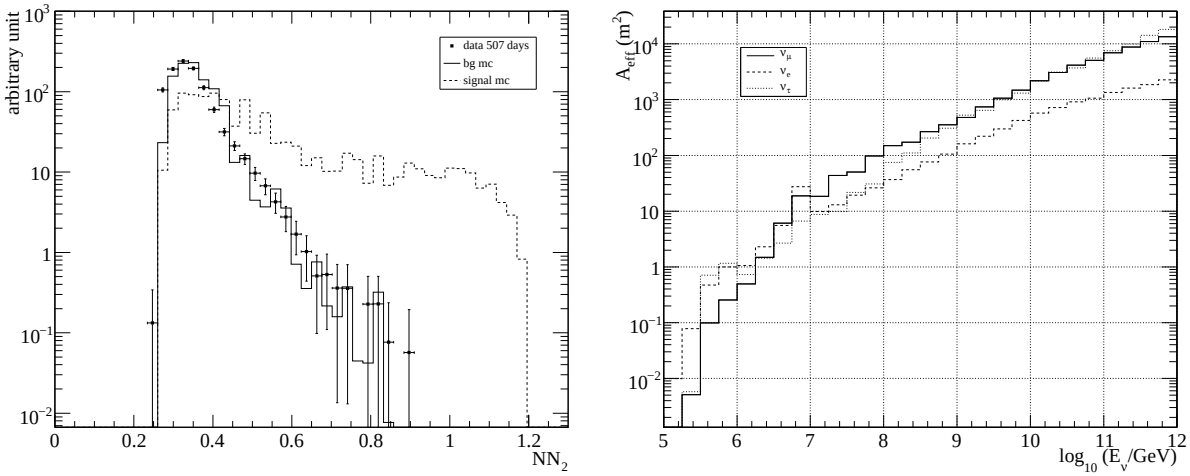

Fig. 1. Left panel: the neural network (NN_2) distribution plotted for data, background and signal simulation. Right panel: detector effective area for muon, electron and tau neutrinos as a function of neutrino energy.

with large number of p.e. pulses recorded in the array. After this level the analysis is refined by developing two independent neural networks. The first neural network mostly incorporates variables from reconstructed events, i.e. the reconstructed zenith angle of the events, which can separate downward going muons from signal mostly concentrated at the horizon. The second neural network uses primarily time dependent variables, like spread in leading edge of the arrival time and time-over-threshold values of the p.e. pulses, which at the higher level of the analysis better discern signal from high energy bundles of atmospheric muons. Variables were developed that exploit the full PMT waveforms, which in turn strongly correlate to signal features and better separate signal-like background events. Selection criteria based on single variable discriminators, like the number of photon-electrons were tested, but demonstrated not to be efficient for retaining signal events. Therefore a new set of variables were developed, which depend on timing and energy of typical signal events [7]. The new developed variables which use multiple photon-electrons in the PMT waveforms are the fluctuation of the time-over-threshold incorporated in the standard deviation of the tot's (σ_{tot}), the mean of the leading edge times of the photon-electron pulses (μ_{le}), and the fluctuation from the standard deviation of the leading edge times (σ_{le}). Simulation of signal shows that distant UHE ν events may not deposit much light in the detector, but the spread in leading edge arrival time σ_{le} and time-over-threshold σ_{tot} values is large compared to typical background events. Background events tend to have large number of muons with relatively small lateral dimensions, which traverse through or close to the detector. Consequently, the arrival time of background photons shows little spread in time. On the other hand, signal events with comparable values of number of photon-electrons do not pass close to the detector. Therefore, these events differ from background because the photons show large variability in the arrival times. To further improve background rejection, neural networks were developed and trained. The most powerful neural network included variables that measure the mean spread in leading edge times and fluctuations of time-over-threshold values. The search is performed with a blind analysis, i.e. 20% of the data sample is used to compare data with simulation while cut optimization is based on simulation solely. Once the analysis criteria are established, the cuts are frozen and applied to the remaining 80% of the data. Fig. 1 left panel shows the neural network (NN_2) before the final cut level for the combined data set, for the simulated atmospheric background and for the neutrino signal following an E^{-2} spectrum.

Background simulation was performed by generating primary cosmic ray using the CORSIKA package [12], propagating particles through the ice with the program MMC [13], recording detector response using the program AMASIM [14] with description of depth-dependent properties of Antarctic ice [15], and including proper treatment of waveform data. Similarly, neutrino signal simulation was performed for all flavors using the program ANIS [16]. Background simulation was biased in energy and spectrum towards high energy events to accommodate available computing resources. The final cut on NN_2 was determined by evaluating the model rejection factor (MRF), as described in [17], and computing the minimum of the ratio $\mathrm{MRF} = \langle \mu_{90}(n|b) \rangle / n_{sig}$. The $\langle \mu_{90}(n|b) \rangle$ is the average 90% C.L. upper limit, determined by using the Feldman-Cousins method [18], computed over the Poisson probabilities for the experiment repeated many times, and n_{sig} is the number of signal events for a given model. The minimum of the MRF determines the cut which is set to $NN_2 > 0.85$. After the final cut one experimental event is observed over a detector live-time of 507 days, consistent with 0.9 $(-0.9, +1.3)$ events from background expectation.

III. RESULTS

The search for a diffusely distributed flux of UHE neutrinos shows no signal events, leading to a prelimi-

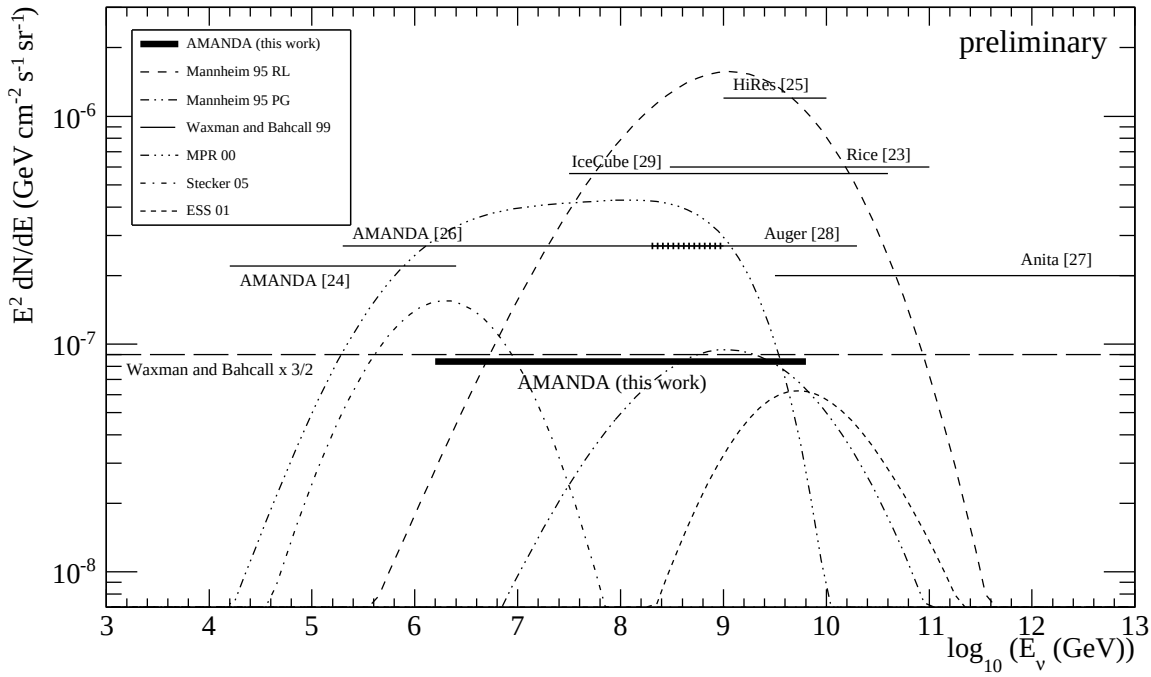

Fig. 2. Experimental limits of this analysis on a diffuse E^{-2} ν-flux for all flavors as a function of neutrino energy, thick solid line. Solid lines represent experimental limits from other experiments [23], [24], [25], [26], [27], [28], [29]. Dotted curves represent model predictions for a diffuse ν-flux, and predictions have been adjusted for all flavor neutrino contribution, where necessary.

nary flux limit, summed over all flavors

$$E^2\Phi_\nu \leq 8.4 \times 10^{-8}\ \mathrm{GeV\ cm^{-2}\ s^{-1}\ sr^{-1}} \quad (1)$$

at 90% C.L. for the energy interval $10^{15.2}$ eV $< E_\nu <$ $10^{18.8}$ eV, defined by the 90% containment of the final neutrino energy distribution, which has a median energy of $\langle E_\nu \rangle = 4 \times 10^{16}$ eV. Fig. 1 right panel shows the detector effective area for all flavor neutrinos for an E^{-2} spectrum as a function of neutrino energy, which for muon neutrinos reaches 100 m^2 for 100 PeV and rapidly increases with energy.

The limits are computed including the contribution of systematic uncertainties by using the method described in [19]. Tab. I summarizes the different sources of systematic uncertainties which impact background and signal simulation in this analysis: The same numbers as given in the table is then repeated in the text. Differences in the simulation for cosmic ray composition by generating proton and iron CR primaries, and interaction models by using two different hadronic models (QGSJET and SIBYLL) were used to estimate variations in background event rate; Uncertainties in detector sensitivity which mostly depend on the absolute sensitivity of the PMT's, were also included; Variations have been estimated due to the difference in detector response observed for the three years studied in the analysis; Variations in the spread of the time-over-threshold for distances $d > 200$ m were evaluated for the impact on signal efficiency; Studying ice properties with two different models gave a max variation of 16% in signal sensitivity; The impact on systematic uncertainties due to ice properties has been further studied by varying the length of photon propagation in ice for distances characteristic of high energy signal, and by incorporating this variation into the effect of detector sensitivity to estimate the impact on signal sensitivity; Background from charm production has been estimated to be negligible in this analysis;

TABLE I
SUMMARY OF SYSTEMATIC UNCERTAINTIES ESTIMATED FROM DIFFERENT SOURCES IMPACTING BACKGROUND AND SIGNAL SIMULATION.

Source	bg	signal (E^{-2})
CR comp. and inter. models	$\pm 80\%$	-
detector sensitivity	$\pm 15\%$	$\pm 15\%$
year-to-year detector variation	$\pm 14\%$	$\pm 14\%$
tot-factor for $d > 200$ m	-	$+10\%$
ice properties	$\pm 20\%$	$\pm 20\%$
charm BG	negl.	-
tot-corr. and N_2-laser cal.	$\pm 100\%$	$\pm 10\%$
neutrino cross section [20]	-	$\pm 4\%$
LPM effect	-	-3%
total (added in quadrature)	$\pm 131\%$	$\pm 32\%$

TABLE II
SUMMARY OF MODEL PREDICTIONS TESTED BY THIS ANALYSIS. MODELS WITH A MRF < 1 ARE EXCLUDED AT 90%, WHILE MODELS WITH A MRF > 1 ARE CONSISTENT WITH THESE RESULTS.

Model	ν_{all}	MRF	Reference
AGN RL A-*jet*	1.10	3.05	Mannheim 95 PG [1]
AGN RL B-*jet*	17.8	0.19	Mannheim 95 RL [1]
AGN-*jet*	14.6	0.23	MPR 00 [2]
AGN-*core*	3.12	1.07	Stecker 05 [3]
Waxman-Bahcall	4.04	0.83	WB 99 [4]
GZK mono-energetic	5.50	0.61	KKSS 02 [21]
GZK index α=2	4.68	0.72	KKSS 02 [21]
GZK full evol.	0.28	12.0	ESS 01 [22]

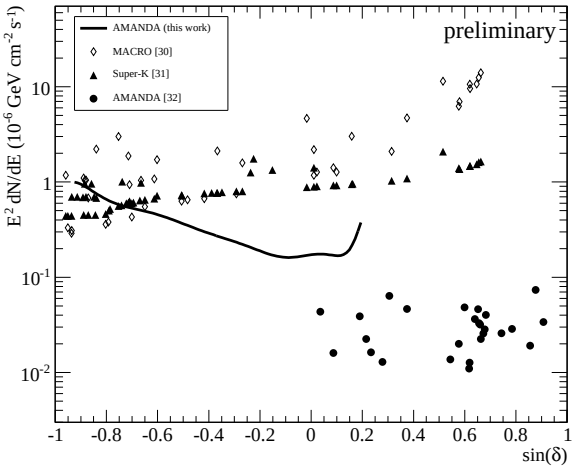

Fig. 3. Point flux limits as a function of declination $sin(\delta)$ for the Southern Sky averaged over azimuth, solid line. Also included are limits from other experiments [30], [31] and for the Northern Sky [32].

Variations in the N_2-laser calibration for the spread of the time-over-threshold were estimated for background event rate and signal efficiency; Uncertainties in the neutrino cross section [20] for energies relevant for this analysis were incorporated, and impact due to LPM effect for signal above 10^8 GeV were also included. The estimated systematic uncertainties have been added in quadrature and incorporated in the final results of the analysis.

The diffuse limit has been used to test a number of model predictions different from the E^{-2} spectrum. Model predictions with a ratio $\langle \mu_{90}(n|b) \rangle / n_{sig} < 1$ are excluded by this analysis. The models tested and the corresponding MRF have been summarized in Tab. II. A class of AGN predictions based on *jet-models* scenario, such as [1] (RL B) and [2] have been excluded, while prediction [1] (RL A) is not, and AGN prediction based on *core-models* scenario [3] is almost excluded. From the class of models excluded by this analysis we can conclude *jet-models* normalized to diffuse x-ray or GeV/TeV emission from individual sources are generally disfavored. These limits are consistent, and below the maximum upper bound to neutrino flux predicted by [4], [6], and also below the maximum neutrino flux due to possible extra-galactic component of low-energy protons of 10^{17} eV [5]. These results are also consistent and below the bounds on neutrino fluxes presented by [2], computed by assuming optically thin (thick) sources to pion photo-production processes. Models on GZK neutrino spectrum were also tested, predictions [21] are excluded, while prediction [22] is still compatible with these results. The limits from this work to an E^{-2} neutrino flux as a function of energy are shown in Fig. 2, thick solid line. Model predictions are represented by dotted curves, and solid lines show limits presented by other experiments [23], [24], [25], [26], [27], [28], [29].

At UHE energies this analysis is sensitive to search for point source of neutrinos in the Southern Sky. Simulation shows that muons are reconstructed with angular resolution of $\sim 7^o$ over the entire Southern hemisphere. Except for a small band near the horizon, signal originating from the Southern Sky will be observed in the Southern Sky. The sensitivity only depends on zenith angle and is roughly independent of azimuth, and maximum sensitivity peaks at the horizon [7]. Since, no excess of events were observed, a flux limit as a function of declination is derived, Fig. 3, and fitted with a function of δ, as $E^2 dN/dE_\nu(\sin\delta) \leq [1.3 \times e^{-(2\ sin\ \delta)}] \times 10^{-7}$ GeV cm^{-2} s^{-1} with 10% accuracy, valid for $-0.98 < sin(\delta) < 0$, and for $10^{15.2}$ eV $< E_\nu < 10^{18.8}$ eV. These point flux limits are valid for energies above PeV, and are compatible with results from other experiments, which cover lower energy intervals between 10 GeV - 100 TeV [30], and between 10 GeV - 100 GeV [31].

To summarize, we have presented in this paper the most stringent limits to date for neutrino energies above 1 PeV. These experimental limits begin to restrict the largest possible fluxes of the WB upper bound [4], [5], [6].

IV. Acknowledgment

The author acknowledges support from U.S. National Science Foundation-Physics Division, and the NSF-supported TeraGrid system at the San Diego Supercomputer Center (SDSC).

References

[1] K. Mannheim, *Astropart. Phys.* **3**, 295 (1995).
[2] K. Mannheim et al., *Phys. Rev. D* **63**, 023003 (2001).
[3] F. Stecker, *Phys. Rev. D* **72**, 107301 (2005).
[4] E. Waxman and J. Bahcall, *Phys. Rev. D* **59**, 023002 (1999).
[5] J. Bahcall and E. Waxman, *Phys. Rev. D* **64**, 023002 (2002).
[6] E. Waxman, *Phil.Trans.Roy.Soc.Lond.* **A 365**, 1323 (2007).
[7] A. Silvestri, *Ph.D. Thesis*, University of California, Irvine (2008).
[8] E. Andres et al., *Nature* **410**, 441 (2001).
[9] W. Wagner et al., *Proc. 28th ICRC*, **2**, 1365 (2003).
[10] A. Silvestri et al., *Proc. 29th ICRC*, **5**, 431 (2005).
[11] A. Silvestri et al., *Mod. Phys. Lett. A* **22**, 1769 (2007).
[12] D. Heck, *DESY-PROC-1999-01*, 227 (1999).
[13] D. Chirkin and W. Rhode, *hep-ph/0407075* (2004).
[14] S. Hundertmark,*Proc.1st νTelescopes Workshop*, Zeuthen (1998).
[15] M. Ackermann et al., *J. Geophys. Res.* **111**, D13203 (2006)
[16] M. Kowalski and A. Gazizov, *Comput. Phys. Comm.* **172**, 203 (2005).
[17] G. Hill and K. Rawlins, *Astropart. Phys.* **19**, 393 (2003).
[18] G. J. Feldman and R. D. Cousins, *Phys. Rev. D* **57**, 3873 (1998).
[19] G. Hill, *Phys. Rev. D* **67**, 118101 (2003).
[20] A. Cooper-Sarkar and S. Sarkar, *JHEP* **75**, 801 (2008).
[21] O. E. Kalashev et al., *Phys. Rev. D* **66**, 063004 (2002).
[22] R. Engel et al., *Phys. Rev. D* **64**, 093010 (2001).
[23] I. Kravchenko et al., *Phys. Rev. D* **73**, 082002 (2006).
[24] A. Achterberg et al., *Phys. Rev. D* **76**, 042008 (2007).
[25] K. Martens et al., *astro-ph/0707.4417*, (2007).
[26] M. Ackermann et al., *Astrophys. J.* **675**, 1014 (2008).
[27] P. Gorham et al., *astro-ph/0812.2715*, (2008).
[28] J. Abraham et al., *astro-ph/0903.3385*, (2009).
[29] K. Mase, A. Ishihara and S. Yoshida et al., *Proc. 31th ICRC*, these Proceedings (2009).
[30] M. Ambrosio et al., *Astrophys. J.* **546**, 1038 (2001).
[31] S. Desai et al., *Astropart. Phys.* **29**, 42 (2008).
[32] R. Abbasi et al., *Phys. Rev. D* **79**, 062001 (2009).

Selection of High Energy Tau Neutrinos in IceCube

Seon-Hee Seo* and P. A. Toale† for the IceCube Collaboration‡

* *Oskar Klein Centre and Dept. of Physics, Stockholm University, SE-10691 Stockholm, Sweden*
† *Dept. of Physics, Pennsylvania State University, University Park, PA 16802, USA*
‡ *See the special section of these proceedings*

***Abstract*. Astrophysical neutrino sources are expected to produce electron and muon flavor neutrinos via charged pion decay. Over cosmological distances, standard neutrino oscillations will change the flavor content to include equal fluxes of all three flavors. Tau neutrinos with energies above a few PeV will produce characteristic signatures known as double-bangs and lollipops. In contrast to searches for cosmological electron and muon neutrinos, which must contend with backgrounds from atmospheric neutrinos, tau neutrinos are expected to be background-free. Thus far no searches for tau neutrino events with these characteristic signatures have been performed because their detection requires a kilometer-scale detector. In this talk, we will present current results from several methods for searching for high energy tau neutrinos in IceCube.**

***Keywords*: Tau neutrinos, Double-bangs, IceCube**

I. INTRODUCTION

One of the main research topics in neutrino telescopes such as ANTARES and IceCube is to search for neutrinos of astrophysical origin. Astrophysical particle accelerators like AGNs and GRBs may produce high energy neutrinos [1], [2]. As daughters of charged pion decay, the emerging neutrinos are expected to have the flavor flux ratio of 1:2:0 (ν_e:ν_μ:ν_τ). Due to neutrino oscillations, this neutrino flux is expected to be observed in the flavor ratio of approximately 1:1:1 on Earth. There are also models which predict different ratios of neutrino flux observed on the Earth but they all lead to non-zero flux of ν_τ [3], [4].

Here we discuss aspects of a search for high energy (greater than a few PeV) ν_τ's with the IceCube 22-string array ("IC-22"). High energy ν_τ's can leave very distinctive signatures in the IceCube detector owing to the very short life time and numerous decay channels of tau leptons. We denote these signatures "lollipops," "inverted lollipops" and "double-bangs" [5], [6]. Although high energy ν_τ's can traverse the Earth through the "regeneration" process [7], they typically emerge with energies too low to create any of the signatures under study here. The low energy (below PeV) ν_τ's can be detected in 4π in IceCube but are seen as "cascade-like" events, which is described elsewhere.

The lollipop and inverted lollipop topologies are characterized by having either the production or decay vertex of the tau lepton well outside the detector fiducial volume, respectively. In these topologies we expect to see a track due to the tau lepton and a single shower at the contained vertex. The double-bang topology as shown in Fig. 1 is characterized by having both production and decay vertices contained within the detector fiducial volume, and the tau track long enough to clearly separate the two showers from one another.

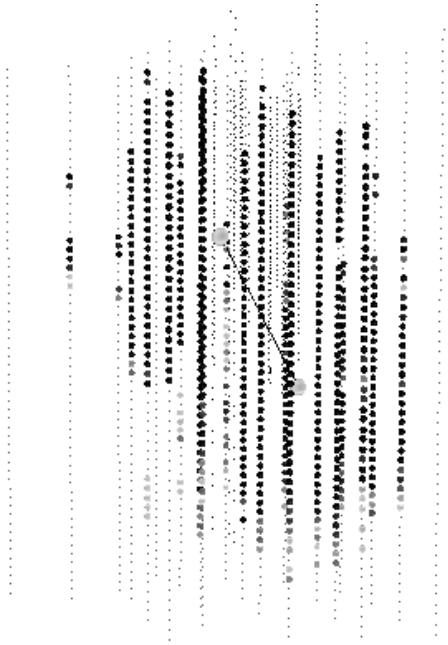

Fig. 1. A simulated double-bang event produced from a primary neutrino energy of 47 PeV that enters the IC-22 detector with 35^o zenith angle. The two showers are separated by a tau track of 332 m long. The colors (online version only) represent the relative hit times, with red for the earliest hits, blue for the latest hits, and other times in between according to the colors of the rainbow.

These astrophysical high energy ν_τ events are contaminated much less by atmospheric background from cosmic ray interactions compared to ν_μ and ν_e [8]. This is because the conventional atmospheric ν_τ flux is nearly zero, and the prompt ν_τ flux produced from charmed meson decay in the atmosphere is also expected to be very small [9], [10].

II. SIGNATURE BASED SEARCH METHOD

In IC-22, the search for high energy ν_τ does not incorporate full event reconstruction [11], but instead relies on a simpler approach that exploits the unique signatures

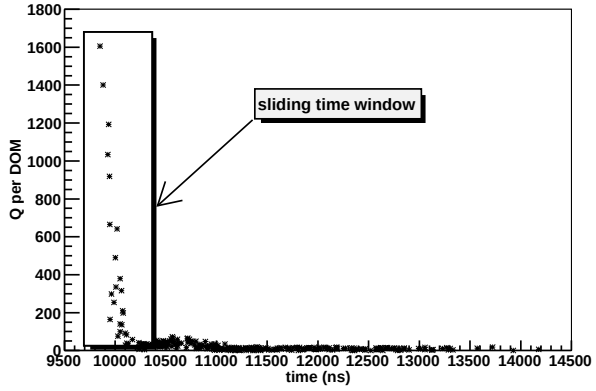

Fig. 2. Charge (number of photo-electrons) per DOM distribution as a function of light arrival time (ns) for a simulated inverted lollipop event produced from a primary neutrino energy of 64 PeV. The initial peak corresponds to a shower from ν_τ charged-current interaction, followed by a tau track.

of these events. An example of a simple criterion is given in Fig. 2 which shows the distribution of detected charge (proportional to the amount of Cherenkov light) per digital optical module (DOM) as a function of the time at which the light arrived, for a simulated inverted lollipop event.

As shown in the figure the inverted lollipop event produces a unique topology consisting of a shower followed by a track inside the detector compared to typical muons that produce simple track-like signatures with smooth light deposition along its track length. A set of simple variables based on the differences in the topologies can select (inverted-)lollipop and double-bang events while removing track-like muon backgrounds. One of the variables invented for this purpose is maximum "current ratio," $I_{\mathrm{R,max}}$. This variable is defined as a ratio of the two currents, I_{R}, themselves defined as the amount of charge per unit time, inside and outside a sliding time window, as shown in Fig. 2. When the sliding time window passes through the event's time-ordered hits, I_{R} is calculated, and its maximum value $I_{\mathrm{R,max}}$ is used as a cut variable. For signal events, $I_{\mathrm{R,max}}$ is expected to be greater than 1 but for simple track-like muon backgrounds it is expected to be closer to 1.

However, energetic muons can leave a big shower from bremsstrahlung during their passage through the fiducial volume so that these events could survive the $I_{\mathrm{R,max}}$ cut due to the similarity of the event topology. To remove these energetic muon events another variable called the "local current," I_{L}, is used. The I_{L} is defined as the current calculated in three equally-spaced time regions of an event's time-ordered hits. Of the first and last third, we choose the one with the largest IL as the selection criterion. We intentionally ignore the middle third to help reject energetic muons that have an accompanying bremsstrahlung somewhere in the middle of its track length. This variable showed good discrimination power between signal and background events.

III. Cuts and Efficiencies

So far the cuts have been developed in six distinct levels after application of a trigger and online filter. The trigger, denoted "SMT8," applies a simple majority condition of 8 hits within 5 μs to the data as it is acquired. The online filter is a logical OR of IceCube's cascade and Extremely High Energy (EHE) filters. The cascade filter is designed to select events which satisfy minimum condition of "cascade-like" events [12]. For the EHE filter, a minimum of 80 hits were required.

The level 0 and 1 (L0, L1) cuts are designed to remove track-like muon backgrounds. The L2 cuts are designed mainly to remove energetic muons accompanying bremsstrahlung in the middle of their passage. The L3 cuts are designed to remove downwards-going events, and the L4 cuts are designed to select events that look more "cascade-like" than "track-like" using different variables from those used in L0 and L1. The L5 cuts are designed to remove events which are not sufficiently contained inside the detector. Fig. 3 shows the relative efficiencies at each cut level for signal and background events.

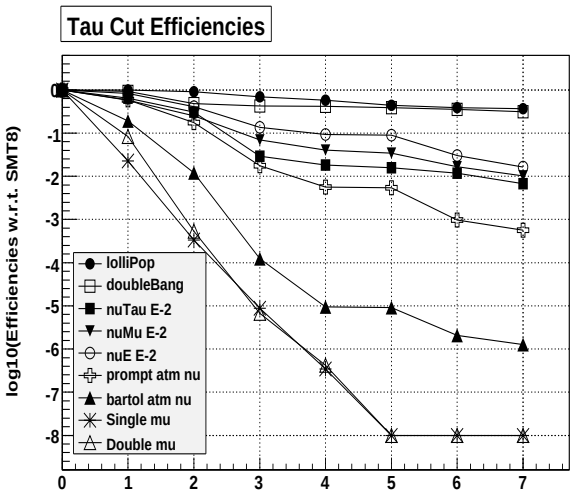

Fig. 3. High energy ν_τ selection cut efficiencies w.r.t. SMT8 for lollipop, double-bang, astrophysical ν_τ, ν_μ and ν_e, and atmospheric background events for IC-22. The numbers from 0 to 8 on the x-axis represent SMT8, the online filter, and L0, L1, L2, L3, L4 and L5 cuts, respectively.

As shown in Fig. 3, lollipop and double-bang events keep the highest efficiencies because they are specially selected from all generated ν_τ's so that they are well contained within the IC-22 detector ("golden events"). Next highest efficiency group is astrophysical neutrinos of all flavors. Note that, for the astrophysical ν_τ's, they are unbiased data samples including all generated ν_τ events unlike the "golden events". Atmospheric neutrino backgrounds, prompt and conventional, come next to astrophysical neutrinos. Atmospheric muon backgrounds, single and coincident, show the lowest efficiencies even

though they run out of statistics from L3 cut which need statistical improvement in near future.

It is good that the cuts developed so far segregate well between astrophysical signal and atmospheric background events. Within astrophysical neutrinos, however, the cuts are almost equally sensitive to all flavors so that we lose the discrimination power for the specific flavor under study, ν_τ. This is due to the fact that the cuts are still quite general. To better distinguish astrophysical ν_τ from astrophysical ν_μ and ν_e, which can more easily mimic lollipop than double-bang signatures, the future direction this analysis will take is to focus exclusively on the double-bang topology.

IV. Double-bang search

Fig. 4 shows charge per DOM distribution as a function of DOM hit time for a simulated double-bang event produced from a primary neutrino energy of 50 PeV. As shown in the figure the double-bang event has two showers separated by a track (403 m long).

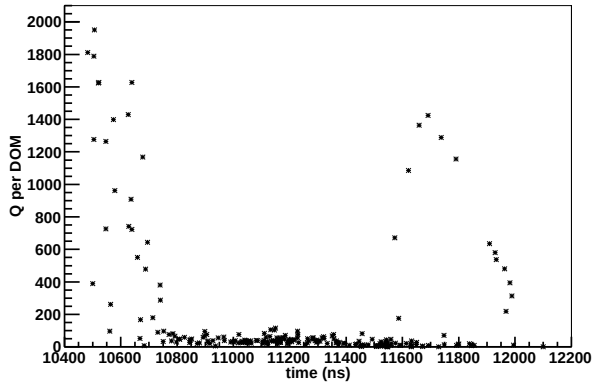

Fig. 4. Charge (number of photo-electrons) per DOM distribution as a function of DOM hit time (ns) for a simulated double-bang event. The first peak corresponds to a shower from ν_τ CC interaction and the second peak from the tau decay. Only hits arriving within 900 ns of residual time were used. (Residual time is the time difference between expected and actual photon arrival time.)

Using the local current variable described above, requiring a large I_{L} in both the first and last parts of the event, double-bang events can be selected. However, very energetic muons which produce two bremsstrahlungs in sequence could survive this cut. Further cuts are still being developed and evaluated.

V. Conclusion

Nature produces high energy neutrinos and they can be observed in all flavors. We try to detect especially high energy ν_τ's which can leave unique signatures inside the IceCube detector. So far our approach is rather simple but we will continue investigate the IceCube potential especially for double-bang type events.

References

[1] F. Halzen and D. Hooper, *Rept. Prog. Phys.* **65**, 1025 (2002).
[2] A. Neronov and M. Ribordy, *arXiv:0905.0509* (2009).
[3] S. Pakvasa, *Nucl. Phys.* **B137** 295 (2004).
[4] D. Meloni and T. Ohlsson, *Phys. Rev.* **D75**, 125017 (2007).
[5] J.G. Learned and S. Pakvasa, *Astropart. Phys.* **3**, 267 (1995).
[6] D. F. Cowen, *J. Phys.* **60**, 227 (2007).
[7] E. Bugaev *et al.*, *Astropart. Phys.* **21**, 491 (2004).
[8] T. DeYoung, S. Razzaque and D. F. Cowen, *J. of Phys.* **60**, 231 (2007).
[9] L. Pasquali and M. H. Reno, *Phys. Rev.* **D59**, 093003 (1999).
[10] R. Enberg *et al.*, *Phys. Rev.* **D78**, 043005 (2008).
[11] M. Ribordy, *Nucl. Inst. Meth.* **A574**, 137 (2006).
[12] J. Kiryluk, "First search for extraterrestrial neutrino-induced cascades with IceCube" *in these proceedings*.

Search for quantum gravity with IceCube and high energy atmospheric neutrinos

Warren Huelsnitz[*] **and John Kelley**[†] **for the IceCube Collaboration**[‡]

[*]*Department of Physics, University of Maryland, College Park, MD 20742, USA*
[†]*Department of Physics, University of Wisconsin, Madison, WI 53706, USA*
[‡]*See the special section of these proceedings*

Abstract. **We present the expected sensitivity of an analysis that will use data from the IceCube Neutrino Observatory to search for distortions in the energy or directional dependence of atmospheric neutrinos. Deviations in the energy and zenith angle distributions of atmospheric neutrinos due to Lorentz invariance violation or quantum decoherence could be a signature of quantum gravity in the neutrino sector. Additionally, a periodic variation as a function of right ascension is a possible consequence of a Lorentz-violating preferred frame. We use a likelihood method to constrain deviations in the energy and zenith angle distributions and a discrete Fourier transform method to constrain a directional asymmetry in right ascension. In the absence of new physics, the likelihood method can also constrain conventional and prompt atmospheric neutrino flux models. Results from a similar analysis using data from the AMANDA-II detector are also discussed.**

Keywords**: quantum gravity, Lorentz violation, atmospheric neutrinos**

I. Introduction

Physicists have so far been unable to reconcile quantum field theory and general relativity into a coherent theory of quantum gravity (QG). Numerous approaches are in development, and common to many is the possibility that Lorentz invariance is violated at extremely small distance scales (high energy scales), due to a discrete structure of spacetime or an invariant minimum length scale. Interactions with a spacetime foam, or virtual black holes, may also induce quantum decoherence in which pure quantum states evolve into mixed states [1].

Neutrinos, lacking any gauge interactions other than weak, and having extremely high Lorentz factors, are sensitive probes of these effects. Violation of Lorentz invariance (VLI) can induce a number of flavor-changing signatures in neutrinos, including oscillations with unique energy dependencies or directional asymmetries due to a Lorentz-violating preferred frame. Quantum decoherence (QD) can also result in flavor-changing effects that depend upon the neutrino energy.

Atmospheric neutrinos are produced in the decay chains of particles resulting from the interaction of cosmic rays with the earth's atmosphere [2,3]. The IceCube neutrino telescope [4], currently under construction in the glacial ice at the South Pole, detects the Cherenkov radiation emitted by charged particles produced by neutrino interactions in the ice or rock. IceCube has already collected a large sample of atmospheric muon neutrinos in the energy range of 100 GeV to a few tens of TeV, and can search for deficits caused by possible QG effects such as VLI or QD.

We will first review the phenomenological models of QG to be tested. Then, we will discuss event selection and the observables used for the analysis, followed by a discussion of the likelihood and discrete Fourier transform (DFT) methods we use. Finally, results from the AMANDA-II detector, and expected sensitivity of the 40-string configuration of IceCube will be discussed.

II. Phenomenology

A. Violation of Lorentz Invariance

For VLI models, we consider the case of a flavor-dependent dispersion relation, or, equivalently, flavor-dependent limiting velocities that differ from the speed of light [5, 6]. Further, we make the simplifying assumption of a two neutrino model in which the new eigenstates are characterized by a mixing angle ξ and a phase η. This leads to a muon neutrino survival probability of the form:

$$P_{\nu_\mu \to \nu_\mu} = 1 - \sin^2 2\Theta \sin^2 \left(\frac{\Delta m^2 L}{4E} \Re \right).$$

E is the neutrino energy and L the propagation distance for the atmospheric neutrino, which is a function of zenith angle. Θ is the effective mixing angle, given by

$$\sin^2 2\Theta = \big(\sin^2 2\theta + R^2 \sin^2 2\xi + 2R \sin 2\theta \sin 2\xi \cos\eta\big)/\Re^2.$$

The effective oscillation wavelength is

$$\Re = \big(1 + R^2 + 2R\,[\cos 2\theta \cos 2\xi + \sin 2\theta \sin 2\xi \cos\eta]\big)^{-1/2}.$$

R is the ratio between the VLI oscillation wavelength and the mass-induced oscillation wavelength:

$$R = \frac{\Delta c}{c} \frac{E}{2} \frac{4E}{\Delta m^2}.$$

$\Delta c/c$ is the velocity splitting between eigenstates. The VLI oscillation length can be generalized to integral

powers of neutrino energy:

$$\frac{\Delta c}{c}\frac{LE}{2} \rightarrow \Delta\delta\frac{LE^n}{2}.$$

Since mass-induced oscillations are suppressed in the energy range for this analysis, we can make a simplifying assumption and set $\eta = \pi/2$ so that $\cos\eta = 0$. We then have two physics parameters: $\Delta c/c$ and $\sin^2 2\xi$.

B. Decoherence

For quantum decoherence, we use a full three-neutrino model, in which the muon neutrino survival probability can be written [7,8]:

$$\begin{aligned} P_{\nu_\mu\rightarrow\nu_\mu} = \frac{1}{3} + \frac{1}{2}\{ & e^{-\gamma_3 L}\cos^4\theta_{23} \\ & + \frac{1}{12}e^{-\gamma_8 L}\left(1 - 3\cos 2\theta_{23}\right)^2 \\ & + 4e^{\frac{-(\gamma_6+\gamma_7)L}{2}}\cos^2\theta_{23}\sin^2\theta_{23} \\ & \times \left[\cos\left(L\sqrt{m}/2\right)\right. \\ & + \left.\sin\left(L\sqrt{m}/2\right)\left(\gamma_6 - \gamma_7\right)/\sqrt{m}\right]\}, \end{aligned} \tag{1}$$

$$\text{with } m \equiv \left|\left(\gamma_6 - \gamma_7\right)^2 - \left(\Delta m^2_{23}/E\right)^2\right|.$$

To limit the number of physics parameters, we assume that $\gamma_3 = \gamma_8$ and $\gamma_6 = \gamma_7$. The γ_i can be generalized to integral powers of neutrino energy:

$$\gamma_i \rightarrow \gamma_i^*\left(\frac{E}{\text{GeV}}\right)^n \text{GeV}.$$

The units of γ_i^* are then GeV^{-n+1}.

C. Directional Asymmetry

The location of IceCube at the South Pole is ideally suited to search for a sidereal variation in the flux of atmospheric neutrinos. Right ascension (RA) is synonymous with sidereal phase, and azimuthal asymmetries in the detector average out over a year. We use a two-neutrino model derived from the Standard Model Extension (SME), known as the vector model [9]. This model predicts a survival probability that depends on the direction of neutrino propagation:

$$\begin{aligned} P_{\nu_\mu\rightarrow\nu_\mu} = 1 - \sin^2\Big(L\Big[& \left(A_s\right)_{\mu\tau}\sin\left(\alpha + \varphi_0\right) \\ & + \left(A_c\right)_{\mu\tau}\cos\left(\alpha + \varphi_0\right)\Big]\Big). \end{aligned}$$

α is the RA of the neutrino and φ_0 is the offset between the origin of our coordinate system and a 'preferred' direction. A_s and A_c are functions of neutrino energy, E, neutrino direction unit vectors, $\hat{N}$, and four coefficients from the SME, the $(a_L)^\mu$ and $(c_L)^{\mu\nu}$:

$$\left(A_s\right)_{\mu\tau} = \hat{N}^Y\left(a_L^X - 2Ec_L^{TX}\right) - \hat{N}^X\left(a_L^Y - 2Ec_L^{TY}\right),$$

$$\left(A_c\right)_{\mu\tau} = -\hat{N}^X\left(a_L^X - 2Ec_L^{TX}\right) - \hat{N}^Y\left(a_L^Y - 2Ec_L^{TY}\right).$$

Typically, we assume $a_L^X = a_L^Y$ and $c_L^{TX} = c_L^{TY}$ in the analysis. Additionally, while constraining the a_L coefficients, the c_L are set to 0, and when constraining the c_L coefficients, the a_L are set to 0.

III. Event Selection

We are interested in upgoing atmospheric ν_μ events, and the main background is cosmic-ray muons. Even after an initial event selection based on zenith angle, the event sample is dominated, by several orders of magnitude, by misreconstructed cosmic-ray muons. This background is further reduced by event selection cuts that are based on track quality parameters and on fits to alternative track hypotheses. Alternative track hypotheses include downgoing versus upgoing tracks, and coincident muon events.

Since the remaining background contamination is difficult to model with simulation, we require an essentially pure neutrino sample. Final event selection to achieve this level of purity is done using a Boosted Decision Tree (BDT) [10]. The event sample for one year of data from 40-string IceCube is expected to be about 20,000 upgoing neutrinos, with zenith angles between 90 and 180 degrees, and neutrino energies from 100 GeV to about 30 TeV.

IV. Flux Modeling and Binning

Simulated events are weighted by their contribution to conventional [2, 3] and prompt [11–13] atmospheric neutrino flux models. These weights are then multiplied by the applicable oscillation or decoherence survival probability. Nuisance parameters are used in the likelihood analysis to account for the more significant theoretical and experimental uncertainties in flux normalization, spectral index, and zenith angle distribution. Individual events are thus weighted as follows:

$$w = A\left\{Bw_{conv} + Cw_{prompt}\right\}P_{\nu_\mu\rightarrow\nu_\mu},$$

where

$$A = \varepsilon\left(\frac{E}{1\text{ TeV}}\right)^{\Delta\gamma}\left[1 + 2\alpha\left(\cos\theta_Z + 1/2\right)\right],$$

$$B = \left[1 + 2\alpha_c\left(\cos\theta_Z + 1/2\right)\right], \text{ and}$$

$$C = A_p\left(\frac{E}{5\text{ TeV}}\right)^{\Delta\gamma_p}.$$

ε accounts for theoretical and experimental uncertainties in the overall flux normalization, such as ice model uncertainties, optical module (OM) sensitivity uncertainty, interaction rate uncertainties, reconstruction errors, etc. $\Delta\gamma$ accounts for the uncertainty in the primary cosmic ray slope as well as the impact of OM and ice model uncertainties on the observed spectral index. α accounts for the impact of OM and ice model uncertainties on the zenith angle tilt of the observed flux. α_c accounts for theoretical uncertainty in the zenith-angle tilt of the conventional atmospheric neutrino flux, primarily due to uncertainty in the pion to kaon ratio. A_p and $\Delta\gamma_p$ account for theoretical uncertainty in the magnitude and spectral index of the prompt atmospheric neutrino flux, primarily due to uncertainties in charm production cross sections and fragmentation functions.

θ_Z is the zenith angle of the neutrino, and $P_{\nu_\mu \to \nu_\mu}$ is the oscillation or decoherence survival probability. The particular forms of the spectral tilt and zenith angle tilt equations were chosen to minimize the impact on overall normalization as the correction factors are varied.

Events are binned in $\log_{10}(dE/dX)$ and $\cos(\theta_Z)$ for tests of VLI, decoherence, and atmospheric flux models, and in RA for the vector model. dE/dX, with units of GeV m^{-1}, is the average energy loss per unit propagation length of a muon that would produce the detected amount of light, and serves as an estimator for the original neutrino energy. The energy resolution is about 0.3 on a log scale, reducing sensitivity to VLI effects by a factor of two as compared to perfect energy resolution. Histograms for $\log_{10}(dE/dX)$ and $\cos(\theta_Z)$ are 10 x 10, and range from -1.9 to 1.1 for $\log_{10}(dE/dX)$ and -1 to 0 for $\cos(\theta_Z)$. 32 bins, from 0 to 360°, are used for RA, and include events in the declination band 0 to -30° (zenith band 90 to 120°).

Since some of the ν_μ are assumed to oscillate to ν_τ, ν_τ-induced muons are included in the simulation chain. Finally, bin counts for toy Monte Carlo (MC) histograms are varied according to Poisson distributions.

V. Likelihood Ratio Test

To determine the compatibility of various new physics hypotheses with the data and identify acceptance regions, we use a likelihood-ratio test and the ordering principle of Feldman and Cousins [14]. The signal we are looking for is a distortion, or a warping, of the event counts in the energy-zenith plane. A likelihood analysis takes advantage of this shape of the distribution and provides a convenient way to include systematic uncertainties in the overall normalization and shape of the atmospheric neutrino flux. Systematic uncertainties are included using the nuisance parameters discussed above, and the profile construction method [15, 16]. The likelihood function is:

$$L\left(\{n_{ij}\}|\{\mu_{ij}\left(\theta_r,\theta_s\right)\}\right) = \prod_{i,j} \frac{\mu_{ij}^{n_{ij}}}{n_{ij}!} e^{-\mu_{ij}}.$$

n is the binned toy MC or real data and μ is the prediction. θ_r represents the physics parameters and θ_s the nuisance parameters. In practice, this function is maximized by finding the minimum of the negative log of the likelihood, using the Minuit2 package in ROOT [17]. The test statistic is the likelihood ratio,

$$R = -2 \ln \frac{L_0}{\hat{L}}.$$

where L_0 is the maximum likelihood, i.e., the best fit to the data or the toy MC histogram, with physics parameters held fixed and nuisance parmaters allowed to vary over the ranges of their uncertainties. $\hat{L}$ is the maximum likelihood when physics as well as nuisance parameters are allowed to vary.

In the absence of new physics effects, the likelihood method will be used to evaluate theoretical uncertainties in conventional and prompt atmospheric neutrino flux models. For these analyses, experimental and theoretical uncertainties are split into separate nuisance parameters, and those associated with theoretical uncertainties in the conventional and/or prompt neutrino flux become physics parameters.

VI. DFT Analysis

Neutrino oscillations in the vector model depend on the x and y components of the neutrino propagation direction. Hence, a phase angle specifying the offset from a preferred direction is required. To conduct a model-independent search for a sidereal signal independent of an arbitrary assumption about this phase angle, we use a DFT analysis. This analysis is done in two stages and has been adapted from a similar analysis performed with the MINOS detector to search for a directional dependence [18]. In the first stage, the data is checked for consistency with the hypothesis of no sidereal signal. In the second stage, constraints are placed on the SME coefficients of the vector model.

First, a large number of toy experiments are performed in which the right ascensions of all events in the data are randomly redistributed. The power spectral densities (PSDs) in the $n = 1$ to $n = 4$ components of a DFT are computed for each of these 'noise-only' toy experiments. The corresponding frequencies are $n/T_\oplus$, where $T_\oplus$ is a sidereal day. The PSDs of the true data histogram are then computed and compared to the range of PSDs from the toy experiments. This indicates whether the data is consistent with the hypothesis of no sidereal signal.

In the vector model, muon neutrino survivial probability varies with RA with a modulation frequency of $4/T_\oplus$. To constrain the vector model, we look for an excess of power in the $n = 4$ harmonic. The energy and zenith angle distributions are modeled using simulated events and the best-fit nuisance parameter values from the data. A large number of toy MC experiments are created, using these best-fit values. The physics parameters of the vector model are then increased, and the simulated events reweighted accordingly, until a PSD greater than the 99th percentile of the PSDs from the noise-only toy experiments is obtained. The values found in each of these trials are then averaged to find the sensitivity of this analysis given the data and the absence of a signal.

VII. Results and Expectations

In a previous analysis of atmospheric muon neutrino events collected from 2000 to 2006 with the AMANDA-II detector [19], the data were consistent with the Standard Model, and upper limits on QG parameters were set. A VLI upper limit at the 90% CL was found of

$$\Delta c/c < 2.8 \times 10^{-27}$$

for VLI oscillations proportional to the neutrino energy. A QD upper limit at the 90% CL was found of

$$\gamma^* < 1.3 \times 10^{-31}\ \mathrm{GeV}^{-1}$$

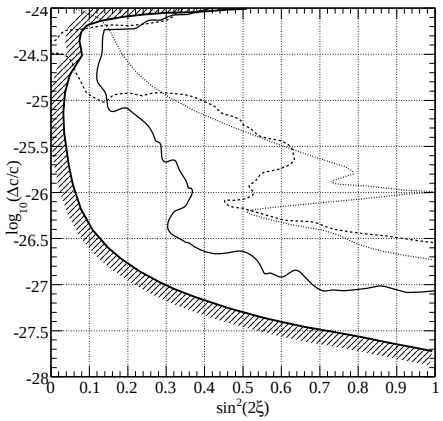

Fig. 1: VLI Model, 90% CL curves. Dashed: AMANDA-II [19]. Dotted: SuperK + K2K [5]. Solid with hash marks: expected 80-string IceCube sensitivity [6]. Solid: expected 40-string IceCube sensitivity (preliminary).

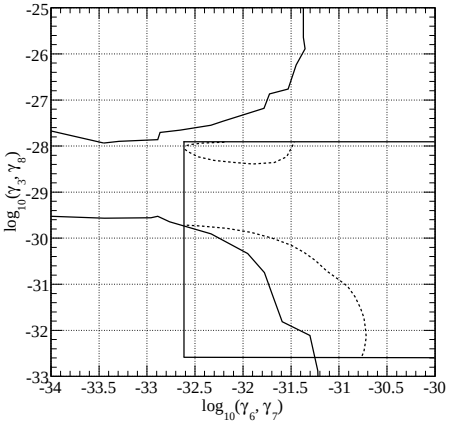

Fig. 2: Decoherence model, 90% CL curves. Dashed: AMANDA-II [19]. Solid: expected 40-string IceCube sensitivity (preliminary). The black box indicates region scanned in AMANDA-II analysis.

for decoherence effects proportional to E^2 and with all γ_i assumed equal. For one year of data from 40-string IceCube, we expect about a factor of three improvement:

$$\Delta c/c < 9.0 \times 10^{-28} \text{ and}$$

$$\gamma^* < 2.5 \times 10^{-32} \text{ GeV}^{-1}.$$

Figure (1) shows 90% CL curves for the $n = 1$ VLI model. Included are the AMANDA-II analysis, SuperK and K2K [5], and expected sensitivity for ten years of data from the full, 80-string, IceCube detector [6]. Also included is the 90% CL curve expected for the 40-string IceCube detector, based on a preliminary treatment of nuisance parameters. Figure (2) shows 90% CL curves for the $n = 2$ decoherence model from the AMANDA-II analysis, and the expected sensitivity for 40-string IceCube (also preliminary).

For the vector model, the sensitivity of the 40-string IceCube detector, at the 99% CL, is expected to be:

$$a_L^X = a_L^Y < 2.0 \times 10^{-23} \text{ GeV},$$
$$c_L^{TX} = c_L^{TY} < 6.6 \times 10^{-27}.$$

These limits are three orders of magnitude lower for the a_L terms and four orders of magnitude lower for the c_L terms than the limits reported in [18]. This is due to the longer baseline of atmospheric neutrinos, and higher energy reach of IceCube.

Data from AMANDA-II were used to find that the best-fit flux Φ for conventional atmospheric neutrinos, starting with the flux (Φ_{Barr}) of reference [2] is:

$$\Phi = (1.1 \pm 0.1) \left(\frac{E}{640 \text{ GeV}} \right)^{0.056} \Phi_{\text{Barr}}.$$

This likelihood methodology will also be used with IceCube data to constrain conventional and prompt atmospheric neutrino flux models.

VIII. Conclusions

Data from IceCube's 40-string configuration will improve constraints on VLI and decoherence models beyond that achieved with AMANDA-II. Additionally, it will significantly improve constraints on a certain class of direction-dependent oscillation models.

The IceCube detector will be able to provide improved constraints on various models of quantum gravity and atmospheric neutrino flux models as the detector grows to its final design configuration and as data collection continues in the following years. The likelihood method and the flux weighting discussed above provide flexibility to adjust nuisance parameter ranges as IceCube systematic uncertainties become better constrained.

References

[1] S.W. Hawking, *Commun. Math. Phys.*, 87:395 (1982).
[2] G.D. Barr *et al.* , *Phys. Rev. D.*, 70:023006 (2004).
[3] M. Honda *et al.* , *Phys. Rev. D.*, 75:043006 (2007).
[4] A. Karle, *arXiv:0812.3981v1*.
[5] M.C. Gonzalez-Garcia and M. Maltoni, *Phys. Rev. D.*, 70:033010 (2004).
[6] M.C. Gonzalez-Garcia, F. Halzen and M. Maltoni, *Phys. Rev. D.*, 71:093010 (2005).
[7] A.M. Gago *et al.* , *arXiv:hep-ph/0208166v1*.
[8] L. Anchordoqui and F. Halzen, *Annals Phys.*, 321:2660 (2006).
[9] V.A. Kostelecky and M. Mewes, *Phys. Rev. D.*, 70:076002 (2004).
[10] A. Hocker *et al.* , *arXiv:physics/0703039v4*.
[11] R. Enberg, M.H. Reno and I. Sarcevic, *Phys. Rev. D.*, 78:043005 (2008).
[12] A.D. Martin, M.G. Ryskin and A.M. Stasto, *Acta Phys. Polon. B*, 34:3273 (2003).
[13] G. Fiorentini, A. Naumov and F.L. Villante, *Phys. Lett. B*, 510:173 (2001).
[14] G.J. Feldman and R.D. Cousins, *Phys. Rev. D.*, 57:3873 (1998).
[15] G.J. Feldman, "Multiple measurements and parameters in the unified approach," Workshop on Confidence Limits, Fermilab (2000).
[16] K. Cranmer, in *Statistical Problems in Particle Physics, Astrophysics and Cosmology: Proceedings of PHYSTAT05*, L. Lyons and M. Ünel, eds., (Univ. of Oxford, U.K., 2005);*arXiv:physics/0511028v2*.
[17] R. Brun and F. Rademakers, *Phys. Res. A*, 389:81 (1997).
[18] P. Adamson *et al.* , *Phys. Rev. Lett.*, 101:151601 (2008).
[19] R. Abbasi *et al.* , *arXiv:0902.0675v1*.

A First All-Particle Cosmic Ray Energy Spectrum From IceTop

Fabian Kislat*, Stefan Klepser†, Hermann Kolanoski‡ and Tilo Waldenmaier‡ for the IceCube Collaboration*

*DESY, D-15738 Zeuthen, Germany
†IFAE Edifici Cn., Campus UAB, E-08193 Bellaterra, Spain
‡Institut für Physik, Humboldt-Universität zu Berlin, D-12489 Berlin, Germany
*See special section of these proceedings

Abstract. **The IceTop air shower array is presently under construction at the geographic South Pole as part of the IceCube Observatory. It will consist of 80 stations which are pairs of Ice-Cherenkov tanks covering an area of $1\,\mathrm{km}^2$. In this paper a first analysis of the cosmic ray energy spectrum in the range $2 \cdot 10^{15}\,\mathrm{eV}$ to $10^{17}\,\mathrm{eV}$ is presented using data taken in 2007 with 26 IceTop stations. The all-particle spectrum has been derived by unfolding the raw spectrum using response matrices for different mass compositions of the primaries. Exploiting the zenith angle dependence of the air shower development we have been able to constrain the range of possible composition models.**

Keywords**: IceTop - Energy - Spectrum**

I. Introduction

The IceTop air shower array is currently under construction as part of the IceCube Observatory at the geographic South Pole [1], [2]. Its 80 detector stations will cover an area of about $1\,\mathrm{km}^2$ at an atmospheric depth of $680\,\mathrm{g/cm}^2$. Each station consists of two ice filled $1.8\,\mathrm{m}$ diameter tanks each equipped with two Digital Optical Modules (DOMs) [3] as photon sensors (the same as used by IceCube in the deep ice). The photomultipliers inside the two DOMs are operated at different gains to increase the dynamic range.

Air showers are detected via the Cherenkov light emitted by charged particles inside the ice tanks. The light intensity is recorded by an 'Analog Transient Waveform Digitizer' (ATWD) at a $300\,\mathrm{MSPS}$ sampling rate. When the signal inside a DOM crosses a threshold a 'local coincidence' signal is sent to neigbouring DOMs. Data taking is started when a local coincidence signal is received from the high gain DOM in the other tank of a station within $250\,\mathrm{ns}$. This ensures that the two tanks of a station always trigger together. This analysis only uses events where at least five stations have triggered.

The analysis uses the signal sizes, obtained by integrating the waveforms, and the arrival times, determined from the leading edge of a waveform. Because of its high altitude of $2835\,\mathrm{m}$, IceTop is located close to the shower maximum for showers of energies between $10^{15}\,\mathrm{eV}$ and $10^{17}\,\mathrm{eV}$ (about $550\,\mathrm{g/cm}^2$ to $720\,\mathrm{g/cm}^2$). Therefore, the signals measured by IceTop are dominated by the electromagnetic component of the air showers.

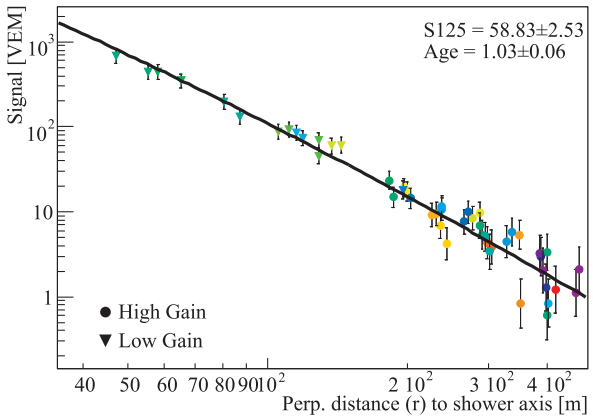

Fig. 1. An example of a lateral signal size distribution from a single event in IceTop. Each data point corresponds to the signal in terms of Vertical Equivalent Muons measured in an IceTop tank. The curve is a fit of the lateral distribution function (1).

II. Energy reconstruction

Generally, the shower direction can be reconstructed from the arrival times of signals, while the core position and the primary energy of the air shower are inferred from the lateral distribution of signal sizes. These signal sizes are calibrated with signals from vertical muons to eliminate differences between the tanks. Signals given in units of Vertical Equivalent Muons (VEM) are a detector independent measure of the intensity of an air shower at the position of a tank.

A first estimate of the shower core position is obtained by finding the signal center-of-gravity which is defined as the average of the tank positions weighted by the square-root of the signal size. The shower direction is obtained by fitting a plane to the measured signal times. These two first guesses are used as an input to a more accurate iterative maximum likelihood fit.

In the latter procedure a lateral distribution function is fitted to the measured signal sizes and an arrival time distribution is fitted to the signal times. The lateral distribution function [4] has been obtained from air shower and detector simulations and corresponds to a second order polynomial on a double logarithmic scale:

$$S(r) = S_{\mathrm{ref}} \left(\frac{r}{R_{\mathrm{ref}}} \right)^{-\beta_{\mathrm{ref}} - \kappa \log_{10}(r/R_{\mathrm{ref}})} \qquad (1)$$

S_{ref} is the signal expectation value at the reference radius R_{ref} from the shower axis, β_{ref} is a slope parameter related to the shower age and κ is a curvature parameter of the lateral signal distribution function. Based on a study of the stability of fit results the reference radius has been fixed to $R_{\mathrm{ref}} = 125\,\mathrm{m}$ which also corresponds to the IceTop grid spacing. An example is shown in Figure 1. The likelihood function used in the fitting procedure is based on a study of signal fluctuations and also takes into account stations that do not trigger [4]. Taking into account the spatial curvature of the shower front, which is assumed to have a fixed profile [5], the arrival time distribution $t(r)$ is given by:

$$t(r) = 19.41\,\mathrm{ns}\left(e^{-\left(\frac{r}{118.1\,\mathrm{m}}\right)^2} - 1\right) - 4.823 \cdot 10^{-4}\,\frac{\mathrm{ns}}{\mathrm{m}^2}\,r^2 \tag{2}$$

This $t(r)$ indicates the time delay of a signal at distance r from the shower axis with respect to a planar shower front through the shower core and perpendicular to the shower axis. Using this shower front parametrisation improves the direction resolution compared to the plane fit first guess result.

The complete log-likelihood function, therefore, has three terms,

$$L = L_{\mathrm{hit}} + L_{\mathrm{nohit}} + L_{\mathrm{time}} \tag{3}$$

L_{hit} is based on the log-normal distribution of signal sizes obtained from the study of signal size fluctuations, L_{time} is based on an assumed Gaussian distribution of arrival times and L_{nohit} is defined by

$$L_{\mathrm{nohit}} = \sum \log\left(1 - P^A_{\mathrm{hit}} P^B_{\mathrm{hit}}\right) \tag{4}$$

P^i_{hit} is the probability that tank i of a station triggers given the signal expectation of the fit at that iteration step, given the shower core position and direction. The likelihood accounts for the 'local coincidence' condition which requires both tanks of a station to trigger before signals are transmitted. The sum in (4) runs over all stations that did not trigger.

The fit procedure is divided into several steps to improve the stability. At first the direction is fixed to the initial first guess value and only the lateral signal distribution (1) is fitted. In a second iteration the direction is also varied but the parameters of the lateral fit are limited to a $\pm 3\sigma$ range around the values obtained in the first step. Finally a last iteration with fixed direction is performed. The slope parameter of the lateral distribution function is limited throughout this procedure to $1.5 \leq \beta_{125} \leq 5$.

Using the results of the fit a first-guess energy is determined as a function of shower size and the zenith angle. As a measure of the shower size, the signal expectation value $S_{\langle \log r \rangle}$, at the distance $\langle \log r \rangle$ from the core is used, where $\langle \log r \rangle$ is the average of the logarithmic distance of tanks to the shower axis. The size parameter $S_{\langle \log r \rangle}$ has been found to be least correlated to the other fit parameters (in general S_{125} and the slope β_{125} are correlated). From air shower simulations an energy estimator $E_{\mathrm{rec}}(S_{\langle \log r \rangle}, \theta)$ for any given $\langle \log r \rangle$ based on a proton hypothesis has been derived.

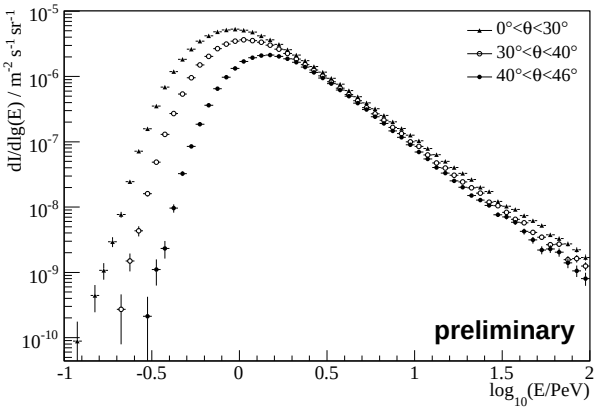

Fig. 2. Raw IceTop energy spectrum divided into three different zenith angle ranges (see text for details).

To ensure the quality of the reconstructed data several quality criteria are applied:

- Only showers with a zenith angle $\theta < 46°$ are considered restricting the analysis to a well understood zenith angle range;
- The value of the slope parameter must be $1.55 \leq \beta_{125} < 4.95$ removing all showers for which the likelihood fit ran into the limits on this parameter;
- The uncertainty on the shower core position must be less than $20\,\mathrm{m}$;
- The core position from the likelihood fit and the center-of-gravity first guess must be inside the IceTop array, $50\,\mathrm{m}$ away from the array border. Furthermore, the station with the largest signal must not be on the border of the IceTop array.

The last item is to exclude showers with a core outside the array which have a high probability to be misreconstructed. Using the likelihood fit result alone is not sufficient because the fit tends to reconstruct these cores inside the array. These strict requirements on the core reconstruction are necessary because the position of the core directly influences the interpretation of the fitted lateral distribution. Data was taken between June 1st 2007 and October 31st 2007 with the 26 IceTop stations operated at that time. The filter level data sample contained 11 262 511 events. After all of the above cuts, 4 131 343 events remained.

The raw energy spectrum, that is the distribution of the reconstructed energies E_{rec} without any further corrections or unfolding applied, but after the abovementioned cuts, is shown in Figure 2. The data is split into three zenith angle ranges, $0 \leq \theta < 30°$, $30° \leq \theta < 40°$ and $40° \leq 46°$.

III. Air shower simulations

The relation between the measured signals and the properties of the primary particle can only be obtained

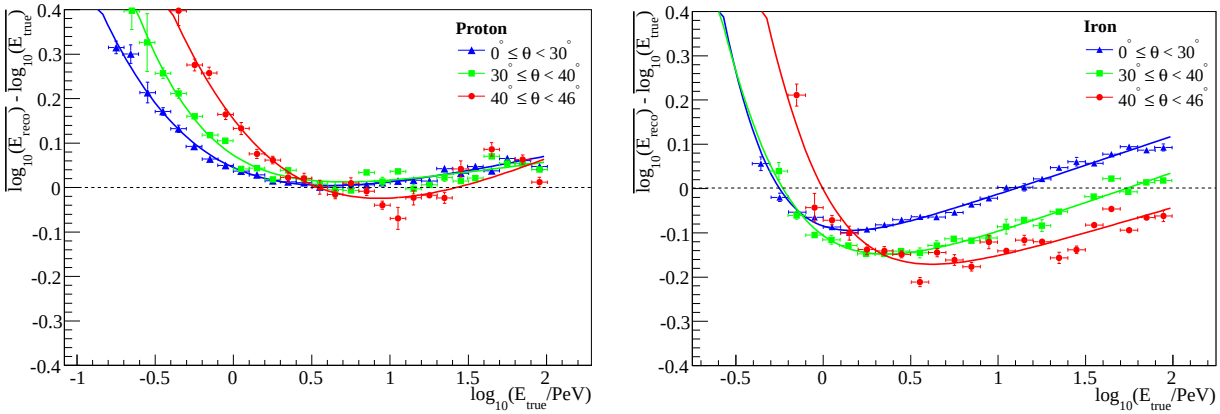

(a) Primary protons (b) Primary iron

Fig. 3. Systematic energy shift for (a) protons and (b) iron when using the energy estimator E_{rec} as a function of the true energy of a particle. This energy mis-reconstruction is one of the parameters describing the energy response of the IceTop detector. The strong increase towards low primary energies is a threshold effect as explained in the text. Since E_{rec} is based on the proton assumption the energy mis-reconstruction for protons is small while that for primary iron larger and shows a clear zenith angle dependance.

from simulations of air showers and the detector. Therefore, a Monte Carlo shower library containing 98 760 proton and iron showers with primary energies between $100\,\mathrm{TeV}$ and $100\,\mathrm{PeV}$ has been generated with CORSIKA [6]. The hadronic interaction models SIBYLL [7] and Fluka 2006.3b [8] and the CORSIKA atmosphere model No. 14 (South Pole, Dec. 31, 1997, MSIS-90-E) were used.

IV. Unfolding the spectrum

The energy estimator E_{rec} does not fully account for the angular and energy dependence of the detector acceptance and smearing. This biases the result especially in the threshold region where the detection efficiency increases strongly with energy. In addition, the calculation of E_{rec} assumes proton primaries and one specific atmosphere profile (CORSIKA atmosphere 12, South Pole July 01, 1997). A different atmosphere profile or a different composition of primary particles can result in a different energy spectrum. All these effects can be taken into account by unfolding the raw energy spectrum.

The unfolding algorithm uses a response matrix which contains the probability that an incident primary particle with true energy E_{true} will be assigned the energy E_{rec}. Response matrices are generated from CORSIKA air shower simulations for proton and iron primaries in three different zenith angle ranges. Response matrices for mixed compositions are obtained as linear combinations of these single primary particle responses.

To calculate the response matrices the simulated data are subdivided into 30 bins of true primary energies, equidistant in $\log_{10}(E_{\mathrm{true}})$. For each bin the energy response is obtained from a distribution of $\log_{10}(E_{\mathrm{rec}}/E_{\mathrm{true}})$ of all reconstructed events which is approximately normally distributed. Non-zero values of this quantity indicate a wrong energy reconstruction. As such the mean of this distribution is the 'energy mis-reconstruction', the width is the energy resolution. The reconstruction efficiency is the ratio between the number of reconstructed and generated events.

Depending on the zenith angle, the IceTop detector gets fully efficient at about $2\,\mathrm{PeV}$ with an effective area of $0.096\,\mathrm{km}^2$. The energy resolution improves with increasing energy and reaches a value of 0.05 in logarithm of energy at $10\,\mathrm{PeV}$ primary energy which corresponds to a statistical uncertainty of roughly $12\,\%$.

An important property of the detector response is the 'energy mis-reconstruction' shown in Figure 3. It is the systematic difference between the true primary energy and the reconstructed energy. The energy mis-reconstruction shows a strong dependence on the primary particle mass and thus on the assumed primary composition. The attenuation of iron induced showers with increasing slant depth is greater than for proton showers. This leads to an underestimation of the primary energy for inclined iron showers when using the proton-based energy estimator E_{rec}. This is nicely visible in Figure 3b.

V. Preliminary energy spectrum from IceTop

Based on these response matrices the three raw energy spectra of Figure 2 are unfolded using an iterative unfolding method [9]. An unfolding based on three different composition assumptions has been made: pure proton, pure iron and the two-component model consisting of proton and iron primaries as motivated in [10].

The results are shown in Figure 4. Above $4\,\mathrm{PeV}$ the spectra have a spectral index ranging from 2.93 to 3.19, depending on the composition assumption and the zenith angle band. The absolute normalization varies between $3.77 \cdot 10^{-15}\,\mathrm{m}^{-2}\mathrm{s}^{-1}\mathrm{sr}^{-1}\mathrm{GeV}^{-1}$ and $7.93 \cdot 10^{-15}\,\mathrm{m}^{-2}\mathrm{s}^{-1}\mathrm{sr}^{-1}\mathrm{GeV}^{-1}$ at an energy of $10\,\mathrm{PeV}$.

The abovementioned mis-reconstruction of the energy of inclined iron showers leads to a relative shift of the

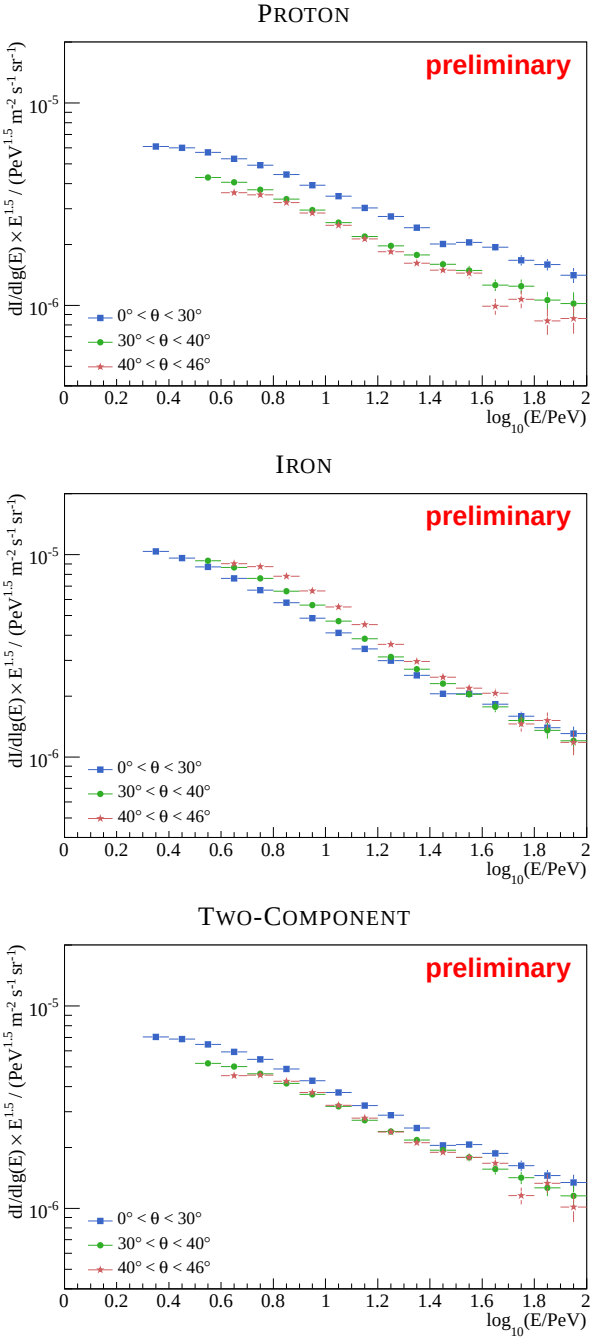

Fig. 4. Unfolding result for three different assumptions on the primary compositions: pure protons, pure iron, two-component model [10].

spectra from different zenith bands in the unfolding. In case of proton primaries the spectrum from the most vertical zenith bin shows the largest flux and the spectrum from the $40°$ to $46°$ zenith band shows the lowest flux. This order is reversed if the primary particles are assumed to be purely iron. Since there are no indications of an anisotropy of the arrival directions of cosmic rays in the energy range under consideration, isotropy has to be assumed. An isotropic flux, however, means that the unfolded spectra obtained from different zenith bands must agree.

VI. Conclusions and Outlook

A first analysis of the energy spectrum of cosmic rays in the range between $2\,\mathrm{PeV}$ and $100\,\mathrm{PeV}$ has been presented. This analysis uses an unfolding procedure to account for detector and atmospheric influences as well as differences in the shower development of different primary particles. Energy spectra have been obtained for three different compositions and three different zenith angle ranges. In case of a pure proton or iron hypothesis the three different inclination spectra do not agree which is in conflict with the assumption of an isotropic flux. Therefore those two pure composition assumptions can be excluded.

Several issues have not yet been addressed in this early study. Most importantly, the systematic uncertainties due to the interaction models used in the simulations must be studied. Also the influence of different atmosphere parametrisations in the simulation must be analysed and understood. This becomes even more important when analysing data from a longer period of time. Currently, in 2009, the detector is running with nearly three quarters of the full detector.

References

[1] T.K. Gaisser *et al. IceTop: The Surface Component of IceCube*, in *Proc. 28th ICRC*, Tsukuba, Japan, 2003.
[2] T.K. Gaisser *et al. Performance of the IceTop Array*, in *Proc. 30th ICRC*, Mérida, Mexico, 2007; arXiv:0711.0353v1.
[3] R. Abbasi *et al.* "The IceCube Data Acquisition System: Signal Capture, Digitization, and Timestamping," Nucl. Instrum. Meth. A **601**, 294 (2009).
[4] S. Klepser *et al. Lateral Distribution of Air Shower Signals and Initial Energy Spectrum above 1 PeV from IceTop*, in *Proc. 30th ICRC*, Mérida, Mexico, 2007; arXiv:0711.0353v1.
[5] S. Klepser *et al. First Results from the IceTop Air Shower Array*, in *Proc. 21st ECRS*, Košice, Slovakia, 2008; arXiv:0811.1671v1.
[6] D. Heck *et al.*, Report **FZKA 6019** (1998), Forschungszentrum Karlsruhe; http://www-ik.fzk.de/corsika/physics_description/corsika_phys.html
[7] R. Engel, T.K. Gaisser, P. Lipari, and T. Stanev, *Air shower calculations with the new version of SIBYLL*, in *Proc. 26th ICRC*, Salt Lake City, USA, 1999.
[8] A. Ferrari, P.R. Sala, A. Fassò, and J. Ranft, "FLUKA: a multi-particle transport code", CERN-2005-10 (2005), INFN/TC 05/11, SLAC-R-773.
[9] G. D'Agostini, "A multidimensional unfolding method based on Bayes' theorem," Nucl. Instrum. Meth. A **362**, 487 (1995)
[10] R. Glasstetter *et al. Analysis of electron and muon size spectra of EAS*, in *Proc. 26th ICRC*, Salt Lake City, USA, 1999.
[11] S. Klepser, "Reconstruction of Extensive Air Showers and Measurement of the Cosmic Ray Energy Spectrum in the Range of $1 - 80\,\mathrm{PeV}$ at the South Pole", Dissertation, Humboldt-Universität zu Berlin, 2008.

Reconstruction of IceCube coincident events and study of composition-sensitive observables using both the surface and deep detector

Tom Feusels*, Jonathan Eisch† and Chen Xu‡, for the IceCube Collaboration§

*Dept. of Subatomic and Radiation Physics, University of Gent, B-9000 Gent, Belgium
†Dept. of Physics, University of Wisconsin, Madison, WI 53706, USA
‡Bartol Research Institute, University of Delaware, Newark, DE 19716, USA
§See the special section in these proceedings

***Abstract*. The combined information from cosmic ray air showers that trigger both the surface and underground parts of the IceCube Neutrino Observatory allows the reconstruction of both the energy and mass of the primary particle through the knee region of the energy spectrum and above. The properties of high-energy muon bundles, created early in the formation of extensive air showers and capable of penetrating deep into the ice, are related to the primary energy and composition.**

New methods for reconstructing the direction and composition-sensitive properties of muon bundles are shown. Based on a likelihood minimization procedure using IceCube signals, and accounting for photon propagation, ice properties, and the energy loss processes of muons in ice, the muon bundle energy loss is reconstructed. The results of the high-energy muon bundle reconstruction in the deep ice and the reconstruction of the lateral distribution of low energy particles in the surface detector can be combined to study primary composition and energy. The performance and composition sensitivity for both simulated and experimental data are discussed.

***Keywords*: Cosmic ray composition, IceTop/IceCube, high-energy muon bundles**

I. Introduction

The cosmic ray spectrum covers many orders of magnitude in both energy and flux. In the energy range accessible to the IceCube Neutrino Observatory ($\sim$0.3 PeV to 1 EeV) the slope of the spectrum remains mostly constant, except for a feature at around 3 PeV where the spectrum steepens. This feature is called the knee of the cosmic ray spectrum, and its origin is unknown. Proposed explanations include changes in acceleration mechanisms or cosmic rays leaking from the galactic magnetic field starting at this energy. Measurement of mass composition in this range could give clues to the origin of these cosmic rays. The IceCube detector, together with the IceTop air shower detector, provides an opportunity to measure the composition of cosmic ray particles in the region of the knee and beyond.

The IceTop detector, high on the Antarctic Plain at an average atmospheric depth of 680 g/cm^2, consists of a hexagonal grid of detector stations 125 m apart. Each station consists of two ice tanks that act as Cherenkov media for measuring mainly the electromagnetic component of cosmic ray air showers. In each tank, two Digital Optical Modules (DOMs) are deployed, which contain a 10 inch PMT and digital readout and control electronics. The primary energy can be reconstructed by the IceTop surface array [1].

Deep below each IceTop station is a string of the IceCube detector with 60 DOMs evenly spaced between 1.5 and 2.5 km in the ice. Combined, the IceTop and IceCube arrays can reconstruct the air shower core position and direction while measuring the shower signal strength at the surface and the energy deposition of the high-energy muon bundle in the deep ice. With these measurements, the energy and mass of the primary cosmic rays can be reconstructed.

A characteristic difference between showers induced by light and heavy nuclei for a fixed primary energy is their number of muons, with higher mass primaries producing more muon-rich showers. However, the muon multiplicity is not directly measured by either the IceTop or IceCube detectors. The deep IceCube detector is sensitive to Cherenkov light coming mainly from energy loss processes of high-energy muon bundles. This energy loss is a convolution of the muon multiplicity of the shower, the muon energy distribution and the energy loss of a single muon. If the energy loss behavior of muon bundles can be reconstructed accurately, it can be used as a primary mass indicator [2]. In Section IV, the reconstructed muon bundle track described in Section III will be used as a seed to reconstruct the muon bundle energy loss. Simulated data is compared to experimental data in Section V to examine the detector performance and its sensitivity to composition.

II. Data Sample and Simulation

Our experimental data sample was taken from the month of September, 2008. At that time, the detector consisted of 40 IceTop stations and 40 IceCube strings. A total livetime of 28.47 days was obtained by selecting only runs where both detectors were stable. The events were processed at the South Pole with a filter which required at least three triggered IceTop stations and at

least 8 triggered IceCube DOMs. After this filter about $3.31{\cdot}10^6$ coincident events remained.

To study the direction and energy reconstruction of muon bundles in the ice, a large number of proton and iron showers between 10 TeV and 46.5 PeV were simulated with the CORSIKA [3] package. SIBYLL 2.1 [4], [5] was used as the high-energy (>80 TeV) hadronic interaction model, while FLUKA08 [6], [7] was used as the low energy hadronic interaction model. For this study, CORSIKA was configured to use a model of the South Pole atmosphere typical for the month of July [8]. The showers were simulated according to an E^{-1} spectrum and then reweighted according to an $E^{-2.7}$ spectrum before the knee (at 3 PeV) and an $E^{-3.0}$ spectrum after the knee.

The IceCube software environment was used to resample each CORSIKA shower 500 times on and around the detector, to propagate the high-energy muons through the ice, and to simulate the detector response and trigger. The simulation was filtered the same way as data and yielded about $9.0{\cdot}10^4$ proton and $9.0{\cdot}10^4$ iron events.

III. Direction Reconstruction

The direction reconstruction by IceTop will be described first because it will be used later as a seed for an IceCube muon bundle reconstruction algorithm.

An initial shower core position and direction is determined using the extracted times and charges of the recorded pulses from the IceTop tanks. The first guess core position is the calculated center of gravity of tank signals, while the initial direction reconstruction assumes a flat shower front. This shower core and direction are then used as a seed to fit the lateral distribution of pulses with the double logarithmic parabola (DLP) function described in [9]. Because the reconstruction of the core and direction are highly correlated, the resolution is improved by fitting the shower core position and the shower direction together, with a curved shower front and the DLP lateral particle distribution. This fit, and some geometrical quality cuts discussed later, gives an angular resolution[1] of 1.0° for iron showers (see the dot-dot-dashed line in Fig. 1) and a core resolution of 15.0 m (see dot-dashed line in Fig. 2).

The resolution depends strongly on where the shower core lands with respect to the IceTop array. This analysis uses only events with a shower core reconstructed within the geometrical area of the IceTop detector. The reconstructed muon bundle track was also required to pass within the instrumented volume of the IceCube detector.

The direction that was already reconstructed by the IceTop algorithms alone can serve as a seed for an algorithm more specialized in reconstructing muon bundles in the ice. This algorithm uses only the charges measured

[1]The resolution of observable Y is defined according to $\int_0^x p(\Delta Y)\,\mathrm{d}\Delta Y = 0.683$, where x is the resolution and $p(\Delta Y)$ the frequency of distances between the true and the reconstructed observable.

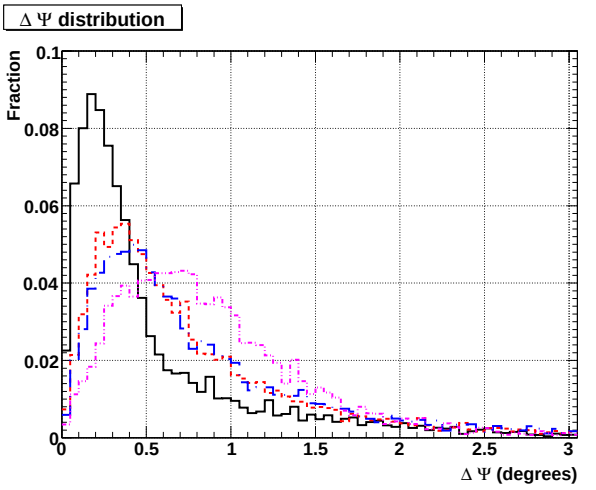

Fig. 1. The distribution of the angles between the true direction and the reconstructed direction for simulations of iron showers is shown for different algorithms. The dot-dot-dashed curve shows the reconstruction which uses IceTop information alone. For the dot-dashed line, the reconstructed core position by IceTop is fixed and the zenith and azimuth are determined by using a muon bundle algorithm seeded with the track determined by IceTop. The solid line illustrates the ideal limit of this reconstruction method by using the true shower core position instead of the reconstructed one. The dashed curve is obtained when a second iteration between IceTop and IceCube algorithms is used.

by the IceCube DOMs and takes into account the range-out of the muons in a bundle [10]. By keeping the reconstructed core position on the surface fixed, a large lever arm of at least 1500 m is obtained. This limits the track parameters (zenith and azimuth) during the minimization procedure and reduces the number of free track parameters from 5 to 2.

In Fig. 1, it can be seen that this method (dot-dashed line) improves on the angular resolution determined by IceTop alone. If the core position can be determined more accurately, the direction reconstruction will be even better. The solid line on Fig. 1 represents the ideal limit, obtained using the true core position. Therefore, to improve the core resolution the new direction is kept fixed and used to seed the IceTop lateral distribution function which then only fits the core position (dashed line on Fig. 2). Iterating over both the surface and the deep detector reconstructions with progressively better core position and direction seeds, leads to the optimal resolution. The ideal limit for the core resolution is acquired by seeding the IceTop algorithm with the true direction and is shown on Fig. 2 (solid line). After the second iteration this limit is already obtained and gives a core resolution of 14.0 m and an angular resolution of 0.9° (see dashed lines in Figures 1 and 2).

Using this combined method for muon bundle direction reconstruction, an almost energy independent angular resolution of 0.8° and a core resolution of 12.5 m is obtained for proton induced showers. An improvement of the core resolution and direction resolution also improves the resolution of the reconstructed shower size and shower age.

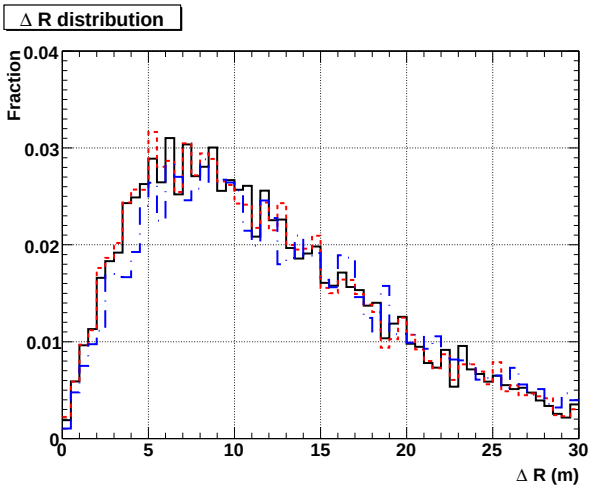

Fig. 2. The distribution of distances between the true shower core position and the reconstructed core position at the surface for iron showers is plotted for different reconstructions. For the dash-dotted line the IceTop DLP function that determines the core position used a first guess direction. The dashed line, where the IceTop algorithm was seeded with a better direction reconstruction from the deep ice, gives a slightly better core reconstruction. When the true direction is used as a seed, the ideal limit represented by the solid line is obtained.

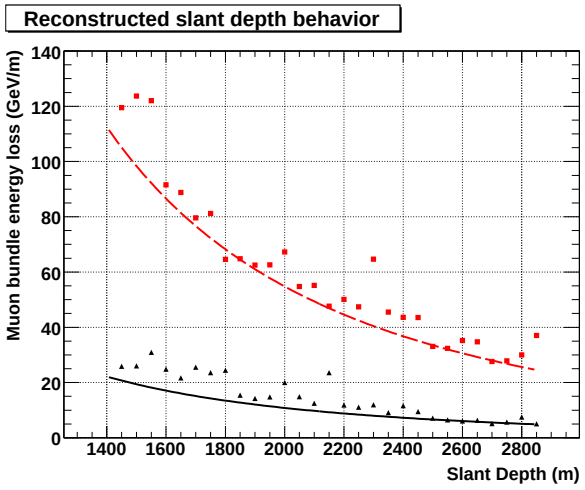

Fig. 3. An example of reconstructed muon bundle energy loss for a single 17 PeV iron and proton shower. The reconstructed slant depth behavior follows the true energy loss reasonably well. The triangles (squares) are the muon bundle energy loss processes for a certain proton (iron) 17 PeV shower with a zenith angle of 28.4° (12.6°). The spread of the points illustrates the stochastic nature. The solid (dashed) line is the reconstructed muon bundle energy loss function, described in the text, for the proton (iron) shower.

IV. Muon Bundle Energy Reconstruction

An energy reconstruction algorithm for single muons was previously reported in Ref. [12]. Using IceCube signals and lookup tables together with a previously reconstructed track a constant energy loss is fit with a likelihood function. The lookup tables model the South Pole ice properties and the propagation of Cherenkov photons through the ice. A single high-energy muon above 730 GeV loses energy mainly by radiative processes like Bremsstrahlung and pair production, which produce secondary electromagnetic cascades in the ice along the muon bundle track. Therefore, an infinite light source with mono-energetic cascades every meter is used as a model for a single muon.

This light model can also be used for muon bundles. The main difference is that a slant depth dependent energy loss will be needed because of the range-out of muons. Here, the slant depth is defined as the distance along the muon bundle track between the point where the muon enters the ice and the point where the Cherenkov light is emitted.

The equation for the muon bundle energy loss is:

$$\left(\frac{dE_\mu}{dX}\right)_{\text{Bundle}}(X) = \int_{E_{\min(\text{surf})}}^{E_{\max(\text{surf})}} \frac{dN_\mu}{dE_\mu}\frac{dE_\mu}{dX} dE_\mu(\text{surf})\,, \tag{1}$$

where $\frac{dN_\mu}{dE_\mu}$ is the energy distribution of the muons and $\frac{dE_\mu}{dX}$ is the energy loss of a single muon. $E_{\min(\text{surf})} = \frac{a}{b}\left(e^{bX}-1\right)$ is the minimum energy that a muon needs to get to depth X. $E_{\max(\text{surf})} \propto \frac{E_0}{A}$ is the maximum energy a muon from a shower induced by a particle with A nucleons and primary energy E_0 can have.

Using a simple power-law as an approximation for the Elbert formula [13], which describes the multiplicity of high-energy muons in air showers, the differential muon energy distribution becomes:

$$\frac{dN_\mu}{dE_\mu} = \gamma_\mu\,\kappa(A)\left(\frac{E_0}{A}\right)^{\gamma_\mu-1} E_\mu^{-\gamma_\mu-1}\,, \tag{2}$$

where $\gamma_\mu = 1.757$ is the muon integral spectral index and κ is a normalization that depends on the shower properties.

With the solution of the single muon energy loss equation, $E_\mu(X) = \left(E_\mu(\text{surf}) + \frac{a}{b}\right) e^{-bX} - \frac{a}{b}$, the average energy loss formula can be expressed as a function of the muon energy at the surface:

$$\begin{aligned}\frac{dE_\mu}{dX}(X) &= -a - bE_\mu(X) \\ &= -b\left(E_\mu(\text{surf}) + \frac{a}{b}\right)e^{-bX}\,,\end{aligned} \tag{3}$$

with $a = 0.260\,\text{GeV/m}$, the ionization energy loss constant and $b = 0.000357\,\text{m}^{-1}$, the stochastic energy loss constant from [11].

The average muon bundle energy loss function is then obtained by integrating Eq. (1) using Eqs. (2) and (3). This energy loss fit function, with κ and E_0/A as free parameters, will be used to scale the expected charges in a DOM from the likelihood formula in [12] instead of scaling it with a constant energy loss.

In Fig. 3, the curves show the reconstructed muon bundle energy loss functions for 17 PeV primaries. The data points are the energy losses calculated from simulations. It can be clearly seen that the muon bundle energy loss function obtained by minimizing the likelihood function describes the depth behavior for these two

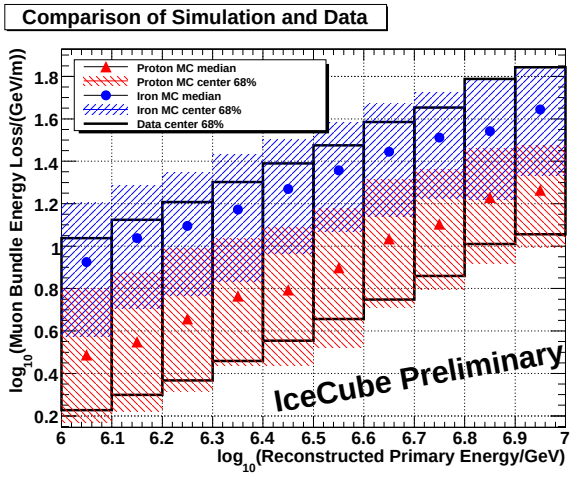

Fig. 4. The reconstructed muon bundle energy loss evaluated at a slant depth of 1650 m versus the reconstructed shower primary energy. Shown are the center 68% of the proton simulation (right diagonal hashes), the iron simulation (left diagonal hashes) and the center 68% of the data (enclosed in the rectangles). The median of the distribution is also shown for the simulated data sets. The events were filtered as described in Section II with the additional quality requirement that the muon bundle reconstruction algorithm used signals from at least 50 DOMs, to remove events with poorly fit energy loss. This quality cut removes a higher portion of muon bundles with low energy loss and will be accounted for in a full composition analysis.

showers better than a constant energy loss function.

It has been shown in [2] that proton and iron showers are separated better by the muon bundle energy loss at smaller slant depths. The reconstructed IceCube composition-sensitive parameter which will be used further on in the coincidence analysis, is the energy loss at the top of the IceCube detector, at a slant depth of 1650 m. At this slant depth, Cherenkov light from showers with a zenith angle up to 30° can still be detected by the upper DOMs, making the energy reconstruction more accurate over the entire zenith range.

V. Combined Primary Mass and Energy Reconstruction

Fig. 4 shows a comparison of proton and iron primary simulation and experimental data described in Section II using the reconstruction methods described in the sections III and IV. While this plot has only rough quality cuts, it can be seen that the spread in the simulation is similar to the spread in the data. The median muon bundle energy loss from an iron primary shower is approximately a factor of 2 higher in the ice than the median muon bundle energy loss from a proton primary shower for the same reconstructed primary energy. There is a large overlap area, where shower to shower fluctuations overcome the effect of the primary mass. It is difficult to reconstruct the primary mass of a single shower with any certainty due to these large fluctuations.

VI. Conclusion and Outlook

The IceTop and IceCube detectors of the IceCube Neutrino Observatory can be used together for an improved air shower core location and direction reconstruction. The promising method of reconstructing the muon bundle energy loss behavior will be further developed to be used in a measurement of cosmic ray mass and energy. This study used only a subsample of the available data; with more statistics and an enlarged detector these methods can be extended up to 1 EeV.

VII. Acknowledgements

This work is supported by the Office of Polar Programs of the National Science Foundation and by FWO-Flanders, Belgium.

References

[1] F. Kislat *et al.*, *A First All-Particle Cosmic Ray Energy Spectrum From IceTop*, These Proceedings.
[2] X. Bai *et al.*, *Muon Bundle Energy Loss in Deep Underground Detector*, These Proceedings.
[3] D. Heck *et al.*, *CORSIKA FZKA 6019*, Forschungszentrum Karlsruhe, 1998.
[4] R. S. Fletcher *et al.*, *SIBYLL: An event generator for simulation of high energy cosmic ray cascades*, Phys. Rev. D, **50** 5710, 1994.
[5] R. Engel *et al.*, *Air shower calculations with the new version of SIBYLL*, In Proc. 26th ICRC, Salt Lake City, 1999.
[6] A. Fassò *et al.*, *FLUKA: a multi-particle transport code* , CERN-2005-10 (2005), INFN/TC_05/11, SLAC-R-773.
[7] G. Battistoni *et al.*, *The FLUKA code: Description and benchmarking* , Proceedings of the Hadronic Shower Simulation Workshop 2006, Fermilab 6–8 September 2006, M. Albrow, R. Raja eds., AIP Conference Proceeding 896, 31-49, (2007).
[8] D. Chirkin, Parameterization based on the MSIS-90-E model, 1997, Private communication.
[9] S. Klepser *et al.*, *Lateral Distribution of Air Shower Signals and Initial Energy Spectrum above 1 PeV from IceTop*, In Proc. 30th ICRC, Merida, Mexico, 2007.
[10] K. Rawlins, Ph.D. Dissertation, UW-Madison (2001).
[11] P. Miočinović, Ph.D. Dissertation, UC Berkeley (2001).
[12] S. Grullon *et al.*, *Reconstruction of high-energy muon events in IceCube using waveforms*, In Proc. 30th ICRC, Merida, Mexico, 2007.
[13] J.W. Elbert, In Proc. DUMAND Summer Workshop (ed. A. Roberts), 1978, vol 2, p.101.

Small air showers in IceTop

Bakhtiyar Ruzybayev*, Shahid Hussain*, Chen Xu* and Thomas Gaisser* for the IceCube Collaboration†

*Bartol Research Institute, Department of Physics and Astronomy, University of Delaware, Newark, DE 19716, U.S.A.
†See the special section of these proceedings.

***Abstract*. IceTop is an air shower array that is part of the IceCube Observatory currently under construction at the geographic South Pole [1]. When completed, it will consist of 80 stations covering an area of 1 km^2. Previous analyzes done with IceTop studied the events that triggered five or more stations, leading to an effective energy threshold of about 0.5 PeV [2]. The goal of this study is to push this threshold lower, into the region where it will overlap with direct measurements of cosmic rays which currently have an upper limit around 300 TeV [3]. We select showers that trigger exactly three or exactly four adjacent surface stations that are not on the periphery of the detector (contained events). This extends the energy threshold down to 150 TeV.**

***Keywords*: IceTop, Air showers, Cosmic rays around the "knee".**

I. Introduction

During 2008, IceCube ran with forty IceTop stations and forty IceCube strings in a triangular grid with a mean separation of 125 m. In the 2008–2009 season, additional 38 IceTop tanks and 18 standard IceCube strings were deployed as shown in Fig.1. When completed, IceCube will consist of eighty surface stations, eighty standard strings and six special strings in the "DeepCore" sub-array [4]. Each IceTop station consists of two ice filled tanks separated by 10 m, each equipped with two Digital Optical Modules (DOMs) [5]. The photo multipliers inside the two DOMs are operated at different gains to increase the dynamic range of the response of a tank. The DOMs detect the Cherenkov light emitted by charged shower particles inside the ice tanks. Data recording starts when local coincidence condition is satisfied, that is when both tanks are hit within a 250 nanoseconds interval. In this paper we used the experimental data taken with the forty station array and compared to simulations of this detector configuration. Here we describe the response of IceTop in its threshold region.

II. Analysis

The main difference between this study and analyzes done with five or more stations triggering is the acceptance criterion. In previous analyzes, we accepted events with five or more hit stations and with reconstructed shower core location within the predefined containment area (shaded area in Fig.1). In addition, the station with the biggest signal in the event must also be located within the containment area.

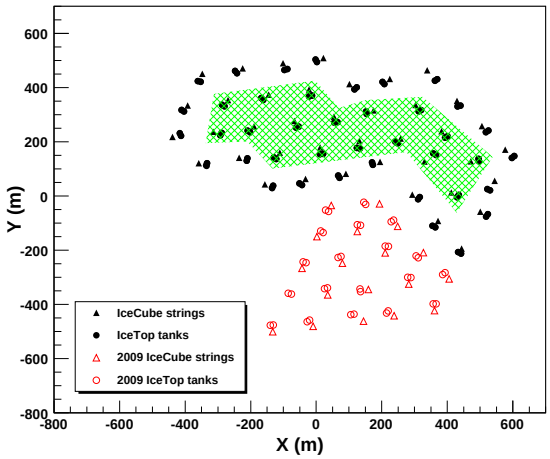

Fig. 1: Surface map of IceCube in 2009. New stations are unfilled markers. The shaded area (200795 m^2) contains stations that are defined as inner stations.

In the present analysis we used events that triggered only three or four stations, thus complementing analyzes with five or more stations. Selection of the events was based solely on the stations that were triggered. The criteria are:

1) Triggered stations must be close to each other (neighboring stations). For three station events, stations form almost an equilateral triangle. For four station events, stations form a diamond shape.

2) Triggered stations must be located inside the array (shaded region in Fig.1). Events that trigger stations on the periphery are discarded.

Since we are using stations on the periphery as a veto, we ensure that our selected events will have shower cores contained within the boundary of the array. In addition, these events will have a narrow energy distribution. We analyzed events in four solid angle bins with zenith angles θ: 0°–26°, 26°–37°, 37°–45°, 45°–53°. Results for the first bin, $\theta = 0°$–26°, are emphasized in this paper. This near-vertical sample will include most of the events with muons seen in coincidence with the deep part of IceCube.

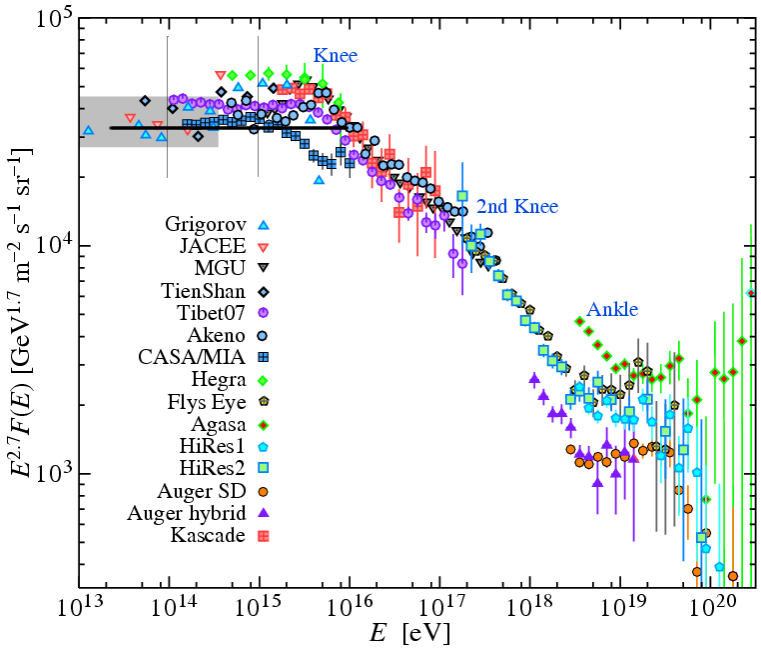

Fig. 2: The all-particle spectrum from air shower measurements as summarized in Figure 24.9 of Review of Particle Physics [3]. The shaded area indicates the range of direct measurements. The thick black line shows the flux model used for this analysis and the vertical lines indicate the energy range responsible for 95% of the 3 and 4 station events.

A. Experimental data and simulations

The experimental data used in this analysis were taken during an eight hour run on September 1st, 2008. Two sets of air shower simulations were produced: pure proton primaries in the energy range of 21.4 TeV–10.0 PeV, and pure iron primaries in the energy range of 45.7 TeV–10.0 PeV. All air showers were produced in zenith angle range: $0^\circ \leq \theta \leq 65^\circ$.

Our simulation used the following flux model:

$$\begin{aligned} \frac{dF}{dE} &= \Phi_0 \left(\frac{E}{E_0}\right)^{-\gamma} \qquad (1)\\ \Phi_0 &= 2.6 \cdot 10^{-4}\,\mathrm{GeV}^{-1}\mathrm{s}^{-1}\mathrm{sr}^{-1}\mathrm{m}^{-2} \\ E_0 &= 1\,\mathrm{TeV} \\ \gamma &= 2.7 \end{aligned}$$

for both proton and iron primaries. The normalizations were chosen such that the fluxes will fit the all particle cosmic ray spectrum as shown in Fig. 2. Simulated showers were dropped randomly in a circular area, around the center of the 40 station array ($X = 100\,m$, $Y = 250\,m$) with a radius of 600 m.

B. Shower Reconstruction

Since the showers that trigger only three or four stations are relatively small, we use a plane shower front approximation and the arrival times to reconstruct the direction. The shower core location is estimated by calculating the center of gravity of the square root of the charges in the stations. For the energy reconstruction we use the lateral fit method [6] that IceTop uses to reconstruct events with five or more stations triggered. This method uses shower sizes at the detector level to estimate the energy of the primary particle. Heavier primary nuclei produce showers that do not penetrate as deeply into the atmosphere as the proton primaries of the same energy. As a result, iron primary showers will have a smaller size at the detector level than proton showers of the same energy. We define a reconstructed energy based on simulations of primary protons and fitted to the lateral distribution and size of proton showers. Therefore the parameter for reconstructed energy underestimates the energy when applied to showers generated by heavy primaries. We observe a linear correlation between true and reconstructed energies in this narrow energy range and use this to correct the reconstructed energies. We reconstruct the experimental data assuming pure proton or pure iron primaries.

C. Effective Area

We use the simulations to determine the effective area as a function of energy. Effective area is defined as

$$A_{\mathrm{eff}} = \frac{\mathrm{Rate}[\mathrm{E_{min}}, \mathrm{E_{max}}]}{\Delta\Omega \cdot F_{\mathrm{sum}}} \qquad (2)$$

$$F_{\mathrm{sum}} = \int_{E_{\mathrm{min}}}^{E_{\mathrm{max}}} \Phi_0 \left(\frac{E}{E_0}\right)^{-\gamma} dE \qquad (3)$$

where Rate[$\mathrm{E_{min}}$,$\mathrm{E_{max}}$] is total rate for a given energy bin, $\Delta\Omega$ is the solid angle of the bin and F_{sum} is the

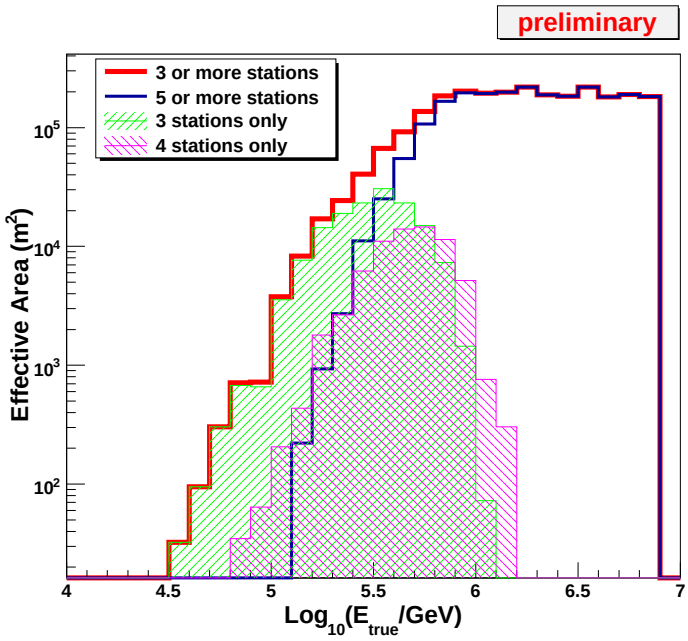

Fig. 3: Effective areas for different triggers in the most vertical zenith angle range: $0° \leq \theta \leq 26°$, derived using true quantities from simulations.

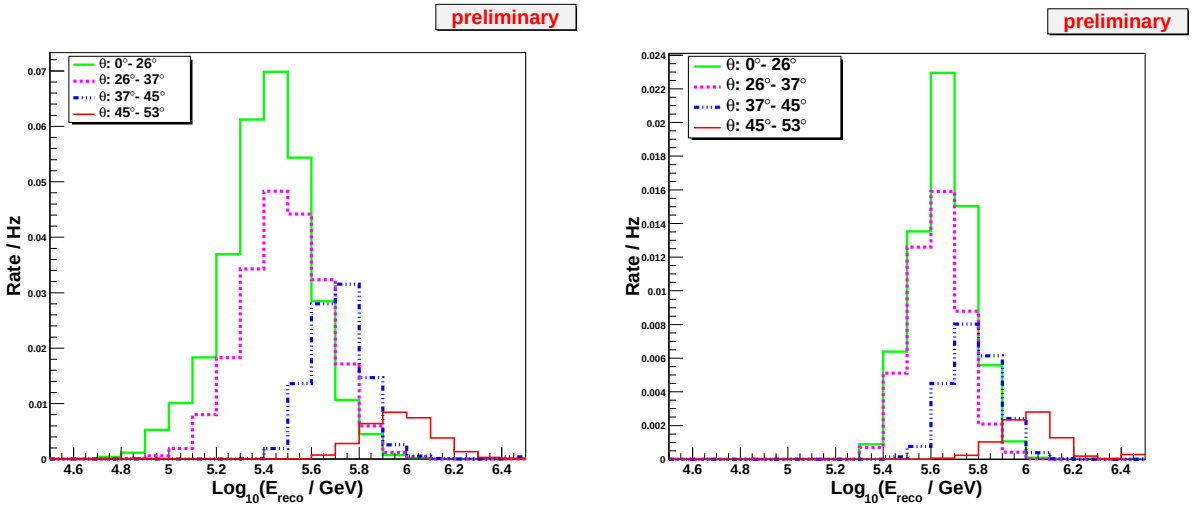

(a) Proton simulation

(b) Iron simulation

Fig. 4: Reconstructed energy distributions for proton and iron simulations for 3 station events in four zenith bins.

total flux in the given energy bin. Figure 3 shows the calculated effective areas, using the true values of energy and direction, for different trigger combinations, in the most vertical bin ($\theta = 0°$–$26°$).

III. Results

We summarize the results of simulations and comparison to data in Figures 4–6.

In Fig.4, we see that the energy distribution of the event rates depends on the zenith angle and the primary type. As expected, the peak of the energy distribution moves to higher energies for larger zenith angles and heavier primaries; these features of the distributions will be very helpful in unfolding the cosmic ray spectrum and composition.

Figure 5 shows the energy distributions in the most vertical zenith bin ($\theta = 0°$–$26°$). Experimental data is reconstructed twice, first with a pure proton assumption, then with a pure iron assumption. For three stations triggered (Fig. 5a), the energy distribution for pure proton simulation with the flux model as defined in (1) has a better agreement to the experimental data than iron simulation. For four stations triggered (Fig. 5b), we have a similar picture but the peaks of the distributions are shifted to the right since on average we need a higher

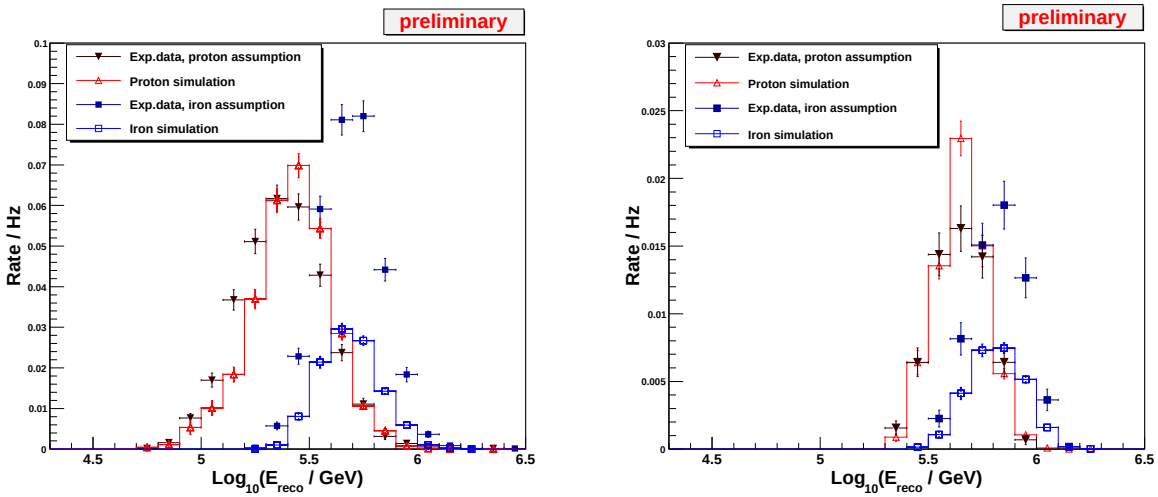

(a) 3 stations (b) 4 stations

Fig. 5: Reconstructed energy distributions for 3 and 4 station events with zenith angles $0°$–$26°$. Experimental data is reconstructed twice: assuming pure proton and pure iron primary.

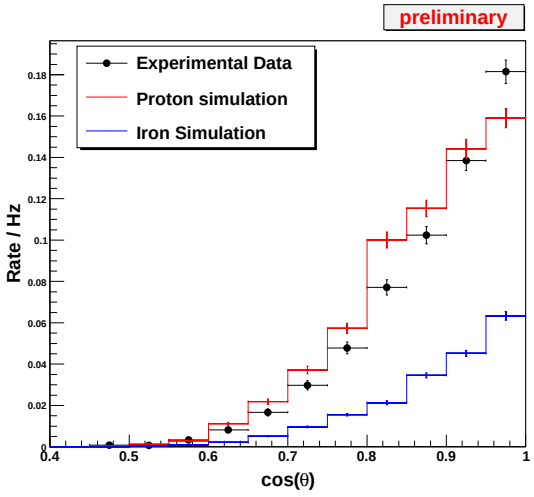

Fig. 6: Reconstructed zenith distributions for 3 station events.

energy primary to trigger four stations. By including three station events we can lower the threshold down to 130 TeV.

Figure 6 shows the zenith distributions of the events. Distribution for pure iron simulation is lower than for proton simulation since fewer iron primaries reach the detector level at lower energies. The deficiency of simulated events in the most vertical bin may be due to the fact that we used a constant γ of 2.7 for all energies and at these energies γ is most probably changing continuously. In the most vertical bin showers must have a lower energy than showers at greater zenith angle. Starting from a lower γ and gradually increasing it for higher energies will increase events in vertical bin and decrease them at higher energies, thus improving the zenith angle distribution. It is possible to further improve the fit of the proton simulation to the experimental data by adjusting the parameters γ and Φ_0 of the model.

IV. Conclusion

We have demonstrated the possibility of extending the IceTop analysis down to energies of 130 TeV, low enough to overlap the direct measurements of cosmic rays. Compared to IceTop effective area for five and more station hits, our results show a significant increase in effective area for energies between 100–300 TeV (Fig. 3). We plan to include three and four station events in the analysis of coincident events to determine primary composition, along the lines described in [7]. Overall results of this analysis encourage us to continue and improve our analysis of small showers.

References

[1] T.K. Gaisser et al., "Performance of the IceTop array", in Proc. 30th ICRC, Mérida, Mexico, 2007.
[2] F. Kislat et al., "A first all-particle cosmic ray energy spectrum from IceTop", this conference.
[3] C. Amsler et al. (Particle Data Group), Physics Letters **B667**, 1 (2008).
[4] A. Karle et al., arXiv:0812.3981, "IceCube: Construction Status and First Results".
[5] R. Abbasi et al., "The IceCube Data Acquisition System: Signal Capture, Digitization, and Timestamping", Nucl. Instrum. Meth. A **601**, 294 (2009).
[6] S. Klepser, PhD Thesis, Humboldt-Universität zu Berlin (2008).
[7] T. Feusels et al., "Reconstruction of IceCube coincident events and study of composition-sensitive observables using both the surface and deep detector", this conference.

Cosmic Ray Composition using SPASE-2 and AMANDA-II

K. Andeen* **and K. Rawlins† For the IceCube Collaboration‡**

*University of Wisconsin-Madison, 1150 University Ave, Madison, WI
†University of Alaska Anchorage, 3211 Providence Dr, Anchorage, AK
‡See special section of these proceedings

***Abstract*. The precise measurement of cosmic ray mass composition in the region of the knee (3 PeV) is critical to understanding the origin of high energy cosmic rays. Therefore, air showers have been observed at the South Pole using the SPASE-2 surface array and the AMANDA-II neutrino telescope which simultaneously measure the electronic air shower component at the surface and the muonic air shower component in deep ice, respectively. These two components, together with a Monte Carlo simulation and a well-understood analysis method will soon yield the relative cosmic ray composition in the knee region. We report on the capabilities of this analysis.**

***Keywords*: composition, cosmic-ray, neural-network**

I. Introduction

The mass composition of high-energy cosmic rays around and above the knee in the energy spectrum ($\sim$3 PeV) is dependent upon the mechanisms of cosmic ray production, acceleration, and propagation. Therefore, the study of mass composition is critical to understanding the origins of cosmic rays in this energy region. At energies up to 10^{14} eV mass composition can be measured directly using balloon and satellite experiments; however, due to the low flux, composition above 10^{14} eV must be obtained from indirect measurements on the ground. Indirect measurements of composition involve a close examination of the air shower produced as a cosmic ray primary smashes into Earth's atmosphere. By utilizing information from more than one component of the shower, such as the electronic and muonic components, the energy and relative mass can be obtained from primary particles with much higher energies than those currently measurable by direct detection techniques.

II. Data and Reconstruction

One such indirect measurement is possible using the South Pole Air Shower Experiment (SPASE-2) in coincidence with the Antarctic Muon And Neutrino Detector Array (AMANDA-II). The SPASE-2 detector is situated on the surface of the South Pole at an atmospheric depth of $\sim$685 g cm^{-2} and is composed of 30 stations in a 30 m triangular grid. Each station contains four 0.2 m^2 scintillators. The AMANDA-II detector lies deep in the ice such that the center-to-center separation between the deep ice and the surface arrays is $\sim$1730 m with an angular offset of 12°. AMANDA-II consists of 677 optical modules (OMs) deployed on 19 detector strings spanning depths from 1500-2000 m below the surface of the ice. Each OM contains a photomultiplier tube (PMT) which is optimized for detection of the Cherenkov light emitted by particles—namely muon bundles—passing through the ice. In addition to the composition analysis, this coincident configuration allows for calibration as well as measurement of the angular resolution of the AMANDA-II detector. [1]

For this analysis, coincident data from the years 2003-2005 are used, for a total livetime of around 600 days. For comparison with the data, Monte Carlo simulated proton, helium, oxygen, silicon and iron air showers with energies between 100 TeV and 100 PeV have been produced using the CORSIKA air shower generator with the SIBYLL/GEISHA hadronic interaction models [2]. At the surface the air showers are injected into GEANT4, which simulates the SPASE-II detector response [3]. The showers are then propagated through the ice and the response of AMANDA-II detector is simulated using the standard software package of the AMANDA collaboration. An E^{-1} spectrum is used for generation, but for analysis the events are re-weighted to the cosmic ray energy spectrum of $E^{-2.7}$ at energies below the knee at 3 PeV and $E^{-3.2}$ above. Both the experimental data and the Monte Carlo simulated data are then put through identical reconstruction chains.

The first step in the reconstruction uses information from SPASE-2 only. The goal of this first reconstruction is to find the shower direction, shower size, and core position of the incoming air shower. The direction can be computed from the arrival times of the charged particles in the SPASE-2 scintillators, while the shower core position and shower size are acquired by fitting the lateral distribution of particle density to the Nishimura-Kamata-Greisen (NKG) function. Evaluating the fit at a fixed distance from the center of the shower (in this case 30 m) [4] gives a parameter called S30, which has units of particles/m^2 and will be used throughout this paper as a measure of the electronic part of the air shower.

The next step in the reconstruction provides a measure of the muon component of the air shower from a combined reconstruction which uses both the surface and deep ice detectors. The core position of the shower from the SPASE-only fit is held fixed while θ and ϕ are varied in the ice to find the best fit of the muon track in the AMANDA-II detector. Holding the core fixed at

the surface allows for a lever arm of about 1730 m when calculating directionality, providing a very tight angular resolution for the track. The expected lateral distribution function (LDF) of the photons resulting from the muon bundle in AMANDA-II is computed and corrected for both the ranging out of muons as they progress downward through the detector, as well as the changing scattering length as a function of depth in the ice caused by dust layers. The LDF is then fit to the hit optical modules and evaluated at a perpendicular distance of 50 m from the center of the shower [5]. This parameter, called K50, has units of photoelectrons/OM and will be used throughout the rest of this paper as the measure of the muon component of the air shower.

III. Analysis Details

Once reconstruction has been completed it is important to find and eliminate poorly reconstructed events. Thus events have been discarded which:

- have a reconstructed shower core outside the area of SPASE-2 or a reconstructed muon track passing outside the volume of AMANDA-II,
- have an unreasonable number of hits in the ice given S30 at the surface (these events represent large showers which landed outside of SPASE-2 and were misreconstructed within the array as having a small S30),
- have an unphysical reconstructed attenuation length of light in the ice (an unphysical reconstruction of attenuation length will lead to a misreconstructed value for K50), or
- are reconstructed independently in SPASE-2 and AMANDA-II as coming from significantly different locations in the sky.

After these cuts have been made, it can be seen in Fig. 1 that our two main observables, S30 and K50, form a parameter space in which primary energy and primary mass separate. This is expected, since the showers associated with the heavier primaries develop earlier in the atmosphere and hence have more muons per electron by the time they reach the surface than the showers associated with lighter primaries [6]. This means that K50, which is proportional to the number of muons in the ice, will be higher for heavier primaries than for lighter primaries of the same S30, as is observed.

In the three-year data set used for this analysis, more than 100,000 events survive all quality cuts. It is interesting to notice that in the previous analysis, using the SPASE-2/AMANDA-B10 detector [5], the final number of events for one year was 5,655. Furthermore, the larger detector used here is sensitive to higher energy events. The significant increases in both statistics and sensitivity, along with a new detector simulation and revised reconstruction algorithm for the SPASE-2 array, are the basis for performing a new analysis.

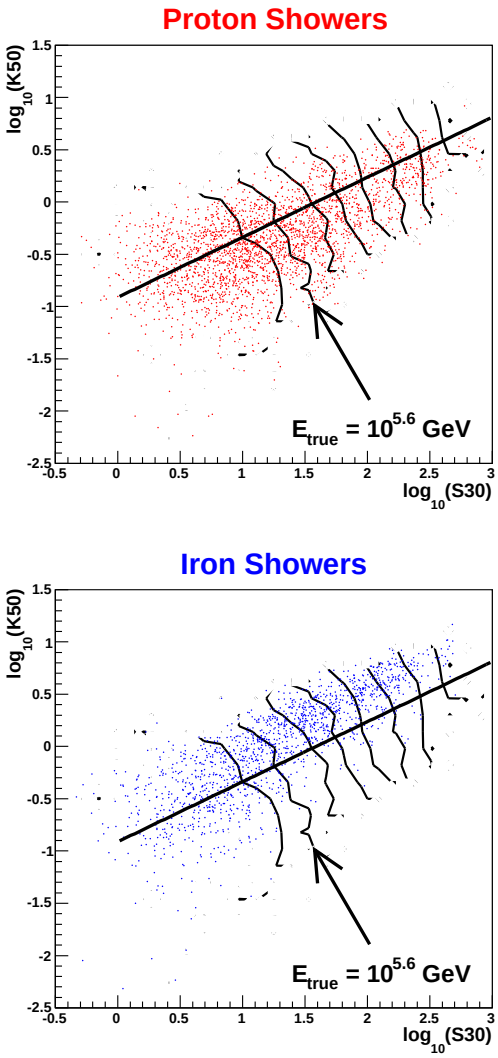

Fig. 1. The two main observables, $\log_{10}$(K50) vs $\log_{10}$(S30), in the Monte Carlo simulation with protons above (red) and iron below (blue). The black contours depict lines of constant energy from $5.4 > \log_{10}(E_{true}/GeV) > 6.8$ marked every $\log_{10}(E_{true}/GeV) = 0.2$. The black line along the energy gradient approximates a division between proton and iron showers and is included merely as a reference between the two plots. It is clear that mass and energy are on a roughly linear axis.

A. Calibration

To accurately measure the composition using both electron and muon information, the Monte Carlo simulations must provide an accurate representation of the overall amplitude of light in ice (measured here as K50). However, due to the model-dependencies displayed by air shower simulations, the overall light amplitude is subject to systematic errors. Therefore, it is important to calibrate the composition measurements at low energies where balloon experiments have provided direct measurements of cosmic ray composition. In light of this, a vertical "slice" in S30 is selected for calibration which corresponds with the highest energies measured directly. At these energies, the direct measurements indicate that $<\ln A> \approx 2$, or 50% protons and 50% iron [7]. The K50 values of the data in this S30 "slice" are thus adjusted by

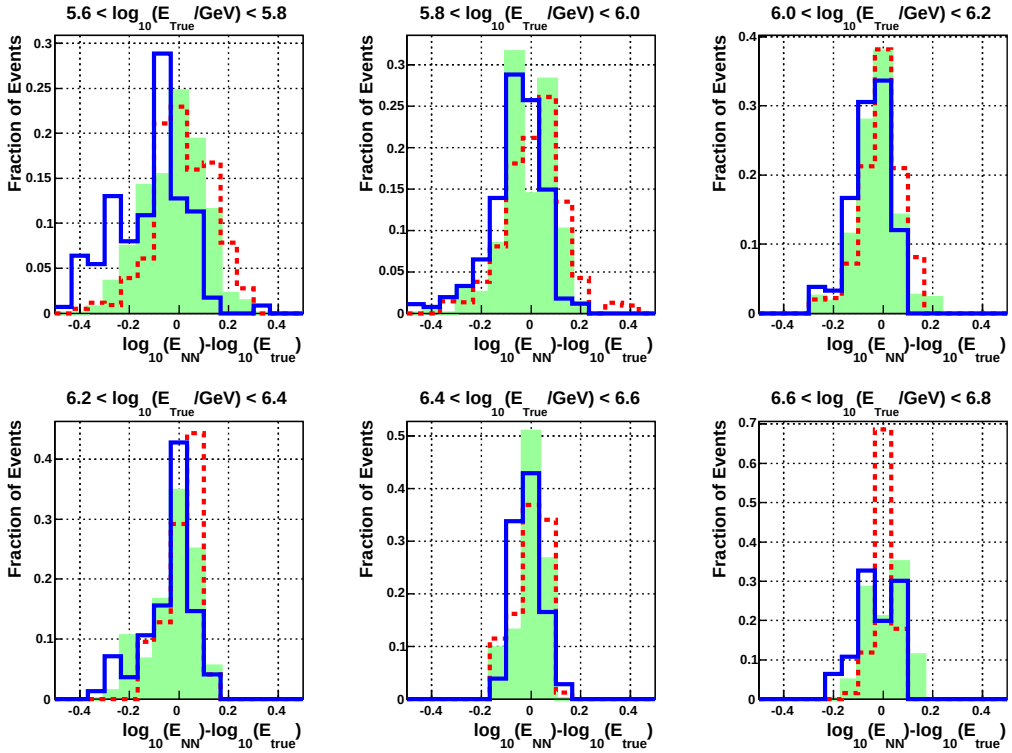

Fig. 2. Energy resolution (the difference between the true primary energy and the energy reconstructed by the neural network) is shown in bins of true energy for iron (solid blue), proton (dashed red) and oxygen (shaded green) primaries. Each energy bin is bounded by two consecutive contours from Fig. 1 (where the indicated energy contour is the lower bound of the first energy bin above). For easier comparison, a Gaussian distribution has been fit to these energy resolution histograms and the mean and sigma of each Gaussian can be found in Table 1.

TABLE I
MEAN AND SIGMA OF A GAUSSIAN DISTRIBUTION FIT TO EACH ENERGY RESOLUTION HISTOGRAM IN FIG. 2.

Shower Type	Gaussian Statistic	True Energy Bins ($\log_{10}$(E) / GeV)					
		5.6 - 5.8	5.8 - 6.0	6.0 - 6.2	6.2 - 6.4	6.4 - 6.6	6.6 - 6.8
Proton	Mean	0.03	0.02	0.00	0.02	0.01	0.00
	σ	0.12	0.11	0.08	0.06	0.05	0.04
Oxygen	Mean	-0.02	-0.01	-0.03	0.00	0.01	0.02
	σ	0.12	0.10	0.07	0.07	0.05	0.09
Iron	Mean	-0.12	-0.05	-0.04	-0.02	-0.01	0.05
	σ	0.15	0.09	0.08	0.08	0.06	0.15

an offset to match the distribution of K50 corresponding to a $50\% - 50\%$ proton and iron sample.

B. Neural Network Reconstruction of Energy and Mass

Similar past investigations utilized the quasi-linear relationship between K50/S30 and mass/energy, as seen in Fig. 1, to employ an analysis wherein, after calibration, the axis is rotated to correspond to the mass/energy coordinate plane [5] [8]. The rotation analysis works quite well up to energies slightly above the knee; however, beyond the knee the relationship between K50/S30 and mass/energy becomes increasingly non-linear as the air showers approach the energy where the shower maximum occurs at the atmospheric depth of the SPASE-2/AMANDA-II detectors. As the data set used here has significantly more statistics at these higher energies than previous studies, it was important to find a new procedure for extracting the composition. A neural network technique has therefore been developed to resolve the mean logarithmic mass at all energies [9].

The main change to the neural network technique since its development has been to distinguish between the calculation for energy and the calculation for mass by using two separate networks. The first neural network (NN1) is trained to find the primary energy by using $\log_{10}$(K50) and $\log_{10}$(S30) as input parameters, followed by one hidden layer. The second network (NN2) is trained to find the primary mass of the air shower. NN2 also takes as input $\log_{10}$(K50) and $\log_{10}$(S30) and also has a single hidden layer of neurons. In both cases the network is trained through a number of "epochs", or training cycles, on half of the simulated proton and iron showers and tested on the other half of the proton and iron showers. The results of testing determine the

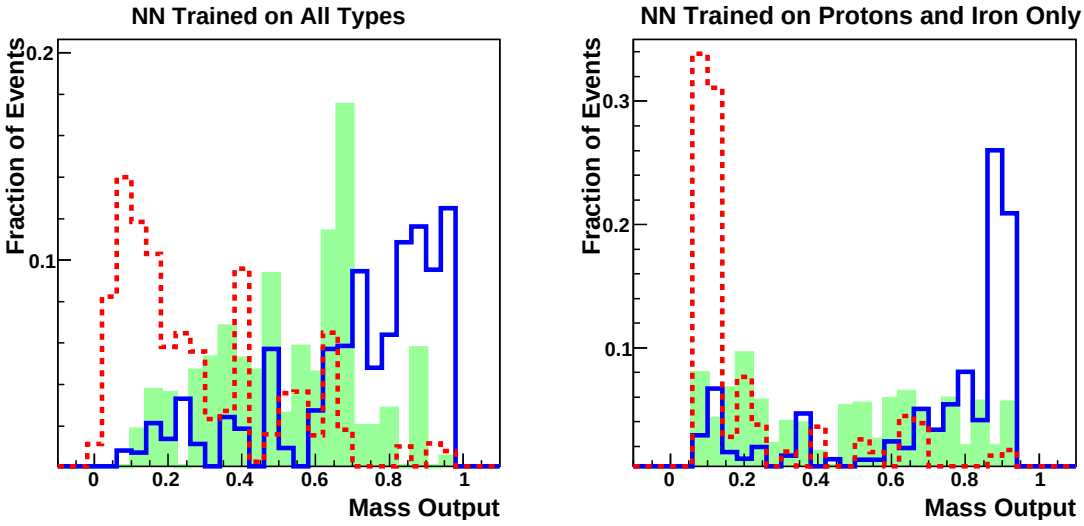

Fig. 3. Mass output of the neural network from the bin $6.2 < \log_{10}(E_{reco}/GeV) < 6.4$ for three primary types: iron (solid blue), oxygen (shaded green), and protons (dashed red). On the left is the output from a network trained on all particle types. On the right is the output from a network trained only on protons and iron. As expected, when the neural network is trained on more particle types it begins to reconstruct the intermediate primaries in their proper location as opposed to attempting to classify them as proton or iron.

number of "epochs" each network can be trained through without overtraining. (The intermediate primaries are currently used only for checking the mass reconstruction of the network. It is hoped that they will soon be plentiful enough to use as inputs for training as well.)

As NN1 is given a full spectrum of energies on which to train, it very successfully reconstructs the energy of each shower. Plots of energy resolution separated into bins of true energy can be found in Fig. 2. The energy resolution is not only very good but also composition independent. This can be seen more clearly in Table I, which shows the Gaussian mean and sigma of each energy bin from Fig. 2. (Currently only six bins in energy are shown: higher energies are being generated and will be available before the conference.)

The mass network outputs a reconstructed mass for each particle in terms of the primaries on which it has been trained. As the neural network is trained only on proton and iron showers, it reconstructs each shower as some combination of proton and iron. Currently a minimization technique is used to find the mean log mass for each energy bin. This minimization technique has been tested on intermediate primaries and proves to reconstruct them reasonably well for a network trained only on protons and iron. However, as the number of intermediate primaries generated is increasing, it is hoped that the mass network can soon be trained on a wider spectrum of primaries. A test of this has been run and a comparison between the output from a network trained on all particle types and a network trained only on protons and iron is shown in Fig. 3. As expected, it is evident that when the network is trained on intermediate primaries oxygen is reconstructed in its own location between protons and iron and no longer as a fraction of one or the other. This method appears very promising and, as more intermediate primaries are simulated, this is the direction in which the analysis will proceed.

IV. Discussion and Outlook

The SPASE-2/AMANDA-II cosmic ray composition analysis has lately acquired new Monte Carlo simulation, a new detector simulation of the surface array and a revised surface-array reconstruction algorithm. Aided by these three new features a great deal of progress has been made. It can clearly be seen that the use of a modified version of the neural network technique seen in the ICRC proceedings of 2007 [9] can very accurately reconstruct the energy of cosmic ray primaries in the region of the knee in the cosmic ray spectrum. The inclusion of a larger variety of primary particles for training the neural network is seen to be very promising and, with increased statistics in the Monte Carlo simulation, a composition result will soon follow.

V. Acknowledgments

The authors would like to acknowledge support from the Office of Polar Programs of the United States National Science Foundation as well as the Arctic Region Supercomputing Center.

References

[1] J. Ahrens et al. *Nuclear Instruments and Methods*, 552:347-359, 2004.
[2] D. Heck and T. Pierog, *Extensive Air Shower Simulations with CORSIKA: A User's Guide* http://www-ik.fzk.de/corsika/usersguide/corsika_tech.html
[3] GEANT4 Collaboration *Nuclear Instruments and Methods, A*, 506:250-303, 2003.
[4] J.E. Dickinson et al. *Nuclear Instruments and Methods A*, 440:95-113, 2000.
[5] K. Rawlins. PhD thesis, University of Wisconsin-Madison, (2001)
[6] T. Gaisser. *Cosmic Rays and Particle Physics*. Cambridge University Press, 1988.
[7] J.R. Hörandel. *International Journal of Modern Physics A*, 20(29):6753-6764, 2005.
[8] J. Ahrens et al. *Astroparticle Physics*, 21: 565-581, 2004.
[9] K. Andeen et al, *Proceedings of the 30th International Cosmic Ray Conference* 2007.

Study of High p_T Muons in IceCube

Lisa Gerhardt*† and Spencer Klein*† for the IceCube Collaboration§

*Lawrence Berkeley National Laboratory, Berkeley, California 94720
†University of California, Berkeley, Berkeley, California 94720
§See the special section of these proceedings

***Abstract*. Muons with a high transverse momentum (p_T) are produced in cosmic ray air showers via semileptonic decay of heavy quarks and the decay of high p_T kaons and pions. These high p_T muons have a large lateral separation from the shower core muon bundle. IceCube is well suited for the detection of high p_T muons. The surface shower array can determine the energy, core location and direction of the cosmic ray air shower while the in-ice array can reconstruct the energy and direction of the high p_T muon. This makes it possible to measure the decoherence function (lateral separation spectrum) at distances greater than 150 meters. The muon p_T can be determined from the muon energy (measured by dE/dx) and the lateral separation. The high p_T muon spectrum may also be calculated in a perturbative QCD framework; this spectrum is sensitive to the cosmic-ray composition.**

***Keywords*: high transverse momentum muons, cosmic ray composition, IceCube**

I. Introduction

The composition of cosmic rays with energies above 10^6 GeV is not well known. At these energies, the flux of cosmic rays is so low that direct detection with balloon or satellite-borne experiments is no longer feasible and indirect measurement with larger ground arrays must be used. These arrays measure the electronic and hadronic components of a cosmic ray air shower, and must rely on phenomemological interaction models to relate observables like muon and electron density to primary composition. These interaction models are based on measurements made at accelerators that reach a maximum energy roughly equivalent to a 10^6 GeV proton cosmic ray [1]. Extrapolation to the energy of the detected cosmic rays leads to uncertainties in the composition of cosmic rays at high energies. An alternate method of determining the composition is to use muons with a high transverse momentum (p_T) [2].

At transverse momenta on the order of a few GeV/c, the muon p_T spectrum can be calculated using perturbative QCD (pQCD). Such calculations have been made for RHIC and the Tevatron, and the data is in quite good agreement with modern fixed order plus next-to-leading log (FONLL) calculations [3]. These experimental studies give us some confidence in pQCD calculations for air showers.

Most of the high-energy muons that are visible in IceCube are produced from collisions where a high-energy (large Bjorken$-x$) parton interacts with a low Bjorken$-x$ parton in a nitrogen target. These collisions will produce heavy (charmed and bottom) quarks and also jets from high p_T partons; the jets will fragment into pions and kaons. Pions and kaons produce "conventional" muons that have a soft spectrum roughly proportional to $E^{-3.7}$ [4] and typicallly have a low p_T. In contrast, charm and bottom quarks are produced early in the shower. The resulting muons ("prompt" muons) have a harder spectrum, a higher p_T, and are the dominant source of atmospheric muons above 10^5 GeV [5].

If these particles are produced in the forward direction (where they will be seen by ground based detectors), they can carry a significant fraction of the energy of the incident nucleon. The muon energy and p_T can be related to the energy of the partons that make up the incident cosmic ray. For example, a 10^{16} eV proton has a maximum parton energy of 10^{16} eV, while the maximum parton energy for a 10^{16} eV iron nucleus (with A=56) is 1.8×10^{14} eV. These two cases have very different kinematic limits for high p_T, high-energy muon production, so measurements of high p_T muon spectra are sensitive to the cosmic-ray composition.

High p_T muons constitute a small fraction of the muons visible in IceCube; the typical muon p_T is of order a few hundred MeV/c. In this domain of "soft physics," the coupling constants are very large, and pQCD calculations are no longer reliable. One is forced to rely on phenomenological models; different hadronic interaction models give rather different results on composition [6].

IceCube, a kilometer-scale neutrino telescope, is well suited for the detection of muons with p_Ts above a few GeV/c [2]. When completed in 2011, it will consist of a 1 km^3 array of optical sensors (digital optical modules, or DOMs) buried deep in the ice of the South Pole and a 1 km^2 surface air shower array called IceTop. IceTop has an energy threshold of 300 TeV and can reconstruct the direction of showers with energies above 1 PeV within 1.5° and locate the shower core with an accuracy of 9 m [7]. The in-ice DOMs (here referred to as IceCube) are buried in the ice 1450 m under IceTop in kilometer-long strings of 60 DOMs with an intra-DOM spacing of 17 m. IceCube can reconstruct high energy muon tracks with sub-degree accuracy. The IceTop measurements can be used to extrapolate the interaction height of the

shower and IceCube can measure the energy, position and direction of the muons. These values, can be used to calculate the p_T:

$$p_T = \frac{dE_\mu}{hc} \quad (1)$$

where E_μ is the energy of the high p_T muon, d is its lateral separation and h is the interaction height of the shower, here taken as an average value of 25 km. The interaction height loosely depends on the composition and a full treatment of this is planned in the future. Taking 150 m, 25 meters more than the separation between strings of DOMs in IceCube, as a rough threshold for the two-track resolution distance of the high p_T muon from the shower core gives a minimum resolvable p_T of 6 GeV/c for a 1 TeV muon.

Multiple scattering and magnetic fields can deflect the muons as they travel to the IceCube detector, but this is only equivalent to a few hundred MeV worth of p_T and is not a strong effect in this analysis. The high p_T muon events are near-vertical which gives them a short slant depth. In order for muons to reach the IceCube detector they must have an energy of at about 500 GeV at the surface of the Earth. These higher energy muons are deflected less by multiple scattering and the Earth's magnetic field.

The combined acceptance for cosmic ray air showers which pass through both IceTop and IceCube is 0.3 km^{2}sr for the full 80-string IceCube array [8]. By the end of the austral summer of 2006/2007, 22 IceCube strings and 26 IceTop tanks had been deployed. The combined acceptance for showers that pass through both IceTop-26 and IceCube-22 is 0.09 km^{2}sr. While this acceptance is too small to expect enough events to generate a p_T spectrum, it offers an excellent opportunity to test reconstruction and background rejection techniques.

II. Previous Measurement of High p_T Muons

MACRO, an underground muon detector, has previously measured the separation between muons in air showers with energies ranging roughly from 10^4 GeV to 10^6 GeV [9]. MACRO measured muon separations out to a distance of about 65 meters. The average separation between muons was on the order of 10 m, with 90% of the muons found with a separation of less than 20 m [9]. MACRO simulated air showers and studied the muon pair separations as a function of the p_T of their parent mesons. They verified the linear relationship between p_T and separation shown in Eq. 1 (with a small offset due to multiple scattering of the muons) out to momenta up to 1.2 GeV/c.

III. High p_T Rate Estimations

The decay of charm will produce roughly 10^6 prompt muons/year with energies in excess of 1 TeV inside the 0.3 km^{2}sr combined acceptance of the full IceCube array [10]. Different calculations agree well in overall rate in IceCube, but, at high (1 PeV) energies, differences in parton distribution functions lead to rates that differ by a factor of 3 [11].

TABLE I: Estimated number of events from charm above different p_T thresholds in 1 year with the 80-string IceCube array

p_T [GeV/c]	Separation [m]	Number
$\geq$6	150	$\sim$500
$\geq$8	200	$\sim$200
$\geq$16	400	$\sim$5

We can roughly estimate the fraction of muons that are produced at high p_T using PYTHIA pp simulations conducted for the ALICE muon spectrometer at a center of mass energy of 14 TeV, which indicate that roughly 0.6% of these events will have a p_T of at least 6 GeV/c [12]. These simulations are done at a higher center of mass energy than the bulk of the IceCube events, and also were for muons produced at mid-rapidity (and, therefore, higher projectile x values and lower target x values than in IceCube). However, they should be adequate for rough estimates. These estimated rates of high p_T muons are further reduced by approximately a factor of 10 by requiring that the high p_T muon be produced in coincidence with a shower that triggers IceTop, leaving a rough expectation of $\sim$500 events per year with a p_T greater than 6 GeV/c in the 80-string configuration of IceCube. The estimated number of events above a given p_T from the decay of charm is given in Table I neglecting the uncertainties mentioned above. At higher p_T, bottom production may also contribute significantly to muon production.

The rate of 1 TeV muons from conventional flux is expected to be about 10^9 events/year in the full IceCube configuration. The vast majority of these muons will have a low p_T. Based on the p_T spectrum measured from pions produced in 200 GeV center of mass energy pp collisions by the PHENIX collaboration, the number of events expected with $p_T > 6$ GeV/c is estimated to be 1 in 6×10^6 [13]. Requiring a $p_T > 6$ GeV/c and an IceTop trigger leaves roughly 20 events/year in the full IceCube configuration from the conventional flux of muons.

IV. Reconstruction Methods

High p_T muons will appear as a separate track coincident in time and parallel with the track from the central core of low p_T muons. Generally the bundle of low p_T muons leaves more light in the detector than the high p_T muon.

Current reconstruction algorithms in IceCube are designed to reconstruct single tracks. In order to reconstruct these double-track events the activated DOMs are split into groups using a k-means clustering algorithm [14]. The first group is the muon bundle and the second group is the high p_T muon. Each group is then reconstructed with a maximum likelihood method that takes into account the scattering of light in ice. After this initial reconstruction, the groups are resplit

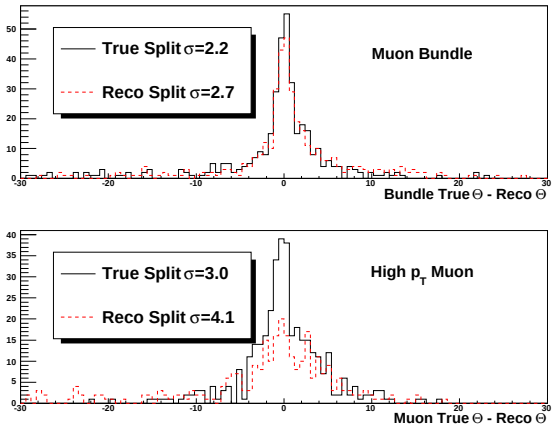

Fig. 1: Zenith angle resolution of the high p_T reconstruction algorithm. The sigma are the results of Gaussian fits to the distributions.

according to their time residual relative to the muon bundle reconstruction and re-fit. The first splitting forces the activated DOMs into two groups, which is not correct for the background events which don't have a high p_T muon and generate only a single shower in the array. Splitting the activated DOMs a second time according to their time residual allows for the possibility for all the activated DOMs to end up in a single group. Figure 1 shows the performance of this clustering algorithm. The zenith angle resolution for groups determined using the true simulation information (black, solid lines) is compared to the resolution for groups determined using the clustering algorithm (red, dashed lines) for the muon bundle (top) and high p_T muon (bottom). Roughly 20% of the events fail to reconstruct because there are not enough DOMs in one of the groups.

These reconstruction algorithms achieve a zenith angle resolution of 2.7° for the muon bundle and 4.1° for a high p_T muon separated by 400 m. The resolution is worse for the high p_T muon because fewer DOMs are activated. While high p_T muons with a greater separation are much easier to resolve with the two track algorithm, they also tend to be lower energy (see Eq. 1) and activate fewer DOMs. The average number of DOMs activated by the high p_T muon is 12, compared to 50 for the muon bundle. Additionally, because high p_T muons have less activated DOMs, a DOM activated by the muon bundle that is incorrectly placed in the high p_T group has a much larger effect on the reconstruction of the high p_T track. These factors lead to a poorer resolution in the high p_T track direction.

V. Signal and Background Separation

Many of the processes that can generate a high p_T muon are not properly modeled or included in CORSIKA [15] with the exception of the modified DPMJET model discussed in [16]. Also, since high p_T muons will occur in only a fraction of simulated showers making simulation very time intensive, a toy model based on CORSIKA proton showers was used to model the signal. A single muon is inserted into an existing CORSIKA event containing a muon bundle from an air shower. This modified shower is then run through the standard IceCube propagation, detector simulation, and reconstruction routines. Simulations insert a muon with energy of 1 TeV separated 100, 150, 200, and 400 m from the shower core. This gave a clean sample ideal for the development of reconstruction routines optimized to identify simultaneous parallel tracks inside the detector.

Cosmic rays air showers that do not generate a high p_T muon are considered a background to this search. Since they generate only a single shower in the array, these events are mostly eliminated by requiring there be two well-reconstructed tracks in the IceCube detector. These single showers are well-reconstructed by a single track hypothesis, while the high p_T muon events are not. Figure 2 shows the negative log of the reduced likelihood of a single track reconstruction for single showers, and showers with an inserted 4, 8, and 16 GeV/c p_T, 1 TeV muon (separation of 100 m, 200 m, and 400 m from the shower core, assuming an average interaction height of 25 km). Well reconstructed events have a lower value on this plot. For large separations, this variable separates single showers from showers which contain a high p_T muon. When the separation between the high p_T muon and the shower core drops below the interstring distance (the blue, dot-dashed line in Figure 2), it is no longer possible to cleanly resolve the high p_T muon from the shower core and the event looks very similar to a single shower.

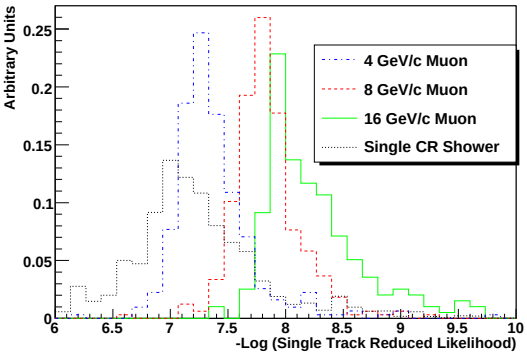

Fig. 2: Negative log of the reduced likelihood for the single track reconstruction

The IceCube 22-string configuration is large enough that the rate of simultaneous events from cosmic rays is significant. Muon bundles from two (or more) air showers can strike the array within the 10 μs event window, producing two separated tracks. These so-called double-coincident events are the dominant background for air showers with high p_T muons. Since these double-coincident events are uncorrelated in direction and time, requiring that both reconstructed tracks be parallel and occur within 1 μs can eliminate most of these events.

Due to misreconstructions some events will survive this selection, and criteria to eliminate these misreconstructed events are being developed. However, an irreducible background remains from double-coincident events that happen to come from roughly the same direction and time.

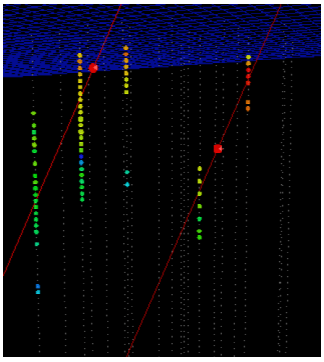

Fig. 3: Candidate shower with a high p_T muon. The colored circles show DOMs that are activated by light. The color and size of the circle corresponds to the time (red being earliest) and magnitude of the signal, respectively and the white dots indicate DOMs that are not activated in the event. The red lines show the reconstructed tracks.

After applying selection criteria to reduce the cosmic ray background, a 10% sample of the IceCube data was scanned by eye for high p_T muon candidates. Several events were found and Figure 3 shows a representative event. The two tracks occur within 600 ns of each other and the spaceangle between the two reconstructions is 5.6°.

VI. Horizontal Events

One possible method to avoid the backgrounds from single and double-coincident cosmic ray air showers is to search for events that come from the horizontal direction. At a zenith angle of 60° the slant depth through the ice is about 3 km. Only muons with energies in excess of several TeV will reach IceCube [17] and the event multiplicity is greatly reduced. Because the intra-DOM spacing is 17 m, compared to the intra-string spacing of 125 m relevant for vertical events, the two-track resolution should improve. A disadvantage to searching in the horizontal direction is the increase in the deflection from the magnetic field and multiple scattering with the slant depth, which could lead to a greater spread in the muon bundle and create event topologies which mimic a high p_T muon event. Nevertheless, the advantage of background suppression is strong. In addition to high p_T muons in cosmic rays, there are a number of other processes (such as the decay of the supersymmetric stau [18]) that can produced horizontal parallel tracks, making the horizon an interesting direction.

A search was conducted in 10% of the IceCube data from 2007 for these horizontal events using simple topological selection criteria. Events which reconstructed within 30° of horizontal were selected and searched for a double track topology. Several interesting candidate events were found, one is shown in Figure 4. The two tracks occur within 1 ns of each other and the spaceangle between the two reconstructions is 33°.

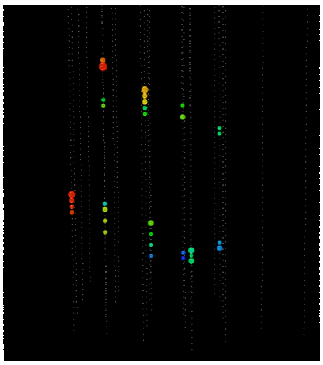

Fig. 4: Candidate double track near-horizontal event

VII. Conclusions

IceCube is large enough that the study of high p_T muons has become viable. Resolution of tracks separated by at least 150 meters from the shower core will allow identification of muons with p_Ts of at least 6 GeV/c. A two-track reconstruction algorithm has been developed and selection criteria for identification of air showers with high p_T muons is under development. A search for horizontal double tracks is also under way. The rate of high p_T muon production is sensitive to the composition of the cosmic rays and offers an alternative to existing composition studies.

This work is made possible by support from the NSF and the DOE.

References

[1] R. Engel, Nuclear Physics B Proc. Suppl., **151**:437 (2006).
[2] S. Klein and D. Chirkin, 30th ICRC (2007), arXiv:0711.0353v1.
[3] R. Vogt, M. Cacciari and P. Nason, Nucl. Phys. **A774**, 661 (2006).
[4] T.K. Gaisser, "Cosmic Ray and Particle Physics," Cambridge University Press, 1990.
[5] L. Pasquali, M. Reno, and I. Sarcevic, Phys. Rev. D **59**:034020 (1998).
[6] W. Apel *et al.* , Astropart. Phys. **29**:412 (2008); J. Bluemer et al,arXiv:0904.0725.
[7] S. Klepser, 21st European Cosmic Ray Symposium (2008), arXiv:0811.1671.
[8] X. Bai, 30th ICRC (2007), arXiv:0711.0353v1.
[9] Ambrosio *et al.* , Phys. Rev. D **60**:032001 (1999).
[10] M. Thunman, P. Gondolo, and G. Ingelman, Astropar. Phys. **5**:309 (1996).
[11] R. Enberg, M. Reno and I. Sarcevic, Phys. Rev. D **78**:043005 (2008).
[12] Z. Conesa del Valle, The European Physical Journal C, **49**:149 (2007).
[13] S. Adler *et al.* , Phys. Rev. Lett. **91**:241803 (2003).
[14] D. MacKay "Information Theory, Inference and Learning Algorithms," Cambridge University Press (2003).
[15] D. Heck, Forschungszentrum Karlsruhe Report FZKA 6019 (1998).
[16] P. Berghaus, T. Montaruli, and J. Ranft, Journal of Cosmology and Astropar. Phys. **6**:003 (2008).
[17] P. Berghaus, these proceedings.
[18] A. Olivas, these proceedings.

Large Scale Cosmic Rays Anisotropy With IceCube

Rasha U Abbasi*, Paolo Desiati* and Juan Carlos Velez* for the IceCube Collaboration †

* *University of Wisconsin, IceCube Neutrino Observatory, Madison, WI 53703, USA*
† *http://icecube.wisc.edu/*

***Abstract*. We report on a study of the anisotropy in the arrival direction of cosmic rays with a median energy per Cosmic Ray (CR) particle of ~ 14 TeV using data from the IceCube detector. IceCube is a neutrino observatory at the geographical South Pole, when completed it will comprise 80 strings plus 6 additional strings for the low energy array Deep Core. The strings are deployed in the deep ice between 1,450 and 2,450 meters depth, each string containing 60 optical sensors. The data used in this analysis are the data collected from April 2007 to March 2008 with 22 deployed strings. The data contain ~ 4.3 billion downward going muon events. A two-dimensional skymap is presented with an evidence of 0.06% large scale anisotropy. The energy dependence of this anisotropy at median energies per CR particle of 12 TeV and 126 TeV is also presented in this work. This anisotropy could arise from a number of possible effects; it could further enhance the understanding of the structure of the galactic magnetic field and possible cosmic ray sources.**

***Keywords*: IceCube, Cosmic rays, Anisotropy.**

I. Introduction

The intensity of Galactic Cosmic Rays (GCRs) have been observed to show sidereal anisotropic variation on the order of 10^{-4} at energies in the range of 1-100 TeV ([1], [2] and [3]). This anisotropy could arise from number of different combination of causes. One possible cause could be the Compton Getting (CG) effect. This effect was proposed in 1935 [4] predicting that CR anisotropy could arise from the movement of the solar system around the galactic center with the velocity of $\sim$ 220 kms^{-1} such that an excess of CR would be present in the direction of motion of the solar system while a deficit would appear in the opposite direction. Another possible effect (proposed by Nagashima *et. al*. [1]) causing the excess in the anisotropy, which was referred to as "tail-in", originates from close to the tail of the hemisphere. While the deficit in the anisotropy, which was referred to as "loss-cone", originates from a magnetic cone shaped structure of the galactic field in the vicinity region.

In this paper we present results on the observation of large scale cosmic ray anisotropy by IceCube. Previous experiments have published a 2-dimensional skymap of the northern hemisphere sky ([2]- [5]). This measurement presents the first 2-dimensional skymap for the southern hemisphere sky. In addition, we present the energy dependence of this anisotropy at median energies per CR particle of 12 TeV and 126 TeV.

The outline of the paper is: the second section will describe the data used in this analysis, the analysis method and the challenges. The third section will discuss the results and the stability checks applied to the data. The fourth section will discuss the anisotropy energy dependence and the last section is the conclusion.

II. Data Analysis

The data used in this analysis are the downward going muons collected by the IceCube neutrino observatory comprising 22 strings. The data were collected from June 2007 to March 2008. The events used in this analysis are those reconstructed by an online one iteration Likelihood (LLH) based reconstruction algorithm. The events selected online require at least ten triggered optical sensors on at least three strings. The average rate of these events is ~ 240 Hz (approximately 40 $\%$ of the events at triggering level). Further selection criteria are applied to the data to ensure good quality and stable runs. The final data set consists of 4.3×10^9 events with a median angular resolution (angle between the reconstructed muon and the primary particle) of 3° and a median energy per CR particle of 14 TeV as simulated according to (CORSIKA [6], SIBYLL [7], Hörandel [8]).

In this analysis we are searching for a high precision anisotropy. The sidereal variation of the CR intensity is induced by the anisotropy in their arrival direction. However, it can also be caused by the detector exposure asymmetries, non-uniform time coverage, diurnal and seasonal variation of the atmospheric temperature. Apart from these effects the remaining variations can only be of galactic origin.

Due to the unique location of IceCube at the South Pole the detector observes the sky uniformly. This is not the case for all the previous experiments searching for large scale cosmic ray anisotropy (e.g. [2], [3], [5]). Due to their locations they need a whole solar day to scan the entire sky. As a result they need to eliminate the diurnal and seasonal variations using various approaches. For IceCube the diurnal variation does not effect the sidereal variation because the whole sky is fully visible to the detector at any given time and because there is only one day and one night per year. In addition, although the seasonal variation is on the order of 20% the variation is slow and does not affect the daily muon intensity significantly.

The remaining challenge for this analysis is accounting for the detector asymmetry, and unequal time coverage in the data due to the detector run selection. To illustrate the detector asymmetry Figure 1 shows the IceCube 22 string geographical configuration. This geographical asymmetry results in a preferred reconstructed muon direction since the muons would pass by more strings in one direction in the detector compared to another. The combination of detector event asymmetry with a non-uniform time coverage would induce an azimuthal asymmetry and consequently artificial anisotropy of the arrival direction of cosmic rays. This asymmetry is corrected for by normalizing the azimuthal distribution.

Figure 2 shows the azimuthal distribution for the whole data set. It displays the number of events vs. the azimuth of the arrival direction of the primary CR particle. Note that the asymmetry in the azimuthal distribution due to detector geometry is modeled well by simulation.

To correct for the detector azimuthal asymmetry we apply an azimuthal normalization. The azimuthal distribution is parameterized by N, n_i, and $\bar{n}$, where N is the total number of bins, n_i is the number of events per bin and $\bar{n}$ is the average number of events, $\bar{n} = \frac{1}{N}\sum_{i=1}^{N} n_i$. $\bar{n}$ is denoted by the horizontal red line in Figure 2. The azimuthal normalization is applied by weighting each event by $\frac{\bar{n}}{n_i}$ for that event.

In addition to the azimuthal asymmetry we also observe a zenith angle asymmetry (more events arrive from the zenith than from the horizon). Due to this declination dependence, the sky is divided into four declination bands such that the data is approximately equally distributed among the declination bands. For each band the azimuthal distribution is normalized for the whole year. The relative intensity for each bin in the 2-dimensional skymap is then calculated by dividing the number of events per bin by the total number of events per declination.

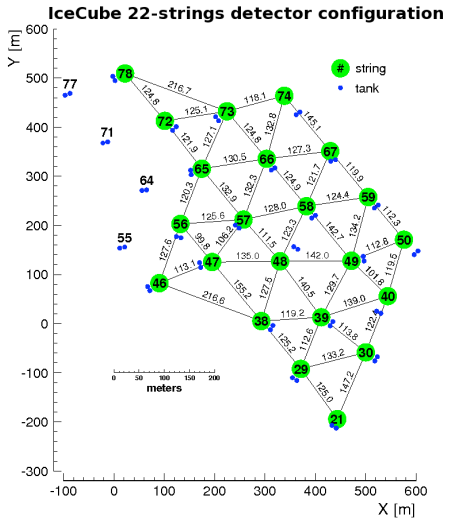

Fig. 1: The IceCube detector configuration. The filled green circles are the positions of IceCube strings and the filled blue circles display the position of the IceTop tanks.

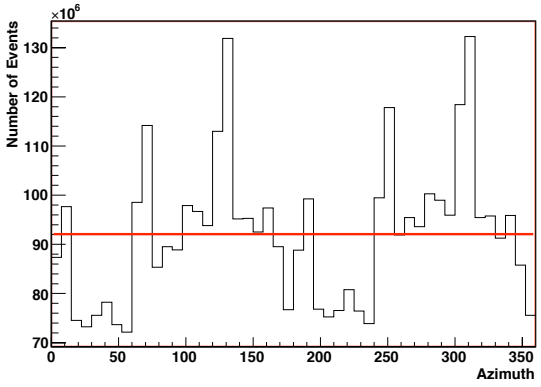

Fig. 2: The azimuthal distribution for the whole data set. This plot shows the number of events vs. the azimuth of the arrival direction of the primary CR particle. The horizontal red line in the average number of events for the distribution.

III. Results:

Figure 3 shows the southern hemisphere skymap for well reconstructed downward going muons for the IceCube 22-Strings data set. The skymap is plotted in equatorial coordinates. The color scale represents the relative intensity of the rate for each bin per declination band where each bin rate is calculated by dividing the number of events for that bin over the average number of events for that bin's declination band. The plot shows a large scale anisotropy in the arrival direction of cosmic rays. The amplitude and the phase of this anisotropy is determined by projecting the 2-dimensional skymap in Right Ascension (RA) as shown in Figure 4. Figure 4 shows the relative intensity vs. the RA. The data are shown in points with their error bars. The fit is the second-order harmonic function in the form of $\sum_{i=1}^{n=2}(A_i \times \cos(i\ ((RA) - \phi_i))) + B$ where A_i is the amplitude and ϕ_i is the phase and B is a constant. The fit A_i, ϕ_i and $\chi^2/ndof$ for the second harmonic fit are listed in table I. The significance of the 2-dimensional skymap is shown in Figure 5. The significance is calculated for each bin from the average number of events for that bin's declination band. Note that the significance of several bins in the excess region is greater than 4σ and in some bins in the deficit region is smaller the -4σ.

A_1. (10^{-4})	ϕ_1	A_2. (10^{-4})	ϕ_2	$\chi^2/ndof$
6.4±0.2	66.4° ±2.6°	2.1±0.3	−65.6° ±4°	22/19

TABLE I: The second harmonic fit amplitude, phase, and $\chi^2/ndof$.

To check for the stability of the measured large scale

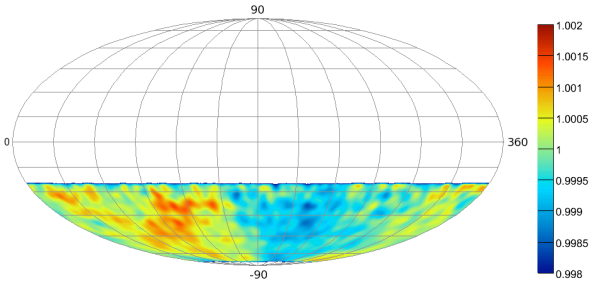

Fig. 3: The IceCube skymap in equatorial coordinates (Declination (Dec) vs. Right Ascension (RA)). The color scale is the relative intensity.

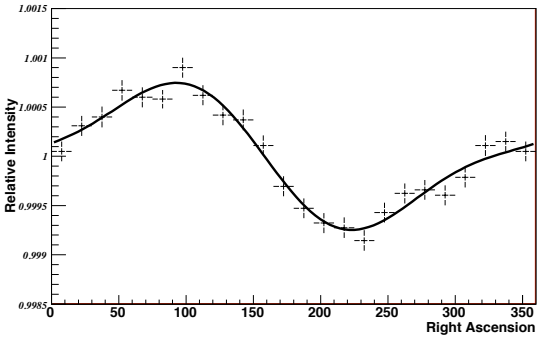

Fig. 4: The 1-dimensional projection of the IceCube 2-dimensional skymap. The line is the second harmonic function fit.

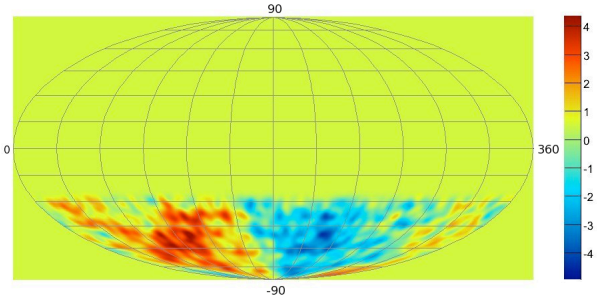

Fig. 5: The IceCube significance skymap in equatorial coordinates (Dec vs. RA). The color scale is the significance.

anisotropy we performed a number of checks with the data set. One check was applied by dividing the data into two sets where one set contains sub-runs with an even index number and the other set contains sub-runs with an odd index number (a sub-run on average contains events collected for $\sim$ 20 minutes at a time). Another check is applied by dividing the data into two sets each set contains half the sub-runs selected randomly. The results for both tests were consistent.

In addition, stability checks are applied to test for daily and seasonal variation effects. To test for the daily variation effect the data were divided in two sets: The first set contains sub-runs with rate values greater than the mean rate value for that sub-run's day. The second set contains sub-runs with rate values less than the mean rate value for that sub-run's day. Furthermore, to test for the seasonal variation effect the data set is divided in two sets: The first set holds the winter month's sub-runs (June-Oct.). The second set holds the summer month's sub-runs (Nov.-March). For both tests we see no significant changes in the value of the anisotropy of the two data sets.

IV. Energy Dependence:

In order to better understand the possible nature of the anisotropy we have searched for energy dependent effects using our data. To determine the energy dependence for the signal we divided the data into two energy bins. To accomplish that and to ensure constant energy distribution along our sky both the number of sensors triggered by the event and the zenith angle of the event are used for the energy bands selection. The first energy bin contains 3.8×10^9 events with a median per CR particle of 12.6 TeV and 90% of the events between 2 and 158 TeV. The second energy bin contains 9.6×10^8 events with a median energy per CR particle of 126 TeV and 90% of the events between 10 TeV and 1 PeV. Each 2-dimensional skymap is projected to 1-dimensional variations in RA. In comparison to previous experiments the 1-dimensional RA distribution is fitted to a first harmonic fit. The first harmonic fit amplitude and phase for the first energy band are $A_1 = (7.3 \pm 0.3) \times 10^{-4}$ and $\phi_1 = 63.4^\circ \pm 2.6^\circ$, while the amplitude and phase for the second energy band are $A_1 = (2.9 \pm 0.6) \times 10^{-4}$ and $\phi_1 = 93.2^\circ \pm 12^\circ$. Figure 6 shows the amplitude of this analysis (in filled circles) in comparison to previous experiments (In empty squares). Note that the amplitude in this analysis shows a decrease of the harmonic amplitude value at the higher energies for the energy ranges of 10-100 TeV.

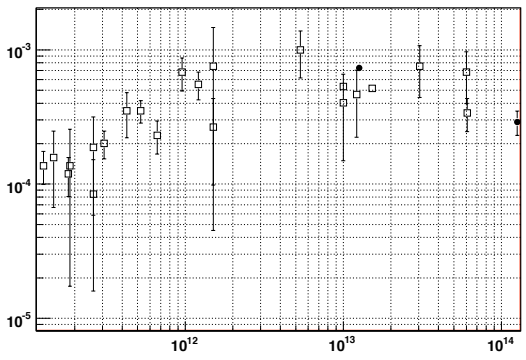

Fig. 6: The filled circles markers are the result of this analysis and the empty square markers are the result from previous experiments ([3], [9], [10], [11], [12], [13], [14], [15], [16], [17], [18], [19], [20], [21], [22], [23], [24], [25]).

V. Conclusion

In this analysis we present the first 2-dimensional skymap for the southern hemisphere of 4.3 billion cosmic rays with a median angular resolution of 3° and a median energy per CR particle of 14 TeV as observed by IceCube. A large cosmic ray anisotropy with a second harmonic vector amplitude of $A_1 = (6.4 \pm 0.2) \times 10^{-4}$ and a phase of $\phi_1 = 66.4^\circ \pm 2.6^\circ$ is observed. The significance of some bins in the excess and the deficit regions were found to be $> |4\sigma|$. This anisotropy is an extension of previously measured large scale anisotropy at the northern hemisphere reported by multiple experiments ([2]- [5]).

In addition, we report on the anisotropy energy dependence. We report the amplitude of the first harmonic vector of the anisotropy for the two energy bands. The first energy band with a median energy per CR particle of 12.6 TeV the amplitude is found to be $A_1 = (7.3 \pm 0.3) \times 10^{-4}$. The second energy band with a median energy per CR particle of 126 TeV the amplitude is found to be $A_1 = (2.9 \pm 0.6) \times 10^{-4}$. The amplitude energy dependence is found to follow a decreasing trend with energy.

VI. Acknowledgments

We acknowledge the support from the following agencies: U.S. National Science Foundation-Oce of Polar Program, U.S. National Science Foundation-Physics Division, University of Wisconsin Alumni Research Foundation, U.S. Department of Energy, and National Energy Research Scientic Computing Center, the Louisiana Optical Network Initiative (LONI) grid computing resources; Swedish Research Council, Swedish Polar Research Secretariat, and Knut and Alice Wallenberg Foundation, Sweden; German Ministry for Education and Research (BMBF), Deutsche Forschungsgemeinschaft (DFG), Germany; Fund for Scientic Research (FNRS-FWO), Flanders Institute to encourage scientic and technological research in industry (IWT), Belgian Federal Science Policy Oce (Belspo); the Netherlands Organisation for Scientic Research (NWO); M. Ribordy acknowledges the support of the SNF (Switzerland); A. Kappes and A. Groß acknowledge support by the EU Marie Curie OIF Program.

References

[1] K. Nagashima *et. al Journal of Geophysical Research*, vol. 103, pp. 17429–17440, Aug. 1998.
[2] M. Amenomori *et. al Science*, vol. 314, pp. 439–443, Oct. 2006.
[3] G. Guillian and for the Super-Kamiokande Collaboration *Physical Review D*, vol. 75, p. 062003, 2007.
[4] A. H. Compton and I. A. Getting *Physical Review*, vol. 47, pp. 817–821, June 1935.
[5] A. Abdo *et. al. ArXiv:astro-ph/0806.2293*, 2008.
[6] CORSIKA *http://www-ik.fzk.de/corsika/*.
[7] R. Engel vol. 1 of *International Cosmic Ray Conference*, p. 415, 1999.
[8] J. R. Hörandel *Astroparticle Physics*, vol. 19, pp. 193–220, May 2003.
[9] K. Munakata *et. al. Physical Review D*, vol. 56, p. 23, 1997.
[10] M. Ambrosio *et. al. Physical Review D*, vol. 67, p. 042002, 2003.
[11] D. Swinson *et. al. Planet. Space Sci.*, vol. 33, p. 1069, 1985.
[12] K. Nagashima *et. al. Planet. Space Sci.*, vol. 33, p. 395, 1985.
[13] H. Ueno *et. al.* vol. 6 of *International Cosmic Ray Conference*, p. 361, 1990.
[14] T. Thambyahpillai vol. 3 of *International Cosmic Ray Conference*, p. 383, Aug. 1983.
[15] K. Munakata *et. al.* vol. 4 of *International Cosmic Ray Conference*, p. 639, 1995.
[16] S. Mori *et. al.* vol. 4 of *International Cosmic Ray Conference*, p. 648, 1995.
[17] M. Bercovitch *et. al.* vol. 10 of *International Cosmic Ray Conference*, p. 246, 1981.
[18] B. K. Fenton *et. al.* vol. 4 of *International Cosmic Ray Conference*, p. 635, 1995.
[19] Y. W. Lee *et. al.* vol. 2 of *International Cosmic Ray Conference*, p. 18, 1987.
[20] D. J. Cutler *et. al. Astrophys. J.*, vol. 376, pp. 322–334, July 1991.
[21] Y. M. Andreyev *et. al.* vol. 2 of *International Cosmic Ray Conference*, p. 22, 1987.
[22] K. Munakata vol. 7 of *International Cosmic Ray Conference*, p. 293, 1999.
[23] V. V. Alexeyenko *et. al.* vol. 2 of *International Cosmic Ray Conference*, p. 146, 1981.
[24] M. Aglietta *et. al.* vol. 2 of *International Cosmic Ray Conference*, p. 800, 1995.
[25] T. Gombosi *et. al.* vol. 2 of *International Cosmic Ray Conference*, pp. 586–591, 1975.

Atmospheric Variations as observed by IceCube

Serap Tilav[*], Paolo Desiati[†], Takao Kuwabara[*], Dominick Rocco[†], Florian Rothmaier[‡], Matt Simmons[*], Henrike Wissing[§¶] for the IceCube Collaboration[‖]

[*] *Bartol Research Institute and Dept. of Physics and Astronomy, University of Delaware, Newark, DE 19716, USA.*
[†] *Dept. of Physics, University of Wisconsin, Madison, WI 53706, USA.*
[‡] *Institute of Physics, University of Mainz, Staudinger Weg 7, D-55099 Mainz, Germany.*
[§] *III Physikalisches Institut, RWTH Aachen University, D-52056 Aachen, Germany.*
[¶] *Dept. of Physics, University of Maryland, College Park, MD 20742, USA.*
[‖] *See the special section of these proceedings*

***Abstract*. We have measured the correlation of rates in IceCube with long and short term variations in the South Pole atmosphere. The yearly temperature variation in the middle stratosphere (30-60 hPa) is highly correlated with the high energy muon rate observed deep in the ice, and causes a $\pm$10% seasonal modulation in the event rate. The counting rates of the surface detectors, which are due to secondary particles of relatively low energy (muons, electrons and photons), have a negative correlation with temperatures in the lower layers of the stratosphere (40-80 hPa), and are modulated at a level of $\pm$5%. The region of the atmosphere between pressure levels 20-120 hPa, where the first cosmic ray interactions occur and the produced pions/kaons interact or decay to muons, is the Antarctic ozone layer. The anti-correlation between surface and deep ice trigger rates reflects the properties of pion/kaon decay and interaction as the density of the stratospheric ozone layer changes. Therefore, IceCube closely probes the ozone hole dynamics, and the temporal behavior of the stratospheric temperatures.**

***Keywords*: IceCube, IceTop, South Pole**

I. Introduction

The IceCube Neutrino Observatory, located at the geographical South Pole (altitude 2835m), has been growing incrementally in size since 2005, surrounding its predecessor AMANDA[1]. As of March 2009, IceCube consists of 59 strings in the Antarctic ice, and 59 stations of the IceTop cosmic ray air shower array on the surface. Each IceCube string consists of 60 Digital Optical Modules (DOMs) deployed at depths of 1450-2450m, and each IceTop station comprises 2 ice Cherenkov tanks with 2 DOMs in each tank.

IceCube records the rate of atmospheric muons with $E_\mu \geq 400$ GeV. Muon events pass the IceCube Simple Majority Trigger (InIce_SMT) if 8 or more DOMs are triggered in 5μsec. The IceTop array records air showers with primary cosmic ray energies above 300 TeV. Air showers pass the IceTop Simple Majority Trigger (IceTop_SMT) if 6 or more surface DOMs trigger within 5μsec.

As the Antarctic atmosphere goes through seasonal changes, the characteristics of the cosmic ray interactions in the atmosphere follow these variations. When the primary cosmic ray interacts with atmospheric nuclei, the pions and kaons produced at the early interactions mainly determine the nature of the air shower. For the cosmic ray energies discussed here, these interactions happen in the ozone layer (20-120 hPa pressure layer at 26 down to 14 km) of the South Pole stratosphere. During the austral winter, when the stratosphere is cold and dense, the charged mesons are more likely to interact and produce secondary low energy particles. During the austral summer when the warm atmosphere expands and becomes less dense, the mesons more often decay rather than interact.

Figure 1 demonstrates the modulation of rates in relation to the temporal changes of the South Pole stratosphere. The scaler rate of a single IceTop DOM on the surface is mostly due to low energy secondary particles (MeV electrons and gammas, $\sim$1 GeV muons)[2] produced throughout the atmosphere, and therefore highly modulated by the atmospheric pressure. However, after correcting for the barometric effect, the IceTop DOM counting rate also reflects the initial pion interactions in the middle stratosphere. The high energy muon rate in the deep ice, on the other hand, directly traces the decay characteristics of high energy pions in higher layers of the stratosphere. The IceCube muon rate reaches its maximum at the end of January when the stratosphere is warmest and most tenuous. Around the same time Icetop DOMs measure the lowest rates on the surface as the pion interaction probability reaches its minimum. The high energy muon rate starts to decline as the stratosphere gets colder and denser. The pions will interact more often than decay, yielding the maximum rate in IceTop and the minimum muon rate in deep ice at the end of July.

II. Atmospheric effects on the IceCube Rates

The Antarctic atmosphere is closely monitored by the NOAA Polar Orbiting Environmental Satellites (POES) and by the radiosonde balloon launches of the South Pole Meteorology Office. However, stratospheric data

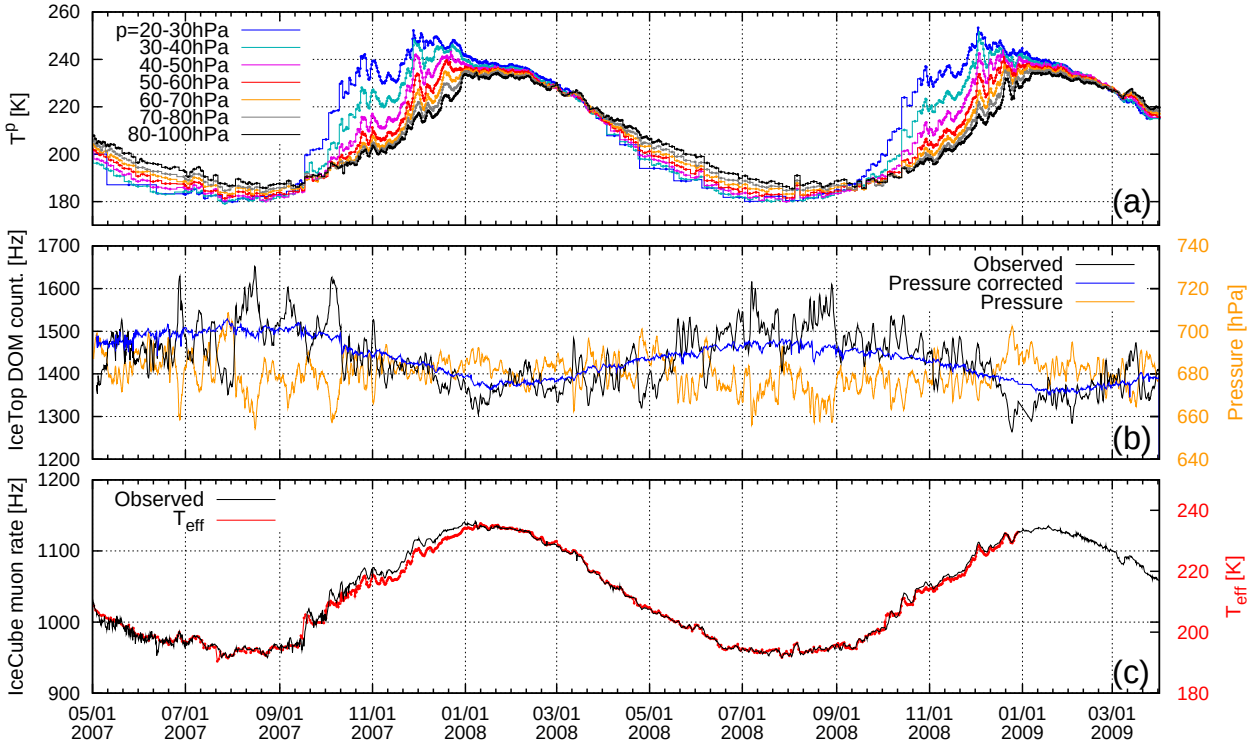

Fig. 1. The temporal behavior of the South Pole stratosphere from May 2007 to April 2009 is compared to IceTop DOM counting rate and the high energy muon rate in the deep ice. (a) The temperature profiles of the stratosphere at pressure layers from 20 hPa to 100 hPa where the first cosmic ray interactions happen. (b) The IceTop DOM counting rate (black -observed, blue -after barometric correction) and the surface pressure (orange). (c) The IceCube muon trigger rate and the calculated effective temperature (red).

is sparse during the winter when the balloons do not reach high altitudes, and satellite based soundings fail to return reliable data. For such periods NOAA derives temperatures from their models. We utilize both the ground-based data and satellite measurements/models for our analysis.

A. Barometric effect

In first order approximation, the simple correlation between log of rate change $\Delta\{lnR\}$ and the surface pressure change ΔP is

$$\Delta\{lnR\} = \beta \cdot \Delta P \tag{1}$$

where β is the barometric coefficient.

As shown by the black line in the Figure 1b, the observed IceTop DOM counting rate varies by $\pm 10\%$ in anti-correlation with surface pressure, and the barometric coefficient is determined to be $\beta = -0.42\%$/hPa. Using this value, the pressure corrected scaler rate is plotted as the smoother line (blue) in Figure 1b. The cosmic ray shower rate detected by the IceTop array also varies by $\pm 17\%$ in anti-correlation with surface pressure, and can be corrected with a β value of -0.77%/hPa. As expected [3], the IceCube muon rate shown in Figure 1c is not correlated with surface pressure. However, during exceptional stratospheric temperature changes, the second order temperature effect on pressure becomes large enough to cause anti-correlation of the high energy muon rate with the barometric pressure. During such events the effect directly reflects sudden stratospheric density changes, specifically in the ozone layer.

B. Seasonal Temperature Modulation

Figure 1 clearly demonstrates the seasonal temperature effect on the rates. The IceTop DOM counting rate, after barometric correction, shows $\pm 5\%$ negative temperature correlation. On the other hand, the IceCube muon rate is positively correlated with $\pm 10\%$ seasonal variation.

From the phenomenological studies [4][5], it is known that correlation between temperature and muon intensity can be described by the effective temperature T_{eff}, defined by the weighted average of temperatures from the surface to the top of the atmosphere. T_{eff} approximates the atmosphere as an isothermal body, weighting each pressure layer according to its relevance to muon production in atmosphere [5][6].

The variation of muon rate $\Delta R_\mu / < R_\mu >$ is related to the effective temperature as

$$\frac{\Delta R_\mu}{< R_\mu >} = \alpha_T \frac{\Delta T_{eff}}{< T_{eff} >}, \tag{2}$$

where α_T is the atmospheric temperature coefficient.

Using balloon and satellite data for the South Pole atmosphere, we calculated the effective temperature as the red line in Figure 1c. We see that it traces the IceCube muon rate remarkably well. The calculated temperature coefficient $\alpha_T = 0.9$ for the IceCube muon

TABLE I
Temperature and correlation coefficients of rates for different stratospheric layers of 20-100 hPa and T_{eff}.

		IceCube Muon		IceTop Count.	
P (hPa)	$< T^p >$ (K)	α_T^p	γ	α_T^p	γ
20-30	214.0	0.512	0.953	-0.194	-0.834
30-40	208.7	0.550	0.986	-0.216	-0.906
40-50	207.3	0.591	0.993	-0.240	-0.946
50-60	206.6	0.627	0.985	-0.261	-0.968
60-70	206.3	0.656	0.971	-0.278	-0.975
70-80	206.3	0.679	0.954	-0.292	-0.975
80-100	206.5	0.708	0.927	-0.310	-0.971
	$< T_{eff} >$	α_T	γ	α_T	γ
	211.3	0.901	0.990	-0.360	-0.969

rate agrees well with the expectations of models as well as with other experimental measurements[7][8].

In this paper, we also study in detail the relation between rates and stratospheric temperatures for different pressure layers from 20 hPa to 100 hPa as

$$\frac{\Delta R}{< R >} = \alpha_T^p \frac{\Delta T^p}{< T^p >}. \quad (3)$$

The temperature coefficients for each pressure layer α_T^p and the correlation coefficient γ are determined from regression analysis. Pressure-corrected IceTop DOM counting rate, and IceCube muon rate are sorted in bins of $\sim$ 10 days, and deviations $\Delta R/ < R >$ from the average values are compared with the deviation of temperatures at different depths $\Delta T^p/ < T^p >$.

We list the values of α_T^p and γ for IceCube muon rate and IceTop DOM counting rate in Table 1. We find that the IceCube muon rate correlates best with the temperatures of 30-60 hPa pressure layers, while the IceTop DOM counting rate shows the best correlation with 60-80 hPa layers. In Figure 2. we plot the rate and temperature correlation for layers which yield the best correlation.

III. Exceptional Stratospheric Events and the Muon Rates

The South Pole atmosphere is unique because of the polar vortex. In winter a large-scale counter clockwise flowing cyclone forms over the entire continent of Antarctica, isolating the Antarctic atmosphere from higher latitudes. Stable heat loss due to radiative cooling continues until August without much disruption, and the powerful Antarctic vortex persists until the sunrise in September. As warm air rushes in, the vortex loses its strength, shrinks in size, and sometimes completely disappears in austral summer. The density profile inside the vortex changes abruptly during the sudden stratospheric warming events, which eventually may cause the vortex collapse. The ozone depleted layer at 14-21 km altitude (ozone hole), observed in September/October period, is usually replaced with ozone rich layer at 18-30 km soon after the vortex breaks up.

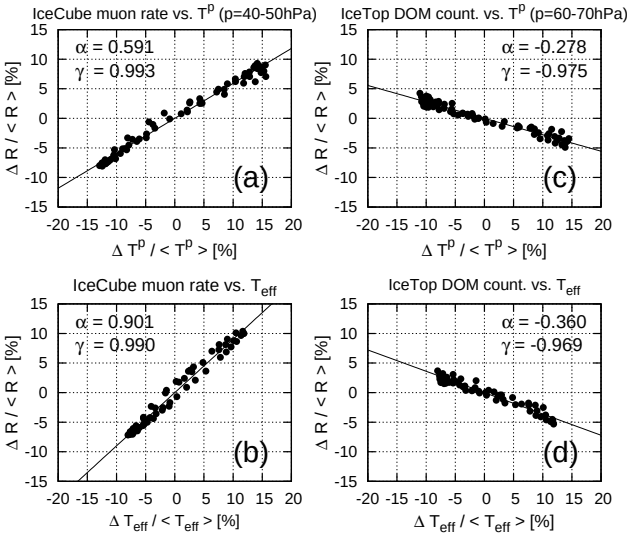

Fig. 2. Correlation of IceCube muon and IceTop DOM counting rates with stratospheric temperatures and T_{eff}. (a) IceCube muon rate vs. temperature at 40-50 hPa pressure layer. (b) IceCube muon rate vs. effective temperature. (c) IceTop DOM counting rate vs. temperature at 70-80 hPa pressure layer. (d) IceTop DOM counting rate vs. effective temperature.

Apart from the slow seasonal temperature variations, IceCube also probes the atmospheric density changes due to the polar vortex dynamics and vigorous stratospheric temperature changes on time scales as short as days or even hours, which are of great meteorological interest.

An exceptional and so far unique stratospheric event has already been observed in muon data taken with IceCube's predecessor AMANDA-II.

A. 2002 Antarctic ozone hole split detected by AMANDA

In late September 2002 the Antarctic stratosphere underwent its first recorded major Sudden Stratospheric Warming (SSW), during which the atmospheric temperatures increased by 40 to 60 K in less than a week. This unprecedented event caused the polar vortex and the ozone hole, normally centered above the South Pole, to split into two smaller, separate off-center parts (Figure 3) [9].

Figure 4 shows the stratospheric temperatures between September and October 2002 along with the AMANDA-II muon rate. The muon rate traces temperature variations in the atmosphere in great detail, with the strongest correlation observed for the 40-50 hPa layer.

B. South Pole atmosphere 2007-2008

Unlike in 2002, the stratospheric conditions over Antarctica were closer to average in 2007 and 2008. In 2007 the polar vortex was off-center from the South Pole during most of September and October, resulting in greater heat flux into the vortex, which decreased rapidly in size. When it moved back over the colder Pole region in early November it gained strength and persisted until the beginning of December. The 2008 polar vortex was

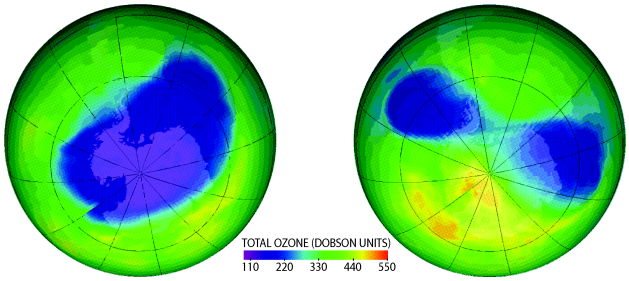

Fig. 3. Ozone concentration over the southern hemisphere on September 20th 2002 (left) and September 25th 2002 (right) [10].

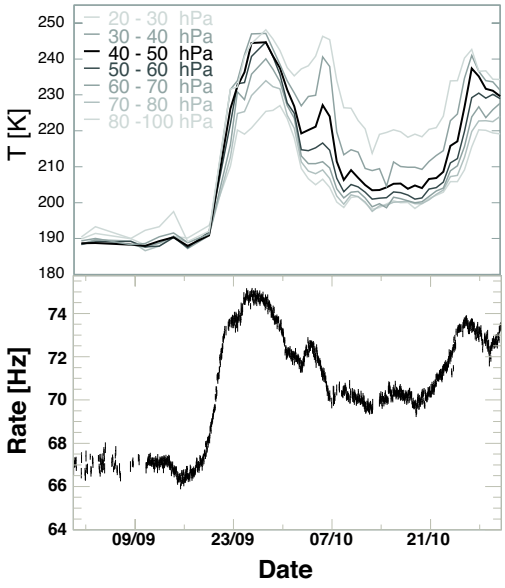

Fig. 4. Average temperatures in various atmospheric layers over the South Pole (top) and deep ice muon rate recorded with the AMANDA-II detector (bottom) during the Antarctic ozone hole split of September-October 2002.

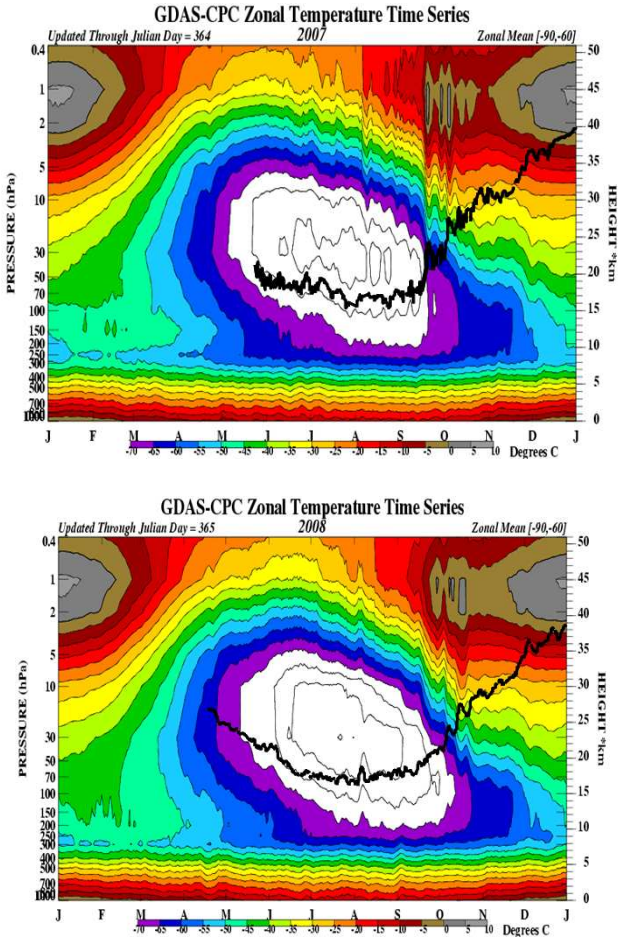

Fig. 5. The temperature time series of the Antarctic atmosphere produced by NOAA[11] are shown for 2007 and 2008. The pattern observed in the deep ice muon rate (black line) is superposed onto the plot to display the striking correlation with the stratospheric temperature anomalies.

one of the largest and strongest observed in the last 10 years over the South Pole. Because of this, the heat flux entering the area was delayed by 20 days. The 2008 vortex broke the record in longevity by persisting well into mid-December.

In Figure 5 we overlay the IceCube muon rate over the temperature profiles of the Antarctic atmosphere produced by the NOAA Stratospheric analysis team[11]. We note that the anomalous muon rates (see, for example, the sudden increase by 3% on 6 August 2008) observed by IceCube are in striking correlation with the middle and lower stratospheric temperature anomalies.

We are establishing automated detection methods for anomalous events in the South Pole atmosphere as well as a detailed understanding and better modeling of cosmic ray interactions during such stratospheric events.

IV. Acknowledgements

We are grateful to the South Pole Meteorology Office and the Antarctic Meteorological Research Center of the University of Wisconsin-Madison for providing the meteorological data. This work is supported by the National Science Foundation.

References

[1] Karle, A. for the IceCube Collaboration (2008), IceCube: Construction Status and First Results, arXiv:0812.3981v1.
[2] Clem, J. et al. (2008), Response of IceTop tanks to low-energy particles, Proceedings of the 30th ICRC, Vol. 1 (SH), p.237-240.
[3] Dorman, L. (2004), Cosmic Rays in the Earth's Atmosphere and Underground, Springer Verlag.
[4] Barrett P. et al. (1952), Interpretation of cosmic-ray measurements far underground, Reviews of Modern Physics, Vol. 24, Issue 3, p.133-178.
[5] Ambrosio, M. et al. (1997), Seasonal variations in the underground muon intensity as seen by MACRO, Astroparticle Physics, Vol. 7, Issue 1-2, p.109-124.
[6] Gaisser, T. (1990), Cosmic rays and particle physics. Cambridge, UK: Univ. Pr.
[7] Grashorn, E. et al., Observation of the seasonal variation in underground muon intensity, Proceedings of the 30th ICRC, Vol. 5 (HE part 2), p.1233-1236.
[8] Osprey, S., et al. (2009), Sudden stratospheric warmings seen in MINOS deep underground muon data, Geophys. Res. Lett., 36, L05809, doi:10.1029/2008GL036359.
[9] Varotsos, C., et al. (2002), Environ. Sci. & Pollut. Res., p.375.
[10] http://ozonewatch.gsfc.nasa.gov
[11] http://www.cpc.noaa.gov/products/stratosphere/strat-trop/

Supernova Search with the AMANDA / IceCube Detectors

Thomas Kowarik*, Timo Griesel*, Alexander Piégsa* for the IceCube Collaboration†

* *Institute of Physics, University of Mainz, Staudinger Weg 7, D-55099 Mainz, Germany*
† *see the special section of these proceedings*

Abstract. **Since 1997 the neutrino telescope AMANDA at the geographic South Pole has been monitoring our Galaxy for neutrino bursts from supernovae. Triggers were introduced in 2004 to submit burst candidates to the Supernova Early Warning System SNEWS. From 2007 the burst search was extended to the much larger IceCube telescope, which now supersedes AMANDA. By exploiting the low photomultiplier noise in the antarctic ice (on average 280 Hz for IceCube), neutrino bursts from nearby supernovae can be identified by the induced collective rise in the pulse rates. Although only a counting experiment, IceCube will provide the world's most precise measurement of the time profile of a neutrino burst near the galactic center. The sensitivity to neutrino properties such as the θ_{13} mixing angle and the neutrino hierarchy are discussed as well as the possibility to detect the deleptonization burst.**

***Keywords*: supernova neutrino IceCube**

I. Introduction

Up to now, the only detected extra-terrestrial sources of neutrinos are the sun and supernova SN1987A. To extend the search to TeV energies and above, neutrino telescopes such as AMANDA and IceCube [1] have been built. It turns out that the noise rates of the light sensors (OMs) in the antarctic ice are very low ($\sim$ 700 Hz for AMANDA, $\sim$ 280 Hz for IceCube) opening up the possibility to detect MeV electron anti-neutrinos from close supernovae by an increase in the collective rate of all light sensors. The possibility to monitor the galaxy for supernova with neutrino telescopes such as AMANDA has first been proposed in [2] and a first search has been performed using data from the years 1997 and 1998 [3].

The version of the the supernova data acquisition (SNDAq) covered in this paper has been introduced for AMANDA in the beginning of the year 2000 and was extended to IceCube in 2007. The AMANDA SNDAq has been switched off in February 2009. We will investigate data recorded by both telescopes concentrating on the 9 years of AMANDA measurements and make predictions for the expected sensitivity of IceCube.

II. Detectors and Data Acquisition

In AMANDA, the pulses of the 677 OMs are collected in a VME/Linux based data acquisition system which operates independently of the main data acquisition aimed at high energy neutrinos. It counts pulses from every connected optical module in a 20 bit counter in fixed 10 ms time intervals that are synchronized by a GPS-clock.

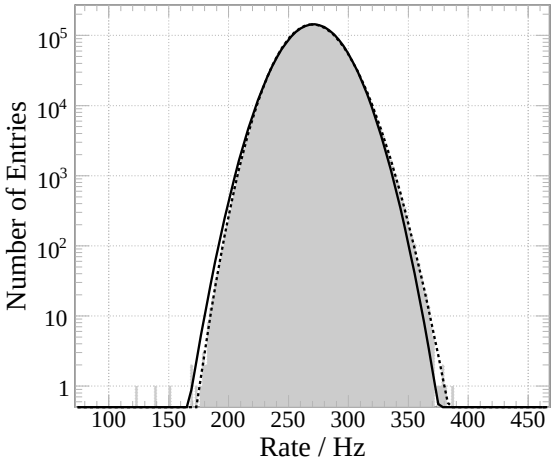

Fig. 1. Rate distribution of a typical IceCube module
The recorded rate distribution (filled area) encompasses about 44 days and has been fitted with a Gaussian (solid line, $\chi^2/N_{\mathrm{dof}} = 56.5$) defined by $\mu = 271\,\mathrm{Hz}$ and $\sigma = 21\,\mathrm{Hz}$. However, a lognormal function (dotted line, $\chi^2/N_{\mathrm{dof}} = 0.66$) with geometric mean $\mu_{\mathrm{geo}} = 6.4\ln(\mathrm{Hz})$, geometric standard deviation $\sigma_{\mathrm{geo}} = 0.03\ln(\mathrm{Hz})$ and a shift of $x_0 = 377\,\mathrm{Hz}$ is much better at describing the data.

In IceCube, PMT rates are recorded in a 1.6384 ms binning by scalers on each optical module. The information is locally buffered and read out by the IceCube data acquisition system. It then transfers this data to the SNDAq, which synchronizes and regroups the information in 2 ms bins.

The software used for data acquisition and analysis is essentially the same for AMANDA and IceCube. The data is rebinned in 500 ms intervals and subjected to an online analysis described later. In case of a significant rate increase ("supernova trigger"), an alarm is sent to the Supernova Early Warning System (SNEWS, [4]) via the Iridium satellite network and the data is saved in a fine time binning (10 ms for AMANDA and 2 ms for IceCube).

III. Sensor Rates

In 500 ms time binning, the pulse distribution of the average AMANDA or IceCube OM conforms only approximately to a Gaussian. It can more accurately be described by a lognormal distribution (see figure 1).

The pulse distributions exhibit Poissonian and correlated afterpulse components contributing with similar

strengths. The correlated component is anticorrelated with temperature and arises form Cherenkov light caused by ^{40}K decays and glass luminescence from radioactive decay chains. A cut at $250\,\mu$s on the time difference of consecutive pulses effectively suppresses afterpulse trains, improves the significance of a simulated supernova at $7.5\,\mathrm{kpc}$ by approximately 20% and makes the pulse distribution more Poissonian in nature.

IV. Effective Volumes

Supernovae radiate all neutrino flavors, but due to the relatively large inverse beta decay cross section, the main signal in IceCube is induced by electron anti-neutrinos (see [5]). The rate R per OM can be approximated weighing the energy dependent anti-electron neutrino flux at the earth $\Phi(E_{\bar{\nu}_e})$ (derived from the neutrino luminosity and spectra found in [6]) with the effective area for anti-electron neutrino detection $A_{\mathrm{eff}}(E_{\bar{\nu}_e})$ and integrating over the whole energy range:

$$R = \int_0^\infty dE_{\bar{\nu}_e}\, \Phi(E_{\bar{\nu}_e}) A_{\mathrm{eff}}(E_{\bar{\nu}_e})\ ,\ \text{with}$$
$$A_{\mathrm{eff}}(E_{\bar{\nu}_e}) = n \int_0^\infty dE_{e^+}\, \tfrac{d\sigma}{dE_{e^+}}(E_{\bar{\nu}_e}, E_{e^+})\, V_{\mathrm{eff},e^+}(E_{e^+})\,.$$

$\frac{d\sigma}{dE_{e^+}}(E_{\bar{\nu}_e}, E_{e^+})$ is the inverse beta decay cross section, n the density of protons in the ice and $V_{\mathrm{eff},e^+}(E_{e^+})$ the effective volume for positron detection of a single OM.

$V_{\mathrm{eff},e^+}(E_{e^+})$ can be calculated by multiplying the number of Cherenkov photons produced with the effective volume for photon detection $V_{\mathrm{eff},\gamma_{\mathrm{ch}}}$.

By tracking Cherenkov photons in the antarctic ice around the IceCube light sensors [7] and simulating the module response one obtains $V_{\mathrm{eff},\gamma_{\mathrm{ch}}} = 0.104\,\mathrm{m}^3$ for the most common AMANDA sensors and $V_{\mathrm{eff},\gamma} = 0.182\,\mathrm{m}^3$ for the IceCube sensors. With a *GEANT-4* simulation, the amount of photons produced by a positron of an energy E_{e^+} can is estimated to be $N^{\gamma_{\mathrm{ch}}} = 270\,E_{e^+}/\,\mathrm{MeV}$. Consequently, the effective volumes for positrons as a function of their energies are $V_{\mathrm{eff},e^+}^{\mathrm{AMANDA}} = 19.5\,E_{e^+}\,\frac{\mathrm{m}^3}{\mathrm{MeV}}$ and $V_{\mathrm{eff},e^+}^{\mathrm{IceCube}} = 34.2\,E_{e^+}\,\frac{\mathrm{m}^3}{\mathrm{MeV}}$. Uncertainties in the effective volumes derive directly from the uncertainties of the ice models ($\sim 5\%$) and in the OM sensitivities ($\sim 10\%$).

In this paper we assume a supernova neutrino production according to the *Lawrence-Livermore* model [8] as it is the only one that provides spectra for up to $15\,\mathrm{s}$. It gives a mean electron anti-neutrino energy of $15\,\mathrm{MeV}$ corresponding to an average positron energy of $(13.4 \pm 0.5)\,\mathrm{MeV}$.

V. Analysis Procedure

A simple investigation of the rate sums would be very susceptible to fluctuations due to variations in the detector response or external influences such as the seasonal variation of muon rates. Medium and long term fluctuations are tracked by estimating the average count rate by a sliding time window. The rate deviation for a collective homogeneous neutrino induced ice illumination is calculated by a likelihood technique. In time bins of $0.5\,\mathrm{s}$ and longer, the pulse distributions can be approximated by Gaussian distributions. For a collective rate increase $\Delta\mu$, the expectation value of the average mean rate μ_i of a light sensor i with relative sensitivity ϵ_i increases to $\mu_i + \epsilon_i\Delta\mu$. The mean value μ_i and its standard deviation σ_i are averaged over a sliding window of $10\,\mathrm{min}$, excluding $15\,\mathrm{s}$ before and after the $0.5\,\mathrm{s}$ time frame r_i studied. By taking the product of the corresponding Gaussian distributions the following likelihood for a rate deviation $\Delta\mu$ is obtained:

$$\mathcal{L} = \prod_{i=1}^{N_{\mathrm{OM}}} \frac{1}{\sqrt{2\pi}\,\sigma_i} \exp - \frac{(r_i - (\mu_i + \epsilon_i\,\Delta\mu))^2}{2\sigma_i^2} \quad .$$

Minimization of $-\ln\mathcal{L}$ leads to:

$$\Delta\mu = \underbrace{\left(\sum_{i=1}^{N_{\mathrm{OM}}} \frac{\epsilon_i^2}{\sigma_i^2}\right)^{-1}}_{=\sigma_{\Delta\mu}^2} \sum_{i=1}^{N_{\mathrm{OM}}} \frac{\epsilon_i\,(r_i - \mu_i)}{\sigma_i^2} \quad .$$

The data is analyzed in the three time binnings $0.5\,\mathrm{s}$, $4\,\mathrm{s}$ and $10\,\mathrm{s}$ for the following reasons: First, the finest time binning accessible to the online analysis is $0.5\,\mathrm{s}$. Second, as argued in [9], the neutrino measurements of SN1987A are roughly compatible with an exponential decay of $\tau = 3\,\mathrm{s}$. The optimal time frame for the detection of a signal with such a signature is $\approx 3.8\,\mathrm{s}$. Last, $10\,\mathrm{s}$ are the approximate time frame where most of the neutrinos from SN1987A fell.

To ensure data quality, the optical modules are subjected to careful quality checks and cleaning. Those modules with rates outside of a predefined range, a high dispersion w.r.t. the Poissonian expectation or a large skewness are disqualified in real time.

Since SNEWS requests one alarm per 10 days, the supernova trigger is set to $6.3\,\sigma$.

To ensure that the observed rate deviation is homogeneous and isotropic, the following χ^2 discriminant is examined:

$$\chi^2(\Delta\mu) = \sum_{i=1}^{N_{\mathrm{OM}}} \left(\frac{r_i - (\mu_i + \epsilon_i\,\Delta\mu)}{\sigma_i}\right)^2 \quad .$$

We demand the data to conform to a χ^2-confidence level of $99.9\,\%$. However, it was found that the χ^2 cannot clearly distinguish between isotropic rate changes and fluctuations of a significant number of OMs: If e.g. 20% of the OMs record rate increases of about $1\,\sigma$ ($\approx 20\,\mathrm{pulses}/0.5\,\mathrm{s}$), the significance for isotropic illumination can rise above $6\,\sigma$ without being rejected by the χ^2 condition. Still, no method was found that performed better than χ^2.

VI. External Perturbations

Figure 2 shows the distribution of the significance $\xi = \frac{\Delta\mu}{\sigma_{\Delta\mu}}$ for AMANDA. From the central limit theorem, one would expect a Gaussian distribution with a width of

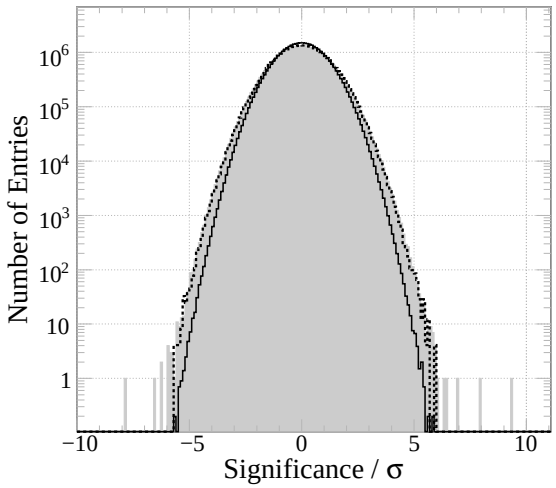

Fig. 2. Significances of AMANDA in $0.5\,\mathrm{s}$ time frames
The filled area shows the significance of the data taken in 2002 with a spread of $\sigma = 1.13$. The solid line denotes the initial background simulation ($\sigma \approx 1$) and the dotted line is a toy monte carlo taking into account the fluctuations due to muon rates ($\sigma \approx 1.11$).

$\sigma = 1$. This expectation is supported by a background simulation using lognormal representations of individual light sensor pulse distributions. However, one finds that the observable is spread wider than expected and exhibits a minor shoulder at high significances.

As this observable is central to the identification of supernovae, its detailed understanding is imperative and a close investigation of these effects is necessary.

Faults in the software were ruled out by simulating data at the most basic level, before entering the SNDAq. Hardware faults are improbable, as the broadening of the rates is seen both for AMANDA ($\sigma = 1.13$) and IceCube ($\sigma = 1.27$) and the detectors use different and independent power and readout electronics.

One can then check for external sources of rate changes as tracked by magnetometers, rio- and photometers as well as seismometers at Pole. All have been synchronized with the rate measurements of the OMs. Only magnetic field variations show a slight, albeit insignificant, influence on the rate deviation of $-4{\cdot}10^{-5}\,\frac{\mathrm{Hz}}{\mathrm{nT}}$ for AMANDA. Due to a μ metal wire mesh shielding, the influence on IceCube sensors is smaller by a factor ~ 30.

It turns out that the main reason for the broadening are fluctuations of the atmospheric muon rates. During $0.5\,\mathrm{s}$, AMANDA detects between $\approx 3.0 \cdot 10^3$ (June) and $\approx 3.4{\cdot}10^3$ (December) sensor hits due to muons. Adding hits from atmospheric muons broadens and distorts the distribution derived from noise rates. A simulation taking into account the muon triggered PMT hits increases the width of the significance distribution to ≈ 1.11 (see figure 2). Although the investigations are still ongoing for IceCube, we expect the larger σ can be ascribed to its lower noise rate leading to a higher resolution and thereby a stronger sensitivity to perturbations.

A Fourier transformation was performed on the data stream. No evidence for periodically recurring events was found, but occasional correlations between subsequent $0.5\,\mathrm{s}$ time frames both in the summed noise rate and the rate deviation could be identified. We determined the mean significance before and after a rate increase exceeding a predefined level. One observes a symmetric correlation in the data mainly between $\pm 10\,\mathrm{s}$. The origin of the effect, which is present both in AMANDA and IceCube data, is under investigation.

VII. Expected Signal and Visibility Range

A preliminary analysis of AMANDA data from 2000 to 2003 yielded a detection range of $R_{4\,\mathrm{s}} = 14.5\,\mathrm{kpc}$ at the optimal binning of $4\,\mathrm{s}$ at an efficiency of 90%, encompassing 81% of the stars of our Galaxy. As signals with exponentially decreasing luminosity (at $\tau = 3\,\mathrm{s}$) have been used as underlying models, the two other binnings were less efficient with $R_{0.5\,\mathrm{s}} = 10\,\mathrm{kpc}$ (56%) and $R_{10\,\mathrm{s}} = 13\,\mathrm{kpc}$ (75%), respectively.

The rates of the IceCube sensors are stable and uniform across the detector. Scaling the observed rates to the full 80 string detector, a summed rate of $\langle R_{\mathrm{IceCube}} \rangle = (1.3{\cdot}10^6 \pm 1.8{\cdot}10^2)\,\mathrm{Hz}$ is expected. While a single DOM would only see an average rate increase of $13\,\mathrm{Hz}$ or $0.65\,\sigma$, the signal in the whole IceCube detector would be $6.1 \cdot 10^4\,\mathrm{Hz}$ or $34\,\sigma$ for a supernova at $7.5\,\mathrm{kpc}$ distance. Using this simple counting method, IceCube would see a supernova in the Magellanic Cloud with $5\,\sigma$ significance.

Figure 3 shows the expected signal in IceCube for a supernova at $7.5\,\mathrm{kPc}$ conforming to the *Lawrence-Livermore* model with $\approx 10^6$ registered neutrinos in $15\,\mathrm{s}$ and a statistical accuracy of 0.1% in the first $2\,\mathrm{s}$. Assuming $2 \cdot 10^4$ events in Super-Kamiokande (scaled from [12]), one arrives at an accuracy of 1% in the same time frame. While IceCube can neither determine the directions nor the energies of the neutrinos, it will provide worlds best statistical accuracy to follow details of

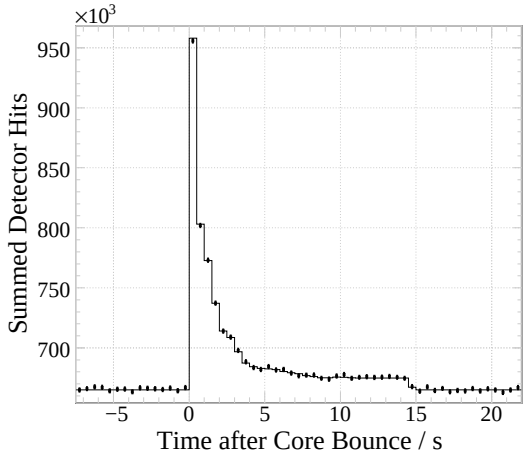

Fig. 3. Expected signal of a supernova at $7.5\,\mathrm{kpc}$ in IceCube.
The solid line denotes the signal expectation and the bars a randomized simulation.

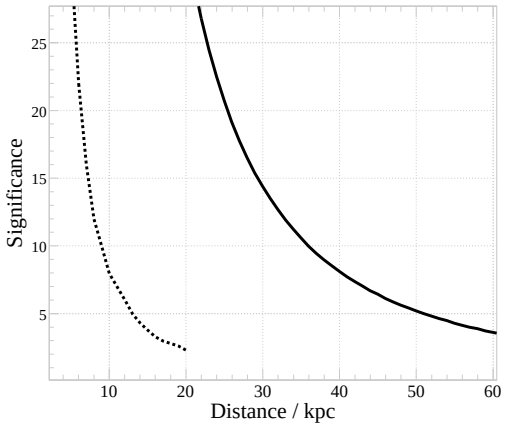

Fig. 4. Supernova detection ranges using $0.5\,\mathrm{s}$ time frames
Significances which supernovae conforming to the *Lawrence-Livermore* model would cause as function of their distance. IceCube performance is described by the solid line, AMANDA by the dotted line. Both are given for the $0.5\,\mathrm{s}$ binning.

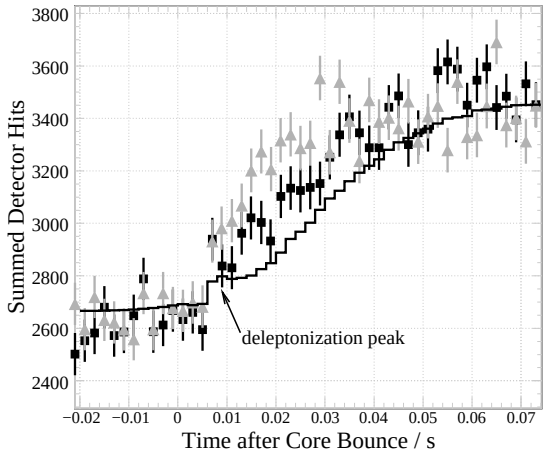

Fig. 5. Neutrino signals of a supernova at $7.5\,\mathrm{kpc}$ distance modified by oscillations as seen in IceCube.
The line shows the expectation without neutrino oscillations, the squares show the simulated signal for the normal mass hierarchy with $\sin^2\theta_{13} > 10^{-3}$ ($\sin^2\theta_{13} < 10^{-5}$ lies nearly on the same line) and the triangles show the signal for inverted mass hierarchy at $\sin^2\theta_{13} > 10^{-3}$.

the neutrino light curve. Its performance in this respect will be in the same order as proposed megaton proton decay and supernova search experiments. As the signal is seen on top of background noise, the measurement accuracy drops rapidly with distance. Figure 4 shows the significance at which IceCube and AMANDA would be able to detect supernovae.

VIII. Deleptonization Peak and Neutrino Oscillations

As mentioned before, the signal seen by AMANDA and IceCube is mostly dominated by electron anti-neutrinos with a small contribution by electron neutrino scattering, thereby leading to a sensitivity which is strongly dependent on the neutrino flavor and is thus sensitive to neutrino oscillations.

As the neutrinos pass varying levels of density within the supernova, the flux of electron and electron anti-neutrinos Φ released is different from the initial flux Φ^0 produced during the collapse:

$$\begin{aligned} \Phi_{\nu_e} &= p\,\Phi^0_{\nu_e} + (1-p)\,\Phi^0_{\nu_x} \quad , \\ \Phi_{\bar{\nu}_e} &= \bar{p}\,\Phi^0_{\bar{\nu}_e} + (1-\bar{p})\,\Phi^0_{\bar{\nu}_x} \quad . \end{aligned}$$

The survival probability $p/\bar{p}$ for the $\nu_e/\bar{\nu}_e$'s varies with the mass hierarchy and the mixing angle θ_{13} [10]:

neutrino oscillation parameters	p	$\bar{p}$
$m_2^2 < m_3^2$, $\sin^2\theta_{13} > 10^{-3}$	$\approx 0\%$	69%
$m_2^1 > m_3^2 < 0$, $\sin^2\theta_{13} > 10^{-3}$	31%	$\approx 0\%$
any hierarchy, $\sin^2\theta_{13} < 10^{-5}$	31%	69%

At the onset of the supernova neutrino burst during the prompt shock, a $\sim 10\,\mathrm{ms}$ long burst of electron neutrinos gets emitted when the neutron star forms. As the shape and rate of this burst is roughly independent of the properties of the progenitor stars, it is considered as a standard candle, allowing one to determine neutrino properties without knowing details of the core collapse.

The first $0.7\,\mathrm{s}$ of a supernova signal were modeled after [11]. Figure 5 shows the expectation for a supernova at a distance of $7.5\,\mathrm{kpc}$ in the $2\,\mathrm{ms}$ binning of IceCube. Due to statistics and the rising background from the starting electron anti-neutrino signal, the identification of the neutronization burst is unlikely at this distance. However, with a supernova at $7.5\,\mathrm{kpc}$ one should be able to draw conclusions for the mass hierarchy, depending on the reliability of the models.

IX. Conclusions and Outlook

With 59 strings and 3540 OMs installed, IceCube has reached 86% of its final sensitivity for supernova detection. It now supersedes AMANDA in the SNEWS network. With the low energy extension DeepCore, IceCube gains 360 additional OMs with a $\sim 30\%$ higher quantum efficiency (rates $\sim 380\,\mathrm{Hz}$). These modules have not been considered in this paper.

References

[1] A. Karle et al. *arXiv:0812.3981v1*
[2] F. Halzen, J. E. Jacobsen and E. Zas *Phys. Rev.*, D49:1758–1761, 1994
[3] J. Ahrens et al. *Astropart. Phys.* 16:345-359, 2002
[4] P. Antonioli et al. *New J. Phys.* 6:114, 2004
[5] W. C. Haxton. *Phys. Rev.*, D36:2283, 1987
[6] M. Th. Keil, G. G. Raffelt and H.-T. Janka. *Astrophys. J.*, 590:971–991, 2003
[7] M. Ackermann et al. *J. Geophys. Res.*, 111:D13203, 2006
[8] T. Totani, K. Sato, H. E. Dalhed and J. R. Wilson *Astrophys. J.*, 496:216–225, 1998
[9] J. F. Beacom and P. Vogel *Phys. Rev.* D60:033007, 1999
[10] A. Dighe. *Nucl. Phys. Proc. Suppl.*, 143:449–456, 2005
[11] F. S. Kitaura, Hans-Thomas Janka and W. Hillebrandt *Astron. Astrophys.* 450:345-350, 2006
[12] M. Ikeda et al. *Astrophys. J.*, 669:519-524, 2007

Physics Capabilities of the IceCube DeepCore Detector

Christopher Wiebusch* for the IceCube Collaboration†

**III.Physikalisches Institut, RWTH Aachen, University, Germany*
† *See the special section of these proceedings*

***Abstract*. IceCube-DeepCore is a compact Cherenkov Detector located in the clear ice of the bottom center of the IceCube Neutrino Telescope. Its purpose is to enhance the sensitivity of IceCube for low neutrino energies (< 1 TeV) and to lower the detection threshold of IceCube by about an order of magnitude to below 10 GeV. The detector is formed by 6 additional strings of 360 high quantum efficiency phototubes together with the 7 central IceCube strings. The improved sensitivity will provide an enhanced sensitivity to probe a range of parameters of dark matter models not covered by direct experiments. It opens a new window for atmospheric neutrino oscillation measurements of ν_μ disappearance or ν_τ appearance in an energy region not well tested by previous experiments, and enlarges the field of view of IceCube to a full sky observation when searching for potential neutrino sources. The first string was succesfully installed in January 2009, commissioning of the full detector is planned early 2010.**

***Keywords*: Neutrino-astronomy, IceCube-DeepCore**

I. INTRODUCTION

Main aim of the IceCube neutrino observatory [1] is the detection of high energy extraterrestrial neutrinos from cosmic sources, e.g. from active galactic nuclei. The detection of high energy neutrinos would help to resolve the question of the sources and the acceleration mechanisms of high energy cosmic rays.

IceCube is located at the geographic South-Pole. The main instrument of IceCube will consist of 80 cable strings, each with 60 highly sensitive photo-detectors which are installed in the clear ice at depths between 1450 m and 2450 m below the surface. Charged leptons with an energy above 100 GeV inside or close to the detector produce enough Cherenkov light to be detected and reconstructed using the timing information of the photoelectrons recorded with large area phototubes. While the primary goal is of highest scientific interest, the instrument can address a multitude of scientific questions, ranging from fundamental physics such as physics on energy-scales beyond the reach of current particle accelerators to multidisciplinary aspects e.g. the optical properties of the deep Antarctic ice which reflect climate changes on Earth.

IceCube is complemented by other major detector components. The surface air-shower detector *IceTop* is used to study high energy cosmic rays and to calibrate

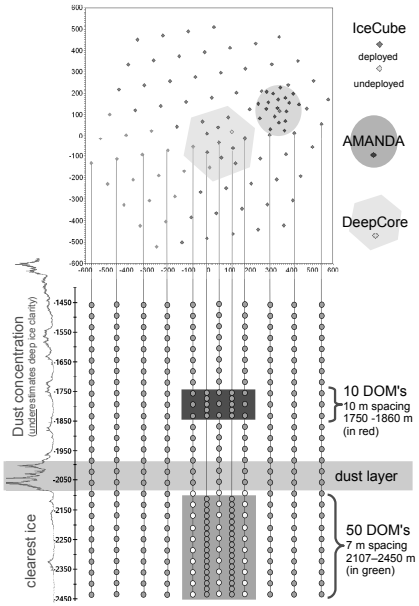

Fig. 1. Geometry of the DeepCore Detector. The top part shows the surface projection of horizontal string positions and indicates the positions of AMANDA and DeepCore. The bottom part indicates the depth of sensor positions. At the left the depth-profile of the optical transparency of the ice is shown.

IceCube. R&D studies are underway to supplement IceCube with radio (*AUR*A) and acoustic sensors (*SPATS*) in order to extend the energy range beyond EeV energies. Six additional and more densely instrumented strings will be deployed in the bottom center of the IceCube detector and form the here considered *DeepCore* detector.

A first DeepCore string has been succesfully installed in January 2009 and is taking data since then. The DeepCore detector will be completed in 2010 and will replace the existing *AMANDA-II* detector, which has been decomissioned in May 2009. DeepCore will lower the detection threshold of IceCube by an order of magnitude to below 10 GeV and, due to its improved design, provide new capabilities compared to AMANDA. In this paper we describe the design of DeepCore and the enhanced physics capabilities which can be addressed.

II. DEEPCORE DESIGN AND GEOMETRY

The geometry of DeepCore is sketched in figure 1. The detector consists out of 6 additional strings of

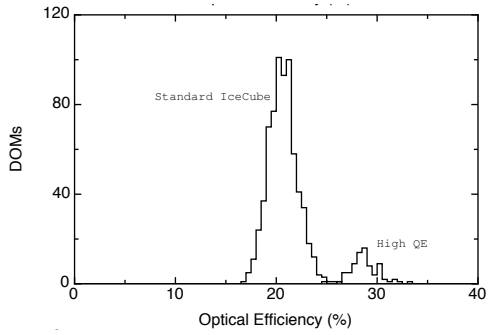

Fig. 2. Results of the quantum efficiency calibration at $\lambda = 405\,\mathrm{nm}$ of the DeepCore phototubes compared to standard IceCube phototubes.

60 phototubes each together with the 7 central IceCube strings. The detector is divided into two components: Ten sensors of each new string are at shallow depths between $1750\,\mathrm{m}$ and $1850\,\mathrm{m}$, above a major dust-layer of poorer optical transparency and will be used as a veto-detector for the deeper component. The deep component is formed by 50 sensors on each string and is installed in the clear ice at depths between $2100\,\mathrm{m}$ and $2450\,\mathrm{m}$. It will form, together with the neighbouring IceCube sensors the main physics volume.

The deep ice is on average twice as clear as the average ice above $2000\,\mathrm{m}$ [2]. The effective scattering length reaches $50\,\mathrm{m}$ and the absorption length $230\,\mathrm{m}$. Compared to AMANDA a substantially larger number of unscattered photons will be recorded allowing for an improved pattern recognition and reconstruction of neutrino events in particular at lower energies.

Another important aspect is a denser spacing of photosensors compared to IceCube: The horizontal inter-string spacing is $72\,\mathrm{m}$ (IceCube: $125\,\mathrm{m}$). The vertical spacing of sensors along a string is only $7\,\mathrm{m}$ (IceCube: $17\,\mathrm{m}$).

The next major improvement with respect to IceCube and AMANDA is the usage of new phototubes (HAMAMATSU R7081-MOD) of higher quantum efficiency. This hemispherical 10" photomultiplier is identical to the standard IceCube PMT [3], but employs a modified cathode material of higher quantum efficiency (typically $33\,\%$ at $\lambda = 390\,\mathrm{nm}$). Calibrations of the phototubes for DeepCore confirm a sensitivity improvement of $30\,\%$-$40\,\%$ with respect to the standard IceCube PMT (figure 2). Also regular IceCube strings will be equipped with these phototubes if within the DeepCore volume.

The net effect of the denser instrumentation is a factor ~ 6 gain in sensitivity for photon detection and superior optical clarity of the ice. This is an imporant prerequisite for a substantially lower detection threshold.

III. DeepCore Performance

The electronic hardware of the optical sensors is identical to the standard IceCube module [3] and this significantly reduces the efforts for maintenance and operations compared to AMANDA. The DeepCore detector is integrated into a homogeneous data aquisition model of IceCube which will be only supplemented by additional trigger. Initial comissioning data of the first installed DeepCore string verifies that the hardware works reliably and as expected.

The IceCube detector is triggered if typically a multiplicity of 8 sensors within $\sim 5\,\mu\mathrm{s}$ observe a signal coincident with a hit in a neighbouring or next to neighbouring sensor. For each trigger, the signals of the full detector are transferred to the surface.

For the sensors within the considered volume the data taking is supplemented with a reduced multiplicity requirement of typically $3-4$. As shown in figure 7, such a trigger is sufficient to trigger atmospheric neutrino events down to a threshold of $1\,\mathrm{GeV}$, sufficiently below the anticipated physics threshold.

The chosen location of DeepCore allows to utilize the outer IceCube detector as an active veto shield against the background of down-going atmospheric muons. These are detected at a $\sim 10^6$ higher rate than neutrino induced muons. The veto provides external information to suppress this background and standard up-going neutrino searches will strongly benefit from a larger signal efficiency and a lower detection threshold as the demands on the maturity of recorded signals decrease.

Even more intriguing is the opportunity to identify down-going ν induced μ, which may, unlike cosmic ray induced atmosperic μ, start inside the DeepCore detector. Simulations [4] show that three rings of surrounding IceCube strings and the instrumentation in the upper part of IceCube are sufficient to achieve a rejection of atmospheric muons by a factor $> 10^6$ maintaining a large fraction of the triggered neutrino signals. A further interesting aspect is the proposal in [6] to veto also atmospheric ν by the detection of a correlated atmospheric μ. This could provide the opportunity to reject a substantial part of this usually irreducable background for extraterrestrial neutrino searches.

Triggered events which start inside the detector will be selected online and transmitted north by satellite. Already simple algorithms allow to suppress the background rate by a factor $> 10^3$ and meet the bandwidth requirements while keeping 90% of the signal [4]. A typical strategy requires that the earliest hits are located inside DeepCore and allows for later hits in the veto-region only if the time is causal consistent with the hypothesis of a starting track. A filter which selects starting tracks in IceCube is active since 2008 and allowed to verify the performance of such filters with experimental data and to benchmark the subsequent physics analysis.

The filtered events are analyzed offline with more sophisticated reconstruction algorithms. Here, the focus is to improve the purity of the sample and to reconstruct direction, energy and the position of the interaction vertex. A particularily efficient likelihood algorithm (finiteReco [4]) capable of selecting starting muons evaluates the hit probabilities of photomultipliers with and without a signal in dependence of the distance to the track. It estimates the most probable position of

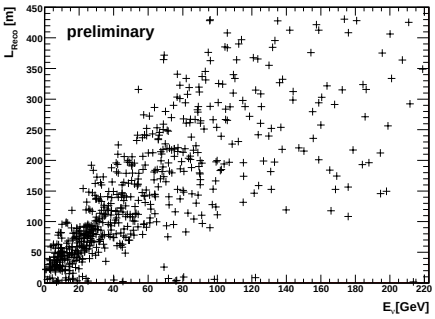

Fig. 3. The reconstructed length of μ contained tracks in DeepCore, based on the reconstructed start- and stop- vertex with the finiteReco algorithm. The data are ν induced μ-tracks from the upper hemisphere, which are reconstructed to start within DeepCore.

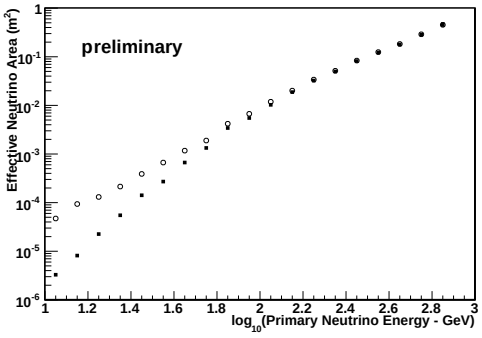

Fig. 4. Effective neutrino detection area of IceCube (trigger level) versus the energy for up-going neutrinos. The squares are IceCube only. The circles represent the area if DeepCore is included.

the start-vertex and provides the probablity that a track may have reached this point undetected by the veto.

The reconstruction algorithms are still under development but initial results are promising. As an example, figure 3 shows the reconstructed length of μ tracks as function of the ν energy. Already the currently achieved resolution of $\sim 50\,\mathrm{m}$ results in a visible correlation with the neutrino energy in particular for energies $\leq 100\,\mathrm{GeV}$. Note, that the resolution is substantially better for vertical tracks.

The effective detection area of IceCube for neutrinos for triggered events is shown in figure 4. Despite DeepCore being much smaller than IceCube, a substantial gain of up to an order of magnitude is achieved by the additional events detected in DeepCore. Higher level event selections for specific physics analysis benefit strongly from the higher information content of events and the gain of DeepCore further improves.

IV. Physics Potential

A. Galactic point sources of neutrinos

The analysis of IceCube data greatly benefits from the location at the geographic South Pole because the celestial sphere fully rotates during one sideral day. Azimuthal detector effects are largly washed out because

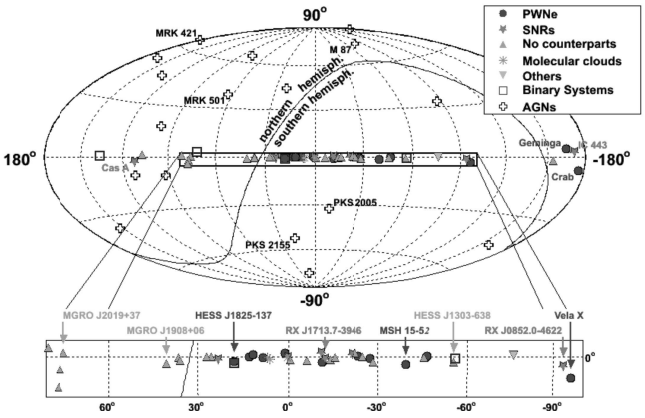

Fig. 5. Interesting celestrial object with known emission of TeV gamma rays.

each portion of the sky is observed with the same exposure and same inclination. However, the aperture of the conventional up-going muon analysis is restricted to only the Northern hemisphere and leaves out a large fraction of the galactic plane and a number of interesting objects such as the galactic center (see figure 5). Extending the field of view of IceCube at low energies ($\leq 1\,\mathrm{TeV}$) to a full sky observation will greatly enlarge the number of interesting galactic sources in reach of IceCube[1] .

The energy spectrum of gamma rays from supernova remnants show indications of a potential cut-off at a few TeV [7]. Under the assumption of a hadronic production mechanism for these gamma rays the corresponding neutrino fluxes would show a similar cut-off at typically half of that cut-off value. The high sensitivity of DeepCore for neutrinos of TeV energies and below will complement the sensitivity of IceCube which is optimized for energies of typically $10\,\mathrm{TeV}$ and above.

B. Indirect detection of dark matter

The observation of an excess of high energy neutrinos from the direction of the Sun can be interpreted by means of annihilations of WIMP-dark matter in its center. The energy of such neutrinos is a fraction of the mass of the WIMP particles (expected on the TeV-scale) and it depends on the decay chains of the annihilation products. The large effective area of DeepCore and the possibility of a highly efficient signal selection greatly improves the sensitivity of IceCube. In particular it is possible to probe regions of the parameter space with soft decay chains and WIMP masses below $\sim$ 200 GeV and which are not disfavored by direct search experiments.

An example of the sensitivity for the hard annihilation channel of supersymmetric neutralino dark matter is

[1]Note, that at high energies $> 1\,\mathrm{PeV}$ the background of atmospheric muons rapidly decreases and also here neutrinos from the Southern hemisphere can be detected by IceCube [8]. However, galactic sources are usually not expected to produce significant fluxes of neutrinos at energies around the cosmic ray knee and above.

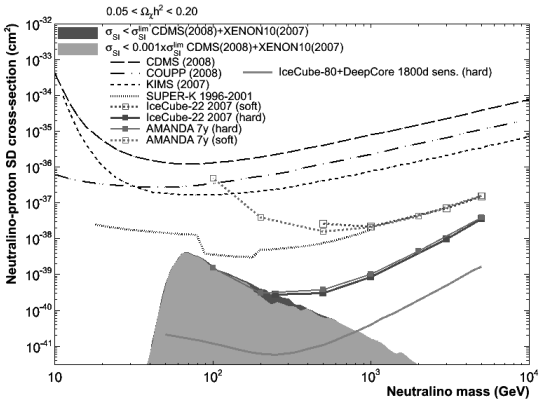

Fig. 6. The expected upper limit of IceCube DeepCore at 90% confidence level on the spin-dependent neutralino-proton cross section for the hard (W^+W^-) annihilation channel as a function of the neutralino mass for IceCube including Deep Core (solid line). Also shown are limits from previous direct and indirect searches. The shaded areas represent MSSM models which are not disfavoured by direct searches, even if their sensitivity would be improved by a factor 1000.

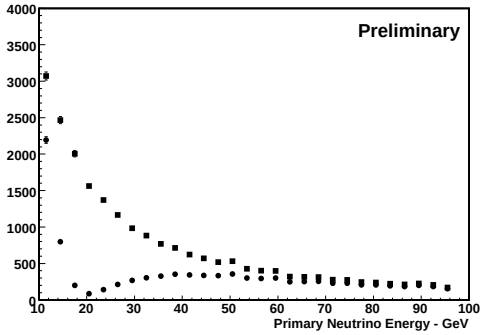

Fig. 7. Number of triggered vertical atmospheric neutrinos per year (per 3GeV) versus the neutrino energy. Events from 1.6π sr are accepted. Shown are the numbers without (squares) and with (circles) the inclusion of oscillations ($\Delta m^2_{atm} = 0.0024\,\mathrm{eV}^2$, $\sin(2\theta_{23}) = 1$).

shown in figure 6.

C. Atmospheric neutrinos

DeepCore will trigger on the order of 10^5 atmospheric neutrinos/year in the energy range from 1 GeV to 100 GeV. Atmospheric neutrinos are largly unexplored in this energy range. Smaller experiments like Super-Kamiokande cannot efficiently measure the spectrum for energies above 10 GeV and measurements done by AMANDA only start at 1 TeV. In the range between $30-50$ GeV decays of charged kaons become dominant over decays of charged pions [10] for the production of atmospheric neutrinos and the systematic error of flux calculations increases. A measurement of this transition could help to reduce systematic errors of the flux of atmospheric neutrinos at TeV energies.

The first maximum of disappearence of atmospheric ν_μ due to oscillations appears at an energy of about 25 GeV for vertically up-going atmospheric neutrinos [5]. The energy threshold of about 10 GeV would allow to measure atmospheric neutrino oscillations by means of a direct observation of the oscillation pattern in this energy range. In addition, DeepCore would aim to observe the appearance of ν_τ by the detection of small cascade-like events in the DeepCore volume at a rate which is anti-correlated with the disappearance of ν_μ.

Similar to ν_τ, the signature of ν_e events are cascade-events with a large local light deposition without the signature of a track. The dominant background to these events are charged current ν_μ interactions with a small momentum transfer to the μ. Analyses like these will have to be performed considering all three flavors and their mixing. Note, that only for a further reduction of the energy threshold smaller than 10 GeV matter effects in the Earth's core would become visible [5].

D. Other physics aspects

Two remaining items are only briefly mentioned here.

Slowly moving magnetic monopoles, when catalizing proton decays, produce subsequent energy depositions of ~ 1 GeV along their path with time-scales of μs to ms. Initial studies are under-way to develop a dedicated trigger for this signature using delayed coincidences.

DeepCore extends the possibility to search for neutrino emission in coincidence with gamma ray bursts (GRB) to lower energies. According to [11] GRB may emit a burst of neutrinos. However, predicted energies are only a few GeV and the event numbers are small ($\sim 10\,\mathrm{yr}^{-1}\,\mathrm{km}^{-2}$). Additional studies are required to evaluate the sensitivity for such signals.

V. Summary and Outlook

This paper summarizes the enhancement of the physics profile of IceCube by the DeepCore detector. The geometry of DeepCore has been optimized and construction has started. Detailed MC studies and experimental analyses are currently under way to optimize and finalize the analysis procedures. First data from the full detector will be available in spring 2010, the veto will be fully completed latest 2011.

Acknowledgement

This work is supported by the German Ministry for Education and Research (BMBF). For a full acknowledgement see [1].

References

[1] J. Ahrens et al. (IceCube Collaboration), Astropart. Phys. **20** (2004) 507-532, 2004
[2] M. Ackermann et al. (IceCube Collaboration), J. of Geophys. Res. **111** (2006) D13203, July 2006
[3] R. G. Stokstad et al. (IceCube Collaboration), Nucl. Phys. B (Proc. Suppl.) **118** (2003) 514.
[4] O. Schulz et al. (IceCube Collaboration), these proceedings.
[5] D. Grant et al. (IceCube Collaboration), these proceedings.
[6] S. Schönert et al., Phys. Rev. D 79, 043009 (2009)
[7] F. Aharonian et al. (HESS Collaboration), Astron. Astrophys. 464, 235-243 (2007)
[8] J. Dumm et al. (IceCube Collaboration), these proceedings.
[9] M. Danninger, priv. Comm., see also R. Abbasi et al. (IceCube Collaboration), arXiv:0902.2460, accept. by Phys. Rev. Lett..
[10] see e.g. Athar, PhysRev.D 71, 103008 (2005)
[11] J. Bahcall,&,P. Meszaros, Phys. Rev. Lett. 85, 1362-1365 (2000).

Fundamental Neutrino Measurements with IceCube DeepCore

Darren Grant*, D. Jason Koskinen*, and Carsten Rott† for the IceCube collaboration.

*Dept. of Physics, Pennsylvania State University, University Park, PA 16802, USA
†Dept. of Physics and Center for Cosmology and Astro-Particle Physics, Ohio State University, Columbus, OH 43210, USA

***Abstract*. The recent deployment of the first string of DeepCore, a low-energy extension of the IceCube neutrino observatory, offers new opportunities for fundamental neutrino physics using atmospheric neutrinos. The energy reach of DeepCore, down to ~ 10 GeV, will allow measurements of atmospheric muon neutrino disappearance at a higher energy regime than any past or current experiment. In addition to a disappearance measurement, a flavor-independent statistical analysis of cascade-like events opens the door for the measurement of tau neutrino appearance via a measurable excess of cascade-like events. In the event of a relatively large value of $\sin^2 2\theta_{13}$, a multi-year measurement of the suppression of muon neutrino disappearance due to earth matter effects may show a measurable dependence on the sign of the mass hierarchy (normal vs. inverted).**

***Keywords*: Oscillations, DeepCore, hierarchy**

I. ICECUBE DEEPCORE

The IceCube neutrino telescope is a multipurpose discovery detector under construction at the South Pole, which is currently about three quarters completed [1]. After completion in 2011, IceCube will have instrumented a volume of approximately one cubic kilometer utilizing 86 strings, each instrumented with 60 Digital Optical Modules (DOMs) at a depth between 1450 m and 2450 m. Eighty of these strings (the baseline design) will be arranged in a hexagonal pattern with an interstring spacing of about 125 m and with 17 m vertical separation between DOMs. This baseline design is complemented by six more strings, that form a more densely instrumented sub-array, located at the center of IceCube. These strings will be spaced in between the regular strings, so that an interstring-spacing of 72 m is achieved. Together with the seven adjacent standard IceCube strings these six strings form the DeepCore array in the center of IceCube (shown in Figure 1). DeepCore strings have a different distribution of the 60 DOMs on them. Fifty out of the 60 DOMs on a DeepCore string will be installed in the deep clear ice, below an ice-layer of short absorption length (1970 2100 m) also labeled "dust-layer". The top 10 DOMs on the DeepCore strings will be deployed above this dust layer. Those DOMs add to the effective veto capability of the surrounding IceCube strings against down-going muons.

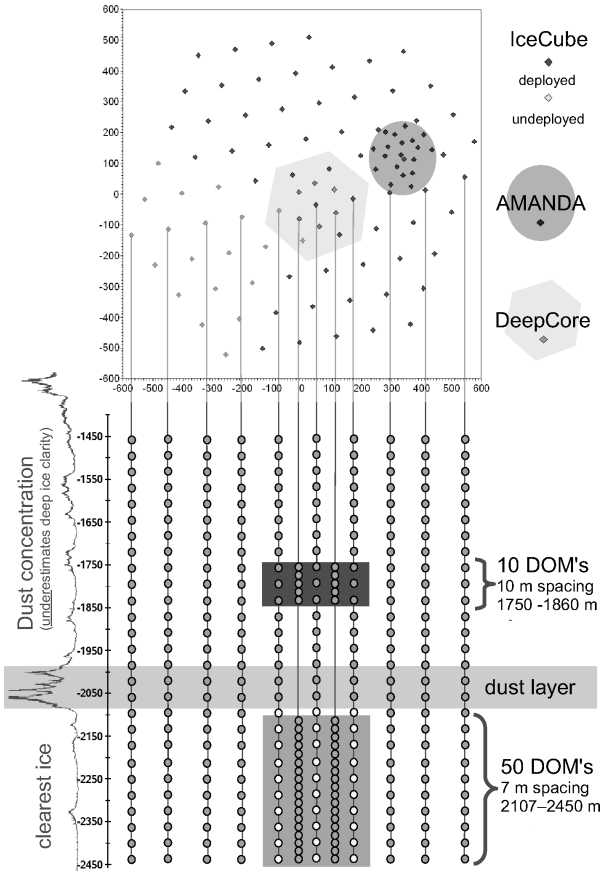

Fig. 1: IceCube with the DeepCore sub-detector in the center deep clear ice. The illustration on the left shows the depth-profile of the optical transparency of the ice.

The DeepCore extension will significantly improve IceCube's low energy performance and allow neutrino detection to approximately 10 GeV (see Figure 2). This is accomplished by having DeepCore strings with a dense vertical spacing of 7 m between DOMs, which are deployed in the deepest ice where the scattering length is approximately twice that compared to the upper part of the IceCube detector [2]. Coupled with the spacing and ice clarity the DOMs themselves are instrumented with high quantum efficiency photomultiplier tubes (HQE PMTs), that have a 40% efficiency increase, wavelength dependent, compared to regular IceCube PMTs [3]. The aforementioned properties make the DeepCore an ideal detector for low energy-low rate neutrino physics.

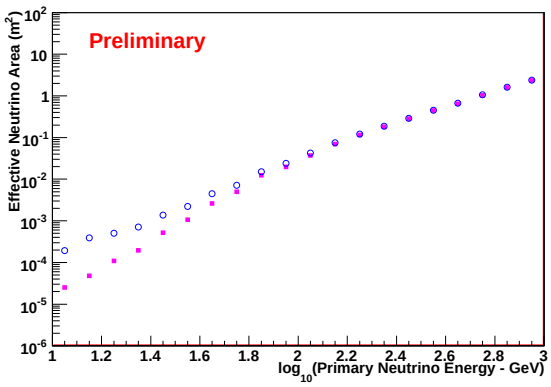

Fig. 2: Comparison of preliminary study of effective area $A_{\rm eff}$ at trigger level for the 80 IceCube string array without DeepCore (squares) and in addition with the six DeepCore strings (open circles). The addition of DeepCore increases the effective area of the detector at low energies significantly.

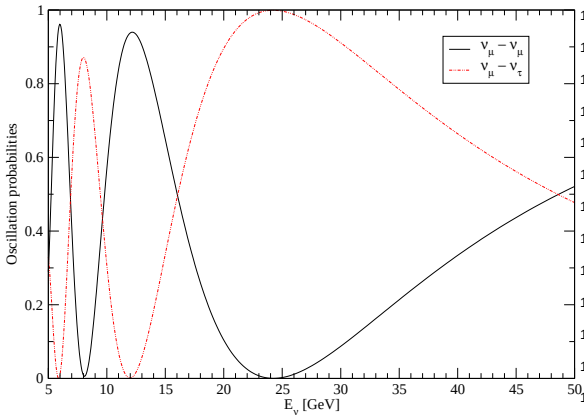

Fig. 3: ν_μ survival probability and $\nu_\mu \longrightarrow \nu_\tau$ oscillation probability for vertically upward going neutrinos, where $\sin^2 2\theta_{13}$ =0.1 [6].

II. DeepCore Neutrino Oscillation Physics

The lower energy reach achieved with the DeepCore opens the possibility to investigate atmospheric neutrino oscillations in the primarily unexplored energy regime of a tens of GeV. In Figure 3 we show the expected ν_μ survival probability and $\nu_\mu \longrightarrow \nu_\tau$ oscillation curves for which the DeepCore will have sensitivity and relate directly to the potential measurements discussed in the following subsections. In addition to the improved energy reach, part of what make such measurements possible is the innate background rejection built into the DeepCore design: increased overburden reduces the number of atmospheric muons and the surrounding IceCube strings provide an in situ veto. Simple veto methods have achieved background reductions of four orders of magnitude with excellent signal retention and have potential for greater than 6 orders of magnitude rejection utilizing reconstruction veto methods [3].

A. Muon-Neutrino Disappearance

Previous measurements of neutrino oscillations at the atmospheric-scale have been significantly decreased in both energy reach and active volume size of the detectors compared to DeepCore. With an approximate 13 MT fiducial volume, DeepCore has the capacity to make a precision measurement of atmospheric neutrino oscillations above 10 GeV [4]. The ν_μ survival probability curve shown in Figure 3 illustrates an expectation for a significant deficit in neutrino flux, shown in Fig. 4 at a previously unexplored energy region. An issue associated with such an analysis is the angular resolution of neutrino induced muon tracks at these energies is fundamentally limited by the kinematics of the neutrino-nucleon interaction. Low energy ν_μ interactions have a much bigger opening angle between the incoming neutrino and outgoing muon than high energy interactions, which leads the muon to have a higher probability of being noncollinear with the incoming neutrino. The intrinsic uncertainty on the opening angle reduces any experiments ability to identify perfectly upward going neutrinos, where the uncertainty can be approximated, in the full data sample, by $\Delta\phi \simeq 30^\circ \times \sqrt{(\mathrm{GeV})/E_{\nu_\mu}}$. However, oscillations can be observed with very high significance with an inclusive measurement over the zenith angle range $-1.0 < \cos\phi < -0.6$, and incorporation of angular dependence will only improve the result. Fig. 4 shows a simulation of this muon disappearance effect, which would be an approximate 20 sigma effect with just one year of IceCube DeepCore data. The current study only discusses the effect on the signal, taking statistical uncertainties into account. Systematic uncertainties remain to be studied, as well as the background prediction to this measurement.

B. Tau-Neutrino Appearance

Returning to Figure 3 and looking at the $\nu_\mu \longrightarrow \nu_\tau$ oscillation curve, we expect a fraction of the incoming atmospheric neutrino flux to have a ν_τ component. Given the higher parent ν_μ flux and different decay kinematics of tau events relative to that of ν_e charge-current (CC) and ν_x neutral current (NC) (x=e, μ, τ) events, we should be able to detect ν_τ both via the excess of cascade (hadronic and electromagnetic shower) events and possibly through the resulting spectral energy distortion. This measurement would not only represent the largest sample of tau neutrinos ever collected (albeit inclusively), it may also be competitive with OPERA [5] in making an appearance measurement of tau neutrinos due to oscillations.

Future components of this analysis comprise developing a dedicated energy reconstruction for low energy cascade events as well as examining the background caused by short muon tracks that mimic cascades as well as the impact of misidentification of up versus down going neutrinos. Good energy resolution will increase sensitivity to ν_τ appearance over regions where neutrino oscillations are maximal.

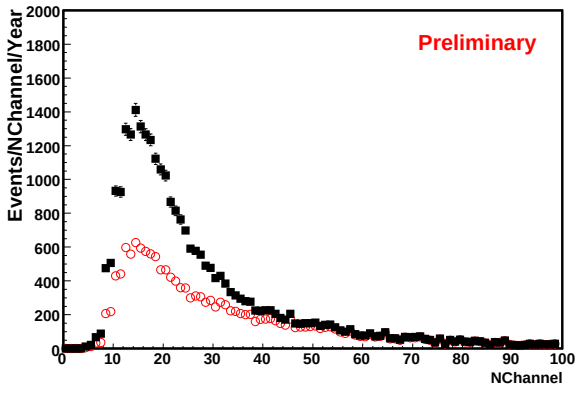

Fig. 4: Simulated ν_μ disappearance with 1 year of DeepCore data. The lower curve (open circles) show the number of upward-going muons observed over the zenith angle cosϕ < -0.6 with oscillations, while the upper curve (squares) is the corollary without oscillations. No systematic errors or background have been included. The effect is approximately 20 sigma based purely on statistical errors (approximately 28000 events per year without oscillations and 16000 events with oscillations assuming $sin^2 2\theta_{23}$=1.0 and Δm^2_{23}=0.0024). Note that NChannel is a crude energy estimator for the detector based on the number of hit DOMs.

C. Matter Effects and Neutrino Mass Hierarchy

Depending on detection efficiency and purity, a sufficiently large value of $\sin^2\theta_{13}$ [6], and control of systematics the DeepCore detector may be used in an ambitious multi-year effort to determine the sign of the neutrino mass hierarchy. This may be accomplished by measuring a small enhancement/supression from the MSW effect [11] of the expected number of ν_μ events. The ν_μ oscillation probability, shown in Figure 5, indicates that the neutrino rate over the 8-25 GeV energy region is enhanced for the normal hierarchy (NH), and enhanced for anti-neutrinos for the inverted mass hierarchy (IH). A complication of this measurement is that DeepCore cannot distinguish between neutrino and anti-neutrinos, however at the relevant energy range of 10 GeV $< E_\nu <$ 30 GeV the interation cross-section between neutrinos and anti-neutrinos differs by a factor of two; $\sigma(\nu_x) \simeq 2\sigma(\bar{\nu_x})$. The difference in interaction cross-section translates into a difference in the number of observed muon neutrino candidate events. Based on statistical discrimination only, it may be possible to distinguish normal from inverted hierarchies. In Fig. 6 we show the expected results from 5 years of DeepCore data, with a statistical separation between the normal and inverted hierarchies of approximately 10 sigma. The described effect is pending on a sufficiently large value of θ_{13} (that is expected to be measured by the time of the data for this measurement has been obtained). Further the signal systematic uncertainties need to be sufficiently small and remaining background need to be effectively removed.

III. Conclusions

We have completed a full Monte Carlo study of the IceCube DeepCore detector that shows the potential for measurements of fundamental neutrino properties. We have discussed the expected effects on the signal for ν_μ disappearance at energies higher than previously measured, a measurement of ν_τ appearance as well as resolution of the neutrino mass hierarchy.

References

[1] A. Achterberg *et al.*, Astropart. Phys. **26**, 155 (2006).
[2] M. Ackermann *et al.*, J. Geophys. Res. **111**, 02201 (2006).
[3] D. Cowen, for the IceCube coll., NUTEL 09, forthcoming.
[4] Y. Fukuda *et al.* [Super-Kamiokande Collaboration], Phys. Rev. Lett. **81**, 1562 (1998) [arXiv:hep-ex/9807003].
[5] R. Acquafredda *et al.* [OPERA Collaboration], New J. Phys. **8**, 303 (2006) [arXiv:hep-ex/0611023].
[6] O. Mena, I. Mocioiu and S. Razzaque, Phys. Rev. D **78**, 093003 (2008)
[7] M. Sanchez [MINOS Collaboration], Moriond EW 2009, forthcoming.
[8] H. L. Ge, C. Giunti and Q. Y. Liu, arXiv:0810.5443 [hep-ph].
[9] G. L. Fogli, E. Lisi, A. Marrone, A. Palazzo and A. M. Rotunno, Phys. Rev. Lett. **101**, 141801 (2008) [arXiv:0806.2649 [hep-ph]].
[10] M. Apollonio *et al.* [CHOOZ Collaboration], Eur. Phys. J. C **27**, 331 (2003) [arXiv:hep-ex/0301017].
[11] E. K. Akhmedov, M. Maltoni and A. Y. Smirnov, JHEP **0705**, 077 (2007)
[12] C. Rott *et al.* for the IceCube coll., these proceedings.
[13] D. Grant *et al.* (DeepCore reconstruction) for the IceCube coll., these proceedings.
[14] C. Wiebusch *et al.* (DeepCore) for the IceCube coll., these proceedings.
[15] R. Abbasi *et al.* [IceCube Collaboration], Nucl. Instrum. Meth. A **601**, 294 (2009)
[16] E. Resconi for the IceCube coll., astro-ph/0807.3891.

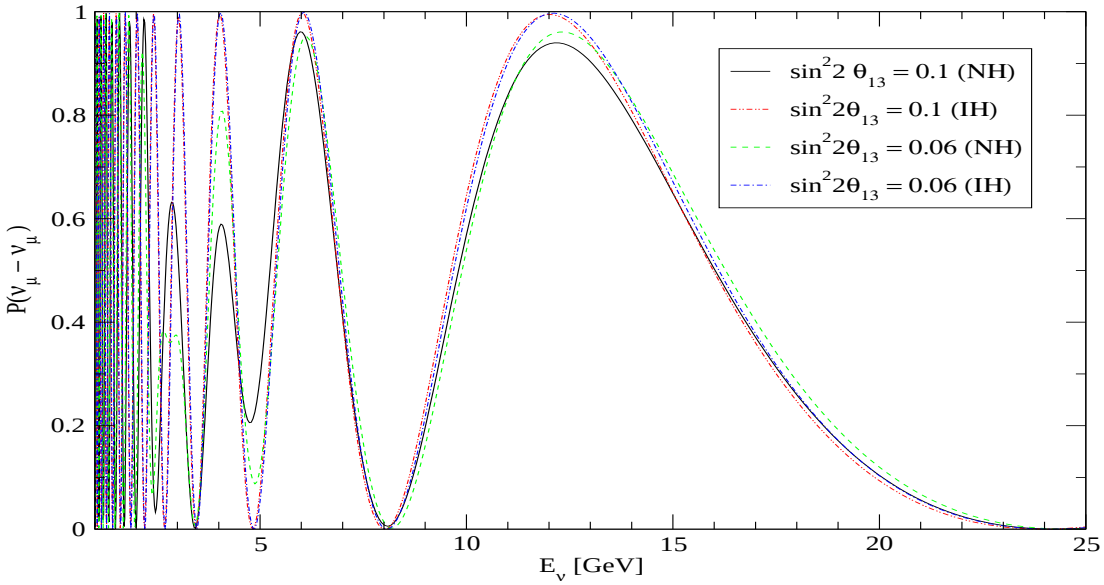

Fig. 5: Oscillation probabilities for $\nu_\mu \longrightarrow \nu_\mu$ transitions for upward going neutrinos [6]. For a value of $\sin^2 2\theta_{13}$=0.1, the difference in the survival probability between the normal hierarchy (solid black line) and inverted hierarchy (dashed red line) is $\approx$ 7%, and increases for higher values of $\sin^2 2\theta_{13}$. Recent measurements [7] as well as global fits [8], [9] prefer that $\sin^2 2\theta_{13}$ is non-zero, while the value of 0.10 reflects the 90% Confidence Limit set by CHOOZ [10].

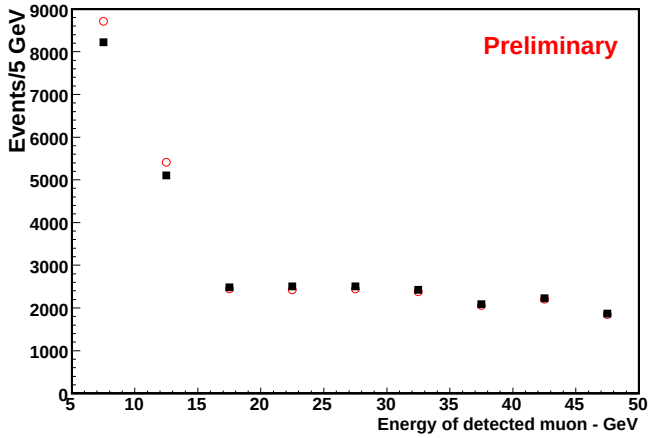

Fig. 6: Predicted rate with 5 years of data for normal (squares) and inverted (open circles) hierarchy, for ν_μ induced muon tracks within 45 degrees of vertical that start within the DeepCore fiducial volume. We find that in the first two bins the rate for the inverted hierarchy is above that for the normal hierarchy and that in the remaining bins the rates overlap. Systematic errors are not yet estimated. Statistical errors are too small to be visible. Note that $\sin^2 \theta_{13}$=0.1 in the presented case.

Implementation of an active veto against atmospheric muons in IceCube DeepCore

Olaf Schulz*, Sebastian Euler† and Darren Grant‡ for the IceCube Collaboration§

*Max-Planck Institut für Kernphysik, Saupfercheckweg 1, 69171 Heidelberg, Germany
†III. Physikalisches Institut, RWTH Aachen University, 52056 Aachen, Germany
‡Dept. of Astronomy and Astrophysics, Pennsylvania State University, University Park, PA 16802, USA
§See the special section of these proceedings

Abstract. **The IceCube DeepCore [1] has been designed to lower the energy threshold and broaden the physics capabilities of the IceCube Neutrino Observatory. A crucial part of the new opportunities provided by DeepCore is offered by the possibility to reject the background of atmospheric muons. This can be done by using the large instrumented volume of the standard IceCube configuration around DeepCore as an active veto region. By thus restricting the expected signal to those neutrino events with an interaction vertex inside the central DeepCore region, it is possible to look for neutrinos from all directions, including the Southern Hemisphere that was previously not accessible to IceCube. A reduction of the atmospheric muon background below the expected rate of neutrinos is provided by first vetoing events in DeepCore with causally related hits in the veto region. In a second step the potential starting vertex of a muon track is reconstructed and its credibility is estimated using a likelihood method. Events with vertex positions outside of DeepCore or with low starting probabilities are rejected. We present here these newly developed veto and vertex reconstruction techniques and present in detail their capabilities in background rejection and signal efficiency that have been obtained so far from full Monte Carlo studies.**

Keywords**: high energy neutrino-astronomy, IceCube, DeepCore**

I. Introduction

The IceCube Neutrino Observatory [2] is currently being built at the geographic South Pole in Antarctica. After completion it will consist of ∼4800 digital optical modules (DOMs) on 80 strings instrumenting one cubic kilometer of ice at a depth between 1450 m and 2450 m. Each DOM consists primarily of a photomultiplier tube and read-out electronics in a glass pressure vessel. IceCube is designed to detect highly energetic neutrino-induced muons as well as hadronic or electro-magnetic showers (cascades) that produce Cherenkov radiation in the medium. Significant backgrounds to the signal, caused by muons from atmospheric air showers above the detector, limit the field of view to the Northern hemisphere for many studies that use neutrino events in IceCube. In addition to its nominal layout, the DeepCore

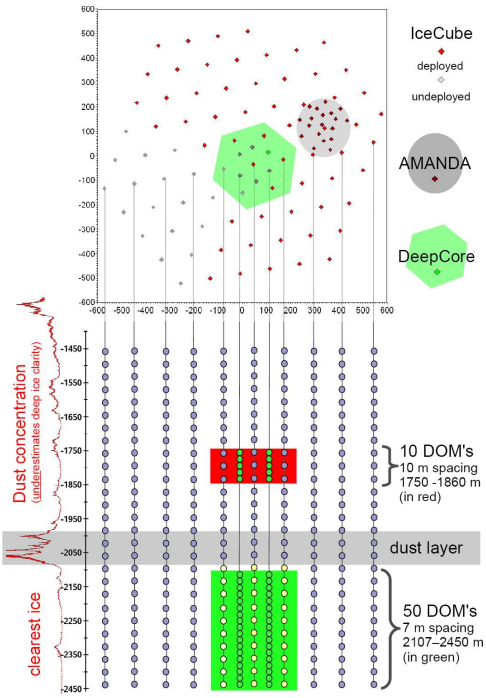

Fig. 1. Schematic view of the IceCube DeepCore

extension to the observatory will lower the IceCube energy threshold from ∼100 GeV down to neutrino energies as low as 10 GeV. This improvement in the detector energy response is achieved by including 6 extra strings, deployed in a denser spacing, around a standard central IceCube string. Each of these strings will be equipped with 60 DOMs, containing Hamamatsu high quantum efficiency photo multiplier tubes (HQE PMTs). 50 of these DOMs will be placed in a dense spacing of ∼7 m in the lowest part of the detector where the ice is clearest and scattering and absorption lengths are considerably longer [3]. The remaining 10 modules are to be placed in a 10 m spacing at a depth from 1760 m to 1850 m. This position has been chosen in order to improve IceCube's capabilities to actively identify and reduce the atmospheric muon background to the central DeepCore volume, as described below. The HQE PMTs have a quantum efficiency that is up to 40% higher, depending on wavelength, compared to the standard IceCube PMTs, while their noise rate of ∼380 Hz is

on average increased by about 32%. Together with the 7 neighboring IceCube strings DeepCore will consist of 13 strings and be equipped with 440 optical modules instrumenting a volume of $\sim$13 megatons water-equivalent.

DeepCore will improve the IceCube sensitivity for many different astrophysics signals like the search for solar WIMP dark matter and for neutrinos from Gamma-Ray Bursts [4]. It also opens the possibility to investigate atmospheric neutrino oscillations in the energy range of a few tens of GeV [5]. An additional intriguing opportunity offered by DeepCore is the possibility to identify neutrino signals from the southern hemisphere. Such a measurement requires a reduction of the atmospheric muon background by more than a factor 10^6 in order to obtain a signal of atmospheric neutrinos to background rate better than one. A first step toward achieving this reduction is implicit in the design of DeepCore. Background events which trigger DeepCore with a minimum number of hits in the DeepCore fiducial volume must pass through a larger overburden resulting in a order of magnitude decrease to the atmospheric muon rate, with respect to the whole IceCube detector. Two additional steps are then performed to attain the remaining 10^5 rejection factor. The first is a veto of DeepCore events with causally related hits in the surrounding IceCube volume, reducing the background rate by 10^2 to 10^3. Then we apply a vertex reconstruction algorithm based on a maximum-likelihood method that determines the approximate neutrino interaction vertex. By rejecting events with a reconstructed vertex outside the central DeepCore volume a full 10^6 background reduction may be achieved.

II. Triggering DeepCore

The first reduction of the atmospheric muon background rate, with respect to IceCube, is achieved by applying a simple majority trigger (SMT) to the DeepCore region, based on number of channels registering a hit in coincidence with a neighbor DOM. The trigger hit coincidence requirement, also known as hard local coincidence (HLC), is such that each channel is accompanied by at least one more hit on one of the four closest neighboring modules within a time window of $\pm$1000 ns. The rate of atmospheric muons triggering DeepCore is largely dependent on the multiplicity that is required. In this study we applied a trigger requirement of 6 HLC hits (SMT6), which translates to an average neutrino energy of approximately 10 GeV.

Table I shows the approximate detector rates for the trigger level and after application of the veto algorithm. The final rates after application of the cuts on the reconstructed vertex are not given in the table, since they are analysis dependent and vary strongly with the cut strength. The background events, muons from cosmic ray air showers, are simulated using CORSIKA [6]. In this study only the most energetic muon is propagated through the full detector simulation. This is a conservative approach since the other muons could only improve

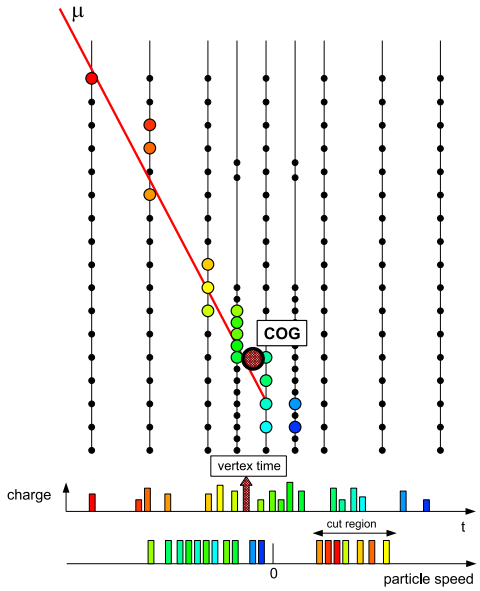

Fig. 2. Scheme of the veto principle: Illustration of the DeepCore hit center of gravity (COG), vertex time and particle speed per hit.

the veto efficiency. The signal rate given here is the rate of neutrinos produced in atmospheric air showers and has been determined following the flux calculations of the Bartol group [7]. Neutrino oscillation effects have not been taken into account. Since the goal is to identify starting muon tracks specifically, the signal is restricted to those events with a simulated interaction vertex within the DeepCore volume. The efficiencies given in Table I relate to events that fulfill this requirement and have a DeepCore SMT6 trigger. The background rejection factors refer to the expected main IceCube trigger rate, build up from an IceCube only SMT8 trigger, a String Trigger which requires 5 out of 7 aligned modules on a string to be fired in a trigger window of 1500 ns, as well as the DeepCore SMT6 trigger itself. Applying the SMT6 trigger gives a background rate which exceeds the signal by a factor $\sim 10^5$. This sets the challenge for the performance of the veto algorithms to be applied.

III. The veto algorithm

DeepCore is surrounded by more than 4500 DOMs that can be used as an active veto volume to reject atmospheric muons. If hits in the surrounding standard IceCube array are consistent with a particle moving downwards with v=c the event is rejected. For the veto algorithm, and also for any following reconstructions, it is essential to keep as many physics hits as possible. Therefore all hits in the detector are used here, including hits on DOMs without HLC (a mode called soft local coincidence, or SLC). To reduce the amount of dark noise hits, we reject any hits that are isolated from others by more than 150 m in distance or by more than 1000 ns in hit time. To determine whether or not to reject an event we initially compute the average hit PMT position and an approximate start time (vertex

TABLE I
BACKGROUND AND SIGNAL RATES AFTER DEEPCORE TRIGGER AND CAUSAL HIT VETO

	atm. μ (CORSIKA)	rejection	atm. ν_μ (Bartol)	eff.	atm. ν_μ upwards	atm. ν_μ down-wards
main IceCube triggers	2279 Hz	-	-	-	-	-
DeepCore event selection	102 Hz	$4.5{\cdot}10^{-2}$	$1.799{\cdot}10^{-3}$ Hz	100%	$0.901{\cdot}10^{-3}$ Hz	$0.895{\cdot}10^{-3}$ Hz
after Veto	1.2 Hz	$5.4{\cdot}10^{-4}$	$1.719{\cdot}10^{-3}$ Hz	95.5%	$0.863{\cdot}10^{-3}$ Hz	$0.856{\cdot}10^{-3}$ Hz

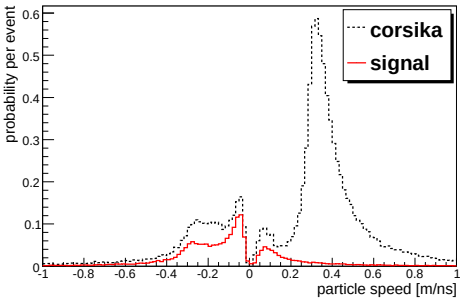

Fig. 3. Particle speed probabilities per event for atmospheric muons (dotted line) and muons induced by atmospheric neutrinos inside DeepCore (solid line).

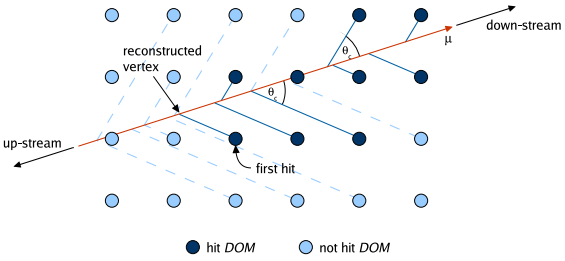

Fig. 4. Principle of the vertex reconstruction

time) of the DeepCore fiducial volume hits (see Fig. 2). The interaction position is determined by using the subset of those hit DOMs that have times within one standard deviation of the first guess vertex time. This has the benefit of reducing the contribution from PMT dark noise and, by weighting the DOMs by their individual charge deposition, a reasonable center of gravity (COG) for the event is computed. By making the assumption that roughly all light in the DeepCore volume originates from the COG a more thorough estimation of the vertex time is possible. For each individual hit the time light would have needed to travel from the COG to the hit module is calculated and subtracted from the original PMT hit time. The average of these corrected PMT hit times is then considered as the vertex time.

Each hit in the veto region gets assigned a particle speed, defined as the spatial hit distance to the DeepCore COG divided by the time difference to the DeepCore vertex time. This speed is defined to be positive if the hit occurred before the vertex time and negative if it appeared after. Causally related hits in the veto region are generally expected to have a speed close to the speed of the muon, which is very close to the speed of light in vacuum (0.3 m/ns). Smaller speeds occur for hits that have been scattered and thus arrive late. Larger speeds are in principle acausal, but since the vertex time represents the start of a DeepCore event, whereas the COG defines its center, the particle speeds for early hits are slightly overestimated. Late hits on the other hand have typically lower speeds. Fig. 3 shows the probability of the occurrence of a particular particle speed per event. The dotted curve describes the simulated muon background from air-showers (CORSIKA) and the solid curve the atmospheric neutrino signal [7] with an interaction vertex inside DeepCore. The peak for the CORSIKA muons is slightly above +0.3 m/ns while muons induced by neutrinos in DeepCore mainly give hits with negative particle speeds. The peak at positive speeds close to zero is mainly due to early scattered light. By cutting out all events with more than one hit within a particle speed window between 0.25 and 0.4 m/ns we achieve an overall background rejection on the order of $5 \cdot 10^{-4}$ (see Table I).

IV. THE VERTEX RECONSTRUCTION

To achieve the remaining background rejection, a second algorithm is used. It analyzes the pattern of hits in an event in conjunction with an input direction and position of a reconstructed track. From the track the algorithm estimates the neutrino interaction vertex and calculates a likelihood ratio which is used as a measurement for the degree of belief that the track is starting at the estimated position.

As shown in Fig. 4, we trace back from each hit DOM to the reconstructed track using the Cherenkov angle of 41° in ice. This projection is calculated for all DOMs within a cylindrical volume of radius 200 m around the track and the DOMs are ordered according to this position. (Note that 200 m is large enough to contain virtually all photons produced by the track.) The projection of the first hit DOM in the up-stream direction defines the neutrino interaction (reconstructed) vertex. A reconstructed vertex inside IceCube indicates a potential starting (neutrino-induced) track. Due to the large distance between neighboring strings, atmospheric muons may leak through the veto, producing their first hit deep inside the detector and thus mimicking the

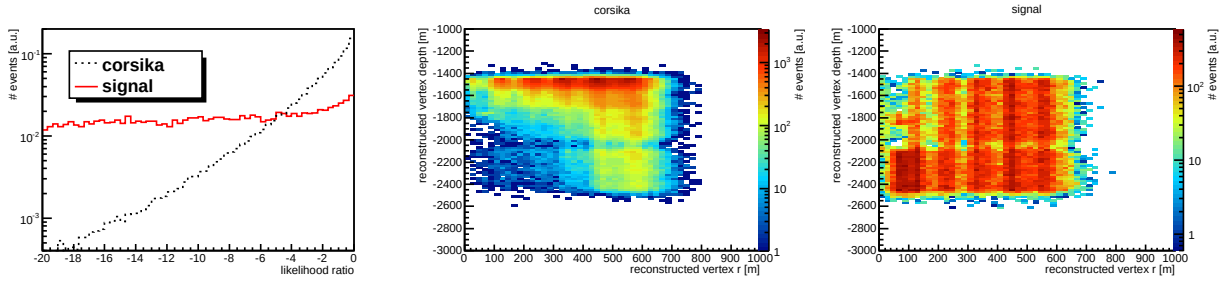

Fig. 5. Distributions of the cut parameters of the vertex reconstruction: Likelihood ratio (left) and position of the reconstructed vertex for atmospheric muons from CORSIKA (middle) and atmospheric neutrinos (right).

signature of a starting track. Therefore it is necessary to quantify for each event the probability of actually starting at the reconstructed vertex. To determine this starting likelihood, one first selects all DOMs without a hit and with a projection on the assumed track upstream of the first hit DOM. The probability that each of these DOMs did not receive a hit is calculated assuming two track hypotheses: a track starting at the reconstructed vertex and a track starting outside the detector volume. Under the assumption of an external track $p(\text{noHit}|\text{Track})$ is calculated. Here, for each DOM the probability of not being hit (in spite of the passing track) depends on track parameters (energy of the light emitting particle, position and direction of the track) and ice properties. The probability is calculated from the expected number of photoelectrons, taken from *Photorec* tables of the *Photonics* project [8], assuming Poisson statistics:

$$p_\lambda(\text{noHit}) = p_\lambda(0) = \frac{\lambda^0}{0!} e^{-\lambda} = e^{-\lambda}. \qquad (1)$$

λ is the expected number of photoelectrons. Under the assumption of a starting track $p(\text{noHit}|\text{noTrack})$ is calculated, which is equal to the probability of a noise hit and can therefore be calculated from measured noise rates.

The likelihood for the observed pattern of hit DOMs may now be constructed as the product of the individual hit probabilities. A track is classified as starting in the detector according to the probability given by the ratio of the likelihoods. For a clearly starting track this ratio is a negative number, and the larger the value the higher the starting probability for the track. To select tracks starting inside the detector, cuts are applied on the position of the reconstructed vertex and on the likelihood ratio. The distributions of the cut parameters are shown in Fig. 5.

Preliminary studies are up to now utilizing the true simulated track, since dedicated low energy track reconstructions are still under development. Even though idealized, these studies strongly indicate that an overall background rejection of $> 10^6$ can be achieved without having to extend the vertex cuts into the densely instrumented DeepCore fiducial region and with keeping the majority of the signal events.

V. Summary and Outlook

We have presented the methods developed thus far to reduce the rate of background muon events within the IceCube DeepCore detector. Utilizing the instrumented standard IceCube volume around DeepCore as an active veto to identify and reject atmospheric muon events improves the possibility of detecting neutrino induced muons and cascades independent of direction. The rate of atmospheric muons is mainly reduced in a two step process. First, a veto algorithm is applied against DeepCore events with causally related hits in the surrounding IceCube region. Second, applied to the veto surviving events, a cut has been defined, using a likelihood ratio, to determine the probability that the event had a starting vertex within the fiducial region of the detector. Monte Carlo studies indicate that both methods together will be suitable to reduce the background muon rate by more than the factor of 10^6 needed to obtain a signal (atmospheric neutrinos) to background ratio of > 1. IceCube and DeepCore are currently under construction and will be finished in 2011. The fully deployed DeepCore detector will provide an effective volume of several megatons of water equivalent for neutrino events with an energy above 10 GeV and a starting vertex in DeepCore. The exact volume will depend on the required signal-to-noise ratio and the individual analysis strategies.

References

[1] E. Resconi, et al., IceCube Collaboration, Proceedings to VLVnT08, (2008).
[2] A. Achterberg, et al., IceCube Collaboration, Astroparticle Physics 26, 155 (2006).
[3] M. Ackermann, et al., IceCube Collaboration, Journal of Geophysical Research, Vol. 111, D13203 (2006).
[4] J. N. Bahcall and P. Meszaros, Physics Review Letters, Vol. 85, p. 1362, (2000).
[5] E. K. Akhmedov, M. Maltoni and A. Y. Smirnov, Journal of High Energy Physics 5, 77 (2007).
[6] D. Heck et al, Report FZKA 6019 (1998).
[7] G. D. Barr, et al., Physical Review D 70, 023006 (2004).
[8] J. Lundberg et al., Nuclear Instruments and Methods, Vol. A581, pp. 619-631, (2007).

Acoustic detection of high energy neutrinos in ice: Status and results from the South Pole Acoustic Test Setup

Freija Descamps* for the IceCube Collaboration†

**Department of Subatomic and Radiation Physics, University of Ghent, 9000 Ghent, Belgium,*
†*See the special section of these proceedings.*

***Abstract*. The feasibility and specific design of an acoustic neutrino detection array at the South Pole depend on the acoustic properties of the ice. The South Pole Acoustic Test Setup (SPATS) has been built to evaluate the acoustic characteristics of the ice in the 1 to 100 kHz frequency range. The most recent results of SPATS are presented.**

***Keywords*: SPATS, acoustic neutrino detection, acoustic ice properties**

I. Introduction

The predicted ultra-high energy (UHE) neutrino fluxes from both hadronic processes in cosmic sources and interaction of high energy cosmic rays with the cosmic microwave background radiation are very low. Therefore extremely large detector volumes, on the order of 100 km^3 or more, are needed to detect a significant amount of these neutrinos. The idea of a large hybrid optical-radio-acoustic neutrino detector has been described and simulated in [1], [2]. The density of detectors in such a possible future UHE neutrino telescope is dictated by the signal to noise behaviour with travelled distance of the produced signals. The ice has optical attenuation lengths on the order of 100 m, enabling the construction and operation of the IceCube [3] detector. The relatively short optical attenuation length makes building a detector much larger than IceCube prohibitively expensive. In contrast, the attenuation lengths of both radio and acoustic waves are expected to be larger [4], [5] and may make construction of a larger detector feasible. The South Pole Acoustic Test Setup (SPATS) has been built and deployed to evaluate the acoustic attenuation length, background noise level, transient rates and sound speed in the South Pole icecap in the 1 to 100 kHz region so that the feasibility and specific design of an acoustic neutrino detection array could be assessed. Acoustic waves are bent toward regions of lower propagation speed and the sound speed vertical profile dictates the refraction index and the resulting radius of curvature. An ultra-high energy neutrino interaction produces an acoustic emission disk that will be deformed more for larger sound speed gradients and so the direction reconstruction will be more difficult. A good event vertex reconstruction allows accurate rejection of transient background. The absolute level and spectral shape of the continuous background noise determine the threshold at which neutrino induced signals can be extracted from the background and thus set the lower energy threshold for a given detector configuration. Transient acoustic noise sources can be misidentified as possible neutrino candidates, therefore a study of transient sources and signal properties needs to be performed. The acoustic signal undergoes a geometric 1/r attenuation and on top of that scattering and absorption. The overall acoustic attenuation influences detector design and hence cost.

II. Instrumentation

A. The SPATS array

The South Pole Acoustic Test Setup consists of four vertical strings that were deployed in the upper 500 meters of selected IceCube holes [3] to form a trapezoidal array, with inter-string distances from 125 to 543 m. Each string has 7 acoustic stages. Figure 1 shows a schematic of the SPATS array and its in-ice and on-ice components. It also shows a schematic drawing of an acoustic stage comprised of a transmitter and sensor module. The transmitter module consists of a steel pressure vessel that houses a high-voltage pulse generator board and a temperature or pressure sensor. Triggered HV pulses are sent to the transmitter, a ring-shaped piezo-ceramic element that is cast in epoxy for electrical insulation and positioned $\sim$13 cm below the steel housing. Azimuthally isotropic emission is the motivation for the use of ring shaped piezo-ceramics. The actual emission directivity of such an element was measured in azimuthal and polar directions [6]. The sensor module has three channels, each 120° apart in azimuth, to ensure good angular coverage.

B. The retrievable pinger

A retrievable pinger was deployed in 10 water-filled IceCube holes down to a depth of 500 m: 6 holes were pinged in December 2007-January 2008 and 4 more holes were pinged using an improved pinger design in December 2008-January 2009. The emitter[1] is a broad band omni-directional transmitter which has a transmission power of 149 dB re (μPa/V) at 1 meter distance. Upon receiving a trigger signal, a short ($\sim 50\mu s$) HV pulse is sent to the piezo-ceramic transmitter that is suspended about 2 m below the housing. A broadband acoustic pulse is then emitted. Both the SPATS array and the pinger are GPS synchronized so that the arrival times of the pinger-pulses can be determined. Data was

[1] ITC-1001 from the International Transducer Company

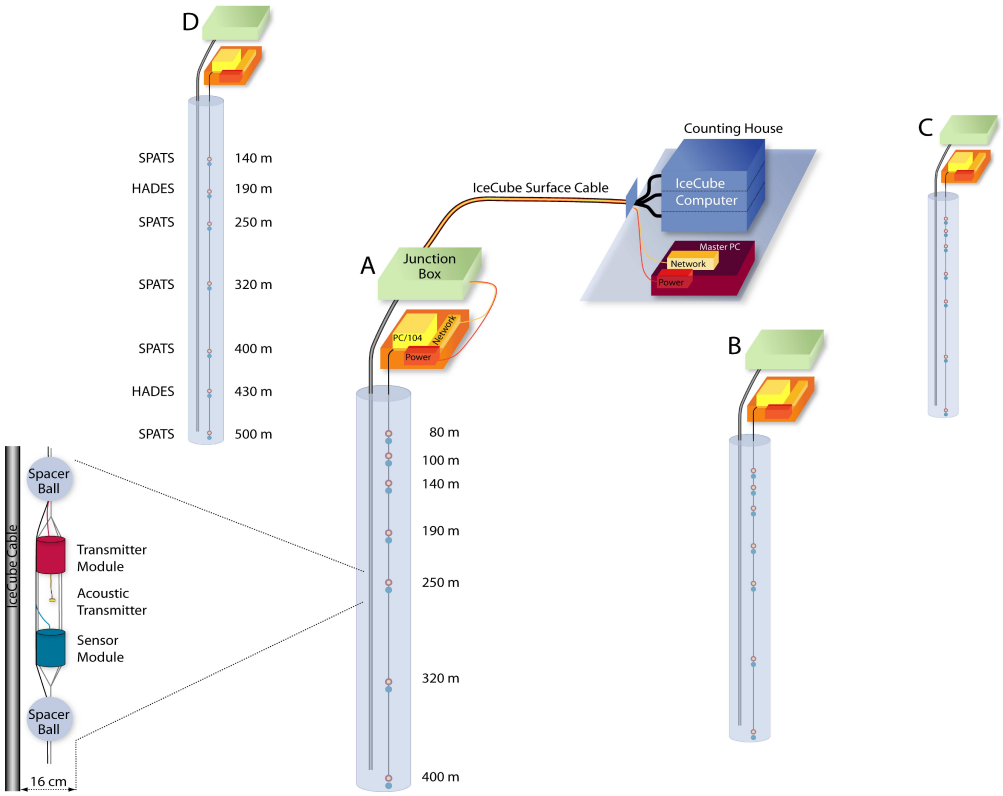

Fig. 1. Schematic of the SPATS detector.

collected for all SPATS-sensor levels at 80, 100, 140, 190, 250, 320, 400, 430 and 500 m depth and the pinger was pulsed at repetition rates of 1, 8 or 10 Hz. At the SPATS instrumented depths, the pinger lowering was stopped for five minutes so that a signal could be recorded with every SPATS sensor at that pinger position. For the December 2008-January 2009 holes, no stop was made at 80, 100, 140 and 430 m depth.

III. Results

A. Sound speed

The sound speed analysis uses data from December 2007-January 2008 geometries where the pinger and sensor were at the same depth and 125 m apart. The pinger emitter was situated in a column of water where no shear waves can propagate, nevertheless shear waves were generated at the water-ice boundary where mode conversion was expected. Therefore transit times can be extracted from the data for both pressure and shear waves for many instrumented SPATS levels. There is agreement with [7] for the pressure wave measurement in the not fully compacted ice of the upper region (firn). The extracted shear wave speed is about half of the pressure wave speed, as expected [8]. A linear fit was made to the data in the deep and fully compacted ice between 250 and 500 m depth. We find following results for the pressure and shear wave sound speeds (v_p and v_s) and their variation with depth (gradient: g_p and g_s):

$$\begin{aligned} v_p(375m) &= (3878 \pm 12)m/s, \\ g_p &= (0.09 \pm 0.13)(m/s)/m, \\ v_s(375m) &= (1975.8 \pm 8.0)m/s, \\ g_s &= (0.067 \pm 0.806)(m/s)/m. \end{aligned}$$

The gradient for both pressure and shear waves is consistent with zero. Both sound speed measurements are performed with a better than 1% precision, taking into account the errors on the horizontal distance, pinger and sensor depths, emission and arrival times. For more details on the SPATS sound speed analysis, see [9].

B. Gaussian noise floor

The noise is monitored in SPATS through a forced 200 kHz read-out of all sensor channels for 0.5 s every hour. The distribution of ADC counts in each of the operational channels is Gaussian and stable during the present observation time of more than 1 year with a typical deviation of the mean noise level of $\frac{\sigma_{RMS}}{<RMS>} < 10^{-2}$. The SPATS sensors on strings A, B and C have been calibrated in liquid water at 0°C in the 10 to 80 kHz frequency range prior to deployment [6]. Lab measurements have shown [6], [10] that the sensitivity of the SPATS sensor in air at atmospheric pressure increases by a factor of 1.5 ± 0.2 when cooled down from 0°C to -50°C. We use this value to estimate the sensitivity of the SPATS sensors after they were deployed in the cold Antarctic ice. A

measurement of the sensitivity at room temperature as a function of static pressure was performed in a pressure vessel and the results indicate a change in sensitivity of $< 30\%$ in the 1 to 100 bar region [10]. The noise level and fluctuations are high for all 4 strings in the firn region, where the transition from a snow/air mixture to compact bulk ice takes place. This is consistent with the effect of a large sound speed gradient in that layer so that the surface noise is refracted back to the surface. In the fully compacted ice, below the firn, noise conditions are more stable and we can derive an average noise level below 10mPa in the relevant frequency range (10 to 50kHz). For more details on the SPATS noise floor analysis, see [11].

C. Transient events

The SPATS detector has been operated in transient mode for 45 minutes of every hour since August 2008. If the number of ADC counts on any of the twelve monitored channels exceeds a certain level above noise, we record a 5ms window of data around the trigger on that channel. The resulting trigger rate is stable and on the order of a few triggers every minute for each of the twelve monitored channels. Most of these events are Gaussian noise events, where only one sample is outside the trigger boundaries. The transient events are processed off-line and analysed for time-coincidence clustering. Figure 2 shows the spatial distribution of a total of 4235 reconstructed transient events as detected by SPATS between 1 September 2008 and 23 April 2009 (4422 hours integrated lifetime). The data shows clear and steady sources or 'hot spots' that can be correlated with the refreezing process of the water in sub-surface caverns. Each IceCube drilling season, a

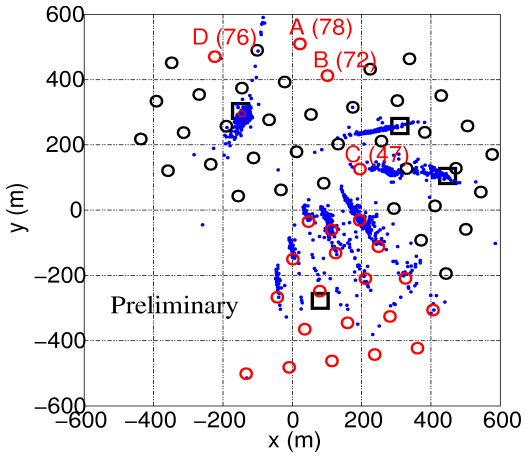

Fig. 2. An overview of the spatial distribution of transient events as detected by SPATS between September 2008 and April 2009. The circles indicate the positions of the IceCube holes, the SPATS strings are indicated by their corresponding letter-ID. The "Rodriguez well" are represented by squares. The smearing-effect is an artefact of the event reconstruction algorithm due to not accounting for refraction in the firn.

"Rodriguez wel" (RW) is used as a water reservoir. The main source of transients is the 07-08 RW. There is also steady detection of the 05-06/04-05 RW. The 06/07 RW was a steady source until October 2008. The 08-09 RW has not yet been detected. Transient data-taking continued during the IceCube 08-09 drilling season and the refreezing of 12 holes nearest to the SPATS array are audible whereas 7 of the farthest are not. No vertices were reconstructed deeper than 400 m.

D. Attenuation length

We have performed 3 classes of attenuation analyses, all of which use the sensors on the frozen-in SPATS strings but with a different sound source: the retrievable pinger, the frozen-in SPATS transmitters and transient events. Table I gives an overview of the SPATS attenuation length studies with their respective uncertainties.

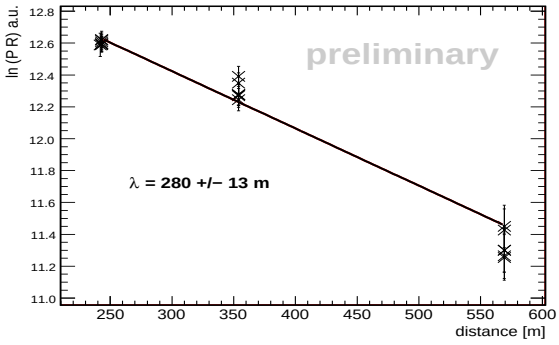

Fig. 3. An example of a (ln(amplitude·distance) vs. distance)-fit for a single channel at 400 m depth.

1) Pinger attenuation length: The retrievable pinger was recorded simultaneously by all SPATS sensors for each of the 4 IceCube holes in which it was deployed during the December 2008-January 2009 period. The pinger holes were almost perfectly aligned relative to the SPATS array, making the single-channel analysis independent of polar and azimuthal sensitivity variation. The energy of the signal, which dominates in the frequency range from 5 to 35 kHz, was extracted both from the waveforms in the time domain (4 pinger holes) and from the power spectrum (3 pinger holes). Figure 3 shows an example of a single-level fit for the energy in the frequency domain (single channel at 400 m depth). For both analyses, the quoted value in Table I is the mean of all fits with the standard deviation as error. The result for the time domain analysis uses all levels as shown in Fig. 4 and points which have large error bar ($\frac{\lambda}{\sigma_\lambda} < 3$) have been excluded (4/47 combinations). There is no evidence for a depth-dependence of the attenuation length.

2) Inter-string attenuation length: The complete SPATS inter-string set of April 2009 consists of all possible transmitter-sensor combinations excluding the shallowest transmitters. The transmitters were fired at 25Hz repetition rate and for each combination a total of 500 pulses was recorded simultaneously by the three channels of the sensor module. An averaged waveform

TABLE I
SPATS ATTENUATION LENGTH STUDIES.

Attenuation analysis	λ (m)	uncertainty	comment on uncertainty
Pinger energy time domain	320	60m	standard deviation of distribution
Pinger energy frequency domain	270	90m	standard deviation of distribution
Interstring energy all levels	320	100m	standard error of weighted mean of distribution
Interstring energy 3-level ratio	193	-	best fit
Transient event analysis	200	-	best fit

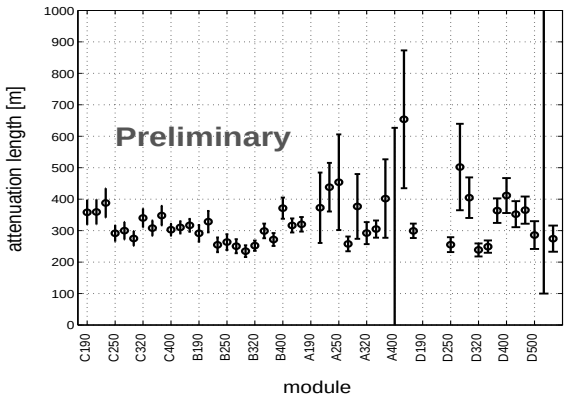

Fig. 4. Pinger energy analysis result from time domain for all recorded levels.

can therefore be obtained and the pressure wave energies extracted. An averaged noise-waveform allows us to subtract the noise contribution. Every transmitter in SPATS can be detected by 3 sensors at the same depth and different distances (strings), this means that only the unknown sensor sensitivities have to be included into the systematic error for a single-level attenuation length fit. We have fitted all data of the transmitters that are detected at three different distances. Each single fit does not constrain the attenuation length very well due to the large sensor-to-sensor variations in sensitivity. By combining all fits, we find a weighted mean and the standard deviation of the weighted mean as value for the attenuation length and its error (Table I). A way to work around the missing calibration of the sensors and transmitters is to build ratios of amplitudes using two transmitter-sensor pairs. For isotropic sensors and transmitters, one such measurement should yield the attenuation length. To minimize the remaining variation of the sensitivity due to the varying polar angle, we limited the amplitude ratios to the levels at 250, 320 and 400 m depth. This ratio-method yields an attenuation length with a large systematic error due to unknown azimuthal and remaining polar sensor orientations, therefore only the best fit is quoted in Table I.

3) Transient attenuation length: If a transient source can be localized, its corresponding signals can be used to estimate the acoustic attenuation length. The strongest transient source (07/08 RW) is excluded since it is too loud so that some channels are saturated. Moreover, all four of the SPATS strings are at similar distances from 07/08 RW. The transient events from the refreezing of hole 37 offer the advantage of mostly being inside the dynamical range of all sensors. In addition, hole 37 was pinged and all sensors recorded signals simultaneously from the pinger at a depth of 320 m. This pinger data can be used to extract relative sensitivity-correction factors for that precise direction for all sensor channels at 320 m depth on all 4 SPATS strings. The best fit of the sensitivity corrected single level transient data yields an attenuation length of 200 m.

IV. CONCLUSIONS

We have presented the most recent results from the SPATS setup. Both pressure and shear wave speeds have been mapped versus depth in firn and bulk ice. This is the first measurement of the pressure wave speed below 190 m depth in the bulk ice, and the first measurement of shear wave speed in the South Pole ice. The resulting vertical sound speed gradient for both pressure and shear waves is consistent with no refraction between 250 and 500 m depth. Extrapolating sensitivities from laboratory calibrations gives a first estimation of the absolute noise level at depths larger than 200 m and indicates values below 10 mPa integrated over the 10 to 50 kHz frequency range. The in-ice transient rates are low, most of the transient events can be correlated with well-know anthropogenic sources. We have presented an overview of the different SPATS attenuation length studies, the preliminary results show that the analyses favour attenuation lengths in the 200-350 m region. The current dataset does not allow a distinction to be made between absorption- or scatter-dominated attenuation length and dedicated measurements are under consideration.

V. ACKNOWLEDGMENT

We are grateful for the support of the U.S. National Science Foundation and the hospitality of the NSF Amundsen-Scott South Pole Station.

REFERENCES

[1] D. Besson *et al.*, Int. J. Mod. Phys. A **21S1** (2006) 259.
[2] D. Besson *et al.*, Nucl. Instr. and Meth. A (2009), doi:10.1016/j.nima.2009.03.047.
[3] A. Achterberg *et al.*, Astropart. Phys. **26** (2009) 155.
[4] S. Barwick *et al.*, J. Glaciol. **51** (2005) 231.
[5] P.B. Price, J. Geophys.Res. **111** (2006) B02201.
[6] J.-H. Fisher, Diploma thesis, Humboldt-Universitat zu Berlin (2006).
[7] J. G. Weihaupt, Geophys. 28 **(4)** (1963) 582.
[8] D.G. Albert, Geophys. Res. Let. **25 No 23** (1998) 4257.
[9] F. Descamps *et al., Nucl. Instr. and Meth.* A(2009), doi:10.1016/j.nima.2009.03.062.
[10] T. Karg *et al.*, these proceedings.
[11] T. Karg *et al.*, Nucl. Instr. and Meth. A (2009), doi:10.1016/j.nima.2009.03.063.

Sensor development and calibration for acoustic neutrino detection in ice

Timo Karg*, Martin Bissok†, Karim Laihem†, Benjamin Semburg*, and Delia Tosi‡ for the IceCube collaboration§

*Dept. of Physics, University of Wuppertal, D-42119 Wuppertal, Germany
†III Physikalisches Institut, RWTH Aachen University, D-52056 Aachen, Germany
‡DESY, D-15735 Zeuthen, Germany
§See the special section of these proceedings.

***Abstract*. A promising approach to measure the expected low flux of cosmic neutrinos at the highest energies (E $>$ 1 EeV) is acoustic detection. There are different in-situ test installations worldwide in water and ice to measure the acoustic properties of the medium with regard to the feasibility of acoustic neutrino detection. The parameters of interest include attenuation length, sound speed profile, background noise level and transient backgrounds. The South Pole Acoustic Test Setup (SPATS) has been deployed in the upper 500 m of drill holes for the IceCube neutrino observatory at the geographic South Pole. In-situ calibration of sensors under the combined influence of low temperature, high ambient pressure, and ice-sensor acoustic coupling is difficult. We discuss laboratory calibrations in water and ice. Two new laboratory facilities, the Aachen Acoustic Laboratory (AAL) and the Wuppertal Water Tank Test Facility, have been set up. They offer large volumes of bubble free ice (3 m^3) and water (11 m^3) for the development, testing, and calibration of acoustic sensors. Furthermore, these facilities allow for verification of the thermoacoustic model of sound generation through energy deposition in the ice by a pulsed laser. Results from laboratory measurements to disentangle the effects of the different environmental influences and to test the thermoacoustic model are presented.**

***Keywords*: acoustic neutrino detection, thermoacoustic model, sensor calibration**

I. Introduction

The detection and spectroscopy of extra-terrestrial ultra high energy neutrinos would allow us to gain new insights in the fields of astroparticle and particle physics. Apart from the possibility to study particle acceleration in cosmic sources, the measurement of the guaranteed flux of cosmogenic neutrinos [1] opens a new window to study cosmic source evolution and particle physics at unprecedented center of mass energies. However, the fluxes predicted for those neutrinos are very low [2], so detectors with large target masses are required for their detection. One possibility to instrument volumes of ice of the order of $100\,\mathrm{km}^3$ with a reasonable number of sensor channels is to detect the acoustic signal emitted from the particle cascade at a neutrino interaction vertex [3].

To study the properties of Antarctic ice relevant for acoustic neutrino detection the South Pole Acoustic Test Setup (SPATS) [4] has been frozen into the upper part of IceCube [5] boreholes. SPATS consists of four vertical strings reaching a depth of 500 m below the surface. The horizontal distances between strings cover the range from 125 m to 543 m. Each string is instrumented with seven acoustic sensors and seven transmitters. The ice parameters to be measured are the sound speed profile, the acoustic attenuation length, the background noise level, and transient noise events in the frequency range from 1 kHz to 100 kHz.

For the design of a large scale acoustic neutrino detector it is crucial to fully understand the *in-situ* response of the sensors as well as the thermoacoustic sound generation mechanism.

II. Sensor calibration

To study the acoustic properties of the Antarctic ice, like the absolute background noise level, and to deduce the arrival direction and energy of a neutrino in a future acoustic neutrino telescope it is essential to measure the sensitivity and directionality of the sensors used, i.e. the output voltage as function of the incident pressure, and its variation with the arrival direction of the incident acoustic wave relative to the sensor. These measurements can be carried out relatively easily in the laboratory in liquid water. The two calibration methods most commonly used are

- the comparison method, where an acoustic signal sent by a transmitter (with negligible angular variation) is simultaneously recorded at equal distance with a pre-calibrated receiver and the sensor to be calibrated. A comparison of the signal amplitudes in the two receivers allows for the derivation of the desired sensitivity from the sensitivity of the pre-calibrated sensor.
- the reciprocity method, which makes use of the electroacoustic reciprocity principle to determine the sensitivity of an acoustic receiver without having to use a pre-calibrated receiver (see e.g. [7]).

All SPATS sensors have been calibrated in $0\,^{\circ}\mathrm{C}$ water with the comparison method [8]. However, both calibration methods are not suitable for in-situ calibration of sensors in South Pole ice. There are no pre-calibrated sensors for ice available, and reciprocity calibration requires large setups which are not feasible for deployment in IceCube boreholes. Further, directionality studies require a change of relative positioning between emitter and receiver which is difficult to achieve in a frozen-in setup.

It is not clear how results obtained in the laboratory in liquid water can be transferred to an in-situ situation where the sensors are frozen into Antarctic ice. We are studying the influence of the following three environmental parameters on the sensitivity separately: low temperature, increased ambient pressure, and different acoustic coupling to the sensor. We will assume that sensitivity variations due to these factors obtained separately can be combined to a total sensitivity change for frozen in transmitters. This assumption can then be checked further using the two different sensor types deployed with the SPATS setup. Apart from the standard SPATS sensors with steel housing two HADES type sensors [9] have been deployed with the fourth SPATS string. These contain a piezoceramic sensor cast in resin and are believed to have different systematics.

A. Low temperatures

The ice temperature in the upper few hundred meters of South Pole ice is $-50\,^{\circ}\mathrm{C}$ [10]. It is not feasible to produce laboratory ice at this temperature in a large enough volume to carry out calibration studies. We study the dependence of the sensitivity on temperature in air. A signal sent by an emitter is recorded with a sensor at different temperatures. To prevent changes in the emissivity of the transmitter, the transmitter is kept at constant temperature outside the freezer, and only the sensor is cooled down. The recorded peak-to-peak amplitude is used as a measure of sensitivity. First results indicate a linear increase of sensitivity with decreasing temperature (cf. Fig. 1). The sensitivity of a SPATS sensor is increased by a factor of 1.5 ± 0.2 when the temperature is lowered from $0\,^{\circ}\mathrm{C}$ to $-50\,^{\circ}\mathrm{C}$ (averaged over all three sensor channels).

B. Static pressure

Acoustic sensors in deep polar ice are exposed to increased ambient static pressure. During deployment this pressure is exerted by the water column in the borehole (max. 50 bar at 500 m depth). During re-freezing it increases since the hole freezes from the top, developing a confined water volume. The pressure is believed to decrease slowly as strain in the hole ice equilibrates to the bulk ice volume. The final static pressure on the sensor is unknown.

A $40.5\,\mathrm{cm}$ inner diameter pressure vessel is available at Uppsala university that allows for studies of sensor

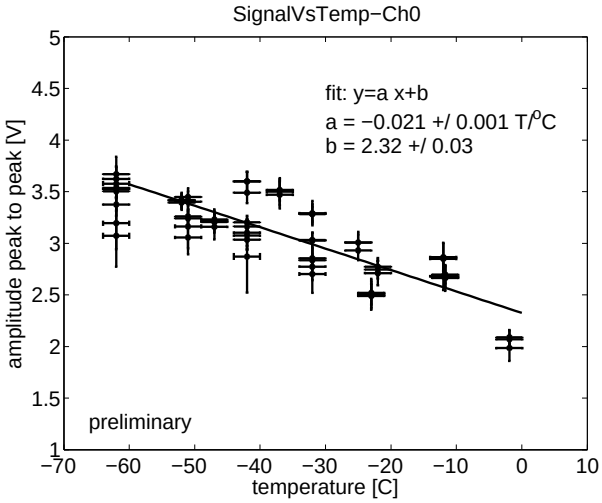

Fig. 1. Measured peak-to-peak amplitude of one SPATS sensor channel in air at different temperatures and linear fit to the data.

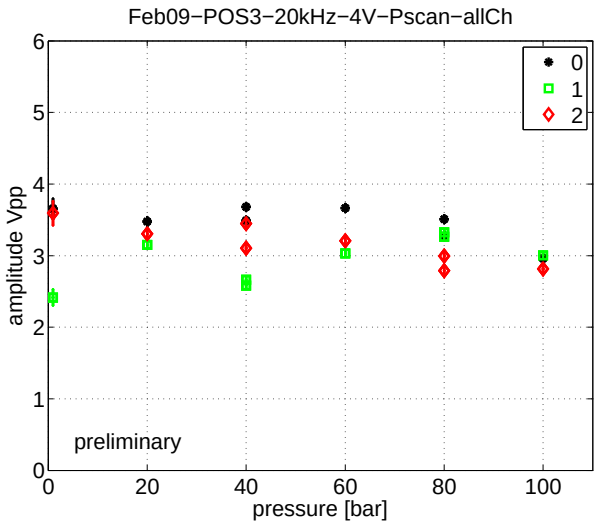

Fig. 2. Measured peak-to-peak amplitude of a SPATS sensor excited by a transmitter coupled from the outside to the pressure vessel. All three channels of the sensor are shown.

sensitivity as function of ambient pressure. Static pressures between 0 and 800 bar can be reached. In this study the pressure is increased up to 100 bar. Acoustic emitters for calibration purposes can be placed inside the vessel or, free of pressure, outside of it. Cable feeds allow one to operate up to two sensors or transmitters inside the vessel. A sensor is placed in the center of the water filled vessel. The transmitter is coupled from the outside to the vessel. The recorded peak-to-peak amplitude is used as a measure of sensitivity while the pressure is increased. The sensor sensitivity is measured by transmitting single cycle gated sine wave signals with different central frequencies from 5 kHz to 100 kHz.

Figure 2 shows the received signal amplitudes for the three sensor channels of a SPATS sensor as a function of ambient pressure. No systematic variation of the sensitivity with ambient pressure is observed. Combin-

ing all available data we conclude that the variation of sensitivity with static pressure is less than 30% for pressures below 100 bar.

C. Sensor-ice acoustic coupling

The acoustic coupling, i.e. the fractions of signal energy transmitted and reflected at the interface of medium and sensor, differs significantly between water and ice. It can be determined using the characteristic acoustic impedance of the medium and sensor, which is the product of density and sound velocity and is equivalent to the index of refraction in optics. Due to the different sound speeds the characteristic acoustic impedance of ice is about 2.5 times higher than in water.

Its influence will be studied in the Aachen Acoustic Laboratory (Sec. III), where it will be possible to carry out reciprocal sensor calibrations in both water and ice, and also to use laser induced thermoacoustic signals as a calibrated sound source.

III. New laboratory facilities

Two new laboratories have been made available to the IceCube Acoustic Neutrino Detection working group for signal generation studies and sensor development and calibration.

a) Wuppertal Water Tank Test Facility: For rapid prototyping of sensors and calibration studies in water, the Wuppertal Water Tank Test Facility offers a cylindrical water tank with a diameter of $2.5\,\mathrm{m}$ and depth of $2.3\,\mathrm{m}$ ($11\,\mathrm{m}^3$). The tank is built up from stacked concrete rings and has a walkable platform on top. It is equipped with a positioning system for sensors and transmitters and a 16-channel PC based DAQ system (National Instruments USB-6251 BNC).

The size of the water volume allows for the clean separation of emitted acoustic signals and their reflections from the walls and surface. This makes it possible to install triangular reciprocity calibration setups with side lengths of up to 1 m. Further, installations to measure the polar and azimuthal sensitivity of sensors are possible.

b) Aachen Acoustic Laboratory: The Aachen Acoustic Laboratory is dedicated to the study of thermoacoustic sound generation in ice. A schematic overview of the setup can be seen in Fig. 3. The main part is a commercial cooling container ($6 \times 2.5 \times 2.5\,\mathrm{m}^3$), which can reach temperatures down to $-25\,^{\circ}\mathrm{C}$. An IceTop tank, an open cylindrical plastic tank with a diameter of 190 cm and a height of 100 cm [6], is located inside the container. The IceTop tank has a freeze control unit by means of which the production of bubble-free ice is possible. The freeze control unit mainly consists of a cylindrical semipermeable membrane at the bottom of the container, which is connected to a vacuum reservoir and a pressure regulation system. The membrane allows for degassing of the water. A total volume of $\approx 3\,\mathrm{m}^3$ of bubble-free ice can be produced. A full freezing cycle takes approximately sixty days with the freezing going from top to bottom.

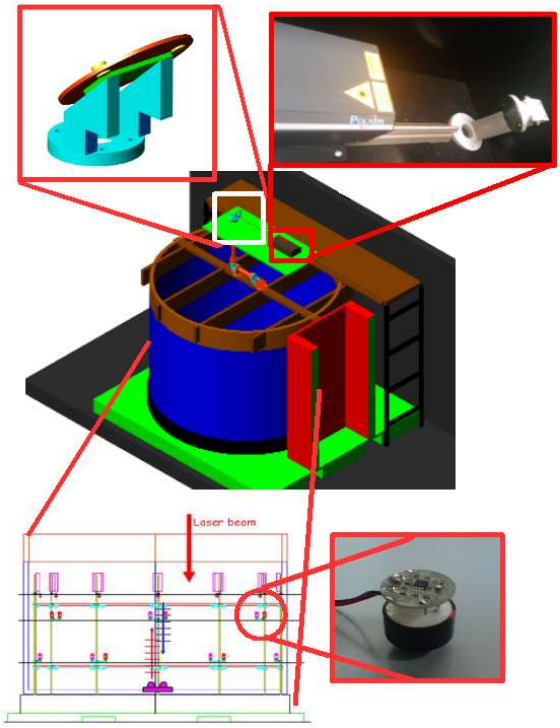

Fig. 3. Overview of the AAL setup with zoom on the mirror holder (top), the sensor positioning system (bottom, left) and a sensor (bottom, right).

On top of the container, a Nd:YAG Laser is installed in a light-tight box with an interlock connected to the laser control unit. The laser has a pulse repetition rate of up to 20 Hz and a peak energy per pulse of 55 mJ at 1064 nm, 30 mJ at 532 nm, and 7 mJ at 355 nm wavelength. The laser beam is guided into the container and deposited in variable positions on the ice surface by a set of mirrors with coatings for the above mentioned frequencies. The optical feed-through consists of a tilted quartz window to avoid damage of the laser cavity by reflected laser light. For the detection of thermoacoustic signals, 18 sensors are mounted on a sensor positioning system. The positioning system has three levels, on each level 6 sensors are placed in a hexagonal geometry. Along with the sensors, 18 sound emitters are deployed for calibration and test purposes. The sensors will be calibrated reciprocally. The positioning system will also include a reciprocal calibration setup for HADES sensors and the ability to install a SPATS sensor for calibration purposes. In addition, two temperature sensors are deployed at each level. The acoustic sensors are pre-amplified low-cost piezo based ultrasound sensors, usually used for distance measurement. The sensors show a strong variation of signal strength with incident angle. This directionality has to be studied but is rather useful for the suppression of reflected signals. The sensors are read out continuously by a LabVIEW-based DAQ framework with a NI PCIe-6259M DAQ card. The framework includes a temperature and acoustic noise monitoring

system.

IV. Studies of thermoacoustic signal generation

A detailed understanding of thermoacoustic sound generation in ice is crucial for designing an acoustic extension to the IceCube detector. The dependence of the signal strength on the deposited energy as well as on the distance to the sensor is of great interest. Also the pulse shape and the frequency content have to be studied systematically with respect to various cascade parameters. The spatial distribution of the acoustic signal has to be investigated, i.e. the acoustic disk and its dependence on the spatial and temporal energy deposition distribution. In addition, the AAL setup will be able to study the thermoacoustic effect in a wide temperature range from $20\,^{\circ}\mathrm{C}$ to $-25\,^{\circ}\mathrm{C}$ and possible differences of the effect in ice and water.

In the Aachen Acoustic Laboratory, the thermoacoustic signal is generated by a Nd:YAG laser. A laser-induced thermoacoustic signal differs from a signal produced in a hadronic cascade. While a cascade's energy deposition profile can be described by a Gaisser-Hillas function, the laser intensity drops of exponentially. Also the lateral profile of a cascade follows a NKG function, where, assuming a TEM_{00} mode in the far field region, the typical laser-beam profile is Gaussian. Knowing this, a recalculation of the signal properties from a laser-induced pulse to a cascade-generated pulse is possible.

The frequency content of the signal is expected to vary with the beam diameter, while a too short penetration depth will result in an acoustic point source rather than a line source. The absorption coefficient of light in water or ice varies strongly with wavelength. The first wavelength of the laser (1064 nm) is absorbed after few centimeters, while the second harmonic (532 nm) has an absorption length of $\approx 60\,\mathrm{m}$. The third harmonic at 355 nm with an absorption length of $\approx 1\,\mathrm{m}$ is expected to be the most suitable wavelength to emulate a hadronic cascade with a typical length of 10 m and a diameter of 10 cm. The diameter of the heated ice volume has to be controlled by optics inside the container that will widen the beam.

With an array of 18 sensors, the Aachen Acoustic Laboratory allows the study of the spatial distribution of the generated sound field, as well as the frequency content with varying beam parameters. The first thermoacoustic signal has been generated and detected in a test setup with preliminary sensor electronics in order to determine a reasonable gain for the pre-amplifier while avoiding saturation. A small volume of bubble-free ice has been produced, containing a sensor and an emitter. Laser pulses (wavelength 1064 nm, 55 mJ per pulse) have been shot at the ice block. A zoom on the first waveform is presented in Fig. 4. The distance between laser spot and sensor is approximately $15\,\mathrm{cm}$ and the sensor gain factor is 22. A Fourier transform of the pulse implies a pulse central frequency of $\approx 100\,\mathrm{kHz}$, which is expected for such a small beam diameter. In order to see the expected bipolar pulse, further studies have to be performed to determine the transfer function of the sensors.

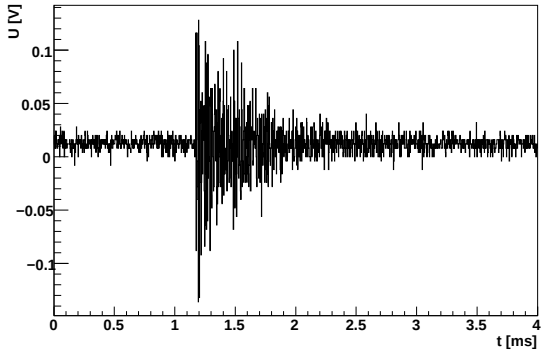

Fig. 4. Thermoacoustic pulse in ice, generated with a laser at 1064 nm wavelength and a beam diameter of $\approx 1\,\mu\mathrm{m}$.

V. Conclusions

Detailed understanding of the thermoacoustic sound generation mechanism and the response of acoustic sensors in Antarctic ice is necessary to design an acoustic extension for the IceCube neutrino telescope. While in-situ calibrations in deep South Pole ice are inherently difficult, different environmental influences can be studied separately in the laboratory. No change in sensor response with increasing ambient pressure was found; a linear increase in sensitivity with decreasing temperature was observed. Intense pulsed laser beams can be used to generate thermoacoustic signals in ice which can also be used as an in-ice calibration source.

Acknowledgments

We are grateful for the support of the U.S. National Science Foundation and the hospitality of the NSF Amundsen-Scott South Pole Station.

This work was supported by the German Ministry for Education and Research.

References

[1] V. S. Berezinsky and G. T. Zatsepin, Phys. Lett. B **28** (1969) 423.
[2] R. Engel, D. Seckel and T. Stanev, Phys. Rev. D **64** (2001) 093010, arXiv:astro-ph/0101216.
[3] G. A. Askaryan, At. Energ. **3** (1957) 152.
[4] J. Vandenbroucke et al., Nucl. Instr. and Meth. A (2009), doi:10.1016/j.nima.2009.03.064, arXiv:0811.1087 [astro-ph].
[5] http://icecube.wisc.edu/
[6] T. K. Gaisser, in Proceedings of the 29th International Cosmic Ray Conference (ICRC 2005), arXiv:astro-ph/0509330.
[7] R. J. Urick, *Principles of underwater sound*, 3rd ed., Peninsula Publishing (1983).
[8] J.-H. Fischer, Diploma Thesis, Humboldt-Universität zu Berlin (2006).
[9] B. Semburg et al., Nucl. Instr. and Meth. A (2009), doi:10.1016/j.nima.2009.03.069, arXiv:0811.1114 [astro-ph].
[10] P. B. Price et al., Proc. Nat. Acad. Sci. U.S.A. **99** (2002) 7844.

A new method for identifying neutrino events in IceCube data

Dmitry Chirkin*

**University of Wisconsin, Madison, U.S.A.*

Abstract. **A novel approach for selecting high-quality muon neutrino events in IceCube data is presented. The rate of air shower events mis-reconstructed as signal is first reduced via the use of the geometrical (software) trigger. The final event selection is performed with a machine-learning method, designed specifically for IceCube data. It takes into account some generic properties of IceCube events, e.g., the fact that separation of signal from background is more difficult (requiring tighter cuts on the quality parameters) for horizontal rather than vertically up-going tracks. The method compares favorably to other techniques in situations with both high and low simulation statistics.**

Keywords**: neutrino search, machine learning, event selection**

I. INTRODUCTION

An important task of a neutrino telescope like IceCube is identifying extra-terrestrial neutrinos that are interspersed between orders of magnitude higher background of particles originating in the showers produced by cosmic rays in the Earth's atmosphere.

As a first step a high purity atmospheric (plus possible extraterrestrial) neutrino event sample is selected, with only a small contaminating fraction of mis-reconstructed atmospheric muon events. Only neutrinos can cross the overburden of the Earth in the upward direction; however, selecting events reconstructed as upward-moving leaves many mis-reconstructed atmospheric muons in the sample, improving the ratio of neutrino to contaminating muon events (initially at $\sim 10^{-6}$) by only a factor of ~ 100.

The problem is further exacerbated by a highly uneven contamination of the mis-reconstructed muons in several of the analysis variables, most importantly the zenith angle. This contamination is smaller for up-going directions and increases for more horizontal tracks, growing rapidly near and above the horizon. It is therefore difficult to arrive at an event selection method that provides optimized cut surfaces simultaneously for all zenith angles. Splitting the cut optimization in different zenith bins leads to fluctuations of the cut parameters from one zenith angle bin to the next that are perceived as unphysical. In situations with limited simulated data, splitting it in several zenith angle bins is undesirable.

This author has also performed an SVM-based event selection optimization and found that training the SVM gets more difficult for zenith angle ranges extending above the horizon.

The above considerations led to the development of a new framework for selecting and applying cuts on quality parameters, that in the following is called "Subset Browsing Method", or *SBM* for short.

The quality parameters used with the event selection method of this paper build upon those discussed previously [1].

II. SIMPLE EXAMPLE

First consider a simple example employing only two parameters that select events with lower background contamination for lower value of the quality parameter. These can be, e.g., zenith angle (0 degrees for up-going to 90 for horizontal tracks) and estimated angular resolution (e.g., describing the half-width of the likelihood function at the minimum corresponding to the reconstructed track direction). Both of these can be used to remove the background of mis-reconstructed events, one through the basic reconstruction property, and the other though our prior knowledge that the contamination is higher for tracks near the horizon.

The toy simulated events are divided into two groups (randomly): the training set that is used for the training of the machine, and the testing set, that is used to judge its performance. Both sets, while drawn from the same parent distribution, are statistically independent. The toy "data" events are also simulated and drawn from a somewhat wider signal distribution (to demonstrate the effect of cuts in the transitional region between signal and background). The 3 steps of the machine application are the steps 1^a, 1^b, and 2 as shown on Figure 1.

The training of the machine in this simple example is achieved by identifying the "outlying" background events (on the signal side of the distribution), and creating the "angle cuts" (shown with black straight lines) by cutting away everything on the rejected sides of such cuts (i.e., everything above and to the right of the background event, including that background event itself).

The cuts so identified will obviously remove all background events in the training dataset. As seen from the second row of Figure 1, these cuts do not remove all of the background events when applied to the testing dataset, so a further step, here called 1^b is necessary. Using the angle cuts derived in step 1^a a quality parameter (*SBM**) is constructed, which is simply the count of "angle cuts" of step 1^a that fall into the bad quadrant (up and to the right) of a tested event, see Figure 2. This quality parameter could also be constructed as a

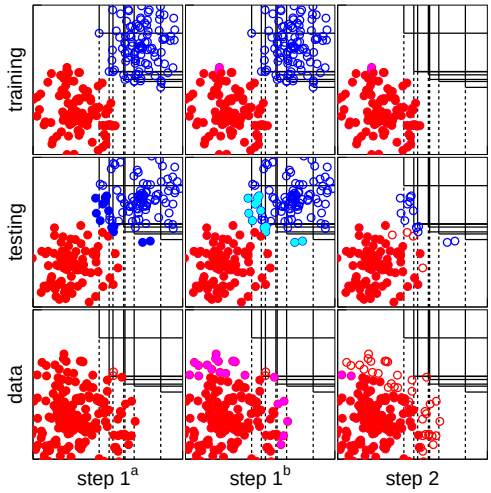

Fig. 1. Two event populations are shown: red is signal for the training and simulated testing event sets, and all data in the data set. Blue points (located up and to the right from red points) describe background events. Lower values on both x and y mean better quality. In steps 1^a and 1^b empty circles show background events removed by the *skeleton cuts*, aqua and pink points show background and signal (or data) events respectively that are removed by the machine quality parameter cut set at 1.5. In the third column events removed by step 2 are shown as empty circles and events additionally removed by the quality parameter cut are shown in pink, same as before. The black lines show the *skeleton cuts* and go through the out-most background events of the training set.

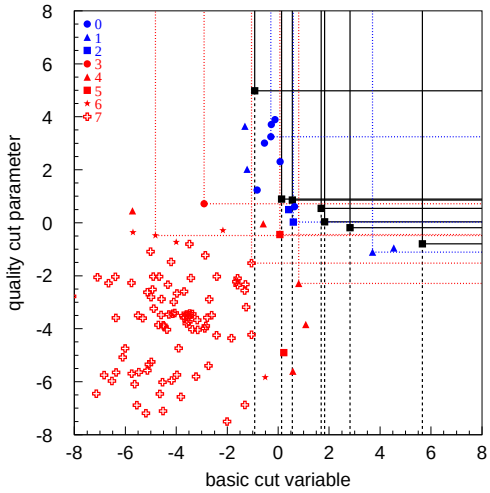

Fig. 2. Shown are events remaining in the testing dataset after the application of step 1^a, signal in red, and background in blue. The legend indicates the value of the *SBM** quality parameter for the shown events. For each value of the *SBM** quality parameter the bad sides of a representative event are shown with straight lines. The *SBM** quality parameter is simply the count of the "outlying" background events of the training dataset that gave rise to the "angle cuts" of step 1^a (indicated with black squares and black solid lines).

weighted sum, as described in the following section, shown for comparison as *SBM* in Figure 4.

A map of the quality parameter (*SBM**) is shown in Figure 3. It is clear that through application of the quality parameter some space is inserted between the cut structure achieved in step 1^a and events with quality parameter greater than 0. Figure 4 shows that a value of *SBM**=2.5 completely separates signal from background in the testing dataset of this simple example.

III. Unsimulated events and step 2

After the application of steps 1^a and 1^b to the real IceCube data it became obvious that, although much of the background events like those present in our simulation was removed, some "unsimulated" background remained in data. This affected agreement in parameter distributions and was particularly evident upon visual inspection. One class of such events appeared to contain two or more coincident but independent muon hit patterns that happened near each other with much overlap in time and failed to be split by the topological trigger. With more simulation we would most likely have been able to correctly identify these events.

Another class of events appeared to contain a bright electromagnetic or hadron shower (*cascade*), with rate of occurrence higher than that predicted by the simulation. While these events, when understood, could be very interesting, making a valuable contribution to the final event selection, it is unclear at this point whether they should be classified as signal or background. Moreover, since they are not simulated as either, the detector effective area to these events cannot be estimated, so they do not contribute to any of the physics results.

A common way to deal with this is by raising the quality parameter of an analysis past the point where all simulated background is removed and to the point where an agreement between data and signal simulation is achieved. This is possible if the quality parameter judges not only how far a given event is from the background region, but also how close it is to the signal region.

In the method presented here the quality parameter is constructed using only the information about the outlying background events that form the "angle cuts" (after some initial amount of signal events is carved out by the step 1^a). Thus, the quality parameter judges only the distance to the background region (contrary to other approaches). To achieve the "similarity with signal events" another step (called step 2) becomes necessary.

This event selection step is achieved by removing all data events, to the bad sides of which there are no signal events of the training set (remaining after the application of steps 1^a and 1^b). The effect of step 2 is demonstrated in the last column of Figure 1: all data events on the background side of the signal region are removed.

IV. Multi-dimensional generalization

First we re-iterate that the SBM method relies on the important observation that most of the quality parameters used in the analysis of IceCube data have the following property: as the fits become less constrained at lower number of channels N_{ch} or strings N_{str} (that received hits), the cuts on the quality parameters necessary to reach a given signal purity need to be tightened. Alternatively, the cuts applied to quality parameters of events with higher N_{ch} or N_{str} can be relaxed somewhat. A

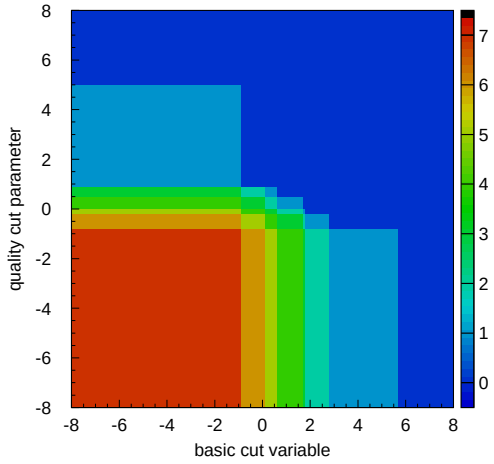

Fig. 3. Map of the quality parameter (*SBM**) calculated according to prescription of Figure 2. Highest-quality region is shown in red.

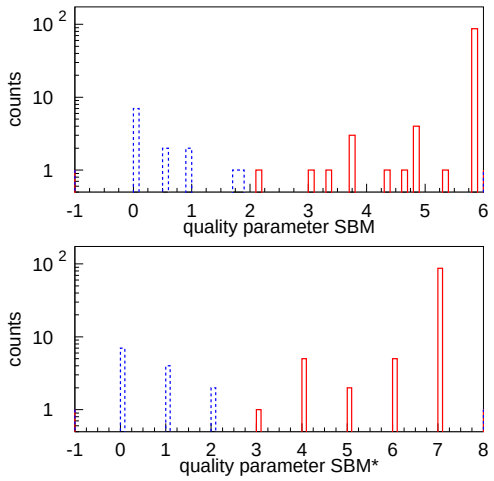

Fig. 4. Quality parameters: simple sum over the "angle cuts" (*SBM**), and weighted sum (*SBM*). Red solid and blue dotted lines show the distribution of signal and background events, respectively.

similar behavior of cuts on quality parameters can be argued for their dependence on the reconstructed zenith angle θ: at angles closer to the horizon the number of background events seeping through is higher than for tracks going up closer to the vertical, so to reach the same purity the cuts on the quality parameters need to be tighter for events with higher reconstructed zenith angle θ. To summarize, we introduce the following

Basic cut property: the cuts necessary to reach the same signal purity satisfy the following conditions:

$$c(\theta^\star, N_{ch}, N_{str}) \leq c(\theta^0, N_{ch}, N_{str}) \text{ for } \theta^\star \geq \theta^0$$

$$c(\theta, N^\star_{ch}, N_{str}) \leq c(\theta, N^0_{ch}, N_{str}) \text{ for } N^\star_{ch} \leq N^0_{ch}$$

$$c(\theta, N_{ch}, N^\star_{str}) \leq c(\theta, N_{ch}, N^0_{str}) \text{ for } N^\star_{str} \leq N^0_{str}$$

This relies on the **assumption** that lower cut values imply tighter cuts[1]. Parameters θ, N_{ch}, and N_{str} that allow such a behavior of cuts are in the following called *basic cut variables*. The following discussion is simplified with a

Definition: a cut $c^\star$ defined for a set of events with $\theta^\star$, $N^\star_{ch}$, and $N^\star_{str}$ is said to be operating on a *subset* of events of a cut c^0 defined for a set of events with θ^0, N^0_{ch}, and N^0_{str} if $\theta^\star \geq \theta^0$, $N^\star_{ch} \leq N^0_{ch}$, and $N^\star_{str} \leq N^0_{str}$.

Main cut property: a cut operating on a given set of events also operates on all its subsets.

To rephrase, a cut c^0 defined for a set of events with θ^0, N^0_{ch}, and N^0_{str} also applies to any set of events with $\theta^\star$, $N^\star_{ch}$, and $N^\star_{str}$ (that has its own cut $c^\star$), if $\theta^\star \geq \theta^0$, $N^\star_{ch} \leq N^0_{ch}$, and $N^\star_{str} \leq N^0_{str}$. To prove we need to show that $c^0 \geq c^\star$. Using 2 intermediate sets of events, and the basic cut property introduced above

$$c^0 = c(\theta^0, N^0_{ch}, N^0_{str}) \geq c(\theta^\star, N^0_{ch}, N^0_{str}) \geq c(\theta^\star, N^\star_{ch}, N^0_{str}) \geq c(\theta^\star, N^\star_{ch}, N^\star_{str}) = c^\star$$

This property allows us to consider all cuts as operating not only on events with $\theta = \theta^0$, $N_{ch} = N^0_{ch}$, and $N_{str} = N^0_{str}$, but rather on all events with $\theta \geq \theta^0$, $N_{ch} \leq N^0_{ch}$, and $N_{str} \leq N^0_{str}$.

Definition: The cut c^0 associated with θ^0, N^0_{ch}, and N^0_{str} is considered *redundant* if there exists another cut $c^\star$ associated with some other $\theta^\star$, $N^\star_{ch}$, and $N^\star$ such that

$$c^\star \leq c^0,\ \theta^\star \leq \theta^0,\ N^\star_{ch} \geq N^0_{ch}, \text{ and } N^\star_{str} \geq N^0_{str}.$$

This is because the new cut $c^\star$ clearly implies c^0 by the main cut property.

For each background event i_b in the simulated training dataset its quality parameters are used to create n cuts associated with θ^{i_b}, $N^{i_b}_{ch}$, and $N^{i_b}_{str}$ of the event. The signal purity $p^{i_b} = s^{i_b}/(s^{i_b} + b^{i_b})$ of the events with $\theta \geq \theta^{i_b}$, $N_{ch} \leq N^{i_b}_{ch}$, and $N_{str} \leq N^{i_b}_{str}$ is then calculated and used to find the i_b that defines cuts in a region with the worst purity. Out of the n cuts associated with i_b the cut that results in a smallest loss of signal events is then chosen and applied to the whole subset on which this cut operates. To accelerate this process if a cut in encountered that removes no signal events it is immediately used without taking into account the purity of the subset of events on which this cut operates.

This procedure is then repeated until the background events in the simulated training dataset are exhausted. At that point all cuts of all background events are cycled through once again, and those that result in no further loss of remaining signal events (which are said to form a *core* or signal events) are saved into the *trained cut set* of the machine. One can further *reduce* this set by removing the *redundant* cuts from it, thus resulting in an *irreducible trained cut set*, which is the result of this machine training procedure.

One can obviously remove all background events (i.e., reach a 100% signal purity) by applying all cuts from the *irreducible trained cut set* to the simulated training dataset. However, when the same is applied to the separately generated *testing* dataset a number of

[1]Some of the quality parameters may need to be taken with a minus sign or as one over their value to satisfy this assumption

background events seep through and the signal purity never reaches 100%.

This may happen, e.g., if we encounter a background event with, say, $N^{\star}_{ch}$ higher than $N^{i_b}_{ch}$ of every background event in the simulated training dataset, thus there are no cuts available that would remove such an event from the testing dataset.

A way around this is to find at least one cut c with $\theta^c \geq \theta^{\star}$, $N^c_{ch} \leq N^{\star}_{ch}$, and $N^c_{str} \leq N^{\star}_{str}$ such that $c^{\star} = q^{\star} \leq c$ ($q^{\star}$ being the quality parameter of the tested event). By the *main cut property* the cut that would achieve the same purity p_c on the subset defined by $\theta^{\star}$, $N^{\star}_{ch}$, and $N^{\star}_{str}$ as the cut c on the subset defined by θ^c, N^c_{ch}, and N^c_{str} is necessarily no more tight as the cut c. That is, applying the cut c on the subset defined by $\theta^{\star}$, $N^{\star}_{ch}$, and $N^{\star}_{str}$ achieves at least the same or higher level of purity as p_c. Now, if an event defined by its quality parameters $c^{\star} = q^{\star}$ but at the *basic cut variables* θ^c, N^c_{ch}, and N^c_{str} of the cut c is passed by the *trained cut set*, cut c is called the *purity cut* defined for the original event (defined by its own $c^{\star}$, $\theta^{\star}$, $N^{\star}_{ch}$, and $N^{\star}_{str}$).

Existence of at least one such cut c for each of the testing dataset events passed by the machine guarantees that the purity in the regions with extrapolated θ, N_{ch}, and N_{str} is at least as good or better than in the regions for which background events existed in the simulated training dataset. This is an important advantage of the discussed method compared to the other machine learning techniques.

Counting all *purity cuts* available for a given testing dataset event provides one with an important machine quality parameter which value is higher for events that are more likely to be signal and lower for events that are more likely to be background. It appears that a cut on this parameter improves the purity in all subsets by equal amount. In order to improve the purity in all subsets to the same final value one may weight the terms in the quality parameter sum with the initial purity of the simulated training dataset on the subsets of the cuts used in the sum (thus leading to the weighted sum definition of SBM, as shown in Figure 4).

We call the machine learning method described here the *subset browsing method* because of the technique in which one has to *browse* through the *subsets* on which the cuts of the *trained cut set* are defined to calculate the quality parameter separating signal from background. The quality parameter itself is called the *SBM quality parameter*: SBM.

The *irreducible trained cut set* forms a "skeleton" of cuts that are applied to the testing dataset achieving the *initial SBM cut level*: $SBM = 0$. The SBM quality parameter is usually normalized so that the highest value of SBM of a background event in a simulated testing dataset is 1 (e.g., in the plot of the SBM in Figure 5).

V. Conclusions and Outlook

We present a new framework for selecting and applying cuts on the quality parameters, here called SBM. It is particularly well-suited for application to IceCube data analysis as it takes into account (both during training and for event classification) some obvious relationships between the quality parameters, which are hardwired into the algorithm.

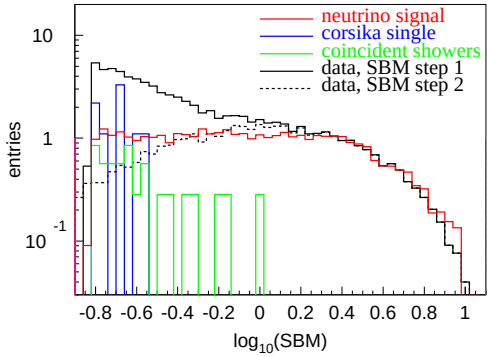

Fig. 5. Distribution of the quality parameter after step 1^a (for 1 year of IC-22 data). The >90% estimated purity is achieved at SBM=0.36.

The SBM appears to separate signal and background well even if the number of simulated training dataset events is low. The SBM extrapolation behavior is very robust and the performance of extrapolation improves as the simulated testing dataset statistics increases, since more *purity cuts* become available to testing events in regions less populated by cuts of the *trained cut set*. The machine will not go around individual background events of the training dataset (a condition that may occur in other methods) because the cuts, by construction, are monotonous functions of the basic parameters.

Additionally, the learning method itself is very simple and has virtually no parameters to set. Most of the machine is implemented with only an application of the $\leq$ operator (and a simple summation for estimating the quality parameter).

The method splits the classification of the data events into two steps: dissimilarity with background, and similarity with signal, thus allowing one to investigate possible "unsimulated" classes of events.

This method was used to identify atmospheric neutrino events in IceCube data taken during the 2007 operation season (see Figure 5 and reference [2]).

As an outlook, this method may be well-suited to analyzes that depend on a veto region around the interesting events in the detector, as most of the cuts on the quality parameters can be relaxed as the veto region is expanded, thus satisfying the basic cut property if veto size is chosen as a basic cut variable.

The method could be further improved in the future by implementing a technique similar to boosting of the BDT.

References

[1] D. Chirkin, et al., *Effect of the improved data acquisition system of IceCube on its neutrino-detection capabilities*, 30th ICRC, Merida, Mexico (arXiv:0711.0353)

[2] D. Chirkin, et al., *Measurement of the atmospheric neutrino energy spectrum with IceCube*, these proceedings

Muon Production of Hadronic Particle Showers in Ice and Water

Sebastian Panknin*, Julien Bolmont†, Marek Kowalski* and Stephan Zimmer‡

*Humboldt-Universität zu Berlin, Germany
†LPNHE, Universite Pierre et Marie Curie Paris 6, Universite Denis Diderot Paris 7, CNRS/IN2P3, France
‡Humboldt-Universität zu Berlin, Germany, now at Uppsala Universitet, Sweden

Abstract. **One of the neutrino signatures in Cerenkov neutrino detectors are isolated, particle showers induced by neutrinos of all flavors. Hadronic showers can produce muons during the shower development and the appearance of the showers can change significantly by such high-energy muons. We use a modified version of the air shower simulation program CORSIKA for the simulation of the generation of muons in salt water. We discuss how the results can be applied for ice. In addition, a simple analytical model is derived, that provides scaling relations for the muon energy spectrum and its dependence on the primary particle.**

Keywords**: shower-simulation, muons, neutrino-detection**

I. INTRODUCTION

Large neutrino telescopes in ice or water, like IceCube[1], Baikal[2] and ANTARES[3], are in operation or construction. They detect Cerenkov light from particles created by neutrino interactions. The most prominent signature are up-going muons generated by charge-current interactions of muon neutrinos. Another possibility is the search for neutrino induced cascades [4]. Such a search is sensitive to electron and tau neutrinos. In addition, unlike a search for neutrino induced muons, one is not restricted to up-going tracks, since the signature of isolated cascades allows in principle good separation from the down-going atmospheric muon background. A requirement for a search of neutrino induced events is their accurate simulation.

In hadronic cascades also muons can be produced. Due to their track-like light signature they may influence the shape and thus should be simulated and parameterized.

We develop a simple analytical calculation for the produced muon flux (section II). We show the results of a full shower simulation with a modified version of the well-known air-shower simulation program CORSIKA [5] (section III) and use this to parameterize the muon flux (section IV). We conclude in section V.

II. ANALYTICAL MODEL FOR THE MUON FLUX

The basic properties of electro-magnetic showers can be understood through the Heitler model [6]. After one interaction length a photon creates an electron-positron pair, and an electron/positron radiates a bremsstrahlung photon. This repeats every interaction length while the energy is distributed over the generated particles, so that more and more particles with lower and lower energies are created. Hadronic showers are more complicated, since in each interaction a wide range of hadronic particles can be created, which through decay increase the complexity further. However, expanding the simple Heitler model helps to get a basic understanding of the muon generation in hadronic cascades.

We follow the extended Heitler model of [7] and consider a hadronic shower generated by a particle of primary energy E_0. In each interaction $N_{\mathrm{mul}} \approx 10$ hadrons are produced. About one third of them will be neutral hadrons like π^0, which will lead to an electromagnetic sub-shower.

So in the generation n we have $N_{\mathrm{H}}(n)$ hadrons with average energy E_{H}:

$$N_{\mathrm{H}}(n) = \left(\frac{2}{3} N_{\mathrm{mul}}\right)^n \tag{1}$$

$$E_{\mathrm{H}}(n) = \frac{E_0}{N_{\mathrm{mul}}^n} \tag{2}$$

Combining this leads to the energy depending number of hadrons per generation

$$\frac{\Delta N_{\mathrm{H}}}{\Delta \log_{N_{\mathrm{mul}}}(E_0/E_{\mathrm{H}})}(E_{\mathrm{H}}) = \left(\frac{E_{\mathrm{H}}}{E_0}\right)^{-\kappa} \quad \text{with } \kappa := 1 + \log_{N_{\mathrm{mul}}} \frac{2}{3} \tag{3}$$

and to the hadronic flux

$$\frac{\mathrm{d}N_{\mathrm{H}}}{\mathrm{d}E_{\mathrm{H}}}(E_{\mathrm{H}}) = -\frac{\ln N_{\mathrm{mul}}}{E_0} \left(\frac{E_{\mathrm{H}}}{E_0}\right)^{-(\kappa+1)} . \tag{4}$$

Next we consider different types of hadrons h. In the following, we will keep using H if a variable is meant for all hadrons. We neglect the different reaction channels for different hadrons and assume a constant branching ratio B_{h} for production of a hadron h, independent of the incident type. (We mainly focus on pions and kaons.)

The muon flux can now be derived as the hadron flux multiplied with the decay probability $P_{\mathrm{h}\to\mu}$ and folded by the energy distribution of the generated muon $\frac{\mathrm{d}n_{\mathrm{h}}}{\mathrm{d}E_\mu}(E_\mu, E_{\mathrm{h}})$:

$$\frac{\mathrm{d}N_\mu}{\mathrm{d}E_\mu}(E_\mu) = \sum_{\mathrm{h}} B_{\mathrm{h}} \int_0^\infty \frac{\mathrm{d}n_{\mathrm{h}}}{\mathrm{d}E_\mu}(E_\mu, E_{\mathrm{h}})\, P_{\mathrm{h}\to\mu} \frac{\mathrm{d}N_{\mathrm{H}}}{\mathrm{d}E_{\mathrm{H}}}(E_{\mathrm{h}})\, \mathrm{d}E_{\mathrm{h}} \tag{5}$$

TABLE I
USED NUMERICAL VALUES FOR PIONS AND KAONS. THEIR CONTRIBUTION A TO THE AMPLITUDE AS WELL AS THE FULL AMPLITUDE ARE PROVIDED.

h	B_h	$b_{\mathrm{h}\to\mu}$	α	r_h	$A_\mathrm{h}\,[\mathrm{GeV}^{-1}]$
π	0.9	1.00	67.1	$5.73\cdot10^{-1}$	$20.03\cdot10^{-3}$
K	0.1	0.64	9.03	$4.58\cdot10^{-2}$	$6.00\cdot10^{-3}$
		$A=\sum_\mathrm{h} A_\mathrm{h}$:			$26.30\cdot10^{-3}$

The decay probability of a hadron with mass m_h and lifetime τ_h and a branching ratio $b_{\mathrm{h}\to\mu}$ for the decay into muons is given by

$$P_{\mathrm{h}\to\mu} = b_{\mathrm{h}\to\mu}\frac{\Lambda}{\lambda_\mathrm{D}} = \frac{b_{\mathrm{h}\to\mu}}{1+\alpha_\mathrm{h}E_\mathrm{h}} \approx \frac{b_{\mathrm{h}\to\mu}}{\alpha_\mathrm{h}E_\mathrm{h}} \quad \text{with } \alpha_\mathrm{h} := \frac{\tau_\mathrm{h}}{m_\mathrm{h}\lambda_\mathrm{I}}, \tag{6}$$

where $\Lambda := \frac{1}{\lambda_\mathrm{I}} + \frac{1}{\lambda_\mathrm{D}}$, λ_I is the interaction length of the hadron and $\lambda_\mathrm{D} = \frac{E_\mathrm{h}\tau_\mathrm{h}}{m_\mathrm{h}}$ is the decay length, assuming $E_\mathrm{h} \gg m_\mathrm{h}$. The approximation holds for $\alpha_\mathrm{h}E_\mathrm{h} \gg 1$. The probability to create a muon of energy E_μ from the decay of a hadron with energy E_h is given by the energy distribution $\frac{\mathrm{d}n_\mathrm{h}}{\mathrm{d}E_\mu}(E_\mu, E_\mathrm{h})$. Unpolarized meson performing a two-body decay will generate mono-energetic muons isotropic distributed over the directions in their rest-frame (see [8]). This transforms in the laboratory system to a constant distribution between the minimal energy $r_\mathrm{h}E_\mathrm{h}$ with $r_\mathrm{h} = \frac{m_\mu^2}{m_\mathrm{h}^2}$ and the maximal energy E_h:

$$\frac{\mathrm{d}n_\mathrm{h}}{\mathrm{d}E_\mu}(E_\mu, E_\mathrm{h}) = \begin{cases} \frac{1}{(1-r_\mathrm{h})E_\mathrm{h}} & r_\mathrm{h}E_\mathrm{h} \le E_\mu \le E_\mathrm{h} \\ 0 & \text{else} \end{cases} \tag{7}$$

Applying eq. (4), (6) and (7) on eq. (5) we obtain the muon flux

$$\frac{\mathrm{d}N_\mu}{\mathrm{d}E_\mu}(E_\mu) = A\left(\frac{E_0}{\mathrm{GeV}}\right)^{\kappa}\left(\frac{E_\mu}{\mathrm{GeV}}\right)^{-(\kappa+2)}$$
$$\text{with } A = \frac{\ln N_\mathrm{mul}}{\kappa+2}\left(\sum_\mathrm{h} B_\mathrm{h}\frac{b_{\mathrm{h}\to\mu}}{\alpha_\mathrm{h}}\frac{1-r_\mathrm{h}^{\kappa+2}}{1-r_\mathrm{h}}\right)\frac{1}{\mathrm{GeV}^2}. \tag{8}$$

This results in the numerical values for the amplitude $A = 26.3\cdot10^{-3}\,\mathrm{GeV}^{-1}$ and for the exponent according to eq. (3) $\kappa = 0.824$. The values used for pions and kaons are summarized in Table I.

III. CORSIKA SIMULATION

For the simulation we used a modified version of CORSIKA based on the official version 6.2040 which enables shower simulation in salt water (see [9]). The used interaction models are Gheisha for low energies and QGSJet 01 for high energies. We simulated 1000 showers at primary energy $E_0 = 1\,\mathrm{TeV}$, 1000 at $10\,\mathrm{TeV}$, 100 at $100\,\mathrm{TeV}$ and ten at $1\,\mathrm{PeV}$ with a proton as primary particle.

The used configuration (Fig. 1) is a CORSIKA observation level $9\,\mathrm{m}$ behind the interaction point. Here the shower is expected to be fully developed, while only the very low energy muons will already be decayed.

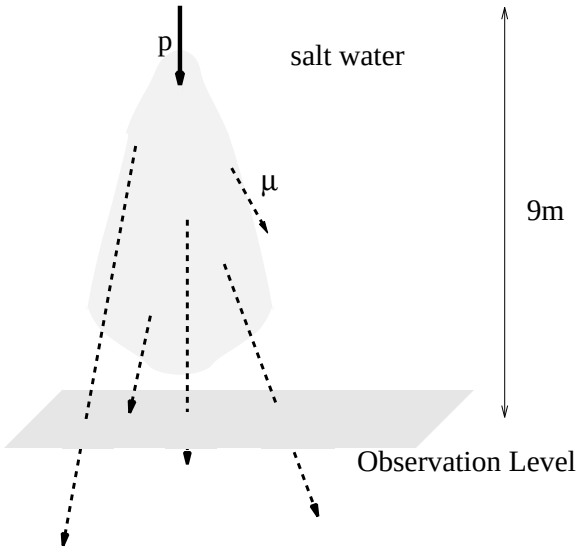

Fig. 1. CORSIKA configuration: the incoming proton p interacts $9\,\mathrm{m}$ above the observation level. The produced muon μ will roughly have the same direction as the incoming particle and are recorded, as they pass through the observation level.

IV. DERIVED MUON FLUX

With the simulation data we calculate the muon flux. To make this comparable to our model we need to calculate the muon energy at generation E_μ from the muon energy at observation level E_μ^obs given in the simulation. This is a small correction, important only for low energetic muons. Muons that are most interesting for us are those with track-lengths above about $10\,\mathrm{m}$, namely those with a range bigger than the typical shower size. These muons have energies above $3\,\mathrm{GeV}$, which is high enough, to reduce systematic error due to the energy correction.

The energy loss can be approximated by:

$$\frac{1}{\varrho}\frac{\mathrm{d}E_\mu}{\mathrm{d}x} = -a - bE_\mu \tag{9}$$

where the medium density is $\varrho = 1.02\,\mathrm{g\,cm^{-3}}$ and the interaction constants are $a = 2.68\,\mathrm{MeV cm^2\,g^{-1}}$ and $b = 4.7\cdot10^{-6}\,\mathrm{cm^2\,g^{-1}}$ (see [10]). Solving this provides the formula for the energy at generation:

$$E_\mu = \left(E_\mu^\mathrm{obs} + \frac{a}{b}\right)\mathrm{e}^{\varrho b x} - \frac{a}{b} \tag{10}$$

Here we choose $x = 7\,\mathrm{m}$, the distance from first interaction point to the observation level reduced by about three radiation length [10].

We show the normalized flux $\frac{E_\mu^2}{E_0^\kappa}\frac{\mathrm{d}N_\mu}{\mathrm{d}E_\mu}(E_\mu)$ which should follow according to eq. (8) a power law with small primary energie dependency (Fig. 2). The power law was fitted for the curves individually (Tab. II). This

leads to the averaged parameterization:

$$\frac{\mathrm{d}N_\mu}{\mathrm{d}E_\mu} = A\left(\frac{E_0}{\mathrm{G}e\mathrm{V}}\right)^{\kappa}\left(\frac{E_\mu}{\mathrm{G}e\mathrm{V}}\right)^{-(2+\kappa)}$$
$$A = (3.5 \pm 0.5\,(\mathrm{stat}) \pm {}^{6.5}_{2.0}\,(\mathrm{sys})) \cdot 10^{-3}\,\frac{1}{\mathrm{G}e\mathrm{V}}$$
$$\kappa = 0.97 \pm 0.07\,(\mathrm{stat}) \pm 0.12\,(\mathrm{sys}). \qquad (11)$$

The systematics were estimated by using different x-values for the energy correction.

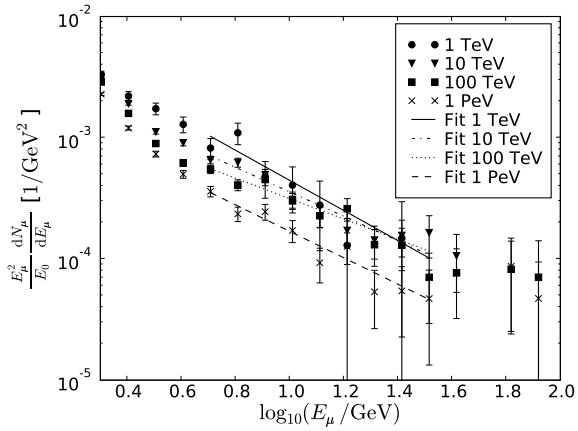

Fig. 2. The muon flux $\frac{\mathrm{d}N_\mu}{\mathrm{d}E_\mu}$ is shown as function of muon energy E_μ. We multiplied by $\frac{E_\mu^2}{E_0}$ to remove the primary energy dependency by some extend and improve readability. The results of the fit are given in Table II.

Using the integral representation (Fig. 3), we can see that on average a hadronic cascade of $100\,\mathrm{T}e\mathrm{V}$ produces e.g. about one muon with an energy above $10\,\mathrm{G}e\mathrm{V}$. Such a muon would have a track length of about $36\,\mathrm{m}$.

CORSIKA provides the information if a muon was generated from a pion. Using this information, Fig. 4 shows the number of pion produced muons over all muons as a function of the energy. As expected, other

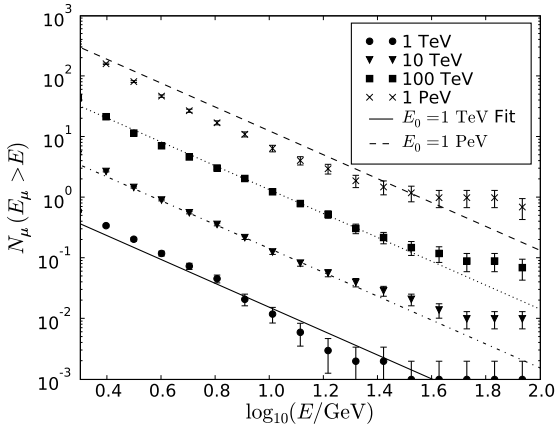

Fig. 3. Integral muon flux $N_\mu(E_\mu > E)$. The fit is taken from the differential muon flux (Fig. 2 and Table II).

TABLE II
PARAMETERIZATION OF MUON FLUX: THE PARAMETERIZATION GIVEN IN (11) WAS FITTED TO THE MUON FLUX INDIVIDUALLY FOR THE DIFFERENT PRIMARY ENERGIES (S. FIG. 2).

E_0	$10^3 \cdot A\,[\frac{1}{\mathrm{GeV}}]$		κ	
$10\mathrm{T}e\mathrm{V}$	4.731	± 0.995	1.007	± 0.104
$100\mathrm{T}e\mathrm{V}$	3.020	± 0.703	0.840	± 0.113
$1\mathrm{T}e\mathrm{V}$	9.457	± 6.792	1.242	± 0.371
$1\mathrm{P}e\mathrm{V}$	3.089	± 0.965	1.091	± 0.156
average	3.490	± 0.492	0.971	± 0.068

production mechanisms (e.g. kaons) become more important with higher energy. However the constant hadron fractions B_h are a reasonable approximation. Our simple model with only pion and kaon ($B_K = 0.1$) predicts a constant $\frac{N_\mu^\pi}{N_\mu} = 77\,\%$.

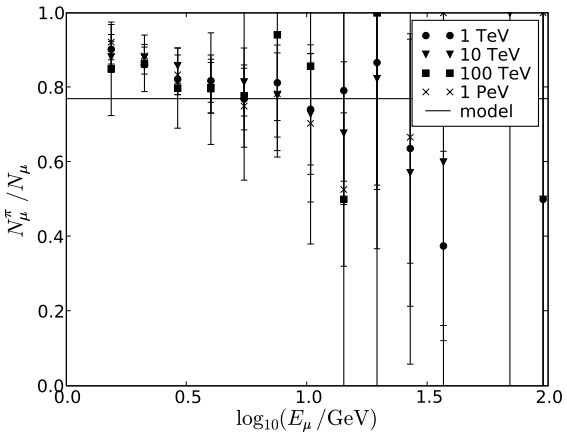

Fig. 4. Muon parent: the ratio of number of muons produced by pions N_μ^π over all number of muons N_μ for each muon energy E_μ is shown. A slight increase with energy of muons produced by other parent hadrons can be observed. However, the comparison to the model shows that the constant fraction is a reasonable approximation.

V. DISCUSSION AND CONCLUSION

We developed an analytical model describing the muon production in hadronic cascades, showing that it follows a power law with exponent $-(2+\kappa)$. The amplitude scales linear with the medium density ϱ and the primary energy E_o^κ. This is an effect of approximately $10\,\%$ in amplitude for changing from salt water to ice.

We compared this model to a full shower simulation with a modified CORSIKA version. The used setup forced us to correct for energy losses. To minimize the influence of the correction and because of the short track length of low energetic muons we focus on energies above $3\,\mathrm{G}e\mathrm{V}$.

We fitted a power law to the results (Fig 2 and Table II) and get the parameters with systematic errors due to the energy correction: $A = (3.5 \pm 0.5\,(\mathrm{stat}) - 2.0 + 6.5\,(\mathrm{sys})) \cdot 10^{-3}\,\mathrm{GeV}^{-1}$ and $\kappa = 0.97 \pm 0.07\,(\mathrm{stat}) \pm 0.12\,(\mathrm{sys})$. Around an energy of $E_\mu = 10\,\mathrm{G}e\mathrm{V}$ and a primary energy $E_0 = 10\,\mathrm{T}e\mathrm{V}$, the value most important to us, the analytical model predicts a flux a factor three higher than the flux from the simulation results.

This study could be checked with a newer modified CORSIKA version [11], which would provide direct results for ice and the possibility to compare different hadronic interaction models and increase the statistic.

The parameterization of muon production in hadronic cascades that we provide can be used to simulate more accurately neutrino induced cascades.

VI. ACKNOWLEDGEMENTS

We would like to thank Terry Sloan for providing us with his modified version of CORSIKA. Sebastian Panknin and Marek Kowalski acknowledge the support of the Deutsche Forschungsgemeinschaft (DFG).

REFERENCES

[1] THE ICECUBE COLLABORATION: J. AHRENS *et al. IceCube Preliminary Design Document* http://www.icecube.wisc.edu/science/publications/pdd/pdd.pdf 2001

[2] G.V. DOMOGATSKII (for THE BAIKAL COLLABORATION), *Status of the BAIKAL neutrino project*, arXiv:astro-ph/0211571v2, 2002

[3] Y. BECHERINI (for THE ANTARES COLLABORATION) *Status report of the ANTARES experiment* J.Phys.Conf.Ser.39:444-446, 2006

[4] AMANDA COLLABORATION: M. ACKERMANN, *et al. Search for Neutrino-Induced Cascades with AMANDA* Astropart.Phys.22:127-138,2004

[5] D. HECK and T. PIEROG, *Extensive Air Shower Simulation with CORSIKA: A Users Guide* http://www-ik.fzk.de/corsika/usersguide/usersguide.pdf Version 6.9xx from April 3, 2009

[6] W. HEITLER, *The Quantum Theory of Radiation*, third edition. Oxford University Press, London 1954

[7] J. MATTHEWS, *A Heitler model of extensive air showers*, Astroparticle Physics 22 (2005), 387-397

[8] T. K. GAISSER, *Cosmic Rays and Particle Physics*, Cambridge, 1990

[9] S. BEVAN *et al.* ., *Astroparticle Physics*, 28, 366, 2007

[10] PARTICLE DATA GROUP, *Particle Physics Booklet*, Berkeley, 2006

[11] J. BOLMONT, *CORSIKA-IW: a Modifed Version of CORSIKA for Cascade Simulations in Ice or Water*, http://nuastro-zeuthen.desy.de/e27/e711/e745/infoboxContent746/corsika-iw_julien_0812.pdf, 2008

Muon bundle energy loss in deep underground detector

Xinhua Bai*, Dmitry Chirkin†, Thomas Gaisser*, Todor Stanev* and David Seckel*

*Bartol research Inst., Dept. of Physics and Astronomy, University of Delaware, Newark, DE 19716, U.S.A.
†Dept. of Physics, University of Wisconsin, Madison, WI 53706, USA

***Abstract*. High energy air showers contain bundles of muons that can penetrate deep underground. Study of these high energy muons can reveal the cosmic ray primary composition and some features of the hadronic interactions. In an underground neutrino experiment like IceCube, high energy muons are also of interest because they are the dominant part of the neutrino background. We study muon bundle energy loss in deep ice by full Monte Carlo simulation to define its fluctuations and relation to the cosmic ray primary nuclei. An analytical formula of muon bundle mean energy loss is compared with the Monte Carlo result. We also use the simulation to set the background for muons with catastrophic energy loss much higher than those of normal muon bundles.**

***Keywords*: cosmic ray, muon bundle, energy loss.**

I. Introduction

When high energy cosmic ray particles interact in the atmosphere and develop extensive air showers (EAS), muons are produced through the decay of mesons, such as pions and kaons. IceCube is primarily a high energy neutrino telescope but it can also study high energy muon bundles which, together with the EAS size determined by the surface array IceTop [1], will contribute to studies of the cosmic ray composition and hadronic interactions.

A proton shower contains one muon above 500 GeV when the primary energy is about 100 TeV. Muons with that energy can reach the underground detector. At higher energies more high energy muons are produced in bundles. The muons above a several hundred GeV in the bundle are highly collimated and closer to each other in space [2], [3] than the distance between IceCube strings. This makes it very hard to count the number of individual muons in the bundle.

In this work we study the energy loss of muon bundles produced by proton and iron showers at different primary energies by carrying out a Monte Carlo simulation. An analytical formula of muon bundle mean energy loss is compared with the Monte Carlo result in Section II. We discuss the fluctuations in the energy loss and their association with cosmic ray primary particles in Section III. With the energy loss limits set by the simulation, we also discuss in Section IV the search for muons above 100 TeV.

We first calculated proton and iron showers with CORSIKA (version 6.735, with SIBYLL 2.1 as high energy hadronic interaction model). This version of CORSIKA does not include charm production. All the muons produced are from pion or kaon decay. Two hundred showers were generated for eight energy points from 1 PeV to 1 EeV for proton and iron primaries. The production was set for the South Pole location (2835 meters above sea level). The atmospheric parametrization for July 01, 1997 was chosen. All muons above 200 GeV in each shower were extracted from the shower ground particle file. Each of these muons was then propagated through the ice to the depth of 2450 meters using the Muon Monte Carlo (MMC) simulation package [4]. All processes in which a muon loses more than 10^{-3} of its energy are treated stochastically. Energy losses due to ionization, bremsstrahlung, photo-nuclear interaction, pair production and their continuous components were kept for each of the five-meter step size along the muon track.

II. High energy muons in air showers: Elbert formula and CORSIKA showers

The number of high energy muons in an EAS depends on the energy and mass of the primary cosmic ray particle. A well-known parametrization was given by Elbert [5] as follows:

$$\begin{aligned} &N_{\mu,B}(E_\mu > E_\mu(0)) \\ &= A\frac{0.0145TeV}{E_\mu(0)cos\theta}(\frac{E_0}{AE_\mu(0)})^{p_1}\cdot(1-\frac{AE_\mu(0)}{E_0})^{p_2} \\ &\simeq \frac{0.0145TeV}{cos\theta}\frac{E_0^{p_1}}{A^{p_1-1}}E_\mu(0)^{-p_1-1}(1-p_2\frac{A}{E_0}E_\mu(0)) \end{aligned} \quad (1)$$

in which A, E_0 and θ are the mass, total energy and zenith angle of the primary nucleus. $p_1 = 0.757$ and $p_2 = 5.25$. The approximation only keeps the first two terms in the Taylor's expansion on $(1-\frac{A}{E_0}E_\mu(0))^{p_2}$. It will be used later in this paper to derive the mean energy loss of muon bundles in matter.

Both Elbert parametrization and the approximation were compared with air shower Monte Carlo results for protons and irons from several hundred TeV up to 1 EeV. Two examples are shown in Fig. 1. Except in the threshold region (where the Elbert parametrization may not be valid) the agreement over the whole energy region is remarkable. This is shown by the two peaks at zero in the two plots at the bottom in Fig. 1. One can also see that CORSIKA with SIBYLL 2.1 has slightly higher yield at higher muon energies. The excess increases with the energy of the primary particle.

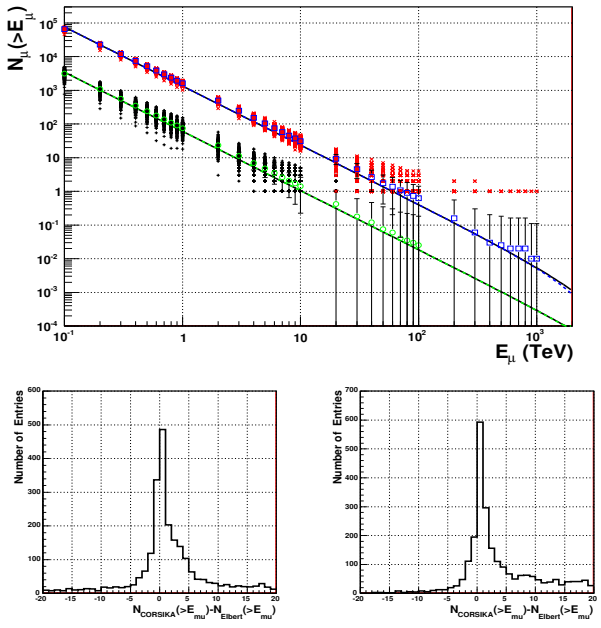

Fig. 1. Number of muons in the bundles as a function of the muon energy. Top entry: 50 PeV proton at 30 degree zenith (lower black $+$) and 1 EeV iron at zero degree zenith (higher red $\times$). The open squares and circles are the averages over all 200 showers at each energy points. The curves represent Elbert formula. Dashed lines are the approximation to the Elbert formula, which correspond to the last line in Eq. (1). Bottom entries: The difference between the number of muons (for $E_\mu \geq 100$ GeV and a increment step size of 100 GeV) in CORSIKA showers and that predicted by the Elbert formula. (left: 50 PeV proton, right: 1 EeV iron)

III. MUON BUNDLE ENERGY LOSS AND COMPOSITION SENSITIVITY

A. *Muon bundle energy loss in ice*

Since IceCube measures the energy loss instead of the number of muons in the bundle, we derive an analytical expression for the muon bundle mean energy loss to understand better the bundle energy loss. Starting from the approximation in Eq. (1) with muon energy loss

$$\frac{dE_\mu(X)}{dX} \approx -a - b \cdot E_\mu(X), \tag{2}$$

the energy loss of a muon bundle at the slant depth X is an integral over the energy loss of the muons in the bundle:

$$\begin{aligned}\frac{dE_{\mu,B}(X)}{dX} &= \int_{E_\mu^{min}(X)}^{E_\mu^{max}(X)} \frac{dE_\mu(X)}{dX}\frac{dN_{\mu,B}(X)}{dE_\mu(X)}dE_\mu(X) \\ &= -\int_{E_\mu^{min}(X)}^{E_\mu^{max}(X)} [a + b \cdot E_\mu(X)] \cdot \frac{dN_{\mu,B}(X)}{dE_\mu(X)}dE_\mu(X).\end{aligned} \tag{3}$$

Here, $E_\mu^{min}(X)$ and $E_\mu^{max}(X)$ represent the possible minimum and maximum energy of muons in the bundle at slant depth X. They can be written as follow [6]:

$$\begin{aligned}E_\mu^{min}(X) &= max\{[(E_\mu(0) + \tfrac{a}{b})e^{-bX} - \tfrac{a}{b}]^{min}, 0\} \\ &= 0 \\ E_\mu^{max}(X) &= (E_\mu^{max}(0) + \tfrac{a}{b})e^{-bX} - \tfrac{a}{b} \\ &= (\tfrac{E_0}{A} + \tfrac{a}{b})e^{-bX} - \tfrac{a}{b}.\end{aligned} \tag{4}$$

The approximate mean energy loss of a muon bundle can be obtained by doing the integration [6]. The expression can be further simplified by assuming that the high energy corrections can be ignored:

$$\begin{aligned}\frac{dE_{\mu,B}(X)}{dX} &= \omega \cdot b \cdot (p_1+1)\tfrac{1}{V+1}[\tfrac{1}{p_1+1}(\tfrac{a}{b})^{-p_1} \\ &\cdot V^{-p_1-1} + \tfrac{1}{p_1}(\tfrac{a}{b})^{-p_1}V^{-p_1} - \tfrac{1}{p_1+1}(\tfrac{a}{b}) \\ &\cdot(\tfrac{E_0}{A})^{-p_1-1} - \tfrac{1}{p_1}(\tfrac{E_0}{A})^{-p_1}]\end{aligned} \tag{5}$$

in which $\omega = \frac{0.0145TeV}{cos\theta}\frac{E_0^{p_1}}{A^{p_1-1}}$ and $V = (e^{bX} - 1)$. For the ice at the South Pole, $a = 0.26\ GeV\,mwe^{-1}$ and $b = 3.60 \cdot 10^{-4}\,mwe^{-1}$ [4] in units of meter water equivalent mwe. X is the slant depth in mwe along the muon bundle track.

The comparison with the full Monte Carlo can be seen in Fig. 2. Despite the large fluctuations in the energy loss mainly due to bremsstrahlung the mean energy loss in the full Monte Carlo (the blue and green dots) can be well described by the analytic approximation of Eq. (5). It needs to be pointed out, however, that for low energy showers, or for the energy loss at larger slant depth, Eq. (5) can have larger offset from the mean Monte Carlo values. This is due to the fact that the Elbert formula (Eq. (1)) is not exact at high E_μ values or a and b can be different from the constant values being used here.

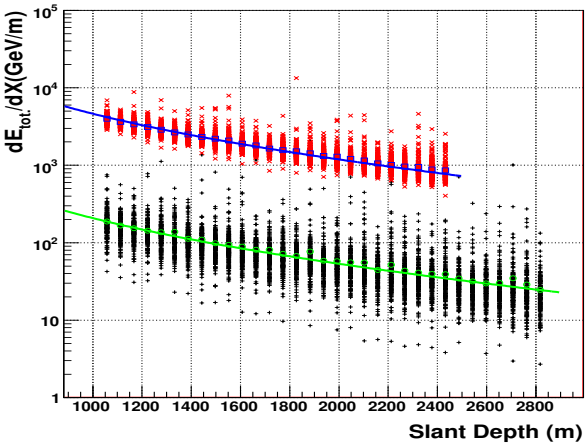

Fig. 2. Muon bundle energy loss as function as slant depth. Two examples are given in the figure: red $\times$ for vertical 1 EeV iron showers and the black $+$ for 30 degree 50 PeV proton showers. Open squares and circles are the mean value of the Monte Carlo results for iron and proton showers. Eq. (5) is represented by the two curves.

B. *Muon bundle energy loss and composition*

To study the muon bundle energy loss and composition sensitivity, in the two component case of this work,

we first define the composition resolving parameters $(A|Y)$ and $(B|Y)$ based on an observable Y as follows:

$$(A|Y) = \frac{\sum_{i=1} N_i^A/(N_i^A + N_i^B)}{\sum_{i=1} P_i^A} \quad (6)$$

$$(B|Y) = \frac{\sum_{i=1} N_i^B/(N_i^A + N_i^B)}{\sum_{i=1} P_i^B} \quad (7)$$

in which $P_i^A = 1.0$ (or $= 0.0$) when $N_i^A \neq 0.0$ (or $= 0.0$), and N_i^A and N_i^B represent the number of proton and iron events in the i^{th} bin on dN/dY distribution as shown in Fig. 3. $(A|Y)$ and $(B|Y)$ have values between 0 and 1. When the two distributions are well separated from each other, both $(A|Y)$ and $(B|Y)$ are equal to 1. When the two distributions are identical and fully overlapped, $(A|Y) = (B|Y) = 0.5$, which means the chance to assign a particle as proton or iron is 50%.

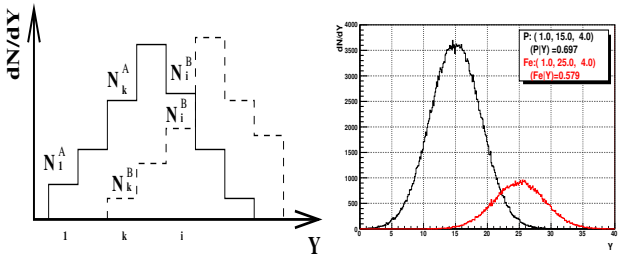

Fig. 3. Left: Definition of composition resolving parameters used in this work, $(A|Y)$ and $(B|Y)$: Two histograms represent the distribution of variable Y (e.g. muon bundle energy loss in deep ice detector) for two types of primary particles (say proton and iron). Right: Particles A and B are represented by two Gaussian shaped distributions with the amplitude, mean and σ in the parentheses. Particle A and B each has 320000 and 80000 samples in this test.

The value of the parameter also depends on the frequency of the detectable signals of different particles. This can be seen in Fig. 3 (right-hand panel), in which $(A|Y) = 0.697$ and $(B|Y) = 0.579$. This definition can be easily extended to cases in which each event has multiple observable variables.

IceCube is sensitive to the Cherenkov light emitted by high energy charged particles. Simulation shows the Cherenkov light yield of an in-ice event is nearly proportional to the particle total energy loss [7]. Since we are not doing the full experiment simulation, we use the total energy loss of muon bundles in small bins along the bundle track as a measure of the signal size. The distributions of muon bundle energy loss in five-meter steps at the slant depths between 1958 m and 2010 m in the ice are shown in Fig. 4. Proton energy loss distribution has a significant overlap with iron, much bigger than the overlap in the muon number distributions.

To improve the separation between the energy loss signals from different nuclei we excluded the large energy loss events caused mostly by bremsstrahlung. The effect from eliminating all energy loss events larger than 85% of the average (cut_1, red) and 500% (cut_2, blue) is shown in the bottom panel of Fig. 4.

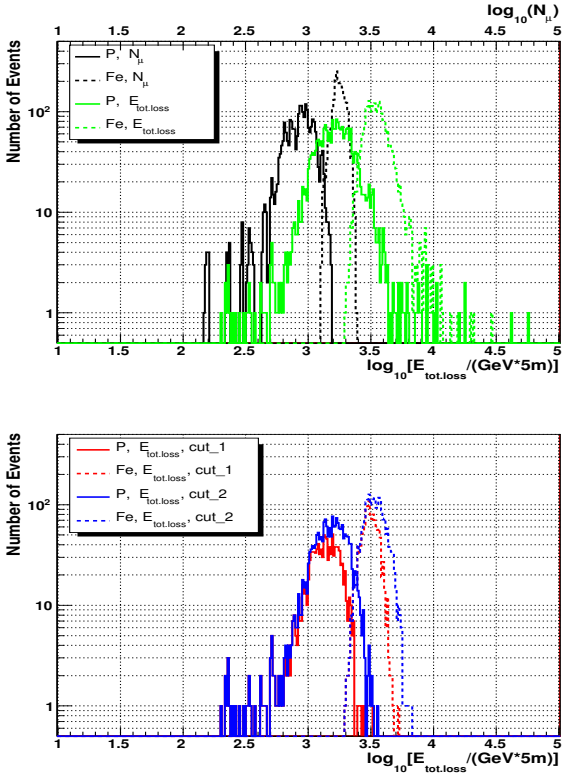

Fig. 4. Top: Histograms of the number of muons and the muon bundle total energy loss in five-meter steps at depths between 1958 m and 2010 m in ice. The example is for 600 PeV proton and iron showers at zenith angle of 30 degrees. Bottom: Histograms of the muon bundle total energy loss for the same Monte Carlo data sample after two cuts were applied. See more details in the text.

Fig. 5 summarizes how the composition resolving parameter varies at different slant depth after these two cuts in proton and iron showers. Several features can be seen in this figure, (1) the tighter cut (cut_1) gives a higher value of resolving parameter corresponding to less overlap between the two histograms shown at the bottom plot of Fig. 4, (2) when tighter cut is applied, the composition resolving power using the muon bundle energy loss can be close to that obtained by the number of muons in the bundle in the simulation, (3) using the same cut, the composition resolving power is slightly better at shallower depth. It would be very interesting to explore these features in real data analysis.

IV. Signature of High Energy Prompt Muons in Muon Bundle Events

Very high-energy muons in air showers are produced either in the decay of very short-lived particles, i.e. charm or from the first interaction whether the parent is conventional (pion or kaon) or charm. The crossing from conventional to prompt muon fluxes was estimated to happen between 40 TeV and 3 PeV [8]. Such muons may be used to study the composition of cosmic ray primaries, as well as heavy quark production in high energy p-N interactions. There are several ways to separate the prompt muons from the conventional ones in

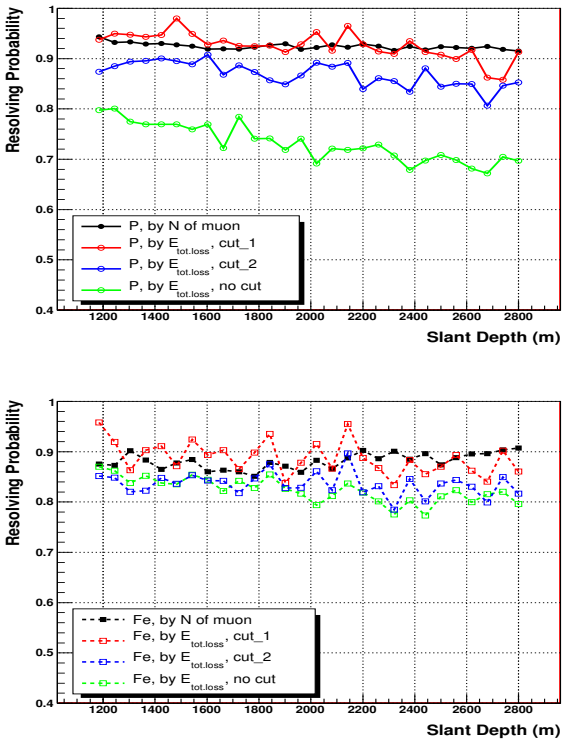

Fig. 5. The values of composition resolving parameters for proton and iron under different cuts at different slant depths. The calculation was done with 200 proton showers and 200 iron showers with 600 PeV primary energy at zenith angle of 30 degrees. The two cuts correspond to the cuts used in Fig. 4

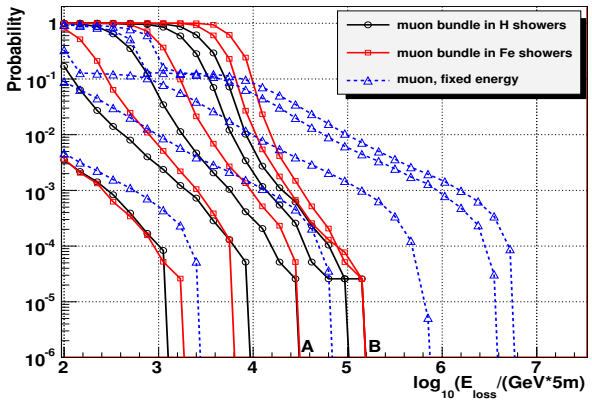

Fig. 6. The probability of the energy loss (in a five-meter step) of muon bundles in air showers (solid lines) and muons with fixed energy (dashed lines). Vertical proton and iron showers with primary energy of 500 TeV, 10 PeV, 100 PeV, 600 PeV and 1EeV are plotted together with vertical muons with fixed energy of 5 TeV, 100 TeV, 1 PeV, 6 PeV, and 10 PeV on the surface. The probability increases at larger energy loss as the energy of primary or single muon goes higher. The energy loss sample for the probability calculation is taken from the depth of 1450. m to the bottom of the in-ice array.

underground experiments, such as using the difference in their zenith angle distributions, the different depth dependence at a given depth and zenith angle [9]. Another technique that is explored here relies on recognizing catastrophic dE/dX signature from these leading muons as bursts of light on an otherwise smoother light deposition from a bundle of lower energy muons.

The probability of finding a certain amount of energy loss in five-meter steps from 1450 to 2450 meters under ice is shown in Fig. 6. The chance to have an energy loss of about 30 TeV (point A in Fig. 6) in a five-meter step is much higher for a muon with energy of 100 TeV than conventional muon bundles from showers below 100 PeV. If one sees a burst energy loss above 160 TeV, it is almost certain ($P > 1\times10^{-3}$ versus $P < 3\times10^{-5}$) that the event consists of a single muon with energy above 1 PeV rather than showers below 1 EeV (point B in Fig. 6).

Since the cosmic ray primary energy can be determined by the surface array in IceCube, this method can be explored further with IceTop and in-ice coincidence data.

V. Summary

In this work, we studied the muon bundle energy loss in ice and its association with cosmic ray primary composition. The analytic formula of the mean muon bundle energy loss given here has reasonably good agreement with the full Monte Carlo. It can be used in muon bundle event reconstruction in IceCube. The parameters (cosmic primary energy and mass) in the formula can be further explored in composition study using IceTop and in-ice coincidence data [10]. Using IceTop in-ice coincidence data, one can also look for signatures from very high energy muons from charm decay by recognizing large catastrophic dE/dX along the muon bundle track.

Acknowledgment This work is supported in part by the NSF Office of Polar Programs and by NSF grant ANT-0602679.

References

[1] T.K. Gaisser for the IceCube Collaboration, Proc. 30th ICRC, Merida (Mexico, 2007), arXiv:0711.0353, p. 15-18.
[2] T. Gaisser, *Cosmic Rays and Particles Physics*, p.208 (Cambridge University Press, 1990).
[3] X. Bai, et al. Proc. 30th ICRC, Merida, Mexico, Vol.5, p.1209-1212, 2007.
[4] D. Chirkin, W. Rhode, "Propagating leptons through matter with Muon Monte Carlo (MMC)", arXiv:hep-ph/0407075v2, 2008.
[5] J.W. Elbert, In Proc. DUMAND Summer Workshop (ed. A. Roberts), 1978, vol. 2, p. 101.
[6] X. Bai, "Energy loss of muon bundles: An analytic approximation", IceTop internal technical report. 2007.
[7] Christopher Henrik V. Wiebusch, Ph.D. thesis, Physicalische Institute, RWTH Aachen, 1995.
[8] Graciela Gelmini, Paolo Gondolo, and Gabriele Varieschi, arXiv:hep-ph/0209111v1.
[9] E. V. Bugaev et al., Phys. Rev. D58(1998)054001
[10] See for example the work by Tom Feusels, Jonathan Eisch and Chen Xu, *Reconstruction of IceCube coincident events and study of composition-sensitive observables using both the surface and deep detector.* These proceedings. More work on data is still needed.

Constraints on Neutrino Interactions at energies beyond 100 PeV with Neutrino Telescopes

Shigeru Yoshida*

*Department of Physics, Faculty of Science, Chiba University, Chiba 263-8522, Japan

Abstract. **A search for extremely high energy cosmic neutrinos has been carried out with the IceCube Neutrino Observatory. These event are neutrino-induced energetic charged leptons and their rate depends on the neutrino-nucleon cross-sections. The resultant event rate has implications for possible new physics beyond the standard model as it is predicted that the cross-sections can be much higher than the standard particle physics prediction if we live in more than four space-time dimensions. In this study we show the capability of neutrino telescopes such as IceCube to constrain neutrino cross-sections at energies beyond 10^7 GeV. The constraints are obtained as a function of the extraterrestrial neutrino flux in the relevant energy range, which accounts for the astrophysical uncertainty of neutrino production models.**

Keywords**: Neutrino, IceCube, cross-sections**

I. INTRODUCTION

High energy cosmic neutrino observations provide a rare opportunity to explore the neutrino-nucleon (νN) interaction behavior beyond energies accessible by the present accelerators. These neutrinos interact druing their propagation in the earth and produce energetic muons and taus. These secondary leptons reach underground neutrino detectors and leave the detectable signals. The detection rate is, therefore, sensitive to neutrino-nucleon interaction probability. The center-of-mass energy of the collision, $\sqrt{s}$, is well above ~ 10 TeV for cosmic neutrino energies on the order of 1 EeV ($= 10^9$ GeV), a representative energy range for the bulk of the GZK cosmogenic neutrinos, generated by the interactions between the highest energy cosmic ray nucleons and the cosmic microwave background photons [1].

The νN collision cross-sections can be varied largely if non-standard particle physics beyond the Standard Model (SM) are considered in the high energy regime of $\sqrt{s} \gg$ TeV. The extra-dimension scenarios, for example, have predicted such effects [2]. The cross-sections of black hole productions via νN collisions can be larger than the SM prediction by more than two orders of magnitude [3]. The effect would be sizable enough to affect the expected annual event rate ($O(0.1-1)$) of the GZK neutrinos by $\sim$ km^3 instrumentation volume of the underground neutrino telescope such as the IceCube observatory, thereby the search for the extremely-high energy (EHE) cosmic neutrinos leads to constraints on the non-standard particle physics.

The IceCube neutrino observatory has already begun EHE neutrino hunting with the partially deployed underground optical sensor array. The 2007 partial IceCube detector realized a ~ 0.5 km^2 effective area for muons with 10^9 GeV and recently placed a limit on the flux of EHE neutrinos at the level approximately an order of magnitude higher than the expected GZK cosmogenic neutrino intensities for 242 days of observation [4]. Since new particle physics may vary the cross section by more than an order of magnitude as we noted above, this result should already imply a meaningful bound on the νN cross-sections. In this paper, we study the constraint on the νN cross-sections ($\sigma_{\nu\mathrm{N}}$) by the null detection of EHE neutrinos with the 2007 IceCube observation. A model-independent bound is derived by estimating the lepton intensity at the IceCube depth with the SM cross-sections scaled by a constant. The constraint is displayed in form of the excluded region on the plane of the cosmic neutrino flux and $\sigma_{\nu\mathrm{N}}$. It is equivalent to upper-bound of $\sigma_{\nu\mathrm{N}}$ for a given flux of astrophysical EHE neutrinos.

II. THE METHOD

The neutrino and charged lepton fluxes at the IceCube depth originated in a given neutrino flux at are calculated by the coupled transportation equations:

$$\begin{aligned}
\frac{dJ_\nu}{dX} &= -N_A\sigma_{\nu N,CC+NC}J_\nu + \frac{m_l}{c\rho\tau_l^d}\int dE_l \frac{1}{E_l}\frac{dn_l^d}{dE_\nu}J_l(E_l) \\
&\quad + N_A\int dE_\nu^{'}\ \frac{d\sigma_{\nu N,NC}}{dE_\nu}J_\nu(E_\nu^{'}) \\
&\quad + N_A\int dE_l^{'}\ \frac{d\sigma_{lN,CC}}{dE_\nu}J_l(E_l^{'}) \qquad (1) \\
\frac{dJ_l}{dX} &= -N_A\sigma_{lN}J_l - \frac{m_l}{c\rho\tau_l^d E_l}J_l \\
&\quad + N_A\int dE_\nu^{'}\frac{d\sigma_{\nu N,CC}}{dE_l}\ J_\nu(E_\nu^{'}) \\
&\quad + N_A\int dE_l^{'}\frac{d\sigma_{lN}}{dE_l}J_l(E_l^{'}) \\
&\quad + \frac{m_l}{c\rho\tau_l^d}\int dE_l^{'}\ \frac{1}{E_l^{'}}\frac{dn_l^d}{dE_l}J_l(E_l^{'}), \qquad (2)
\end{aligned}$$

where $J_l = dN_l/dE_l$ and $J_\nu = dN_\nu/dE_\nu$ are differential fluxes of charged leptons and neutrinos, respectively. X is the column depth, N_A is the Avogadro's number, ρ is the local density of the medium (rock/ice) in the propagation path, σ is the relevant interaction cross-sections, dn_l^d/dE is the energy distribution of the decay products which is derived from the decay rate per unit energy, c is the speed of light, m_l and τ_l^d are the mass

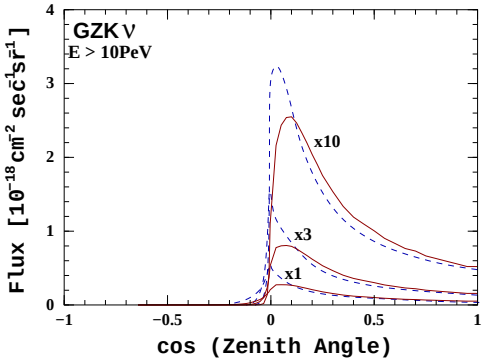

Fig. 1. Integral fluxes of the muon and taus above 10 PeV ($= 10^7$ GeV) at IceCube depth ($\sim$ 1450m) of the GZK cosmogenic neutrinos [5]. The solid lines represent the muons while the dashed lines represent the taus. Numbers along each of the curves are the multiplication factors ($\mathrm{N_{scale}}$) that enhance the standard νN cross-sections [6] in the relevant calculations.

and the decay life time of the lepton l, respectively. In this paper we scale $\sigma_{\nu\mathrm{N}}$ to that of the SM prediction with the factor $\mathrm{N_{scale}}$, *i.e.*, $\sigma_{\nu\mathrm{N}} \equiv \mathrm{N_{scale}}\sigma^{\mathrm{SM}}_{\nu\mathrm{N}}$. It is an extremely intensive computational task to resolve the coupled questions above for every possible values of $\sigma_{\nu\mathrm{N}}$. To avoid this difficulty, we introduce two assumptions to decouple calculation of J_ν from the charged lepton transportation equation. The first is that distortion of the neutrino spectrum by the neutral current reaction is small and the other is that the contribution of muon and tau decay to enhance the neutrino flux, which is represented by the second term on the right hand side of Eq. 1, is negligible. These are very good approximation in the energy region above 10^8 GeV where even the tau is unlikely to decay before reaching the IceCube instrumentation volume. Then the neutrino flux is simply given by the beam dumping factor as

$$J_\nu(\mathrm{E_\nu}, \mathrm{X_{IC}}) = J_\nu(\mathrm{E_\nu}, 0) e^{-N_{\mathrm{scale}}\sigma^{SM,CC}_{\nu\mathrm{N}}\mathrm{X_{IC}}}, \qquad (3)$$

where $\mathrm{X_{IC}}$ is column density of the propagation path from the earth surface to the IceCube depth. The charged lepton fluxes, $J_{l=\mu,\tau}(\mathrm{E_l}, \mathrm{X_{IC}})$, are obtained as

$$J_{\mu,\tau}(\mathrm{E}_{\mu,\tau}, \mathrm{X_{IC}}) = N_A \int_0^{\mathrm{X_{IC}}} dX \int dE'_{\mu,\tau} \frac{dN_{\mu,\tau}}{dE_{\mu,\tau}} (\mathrm{E}'_{\mu,\tau} \to \mathrm{E}_{\mu,\tau})$$

$$\int d\mathrm{E_\nu} \mathrm{N_{scale}} \frac{d\sigma^{SM,CC}_{\nu N}}{dE'_{\mu,\tau}} J_\nu(\mathrm{E_\nu}, 0) e^{-N_{\mathrm{scale}}\sigma^{SM,CC}_{\nu\mathrm{N}}\mathrm{X}}. \qquad (4)$$

Here $dN_{\mu,\tau}/dE_{\mu,\tau}(\mathrm{E}'_{\mu,\tau} \to \mathrm{E}_{\mu,\tau})$ represents distributions of muons and taus with energy of $\mathrm{E}_{\mu,\tau}$ at $\mathrm{X_{IC}}$ originated in those with energy of $\mathrm{E}'_{\mu,\tau}$ produced by νN collisions at depth X. This is calculated in the transportation equation, Eq. 2, with a replacement of $J_\nu(E'_\nu)$ by Eq. 3.

Calculation of the neutrino and the charged lepton fluxes with this method is feasible for a wide range of $\mathrm{N_{scale}}$ without any intensive computation. A comparison of the calculated fluxes with those obtained without the introduced simplification for a limited range of $\mathrm{N_{scale}}$ indicates that the relative difference we found in the resultant $J_{\nu,\mu,\tau}(X_{IC})$ is within 40%. Since this analysis is searching for at least an *order* of magnitude difference in $\sigma_{\nu\mathrm{N}}$, the introdced simplifications provide sufficient accuracy for the present study.

Fig. 1 shows the calculated intensities of the secondary muons and taus for various $\mathrm{N_{scale}}$ factors. One can see that the intensity is almost proportional to $\mathrm{N_{scale}}$ as expected since the interaction probability to generate muons and taus linearly depends on $\sigma_{\nu\mathrm{N}}$. It should be pointed out, however, that the dependence starts to deviate from the complete linearity when the propagation distance is comparable to the mean free path of neutrinos, as one can find in the case of $\mathrm{N_{scale}} = 10$ in the figure. This is because the neutrino beam dumping factor in Eq. 3 becomes significant under this circumstances.

The flux yield of leptons, Y^l_ν ($l = \nu'\mathrm{s}$, μ, τ) from neutrinos with a monochromatic energy at earth surface, E^s_ν, is given by Eq. 4 with an insertion of $J_\nu(E_\nu, 0) = \delta(E_\nu - E^s_\nu)$. The resultant event rate per *neutrino energy decade* is then obtained by,

$$N_\nu(E^s_\nu) = \sum_{\nu=\nu_e,\nu_\mu,\nu_\tau} \frac{1}{3} \frac{dJ_{\nu_e+\nu_\mu+\nu_\tau}}{d\log E_\nu}(E^s_\nu) \int d\Omega$$

$$\sum_{l=\nu,\mu,\tau} \int dE_l A_l(E_l)\ Y^l_\nu(E^s_\nu, E_l, \mathrm{X_{IC}}(\Omega), \mathrm{N_{scale}}) \qquad (5)$$

where A_l is the effective area of the IceCube to detect the lepton l. Note that the differential limit of the neutrino flux is given by Eq. 5 for $\mathrm{N_{scale}} = 1$ with $N_\nu = \bar{\mu}_{90}$ which corresponds to the 90 % confidence level average upper limit. This calculation is valid when the cosmic neutrino flux J_ν and the cross section $\sigma_{\nu\mathrm{N}}$ do not rapidly change over a decade of neutrino energy around E^s_ν. Limiting $\sigma_{\nu\mathrm{N}}$ in the present analysis corresponds to an extraction of the relation between $\mathrm{N_{scale}}$ and the (unknown) cosmic neutrino flux $J_{\nu_e+\nu_\mu+\nu_\tau}$ yielding $N_\nu = \bar{\mu}_{90}$. The obtained constraints on $\sigma_{\nu\mathrm{N}}$ is represented as a function of $J_{\nu_e+\nu_\mu+\nu_\tau}$ for a given energy of E^s_ν. It consequently accounts for astrophysical uncertainties on the cosmic neutrino flux.

In scenarios with extra dimensions and strong gravity, Kaluza-Klein gravitons can change only the neutral current (NC) cross-sections because gravitons are electrically neutral. Any scenarios belonging to this category can be investigated by scaling only $\sigma^{NC}_{\nu\mathrm{N}}$ in the present analysis. The event rate calculation by Eq. 5 is then performed for $Y^l_\nu(\mathrm{N_{scale}} = 1)$ with effective area for ν's, A_ν, enhanced by $(\sigma^{SM,CC}_{\nu\mathrm{N}} + \mathrm{N_{scale}}\sigma^{SM,NC}_{\nu\mathrm{N}})/(\sigma^{SM,CC}_{\nu\mathrm{N}} + \sigma^{SM,NC}_{\nu\mathrm{N}})$ since the rate of detectable events via the NC reaction by IceCube is proportional to $\sigma^{NC}_{\nu\mathrm{N}}$. We also show the constraint in this case.

III. Results

In this analysis we use the IceCube observation results with 242 days data in 2007 to limit $\sigma_{\nu\mathrm{N}}$ using Eq. 5. No detection of signal candidates in the measurement has led to an upper limit of the neutrino flux at 6×10^{-7}

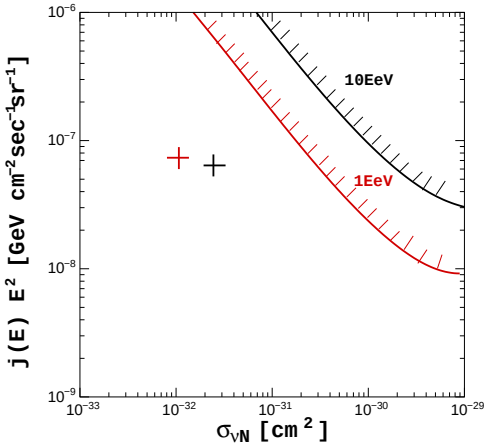

Fig. 2. Constraints on the all-flavor cosmic neutrino flux and the charged current νN cross-sections based on the null detection of neutrino signals by the IceCube 2007 observation. The right upper region is excluded by the present analysis. The cross points provide reference points where the standard cross section [6] and the expected GZK cosmogenic neutrino fluxes [7] is located.

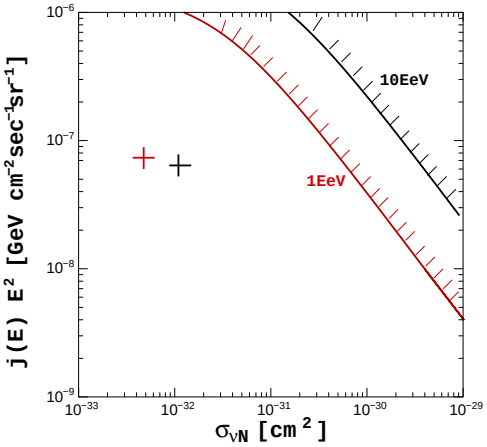

Fig. 3. Constraints on the all-flavor cosmic neutrino flux and the neutral current νN cross-sections for the scenario that only the neutral current reaction is enhanced by a new physics beyond the standard model. The right upper region is excluded by the present analysis. The crosses provide reference points for the standard cross section [6] and the expected GZK cosmogenic neutrino fluxes [7] is located.

GeV cm^{-2} sec^{-1} sr^{-1} [4]. The effective area A_l is 0.5 km^2 for μ, 0.3 km^2 for τ, and 3×10^{-4} km^2 for $\nu^{'}$s. Constraints on $\sigma_{\nu \mathrm{N}}$ are then derived with Eq. 5. Here we assume that the effective area for $\nu^{'}$s is proportional to $\mathrm{N_{scale}}$. The results for $E_\nu^s = 10^9$ and 10^{10} GeV are shown in Fig. 2. Enhancing the charged current cross-sections by more than a factor of 30 for $E_\nu = 1$ EeV (10^9 GeV) is disfavored if the astrophysical neutrino intensities are around $\sim 10^{-7}$ GeV cm^{-2} sec^{-1} sr^{-1}, the expected range of the GZK cosmogenic neutrino bulk. Note that neutrino-nucleon collision with $E_\nu = 1$ EeV corresponds to $\sqrt{s} \sim 40$ TeV and the present limit on $\sigma_{\nu \mathrm{N}}$ would place a rather strong constraint on scenarios with extra dimensions and strong gravity, although more accurate estimation requires studies with a model-dependent approach which implements the cross-sections and the final-state particles from the collision predicted by a given particle physics model in the neutrino propagation calculation. Taking into account uncertainty on the astrophysical neutrino fluxes, any model that increases the neutrino-nucleon cross-section to produce charged leptons by more than two orders of magnitude at $\sqrt{s} \sim 40$ TeV is disfavored by the IceCube observation. However, we should point out that the IceCube 2007 data could not constrain the charged current cross-sections if the intensity of cosmic neutrinos in the relevant energy region is fewer than $\sim 10^{-8}$ GeV cm^{-2} sec^{-1} sr^{-1}, approximately an order of magnitude lower than the predicted cosmogenic neutrino fluxes discussed in the literature. Absorption effects in the earth becomes sizable in this case, resulting in less sensitivity to the cross-section. This limitation will be improved for larger detection area of the full IceCube detector.

Fig. 3 shows the constraint when only the NC cross section is varied. Enhancement of $\sigma_{\nu \mathrm{N}}^{NC}$ by a factor beyond 100 at $\sqrt{s} \sim 40$ TeV is disfavored, but this strongly depends on the cosmic neutrino flux one assumes. Because the NC interaction does not absorb neutrinos during their propagation though the earth, even the case when the neutrino flux is small could bound the cross-section, but the limit becomes rather weak; the allowed maximum enhancement factor is an order of $\sim 10^3$.

IV. Summary and Outlook

The IceCube 2007 observation indicated that any scenario to enhance either the NC or both NC and CC equivalent cross-sections by more than 100 at $\sqrt{s} \sim 40$ TeV is unlikely if the astrophysical neutrino fluxes are $\sim 10^{-7}$ GeV cm^{-2} sec^{-1} sr^{-1} in EeV region. A study of constraints on the model-dependent cross-sections predicted by the theories of the black holes creation with extra dimensions is underway with a dedicated treatment of final state particles produced from the black hole evaporation.

Acknowledgments

This work was supported in part by the Grants-in-Aid in Scientific Research from the MEXT (Ministry of Education, Culture, Sports, Science, and Technology) in Japan.

References

[1] V. S. Beresinsky, G. T. Zatsepin, Phys. Lett. **28B**, 423 (1969).
[2] C. Tyler, A. V. Olinto, G. Sigl, Phys. Rev. **D63** 05501 (2001).
[3] J. Alvarez-Muñiz *et. al.*. Phys. Rev. **D65** 124015 (2002).
[4] K. Mase, A. Ishihara, S. Yoshida for the IceCube collaboration, *this proceedings*.
[5] S. Yoshida, H. Dai, C.C.H. Jui, P. Sommers, Astrophys. J. **479**, 547 (1997).
[6] R. Gandhi, C. Quigg, M. H. Reno, and I. Sarcevic, Astropart. Phys. **5**, 81 (1996); Phys. Rev. D **58** 093009 (1998).
[7] O. E. Kalashev *et.al.*, Phys. Rev. D **66**, 063004 (2002).

Constraints on Extragalactic Point Source Flux from Diffuse Neutrino Limits

Andrea Silvestri* **and Steven W. Barwick***

*Department of Physics and Astronomy, University of California, Irvine, CA 92697, USA.

***Abstract*. We constrain the maximum flux from extragalactic neutrino point sources by using diffuse neutrino flux limits. We show that the maximum flux from extragalactic point sources is $\mathrm{E}^2(\mathrm{dN}_\nu/\mathrm{dE}) \leq \mathbf{5.1 \times 10^{-9}}$ $(\mathbf{L}_\nu/\mathbf{10^{45}}\ \mathrm{erg/s})^{\mathbf{1/3}}\ \mathrm{GeV\ cm^{-2}\ s^{-1}}$ from an ensemble of sources with average neutrino luminosity per decade, $\mathbf{L}_\nu$. It depends only slightly on factors such as the inhomogeneous matter density distribution in the local universe, the luminosity distribution, and the assumed spectral index.**

***Keywords*: Extragalactic sources, diffuse and point sources, high energy neutrinos**

I. Introduction

The origin of ultra high energy cosmic rays (UHECR), is still unknown. AGN, GRB's, or processes beyond the standard model have been hypothesized to be the sources of UHECR's, and may originate from regions of the sky correlated with AGN sources [1]. Therefore, if nearby AGN are the sources of the highest energy CR's, and if AGN emit ν's in addition to photons, protons and other charged particles, then the fluxes from individual AGN may be observable by current generation of neutrino detectors. Several models predict a diffuse neutrino flux from AGN, in particular ν-production has been predicted from the core of radio-quite AGN as presented in [2], [3], and from AGN jets and radio lobes as suggested in [4], [5], [6]. There are good but speculative reasons to expect a correlation between sources of cosmic rays and sources of neutrinos. Direct searches for diffuse [7] and point flux [8] by current telescopes have set the most stringent upper limits, but generally have not reached the sensitivity required, and the models suggest that challenges exist even for next generation telescopes.

Of course, one of the primary motivations for the construction of ν-telescopes is to search for unexpected sources with no obvious connection to the power emitted in the electromagnetic (EM) band. However, we show in this paper that the ν-flux from EG point sources can be constrained by the measured diffuse ν-flux limits. We also test models from individual sources with the constraints.

II. Analysis

If the diffuse ν-flux is generated by an ensemble of extragalactic (EG) sources, then only the nearest of the diffusely distributed sources would be detectable as point sources. Point sources of neutrinos are observed when several neutrinos originate from the same direction, and in the context of this study, only the very nearest of the uniformly distributed sources are detectable as point sources. The number of detectable (or resolvable) point sources, N_s, first proposed in [9], is determined for a given diffuse ν-flux limit and point source sensitivity. The N_s calculation is based on three general assumptions: (1) the sources are extragalactic and uniformly distributed in space; (2) the ν-luminosity follows a power law or broken power law distribution; (3) the sources are assumed to emit neutrinos with an E^{-2} energy spectrum. Later, we discuss the robustness of the constraint by investigating the validity and caveats of the assumptions.

The number of resolvable sources N_s for a distribution of luminosities L_ν per decade in energy is given by:

$$N_s \simeq \frac{\sqrt{4\pi}}{3} \frac{1}{\sqrt{\ln\left(\frac{E_{max}}{E_{min}}\right)}} \frac{H_0}{c} \frac{K_\nu^{diff}}{(C_{point})^{3/2}} \frac{\langle L_\nu^{3/2}\rangle}{\langle L_\nu\rangle} \frac{1}{\xi} \quad (1)$$

where the parameter ξ depends on cosmology and source evolution as described in [9]. The ν-luminosity of the source, L_ν has units of (erg/s), and (E_{min}, E_{max}) defines the energy range of the flux sensitivity, where $E_{max} = 10^3 E_{min}$ for a typical experimental condition. For canonical energy spectrum proportional to E^{-2}, we use the results for all-flavor diffuse flux limits presented in [7] to obtain the ν_μ-diffuse flux: $K_\nu^{diff} \equiv \mathrm{E}^2\Phi_{\nu_\mu} = (1/3) * \mathrm{E}^2\Phi_{\nu_{all}} = (1/3) * 8.4 \times 10^{-8}$ GeV $\mathrm{cm^{-2}s^{-1}sr^{-1}} = 2.8 \times 10^{-8}$ GeV $\mathrm{cm^{-2}s^{-1}sr^{-1}}$ valid for the energy interval of 1.6 PeV $< \mathrm{E} <$ 6.3 EeV. This is the energy interval of interest for CR interaction with energies above the ankle. Below PeV energies K_ν^{diff} can be obtained from [10], $K_\nu^{diff} < 7.4 \times 10^{-8}$ GeV $\mathrm{cm^{-2}\ s^{-1}\ sr^{-1}}$, valid between 16 TeV to 2.5 PeV. So, similar diffuse flux limits, K_ν^{diff}, exist for the entire interval from TeV to EeV energies. C_{point} is the experimental sensitivity to ν-fluxes from point sources for an E^{-2} spectrum, and we used $C_{point} = \mathrm{E}^2(\mathrm{dN}_\nu/\mathrm{dE}) < 2.5 \times 10^{-8}$ GeV $\mathrm{cm^{-2}\ s^{-1}}$ [8].

The diffuse flux K_ν^{diff} and the point flux sensitivity C_{point} are linearly correlated by the following equation:

$$4\pi K_\nu^{diff} = \left[3 \left(\frac{c}{H_0}\right) \frac{1}{r_{max}}\ N_s\right] \times C_{point} \quad (2)$$

where (c/H_0) represents the Hubble distance given by $c/H_0 = 3 \times 10^5\ (\mathrm{km\ s^{-1}})/77\ (\mathrm{km\ s^{-1}\ Mpc^{-1}}) \sim 4$

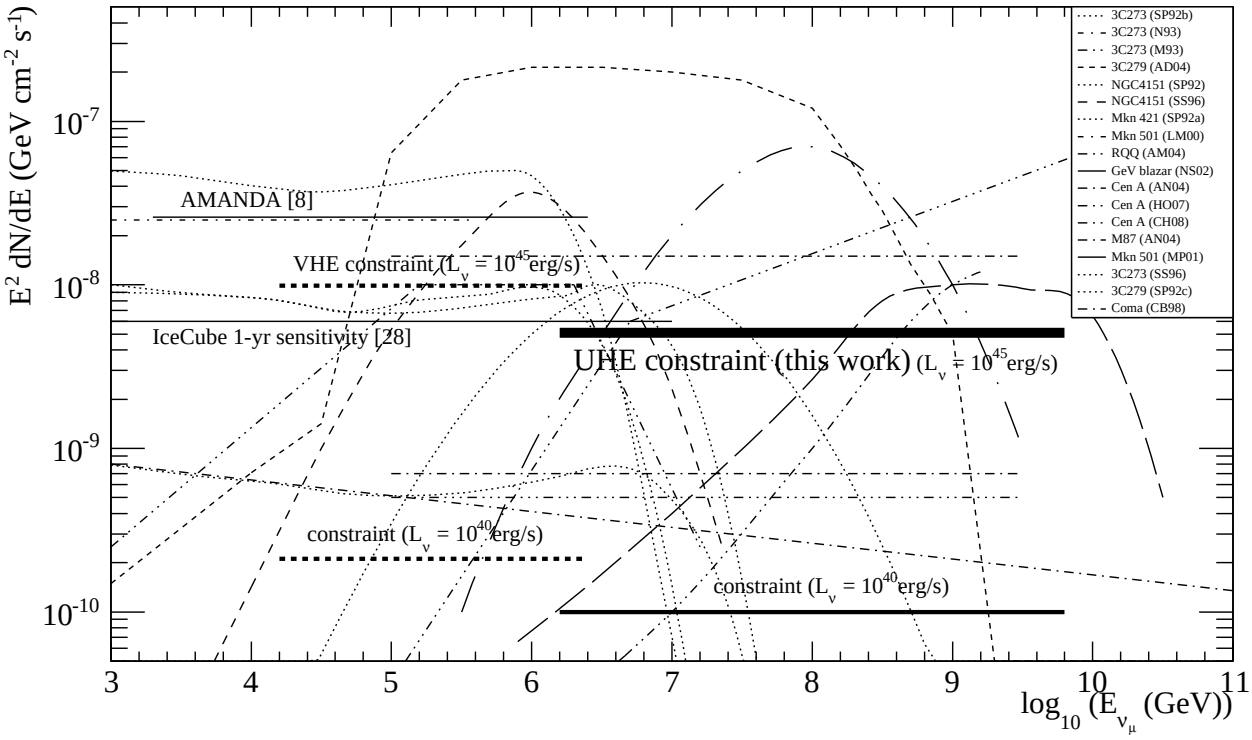

Fig. 1. Constraints on neutrino point fluxes derived from the UHE diffuse ν-flux limit [7], and from VHE limit [10], and assuming a range of neutrino luminosities $L_\nu = (10^{40} - 10^{45})$ erg/s. Current AMANDA limit [8] and IceCube sensitivity [28] to ν-point fluxes are also shown (thin solid lines). Model predictions for ν_μ-point flux from EG sources are displayed in thin dotted-dashed lines: emission from 3C273 predicted by [$3C273$ $(SP92)$] [13], core emission due to pp interactions [$3C273$ $(N93)$] [14], including pp and $p\gamma$ interactions [$3C273$ $(M93)$] [15]; core emission due to $p\gamma$ interaction [$3C273$ $(SS96)$] [24]; AGN jet, calculated for a 3C279 flare of 1 day period [$3C279$ $(AD04)$] [16] and continuous emission [$3C279$ $(SP92)$] [13]; emission from NGC4151 by [$NGC4151$ $(SP92)$] [13] and core emission from NGC4151 due to $p\gamma$ interaction [$NGC4151$ $(SS96)$] [2]; Spectra predicted for Mkn 421 [Mkn 421 $(SP92)$] [13], and for Mkn 501 during the outburst in 1997 [Mkn 501 $(LM00)$] [17] and blazar flaring Mkn 501 [Mkn 501 $(MP01)$] [23]; radio-quiet AGN [RQQ $(AM04)$] [18] and GeV-loud blazars [GeV $blazar$ $(NS02)$] [19]; emission from Cen A as described in [Cen A $(AN04)$] [20], [Cen A $(HO07)$] [21] and [Cen A $(CH08)$] [22]; emission from M87 [$M87$ $(AN04)$] [20], and emission from Coma galaxy cluster [$Coma$ $(CB98)$] [25].

Gpc, and r_{max} defines the maximum observable distance for a point source of luminosity L_ν, which is given by:

$$r_{max} = \left[\frac{L_\nu}{4\pi \, \ln(E_{max}/E_{min}) \, C_{point}} \right]^{1/2} \qquad (3)$$

The constraint also holds for time variable sources, since it depends only on the observed luminosity and is independent of the duration of the variability [11]. Similarly, it holds for beamed sources, such as GRB's. However for luminosities of the order of 10^{51} erg/s typical of GRB emission, we found that a dedicated search for GRB's leads to more restrictive limits [12].

III. Results

We can now estimate a numerical value for N_s by incorporating the ν-diffuse flux limit and the sensitivity to point sources in Eq. 1: $N_s \simeq (3.7 \cdot 10^{-29} \mathrm{cm}^{-1}) \times (K_\nu^{diff}) \times (C_{point})^{-3/2} \times (L_{45})^{1/2} \times 1/\xi \simeq 0.07$ computed assuming $L_{45} = 10^{45}$ erg/s, and $\xi = \xi_{AGN} \simeq 2.2$ which defines the effects due to cosmology and source evolution that follows AGN [9]. The estimate for $N_s \simeq 0.07$, which is compatible with the non-detection of any point sources.

The constraint on ν-flux is determined by setting $N_s = 1$ and inverting Eq. 1 to solve for C_{point}:

$$\mathrm{E}^2 \frac{\mathrm{dN}_\nu}{\mathrm{dE}} \leq \left[\frac{\sqrt{4\pi}}{3} \frac{1}{\sqrt{\ln\left(\frac{E_{max}}{E_{min}}\right)}} \frac{H_0}{c} \cdot K_\nu^{diff} \sqrt{L_\nu} \cdot \frac{1}{\xi} \right]^{2/3}$$

$$\mathrm{E}^2 \frac{\mathrm{dN}_\nu}{\mathrm{dE}} \leq 5.1 \times 10^{-9} \left(\frac{L_\nu}{10^{45} \ \mathrm{erg/s}} \right)^{1/3} \left(\frac{\mathrm{GeV}}{\mathrm{cm}^2 \ \mathrm{s}} \right) \qquad (4)$$

valid for the same energy range 1.6 PeV $<$ E $<$ 6.3 EeV of the diffuse flux limit K_ν^{diff}. This result defines a benchmark flux constraint $\Phi_C \equiv \mathrm{E}^2(\mathrm{dN}_\nu/\mathrm{dE}) \leq 5.1 \times 10^{-9}$ GeV cm^{-2} s^{-1} on neutrino fluxes from bright ($L_\nu = 10^{45}$ erg/s) extragalactic point sources, which is a factor five lower than present experimental limits from direct searches. Note from Eq. 2, that for the case of $N_s < 1$ the distance ratio $(c/H_0)/r_{max} > 1$, which occurs for sources well within the Hubble distance.

Fig. 1 shows these results represented by the constraint derived from the Ultra High Energy (UHE) diffuse ν-flux limit for energies above PeV (thick solid line), and from the Very High Energy (VHE) limit in the TeV-PeV range (thick dotted line). Model predictions for ν_μ-point flux from EG sources (dotted/dashed lines),

TABLE I
SUMMARY OF MODELS FOR ν_μ POINT FLUX FROM EXTRAGALACTIC SOURCES CONSTRAINED BY THE RESULTS FROM THIS WORK. MODELS ARE ORDERED ACCORDING TO THE TYPE OF THE NEUTRINO SOURCE. THE PARAMETER BAND$_\gamma$ REPRESENTS THE PHOTON ENERGY-BAND ASSUMED IN THE GIVEN MODEL. THE NEUTRINO FLUX PREDICTED BY A GIVEN MODEL FOR AN E^{-2} SPECTRUM IS DENOTED BY Φ_ν^{model} AND NEUTRINO FLUXES FOR MODELS WHICH ARE ALMOST CONSTANT TO AN E^{-2} SPECTRUM FOR A LARGE ENERGY RANGE. THE CORRESPONDING FLUX CONSTRAINED FOR AN E^{-2} SPECTRUM IS DEFINED BY THE BENCHMARK FLUX Φ_C. IF THE SOURCE IS COMMONLY REPLICATED IN THE UNIVERSE WITH OUR ASSUMPTIONS, THEN THE RATIO $R_{flux} = \Phi_C/\Phi_\nu^{model} < 1$ DETERMINES A MODEL CONSTRAINED BY THIS WORK.

Model	Band$_\gamma$	Φ_ν^{model} (GeV/cm^2 s)	R_{flux}	Reference
$[3C273\ (SP92)]$	IR/x-ray	1.0×10^{-8}	0.51	[13]
$[3C273\ (N93)]$	x-ray	2.5×10^{-8}	0.20	[14]
$[3C273\ (M93)]$	γ-ray/IR	1.0×10^{-8}	0.51	[15]
$[3C279\ (AD04)]$	GeV	2.0×10^{-7}	0.03	[16]
$[NGC4151\ (SP92)]$	IR/x-ray	3.5×10^{-8}	0.14	[13]
$[Mkn\ 421\ (SP92)]$	IR/x-ray	9.0×10^{-9}	0.10	[13]
$[Mkn\ 501\ (LM00)]$	TeV	2.5×10^{-8}	0.57	[17]
$[RQQ\ (AM04)]$	x-ray/UV	1.0×10^{-8}	0.51	[18]
$[Cen\ A\ (AN04)]$	TeV	1.5×10^{-8}	0.34	[20]
$[Cen\ A\ (CH08)]$	TeV	6.0×10^{-9}	0.85	[22]

have been tested by this analysis and are summarized in Tab. I.

Tab. I summarizes the results from the constraint Φ_C compared to a number of models of neutrino point fluxes from extragalactic sources. The fluxes Φ_ν^{model} predicted from these models can be directly compared to Φ_C since either follow an E^{-2} spectrum, or do cover a large energy range almost constant to an E^{-2} spectrum. These models are constrained since their predicted fluxes exceed the benchmark flux set by Φ_C. If the source is commonly replicated in the universe with the assumptions defined in Sec II, then the ratio $R_{flux} = \Phi_C/\Phi_\nu^{model} < 1$ determines a model constrained by this analysis.

Models have also been presented which predict ν-fluxes from nearby AGNs [20], [21], [22], such as Centaurus A (Cen A) and M87 at a distance of 3.4 Mpc and 16 Mpc, respectively. We note these predictions lie below the upper value of the constraint Φ_C, and are compatible with our results.

A few other models, as shown in Fig. 1, present flux predictions which strongly deviate from an E^{-2} spectrum and in this class of models a direct comparison with the benchmark flux Φ_C is less straightforward. In these cases, the predicted energy spectra should be integrated over the energy interval that defines the constraint to obtain the total neutrino event rate, N_ν^{model}. This result should be compared to the integrated neutrino event rate N_C determined by the constraint and by the given neutrino detector characteristics.

IV. DISCUSSION

The thick dark horizontal line in Fig. 1 indicates our primary constraint Φ_C. It was derived for a mean neutrino luminosity that characterizes the brightest AGN in the EM band. The constraint is even stronger for less luminous classes of sources. In this section we address the robustness of the constraint by focusing the discussion on the three assumptions listed in Sec. II.

A. Homogeneity of source distribution

The matter distribution within 50 Mpc of the Milky Way is far from uniform, which suggests the possibility that the number density of neutrino sources, n_s, may be higher than the universal average if n_s is correlated with matter density. We argue that, in practice, the local inhomogeneity affects only the class of sources characterised by low luminosities. The bright sources are too rare to be affected by local matter density variation - the likelihood of finding a bright neutrino source within 50 Mpc is small to begin with (if EM luminosity and neutrino luminosity are comparable), and the local enhancements in matter density insufficient to change the probability of detection.

On the other hand, low luminosity sources are more likely to be within 50 Mpc, and their density could be affected by fluctuations (e.g. by a factor of 15 [26] at 5 Mpc) in the local matter density. In this case, the flux constraint (Eq. 4) should be adjusted to account for the higher density of local matter, $\Phi' = \Phi * (n_{local}/\langle n_s \rangle)^{2/3}$ (Tab II). However, the adjusted fluxes are below the benchmark flux constraint Φ_C.

To exceed Φ_C a source of a given luminosity L_ν must be within a distance $d_l = (4\pi/3)^{1/3} \cdot r_{max} * (\Phi'/\Phi_C)^{1/2}$. However, we found no counterparts in the EM band within a distance d_l that would violate the constraint Φ_C.

TABLE II
ADJUSTED Φ' TO ACCOUNT FOR LOCAL n_s ENHANCEMENT.

L_ν erg/s	Φ GeV/^{2}s	$n_l/\langle n_s \rangle$ [26]	Φ' GeV/cm^{2}s	d_l Mpc
8×10^{41}	0.5×10^{-9}	15	2.8×10^{-9}	3.7
1×10^{43}	1.1×10^{-9}	5	3.1×10^{-9}	16
1×10^{44}	2.4×10^{-9}	2.5	4.3×10^{-9}	55

B. Distribution function of ν-luminosity

The number of detectable sources N_s depends on $\langle L_\nu^{3/2} \rangle / \langle L_\nu \rangle$, but the luminosity distribution for neutrino sources is not known. However, if the distribution

function follows a broken power law, which is measured for several class of energetic sources in various electromagnetic bands, then the estimate for N_s based on a full distribution agrees with an estimate using the mean luminosity of the distribution to within few percent, as shown in [11]. So, to an excellent approximation, the mean value of the luminosity distribution is sufficient to predict $N_s \sim \langle L_\nu \rangle^{1/2}$ for power law or broken power law distributions. The most common distribution of luminosities can only be observed at relatively small distances, so source evolution and cosmological effects are negligible. Larger values of luminosity are too rare to contribute significantly.

C. Energy spectrum of the source

The constraint can be extended to energy spectra that differ from the assumed E^{-2} dependence, but the constraint applies over a restricted energy interval that matches the energy interval of the diffuse neutrino limits. Experimental diffuse limits span two different energy regions, VHE and UHE, and either limit can be inserted into Eq. 4. The restriction in energy range is required to avoid extrapolating the energy spectrum to unphysical values. In other words, for power law indices far from 2, the spectrum must cut-off at high energies for indices $\gamma < 2$, or at low energies for indices $\gamma > 2$. Subject to this restriction, we find that the constraint depends weakly on the assumed spectral index. For example, the constraints improve by a factor 2 for hard spectra ($\gamma = 1$) and weaken by roughly the same factor for soft spectra ($\gamma = 3$) [11].

On the other hand, it could be argued that the energy spectrum dN_ν/dE is completely unknown. In this case, instead of relying on the power law of neutrino luminosity L_ν, one could derive the constraints by examining the measured number density n_s, ($n_s \propto 1/L_\nu$) for a given class of sources [27].

V. Conclusion

The constraint on neutrino fluxes from extragalactic point sources is $\mathrm{E}^2(\mathrm{dN}_\nu/\mathrm{dE}) \leq 5.1 \times 10^{-9}\ (L_\nu/10^{45}\ \mathrm{erg/s})^{1/3}\ \mathrm{GeV\ cm^{-2}\ s^{-1}}$, which is a factor 5 below current experimental limits from direct searches if the average L_ν distribution is comparable to the EM luminosity that characterizes the brightest AGN. We tested a number of model predictions for ν-point fluxes, and models which predict fluxes higher than the constraint have been restricted by this analysis. The constraint is strengthened for less luminous sources, and noncompetitive with direct searches for highly luminous explosive sources, such as GRB. We found that the constraint is robust when accounting for the non-uniform distribution of matter that surrounds our galaxy, or considering energy spectra that deviate from E^{-2}, or various models of cosmological evolution. The constraint suggests that the observation of EG neutrino sources will be a challenge for kilometer scale detectors unless the source is much closer than the characteristic distance between sources, d_l, after accounting for local enhancement of the matter density. Although the constraint cannot rule out the existence of a unique, nearby EG neutrino sources, we note that we found no counterparts in the EM band with the required luminosity and distance to violate the constraint, assuming $L_\nu \sim L_\gamma$.

VI. Acknowledgment

The authors acknowledge support from U.S. National Science Foundation-Physics Division, and the NSF-supported TeraGrid system at the San Diego Supercomputer Center (SDSC).

References

[1] J. Abraham et al., *Science* **318**, 938 (2007).
[2] F. Stecker et al., *Phys. Rev. Lett.* **66**, 2697 (1991); erratum *Phys. Rev. Lett.* **69**, 2738 (1992).
[3] F. Stecker, *Phys. Rev. D* **72**, 107301 (2005).
[4] K. Mannheim, *Astropart. Phys.* **3**, 295 (1995).
[5] F. Halzen and E. Zas, *Astrophys. J.* **488**, 669 (1997).
[6] R. J. Protheroe, *astro-ph/9607165* (1996).
[7] A. Silvestri et al., *Proc. 31th ICRC*, these Proceedings (2009).
[8] R. Abbasi et al., *Phys. Rev. D* **79**, 062001 (2009).
[9] P. Lipari, *Nucl. Instrum. Meth.* **A 567**, 405 (2006).
[10] A. Achterberg et al., *Phys. Rev. D* **76**, 042008 (2007).
[11] A. Silvestri, *Ph.D. Thesis*, University of California, Irvine (2008).
[12] A. Achterberg et al., *Astrophys. J.* **674**, 357 (2008).
[13] A. P. Szabo and R. J. Protheroe, in *High Energy Neutrino Astrophysics*, World Scientific (Singapore), 24 (1992).
[14] L. Nellen et al., *Phys. Rev. D* **47**, 5270 (1993).
[15] K. Mannheim, *Phys. Rev. D* **48**, 2408 (1993).
[16] A. Atoyan and C. Dermer, *New Astron. Rev.* **48**, 381 (2004).
[17] J. G. Learned, and K. Mannheim, *Annu. Rev. Nucl. Part. Sci.* **50**, 679 (2000).
[18] J. Alvarez-Muniz and P. Meszaros, *Phys. Rev. D* **70**, 123001 (2004).
[19] A. Neronov and D. Semikoz, *Phys. Rev. D* **66**, 123003 (2002).
[20] L. A. Anchordoqui et al., *Phys. Lett. B* **600**, 202 (2004).
[21] F. Halzen and A. O'Murchadha, *astro-ph/0802.0887* (2008).
[22] A. Cuoco and S. Hannestad, *Phys. Rev. D* **78**, 023007 (2008).
[23] A. Mücke and R. J. Protheroe, *Astropart. Phys.* **15**, 121 (2001).
[24] F. Stecker and M. H. Salamon, *Space Sci. Rev.* **75**, 341 (1996).
[25] S. Colafrancesco and P. Blasi, *Astropart. Phys.* **9**, 227 (1998).
[26] T. Jarrett, private communication.
[27] M. Kowalski, private communication.
[28] J. Ahrens et al., *Astropart. Phys.* **20**, 507 (2004).

Study of electromagnetic backgrounds in the 25-300 MHz frequency band at the South Pole

Jan Auffenberg*, Dave Besson†, Tom Gaisser‡, Klaus Helbing*, Timo Karg*, Albrecht Karle§, and Ilya Kravchenko¶

*Bergische Universität Wuppertal, Fachbereich C- Astroteilchenphysik, 42097 Wuppertal, Germany
†Dept. of Physics & Astronomy, University of Kansas, Lawrence, KS 66045, USA
‡Bartol Research Institute, University of Delaware, Newark, DE 19716, USA
§Dept. of Physics, University of Wisconsin, Madison, WI 53706, USA
¶Dept. of Physics & Astronomy, University of Nebraska, Lincoln, NE 68588, USA

***Abstract*. Extensive air showers are detectable by radio signals with a radio surface detector. A promising theory of the dominant emission process is the coherent synchrotron radiation emitted by e+ e- shower particles in the Earth's magnetic field (geosynchrotron effect). A radio air shower detector can extend IceTop, the air shower detector on top of IceCube. This could increase the sensitivity of IceTop to higher shower energies and for inclined showers significantly. Muons from air showers are a major part of the background of the neutrino telescope IceCube. Thus a surface radio air shower detector could act as a veto detector for this muonic background. Initial radio background measurements with a single antenna in 2006 revealed a continuous electromagnetic background promising a low energy threshold of radio air shower detector. However, short pulsed radio interferences can mimic real signals and have to be identified in the frequency range of interest. These properties of the electromagnetic background are being measured at the South Pole during the Antarctic winter 2009 with two different types of surface antennas. In total four antennas are placed at distances ranging up to 400m from each other. They are read out using the RICE DAQ with an amplitude threshold trigger and a minimum bias trigger. Results of the first three months of measurement are presented.**

***Keywords*: Radio air shower detection, EMI background, South Pole**

I. Introduction

The emission of coherent synchrotron radiation by e^+ e^- shower particles in the Earth magnetic field provides a measurable broadband signal from 10 MHz-150 MHz on ground [1]. The South Pole site with its dedicated infrastructural environment and a limited number of radio sources is possibly one of the best places in the world for the detection of air showers by their low frequency radio emission. Another feature of the South Pole site in comparison to other radio quiet regions in the world is the possibility to make studies in coincidence with other astrophysical experiments like the neutrino detector IceCube and the air shower detector IceTop. IceCube is a neutrino detector [2] embedded in the Antarctic ice. One of the main aims of IceCube is to measure neutrinos from cosmic sources. The strategy of IceCube is to measure up-going particles from the northern hemisphere. Only neutrinos or other weakly interacting particles are not absorbed by the Earth and are able to interact in the South Pole ice and produce measurable particles like muons. IceTop is built on the surface above IceCube (Fig. 1). It is designed to detect cosmic air showers from 10^{15} eV up to 10^{18} eV.

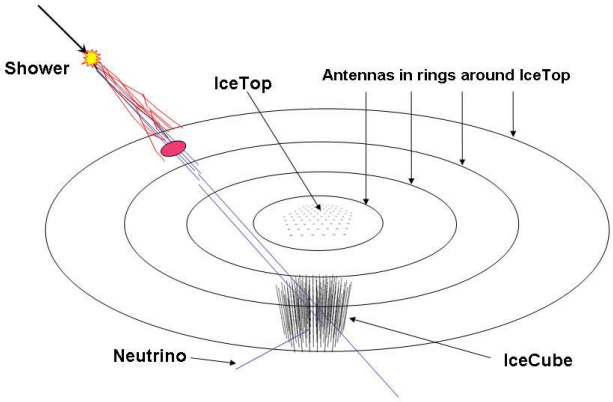

Fig. 1. Schematic view of a high energy radio air shower detector expanding the active area of IceTop. The distance between single antenna stations can be several hundred meters.

This special environment leads to two different options with different focus for a radio air shower detector on top of IceCube and its ambit [3].

- An **infill detector** built up of radio antennas on the same footprint as IceTop in similar distances but shifted with respect to the tank array. This provides an additional powerful observation technique in cosmic ray research of air showers at the South Pole. It would be possible to study air showers by three independent detector systems, IceTop, IceCube and the radio detector.
- An **areal expansion of IceTop** with radio surface antennas is an extension of the air shower detector

to higher energy primary particles and to higher inclination angles [6]. The idea is to build an antenna array in rings with increasing radius around the IceTop array. For ultra-high energetic neutrinos, $E > 300$ TeV, the neutrino nucleon cross section is large enough for absorption in the Earth to become increasingly important. For cosmogenic neutrinos, produced by the GZK mechanism, for example, most of the signal comes from near the horizon. Thus Muon bundles induced by air showers can be misinterpreted as a neutrino signal in the IceCube detector. The role of an antenna array field expansion of the IceTop detector is to detect these air showers with high inclination angle as a veto for the IceCube detector.

II. Electromagnetic Background Measurements At The South Pole With RICE

Initial background measurements with a single antenna in 2006 indicated a continuous electromagnetic background promising a low detector threshold [3]. Together with air shower simulations of the radio emission the background measurements seem to allow the detection of air showers with a threshold lower than 10 PeV in primary energy. The study presented here is aimed at long-term studies of the electromagnetic background for several months to investigate the amount of pulsed radio frequency interference (RFI) and potential long-term variations in the continuous background. The data acquisition of the RICE experiment, constructed to investigate radio detection methods of high energy neutrinos in ice [7], is suited to be extended by four surface antennas. The RICE DAQ consists of 6 oscilloscopes with 4 channels each. The sampling rate of each channel is 1GHz. The dynamic range of the scopes is ± 2 V with 12 Bit digitization.

Three different kinds of trigger are implemented in RICE:

1) Unbiased events every 10 min which is a forced read out of all channels.
2) The RICE simple multiplicity trigger. It is read out if the signal in four or more RICE antennas is above a threshold. The threshold is calculated at the beginning of every run to be 1.5 times above the RMS of unbiased events. These events should have no signal over threshold in the surface antennas.
3) The RICE surface trigger. This is a RICE simple multiplicity trigger with one or more surface antennas above the threshold as part of the trigger. This includes RICE triggers where only surface antennas have a signal over threshold.

The first and the third kind of trigger are of great interest for the surface radio background studies. The second trigger strategy is interesting to understand the in-ice RFI not reaching the surface. It is the most interesting event class for the RICE neutrino detection.

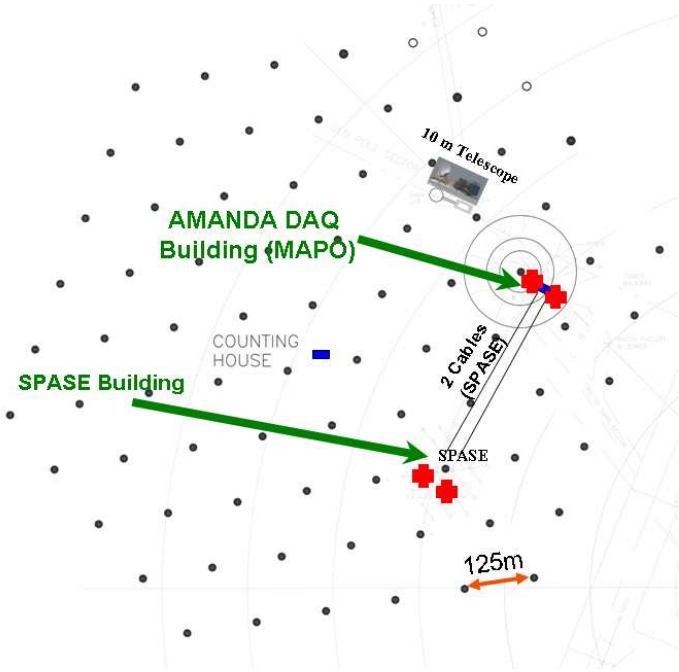

Fig. 2. Top view of the IceCube footprint. Two Fat Wire Dipole antennas were deployed in 350 m distance from the MAPO building (crosses near the SPASE building). The signals are amplified with 60dB MITEQ AU-4A-0150 low noise amplifiers and connected with RG59 cables to the MAPO building. Two four arm dipole antennas are located on the roof of the MAPO building and amplified with 39 dB MITEQ AU-1464-400.

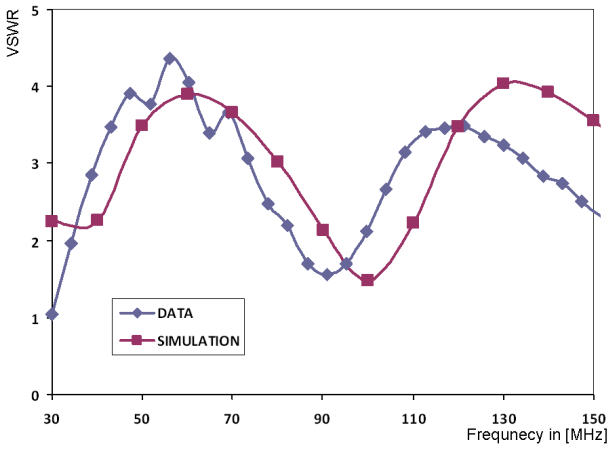

Fig. 3. Comparison of results from antenna simulations and measured properties (DATA). The data is a measurement of the voltage standing wave ratio (VSWR) of the Fat Wire Dipole on the South Pole snow at the final position of the antenna. The Simulation is made with EZNEC+ v. 5.0 without ground effects from the snow surface. The frequency response of the antenna is well described by the simulation. Including ground effects should even improve the agreement between simulation and data.

In total four surface antennas were deployed in the South Pole season 2008/2009 on the IceCube footprint (Fig. 2). Two Fat Wire Dipole antennas (Fig. 4) are connected to RICE with RG59 signal cables (1505A Coax) of the decommissioned SPASE experiment (Fig. 2). These broad band antennas allow for measurements

TABLE I
ANTENNA POSITION AND CABLE DELAYS TO THE RICE DAQ.

Antenna	x [m]	y [m]	z [m]	cable delay [ns]
MAPO1	47	-28.0	18	144
MAPO2	25	-20	18	129
SPASE1	-135	-366	1	2126
SPASE2	-148	-348	1	2729

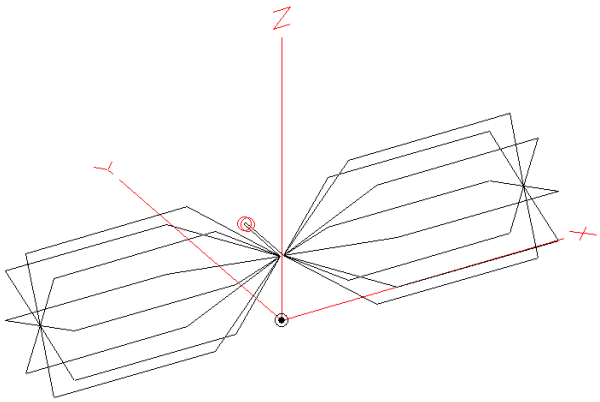

Fig. 4. Conducting elements of the Fat Wire Dipole Antenna deployed near the SPASE building. It is 3 m long and 0.8 m in diameter. The wires are mounted to a wooden carcass.

in the frequency range from 25-500 MHz. Figure 3 shows measurements of the voltage standing wave ratio (VSWR) of a Fat Wire Dipole lying on the Antarctic snow in its final position compared to simulations of the antenna using the NEC2 software package [4]. The frequency response is already well described by simulations without snow ground. The connection with the SPASE cables allows measurements over distances of several hundred meters from the MAPO building on the IceCube footprint, housing electronics, which is a potentially large RFI source, and the antennas on its roof. To compensate for the attenuation of the long signal cable (ca. 40 dB at 75 MHz) 60dB low noise preamplifiers (MITEQ AU-4A-0150) are implemented between antenna and signal cable. The power is transmitted through the same cable using bias tees. To avoid saturation of the preamplifiers by the input power, 25 MHz high pass filters and 300 MHz low pass filters were implemented between amplifiers and Fat Wire Dipole antenna. The antennas near the SPASE building are lying on the snow surface orthogonal to each other. Thus they measure orthogonal polarization of the signals. The other two antennas are deployed on the roof of the MAPO building. These four arm dipole antennas with an amplification of about -2 dB at $>$70 MHz are difficult to calibrate in the surrounding of the MAPO building and thus will only be used for event reconstruction (Fig. 6). The signal of the antennas on the roof of the MAPO building are amplified with 39 dB preamplifiers (AU-1464-400). 300 MHz low pass Filters are used for these roof antennas, too. Table I shows the position of the surface antennas in AMANDA coordinates and their cable delays.

Fig. 5. Picture of the four arm dipole antennas MAPO1 and MAPO2. Every arm has a length of 0.7 m. The wooden stand is 1.2 m high. The final position of the antennas is the roof of the MAPO building.

III. ANALYSIS STRATEGIES

From the technical point of view one can divide the analysis of the data into two parts.

A. Event Reconstruction And Mapping

The reconstruction of the origin of RFI events seen in more than two antennas will indicate possible noise sources at the South Pole e.g. the IceCube counting house or the South Pole Station. A map of these sources will help to improve air shower detection.
A χ^2 minimization on time residuals is used to reconstruct the source location of single events. To test the event reconstruction algorithm, we use signals generated with a GHz horn antenna in front of the MAPO building. Considering the cable delays and the antenna positions (Table I) we are able to make a 3D and time reconstruction of the events. Figure 6 shows the reconstruction with horn antenna signal data is working well. It is accurate within several meters and shows clearly the horn antenna lies in front of the MAPO building near the antenna MAPO1. The horn antenna data reconstructs to the actual position within 50 m with an RMS of 2.3 m. Figure 7 shows a typical noise event triggered with the RICE surface trigger. The event can be nicely reconstructed to have its origin in the building of the 10 m Telescope which is the topmost building in Fig. 2.

B. Events and background in the frequency domain

Another Topic is the rate and variation of the different RFI sources during a whole year of measurement. It is expected that RFI events have a typical signature in the frequency domain. This will help to find an ideal frequency region for a radio air shower detector. The continuous background is monitored over a whole year using the unbiased RICE events. One of the highest peaks on top of the continuous radio background is expected to be the meteor radar at 46.6 MHz to 47.0 MHz and 49.6 MHz to 50.0 MHz [5]. It is clearly observable in the DFT of the recorded data together with a few other expected sources of filterable continuous narrow

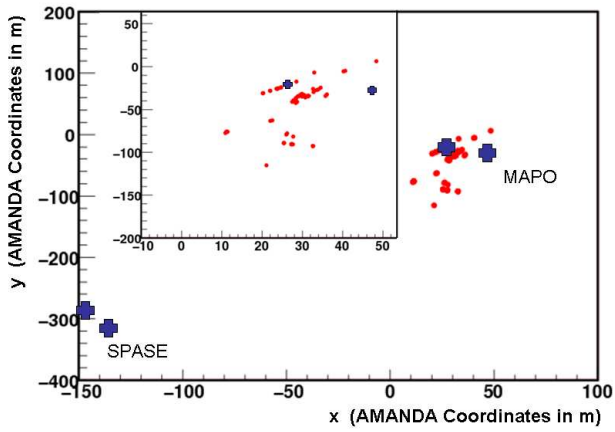

Fig. 6. Distribution of the reconstructed transmitter events in the xy-plane. The four crosses indicate the position of the antennas on the roof of the MAPO building (18m above the snow) and on the snow surface near the SPASE building. The dots are reconstructed positions of triggered signals from a GHz horn antenna, measured with all four antennas. The reconstructed events are in very good agreement to the transmitter position in front of the MAPO1 antenna and demonstrate the potential of the instrument.

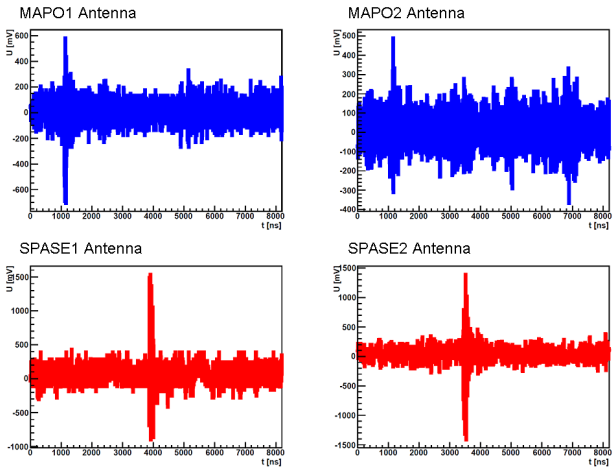

Fig. 7. Example of a triggerd event, seen by all four surface antennas in the time domain. The signal of the event reconstructs to be coming from the building of the 10m telescope.

band RF signals.

The DFT of the constant background measured with the fat wire dipoles is the basis to evaluate the limit of detectable signal strength. For this it is of great importance to correct the measured data for the antenna properties, the high- and low pass filtering, the amplifier response, and the attenuation of the signal cable. Another important topic will be to determine long term variations of the background during one year.

RICE triggered surface events are studied in the frequency domain whether a discrimination of air shower radio signals from RFI noise is feasible. Most of the narrow band noise events could e.g. be filtered in a future air shower detector system.

IV. Conclusion

As a part of RICE the four antenna surface detection system for radio signals, is able to study the conditions of the radio background in the frequency range from 25-150 MHz and higher at the South Pole. The threshold trigger strategy together with RICE allows for the estimation of the amount of RFI noise and its sources on the IceCube site. An analysis of the signals in the frequency domain shall be used to develop strategies to suppress the false trigger rate of a radio air shower detector. Measurements of the continuous background and its variations are the basis to estimate the energy threshold of a radio air shower detector in different frequency bands. The RFI measurements of the surface antennas will help to understand the signals measured with in ice radio detection systems.

References

[1] T. Huege, H. Falcke, Astron. & Astrophys. 412, 1934, (2003).
[2] http://www.icecube.wisc.edu.
[3] J. Auffenberg *et al.* ICRC arXiv:0708.3331 (2007).
[4] http://www.nec2.org.
[5] E. M. Lau *et al.* Radio Sci. 41, RS4007, (2006).
[6] J. Auffenberg *et al.* Arena, doi:10.1016/j.nima.2009.03.179 (2008).
[7] I. Kravchenko *et al.* Phys. Rev. D 73, 082002 (2006).

Neutrino signal from γ-ray loud binaries powered by high-energy protons

Andrii Neronov*† and Mathieu Ribordy‡

*INTEGRAL Science Data Centre, Ch. d'Ecogia 16, 1290, Versoix, Switzerland
†Geneva Observatory, University of Geneva, 51 ch. des Maillettes, 1290, Sauverny, Switzerland
‡Ecole Politecnique Federale de Lausanne, 1015, Ecublens, Switzerland

***Abstract*. We consider hardonic model of activity of Galactic γ-ray-loud binaries. We show that in such a model multi-TeV neutrino flux from the source can be much higher and/or harder than the detected TeV γ-ray flux. This is related to the fact that most of the neutrinos can be produced in pp interactions close to the bright massive star, in a region which is optically thick for the TeV γ-rays. Considering the example of LS I +61° 303, we show that the expected neutrino signal, detectable within ~ 3 years of exposure with ICECUBE, will be marginally sufficient to constrain the spectral characteristics of neutrino signal.**

***Keywords*: Neutrinos, gamma-ray astronomy.**

I. INTRODUCTION

Recently discovered "γ-ray-loud" binaries (GRLB) form a new sub-class of Galactic binary star systems which emit GeV-TeV γ-rays. These are high-mass X-ray binaries (HMXRB) composed of a compact object (a black hole or a neutron star) orbiting a massive star. The detection of γ-rays with energies up to 10 TeV from these systems shows that certain HMXRBs host powerful particle accelerators producing electrons and/or protons with energies above 10 TeV.

Different theoretical models of γ-ray activity of HMXRBs (see [1] for a review) have at least one common point: they are all based on the assumption that the γ-ray emission is produced in result of interaction of a relativistic outflow from the compact object (jet from a black hole, or wide angle wind from a pulsar) with the wind and radiation emitted by the companion massive star. With the exception of Cyg X-1, all the known GRLBs have similar spectral energy distributions (SED), peaking in the MeV-GeV energy band. The physical mechanism of production of the MeV-GeV bump in the spectra is not clear. It can be the synchrotron emission from electrons with the energies much above TeV [2], [3]. Otherwise, it can be produced via inverse Compton (IC) scattering of the UV thermal emission from the massive star by electrons of the energies $E \sim 10$ MeV [4], [5].

The available multi-wavelength data do not allow to constrain the composition of the relativistic outflow from the compact object. On one side, the multi-TeV or 10 MeV electrons, responsible for the production of the MeV-GeV bump in the SED, could be injected into the emission region from the e^+e^- pairs loaded wind. Otherwise, these electrons can be secondary particles produced in e.g. proton-proton collisions, if the relativistic wind is proton-loaded. The only direct way to test if relativistic protons are present in the γ-ray emission region would be detection of neutrinos of the muli-TeV energies. A general problem for the estimates of expected neutrino flux is the uncertainty of the attenuation of the γ-ray flux in the TeV band, which makes the derivation of the estimate of the neutrino flux and spectral characteristics based on the observed TeV γ-ray emission highly uncertain (see [6] for the discussion of the particular case of LS I +61° 303).

In the absence of direct relation between the characteristics of the observed TeV γ-ray and neutrino emission from a GRLB, the only way to constrain possible neutrino signal from the source is via detailed modelling of the broad band spectrum of the source within the hadronic model of activity. The idea is that the pp interactions, which result in the production of neutrinos, also result in production of the e^+e^- pairs, which release their energy via synchrotron, IC and bremsstrahlung emission. The total power released in the pp interactions determines the overall luminosity of emission from the secondary pairs. The knowledge of the electromagnetic luminosity can be used to constrain the power released in pp interactions and hence the neutrino luminosity of the source.

In this contribution we implement this method of estimation of neutrino flux to explore the possibility of detection of neutrino signal from GRLBs. We concentrate mostly on the particular example of LS I +61° 303 system, because it is the only known persitent GRLB in the Northern hemisphere, available for observations with ICECUBE neutrino telescope [7].

II. HADRONIC MODEL OF γ-RAY ACTIVITY

In the hadronic model, the primary source of the high-energy activity of the system are high-energy protons. The presence of the high-energy protons in relativistic outflows from compact objects (stellar mass and supermassive black holes, neutron stars) is usually difficult to detect, because of the very low energy loss rates of protons. GRLBs provide a unique possibility to "trace" the presence of protons/ions in the relativistic outflows

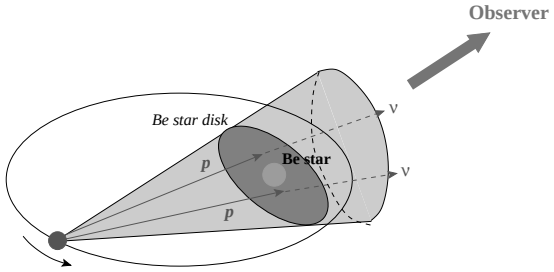

Fig. 1. Mechanism of production of neutrinos in interactions of high-energy protons ejected by the compact object with the dense equatorial disk of Be star.

generated by compact objects. The dense matter and radiation environment, created by the companion massive star provides abundant target material for the protons in the relativistic outflow. Interactions of high-energy protons with the ambient matter and radiation fields, created by the presence of a bright massive companion star, lead to the production and subsequent decays of pions. This results in emission of neutrinos and γ-rays from the source and to the deposition of e^+e^- pairs throughout the proton interaction region. Radiative cooling of the secondary e^+e^- pairs leads to the broad-band synchrotron and IC emission from the source.

Interactions of the high-energy protons with the radiation field produced by the bright massive star in the system (e.g. a Be star with the temperature $T_* \sim 3\times10^4$ K in the case of LS I +61° 303 and PSR B1259-63) are efficient only for protons with the energies above $E_p \geq [200\ \mathrm{MeV}/\epsilon_*]m_p \simeq 2\times10^{16}\,[\epsilon_*/10\ \mathrm{eV}]$ eV, where $\epsilon_* \simeq 3kT_*$ is the typical energy of photons of the stellar radiation. To the contrary, interactions of the high-energy protons with the protons from the dense stellar wind can be efficient for the protons of much lower energies.

In the case when the massive star is a Be-type star, the rate of pp interactions can be highly enhanced if the high-energy protons are able to penetrate into the dense equatorial disk known to surround this type of stars. An obstacle for the penetration of the high-energy protons accelerated e.g. close to the compact object into the disk could be the presence of magnetic field, which would deviate proton trajectories away from the disk. However, the Larmor radius of the highest energy protons, $R_L \simeq 4\times10^{12}\left[E_p/10^{15}\ \mathrm{eV}\right][B/1\ \mathrm{G}]^{-1}$ cm, where B is the magnetic field, could be comparable to the size of the system. Thus, if the magnetic field in the region of contact between the stellar wind and the relativistic outflow is not larger than several Gauss, the highest energy protons can freely penetrate into the dense stellar wind region.

pp interactions result in the production of pions, which subsequently decay onto γ-rays, neutrinos and electrons/positrons. If the Larmor radius of the highest energy protons is comparable to the size of the disk, most of the pions are produced by the protons propagating toward the companion star. In this case the neutrino and γ-ray emission from the pion decays is expected to be anisotropic, with most of the neutrino flux emitted toward the massive star, as it is shown in Fig. 1. To the contrary, the synchrotron and IC emission from the e^+e^- pairs is, most probably, isotropized at the energies at which the radiative cooling time of electrons becomes longer than the period of giration in the magnetic field. Difference in the anisotropy patterns of neutrino emission and of the broad band emission from the secondary e^+e^- pairs should, in principle, lead to significant difference in the expected orbital lightcurves of neutrino and electromagnetic emission from the source.

The flux of γ-rays from the pp interaction region is absorbed due to the pair production on the ultra-violet photon background in the vicinity of Be star. Maximal optical depth with respect to the pair production is achieved at the energies $E_\gamma \simeq 4m_e^2/\epsilon_* \simeq 0.2\left[T_*/3\times10^4\ \mathrm{K}\right]^{-1}$ TeV, where the pair produciton cross section reaches the maximum $\sigma_{\gamma\gamma} \simeq 1.5\times10^{-25}$ cm^2. The optical depth for the γ-rays of this energy produced close to the masive star can be about $\tau_{\gamma\gamma} \geq 10$. At higher γ-ray energies, $E_\gamma T_* \gg (m_\mathrm{e}c^2)^2$, the pair production cross-section and, respectively, the optical depth decrease as $E^{-1}\ln E$. The attenuation of the γ-ray flux due to the pair produciton becomes small only at the energies above ~ 10 TeV.

The power of the absorbed γ-rays is re-distributed to the secondary e^+e^- pairs, which subsequently loose their energy onto the synchrotron and inverse Compton emission. Depending on the magnetic field strength in the pair production region, the bulk of electromagnetic emission from the secondary pairs of the energies 10 GeV-10 TeV can be either re-emitted back in the GeV-TeV energy band, if the inverse Compton loss dominates, or in the X-ray band, in the case of the dominant synchrotron loss.

The results of numerical modeling of the spectra of (isotropic) emission from the secondary e^+e^- pairs produced in pp and $\gamma\gamma$ interactions are shown in Fig. 2. Our numerical code follows evolution of the spectra of the secondary particles, produced in interactions of the high-energy protons with the stellar wind protons from the dense equatorial disk of Be star. We assume that the high-energy protons are initially injected close to the massive star and then escape, together with the secondary particles produced in pp interactions, toward larger distances. The primary proton injection spectrum is assumed to be hard, with $\Gamma_p \simeq 0$, so that most of the protons have the energy close to the cut-off energy assumed to be $E_\mathrm{cut} = 10^{15}$ eV. Such an almost monochromatic spectrum of protons injected into the stellar wind can be produced either if the high-energy protons originate from a "cold" relativistic wind with the bulk Lorentz factor $\sim 10^6$, or because only the highest energy protons have large enough Larmor radii to be able to penetrate deep into the stellar wind. The magnetic

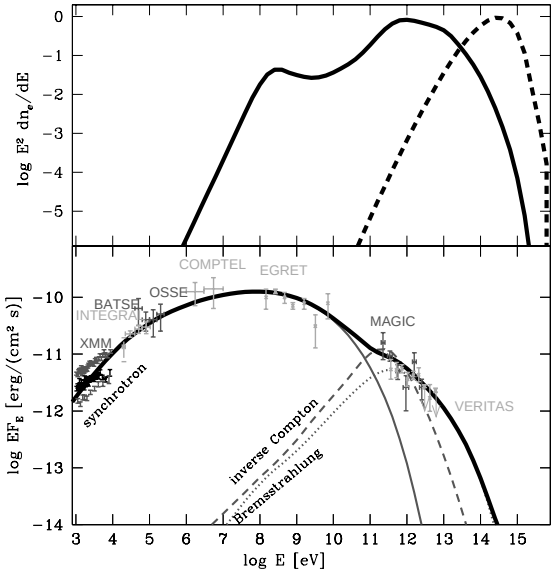

Fig. 2. Broad band spectrum of emission from secondary e^+e^- pairs produced in pp interactions close to the surface of Be star, calculated assuming almost monochromatic proton injection spectrum with $\Gamma_p = 0$, $E_{p,\rm cut} = 10^{15}$ eV. Upper panel shows the injection spectrum of e^+e^- pairs (dashed line) and the spectrum formed in result of cooling via synchrotron, IC and bremsstrahlung emission as well as Coulomb energy loss. In the lower panel, thin red solid, dashed and dotted lines show, respectively, the synchrotron, IC and Bremsstrahlung emission from the pairs. The black thick solid line shows the overall broadband model spectrum.

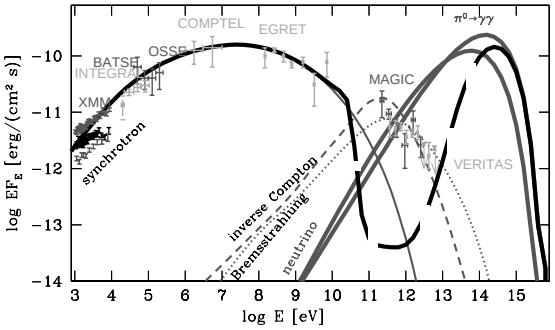

Fig. 3. Broad band spectrum of emission from pp interactions, calculated assuming the same parameters as in Fig. 2, but considering the possibility of strong neutrino emission from the source. Notations for the γ-ray spectrum are the same as in the lower panel of Fig. 2. Green thick solid line shows the spectrum of neutrinos.The black thick solid and dashed lines show the overall broadband model spectra, calculated Solid line shows the case of almost radial escape of the γ-rays, dashed line corresponds to the attenuation of the γ-rays emitted normally to the direction from the massive star. Dotted thick black line shows the modification of the broad band spectrum, if the emission from the tertiary e^+e^- pairs produced via the $\gamma\gamma \to e^+e^-$ process is taken into account.

field is supposed to be characterized by the radial profile $B = B_0 \left(D/R_*\right)^{-\alpha_B}$ with $\alpha_B = 1$ and $B_0 = 5$ G.

Fig. 3 shows modifications of the spectrum introduced by (a) possible presence of an anisotropic γ-ray emission component produced by the π^0 decays and (b) by the strong anisotropic attenuation of the γ-ray flux by the pair production. Both effects are expected to be strongly variable with orbital phase. It is not possible to estimate the real value of average $\tau_{\gamma\gamma}$ as long as the details of the 3-dimenisonal geometry of the emission region and the mutual orientation of the extended emission region, of the Be star and of the observer are not known. Taking into account this uncertainty, we choose the minimal value of $\tau_{\gamma\gamma}$ at which the absorbed spectrum does not violate the upper bound on the flux at the energies above $\sim (several)$ TeV, found in VERITAS observations of the source.

III. Estimate of the number of neutrino events for ICECUBE

Within the hadronic models of activity, the MeV-GeV bump in the spectral energy distribution of GRLBs is produced by the emission from the secondary e^+e^- pairs from the pp interactions. This fact enables an estimate of the neutrino luminosity of the source, based on its MeV-GeV band luminosity. The only uncertainty of such an estimate is that the synchrotron emission from the secondary e^+e^- pairs in the MeV-GeV energy band is, most probably, isotropic, while the neutrino and π^0 decay γ-ray emissions are not.

Although the total power of neutrino emission can be estimated from the MeV-GeV luminosity of the γ-ray-loud binary, modelling of the broad band emission spectrum of the source gives only mild constraints on the neutrino emission spectrum: acceptable models of the broad band spectra can be found assuming the initial proton injection spectra ranging from E^{-2} powerlaw to almost monochromatic injection spectra (see [8] for details). The properties of the neutrino signal can be used to distinguish between different primary proton spectra, if one is able to derive the information on the energies of the detected neutrinos from the observational data.

Extraction of information about the properties of the source neutrino spectrum from the data is complicated by the fact that (a) the neutrino telescopes measure only the energies of the detected muons, rather than that of the primary neutrinos, (b) the flux of the primary neutrinos and the energies of the secondary muons are attenuated by the effect of propagation through the Earth. The differential induced muon spectrum at the detector, which strongly depends on the source declination δ, could be obtained after propagation of neutrinos up to the interaction point and further propagation of the muons to the detector. A semi-analytical method of calculation of the muon spectra, which is based on the use of the muon effective area and the knowledge of the details of the detector, namely the angular and energy resolution was developed in the Ref. [8].

The results of such semi-analytical calculation of the atmospheric background-subtracted muon spectra, for the particular case of neutrinos from LS I +61° 303, are presented Fig. 4. The exposure time is taken to be 3 years of running the full ICECUBE array. For comparison, we also show by the solid thick line the level of the signal which is 5σ above the atmospheric background. Dotted line show the detected muon spectrum for the

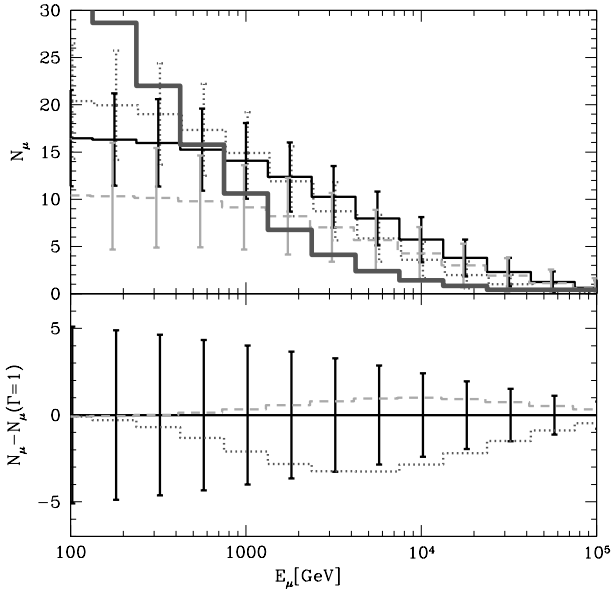

Fig. 4. Background-subtracted cumulative muon spectra $N(E_{\mu,\rm thr})$, expected after the 3-year ICECUBE exposure for the three model neutrino spectra of LS I +61° 303, discussed in the previous sections (error bars of signal muon spectra are the sum in quadrature of statistical errors of signal + atmospheric neutrino background). Dotted line shows the spectrum for the proton injection spectrum with the spectral index $\Gamma = 2$. Thin solid line corresponds to the initial proton injection spectrum with $\Gamma = 1$, while the dashed line is for the proton injeciton spectrum with $\Gamma = 0$. Thick solid line shows the 5σ excess above the atmospheric neutrino backgorund (the "discovery threshold"). The bin radius is set to $\psi = 1.3°$.

model with the proton injection spectrum with spectral index $\Gamma_p = 2$, thin solid line corresponds to the proton injection spectrum with $\Gamma_p = 1$ and cut-off at the same energy, while the dashed line corresponds to $\Gamma_p = 0$. In all three cases the cut-off energy is assumed to be $E_{\rm cut} = 1$ PeV.

Inspecting the muon spectra shown in the upper panel of Fig. 4, one can see that softed proton injection spectrum results in a slight excess of muon events at lower energies. If the overall normalization of the neutrino flux would be known, measurement of the spectrum of muon events would allow to constrain the spectrum of the primary protons in the source. However, taking into account the uncertainty of the overall normalization of neutrino flux introduced by the uncertainty of the anisotropy pattern of neutrino emission, one can find that the statistics of the signal will not be enough for such a task. This is illustrated in the lower panel of Fig. 4, where a comparison of the shapes of the muon spectra is shown. If one assumes the same total number of muon events, the difference in the spectra for the three models is always within $\sim 1\sigma$ errorbars, over the entire energy range.

IV. Conclusions

We have estimated the neutrino flux from GRLBs expected within the hadronic model of activity of these sources. Within such a model, the measured spectral characteristics of γ-ray emission from the source in the TeV energy band are not directly related to the spectral characteristics of the neutrino emission, because of absorption of the TeV γ-rays on the thermal photon background produced by the massive star in the system. The uncertainty of the calculation of the attenuation of the TeV γ-ray flux introduces a large uncertainty to the estimate of the neutrino flux based on the measured TeV γ-ray lfux.

Taking into account this uncertainty, we have adopted a different approach for the estimate of the neutrino flux from a GRLB. Namely, we have noted that the energy output of proton-proton interactions, and hence the neutrino flux, can be instead constrained by the broad-band spectrum of the source.

Although the observed bolometric luminosity of the source (i.e. the height of the MeV-GeV bump of the SED) constrains the overall neutrino luminosity, the shape of the neutrino spectrum and the overall normalization of the neutrino flux are only mildly constrained by the multi-wavelength data. Taking into account these uncertainties of the neutrino emission spectrum, we have estimated the expected number of neutrinos which will be detected by the ICECUBE, assuming that the neutrino flux saturates the upper bound imposed by the observed γ-ray flux in the MeV-GeV energy band. Considering the particular example of LS I +61° 303, we have found that if the spectrum of high-energy protons in the source extends to the PeV energies, the source could be readily detectable with 3 years of exposure with ICECUBE.

We have also explored the potential of the full ICECUBE detector for the measurement of the spectral characteristics of the neutrino signal from LS I +61° 303. We find that in the case when the neutrino flux is at the level of the upper bound imposed by the observed MeV-GeV γ-ray flux, exposure time much longer than 3 years is required to constrain the spectral index of the primary high-energy proton spectrum via observations of neutrino signal in ICECUBE.

References

[1] I.F. Mirabel, Science, 312, 1759, (2006).
[2] M. Tavani, J. Arons, Ap.J., 477, 439 (1997).
[3] V. Bosch-Ramon et al., A&A, 447, 263 (2006).
[4] L. Maraschi, A. Treves, MNRAS, 194, 1 (1981).
[5] M. Chernyakova, A. Neronov, et al. MNRAS, 367, 1201 (2006).
[6] D.F. Torres, F. Halzen, A.Ph., 27, 500, (2007).
[7] `http://icecube.wisc.edu/`
[8] A. Neronov, M. Ribordy, Phys. Rev. D79, 043013 (2009).

Acoustic sensor development for ultra high energy neutrino detection

Matt Podgorski[†] **and Mathieu Ribordy**[*]

[*] *High Energy Physics Laboratory, EPFL, CH - 1015 Switzerland*
[†]*RWTH Aachen, visiting EPFL*

***Abstract*. The GZK neutrino flux characterization would give insights into cosmological source evolution, source spectra and composition at injection from the partial recovery of the degraded information carried by the ultra high energy cosmic rays. The flux is expected to be at levels necessitating a much larger instrumented volume (>100 km^3) than those currently operating. First suggested by Askaryan, both radio and acoustic detection techniques could render this quest possible thanks to longer wave attenuation lengths (predicted to exceed a kilometer) allowing for a much sparser instrumentation compared to optical detection technique.**

We present the current acoustic R&D activities at our lab developing adapted devices, report on the obtained sensitivities and triangulation capabilities we obtained, and define some of the requirements for the construction of a full scale detector.

***Keywords*: Ultra high energy neutrinos. Acoustic detection techniques. Acoustic sensor studies.**

I. INTRODUCTION

The IceCube detector [1] may well soon identify the first ultra high energy neutrino of cosmogenic origin, following interactions of ultra high energy cosmic rays with the cosmic microwave background [2]. Predictions for the cosmogenic neutrino flux, i.e. neutrinos from photo-disintegration, is at levels of the order of $EdN/dE \sim 10^{-17}\,\mathrm{s}^{-1}\,\mathrm{cm}^{-3}\mathrm{sr}^{-1}$ at $E = 10^{18}$ eV, resulting in 0.01 - 1 event / year / km^3 in ice [3]. These predictions strongly depend on the primary cosmic ray composition [4]. Currently, the situation is uncertain: While the observed correlation of UHE CR sources with the AGN distribution by AUGER [5] hints toward a light composition (and in this case we lie close to the upper flux predictions), dedicated AUGER composition studies favor a composition turning heavier at UHE [6]. GZK neutrinos are astronomical messengers keeping track of the original CR direction, GZK interactions mostly occur close to the source. In case of the existence of a few UHE cosmic accelerators located close-by (Gpc), the detection of a substantial flux of GZK neutrinos from these directions using a multi-messenger approach would allow the possibility of pinpointing the nature of these CR accelerators.

The characterization of the GZK neutrino flux spectrum, and thus the recovery of the degraded information information carried by UHE CR, would allow the delineation of cosmological source evolution scenarios from source spectrum characteristics. To fulfill this goal, the event detection rate should be vastly increased. Therefore a much larger volume should be instrumented with an adequate technology for the detection of ultra high energy neutrino interactions. Two novel detection methods have been proposed, following signatures first discussed by Askaryan [7], [8]. An interacting neutrino emits a coherent Cherenkov pulse in the range of 0.1-1 GHz [9] close to the shower axis and a thin thermoacoustic pancake normal to the shower axis. Both detection techniques are currently exploited by several detectors. In ice, both radio and acoustic emissions have rather large theoretical attenuation lengths [10]. While this has been convincingly demonstrated for the radio emission, it is still a work in progress for the acoustic emission and is one of the main goals for the South Pole Acoustic Test Setup (SPATS) [11]. With the data collected by the SPATS array, the sound speeds w.r.t. the depth have been determined with great accuracy, meeting theoretical expectations [12] and S-waves have been found as well. Unknown, however, remains the exact nature of the local source of noise and the exact value of the attenuation length. Newest experimental results hint toward a reduced pressure wave attenuation length on one hand and demonstrate favorable noise level below 10 mPa on the other hand [13].

Contrary to salt and water, ice is unique. It allows the detection of three distinct signatures accompanying a neutrino event: Optical Cherenkov light, coherent radio Cherenkov and thermoacoustic emissions, thus firmly establishing the event origin by a strong background reduction. A possible layout for the hybrid instrumentation of a large volume of order of 100 km^3 at the South Pole would consist of strings deployed one kilometer apart down to a depth of 2 km (radio and acoustic attenuation lengths strongly vary with temperature and are decreasing with depth). Given the topologies for the radio & acoustic emissions, a string should be densely equipped with radio and acoustic devices with an option of supplementing it with PMT devices for optical detection. $10 - 10^3$ interacting GZK neutrinos in 100 km^3 instrumented volume can be expected after 10 years. The cosmogenic spectrum could be characterized (and consequently insights into the underlying physics), provided a high detection efficiency, a deep knowledge of the local source of noise and good energy resolution. Thermoacoustic models and Monte Carlo simulations

predict that a signal from a neutrino with an energy $E = 10^{18}$ eV will typically have an amplitude of 10 mPa at a distance of one kilometer [14] (to be rescaled for finite attenuation length). To keep a good S/N ratio, the sensitivity of the devices should be at the sub mPa level. Also, a good pointing resolution may serve the purpose of UHE point source search. Given the giant array layout introduced above, an acoustic signal will be recorded by a small number of acoustic devices. It is therefore desirable to design acoustic sensor devices with pointing capabilities of their own.

In the next section, we present R&D activities which are taking place at our lab in regard of sensor design and construction and discuss its performances.

II. R&D ACTIVITIES

The design and construction of a multi-channel sensor was conducted at our lab, which use piezo transducers (PZT) as sensitive elements. A noise level level $S/N < 5$ mPa ($S/N \equiv S_{\rm RMS}/N_{\rm RMS}$) and a good angular resolution were demonstrated, suggesting the possibility for excellent vertex localization combining the responses from all sensor hits. The design, which must still be improved to meet our design goals, could eventually allow for diffuse acoustic noise reduction through spectral shape analysis and accurate energy estimate of physical events.

The setup for conducting the R&D activities consists of a bath, topped with a support structure for one absolutely calibrated hydrophone (Sensortech SQ03), one homemade sensor and one transmitter. A datataking LabView program interfaced to a National Instrument board is used for analog response digitization (12 bits $\times$ 12 channels, total 1.25 MHz), transmitter pulse generation and 4π relative orientation between the transmitter and the sensors for automatized sensor profiling.

The experimental setup shown in Fig. 1 consists of the homemade hydrophone, a transmitter and the reference hydrophone. In the following, two different electric signal shapes have been considered: a damped sin pulse and a gaussian pulse, resulting in a tripolar pressure pulse (the neutrino-induced thermoacoustic pulse is bipolar).

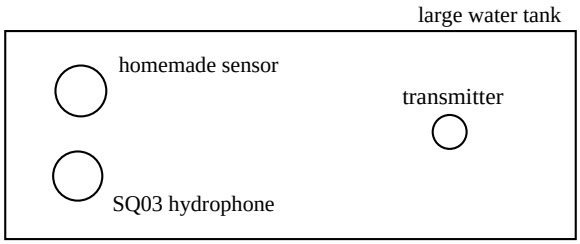

Fig. 1. Experimental setup.

A. Acoustic sensor design

The sensor consists of an aluminium pressure vessel housing 4 channels to provide triangulation capabilities. The noise level at the amplifier input to 130 nV, reached at the expense of some bandwidth reduction, peaking at 22 kHz with $\sim$90 dB amplification and sharply decreasing below 10 kHz and above 40 kHz. Whether that is optimal has to be studied further. It is manufacturable at relatively low cost. While aluminium is an adequate medium for use in a liquid water bath, it will be replaced by steel for application in ice (more adequate given both impedance and resistance to pressure).

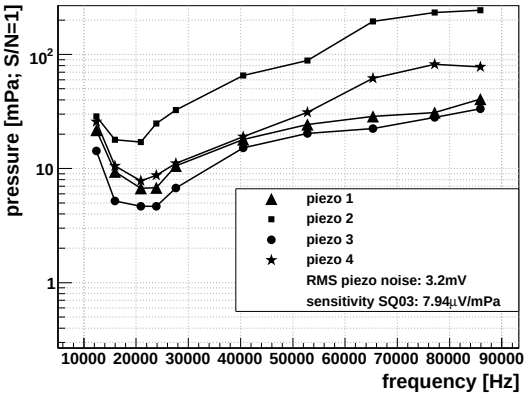

Fig. 2. Pressure sensitivity as a function of frequency of damped sin transmitted pulses normalized to $S/N = 1$ ratio.

B. Sensitivity calibration

Signals with peak frequencies in the range 10 - 90 kHz were recorded with a sampling rate of 330 kHz. A strong frequency correlation between the transmitted pulse and the sensor response was observed. Due to the finite size of the bath tub and given the sound speed velocity in water, only the first 150 μs following the pulse arrival time were analysed in what follows to avoid reflexion artefacts.

With the collected data from the 4-channel sensor and from the commercial hydrophone, the absolute pressure sensitivity was calculated in the time domain using RMS values for signal and noise. Fig. 2 shows the absolute pressure sensitivity (defined as $S/N = 1$) w.r.t. the dominant frequency of the sent signals.

The measurements demonstrate the importance of the state of surface coupling the PZT to the housing: The polished surfaces for piezos 1 and 3 show a response $\sim$2 times stronger than piezos 2 and 4 coupled to the housing through porous surfaces.

C. Triangulation

Time resolution is essential for triangulation and therefore a digitization frequency of 100/200 kHz is required in order to reach cm resolution in aluminium/steel. This suggests that a sensor design should include digital electronics with at least 200 kHz sampling rate per channel[1], in order to reach 0.5-5 ms

[1]100 kHz (and therefore 200 kHz sampling rate) is by coincidence the value above which the ice attenuation length drops quickly and roughly the extension of the neutrino-induced thermoacoustic pulse spectrum.

pulse start time resolution (depending on amplitude) which roughly corresponds to 2°-20° ($4\pi/10^2$ - $4\pi/10^4$) angular resolution with the current multi-channel sensor. The design of a new digital (0.2 MHz/channel) 4-channel amplifier board has been started, with long range communication protocols. It does not yet include trigger logic. Digitization is necessary for a viable acoustic detector design in order to avoid losses in km long cables (of order of 3 dB/100 m in high quality cables) and thus keep both good sensitivity and time resolution. Once in operation, this will allow to define the requirements for future efficient trigger concept at the sensor level.

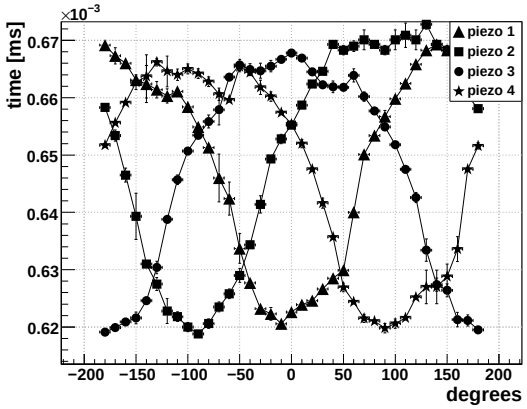

Fig. 3. Time of first signal maximum as a function of the polar orientation of the sensor.

Figure 3 demonstrates triangulation capabilities. Coupling between channels was found to provide in any sampled sensor positions 2 channels with signal within a factor 2 of the channel with the highest response. The resolution will nevertheless depend on the individual signal-to-noise ratios, but it shows potential for vertex reconstruction with a single sensor module.

D. Outlook

First positive results in the time domain were obtained. Absolute sensitivities are currently analyzed in the frequency domain. A second 4-channel sensor of similar design in a steel housing will be soon equipped with digital electronics. Further sensor tests are foreseen to happen next. Low temperature behavior test will be conducted in the laboratory and at large distances and depths in the lake Geneva ($\sim$ 400 m depth) to avoid reflexions, assess the acoustic noise characteristics and probe the sensor design.

III. CONCLUSIONS

Acoustic neutrino detection techniques should be further developed, pushing the sensitivity at sub mPa levels, together with the characterization of noise sources which may impede the applicability of the technique. Noise measurement in an open media (water / ice) are required to characterize the noise rate and its spectral shape in order to investigate improved trigger schemes relying on signal processing within the sensors. These developments have been started with digitization board in the sensor, a necessary step for a viable acoustic array design, where signal attenuation along km transmission cable is excluded.

While it seems clear that sub mPa sensors should be designed, the uncertain detection conditions at the South Pole make predictions concerning the detection efficiency difficult. The potential can be dangerously spoiled in the case the local source of acoustic noise mimick a neutrino event. Further dedicated studies are on-going to ensure that it could be possible to distinguish the event origin with high efficiency. The deployement of an acoustico-radio-optical hybrid detector would constitute a welcome option, allowing to reduce further possible background noises. Also, complementing the hybrid radio-acoustic strings with a few optical DOMs such as in IceCube would allow to unambiguously tag neutrino events (at these energies, given a $>$100m absorption length in the ice at these depths [15], photons may likely accompany a radio-acoustic signal in the case of a neutrino event).

REFERENCES

[1] R. Abbasi et al., Nucl. Instr. Meth.A601:294-316,2009.
[2] V. Berezinsky and G. Zatsepin, Phys. Lett. B 28 (1969) 423.
[3] R. Engel, D. Seckel & T. Stanev, Phys. Rev. D **64** (2001) 093010.
[4] L. A. Anchordoqui, H. Goldberg, D. Hooper, S. Sarkar & A. M. Taylor, Phys. Rev. D **76** (2007) 123008.
[5] J. Abraham et al. [Pierre Auger Collaboration], Astropart. Phys. **29** (2008) 188. [Erratum-ibid. **30** (2008) 45]
[6] K. H. Kampert [Pierre Auger Collaboration], AIP Conf. Proc. **1085** (2009) 30.
[7] G. Askaryan, JETP 14 (1962) 441; G. Askaryan, JETP 21 (1965) 658.
[8] G. Askaryan, Sov. J. Atom. Energy 3 (1957) 921.
[9] E. Zas, F. Halzen & T. Stanev, Phys. Rev. D45 (1992) 362.
[10] B. Price and L. Bergstrm, Appl. Opt. 36 (1997) 4181; L. Bergstrm, B. Price et al., Appl. Opt. 36, 4168 (1997); B. Price, J. Geophys. Res.111, B02201 (2006).
[11] S. Boeser et al., arXiv:0807.4676 [astro-ph]; S. Boeser et al., Int. J. Mod. Phys. A21S1 (2006) 107.
[12] J. Vandenbroucke et al., arXiv:0811.1087 [astro-ph].
[13] F. Descamps et al. [IceCube coll.], in these proceedings.
[14] D. Besson et al., Int. J. Mod. Phys. A21S1 (2006) 259.
[15] M. Ackermann et al., J. Geophys. Res. 111, D13203 (2006).